

**THE INFLUENCE OF CONTINUOUS
CASTING PARAMETERS ON HOT
TENSILE BEHAVIOUR IN LOW
CARBON, NIOBIUM AND BORON
STEELS**

Lesley H. Chown

A thesis submitted to the Faculty of Engineering and the
Built Environment, University of the Witwatersrand, Johannesburg,
in fulfilment of the requirements for the degree of

DOCTOR OF PHILOSOPHY

Johannesburg, 2008

Declaration

I declare that this thesis is my own, unaided work. It is being submitted for the Degree of Doctor of Philosophy in the University of the Witwatersrand, Johannesburg. It has not been submitted before for any degree or examination in any other University.

day of 2008

Abstract

This thesis studies the factors that govern transverse cracking during continuous casting of low carbon, niobium microalloyed and boron microalloyed steels. Crack susceptibility in the thick slab, billet and thin slab casting processes are compared by using typical conditions in laboratory hot ductility tests.

There is limited published literature on hot ductility in aluminium-killed and silicon-killed boron microalloyed steels and the proposed mechanisms of failure by transverse cracking are contradictory. Few published papers specifically compare hot ductility behaviour of any steels between thick slab, billet and thin slab continuous casting processes. Thus, the basis of this research is to assess the influence of casting parameters and compositional variations on hot ductility behaviour in low carbon steels, niobium microalloyed steels, aluminium-killed boron microalloyed steels and silicon-killed, boron microalloyed steels.

The typical temperature ranges, cooling rate and strain rate conditions of the continuous casting processes were used in reheated and *in situ* melted hot tensile tests performed on steel specimens. Solidification, transformation and precipitation temperatures were calculated using solubility equations and modelled using the Thermo-CalcTM thermodynamics program. Scanning electron microscopy and transmission electron microscopy were used to determine the modes of failure in the tested specimens.

In the low carbon steels, hot ductility was improved by increasing the strain rate; by calcium treatment, which minimises copper sulphide and iron sulphide formation; and by maintaining a nickel to copper ratio of 1:1. It was shown that thin slab casting conditions provided the best hot ductility results for the low carbon steels.

All the niobium steels showed poor ductility in the single-phase austenite temperature region, indicating that intergranular precipitation of fine niobium carbonitrides was the cause of the poor ductility. It was shown that the hot ductility was greatly improved by calcium treatment, by decreasing the cooling rate and by increasing the strain rate. Slow

thin slab and thick slab casting conditions provided the best hot ductility results for the niobium steels.

Hot ductility was substantially improved in the aluminium-killed boron steels by increasing the boron to nitrogen ratio from 0.19 to 0.75. The results showed that, at cooling rates generally associated with thick slab, bloom and slow thin slab casting, a boron to nitrogen ratio of ≥ 0.47 was sufficient to avoid a ductility trough altogether. However, under conditions typically experienced in fast thin slab and billet casting, a boron to nitrogen ratio of 0.75 was required to provide good hot ductility. The mechanism of the ductility improvement with increasing boron to nitrogen ratio was found to be enhanced precipitation of boron nitride, leading to a decrease in nitrogen available for aluminium nitride precipitation.

In the silicon-killed boron steels, it was found that the boron to nitrogen ratio had the overriding influence on hot ductility and hence on crack susceptibility. Excellent hot ductility was found for boron to nitrogen ratios above 1. Additionally, analysis of industrial casting data showed that the scrap percentage due to transverse cracking increased significantly at manganese to sulphur ratios below fourteen. An exponential decay relationship between the manganese to sulphur ratio and the average scrap percentage due to transverse cracking was determined as a tool to predict scrap levels in the casting plant.

To my dear Graeme,
to Matthew and Darren who
were born during the course of this work
and especially
to my Lord Jesus Christ

“For the LORD gives wisdom and from his
mouth come knowledge and understanding.”
Proverbs 2:6

Acknowledgements

I would like to express my deep thanks to Professor Lesley Cornish whose constant guidance and encouragement helped me to remain focused throughout this work. I really appreciate the hours she spent editing my thesis and working on Thermo-Calc for this project.

I want to thank Mintek for funding my studies. Special thanks to Lizelle Glaner who helped with some of the SEM work and always listened and to Elma van der Lingen who went out of her way to help me finish the thesis.

I also want to thank Dr. Tom von Moltke, IMMRI, Pretoria University, and Iscor Ltd. (now Arcelor Mittal) for providing funding, steel specimens and use of the testing equipment. Special thanks go to Johan van Wyk who performed many of the hot tensile tests, Carel Coetzee who patiently instructed me in the use of the SEM, Thomas Mabena who prepared over a hundred metallography specimens and Alison Tuling and Alan Bentley who did the TEM work.

To my dear, dear family, who have been quietly suffering these long years –

MOMMY’S BACK

REALLY!!

Table of Contents

CHAPTER 1: INTRODUCTION.....	1
1.1 BACKGROUND OF CONTINUOUS CASTING AND CRACK SUSCEPTIBILITY	1
1.2 OBJECTIVE OF THESIS AND CONTRIBUTION TO ENGINEERING	2
1.3 CONTRIBUTIONS TO LITERATURE	2
1.4 THESIS STRUCTURE	3
CHAPTER 2: LITERATURE REVIEW.....	5
2.1 OVERVIEW OF CHAPTER 2.....	5
2.2 CONTINUOUS CASTING PROCESS.....	6
2.3 CRACK SUSCEPTIBILITY IN CONTINUOUS CASTING.....	8
2.4 INFLUENCE OF PROCESS VARIABLES ON SURFACE CRACKING.....	10
2.4.1 Mould heat transfer.....	10
2.4.2 Mould oscillation	10
2.4.3 Secondary cooling and casting speed	11
2.4.4 Straightening.....	12
2.5 INFLUENCE OF HOT DUCTILITY BEHAVIOUR ON CRACKING	12
2.5.1 Metallurgical mechanisms of cracking	12
2.5.2 Strain rate.....	18
2.5.3 Cooling rate.....	18
2.5.4 Solution treatment temperature and time	19
2.5.5 Thermal oscillations.....	20
2.5.6 Steel composition.....	21
2.6 DETERMINING THE PRECIPITATION AND TRANSFORMATION TEMPERATURES IN STEEL.....	31
2.7 LABORATORY TESTING OF HOT DUCTILITY	35
2.7.1 Overview.....	35
2.7.2 Secondary cooling patterns	36
2.7.3 Strain approximation of straightening	36
2.7.4 Strain rate conditions in hot tensile testing	38
2.7.5 Comparison of hot tensile testing techniques	39
2.7.6 Method 1: Heat to test temperature.....	39

2.7.7	Method 2: Heat to solution treatment temperature	39
2.7.8	Method 3: Melting	40
CHAPTER 3: EXPERIMENTAL PROCEDURE.....		42
3.1	OVERVIEW OF CHAPTER 3	42
3.2	DETERMINATION OF INDUSTRIAL CASTING CONDITIONS.....	43
3.3	TESTING SPECIFICATIONS AND PROCEDURES	45
3.4	STEEL SPECIMENS	46
3.4.1	Material sampling	46
3.4.2	Steel compositions	46
3.4.3	Tensile specimens	49
3.5	HOT TENSILE TESTING FACILITIES	50
3.5.1	Instron [®] tensile testing	50
3.5.2	Gleeble [®] 1500 tensile testing	52
3.6	TENSILE TESTING SCHEDULES	55
3.7	SCHEDULES A-H	57
3.8	SCHEDULES J AND K	57
3.9	INTERPRETATION OF TEST RESULTS	59
3.9.1	Determination of stress – strain curves	59
3.9.2	Calculation of maximum stress.....	59
3.9.3	Calculation of total elongation.....	60
3.9.4	Hot ductility measurement.....	60
3.10	METALLOGRAPHY	61
3.10.1	Specimen preparation	61
3.10.2	Optical microscopy	61
3.11	SCANNING ELECTRON MICROSCOPY: JEOL [®] SEM	62
3.12	SCANNING ELECTRON MICROSCOPY: FEI NOVA [®] NANOSEM.....	62
3.13	TRANSMISSION ELECTRON MICROSCOPY	63
3.14	TEMPERATURE CALCULATIONS: TRANSFORMATION AND PRECIPITATION	63
3.15	ANALYSIS OF INDUSTRIAL BILLET CASTING DATA	64
3.16	DATABASE GENERATION	64
CHAPTER 4: DISCUSSION OVERVIEW.....		65
4.1	OVERVIEW OF CHAPTER 4	65
4.2	DEPENDENCE OF DUCTILITY ON FAILURE MODE	66
4.3	RELEVANCE OF THE HOT DUCTILITY TEST IN ASSESSING SUSCEPTIBILITY TO TRANSVERSE CRACKING.....	68

4.3.1	Background.....	68
4.3.2	Limitations of the hot tensile testing technique in assessing the problem of transverse cracking.....	68
4.3.1	Analysis of the hot ductility curve.....	71
4.1	SUMMARY – USING THE HOT DUCTILITY CURVE TO IMPROVE THE INDUSTRIAL CONTINUOUS CASTING OPERATION.....	75
CHAPTER 5: LOW CARBON STEELS		76
5.1	OVERVIEW OF CHAPTER 5.....	76
5.2	TRANSFORMATION IN THE LOW CARBON STEELS.....	77
5.3	PRECIPITATE DISSOLUTION IN THE LOW CARBON STEELS.....	80
5.4	LOW CARBON STEEL <i>LC-1</i>	85
5.4.1	Introduction.....	85
5.4.2	Maximum strength.....	87
5.4.3	Reduction in area	88
5.4.4	Total elongation	89
5.4.5	Scanning electron microscopy	90
5.5	LOW CARBON STEEL <i>LC-2</i>	93
5.5.1	Introduction.....	93
5.5.2	Maximum strength.....	93
5.5.3	Reduction in area	95
5.5.4	Total elongation	96
5.5.5	Scanning electron microscopy	97
5.6	LOW CARBON STEEL <i>LC-3</i>	101
5.6.1	Introduction.....	101
5.6.2	Maximum strength.....	101
5.6.3	Reduction in area	103
5.6.4	Total elongation	104
5.6.5	Scanning electron microscopy	105
5.7	LOW CARBON STEELS <i>LC-4</i> AND <i>LC-5</i>	106
5.7.1	Maximum strength.....	106
5.7.2	Reduction in area	108
5.7.3	Total elongation	109
5.7.4	Scanning electron microscopy	110
5.8	SUMMARY OF HOT DUCTILITY RESULTS FOR THE LOW CARBON STEELS	112
5.9	EFFECT OF STRAIN RATE ON HOT TENSILE BEHAVIOUR IN LOW CARBON STEELS <i>LC-1</i> AND <i>LC-2</i>	116

5.9.1	Maximum strength	116
5.9.2	Hot ductility	116
5.10	EFFECT OF COOLING RATE ON HOT TENSILE BEHAVIOUR IN LOW CARBON STEELS <i>LC-1</i> AND <i>LC-2</i>	118
5.10.1	Maximum strength	118
5.10.2	Hot ductility	118
5.11	PRECIPITATION IN THE LOW CARBON STEELS.....	120
5.12	EFFECT OF COMPOSITION ON HOT TENSILE BEHAVIOUR IN THE LOW CARBON STEELS.....	122
5.12.1	Maximum strength	122
5.12.2	Hot ductility	122
5.13	MECHANISMS OF HOT TENSILE BEHAVIOUR IN THE LOW CARBON STEELS	123
5.13.1	Zone II embrittlement: High temperature ductility drop above the A_{e3} temperature	123
5.13.2	Zone III embrittlement: High temperature ductility drop below the A_{e3} temperature	125
5.13.3	Low temperature ductility recovery below Zone III.....	125
5.14	APPLICATION AND RELEVANCE TO INDUSTRY	126
CHAPTER 6: NIOBIUM STEELS		128
6.1	OVERVIEW OF CHAPTER 6.....	128
6.2	CALCULATED TRANSFORMATION TEMPERATURES IN THE NIOBIUM STEELS	129
6.3	CALCULATED PRECIPITATE DISSOLUTION IN THE NIOBIUM STEELS	131
6.4	NIOBIUM STEEL <i>NB-1</i>	138
6.4.1	Maximum strength	138
6.4.2	Reduction in area	140
6.4.3	Total elongation	141
6.4.4	Scanning electron microscopy	142
6.5	NIOBIUM STEELS <i>NB-2</i> , <i>NB-3</i> AND <i>NB-4</i>	144
6.5.1	Maximum strength	144
6.5.2	Reduction in area	146
6.5.3	Total elongation	147
6.5.4	Scanning electron microscopy	148
6.6	NIOBIUM STEEL <i>NB-5</i>	150
6.6.1	Maximum strength	150
6.6.2	Reduction in area	152

6.6.3	Total elongation	153
6.6.4	Scanning electron microscopy	154
6.7	SUMMARY OF HOT DUCTILITY RESULTS FOR THE NIOBIUM STEELS	157
6.8	EFFECT OF SOLUTION TREATMENT TIME ON HOT TENSILE BEHAVIOUR IN NIOBIUM STEEL <i>NB-1</i>	158
6.9	EFFECT OF THERMAL OSCILLATION ON HOT TENSILE BEHAVIOUR IN NIOBIUM STEEL <i>NB-1</i>	159
6.10	EFFECT OF STRAIN RATE ON HOT TENSILE BEHAVIOUR IN NIOBIUM STEEL <i>NB-5</i>	160
6.11	EFFECT OF COOLING RATE ON HOT TENSILE BEHAVIOUR IN NIOBIUM STEEL <i>NB-5</i>	160
6.12	PRECIPITATION IN THE NIOBIUM STEELS	163
6.13	EFFECT OF COMPOSITION ON HOT TENSILE BEHAVIOUR IN THE NIOBIUM STEELS.....	164
6.13.1	Maximum strength.....	164
6.13.2	Reduction in area	165
6.13.3	Total elongation	166
6.14	MECHANISMS OF HOT TENSILE BEHAVIOUR IN THE NIOBIUM STEELS	166
6.15	APPLICATION AND RELEVANCE TO INDUSTRY	167
CHAPTER 7: AL-KILLED BORON STEELS		169
7.1	OVERVIEW OF CHAPTER 7.....	169
7.2	TRANSFORMATION IN THE AL-KILLED BORON STEELS	170
7.3	PRECIPITATE DISSOLUTION IN THE AL-KILLED BORON STEELS.....	171
7.4	AL-KILLED BORON STEEL <i>B-1</i>	177
7.4.1	Introduction.....	177
7.4.2	Maximum strength.....	178
7.4.3	Reduction in area	180
7.4.4	Total elongation	182
7.4.5	Scanning electron microscopy	183
7.4.6	Transmission electron microscopy	188
7.5	AL-KILLED BORON STEEL <i>B-2</i>	191
7.5.1	Introduction.....	191
7.5.2	Maximum strength.....	191
7.5.3	Reduction in area	193
7.5.4	Total elongation	195
7.5.5	Scanning electron microscopy	196

7.5.6	Transmission electron microscopy	202
7.6	AL-KILLED BORON STEEL <i>B-3</i>	206
7.6.1	Introduction.....	206
7.6.2	Maximum strength.....	207
7.6.3	Reduction in area	208
7.6.4	Total elongation	209
7.6.5	Scanning electron microscopy	210
7.6.6	Transmission electron microscopy	214
7.7	SUMMARY OF HOT DUCTILITY RESULTS FOR THE AL-KILLED BORON STEELS	216
7.8	EFFECT OF STRAIN RATE ON HOT TENSILE BEHAVIOUR IN THE AL-KILLED BORON STEELS	217
7.8.1	Maximum strength.....	217
7.8.2	Reduction in area	217
7.8.3	Total elongation	218
7.9	EFFECT OF COOLING RATE ON HOT TENSILE BEHAVIOUR IN THE AL-KILLED BORON STEELS	218
7.9.1	Maximum strength.....	218
7.9.2	Reduction in area	220
7.9.3	Total elongation	223
7.10	PRECIPITATION IN THE AL-KILLED BORON STEELS	224
7.11	EFFECT OF COMPOSITION IN AL-KILLED BORON STEELS	226
7.11.1	Maximum strength.....	226
7.11.2	Hot ductility	227
7.12	MECHANISMS OF HOT TENSILE BEHAVIOUR IN THE AL-KILLED BORON STEELS	231
7.13	APPLICATION AND RELEVANCE TO INDUSTRY	232
CHAPTER 8: SILICON-KILLED BORON STEELS		235
8.1	OVERVIEW OF CHAPTER 8.....	235
8.2	TRANSFORMATION IN THE SI-KILLED BORON STEELS	236
8.3	PRECIPITATE DISSOLUTION IN THE SI-KILLED BORON STEELS	237
8.4	SI-KILLED BORON STEEL <i>SIB-1</i>	242
8.4.1	Introduction.....	242
8.4.2	Maximum strength.....	244
8.4.3	Reduction in area	245
8.4.4	Total elongation	246
8.4.5	Scanning electron microscopy	247

8.4.6	Transmission electron microscopy	254
8.5	SI-KILLED BORON STEEL <i>SIB-2</i>	256
8.5.1	Introduction.....	256
8.5.2	Maximum Strength	256
8.5.3	Reduction in area	258
8.5.4	Total elongation	259
8.5.5	Scanning electron microscopy	260
8.6	SI-KILLED BORON STEEL <i>SIB-3</i>	264
8.6.1	Introduction.....	264
8.6.2	Maximum Strength	264
8.6.3	Reduction in area	266
8.6.4	Total elongation	267
8.6.5	Scanning electron microscopy	268
8.7	SI-KILLED BORON STEEL <i>SIB-4</i>	270
8.7.1	Introduction.....	270
8.7.2	Maximum Strength	270
8.7.3	Reduction in area	272
8.7.4	Total elongation	273
8.7.5	Scanning electron microscopy	274
8.8	SUMMARY OF HOT DUCTILITY RESULTS FOR THE SI-KILLED BORON STEELS	277
8.9	PRECIPITATION IN THE SI-KILLED BORON STEELS	278
8.10	INTERRUPTED COOLING TESTS	279
8.11	EFFECT OF COMPOSITION IN THE SI-KILLED BORON STEELS	281
8.11.1	Maximum strength.....	281
8.11.2	Hot ductility	282
8.12	ANALYSIS OF PRODUCTION DATA.....	287
8.13	MECHANISMS OF HOT DUCTILITY FAILURE IN THE SI-KILLED BORON STEELS	292
8.14	APPLICATION AND RECOMMENDATIONS TO INDUSTRY	294
CHAPTER 9: HOT DUCTILITY DATABASE		295
9.1	OVERVIEW OF CHAPTER 9.....	295
9.2	HOT DUCTILITY DATABASE PARAMETERS	296
9.3	HOT DUCTILITY DATABASE EXAMPLE.....	298
9.4	HOT DUCTILITY DATABASE APPLICATION	299
CHAPTER 10: CONCLUSIONS		300

CHAPTER 11: RECOMMENDATIONS.....	308
CHAPTER 12: REFERENCES.....	310
APPENDIX I: PUBLICATIONS, PRESENTATIONS AND CONTRIBUTIONS TO LITERATURE	A-1
APPENDIX II: SUMMARY OF THE WORK DONE BY LESLEY CHOWN AND THE WORK DONE BY COLLEAGUES AND INDUSTRY	A-23

List of Figures

Figure 2.1:	Curved mould, vertical continuous casting machine (Irving, 1993).....	7
Figure 2.2:	Surface defects on continuously cast strand (IISI, 1985).	9
Figure 2.3:	Schematic diagram showing the three low ductility temperature zones in steel. (Suzuki, 1982).....	13
Figure 2.4:	Schematic models showing formation of wedge cracks by grain boundary sliding. Arrows indicate sliding boundary and sense of translation (Yue, 1995).....	15
Figure 2.5:	Schematic illustrations showing intergranular microvoid coalescence by deformation in the low temperature austenite region (<i>a-c</i>) and in the two-phase γ - α region (<i>d-f</i>) (Maehara <i>et al.</i> , 1990).	16
Figure 2.6:	Intergranular failure by suppression of recrystallization in austenite (Maehara <i>et al.</i> , 1990).	17
Figure 2.7:	Strain distribution across the solidified strand during single point unbending (Irving, 1993).....	37
Figure 2.8:	Three tensile testing methods used to determine hot ductility:	40
Figure 3.1:	Sampling position and orientation for machining of tensile specimens from continuously cast slab or billet.....	46
Figure 3.2:	Schematic diagram of machined round tensile specimen according to standard ASTM E8M (ASTM, 1997a).....	48
Figure 3.3:	DSI Gleeble standard specimen with threaded ends for hot tensile testing with <i>in situ</i> melting, showing approximate width of the molten zone.	49
Figure 3.4:	Photograph of the Instron [®] tensile testing facility.....	50
Figure 3.5:	Schematic diagram of the tensile testing facility.....	51
Figure 3.6:	Photograph of the hot tensile specimen setup.	52
Figure 3.7:	Photograph of the Gleeble 1500 [®] facility at Pretoria University.	53
Figure 3.8:	View of the hot specimen, grips, and thermocouples.....	54
Figure 3.9:	Testing conditions showing the strain rate and cooling rate variations for schedules A, B, C, D, F, G, H, J and K.....	56
Figure 4.1:	Dependence of reduction in area on failure mode in this work.....	67
Figure 4.2:	Schematic diagram showing the ductility trough (LD trough) flanked by a low temperature high ductility region (LT-HD) and a high temperature high ductility region (HT-HD)..	72
Figure 4.3:	Schematic diagram showing the effect of dynamic recrystallisation on reduction of area for carbon and niobium steels (Cowley <i>et al.</i> , 1998).	74

Figure 5.1:	Comparison of the calculated <i>GAS</i> , modelled TCFe3 and SSOL2 Ae_3 temperatures with the calculated <i>Andrews</i> Ae_3 temperature.	78
Figure 5.2:	Comparison of the modelled TCFe3 and SSOL2 Ae_1 temperatures with the calculated <i>Andrews</i> Ae_1 temperature.	79
Figure 5.3:	Logarithmic dependence of the AlN dissolution temperature on [Al][N] for the low carbon steels (Thermo-Calc™ TCFe3 and Turkdogan equation).	81
Figure 5.4:	Logarithmic dependence of the MnS dissolution temperature on [Mn][S] for the low carbon steels modelled using Thermo-Calc™ and calculated using the Turkdogan (1987) equation.	82
Figure 5.5:	Thermo-Calc™ graphs modelled using database TCFe3, showing the equilibrium phases for low carbon steels a) <i>LC-1</i> and b) <i>LC-2</i>	83
Figure 5.6:	Thermo-Calc™ graphs modelled using database TCFe3, showing the equilibrium phases for low carbon steels a) <i>LC-3</i> and b) <i>LC-4</i>	84
Figure 5.7:	Thermo-Calc™ graph modelled using database TCFe3, showing the equilibrium phases for low carbon steel <i>LC-5</i>	85
Figure 5.8:	Engineering stress as a function of elongation for steel <i>LC-1</i> . The key to the testing schedules is also shown. The arrows indicate the onset of dynamic recrystallisation.	86
Figure 5.9:	Maximum strength for steel <i>LC-1</i> as a function of testing temperature, strain rate and cooling rate.	87
Figure 5.10:	Reduction in area for steel <i>LC-1</i> as a function of testing temperature, strain rate and cooling rate.	88
Figure 5.11:	Elongation for steel <i>LC-1</i> as a function of testing temperature, strain rate and cooling rate.	89
Figure 5.12:	SEM backscatter images of steel <i>LC-1</i> tested under schedule G conditions, showing cracks along prior austenite grain boundaries formed by microvoid coalescence.	91
Figure 5.13:	SEM backscatter images of steel <i>LC-1</i> tested under schedule C conditions, showing microvoid coalescence between precipitates.	91
Figure 5.14:	SEM backscatter images of steel <i>LC-1</i> tested under schedule F, D and H conditions, showing precipitates and cracks along prior austenite grain boundaries.	92
Figure 5.15:	Engineering stress as a function of elongation for steel <i>LC-2</i>	94
Figure 5.16:	Maximum strength for steel <i>LC-2</i> as a function of testing temperature, strain rate and cooling rate.	94
Figure 5.17:	Reduction in area for steel <i>LC-2</i> as a function of testing temperature, strain rate and cooling rate.	95
Figure 5.18:	Elongation for steel <i>LC-2</i> as a function of testing temperature, strain rate and cooling rate.	96
Figure 5.19:	SEM backscatter images of steel <i>LC-2</i> showing precipitation and void formation along austenite grain boundaries ($1.2\text{ }^{\circ}\text{C}\cdot\text{s}^{-1}$, 10^{-3} s^{-1}).	97

Figure 5.20: SEM backscatter images of steel <i>LC-2</i> tested under Schedule G conditions: (10^{-3} s^{-1} , $3.0 \text{ }^\circ\text{C.s}^{-1}$), showing a) many precipitates and extensive cracking and b) less cracking.	98
Figure 5.21: SEM backscatter images of steel <i>LC-2</i> tested under Schedule F and D conditions: $10^{-4} \text{ s}^{-1} + 0.3$ and 1.2 C.s^{-1} respectively, showing cracking and many precipitates.	99
Figure 5.22: SEM backscatter images of steel <i>LC-2</i> tested under Schedule H conditions: (10^{-4} s^{-1} , $3.0 \text{ }^\circ\text{C.s}^{-1}$).	100
Figure 5.23: Engineering stress as a function of elongation for steel <i>LC-3</i> . The key to the testing schedules is also shown.	102
Figure 5.24: Maximum strength for steel <i>LC-3</i> as a function of testing temperature, strain rate and cooling rate.	102
Figure 5.25: Reduction in area for steel <i>LC-3</i> as a function of testing temperature, strain rate and cooling rate.	103
Figure 5.26: Elongation for steel <i>LC-3</i> as a function of testing temperature, strain rate and cooling rate.	104
Figure 5.27: SEM backscatter images of Steel <i>LC-3</i> tested under Schedule C and H conditions: (10^{-3} s^{-1} , 1.2°C.s^{-1} and 10^{-4} s^{-1} , 3.0°C.s^{-1} respectively). Dark lines show cracking between precipitates.....	105
Figure 5.28: Engineering stress as a function of total elongation for steels <i>LC-4</i> and <i>LC-5</i> . All tests were done according to schedule C conditions (1.2°C.s^{-1} , 10^{-4} s^{-1}). Arrows indicate the onset of dynamic recrystallisation.	107
Figure 5.29: Maximum strength for steels <i>LC-4</i> and <i>LC-5</i> as a function of testing temperature.....	107
Figure 5.30: Reduction in area for steels <i>LC-4</i> and <i>LC-5</i> as a function of testing temperature.....	108
Figure 5.31: Elongation for steels <i>LC-4</i> and <i>LC-5</i> as a function of testing temperature.....	109
Figure 5.32: SEM backscatter images of steel <i>LC-4</i> tested under Schedule C conditions: (10^{-3} s^{-1} , $1.2 \text{ }^\circ\text{C.s}^{-1}$), showing microvoid coalescence along prior austenite grain boundaries.	110
Figure 5.33: SEM backscatter image of steel <i>LC-5</i> tested under Schedule C conditions: (10^{-3} s^{-1} , $1.2 \text{ }^\circ\text{C.s}^{-1}$), showing precipitate-containing voids.	111
Figure 5.34: Variation in maximum stress between the low carbon steels <i>LC-1</i> to <i>LC-5</i> , as a function of strain rate cooling rate and testing temperature.....	113
Figure 5.35: Reduction in area for low carbon steels <i>LC-1</i> to <i>LC-5</i> , as a function of strain rate, cooling rate and temperature.	114
Figure 5.36: Total elongation for low carbon steels <i>LC-1</i> to <i>LC-5</i> , as a function of strain rate, cooling rate and temperature.	115
Figure 5.37: The effect of strain rate (10^{-4} - 10^{-3} s^{-1}) on hot ductility of steel <i>LC-1</i>	117
Figure 5.38: The effect of strain rate (10^{-4} - 10^{-3} s^{-1}) on hot ductility of steel <i>LC-2</i>	117

Figure 5.39:	The effect of cooling rate on hot ductility of steel <i>LC-1</i>	119
Figure 5.40:	The effect of cooling rate on hot ductility of steel <i>LC-2</i>	119
Figure 6.1:	Comparison of the calculated <i>GAS</i> , modelled TCFE3 and SSOL2 Ae_3 temperatures with the calculated Andrews Ae_3 temperature for the niobium steels.	130
Figure 6.2:	Logarithmic dependence of the AlN dissolution temperature on [Al][N] for the niobium steels modelled using Thermo-Calc™ and calculated using the Turkdogan (1987) equation.	132
Figure 6.3:	Logarithmic dependence of the MnS dissolution temperature on [Mn][S] for the niobium steels using Thermo-Calc™ modelling and the Turkdogan equation (1987).	133
Figure 6.4:	Logarithmic dependence of the various Nb(C,N) precipitate dissolution temperatures on [Nb][C] _x [N] _y for the niobium steels, using Thermo-Calc™ TCFE3 and SSOL4, and the Turkdogan equation(1987).	134
Figure 6.5:	Thermo-Calc graph modelled using database TCFE3, showing the equilibrium phases for niobium steel <i>Nb-1</i>	135
Figure 6.6:	Thermo-Calc™ graphs modelled using database TCFE3, showing the equilibrium phases for niobium steels a) <i>Nb-2</i> and b) <i>Nb-3</i>	136
Figure 6.7:	Thermo-Calc™ graphs modelled using database TCFE3, showing the equilibrium phases for niobium steels a) <i>Nb-4</i> and b) <i>Nb-5</i>	137
Figure 6.8:	Engineering stress as a function of elongation for steel <i>Nb-1</i> . The arrow in b) indicates the onset of dynamic recrystallisation. The key to the testing schedules A, B and C is also shown.	139
Figure 6.9:	Maximum strength for steel <i>Nb-1</i> as a function of testing temperature, solution treatment time and cooling pattern.	139
Figure 6.10:	Reduction in area for steel <i>Nb-1</i> as a function of testing temperature, strain rate and cooling rate.	140
Figure 6.11:	Elongation for steel <i>Nb-1</i> as a function of testing temperature, strain rate and cooling rate.	141
Figure 6.12:	SEM backscatter images of steel <i>Nb-1</i> tested under schedule A, B and C conditions (cooling rate = 1.2 °C.s ⁻¹ , strain rate = 10 ⁻³ s ⁻¹), showing discrete precipitates without any cracking (b), microvoid coalescence (a and d) and extensive cracking (c).	143
Figure 6.13	Engineering stress as a function of elongation for steels <i>Nb-2</i> , <i>Nb-3</i> and <i>Nb-4</i> . The key to the testing schedules is shown above. Arrows indicate the onset of dynamic recrystallisation	145
Figure 6.14:	Maximum strength for steels <i>Nb-2</i> , <i>Nb-3</i> and <i>Nb-4</i> as a function of testing temperature. All tests were conducted according to Schedule C conditions (10 ⁻³ s ⁻¹ , 1.2 °C.s ⁻¹).	145
Figure 6.15:	Reduction in area for steels <i>Nb-2</i> , <i>Nb-3</i> and <i>Nb-4</i> as a function of testing temperature. All tests were conducted according to Schedule C conditions (10 ⁻³ s ⁻¹ , 1.2 °C.s ⁻¹).	146

Figure 6.16:	Elongation for steels <i>Nb-2</i> , <i>Nb-3</i> and <i>Nb-4</i> as a function of testing temperature. All tests were conducted according to Schedule C conditions (10^{-3} s^{-1} , $1.2 \text{ }^\circ\text{C}\cdot\text{s}^{-1}$).	147
Figure 6.17:	SEM backscatter images of steel <i>Nb-2</i> tested under schedule C conditions ($1.2 \text{ }^\circ\text{C}\cdot\text{s}^{-1}$, 10^{-3} s^{-1}), showing microvoid coalescence with single line cracking (a) and network cracking (b).	148
Figure 6.18:	SEM backscatter images of steels <i>Nb-3</i> and <i>Nb-4</i> tested under schedule C conditions ($1.2 \text{ }^\circ\text{C}\cdot\text{s}^{-1}$, 10^{-3} s^{-1}).	149
Figure 6.19:	Engineering stress as a function of elongation for steel <i>Nb-5</i> .	151
Figure 6.20:	Maximum strength for steel <i>Nb-5</i> as a function of testing temperature, strain rate and cooling rate.	151
Figure 6.21:	Reduction in area for steel <i>Nb-5</i> as a function of testing temperature, strain rate and cooling rate.	152
Figure 6.22:	Elongation for steel <i>Nb-5</i> as a function of testing temperature, strain rate and cooling rate.	153
Figure 6.23:	SEM backscatter images of steel <i>Nb-5</i> tested under schedule C, G, D and H conditions, showing precipitates, microvoid coalescence, Nb(C,N) eutectic phase and extensive cracking.	155
Figure 6.24:	SEM backscatter images of steel <i>Nb-5</i> tested under schedule F conditions, showing three types of intergranular cracking: a) wedge cracking b) parallel cracking along prior austenite grain boundaries and c) limited microvoid coalescence.	156
Figure 6.25:	Effect of composition on maximum strength in niobium steels <i>Nb-1</i> to <i>Nb-5</i> . The Ae_3 and Ae_1 temperatures for Nb-1 are shown.	161
Figure 6.26:	Effect of composition on: a) Reduction in area and b) Total elongation in niobium steels <i>Nb-1</i> to <i>Nb-5</i> . The Ae_3 and Ae_1 temperatures for Nb-1 are shown on the graphs.	162
Figure 7.1:	Dependence of the AlN dissolution temperature on [Al][N] for the boron steels modelled using Thermo-Calc TM and calculated using the Turkdogan (1987) equation.	173
Figure 7.2:	Logarithmic dependence of the MnS dissolution temperature on [Mn][S] or the boron steels modelled using Thermo-Calc TM and calculated using the Turkdogan (1987) equation.	174
Figure 7.3:	Logarithmic dependence of the BN dissolution temperature on [B][N] for the boron steels, calculated using equations published by Turkdogan (1987), Fountain (1962) and Maitrepierre (1979).	174
Figure 7.4:	Thermo-Calc TM graphs modelled using database TCFE3, showing the equilibrium phases for boron steels a) <i>B-1</i> and b) <i>B-2</i> .	175
Figure 7.5:	Thermo-Calc TM graphs modelled using database TCFE3, showing the equilibrium phases for boron steel <i>B-3</i> .	176
Figure 7.6:	Engineering stress as a function of elongation for steel <i>B-1</i> .	179
Figure 7.7:	Maximum strength for steel <i>B-1</i> as a function of testing temperature, strain rate and cooling rate.	179

Figure 7.8:	Reduction in area for steel B-1 as a function of testing temperature, strain rate and cooling rate.	180
Figure 7.9:	Elongation for steel B-1 as a function of testing temperature, strain rate and cooling rate.	182
Figure 7.10:	SEM backscatter images of Steel <i>B-1</i> tested under Schedule C conditions: (10^{-3} s^{-1} , $1.2 \text{ }^{\circ}\text{C}\cdot\text{s}^{-1}$).	184
Figure 7.11:	SEM backscatter images of Steel <i>B-1</i> tested under Schedule G conditions: (10^{-3} s^{-1} , $3.0 \text{ }^{\circ}\text{C}\cdot\text{s}^{-1}$).	185
Figure 7.12:	SEM backscatter images of Steel <i>B-1</i> tested under Schedule F conditions: (10^{-4} s^{-1} , $0.3 \text{ }^{\circ}\text{C}\cdot\text{s}^{-1}$).	186
Figure 7.13:	SEM backscatter images of Steel <i>B-1</i> tested under Schedule D conditions: (10^{-4} s^{-1} , $1.2 \text{ }^{\circ}\text{C}\cdot\text{s}^{-1}$), showing precipitate-containing microvoids and cracking along prior austenite grain boundaries.	187
Figure 7.14:	SEM backscatter images of Steel <i>B-1</i> tested under Schedule H conditions: (10^{-4} s^{-1} , $3.0 \text{ }^{\circ}\text{C}\cdot\text{s}^{-1}$), showing cracking between microvoids.	188
Figure 7.15:	X-ray maps of Steel <i>B-1</i> tested under Schedule F conditions.	189
Figure 7.16:	X-ray maps of a grain boundary filament in Steel <i>B-1</i> tested under Schedule F conditions ($R. A. = 20\%$, 10^{-4} s^{-1} , $0.3 \text{ }^{\circ}\text{C}\cdot\text{s}^{-1}$).	190
Figure 7.17:	Engineering stress as a function of elongation for steel <i>B-2</i>	192
Figure 7.18:	Maximum strength for steel <i>B-2</i> as a function of testing temperature, strain rate and cooling rate.	193
Figure 7.19:	Reduction in area for steel <i>B-2</i> as a function of testing temperature, strain rate and cooling rate.	194
Figure 7.20:	Elongation for steel <i>B-2</i> as a function of testing temperature, strain rate and cooling rate.	195
Figure 7.21:	SEM backscatter images of Steel <i>B-2</i> tested under Schedule C conditions: (10^{-3} s^{-1} , $1.2 \text{ }^{\circ}\text{C}\cdot\text{s}^{-1}$), showing large Fe-O-B-N precipitates.	197
Figure 7.22:	SEM backscatter images of Steel <i>B-2</i> tested under Schedule G conditions: (10^{-3} s^{-1} , $3.0 \text{ }^{\circ}\text{C}\cdot\text{s}^{-1}$), showing various precipitates and microvoid coalescence.	198
Figure 7.23:	SEM backscatter images of Steel <i>B-2</i> tested under Schedule F conditions: (10^{-4} s^{-1} , $0.3 \text{ }^{\circ}\text{C}\cdot\text{s}^{-1}$), showing EDS analyses of various precipitates.	199
Figure 7.24:	SEM backscatter images of Steel <i>B-2</i> tested under Schedule D conditions (10^{-4} s^{-1} , $1.2 \text{ }^{\circ}\text{C}\cdot\text{s}^{-1}$).	200
Figure 7.25:	SEM backscatter images of Steel <i>B-2</i> tested under Schedule H conditions (10^{-4} s^{-1} , $3.0 \text{ }^{\circ}\text{C}\cdot\text{s}^{-1}$), showing various precipitates and intergranular cracking.	201
Figure 7.26:	Dark field image, bright field image, X-ray maps and EDS spectrum of a precipitate in Steel <i>B-2</i> tested under Schedule G conditions.	203

Figure 7.27: Bright field, dark field images and X-ray map of CuS filaments and small spherical CuS precipitates in steel <i>B-2</i> tested under Schedule G conditions (10^{-3} s^{-1} , $3.0^\circ\text{C}\cdot\text{s}^{-1}$).....	204
Figure 7.28: Dark field image & X-ray maps of alumina inclusion covered by BN in steel <i>B-2</i> tested under Schedule F conditions (10^{-4} s^{-1} , $0.3^\circ\text{C}\cdot\text{s}^{-1}$).....	205
Figure 7.29: Engineering stress as a function of elongation for steel <i>B-3</i> . The key to the testing schedules is also shown. Arrows indicate the onset of dynamic recrystallisation.....	207
Figure 7.30: Maximum strength for steel <i>B-3</i> as a function of testing temperature, strain rate and cooling rate.	208
Figure 7.31: Reduction in area for steel <i>B-3</i> as a function of testing temperature, strain rate and cooling rate.	208
Figure 7.32: Elongation for steel <i>B-3</i> as a function of testing temperature, strain rate and cooling rate.	209
Figure 7.33: SEM backscatter images of Steel <i>B-3</i> tested under Schedule C conditions: (10^{-3} s^{-1} , $1.2^\circ\text{C}\cdot\text{s}^{-1}$), showing various precipitates.....	211
Figure 7.34: SEM backscatter images of Steel <i>B-3</i> tested under Schedule F conditions: (10^{-4} s^{-1} , $0.3^\circ\text{C}\cdot\text{s}^{-1}$), showing large precipitates with varying compositions.	212
Figure 7.35: SEM backscatter images of Steel <i>B-3</i> tested under Schedule H conditions: (10^{-4} s^{-1} , $3.0^\circ\text{C}\cdot\text{s}^{-1}$), showing complex precipitates.....	213
Figure 7.36: a) Dark field image and b) X-ray maps of Steel <i>B-3</i> tested under Schedule F conditions (10^{-4} s^{-1} , $0.3^\circ\text{C}\cdot\text{s}^{-1}$), showing a large, complex precipitate (oxide with BN and C) and a smaller CuS precipitate in the top right-hand corner.	214
Figure 7.37: a) Dark field image b) Line scan across the precipitate and c) X-ray map of steel <i>B-3</i> tested under Schedule F conditions (10^{-4}s^{-1} , $0.3^\circ\text{C}\cdot\text{s}^{-1}$), showing a complex precipitate (CuS+BN).	215
Figure 7.38: The effect of composition (increase in B:N ratio), strain rate and cooling rate on maximum strength in Al-killed boron steels <i>B-1</i> , <i>B-2</i> and <i>B-3</i> . The Ae_3 temperatures of <i>B-1</i> (888°C) <i>B-2</i> and <i>B-3</i> (both 895°C) are shown.....	219
Figure 7.39: The effect of composition (increase in B:N ratio), strain rate and cooling rate on reduction in area in Al-killed boron steels <i>B-1</i> , <i>B-2</i> and <i>B-3</i> . The Ae_3 and BN dissolution temperatures for the three steels are shown.....	220
Figure 7.40: Graphs showing the improvement of hot ductility by increasing strain rate from 10^{-4} to 10^{-3} s^{-1} at fast and intermediate cooling rates for steel <i>B-1</i> (a and b). There is very little effect of strain rate for steel <i>B-2</i> (c and d).....	221
Figure 7.41: Graphs showing the improvement of hot ductility by decreasing cooling rate at high strain rate for steel <i>B-1</i> (no change at low strain rate) and at both high and low strain rates for steel <i>B-2</i>	222
Figure 7.42: The effect of composition (increase in B/N ratio), strain rate and cooling rate on total elongation in Al-killed boron steels <i>B-1</i> , <i>B-2</i>	

	and <i>B-3</i> . The A_{e_3} temperatures of <i>B-1</i> (888°C), <i>B-2</i> and <i>B-3</i> (both 895°C) are shown.	223
Figure 7.43:	Contour plots showing the effects of temperature, cooling rate, strain rate and B:N ratio on reduction in area, and hence on hot ductility, in the Al-killed boron steels.	228
Figure 7.44:	Hot ductility in the Al-killed boron steels <i>B-1</i> , <i>B-2</i> and <i>B-3</i> tested by Banks and Verdoorn (1996).	229
Figure 7.45:	The influence of B:N ratio on hot ductility in Al-killed boron steels.	233
Figure 8.1:	Logarithmic dependence of the MnS dissolution temperatures on [Mn][S] for the Si-killed steels using Thermo-Calc™ modelling and calculation using the Turkdogan (1987) equation.	238
Figure 8.2:	Logarithmic dependence of the BN dissolution temperature on [B][N] for the Si-killed boron steels.	239
Figure 8.3:	Thermo-Calc™ graphs modelled using database TCFE3, showing equilibrium phase fractions as a function of temperature for steels.	240
Figure 8.4:	Thermo-Calc™ graphs modelled using database TCFE3, showing equilibrium phase fractions as a function of temperature for steels.	241
Figure 8.5:	Engineering stress as a function of elongation for Si-killed steel <i>SiB-1</i> after <i>in situ</i> melting, followed by cooling to the test temperature at a) 2 °C.s ⁻¹ and b) 1 °C.s ⁻¹ . The key to the tests is shown, the onset of dynamic recrystallisation is indicated by arrows on the graphs.	243
Figure 8.6:	Maximum strength for steel <i>SiB-1</i> as a function of testing temperature and cooling rate.	244
Figure 8.7:	Reduction in area for steel <i>SiB-1</i> as a function of testing temperature and cooling rate.	245
Figure 8.8:	Elongation for steel <i>SiB-1</i> as a function of testing temperature and cooling rate.	246
Figure 8.9:	Photograph of a section of industrially cast steel <i>SiB-1</i> billet, showing a severe transverse corner crack.	247
Figure 8.10:	SEM images of the transverse surface crack in steel <i>SiB-1</i> , showing microvoid coalescence, with many large MnS precipitates (1-3 µm) and C, Cu, B, O, Al and Si.	248
Figure 8.11:	SEM images of the hot tensile specimen fracture surfaces: a) and b) 800 °C testing temperature (transgranular fracture) and c – e) 825 °C (intergranular fracture).	250
Figure 8.12	a-e: SEM backscatter images of the brittle hot tensile specimen fracture surfaces for testing temperature 825 °C, showing intergranular fracture and copious precipitation of MnS-rich spherical precipitates.	251
Figure 8.13	a-c: SEM secondary electron images of the hot tensile specimen fracture surfaces for testing temperature 1175 °C showing intergranular fracture. The fracture surfaces are covered with large MnS precipitates.	252

Figure 8.14	SEM backscatter electron images of the hot tensile specimen fracture surface (testing temperature 1175 °C) showing grain boundary precipitation, precipitate free zone (PFZ) and matrix precipitation.....	253
Figure 8.15:	TEM bright field images of a brittle hot tensile sample from <i>SiB-1</i> cooled at 2 °C.s ⁻¹ to a test temperature of 1175 °C.....	255
Figure 8.16:	Engineering stress as a function of elongation for S-killed steel <i>SiB-2</i> after <i>in situ</i> melting, followed by cooling to the test temperature at 2 °C.s ⁻¹ . The arrow shows the onset of dynamic recrystallisation.....	257
Figure 8.17:	Maximum strength for steel <i>SiB-2</i> as a function of test temperature. The arrow shows the onset of dynamic recrystallisation.	257
Figure 8.18:	Reduction in area for steel <i>SiB-2</i> as a function of test temperature.	258
Figure 8.19:	Elongation for steel <i>SiB-2</i> as a function of test temperature.	259
Figure 8.20:	SEM backscatter images of the fracture surface of a brittle hot tensile sample from <i>SiB-2</i> (850 °C, <i>R.A.</i> = 3%).....	261
Figure 8.21	a) and b) SEM backscatter images of the fracture surface of a brittle hot tensile sample from <i>SiB-2</i> (850 °C, <i>R.A.</i> = 3%) showing austenite grain boundary triple points, microvoid coalescence between MnS precipitates and cracking along the austenite grain boundaries.	262
Figure 8.22:	SEM backscatter images of the fracture surface of a brittle hot tensile sample from <i>SiB-2</i> (850 °C, <i>R.A.</i> = 3%).....	263
Figure 8.23:	Engineering stress as a function of elongation for Si-killed steel <i>SiB-3</i> after <i>in situ</i> melting, followed by cooling to the test temperature at 2 °C.s ⁻¹ . The arrow shows the onset of dynamic recrystallisation.....	265
Figure 8.24:	Maximum strength for steel <i>SiB-3</i> as a function of test temperature.	265
Figure 8.25:	Reduction in area for steel <i>SiB-3</i> as a function of test temperature.	266
Figure 8.26:	Elongation for steel <i>SiB-3</i> as a function of test temperature, strain rate and cooling rate.	267
Figure 8.27	a) and b) SEM backscatter images of the fracture surface of a ductile hot tensile sample from <i>SiB-3</i> (1185 °C, <i>R.A.</i> = 86%).....	269
Figure 8.28:	Engineering stress as a function of elongation for Si-killed steel <i>SiB-4</i> after <i>in situ</i> melting, followed by cooling to the test temperature at 2 °C.s ⁻¹ . Dynamic recrystallisation is shown by an arrow.....	271
Figure 8.29:	Maximum strength for steel <i>SiB-4</i> as a function of testing temperature. The arrow shows the onset of dynamic recrystallisation.	271
Figure 8.30:	Reduction in area for steel <i>SiB-4</i> as a function of test temperature.	272
Figure 8.31:	Elongation for steel <i>SiB-4</i> as a function of test temperature.	273
Figure 8.32	a) and b) SEM backscatter images of the fracture surface of a brittle hot tensile sample from <i>SiB-4</i> (1000°C, <i>R.A.</i> = 16%), showing flat fracture surfaces indicative of grain boundary sliding.....	275
Figure 8.33	a) and b) SEM backscatter images of the fracture surface of a brittle hot tensile sample from <i>SiB-4</i> (1000°C, <i>R.A.</i> = 16%) showing <1 µm diameter MnS precipitates randomly situated in the austenite matrix.	276

Figure 8.34:	Schematic temperature - time diagram showing the hot tensile tests with interrupted cooling.....	279
Figure 8.35	Interrupted cooling test results, showing low ductility for samples cooled directly to 1150 °C (no hold: 14%, 10 minutes hold: 11%), and higher ductility for samples cooled first to 1220 °C (5 minutes: hold 49%, 10 minutes hold: 51%).....	280
Figure 8.36:	Maximum strength results for the Si-killed steels.....	281
Figure 8.37:	Hot ductility results for the Si-killed steels.....	282
Figure 8.38:	Total elongation results for the Si-killed steels.....	283
Figure 8.39:	Effect of Mn:S ratio on reduction in area in the Si-killed steels (the angular shape of the 3-D plot is due to the limited data).....	284
Figure 8.40:	Effect of B:N ratio on reduction in area in the Si-killed steels.....	286
Figure 8.41:	Actual scrap percentage as a function of the actual Mn:S ratio.....	288
Figure 8.42:	Average scrap percentage as a function of the average Mn:S ratio, including the exponential decay equation determined by regression analysis. The 5% scrap level is indicated on the graph.....	289
Figure 8.43:	Predicted scrap % as a function of Mn:S ratio for the Si-killed boron steels.....	290
Figure 8.44:	Average scrap % as a function of average B:N ratio.....	291
Figure 8.45:	The influence of B:N ratio on hot ductility in a) Si-killed steels and b) Si-killed and Al-killed steels (from Chapter 7).....	293
Figure 9.1:	“Choose steel type” selection boxes, showing cooling rate and strain rate options.....	297
Figure 9.2:	“Chemical composition” menu, where minimum or maximum limits can be set for various steel elements.....	297
Figure 9.3:	Reduction in area (%) results plotted as a function of temperature for the high carbon steel numbers listed in Table 9.1.....	298

List of Tables

Table 2.1	Effect of steel composition on transverse surface cracking.	33
Table 2.2	Equilibrium solubility equations for carbides and nitrides in austenite.	34
Table 2.3:	Equations used to determine transformation temperatures.....	35
Table 3.1:	Casting parameters for thick slab casting, thin slab casting and billet casting, determined from the casting machines used in this work, including calculated cooling rates, strain and strain rate values.....	44
Table 3.2:	Chemical composition of steels (mass %, N and B ppm), grouped by general steel type: low carbon, niobium, boron and high sulphur.....	47
Table 3.3:	Summary of tensile testing schedules.....	56
Table 3.4:	Programmed cooling times from solution treatment temperature to testing temperatures.....	58
Table 3.5.:	Relationship between strain rate and crosshead speed.	58
Table 5.1:	Chemical composition of low carbon steels (in mass %).	77
Table 5.2:	Calculated transformation temperatures (in °C) for low carbon steel compositions in this work.	77
Table 5.3:	Critical and actual Mn:S ratios for all of the steels.	81
Table 5.4:	Solubility of precipitates in austenite in the low carbon steels – calculated equilibrium precipitate dissolution temperatures.	81
Table 5.5:	Summary of the hot ductility results for the low carbon steels.	112
Table 5.6:	Summary of the precipitation elements and species found in the low carbon steels.	121
Table 5.7:	Application of the hot ductility results to casting parameters.	126
Table 6.1:	Chemical composition of niobium microalloyed steels (mass %).	129
Table 6.2:	Calculated Ae_3 and Ae_1 transformation temperatures (in °C) for niobium microalloyed steels in this work.....	129
Table 6.3:	Critical (Mn:S) _c and actual (Mn:S) _a ratios for all of the steels calculated using the De Toledo (1993) criterion.	131
Table 6.4:	Solubility of precipitates in austenite in niobium steels – calculated equilibrium precipitate dissolution temperatures (°C).	131
Table 6.5:	Solubility of precipitates in austenite in niobium steels: Thermo-Calc modelled equilibrium precipitate dissolution temperatures (°C).....	142
Table 6.6:	Summary of the hot ductility results for niobium steel <i>Nb-1</i> . (Strain rate = 10^{-3} s^{-1} , cooling rate = $1.2 \text{ °C}\cdot\text{s}^{-1}$).....	157
Table 6.7:	Summary of hot ductility results for niobium steels <i>Nb-2-Nb-5</i>	158
Table 6.8:	Summary of the precipitate species found in the niobium steels.	164

Table 6.9:	Application of the hot ductility results to casting parameters.	167
Table 7.1:	Chemical composition of Al-killed boron microalloyed steels	170
Table 7.2:	Calculated and modelled transformation temperatures (in °C) for Al-killed boron steels.	170
Table 7.3:	Critical (Mn:S) _c & actual (Mn:S) _a ratios for Al-killed boron steels.	172
Table 7.4:	Solubility of precipitates in austenite in Al-killed boron steels – calculated equilibrium precipitate dissolution temperatures.	172
Table 7.5:	Solubility of precipitates in austenite in Al-killed boron steels – Thermo-Calc™ modelled equilibrium precipitate dissolution temperatures (°C).	173
Table 7.6:	Summary of the hot ductility results for Al-killed boron steels.	216
Table 7.7:	List of precipitate species found in Al-killed boron steels.	225
Table 7.8:	Summary of precipitate species relevant to Al-killed boron steels.	226
Table 7.9:	Chemical composition of Al-killed boron steels (mass %), showing B:N ratio, %N tied up in BN formation, excess %N available for AlN formation and the hot ductility ranking (1: best, 3: worst).	230
Table 7.10:	Application of the hot ductility results to casting parameters.	232
Table 8.1:	Chemical composition of the Si-killed boron steels (in mass %).	236
Table 8.2:	Calculated transformation temperatures (°C) for the Si-killed steels in this work.	236
Table 8.3:	De Toledo (1995) hot cracking criterion, showing critical (Mn:S) _c and actual (Mn:S) _a ratios for the Si-killed boron steels.	237
Table 8.4:	Solubility of precipitates in austenite in the Si-killed boron steels – calculated and Thermo-Calc™ modelled equilibrium precipitate dissolution temperatures (°C).	238
Table 8.5:	Summary of the hot ductility results for the Si-killed boron steels (low and high temperature recovery, minimum <i>R.A.</i> and dynamic recrystallisation temperature).	277
Table 8.6:	List of precipitates found in the Si-killed boron steels.	278
Table 8.7:	Hot ductility (% <i>R.A.</i>) of interrupted cooling tests. All tensile tests were performed at 1150 °C on samples from steel <i>SiB-2</i>	280
Table 8.8:	Chemical composition of the Si-killed boron steels (in mass %), showing Mn:S ratio, %S required for MnS formation, excess %S and the hot ductility ranking (1: best, 4: worst).	283
Table 8.9:	Mn:S ratio, equilibrium volume % MnS of the Si-killed boron steels (in mass %) and hot ductility ranking (1: best, 4: worst).	285
Table 8.10:	B:N ratio of the Si-killed boron steels (in mass %) showing the hot ductility ranking (1: best, 4: worst).	286
Table 8.11:	Ni:Cu ratio of the Si-killed boron steels (in mass %) showing the hot ductility ranking (1: best, 4: worst).	287
Table 9.1:	Example of hot ductility database retrieval, showing high carbon steel parameters. Compositions are given in mass %.	298

Chapter 1: Introduction

General introduction to the thesis

1.1 BACKGROUND OF CONTINUOUS CASTING AND CRACK SUSCEPTIBILITY

The occurrence of transverse corner and facial cracking on the surface of continuously cast slabs has been a problem for steelmakers since the commercialization of the continuous casting process. Cracks initiate in the casting machine and usually propagate during the strand straightening process. This issue is not confined to thick strand casting, but is also found in bloom, billet and the rapidly developing thin slab casting routes. With the ever-increasing drive to reduce processing costs, reheating stages may be avoided by hot charging and direct rolling, which eliminates the possibility of detailed strand inspection and dressing. Steelmakers gain experience in avoiding specific casting conditions that cause transverse cracking. However, relatively small changes in steel composition or in casting practice can lead to production losses through scrapping or intensive dressing of severely cracked slabs.

Fortunately, it is possible to attain significant understanding of the factors that govern transverse cracking by undertaking simple and inexpensive laboratory testing. This experimental work usually takes the form of hot tensile, compressive or bend testing. In this work, the two techniques: reheated hot tensile testing and *in situ* melted tensile testing were used. Many variables can be addressed, such as: strand cooling rate and casting speed (through testing strain rate variations) and comparisons can be drawn to explain the effects of changing steel composition.

1.2 OBJECTIVE OF THESIS AND CONTRIBUTION TO ENGINEERING

Hot ductility of conventionally cast thick slab, particularly in low carbon and niobium microalloyed steels, is a well-researched area, whereas literature on hot ductility in low carbon, boron microalloyed steels is limited. Specific comparisons of hot ductility in thick slab, billet and thin slab casting are also not widely published. Thus, the basis of this investigation is to assess the influences of the following parameters on hot tensile behaviour:

- The tensile testing variables: cooling rate and strain rate, including comparisons of typical thick slab, billet and thin slab parameters.
- Variations in composition, particularly carbon, manganese, sulphur and calcium, in five low carbon steels.
- Variations in composition in five niobium microalloyed steels.
- Variations in composition, specifically the boron: nitrogen ratio, in three low carbon, aluminium-killed boron microalloyed steels.
- Variations in composition, in particular the boron: nitrogen and manganese: sulphur ratios, in four silicon-killed, boron microalloyed steels.

1.3 CONTRIBUTIONS TO LITERATURE

The following paper on this work (attached in the Appendix) has been submitted for publication and is under review:

- L. H. CHOWN and L. A. CORNISH, Investigation of hot ductility in Al-killed boron steels, *Materials Science and Engineering A*, vol. 494, 2008, pp. 263-275.

The following papers on this work were presented by the author at conferences and colloquia, and are attached in the Appendix:

- L. H. CHOWN and A. S. TULING, *Proceedings of the 15th International ICEM conference*, Sep. 2002, vol. 2, pp. 767-768.
- L. H. CHOWN, A. P. BENTLEY and F. A. VERDOORN, *Proceedings of the 40th Microscopy Society of Southern Africa Conference*, Dec. 2001, vol. 31, pg. 25. [ANASPEC Award: “The Best Application in Industry” Presentation.]

- L.H. CHOWN, The effects of boron, cooling rate and strain rate on hot ductility of extra low carbon steel, *SAIMM Colloquium*, Pretoria, 18 July 2000.
- L.H. CHOWN, Continuous casting of steels - prediction and prevention of cracking, *Centre of Excellence in Strong Materials Colloquium*, University of the Witwatersrand, Johannesburg, 20 February 2005.

The following reports on this work were written by the author while working at Iscor Ltd. (now Arcelor Mittal) and at IMMRI, Pretoria University:

- L. H. Chown and F. A. Verdoorn, *Final Report: The influence of cooling rate on hot ductility in a low carbon boron billet steel*, Iscor report P40-02 to Cape Gate (Pty.) Ltd., 20 June 2002.
- L. H. Chown and F. A. Verdoorn, *Results report: Examination of the cracks on billet material and the influence of cooling rate on hot ductility in low carbon boron billet steel SAE1006*, Iscor Results report P40-01R to Cape Gate (Pty.) Ltd., 21 December 2001.
- L. H. Chown and F. A. Verdoorn, *Hot ductility of uncracked vs. cracked boron steel SAE1006 and the effect of Mn/S ratio on transverse cracking*, Iscor report P40-001 to Cape Gate (Pty.) Ltd., 7 July 2001.
- L. H. Chown, *Hot ductility of steels during continuous casting – Part I: Database generation*, Iscor internal report, 7 August 1997.
- L. H. Chown, *Hot ductility and ultimate tensile strength of ULC steel SC6*, Iscor internal report, 1 April 1996.
- L. H. Chown, *Thin slab casting – the effect of strain*, Iscor internal report, 8 December 1994.

1.4 THESIS STRUCTURE

In Chapter 2, relevant literature is reviewed in five sections. The first section provides an overview of the continuous casting process. This is followed in the second section by a summary of crack susceptibility in continuous casting. The third section discusses the influence of the processing variables that affect surface cracking. The influence of hot

ductility behaviour on cracking is detailed in the fourth section. The final section in Chapter 2 explains the laboratory testing methods and calculations used in this work.

In Chapter 3, the experimental methodology, equipment and materials are described. Schematic diagrams and photographs of the tensile testing facility are presented and the tensile testing procedure is detailed. The scanning electron microscopy and transmission electron microscopy procedures, used to examine specimens after testing, are described. The type of testing material is detailed, from sampling and machining, to steel composition analysis.

Chapter 4 gives a brief overview of and introduction to the results. The critical minimum reduction in area required to avoid transverse cracking is discussed and determined. The relevance and limitations of the hot ductility test in assessing susceptibility to transverse cracking are outlined. The results are described in detail in Chapters 5 to 8:

- Chapter 5 – low carbon steels
- Chapter 6 – niobium steels
- Chapter 7 – aluminium-killed boron steels
- Chapter 8 – silicon-killed boron steels

In each results chapter, a similar format is followed. First, the calculated and modelled transformation and equilibrium precipitate dissolution temperatures for each steel are presented. Then the stress - elongation, maximum strength, reduction in area, total elongation, scanning electron microscopy and transmission electron microscopy, where relevant, and results for each steel are reported separately. The influences of cooling rate, strain rate and compositional changes on hot tensile behaviour are determined. Proposed mechanisms of hot tensile failure are given, with reference to literature. The relevance of this to the industrial problem of transverse surface cracking is discussed.

A hot ductility database compiled by the author is described in Chapter 9 and the results obtained from the database are illustrated by means of an example.

Conclusions drawn from the discussions in the Chapters 5 to 9 and recommendations for further work are presented in Chapters 10 and 11 respectively. References from literature are listed in Chapter 12. The Appendix contains the papers, abstracts and presentations discussed in Section 1.3.

Chapter 2: Literature Review

Overview of continuous casting, transverse cracking, hot ductility behaviour and laboratory testing

2.1 OVERVIEW OF CHAPTER 2

This chapter provides an overview of surface crack susceptibility during the continuous casting process. The influences of process variables such as casting speed and hot ductility behaviour on surface cracking are discussed. The metallurgical mechanisms of cracking and the influence of strain rate, cooling rate and steel composition on hot ductility are examined in detail. The various types of laboratory tests to determine hot ductility are then compared.

2.2 CONTINUOUS CASTING PROCESS

Since the early 1800s, the traditional method of ingot casting was used to convert liquid steel to a useable solid form. It was only in 1887 that R. M. Daelen (Daelen, 1890) envisaged a process where a stream of liquid steel would be poured vertically into an open-ended mould, passed through a secondary cooling system and withdrawn by pinch rolls prior to being cut by a torch device. This was the birth of the modern continuous casting process. In 1950, a production plant was commissioned at Mannesmann AG, and in 1951, a continuous billet casting plant was installed at Barrow Steel in Great Britain. Continuous casting of slab became a commercially viable alternative to ingot casting in the early 1960s, providing a product with consistent properties at higher production rates. By 1990, the continuous casting to ingot casting ratio for the western world had reached 85% (Irving, 1993).

The definitions of various as-cast sections in steel production are as follows:

- **Billets** small square sections up to 150 mm square, or round sections up to 150 mm diameter (Kumar *et al.*, 1997).
- **Blooms** square or rectangular cross-sections, larger than 150 mm square and smaller than 800 x 400 mm, with aspect ratios less than 2 (Anelli *et al.*, 1993).
- **Slabs** larger than blooms, usually with aspect ratios greater than 2 and less than 10. Typical dimensions are 1200 x 200 mm (Cicutti *et al.*, 1997).
- **Thin slabs** thinner than slabs with the as-cast thickness ranging from 20 – 90 mm. Aspect ratios are typically greater than 10 (Brimacombe *et al.*, 1997).

There are a number of different types of continuous casters in operation, but the basic process is the same: molten steel is transported to the continuous casting machine by a ladle and is then poured via a tundish into the caster. The caster consists of an oscillating, water-cooled copper mould, which can be straight or curved. The solidifying steel strand (slab, bloom or billet) is usually cast vertically. A lubricant, usually a synthetic casting powder, is used to form a slag on top of the liquid steel (Irving, 1993). Slag infiltrates the gap between the steel and mould at the meniscus to provide lubrication. The solidifying shell is withdrawn from the mould by driven pinch rolls further down in the machine. The

strand is cooled by means of water sprays, is then straightened (in the case of a curved mould) or bent (for a straight mould) by segments of rollers and is cut into the required lengths. The straightening operation occurs when the strand temperature is typically in the region of 700-1000°C (Mintz *et al.*, 1991).

In recent years, the curved mould machine has been widely used (De Toledo *et al.*, 1993). This enables the radius of curvature of the strand in such a machine to be 7-12 m, depending on the product thickness. A schematic diagram of a modern vertical slab casting machine is given in **Figure 2.1** (Irving, 1993).

In the metallurgical view of the continuous casting of steel, the liquid steel begins to solidify in the mould, forming a thin solid shell. Segregation of solute atoms and the formation of some precipitates occur in the solid steel on cooling. The cooling below the mould, known as secondary cooling, determines the extent and type of segregation and precipitation. The distance to the point of through-thickness solidification, known as the metallurgical length of the strand, is also largely determined by the secondary cooling. The strand should be completely solidified by the time it reaches the straightening zone to prevent internal cracking at the solid-liquid interface (Patrick *et al.*, 1992).

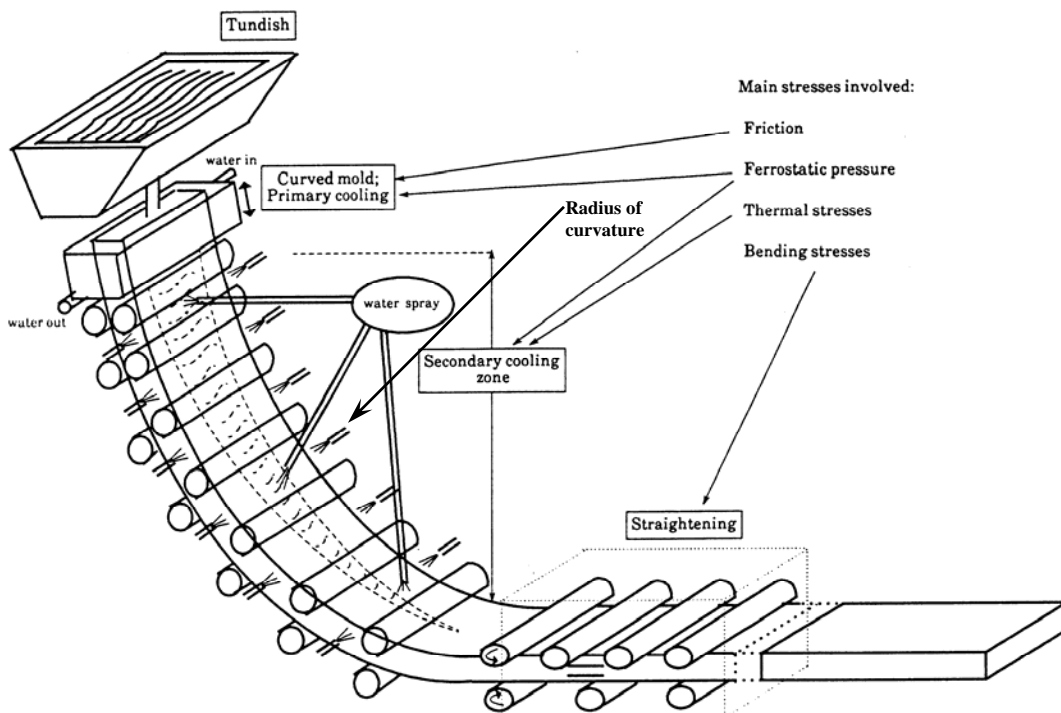


Figure 2.1: Curved mould, vertical continuous casting machine (Irving, 1993).

SMS Schloemann Siemag developed the first thin slab CSP[®] (Compact Strip Production) process, with Nucor Steel opening the first CSP[®] plant in 1989. There were 35 thin slab plants operational or planned in 2003 (Trippelsdorf *et al.*, 2003). Minimills with thin slab casters have become rivals to conventional (thick) slab casters, as thin slab casting is a more cost-effective process (less reheating and rolling).

In comparison to conventional slab casting, thin slab casting has more rapid solidification and faster cooling rates, which lead to less interdendritic segregation, a more refined as-cast structure, and finer precipitation of sulphides and oxides (Liu *et al.*, 2003). However, conventional slab casting has some steel quality advantages over thin slab casting in terms of cleanliness and mould powder entrapment (Trippelsdorf *et al.*, 2003).

2.3 CRACK SUSCEPTIBILITY IN CONTINUOUS CASTING

Cracks are of great concern in continuous casting. Internal cracks cause subsurface defects, which often only become evident during manufacturing of the final product. Shallow surface cracks require scarfing (surface grinding), while deep transverse facial and corner cracks lead to scrapping of the slab, which has a negative impact on profitability (Hassani and Yue, 1993). An entirely crack-free strand is a prerequisite for Hot Charge Rolling (HCR), Hot Direct Rolling (HDR) and for near-net shape processes such as Thin Slab Casting (TSC), as there is no possibility of detailed inspection or dressing of the strand between casting and hot rolling. **Figure 2.2** shows the International Iron and Steel Institute (IISI) categorization of the types of surface defects that can occur on continuously cast strand (IISI, 1985).

At temperatures from ~1200 °C to the solidus temperature, the presence of a liquid film in the interdendritic region can cause embrittlement (Suzuki *et al.*, 1982). Low strength and low ductility in this region is the cause of high temperature cracking, particularly longitudinal mid-face cracks (Hassani and Yue, 1993). However, liquid film embrittlement can extend to even lower temperatures if a low melting temperature phase is present.

Cracking occurs when the strand is subjected to thermal and mechanical strains, which induce stresses greater than the inherent material strength (Patrick, 1994). It has been shown by Hassani and Yue (1993) that transverse surface crack susceptibility in continuous casting relates directly to specific temperature regions of low hot ductility, depending on the chemical composition of the steel (discussed in **Section 2.6**). Deep oscillation marks act as stress raisers for crack initiation.

Transverse facial and corner cracking usually occur when the strand surface temperature drops into a ductility trough in the temperature region 700 to 1000 °C at any point in the spray chamber and at the straightening zone (Barber *et al.*, 1989). Ductility does not fully recover even if the surface reheats to above the ductility trough temperature. Cracking is strain-induced, occurring particularly at the straightening zone where the top surface of the strand is in tension (Brimacombe *et al.*, 1977).

The surface transverse cracks initiate in oscillation marks and propagate below the surface along austenite grain boundaries. The surface cracks are always filled with scale and show internal oxidation. Sub-surface, intergranular cracks caused by sulphide, nitride and carbonitride precipitates at the prior austenite grain boundaries, are neither oxidised nor related to oscillation marks (Turkdogan, 1987).

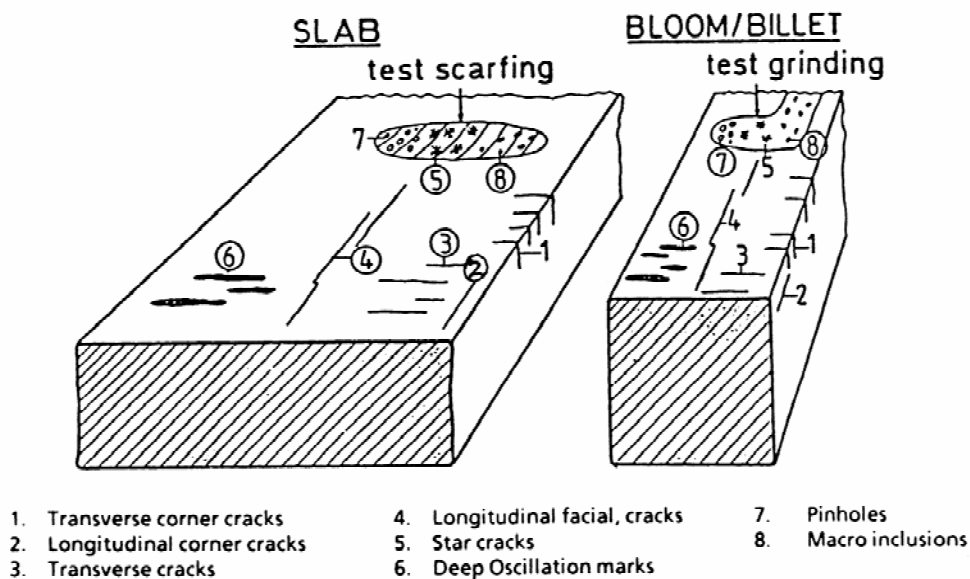


Figure 2.2: Surface defects on continuously cast strand (IISI, 1985).

2.4 INFLUENCE OF PROCESS VARIABLES ON SURFACE CRACKING

Process factors that influence surface transverse cracking during continuous casting are:

- Mould heat transfer
- Mould oscillation
- Secondary cooling and casting speed
- Straightening

2.4.1 Mould heat transfer

The strand surface structure and thermal stresses can vary greatly with variable heat transfer (Mahapatra *et al.*, 1985). A coarse-grained columnar layer near the strand surface caused by non-uniform solidification in the mould increases the risk of cracking.

The control of mould heat transfer can be improved (Irving, 1993) by:

- Optimizing the casting powders in terms of properties such as viscosity
- Ensuring consistent powder feeding
- Maintaining stable mould level control
- Reducing mould turbulence
- Optimizing mould taper to ensure good contact between slag layer and mould.

2.4.2 Mould oscillation

Mould oscillation causes transverse ripples (oscillation marks) on the strand surface. Patrick *et al.* (1994) showed that deep oscillation marks have the following effects:

- Aggravating cracks arising in the mould, secondary cooling zones and straightening zone by acting as stress raisers
- Increasing the local variation in heat transfer in the mould or sprays
- Promoting segregation of P, S and Mn below the oscillation mark, which present a preferred path for cracks.

Under specific conditions, cracks can initiate along the oscillation marks on the top surface and edges of the strand (Takeuchi *et al.*, 1997). The cracks propagate during strand straightening when the top surface and edges are in tension. The intergranular cracks are fine, and are able to penetrate along prior austenite grain boundaries to a depth of 5-8 mm below the surface. Scarfing is usually required to reveal and remove cracks and, in the case of edge cracks, the steel is rolled wider than required by the customer to allow for edge trimming. Both scarfing and edge trimming are time- and material-intensive and add to the cost of the finished product (Mintz *et al.*, 1991).

According to Patrick *et al.* (1994), the oscillation mark depth can be reduced by:

- Correct choice and application of mould powder
- Reducing negative strip time by increasing mould oscillation frequency or reducing stroke length
- Avoiding the peritectic carbon range (Maehara *et al.*, 1985)

2.4.3 Secondary cooling and casting speed

Many steels have an area of low ductility in the temperature range of ~700-1000°C. Once the ductility trough has been defined by laboratory testing, a secondary cooling strategy to avoid transverse cracking can be used. This is usually done by adjusting the casting speed and the water spray pattern, as described by Kuo *et al.* (1991), Nazaki *et al.* (1978) and Offerman (1997).

The two main types of cooling are known as *soft* and *hard* cooling. Soft cooling uses little water, often in an air-water mist spray, resulting in surface temperatures higher than the ductility trough at the straightener. Hard cooling uses maximum water to decrease the strand temperature to below 700 °C at the straightening zone. Blocked nozzles, excess water, static spray control or poor cooling design often cause problems with surface temperature control (Patrick *et al.*, 1994).

2.4.4 Straightening

Straightening leads primarily to transverse cracking on the slab upper face as a result of tensile strains (Patrick *et al.*, 1994). Strain rate is the factor that exerts the greatest influence on cracking during straightening. Lower strain rates promote grain boundary sliding, strain-induced precipitation and formation of deformation induced ferrite on the austenite grain boundaries, which cause deterioration of hot ductility (Maehara *et al.*, 1990). Multiple point unbending effectively reduces the average strain rate and can therefore have an adverse effect on hot ductility at lower temperatures such as 850-750 °C (Mintz, 1993), although it has been found to promote stress relaxation at higher temperatures such as ~1300 °C (Mintz *et al.*, 1991).

2.5 INFLUENCE OF HOT DUCTILITY BEHAVIOUR ON CRACKING

It has been found that the hot ductility behaviour of steel can be used as an indication of crack susceptibility in continuous casting, particularly for transverse cracking. The same variables that cause low ductility in the hot tensile test also cause transverse cracking. When serious cracking problems have been encountered, steel companies have used hot ductility information to either reduce or increase the temperature at the straightener (Mintz *et al.*, 1990).

2.5.1 Metallurgical mechanisms of cracking

There are three low ductility temperature zones that can occur in steel (Maehara *et al.*, 1990), as shown in **Figure 2.3**:

Zone I extends from around 1200 °C to the solidus temperature (onset of melting). Both strength and ductility decline markedly in this temperature region (Brimacombe *et al.*, 1977). The cause of embrittlement is the presence of liquid film in the interdendritic

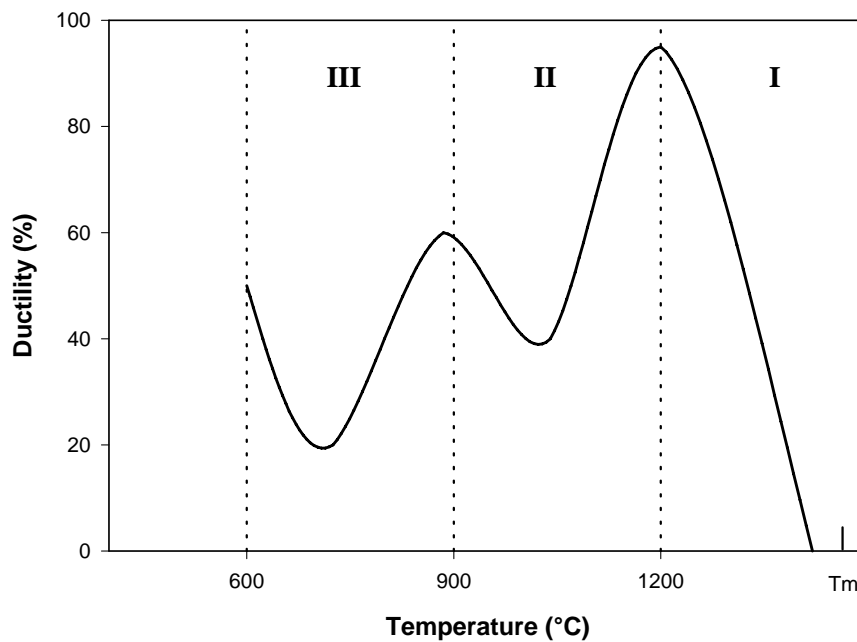


Figure 2.3: Schematic diagram showing the three low ductility temperature zones in steel. (Suzuki, 1982)

region, which does not freeze until temperatures well below solidus are reached (Adams, 1971; Fuchs, 1975). Hot tearing of the strand shell can occur due to strains in the mould or spray zones of the casting machine (Weinberg, 1979). The ductility is independent of strain rate and is mainly affected by the chemical composition, particularly microsegregation of elements such as carbon, sulphur and phosphorus (Hassani *et al.*, 1993). With the exception of transverse cracks, all surface cracks probably form in Zone I, the high temperature, low ductility region (Brimacombe and Sorimachi, 1977).

Zone II is found between 900 and 1200 °C. This zone is usually attributed to the fine intergranular precipitation of sulphides, oxides or oxy-sulphides at the austenite grain boundaries, leading to the formation of soft precipitate-free zones (PFZs) adjacent to the grain boundaries (Yue *et al.*, 1995), or to microvoid creation around the precipitates and subsequent microvoid coalescence. The PFZs are sites for strain concentration, which lead to failure at low strains in continuous casting (Suzuki *et al.*, 1982). Grain boundary sliding is also enhanced by particles at the austenite grain boundaries (Mintz *et al.*, 1991). It is generally accepted that a Mn:S ratio in excess of 50 will eliminate Zone II, so most

low sulphur continuously cast steels today will only exhibit the two ductility troughs I and III.

Zone III occurs in the low temperature austenite region, including the austenite to ferrite phase transformation *i.e.* from 700 °C to approximately 900 °C, depending on the steel composition (Cardoso and Yue, 1989). Ductility recovery corresponds to a large amount of α ferrite ($\geq 45\%$) present before deformation or α forming in large quantities during deformation close to the A_{e3} temperature (Mintz *et al.*, 1998). Just before the A_{r3} temperature, a large volume fraction of α is present before the test, allowing the strain to be dispersed. The ductility then recovers fully $\sim 20\text{-}30$ °C below the undeformed A_{r3} , which is ~ 745 °C for 0.10% C and ~ 710 °C for 0.16% C in plain C steels (Mintz, 1996). A fully ferritic structure shows good ductility because recovery occurs readily, the subgrain size is large and the flow stress is low. Zone III coincides with typical strand straightening temperatures during continuous casting. The origin of transverse surface or subsurface cracks has been attributed to tensile stresses applied by straightening rolls on material with poor ductility (Mintz *et al.*, 1991).

This low ductility zone is explained by four possible mechanisms:

- Grain boundary sliding (Yue *et al.*, 1995)
 - Precipitate free zones (PFZs) (Patrick *et al.*, 1994)
 - Formation of thin ferrite films on the austenite grain boundaries (Maehara *et al.*, 1990)
 - Suppression of austenite dynamic recrystallization, as detailed below (Yue *et al.*, 1995).
-
- **Grain boundary sliding** is defined as plastic deformation that is confined to the grain boundaries (Yue *et al.*, 1995). This mechanism is seen in austenite rather than ferrite, as austenite shows only limited dynamic recovery (Mintz *et al.*, 1991). Grain boundary fracture is initiated when stresses that are built up at grain boundary triple points exceed the stress required for grain boundary failure, as seen in **Figure 2.4**. This is considered to be the main deformation and fracture mechanism under conditions of creep *i.e.* for strain rates at and below 10^{-4} s⁻¹ (Yue *et al.*, 1995).

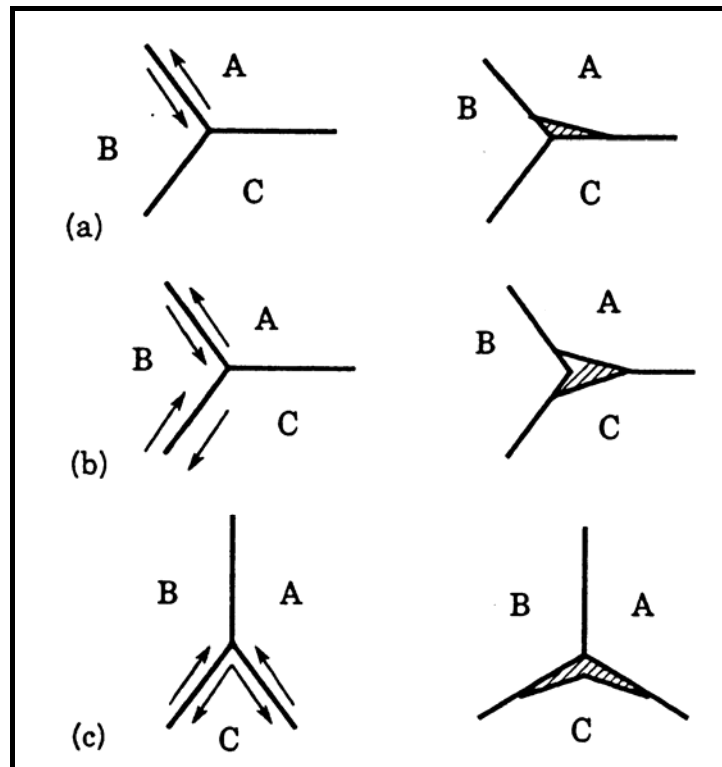


Figure 2.4: Schematic models showing formation of wedge cracks by grain boundary sliding. Arrows indicate sliding boundary and sense of translation (Yue *et al.*, 1995).

- Precipitate free zones (PFZs):** As previously discussed in **Section 2.4.4**, the straightening strain rates during continuous casting are low. Dynamic or strain-induced precipitation of Nb(C,N), AlN or V(C,N) occur at low strain rates and within a critical temperature range (Patrick and Ludlow, 1994). In the single-phase austenite region, precipitates form preferentially at the austenite grain boundaries. This leads to soft PFZs adjacent to the grain boundary, where strain is then concentrated during strand deformation. Microvoids are formed by decohesion of the precipitate-matrix interface during deformation, eventually resulting in void coalescence and crack propagation along the grain boundaries (intergranular fracture), as shown in **Figure 2.5 a-c** (Maehara *et al.*, 1990). Failure by this mechanism is primarily associated with fine precipitation on the grain boundaries (Turkdogan, 1987).

- Thin ferrite films:** On cooling, strain-induced ferrite can form at temperatures above the undeformed A_{r3} temperature (transformation start temperature at a constant cooling rate), even as high as the A_{e3} , the equilibrium transformation temperature of austenite to ferrite (Yue *et al.*, 1995). This ferrite forms as thin films along the austenite grain boundaries (Suzuki *et al.*, 1982). Ferrite has lower flow stresses than austenite at any temperature due to the higher recovery rate of ferrite. This leads to preferential strain concentration in the softer ferrite which, according to Cowley *et al.* (1998), causes decohesion at precipitates on the prior austenite grain boundaries (**Figure 2.5 d-f**). Thus, the ferrite acts in a similar manner to the PFZs described above (Yue *et al.*, 1995). Precipitates such as MnS are often found in the ferrite films. The ductility improves as the ferrite film thickens, reducing the strain concentration at the grain boundaries.

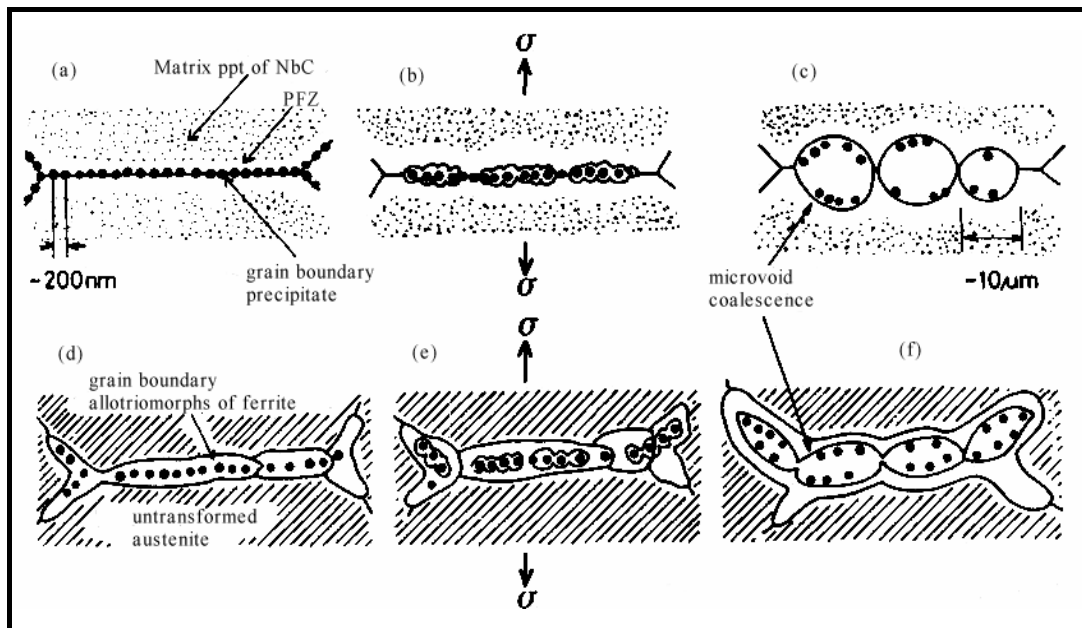


Figure 2.5: Schematic illustrations showing intergranular microvoid coalescence by deformation in the low temperature austenite region (a-c) and in the two-phase γ - α region (d-f) (Maehara *et al.*, 1990).

- **Suppression of dynamic recrystallization in austenite** occurs due to grain boundary precipitation of fine carbides or nitrides during deformation, known as dynamic precipitation (Wilcox and Honeycombe, 1987). Grain boundary mobility is reduced, leading to growth of voids around the precipitates, thus facilitating intergranular crack propagation, even in a fully austenitic microstructure (Turkdogan, 1987). This mechanism is usually associated with HSLA (high strength low alloy) steels, as shown in **Figure 2.6**. Initially, near-continuous precipitation of particles such as $M_{23}C_6$ and $Nb(C,N)$ occurs on the austenite grain boundaries (**Figure 2.6 a**) then microvoids form (**Figure 2.6 b**), followed by coalescence of the microvoids (**Figure 2.6 c**). Mintz and Arrowsmith (1979) found that slabs which gave no plate rejections due to cracking had a coarse distribution of niobium carbonitride $Nb(C,N)$ at the austenite grain boundaries; whereas slabs rejected for cracks had fine grain boundary precipitates. The observed particle size effect on hot ductility is related to the particle size effect on grain boundary mobility: coarser particles with a larger interparticle spacing are less detrimental to grain boundary mobility and hot ductility than fine, densely-spaced particles (Turkdogan, 1987).

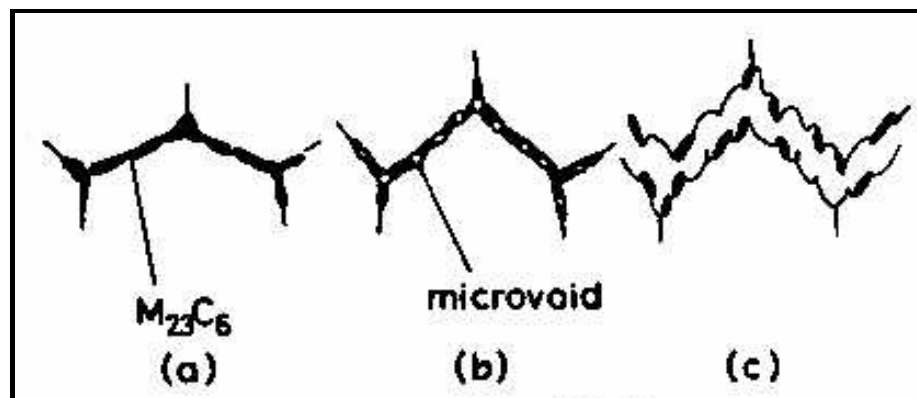


Figure 2.6: Intergranular failure by suppression of recrystallization in austenite (Maehara *et al.*, 1990).

- a) Almost continuous precipitation of $M_{23}C_6$ particles.**
- b) Microvoid formation around $M_{23}C_6$ particles.**
- c) Coalescence of microvoids.**

2.5.2 Strain rate

Decreasing the strain rate decreases the maximum strength (S_u) by the following mechanisms:

- A longer time for grain boundary sliding as well as for the austenite and ferrite to recover and remain soft during deformation (Mintz and Jonas, 1994)
- In the γ region, the ability of screw dislocations to cross-slip increases, promoting dynamic recovery (Michalak, 1991)
- Deformation-induced ferrite forms more easily on straining, as there is more time available for transformation (Mintz *et al.*, 1991)
- The transformed α is able to recover more readily and the S_u is substantially lower than that of γ (Mintz and Jonas, 1994).

It has been found that the reasons for decreased ductility with decrease in strain rate are:

- Increased time for strain-induced precipitation, as deformation is still occurring when the incubation time for dynamic precipitation has been reached (Mintz *et al.*, 1991)
- The amount of grain boundary sliding increases (Ouchi *et al.*, 1982)
- There is increased time for the formation and diffusion-controlled growth of voids next to the precipitates at grain boundaries (Mintz *et al.*, 1990)
- Strain is concentrated in the ferrite films, which recover and remain soft at lower strain rate (Lewis *et al.*, 1998).

2.5.3 Cooling rate

In **low carbon steels**, Abushosha (1998a, 1998b) found that a decrease in cooling rate resulted in:

- Coarser MnS precipitate distribution in the ferrite surrounding the austenite grains, which decreased the ease of microvoid coalescence.
- Wider ferrite films, which decreased the strain concentration; both favouring transgranular failure and improving hot ductility.

In **niobium microalloyed steels**, the improvement in hot ductility with decrease in cooling rate has been found to be as a result of favoured static precipitation on cooling (Abushosha, 1998b). This removes Nb, N and C from solution before the finer Nb(C,N) can form dynamically on dislocations during straining (Mintz et al., 1991). These fine precipitates lead to worse hot ductility. Weiss and Jonas (1979) showed that in a solution-treated Nb steel, dynamic precipitation at 900 °C started after 1 second and was complete after 2 minutes.

Boron steels: Yamamoto *et al.* (1987) reported that the embrittlement zone disappeared completely at an average cooling rate of 0.1 °C.s⁻¹ and strain rate of 0.5 s⁻¹ in a steel containing 0.14% C, 1.20% Mn, 0.06% V, 0.0011% B and 0.0041% N. They showed that a decrease in cooling rate from 20 – 0.1 °C.s⁻¹ moved BN precipitation from γ grain boundaries to the matrix, where BN precipitated on MnS nuclei. This coarsened the B-containing precipitates, rendering them ineffective to influence hot ductility.

Chung and Cho (1993) studied the hot ductility of 0.0012 - 0.0029% B addition to a 0.2% C - 0.6% Mn - 0.02% Al - 0.005% N steel between 650 - 850 °C. They showed that hot ductility was improved by decreasing the cooling rate from 40 to 10 °C.s⁻¹ due to lower occupation of BN precipitates on the grain boundary. Suzuki *et al.* (1983) found that the embrittlement temperature zone extended over ~60 °C for an average cooling rate from the melting point to 900 °C of 1.0 °C.s⁻¹ (steel containing 0.0015% B and 0.0060% N).

2.5.4 Solution treatment temperature and time

The austenite grain size is increased by an increase in solution treatment time (Pickering, 1978; and Uhm *et al.* 2004) and by an increase in solution treatment temperature (Yue *et al.* 1995), especially if the temperature is above the dissolution temperatures of precipitates that may cause pinning of grain boundaries (Gladman, 1997; Bhadeshia and Honeycombe, 2006).

The dependence of grain size on time and temperature is given by the following relationship:

$$D^{1/n} - D_0^{1/n} = K \cdot t \quad (2.1)$$

where the constant $K = A \cdot \exp\left(\frac{-Q_{gg}}{RT}\right)$

D is an average final grain diameter, D_0 is the initial grain size at time $t = 0$ s, n is the time exponent, A is a constant, Q_{gg} is the activation energy for grain growth, R is the universal gas constant, T is the temperature in Kelvin and t is the solution treatment time. Constant n depends on the alloy composition and processing conditions. The value of n appears to approach 0.5 as an upper limit with increasing temperature (Guy and Hren, 1974). The grain growth occurring with increasing time at constant temperature is small compared to that occurring with increasing temperature at constant time.

Intergranular fracture is easier with a coarser grain size, as the crack aspect ratio increases, which increases the stress concentration at the crack tip. Also, for a given volume fraction of precipitates, a decrease in the grain boundary area per unit volume, *i.e.* a coarser grain size, will increase the number of precipitates per unit area of grain boundary, thus having a more detrimental effect on hot ductility (Fu *et al.*, 1988).

2.5.5 Thermal oscillations

Mintz *et al.* (1987) showed that oscillated cooling, as found in industrial continuous casting from roll to inter-roll regions, is detrimental to hot ductility. Increased oscillation amplitude increases the width and depth of the hot ductility trough (El-Wazri *et al.*, 1998a). Also, when the strand temperature falls below the $\gamma \rightarrow \alpha$ transformation temperature, precipitation of nitrides and carbonitrides in niobium microalloyed steels is enhanced due to the lower solubility of Nb(C,N) in α than in γ , which again decreases the ductility (El-Wazri *et al.*, 1998b).

Cardoso and Yue (1989) found that the hot ductility decreases if the temperature drops below the final testing temperature due to the increase in precipitation rate and decrease in precipitate size.

2.5.6 Steel composition

Various elements have a specific detrimental impact on hot ductility, particularly when combined with high levels of other elements *e.g.* Nb, C and N, which can form precipitates on the austenite grain boundaries. **Table 2.1** lists the elements that are accepted to have the largest influences, although there are also contradicting reports of the effects of some of these elements. In a number of cases, the noted effects on hot ductility are specific to the composition of the steels and the specific testing procedure used in the investigation. For example, the effect of increasing sulphur content may not be as severe in high carbon steel as in low carbon steel (Patrick *et al.*, 1994).

Low carbon steels

- **Carbon**

Peritectic steels are generally defined as having carbon contents of ~0.10 - 0.17% C, but this varies depending on the author (Wolff, 1997). Peritectic steels are well known for their tendency to crack during continuous casting (Walmag *et al.*, 2002) and are more difficult to cast than others (Wolf, 1997). The higher susceptibility of the peritectic steels to cracking is induced by the uneven solidification and high shrinkage of the strand shell in the mould, influenced by the delta ferrite to austenite transformation. This causes uneven meniscus shell growth (Pierer and Bernhard, 2006) and deeper oscillation marks on the strand surface than in other carbon steels (Wolf, 1997). In addition, coarser austenite grains form in these peritectic steels, which are also detrimental to hot ductility (Mintz, 1991).

Including the influence of other alloying additions such as Ni, Mn and Si, the *carbon equivalent for the peritectic reaction* (c_p) can be used to classify steels by their solidification behaviour:

- Hypoperitectic $c_p < 0.10\%$
- Peritectic $0.10\% < c_p < 0.17\%$
- Hyperperitectic $0.17\% < c_p < 0.51\%$

c_p in low alloy steels is defined according to Howe (1991) as:

$$c_p = [\%C] + 0.04 [\%Mn] + 0.1 [Ni] - 0.14 [\%Si] \quad (2.2)$$

where the %C, Mn, Ni and Si are in mass %.

The austenite stabilising elements are added to, and the ferrite forming elements are subtracted from, the carbon content. Wolf (1991) has proposed the following average values, developed by examining plant data of crack occurrences:

$$c_p = [\%C] + 0.02 [\%Mn] + 0.4 [Ni] - 0.1 [\%Si] - 0.04 [\%Cr] - 0.1 [\%Mo] \quad (2.3)$$

For validation, this equation was also tested against the *ferrite potential* (FP):

$$FP = 2.5 (0.5 - [\%c_p]) \quad (2.4)$$

Steels with $FP > 1.0$ are hypoperitectic, $FP < 0$ (*i.e.* negative) are hyperperitectic and the peritectic range extends between $0 < FP < 1.0$.

- **Mn:S ratio**

A low Mn:S ratio increases the tendency to form iron-rich sulphides, which are detrimental to hot ductility. Sulphur segregates more strongly to grain boundaries than manganese due to the large difference in misfit strain energy (McLean, 1957). At 1090 °C the mobility of S is 1000 times higher than that of Mn (Seibel, 1964). Upon rapid cooling from 1400 – 1090 °C (below the solubility limit of S in pure Fe), metastable FeS will precipitate at grain boundaries due to the availability of iron (Lankford, 1972). With slower cooling rates, Mn has time to diffuse to the grain boundaries, and the precipitates will be Mn-enriched. Nagasaki and Kihara (1999) found that FeS on the grain boundaries ranged in size from less than 30 nm to ~100nm. Voids are initiated due to the incoherence of FeS with the matrix, as FeS has a hexagonal close packed structure.

Suzuki (1982) found that that during cooling after solidification, in the temperature region 900-1150 °C, supersaturated S or O precipitates as (Fe, Mn)O or (Fe, Mn)S along the γ grain boundaries. Even Mn(O)S can form as a liquid below 1150 °C (Lankford, 1972). Voids nucleate along these precipitates and fine precipitation enhances intergranular embrittlement.

Wilber (1975) proposed that an eutectic FeS phase with a low melting point (~900 °C) forms as a liquid grain boundary film, thus causing intergranular failure by incipient melting. Sridhar (1999) found that the melting point of (Fe,Mn)S was 915-940 °C, which is lower than the invariant ternary peritectic temperature of 997 °C, and thus these precipitates included other impurities. Salter (1979) showed that, at sulphur levels of 0.25% S, FeS was still present at a Mn:S ratio of 1.4, but not at a Mn:S ratio of 2.8. Kiessling and Lange (1966) determined that the melting point of the FeO-FeS eutectic is ~940 °C.

Hot shortness in the presence of oxygen can occur, as low melting phases with FeS, FeO and often silicates can be formed in eutectics with melting points down to 900 °C. They also stated that there is extensive solubility of FeS in MnS, requiring a minimum Mn:S ratio of 4 to replace FeS by the higher melting MnS.

De Toledo *et al.* (1993) studied the influence of S and Mn:S ratio on crack susceptibility and hot ductility of steels. They theoretically demonstrated that there is a critical value of the (Mn:S) ratio, $(Mn:S)_c$ below which a high susceptibility to cracking, during casting or deformation of as-cast material, is expected. The value of $(Mn:S)_c$ increases as the S content of the steel decreases and below the $(Mn:S)_c$, the defect index showed a sharp increase. In a low sulphur steel (0.030% S) the critical Mn:S ratio was found to be $(Mn:S)_c = 40$, and in a high sulphur steel (0.300% S) the critical Mn:S ratio was found to be $(Mn:S)_c = 3.5$. Based on experimental data, an expression for the critical Mn:S ratio was deduced:

$$(Mn:S)_c = 1.345 S^{-0.7934} \quad (2.5)$$

where S is the mass % of sulphur in the steel.

Wintz *et al.* (1995) developed a model to predict the FeS content of (Mn, Fe)S sulphides in plain carbon steels. They found that for sulphur contents of 0.015 - 0.025% S, the FeS content of the sulphides was ~5 % throughout solidification for a Mn:S ratio of 20-50. When the Mn:S = 12, the FeS content is higher, increasing from ~19% at the start of sulphide precipitation, to ~37% at the end of solidification.

- **Copper**

Copper is detrimental to hot ductility under certain conditions. The melting point of pure Cu is 1085 °C, so most Cu-rich phases will be molten at reheating temperatures of 1300 °C. Copper is known to penetrate grain boundaries, leading to surface cracks in hot rolling, also called hot shortness. In hot ductility testing, Cu has been found to have no effect on hot ductility under a protective atmosphere, such as argon, whereas testing in air decreases the hot ductility due to the formation of fine copper (oxy) sulphides (Mintz *et al.*, 1995):



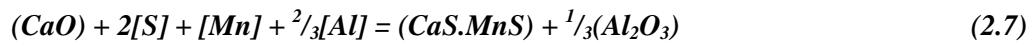
The precipitation of copper sulphide uniquely in welds, first identified by Harbottle in 1982, is thought to arise from the high temperature oxidising environment experienced during welding. This favours the formation of Cu_{1.8}S (digenite) in the presence of soluble copper from the less stable FeS commonly found in sulphur-bearing steels (Harbottle and Fischer, 1982). With the advent of thin slab casting, much attention has been given recently to the formation of copper sulphide in low carbon steels, in the form of Cu₂S (Liu *et al.* 2003).

There is little information for copper sulphide solubility in steel, but Shimazu (1985) has defined the solubility of Cu₂S in silicon-killed steel (**Table 2.2**). Lee *et al.* (2007) predicted that the Cu₂S phase is thermodynamically unstable, and can precipitate when the thermodynamic equilibrium state is not reached during the steelmaking process. The melting point of Cu₂S is 1127 °C (WebElements, 2007) indicating that Cu₂S is molten at the solution treatment temperature (1300 °C) and can thus re-precipitate on cooling.

Liu *et al.* (2004) and Kobayashi and Nagai (2005) found that very rapid solidification in strip casting (as-cast thickness = 2.2 mm) produces extremely fine Cu_{2-x}S precipitates ~15nm diameter. Four kinds of copper sulphide with different morphologies were observed: duplex oxide-sulphides based on manganese silicate (Mn₂SiO₄) with (Mn, Fe, Cu)S; plate-like copper sulphide (Cu_{2-x}S); shell-like copper sulphide (Cu_{2-x}S) and nano-sized Cu₂S (Liu *et al.*, 2006). Comineli *et al.* (2003) found 100-200 nm diameter copper sulphide precipitates in low carbon steels tested under argon, whereas Mintz *et al.* (1995) had only observed CuS precipitates in steels tested under oxidising conditions.

- **Calcium**

Calcium addition, also known as calcium modification, improves hot ductility in steels. The beneficial effect is achieved via a reduction in free S in the steel by the formation of CaMnS during steelmaking, which decreases the volume fraction of sulphides precipitated in the interdendritic regions and on γ grain boundaries (Mintz *et al.*, 1989a). In Al-killed low S steels, Mn and S are combined with Ca to form large CaS.MnS - type precipitates by the reaction:



Treatment of liquid steel with calcium has become an important means of deoxidation ($CaO + S = CaS + O$) and, more importantly, desulphurisation to very low levels. Equally significant is the now routine use of calcium to control the shape, size and distribution of oxide and sulphide inclusions (Turkdogan 1996). No matter what addition technique is used, however, calcium will have two beneficial effects: it will reduce the total number of inclusions remaining in the steel - sulphur, for example, can be brought down to 0.001-0.003% S with a little extra care and down to 0.007% S in routine practice - and it will modify the shape of the remaining inclusions into one that is less detrimental to mechanical properties in the final product (Shieldalloy, 2002).

- **Nickel**

Nickel has a beneficial effect on hot ductility, as it stabilizes austenite and increases the solubility of Cu in austenite, thus decreasing the precipitation of Cu sulphides (Suzuki, 1997). A Ni:Cu ratio of 1.5-2.0:1 is required to increase the solubility of copper in austenite to prevent hot shortness (Mintz *et al.*, 1995). Fisher (1969) found that a Ni:Cu = 1 balances the detrimental effect of Cu by promoting internal oxidation and subscale occlusion, thus removing Cu from solution.

Mintz *et al.* (2004) showed that in a steel with 0.5% Cu, the addition of 0.3-0.49% Ni prevents precipitation of fine copper sulphides, but the mechanism of this was not discussed. Imai (1997) also found that 0.3% Ni added to a steel containing 0.3% Cu suppressed surface cracking.

- **Silicon**

Silicon addition may also improve hot ductility in Cu-bearing steel by internal oxidation of Cu into larger oxidized particles (Seo *et al.*, 1997).

- **Phosphorus**

Phosphorus is likely to improve hot ductility of continuously cast strand, provided segregation is reduced (Mintz, 1999). P is also known to enhance the oxidation rate of iron at 1000 °C, which could decrease the formation of iron sulphides (Seo *et al.*, 1997). Phosphorus also refines the austenite grain structure (γ grain size is halved by addition of 0.20% P) and promotes dispersion of Mn in the interdendritic region, both which improve hot ductility (Yoshida *et al.* 2003).

- **Aluminium**

Aluminium is added to low carbon steels during steelmaking to remove oxygen from solution by forming alumina inclusions. These aluminium-killed steels show improved strain-ageing resistance and enhanced deep drawability by the formation of AlN precipitates (Wilson and Gladman, 1998). Aluminium nitride nucleates with difficulty in steel and does not precipitate readily in austenite, unless precipitation is enhanced by thermal or mechanical treatments. The rate of diffusion of aluminium, and hence the rate of precipitation of AlN, is significantly higher in ferrite than in austenite. Precipitation of AlN is very sensitive to cooling rate and can be suppressed entirely at cooling rates greater than ~ 1 °C per second.

Increasing aluminium content of steel causes a progressive drop in hot ductility, especially below 900 °C. AlN precipitates at the austenite grain boundaries. At low strain rates, fine AlN precipitates at the grain boundaries provide initiation sites for void nucleation and hinder grain boundary mobility. Cavities that nucleate can continue to grow at pinned grain boundaries, leading to void coalescence and ultimate intergranular failure. At 1100 °C, AlN precipitates are too coarse (1-2 μm) to impede grain boundary movement, and the hot ductility is unimpaired (Wilson and Gladman, 1998).

At commercial levels of Al and N (0.02 – 0.04% Al and 0.005% N) aluminium has been found to have no influence on the hot ductility for samples solution treated and cooled to the test temperature (Hannerz *et al.*, 1985 and Vodopivec *et al.*, 1987).

Niobium steels

In Nb-microalloyed HSLA (high strength low alloy) steels, the low hot ductility associated with intergranular fracture is caused by either suppression of dynamic recrystallization or by formation of PFZs.

- **Carbon**

In C-Mn-Nb-Al steels with $\leq 0.03\%$ Nb, C has little influence on the position of the hot ductility trough, except at $\leq 0.05\%$ C, when both the width and depth of the trough are reduced *i.e.* an improvement in ductility (Mintz *et al.*, 1989b). This is because of the overriding influence of Nb(C,N) precipitation in austenite: a decrease in carbon content decreases the volume fraction of Nb carbonitride precipitates. For a steel with 0.03% Nb and $\geq 0.05\%$ C, there is little further increase in the volume fraction precipitated, and the hot ductility will be insensitive to C level.

- **Niobium**

Increasing the niobium content in the range 0 – 0.08% Nb deteriorates the hot ductility by increasing the precipitation of Nb(C,N) on the austenite grain boundaries (Ouchi and Matsumoto, 1982).

- **Nitrogen**

Higher N levels give rise to worse ductility (Mintz and Arrowsmith, 1979). The amount of Nb carbonitride precipitated at a given temperature depends on the amount of N, but to a lesser extent than C (Mintz *et al.*, 1989b).

- **Sulphur**

Initiation of microvoids by decohesion of grain boundary precipitates from the matrix occurs by segregation of impurity atoms such as sulphur on the precipitate/matrix interfaces (Maehara *et al.*, 1991). Ductility loss resulting from precipitation of carbides or nitrides can be reduced significantly by a decrease in S content (Maehara *et al.*, 1990).

- **Calcium**

Calcium improves hot ductility in Nb microalloyed steels. This is achieved by a reduction in free S in the steel, by the formation of CaS (Mintz *et al.*, 1989a).

Boron steels

There are three main types of precipitates that can form in boron-containing low alloy steels: BN, Fe₂₃(CB)₆ and Fe(CB)₃. Little work has been done on the influence of boron on hot ductility in steels. The following references to literature were found after extensive research by the author.

Low carbon steel for drawing and cold heading applications should have low strength, high ductility and low strain ageing rates. To achieve these properties, nitrogen must be removed from solid solution. Boratto *et al.* (1993) showed that the B:N ratio must be above 0.8, *i.e.* above stoichiometry, to remove all nitrogen from solid solution.

Cho and Kim (2004) demonstrated the influence of boron addition to room temperature mechanical properties of hot rolled low carbon steel: lowered yield strength and increased total elongation. This is due to the scavenging effect of B on N, by removing the N from solid solution to form coarse BN precipitates that nucleate in the matrix on CuS or MnS precipitates.

Yamamoto *et al.* (1987) found that poor ductility occurred between 700 – 900 °C in peritectic steels with boron contents below 0.0020% B. Facial cracking on the surface of continuously cast slabs resulted from intergranular cracking due to precipitation of BN on austenite grain boundaries. The authors found that it is possible to prevent transverse

facial cracking in low carbon steels containing boron, when the nitrogen content available to react with boron is reduced by the following equation:

$$(N_t - 0.2 \cdot Ti) < 0.003 \% \quad (2.8)$$

where N_t is the total nitrogen content (mass %) and Ti is the mass % titanium.

However, it was noted that reducing the nitrogen content alone did not entirely eliminate the cracking problem. Maintaining the cooling rate at less than $0.5 \text{ }^\circ\text{C s}^{-1}$ in the secondary cooling zone (*i.e.* when slab is under water sprays) precipitated coarse BN in the matrix, which had a positive influence on the hot ductility.

Wilson and Gladman (1988) stated that aluminium addition is used in steelmaking to protect boron additions *i.e.* to form AlN instead of BN, thus leaving B available for hardenability. Although BN is thermodynamically less stable than AlN, BN is less soluble in austenite than AlN. Due to the high diffusion rate of B in austenite, which approaches that of N, BN usually precipitates in preference to AlN. The precipitation of BN in austenite is very rapid.

Luo *et al.* (2001) investigated the influence of boron on the hot ductility of 0.2%C – 1%Mn – 0.03%Al – 1.0%Cr steel between 700 – 1000 °C. They found that the addition of 0.0037% B improved the hot ductility by either precipitation of Fe(CB)₃ below 980 °C, or by segregation of solute B atoms to vacancies on the austenite grain boundaries, thus reducing the formation and propagation of cracks on the grain boundaries.

Marique and Messien (1990) investigated the crack susceptibility of extra-mild boron steel billets during the commissioning phase of industrial production. They recommended a minimum for the boron to nitrogen ratio ($B:N \geq 0.8$), reducing the total nitrogen content ($\%N < 0.0060$) and keeping a constant manganese to sulphur ratio ($Mn:S > 30$).

The hot ductility of 0.0012 – 0.0029% B addition to a 0.2% C – 0.6% Mn – 0.23% Si – 0.02% Al – 0.005% N steel was studied by Chung and Cho (1993). They concentrated on the effects of cooling rate (10, 20 and $40 \text{ }^\circ\text{C s}^{-1}$) and strain rate ($10^{-1} - 10^{-3} \text{ s}^{-1}$) on the hot ductility between 650 – 850 °C. They showed that hot ductility was improved by decreasing the cooling rate (lower occupation of precipitates on the grain boundary) and

by increasing the strain rate (deformation mechanism changes from grain boundary sliding to grain deformation).

Tanino (1983) showed that boron has a tendency to segregate to high angle grain boundaries, which also suggested that B will also tend to segregate to interfaces of incoherent particles such as MnS, FeS and Al₂O₃. This leads to the formation of complex [MnS + BN] precipitates, in which a spherical MnS precipitate is surrounded by polycrystalline aggregates of hexagonal BN.

Song *et al.* (2003) investigated the effect of boron (0.00075 - 0.0035% B) on hot ductility of a 2.25Cr1Mo (0.12% C – 0.5% Mn – 0.25% Si – 0.016% Al) steel. They found that increasing boron content shifted the ductility trough to lower temperatures (~950-800 °C) and the trough became narrower and shallower. They proposed that the addition of boron may retard the formation of pro-eutectoid ferrite and increase grain boundary cohesion in the austenite region.

It has been shown that steels with 0.001% B, have poor hot ductility (23-39 % reduction in area, *R. A.*, in the temperature range 900-1300 °C). Steels with 0.0029 % B. show improved hot ductility over the samples without boron at temperatures between 1100 - 1300 °C (Wenying *et al.*, 2006).

Wolańska *et al.* (2007) investigated the hot ductility of a low carbon boron steel (0.10% C – 0.47% Mn – 0.08% Si – 0.023% S – 0.17% Cu – 0.0060% B – 0.0090% N). They found that increasing the strain rate from 0.01 to 6.5 s⁻¹ greatly improved the hot ductility. The minimum %*R.A.* increased from 30 to 65% and the width of the ductility trough at 65% *R.A.* narrowed from ~350 °C to ~10 °C.

In recent work, López-Chipres *et al.* (2007) commented that the effect of boron on hot ductility in the austenite single-phase region has not yet been studied in depth. They showed that increasing the boron content in a low carbon steel (0.04% C – 1.4% Mn – 0.002% Al – 0.008% N) from 0.0029 - 0.0105% B *i.e.* B:N of 0.36 to 1.31, improved the ductility by up to 25% at all temperatures between 700-1000 °C. They proposed that the improved ductility with increased boron content was associated with enhanced grain boundary cohesion and an easier flow in the austenite lattice.

2.6 DETERMINING THE PRECIPITATION AND TRANSFORMATION TEMPERATURES IN STEEL

The influence of precipitation and transformation on hot ductility of steel is well documented in literature. Transverse cracks on the surface of continuously cast strand are caused by formation of fine precipitates, such as sulphides, nitrides or carbonitrides, or a thin ferrite layer at the prior austenite grain boundaries. This is usually indicated by the hot ductility trough from tension testing, which can occur over a wide temperature range such as 700-1000°C.

The equilibrium equations for the solubility of carbides and nitrides in iron (**Table 2.2**), could give an indication of precipitation temperatures on cooling in the hot ductility test, and hence, be applied to the continuous casting process. These equations could be used to predict the onset temperature of the hot ductility trough in steels that show fine precipitation.

Equilibrium precipitation occurs only in the isothermal treatment of steel after long treatment times and precipitation on cooling occurs only under very low cooling rates. However, strain-induced precipitation can occur at low strain rates and higher cooling rates. In continuous casting, the strain exerted on the surface of the strand during bending is sufficiently high to initiate precipitation of carbides and nitrides.

The solubility of sulphur in iron in the austenite temperature range (Gladman, 1997) is given by the following equation:

$$K = \frac{[\%Mn] \cdot [\%S] \cdot f_S^{Mn}}{a_{MnS}} \quad (2.9)$$

The activity a_{MnS} can be regarded as unity.

In the manganese content range 0.37–1.30% Mn and in the temperature range 1200–1435 °C, f_S^{Mn} has been experimentally determined to be:

$$\log f_S^{Mn} = \left(-\frac{215}{T} + 0.097 \right) \cdot [\%Mn] \quad (2.10)$$

Similarly, knowledge of the equilibrium (isothermal) phase transformation temperatures (Ae_3) could give an indication of a lower temperature hot ductility trough, or widening of the trough initiated at higher temperatures by precipitation. Equations relating steel composition to these calculated transformation temperatures are shown in **Table 2.3**.

Additionally, melting temperatures of precipitates such as FeS and CuS are also critical in determining hot ductility.

Table 2.1: Effect of steel composition on transverse surface cracking.

From Mintz (1991 and 1989a); Patrick (1994); Wolf (1981); McPherson (1997) and Turkdogan (1996).

Carbon	Transverse cracking is increased in the peritectic composition region (0.10-0.15% C) which coincides with maximum oscillation mark depth. Peritectic steels show the most shrinkage upon solidification (at a maximum around 0.11% C), which leads to uneven heat removal from the solidifying steel shell, hence irregular shell growth, creating stress raisers in the steel surface, which in tension increases the susceptibility to cracking. The peritectic steels are also more prone to intergranular fracture, as a result of large as-cast austenite grain size.
Aluminium	Total Al levels above 0.035% increase cracking by widening the low ductility region, specifically by extending the trough to higher temperatures. In the presence of nitrogen the aluminium precipitates as AlN. Increasing the amount of AlN also widens the ductility trough. Al levels of more than 0.035% can be used if the nitrogen content is kept to less than 40 ppm. The detrimental effect of Al is aggravated by the addition of niobium.
Niobium	Niobium precipitates as niobium carbide, nitride or carbonitride, depending on the steel composition. An increase in niobium content both widens and deepens the ductility trough.
Vanadium	Vanadium causes transverse cracking at high nitrogen levels (90-120 ppm), but below 50 ppm N, V has little effect. Vanadium has less effect on ductility than Nb, as V precipitates are coarser and more random.
Nitrogen	Nitrogen content controls the extent of transverse cracking in Al-killed and microalloyed steels. The ductility trough is widened and deepened by increasing nitrogen. Cracking is minimized at nitrogen levels below 40 ppm, and problems are experienced in high nitrogen steels with 120-150 ppm nitrogen.
Nickel	Nickel reduces the intergranular ferrite film thickness as it is an austenite stabilizer. Nickel reduces the solubility of nitrogen in austenite, which increases the formation of AlN precipitates thus reducing ductility.
Copper	Copper causes deterioration in ductility, by increasing the ferrite film thickness at the austenite grain boundaries. Cu also increases the extent of sulphide precipitation.
Titanium	Transverse cracking is reduced by addition of 0.015-0.04% Ti, by forming coarse TiN, reducing the formation of fine AlN and Nb(C,N) precipitates.
Boron	Boron additions reduce transverse cracking especially in the presence of titanium. The high affinity of nitrogen for boron results in the preferential precipitation of boron nitrides, which reduces the formation of other nitrides.
Sulphur	Reducing the S reduces the incidence of transverse cracking. Manganese sulphides are associated with intergranular fracture in the low temperature austenite range, particularly when the Mn/S ratio is less than 20.
Phosphorus	Raising the P level in the range 0.005-0.015% improves hot ductility.
Calcium	Ca modification, improves hot ductility in steels: reduction in free S in the steel, formation of CaMnS, decreases the amount of sulphides precipitated in the interdendritic regions and on γ grain boundaries. Sulphide shape control, MnS precipitation is suppressed. In Al-killed low S steels, Mn, S and Ca form large CaS.MnS precipitates.

Table 2.2: Equilibrium solubility equations for carbides and nitrides in austenite.

<u>Turkdogan (1987):</u>	
$\log K_{\gamma} [Al] \cdot [N] = -\frac{6770}{T} + 1.03$	<p>where:</p> <p>K_{γ} Equilibrium solubility product in austenite</p> <p>$[X]$ mass % of element dissolved in steel</p> <p>$[]^y$ mass ratio of elements in precipitate</p> <p>T Temperature (K)</p>
$\log K_{\gamma} [B] \cdot [N] = -\frac{13970}{T} + 5.24$	
$\log K_{\gamma} [Nb] \cdot [N] = -\frac{10150}{T} + 3.79$	
$\log K_{\gamma} [Nb] \cdot [C]^{0.87} = -\frac{7020}{T} + 2.81$	
$\log K_{\gamma} [Nb] \cdot [C]^{0.7} \cdot [N]^{0.2} = -\frac{9450}{T} + 4.12$	
$\log K_{\gamma} [Ti] \cdot [N] = -\frac{15790}{T} + 5.40$	
$\log K_{\gamma} [Ti] \cdot [C] = -\frac{7000}{T} + 2.75$	
$\log K_{\gamma} [V] \cdot [N] = -\frac{7700}{T} + 2.86$	
$\log K_{\gamma} [V] \cdot [C]^{0.75} = -\frac{6560}{T} + 4.45$	
$\log K_{\gamma} [Mn] \cdot [S] = -\frac{9020}{T} + 2.93$	
<u>Stuart (1981):</u>	
$\log K_{\gamma} [Nb] \cdot [C]^{0.87} = -\frac{7170}{T} + 3.43$	
$\log K_{\gamma} [Nb] \cdot [C] = -\frac{7510}{T} + 2.96$	
$\log K_{\gamma} [Nb] \cdot [C]^{0.83} \cdot [N]^{0.14} = -\frac{9800}{T} + 4.46$	
$\log K_{\gamma} [Nb] \cdot [C]^{0.24} \cdot [N]^{0.65} = -\frac{10400}{T} + 2.09$	
$\log K_{\gamma} [Nb] \cdot [N] = -\frac{8500}{T} + 2.80$	
<u>Maitrepierre (1979):</u>	
$\log K_{\gamma} [B] \cdot [N] = -\frac{6700}{T} + 0.2$	
<u>Fountain (1962):</u>	
$\log K_{\gamma} [B] \cdot [N] = -\frac{15000}{T} + 5.9$	
<u>Liu (2004):</u>	
$\log K_{\gamma} [Cu]^2 \cdot [S] = -\frac{44971}{T} + 26.31$	

Table 2.3: Equations used to determine transformation temperatures.

<p><u>Deo et al. (1995):</u></p> $Ae_3 = 912 - 660 X_C^{0.88} + 454 X_C^{1.11} - 38 X_{Mn}^{0.92} + 10 X_{Si}^{4.38} + 71 X_{Si}^{1.13} - 516 X_{Ni}^{1.18} + 468 X_{Ni}^{1.22} - 196 X_{Cr}^{1.34} + 180 X_{Cr}^{1.37} + 1.13 X_{Mo}^{4.09} + 29.4 X_{Mo}^{1.24} - 24 X_{Cu}^{0.96} + 38.07 X_C^{0.4} \cdot X_{Mn}^{0.74} + 58.48 X_C^{0.33} \cdot X_{Ni}^{0.46} - 78.89 X_C^{0.32} \cdot X_{Si}^{2.04} - 6.54 X_C^{0.33} \cdot X_{Ni}^{1.47} - 68.9 X_C^{1.47} \cdot X_{Mo}^{1.33} + 39.64 X_C^{3.3} \cdot X_{Cr}^{1.86} + 4.48 X_{Ni}^{1.88} \cdot X_{Cr}^{1.31} \cdot X_{Mo}^{0.59}$
<p><u>Andrews (1965):</u></p> $Ae_3 = 913 - \Delta T - 25X_{Mn} - 11X_{Cr} - 20 X_{Cu} + 60X_{Si} + 60X_{Mo} + 40X_N + 100X_V + 700X_P$ <p>where: ΔT is dependent on the equivalent carbon content obtained by adding (0.1%Ni) to the %C. Values of ΔT are listed as follows (equivalent C; ΔT): (0.05 ; 24), (0.10; 48), (0.15 ; 64).</p> $Ae_1 = 723 - 25X_{Mn} - 26X_{Ni} + 40X_{Si} + 42X_{Cr}$

2.7 LABORATORY TESTING OF HOT DUCTILITY

2.7.1 Overview

The test which best simulates the straightening operation during continuous casting is the hot bend test. However, because of the problem of quantifying the severity of surface cracking from the hot bend test, it has only been used rarely (Blake, 1987). Compression testing (Fu *et al.*, 1988b) and torsion testing (Cepeda *et al.*, 1989) have also been used, but the difficulties in testing and interpreting of the test results make these tests unsuitable (Mintz *et al.*, 1991). The one test that has proved popular for the study of cracking is the simple hot tension test. The major advantage of the hot tension test is that the stress/strain state closely simulates hot working conditions *e.g.* during continuous casting (Bailey, 1982). Meaningful results are obtained from hot ductility testing if the testing parameters approximate industrial conditions, such as cooling patterns and strain rate.

2.7.2 Secondary cooling patterns

In the secondary cooling zone, the strand surface experiences thermal oscillations of up to 300 °C as it moves from making contact with each set of water sprays and rolls to the inter-roll gaps (Mintz *et al.*, 1987). The cooling and heating rates can be as high as 3 °C.s⁻¹, which, when thermal oscillations are added, are difficult to simulate in a typical hot tensile test with an infrared or induction furnace. The only heating method that is capable of simulating a number of fast thermal oscillations is resistance heating, such as that found on the Gleeble 1500[®] machine.

If the surface temperature of a continuously cast strand has not been measured directly by means of a thermocouple (Barber *et al.*, 1996 and 1997), it is not possible to determine the magnitude of the thermal oscillations. The alternative is to only consider the average cooling rate, which is calculated from the following equation:

$$\dot{T} = \left(\frac{v}{l} \right) dT_{\text{mould exit} \rightarrow \text{straightening}} \quad (2.11)$$

where \dot{T} is the cooling rate in °C.s⁻¹, v is the average casting speed in m.s⁻¹, l is the length of the caster from the mould exit to the straightener in m and dT is the difference in temperature from mould exit to the straightener.

2.7.3 Strain approximation of straightening

Hard box theory

Elementary bending theory can be applied to strand straightening operations (Deisinger *et al.*, 1997). In hard box theory, where the strand is solid throughout, a neutral axis is assumed in the strand midplane. The initial strand curvature is $1/R$, where the machine radius R is measured through the strand centre. Lankford (1972) first proposed that the surface strain during straightening is given by the ratio of half the strand thickness t to the bending radius R of the strand (**Figure 2.7**):

$$\varepsilon = \left(\frac{t}{2R} \right) \quad (2.12)$$

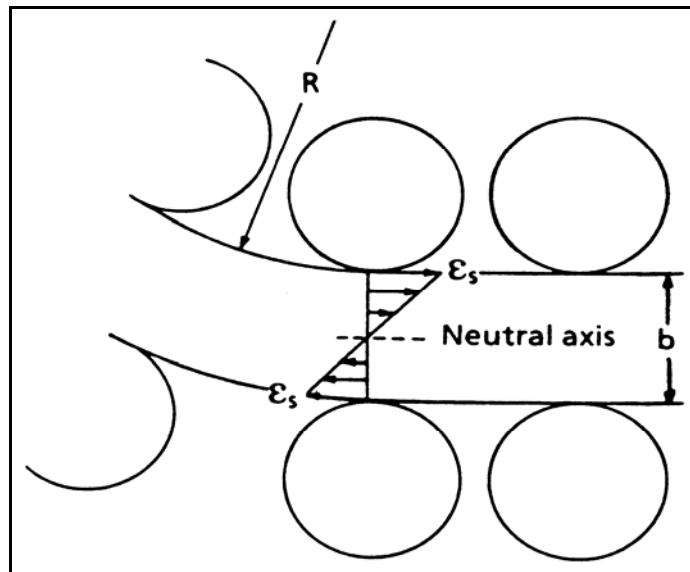


Figure 2.7: Strain distribution across the solidified strand during single point unbending (Irving, 1993).

The strain rate depends on the design of the unbending system. In one-point unbending, an acute strain rate peak develops near the tangent point since the curvature change is enforced rapidly. With multi-point unbending, the strain rate is reduced (Deisinger *et al.*, 1997).

The theoretical minimum strain rate is given by the following relation (Lankford 1972):

$$\dot{\epsilon} = \left(\frac{t}{2R} \right) \cdot \left(\frac{v}{l} \right) \quad (2.13)$$

where t is the strand thickness, v is the casting speed, R is the bending radius and L is the gauge length to develop the full bending strain.

Lankford assumed that the bending strain develops between the smallest and largest of the following gauge lengths: the distance from a tangent point to the first bending roll, the slab thickness, or the skin thickness (in the case of straightening with a liquid core). In other words, Lankford perceived L to be an ill-defined term. However, Irving (1993) and Deisinger (1997) define L as the length of the unbending zone.

Strain rates during straightening are usually around $1 \times 10^{-4} \text{ s}^{-1}$ in continuous casting of slab, $5 \times 10^{-4} \text{ s}^{-1}$ in billet casting and $1 \times 10^{-3} \text{ s}^{-1}$ in thin slab casting.

2.7.4 Strain rate conditions in hot tensile testing

In the hot tensile test, the strain rate decreases as the specimen elongates (Bailey *et al.*, 1982):

$$\dot{\epsilon} = \frac{d\epsilon}{dt} = \frac{1}{L} \cdot \frac{dL}{dt} \quad (2.14)$$

where $\dot{\epsilon}$ is the true strain rate, ϵ is the true strain, L is the specimen gauge length (in mm) and $\frac{dL}{dt}$ is the machine crosshead speed (in mm.s⁻¹ or mm.min⁻¹).

For a constant crosshead speed in a test, the strain rate is at a maximum at the beginning of the test (the gauge length is at a minimum). The strain rate then decreases until the onset of necking, after which it increases and then gradually decreases to the point of fracture (Bailey *et al.*, 1982).

Calculated elastic strain rates will be slightly higher than the actual elastic strain rate, as some of the elastic strain will occur outside the gauge length. However, this equation is valid for estimating the plastic strain rate once the maximum load has been reached, where the plastic deformation occurs uniformly throughout the gauge length (Christ, 1991).

Strain rate cannot easily be held constant in a tensile test, but similar variations occur in industrial processes. Tensile tests should thus be conducted in the same order-of-magnitude strain rate range that simulates the industrial conditions. Thus the mean strain rate ($\bar{\epsilon}$) of the hot tensile test can be calculated and used (Bailey *et al.*, 1982):

$$\bar{\epsilon} = \left(\frac{1}{\Delta t} \right) \cdot \ln \left(\frac{d_0}{d_f} \right)^2 \quad (2.15)$$

where Δt is the time during which the specimen was under stress, d_0 is the initial specimen diameter and d_f is the final specimen diameter at fracture.

2.7.5 Comparison of hot tensile testing techniques

In hot ductility testing, the strength and ductility are determined under controlled temperature and strain rate conditions on a tensile testing machine. Hot tensile tests are usually carried out using a servo-hydraulic machine equipped with a furnace or induction coil, in a protective atmosphere. The Gleeble machine has been used quite extensively for hot ductility research, as it is possible to melt samples. Heating on the Gleeble is by electrical resistance, which can be quite versatile in simulating thermal cycles (Suzuki *et al.*, 1982; and Zheng *et al.*, 1990).

Three tensile testing methods have commonly been used to determine hot ductility during the continuous casting process, as discussed below.

2.7.6 Method 1: Heat to test temperature

Shown in **Figure 2.8 a**, the specimen is heated directly to the tensile test temperature, stabilized at the temperature for a short time, then pulled under the required strain rate conditions (Nachtrab, 1986; and Mintz *et al.*, 1989c).

2.7.7 Method 2: Heat to solution treatment temperature

The specimen is heated to a temperature above phase transformation temperatures or, in most cases, above precipitate dissolution temperatures. It is held at the desired soaking temperature, then cooled at a specified cooling rate to the test temperature and pulled at a specified strain rate, as shown in **Figure 2.8 b** (Mintz *et al.*, 1989c). Various cooling patterns can be used, for example to simulate the thermal oscillations of the strand surface as it makes contact with each set of water sprays and rolls in the secondary cooling zone (Mintz *et al.*, 1991). Thermal oscillations can increase the amount of fine precipitation, which can then be detrimental to the ductility (Cardoso and Yue, 1989).

2.7.8 Method 3: Melting

The specimen is heated to 15-30 °C above the liquidus temperature in a quartz tube, then cooled to the test temperature at a specified cooling rate and can be carried out either with or without directional solidification, the latter being preferred but more difficult to achieve (Revaux *et al.*, 1994; Deprez *et al.*, 1993; and Schmidtman *et al.*, 1987). The specimen is then pulled to failure, as shown in **Figure 2.8c**.

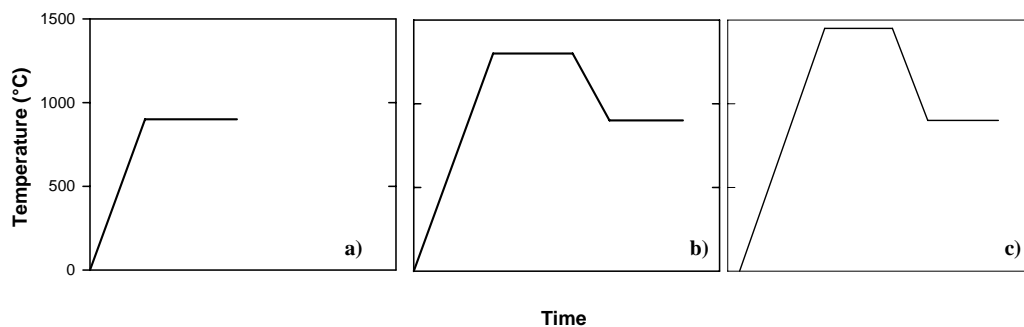


Figure 2.8: Three tensile testing methods used to determine hot ductility:

- a) **Method 1: Heat directly to test temperature**
- b) **Method 2: Heat to a solution treatment temperature**
- c) **Method 3: Heat to above liquidus temperature.**

Of the three methods given above, **Method 1** is the least accurate representation of continuous casting conditions. The temperature range of straightening can extend from temperatures below, to well above, phase transformation regions, *e.g.* ferrite to austenite, or precipitation regions. Thus, tests performed below, in and above the transformation temperature region do not have the same initial conditioning of the microstructure. For example, in a directly heated sample, the thin ferrite film at austenite grain boundaries does not form (Mintz *et al.*, 1991). Method 1 does not allow for the influence of cooling conditions on transformation and precipitation behaviour. Direct heating produces a fine-grained structure with precipitates at the grain boundaries.

In theory, **Method 3** should provide the most accurate simulation of continuous casting conditions, as it includes the influences of solidification behaviour, segregation of elements and cooling rate. However, it is difficult to simulate the surface chill zone and

directional solidification of the columnar zone of a continuously cast strand in a laboratory tensile test. The length of the columnar grains cannot be replicated in a tensile sample. The control of melting and solidification is also not a simple process and leads to non-uniform initial specimen conditioning.

Method 2 is the most commonly used laboratory technique for hot ductility testing. Usually, specimens are heated to a temperature above the dissolution temperature of the precipitates in the steel. This is to dissolve the precipitates and to produce a grain structure as coarse as the cast structure before the straightening operation. The sample is cooled at the average rate of the strand surface during the secondary cooling stage to the testing temperature and is then strained at the strain rate calculated from **Equation 2.5**. Method 2 is a reliable, easily controlled process. The influence of cooling conditions on precipitation and transformation can also be studied. The main disadvantage of this method is that the conditioning of the microstructure is not the same as in continuous casting, as cooling does not begin from above the liquidus temperature. However, by following the same solution treatment conditions for each set of tests, the results can be directly compared to other tests with the same solution treatment.

Chapter 3: Experimental Procedure

Definition of casting parameters, simulation procedures, materials and analysis techniques used in this work

3.1 OVERVIEW OF CHAPTER 3

The industrial casting parameters for thick slab, thin slab and billet casting are determined. The parameters for hot tensile testing simulations are defined based on typical industrial conditions. The material sampling, machining and testing procedures used for the two hot ductility test procedures - reheating and *in situ* melting - are then detailed. Analysis and modelling techniques used to examine the test results and the steel samples are discussed.

3.2 DETERMINATION OF INDUSTRIAL CASTING CONDITIONS

The hot tensile testing technique with solution treatment was chosen for this study, as it is a simple and repeatable procedure, which is easily controlled. To closely approximate continuous casting conditions near the strand surface by tensile testing, it is necessary to know the following parameters:

- Casting speed
- Secondary cooling rate
- Length of the unbending zone
- Tensile strain rate on the top surface (loose face) of the strand at unbending.

Table 3.1 shows typical values of thick and thin slab casting parameters. The steady-state casting speed is set at the start of a casting sequence for a particular steel composition. It was not possible to determine strand surface temperatures directly throughout the casting process as described in literature (Barber, 1996 and 1997), as there are no pyrometers or thermocouples installed in the casting machines used in this work. In addition, the high temperatures and steam generated are too dangerous to allow the use of hand-held pyrometers to measure the temperature. Thus, for the purposes of this work, an average cooling rate was calculated using **Equation 2.4**, based on typical strand surface temperatures at the mould exit and at the unbending segment, which are directly measured temperatures. The tensile strain on the loose face was calculated from **Equation 2.5** and the tensile strain rate was determined by using **Equation 2.6**.

Under normal, steady state casting conditions, conventional slab casting of 200 mm thick strand is performed at speeds of 0.8 – 1.3 m.min⁻¹. The average secondary cooling rate is 0.15 – 0.40 °C.s⁻¹ and the tensile strain rate at straightening on the loose face of the strand is approximately 1 x 10⁻⁴ s⁻¹, as calculated by **Equations 2.4** and **2.6**.

Thin slab casting of 50 – 90 mm thick strand is typically performed at speeds of 3.0 – 6.5 m.min⁻¹. This gives an average secondary cooling rate of 1.2 – 3.0 °C.s⁻¹ as calculated by **Equation 2.4**. The straightening strain rate is 5 x 10⁻⁴ – 1 x 10⁻³ s⁻¹ (**Equation 2.6**).

Billet casting of squares measuring 100 x 100 to 140 x 140 mm is typically performed at speeds of 1.2 – 2.4 m.min⁻¹. The average secondary cooling rate is approximately 1.0 °C.s⁻¹ (Equation 2.4), with corner cooling rates of up to 3.0 °C.s⁻¹. The straightening strain rate is 1 x 10⁻⁴ – 5 x 10⁻³ s⁻¹ (Equation 2.6).

Table 3.1: Casting parameters for thick slab casting, thin slab casting and billet casting, determined from the casting machines used in this work, including calculated cooling rates, strain and strain rate values.

Parameter	Unit	Thick slab casting	Thin slab casting	Billet casting (1)	Billet casting (2)
Strand thickness (b)	m	0.20	0.09	0.10	0.115
Mould length	mm	900	1050	780	
Support length (sl)	m	27.8	14.8	11	7.85
Length to unbending (l)	m	27.8	10.2	11	7.85
Bending radius (R)	m	7.5	5.6	7	5
Casting speed (min.) v	m.min ⁻¹	0.8	3	1.2	2.4
Casting speed (av.) v	m.min ⁻¹	1	5	1.7	2.65
Casting speed (max.) v	m.min ⁻¹	1.3	6.5	2.4	2.9
Temperature (mould exit)	°C	1250	1250	1250	1400
Temperature (unbending)	°C	900	900	900	1000
Cooling rate (min.)	°C.s ⁻¹	0.17	1.47	0.64	2.04
Cooling rate (av.)	°C.s ⁻¹	0.21	2.45	0.90	2.25
Cooling rate (max.)	°C.s ⁻¹	0.27	3.19	1.27	2.46
Bending/unbending zone length (d)	m	1.0	0.7	1.0	1.0
Strain (av.)		0.013	0.008	0.007	0.012
Strain rate (min.)	s ⁻¹	1.8E-04	5.7E-04	1.4E-04	4.6E-04
Strain rate (av.)	s ⁻¹	2.2E-04	9.6E-04	2.0E-04	5.1E-04
Strain rate (max.)	s ⁻¹	2.9E-04	1.2E-03	2.9E-04	5.6E-04

3.3 TESTING SPECIFICATIONS AND PROCEDURES

The following relevant testing specifications and standard testing procedures were used:

- ASTM E8M: Standard test method for tension testing of metallic materials [metric] (ASTM, 1997a)
- ASTM E 21-92: Standard test methods for elevated temperature tension tests of metallic materials (ASTM, 1997b)
- ASTM E 112-96: Standard test method for determining average grain size (ASTM, 1997c)

The following information was used from the DSI Gleeble[®] manual (1986):

- Application Note APN001 – Axisymmetric Uniaxial Compression Testing Using ISO-T Anvils on Gleeble[®] Systems
- Chapter 11 – Melting and controlled solidification with thermocouple support
- Application Note APN007 – Unidirectional Tension/ Compression Test
- Type B standard specimens for hot ductility testing
- Application Note APN021 – Steel Melt Testing on Series 3 Digital Control Gleeble Systems

3.4 STEEL SPECIMENS

3.4.1 Material sampling

All material was taken from industrial continuously cast slabs (200-240 mm thick), with the exception of the high sulphur boron steels, which were sampled from continuously cast billet (100x100mm). All specimens were machined with their axes parallel to the casting direction and about 10 mm below the top (loose) surface of the slab or billet, as shown in **Figure 3.1**.

This position and orientation provide specimens for laboratory hot ductility testing that are representative of the crack-sensitive region of a continuously cast strand *i.e.* perpendicular to the dendrites in the outer region of the columnar zone on the top face.

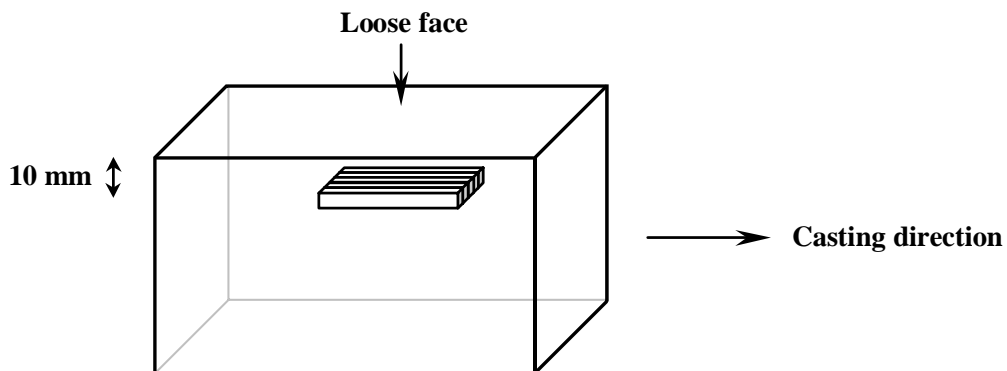


Figure 3.1: Sampling position and orientation for machining of tensile specimens from continuously cast slab or billet.

3.4.2 Steel compositions

Four general steel types were used:

- **Low carbon** (aluminium-killed or silicon-killed)
- **Niobium** microalloyed, low carbon
- **Boron** microalloyed, extra-low carbon
- **High sulphur**, boron microalloyed, low carbon

The compositions of the steels were determined by the *Glow Discharge Emission Spectroscopy* (GDOES) method and are listed in **Table 3.2**, in mass % (N and B are listed in ppm).

Table 3.2: Chemical composition of steels (in mass %, N and B in ppm*), grouped by general steel type: low carbon, niobium, boron and high sulphur.

Steel type	Grade	C	Mn	P	S	Si	Al	N*	Nb	Ni	Cu	Cr	B*
Low carbon	LC-1	0.100	0.43	0.012	0.006	0.04	0.042	85		0.03	0.02	0.02	
	LC-2	0.120	0.65	0.010	0.009	0.01	0.045	62		0.02	0.01	0.03	
	LC-3	0.140	1.10	0.010	0.007	0.25	0.021	38		0.02	0.02	0.02	
	LC-4	0.160	0.72	0.010	0.011	0.18	0.021	91		0.09	0.27	0.02	
	LC-5	0.120	0.32	0.100	0.012	0.53	0.028	60		0.26	0.34	0.55	
Niobium	Nb-1	0.040	0.34	0.009	0.001	0.12	0.047	67	0.018	0.02	0.01	0.02	
	Nb-2	0.070	0.54	0.008	0.003	0.15	0.032	70	0.020	0.02	0.02	0.01	
	Nb-3	0.070	0.87	0.005	0.006	0.19	0.042	106	0.027	0.02	0.01	0.02	
	Nb-4	0.120	0.83	0.007	0.014	0.03	0.045	71	0.028	0.02	0.02	0.02	
	Nb-5	0.160	1.48	0.007	0.008	0.34	0.036	93	0.030	0.01		0.02	
Boron (Al-killed)	B-1	0.036	0.30	0.008	0.016	0.02	0.036	54		0.03	0.01	0.03	10
	B-2	0.026	0.31	0.009	0.005	0.02	0.055	47		0.01	0.01	0.03	22
	B-3	0.033	0.25	0.009	0.015	0.01	0.055	44		0.02	0.01	0.03	33
Boron (Si-killed)	HS-1	0.056	0.36	0.025	0.035	0.11		90		0.09	0.15	0.08	40
	HS-2	0.048	0.30	0.004	0.025	0.11		100		0.09	0.18	0.07	40
	HS-3	0.059	0.44	0.008	0.018	0.15		59		0.07	0.20	0.06	70
	HS-4	0.039	0.41	0.014	0.034	0.14		80		0.09	0.15	0.03	80

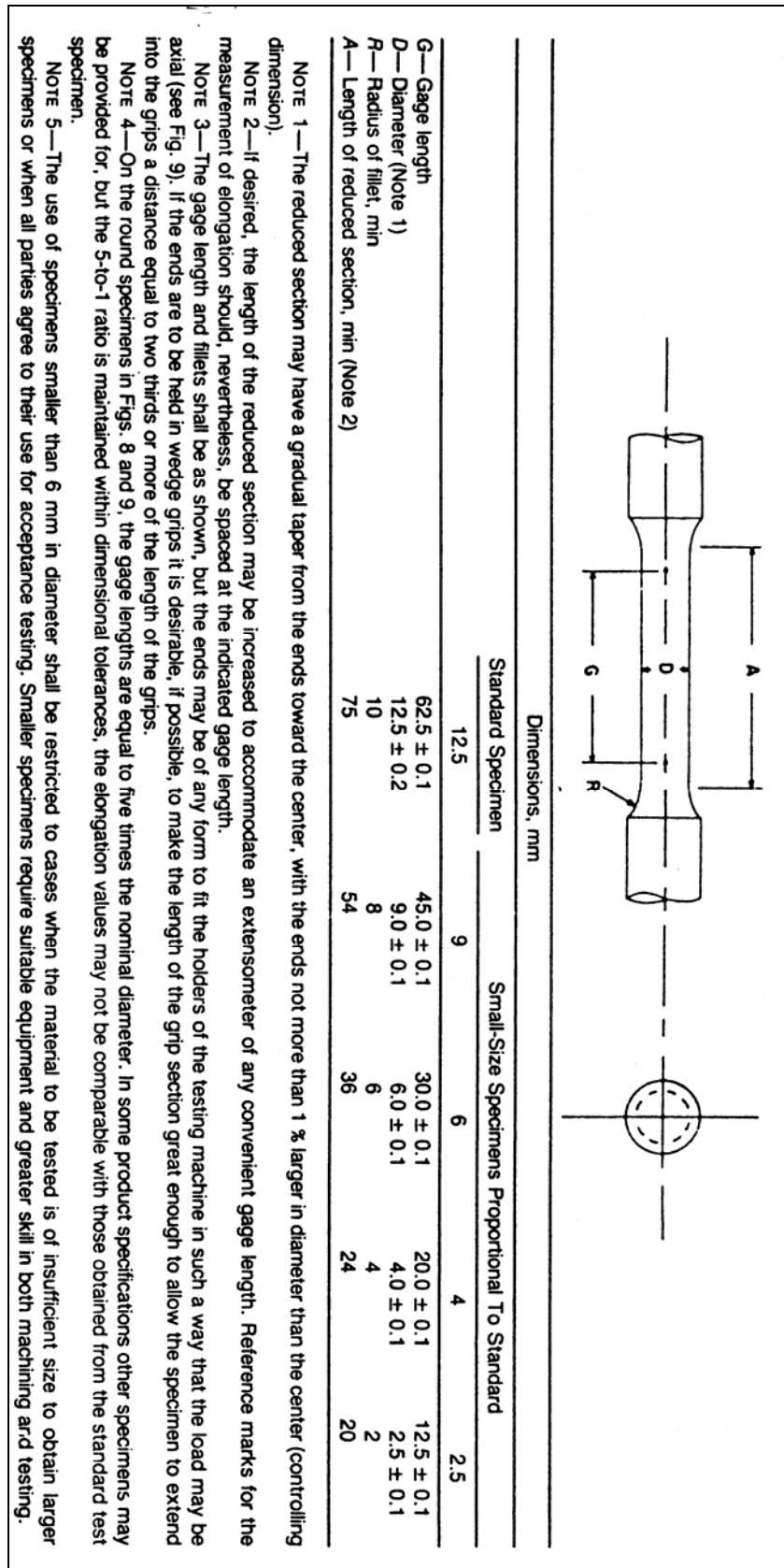


Figure 3.2: Schematic diagram of machined round tensile specimen according to standard ASTM E8M (ASTM, 1997a).

3.4.3 Tensile specimens

For the Instron[®] tensile tests, using infrared heating to 1300°C, the round, threaded-end tensile specimens (**Figure 3.2**) were machined according to ASTM E8M (1997a) with the following dimensions:

- Gauge length (G): 30 ± 0.1 mm
- Length of reduced section (A): 36 mm (minimum)
- Diameter (D): varying from 5.50 to 6.50 mm
- Radius of fillet (R): 6 mm

For the Gleeble[®] tensile tests, using resistance heating with *in situ* melting, round, threaded-end tensile specimens having no reduced section, were machined according to the DSI (1986) standard Type B specimen dimensions (**Figure 3.3**):

- Specimen length: 120 mm
- Threaded ends: 10 mm x 1.5
- Length between grips: 30 mm
- Diameter: 10 ± 0.04 mm
- Quartz tube: Length 20 ± 1 mm, outer diameter 12 mm

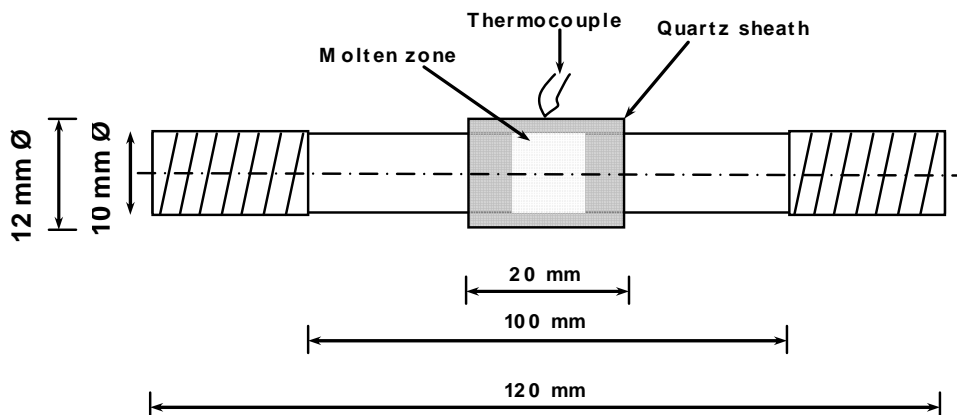


Figure 3.3: DSI Gleeble standard specimen with threaded ends for hot tensile testing with *in situ* melting, showing approximate width of the molten zone.

3.5 HOT TENSILE TESTING FACILITIES

3.5.1 Instron[®] tensile testing

Hot tensile tests were performed on an Instron[®] mechanical tensile testing machine, shown in **Figure 3.4** and schematically in **Figure 3.5**. A round tensile specimen with threaded ends was screwed into the upper and lower grips, which were then attached to the frame of the tensile machine by pins. An S-type thermocouple was spot-welded onto the reduced section of the tensile specimen to control and record the temperature. The specimen and part of the two grips were centred inside a cylindrical quartz tube, which was fitted onto a brass ring at the lower grip end. An infrared furnace was fitted around the quartz tube. The specimen setup is shown in **Figure 3.6**.

After the specimen setup had been mounted in the machine, the spaces between the quartz tube, the brass ring and the grips were packed with the heat-resistant material Kaowool[®]. Argon gas was blown into the partially sealed cylinder for the duration of the hot tensile



Figure 3.4: Photograph of the Instron[®] tensile testing facility.

test to limit surface oxidation of the steel specimens. The infrared furnace heated the specimen through the controlled temperature cycle, which was programmed into the REX-P200[®] control system.

The tensile testing program was activated by the operator when the specimen had reached the required testing temperature. The program moved the crosshead (lower mobile arm) downwards at the specified speed. A 5 kN load cell measured the tensile force. The specimen elongation was determined by measuring the crosshead movement.

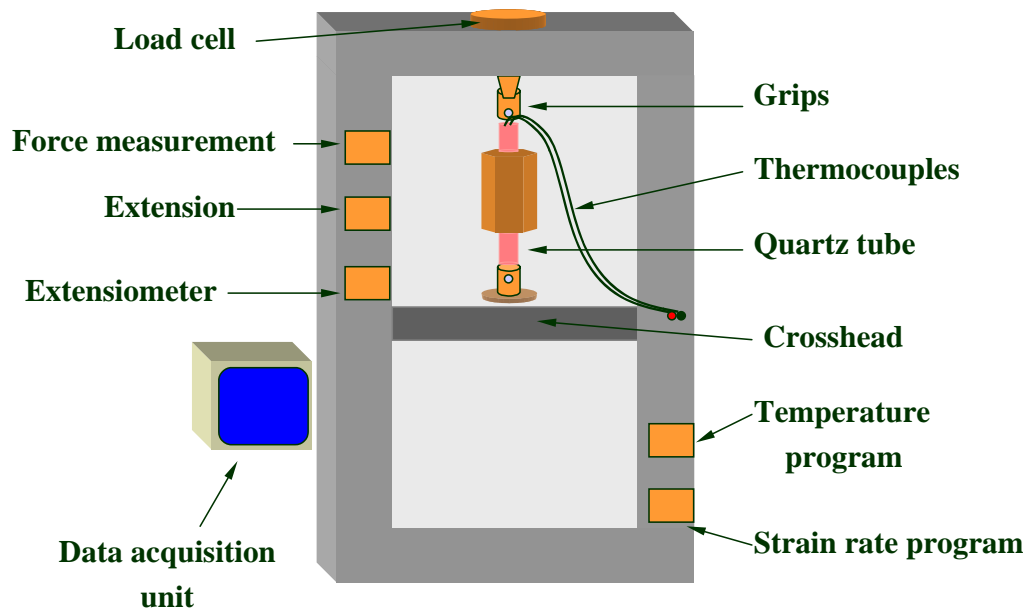


Figure 3.5: Schematic diagram of the tensile testing facility.

The testing temperature, force and crosshead movement were recorded in two ways onto a data acquisition unit:

- Graphically as temperature - time and force - crosshead displacement.
- In ASCII format onto diskette (temperature, time, force and crosshead displacement). The ASCII data was then converted to stress – strain and total elongation values by using the computer program Jandel SigmaPlot®.

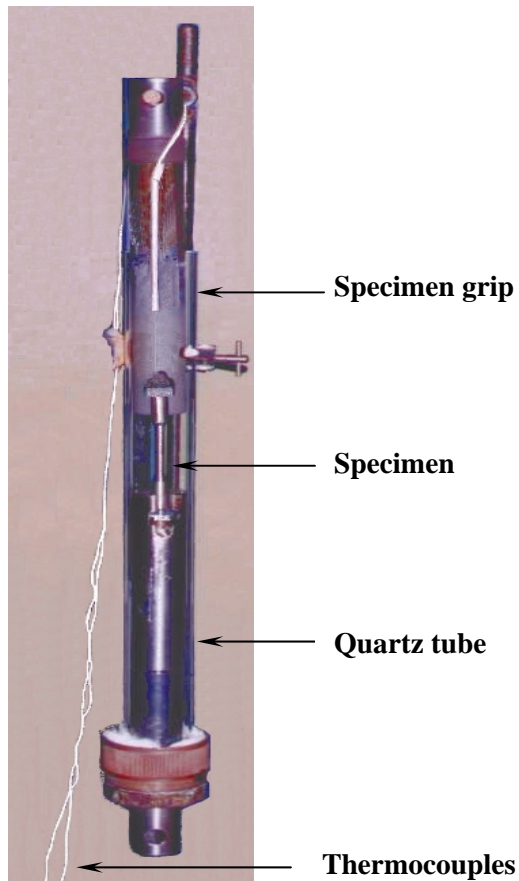


Figure 3.6: Photograph of the hot tensile specimen setup.

3.5.2 Gleeble® 1500 tensile testing

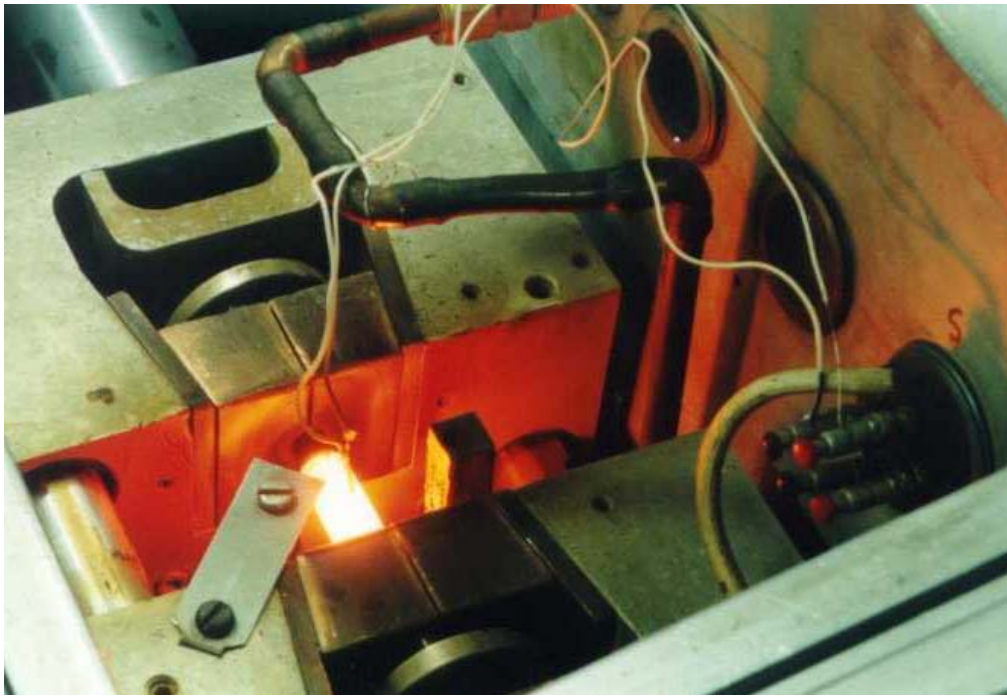
Hot tensile tests with *in situ* melting were performed on only the silicon-killed boron steels on a Gleeble 1500® servo-hydraulic machine (shown in **Figure 3.7**). A solid cylindrical tensile specimen with threaded ends and no machined gauge section was screwed into the sample grips of the Gleeble. An S-type thermocouple was welded onto the specimen and a quartz sleeve was placed around the centre of the specimen to support the melting zone, as shown in **Figure 3.8**.



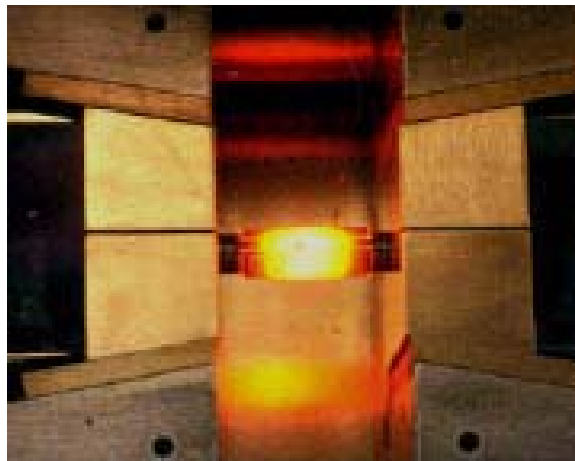
Figure 3.7: Photograph of the Gleeble 1500[®] facility at Pretoria University.

As the thermocouple was attached to the surface of the tensile specimen through a slit in the quartz sleeve, the temperature recorded was from the surface and not the centre of the specimen. Suzuki *et al.* (1982) found that there was a temperature gradient of up to 100 °C between the surface and centre of a Gleeble[®] specimen above 1400 °C. This radial thermal gradient is due mainly to radiative heat loss under vacuum conditions (Moon, 2003). The heating, cooling and tensile testing program was controlled by the Gleeble[®] computer up to a surface temperature of 1400 °C. Thereafter, the temperature was slowly increased manually to between the solidus and liquidus temperatures of the steel, where the surface temperature varied from 1420-1430 °C. Melting was visually observed by a slumping of the specimen and the formation of small bubbles, and seen on the force measurement as a region of unstable force. A small compressive force of 4MPa was applied from a temperature of 1300 °C to avoid any changes in shape and area of the specimen, in the current passing through the specimen and thus, in the temperature. After ~40 seconds, the Gleeble[®] programme was then used to cool the specimen down to the testing temperature at the specified cooling rate.

Crosshead movement, force and actual temperature measurements were recorded on the Gleeble[®] in ASCII format, which were then converted to engineering strain and engineering stress in MS Excel[®].



a)



b)

Figure 3.8: a) View of the hot specimen, grips, and thermocouples inside the Gleeble[®] testing chamber.
b) Top view showing *in situ* molten zone of specimen contained in a quartz tube with a slit for the thermocouple.

3.6 TENSILE TESTING SCHEDULES

The testing schedules were based on typical industrial casting conditions (**Section 3.1**). The seven schedules were designed to show the following influences of steel composition, cooling rate and tensile strain rate on hot ductility and strength:

- The differences between conventional thick casting and two thin slab casting conditions.
- The influence of cooling rate (0.3, 1.2, 3.0 °C.s⁻¹) at a slow strain rate of 10⁻⁴ s⁻¹.
- The influence of cooling rate (1.2 and 3.0 °C.s⁻¹) at a fast strain rate of 10⁻³ s⁻¹.
- The influence of strain rate (10⁻³ and 10⁻⁴ s⁻¹) at a cooling rate of 1.2 °C.s⁻¹.
- The influence of strain rate (10⁻³ and 10⁻⁴ s⁻¹) at a cooling rate of 3.0 °C.s⁻¹.
- The influence of solution treatment time (1 and 5 minutes) at a fast cooling rate of 1.2 °C.s⁻¹ and fast strain rate of 10⁻³ s⁻¹.
- The influence of temperature oscillation at a fast cooling rate of 1.2 °C.s⁻¹ and fast strain rate of 10⁻³ s⁻¹.
- The influence of cooling rate (1.0 and 2.0 °C.s⁻¹) on sulphide precipitation in high sulphur boron steels.

The parameters of the schedules are summarized in **Figure 3.9** and **Table 3.3**.

For the Instron[®] tensile tests, the heating rate (2.7 °C.s⁻¹) and solution treatment temperature (1300 °C) were kept constant for all schedules. A solution temperature of 1300 °C was chosen for all the tests, as it is above all calculated transformation and precipitate dissolution temperatures for the tested steels, except for the MnS dissolution temperatures. Thus, after the solution treatment, the specimens should contain no Nb, Al and B precipitates that influence hot ductility. The solution treatment time was kept constant at 5 minutes except for Schedules A and B where the time was reduced to 1 minute to examine the effect of solution treatment time on ductility and strength in a niobium steel.

For the Gleeble® tensile tests, the heating rate of 8 °C.s⁻¹ to the melting temperature was used. A holding time of 1 minute at the melting temperature was deemed sufficient to allow homogeneous melting without excessive bubbling in the molten zone, which would cause deleterious porosity upon cooling, and would thus not be representative of the conditions being simulated.

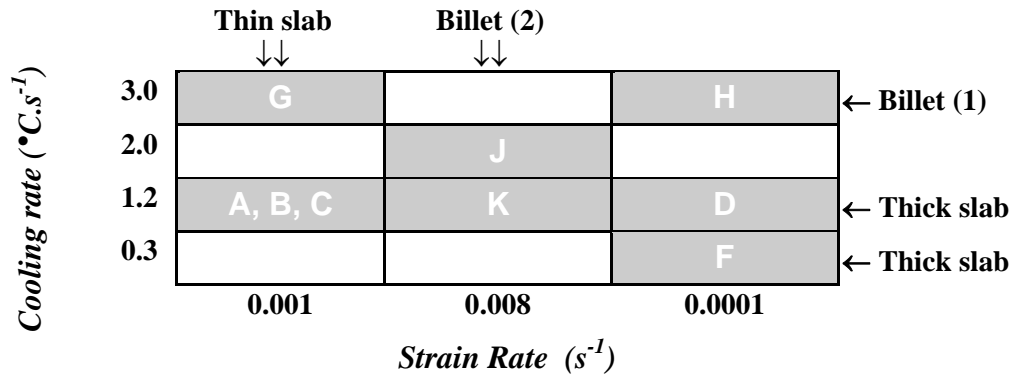


Figure 3.9: Testing conditions showing the strain rate and cooling rate variations for schedules A, B, C, D, F, G, H, J and K.

Table 3.3: Summary of tensile testing schedules.

Schedule	Solution treatment		Cooling rate (°C.s ⁻¹)	Strain rate (s ⁻¹)
	Temperature (°C)	Time (minutes)		
A	1300	1	1.2	1 x 10 ⁻³
B	1300	1	1.2 + oscillation	1 x 10 ⁻³
C	1300	5	1.2	1 x 10 ⁻³
D	1300	5	1.2	1 x 10 ⁻⁴
F	1300	5	0.3	1 x 10 ⁻⁴
G	1300	5	3.0	1 x 10 ⁻³
H	1300	5	3.0	1 x 10 ⁻⁴
J	~1430	1	2.0	8 x 10 ⁻⁴
K	~1430	1	1.0	8 x 10 ⁻⁴

3.7 SCHEDULES A-H

The specimens were heated in an infrared furnace to 1300 °C in 7 minutes, held for 5 minutes (or 1 minute for Schedules A and B) at 1300 °C and then cooled to testing temperatures in the range of 750-1100 °C at cooling rates of 0.3, 1.2 or 3.0 °C.s⁻¹, depending on the schedule. The programmed cooling times from 1300 °C to the testing temperatures are given in **Table 3.4**. After holding at the testing temperature for 30-60 s, the specimens were strained to failure at the specified initial strain rate of 1 x 10⁻⁴ or 1 x 10⁻³ s⁻¹. The crosshead speed values were calculated from the initial strain rates by **Equation 2.8** (Crosshead speed = 50/time) and are listed in **Table 3.5**. The time to pull 50 mm for a gauge length of 30 mm is calculated as: $t = 50/(30 \times \text{strain rate})$.

3.8 SCHEDULES J and K

The tensile specimens were resistance heated at a heating rate of ~8 °C.s⁻¹ to the melting temperature (~1420-1430 °C), with a quartz crucible around the specimen to contain the molten zone, and in an argon atmosphere to limit oxidation. After holding at the melting temperature for 1 minute, the specimens were cooled at a rate of 2.0 °C.s⁻¹ (and 1 °C.s⁻¹ for steel *SiB-1*) to testing temperatures in the range 750-1250 °C. The programmed cooling times from 1430 °C to the testing temperatures are given in **Table 3.4**. The tensile strain rate was calculated for the billet top surface during straightening. The specimens were then pulled to failure at constant speed = 24/time as listed in **Table 3.5**, calculated from **Equation 2.8** using an initial strain rate of 8 x 10⁻⁴ s⁻¹. The time to pull 24 mm for a gauge length of 12 mm is calculated as $t = 24 / (12 \times \text{strain rate})$.

Table 3.4: Programmed cooling times from solution treatment temperature to testing temperatures.

Test T (°C)	Time from 1300 °C (min:sec)				Test T (°C)	Time from 1430 °C (min:sec)	
	A, C, D	F	G, H	B*		J	K
1250	0:42	2:47	0:17		1250	01:30	03:00
1200	1:23	5:33	0:55		1225	01:43	03:25
1150	2:05	8:20	0:83		1200	01:55	03:50
1100	2:47	11:07	1:07		1185	02:03	04:05
1050	3:28	13:53	1:23		1175	02:08	04:15
1000	4:10	16:40	1:40	2:50*	1150	02:20	04:40
975	4:31	18:06	1:48		1100	02:45	05:30
950	4:51	19:27	1:57	3:30*	1050	03:10	06:20
925	5:12	20:50	2:05		1000	03:35	07:10
900	5:33	22:13	2:13	4:10*	950	04:00	
875	5:54	23:37	2:22		900	04:25	
850	6:15	25:00	2:30		850	04:50	
825	6:36	26:23	2:38		825	05:03	
800	6:56	27:47	2:46		800	05:15	
775	7:17	29:10	2:55		750	05:40	
750	7:38	30:33	3:03		700	06:05	
700	8:20	33:20	3:20		650	06:30	

B:

Temp (°C)	time (min:sec)
1300	1:00
1000	4:10
1200	2:50

* Schedule B has an initial temperature oscillation:
1300 - 1000 - 1200 °C
so cooling times are quoted from 1200 °C

Table 3.5: Relationship between strain rate and crosshead speed.

Parameter	Unit	A,B,C,G	D,F,H	J,K
Strain rate	s ⁻¹	1 x 10 ⁻³	1 x 10 ⁻⁴	8 x 10 ⁻⁴
Time to pull 50mm	min:sec	29:00	278:00	
Crosshead speed = 50/time	mm.s ⁻¹	0.029	0.003	
	mm.min ⁻¹	1.74	0.18	
Time to pull 24mm	min:sec			23:10
Crosshead speed = 24/time	mm.s ⁻¹			0.017
	mm.min ⁻¹			1.04

3.9 INTERPRETATION OF TEST RESULTS

3.9.1 Determination of stress – strain curves

The recorded force (in kN) is converted to engineering stress (MPa) by **Equation 3.1** (Bailey *et al.*, 1982):

$$S_i = \left(\frac{1000 \cdot F_i}{A_0} \right) \quad (3.1)$$

where: S_i is the engineering stress in MPa, F_i is the recorded force in kN. A_0 is the initial cross-sectional area of the reduced section in mm^2 ($A_0 = \pi \cdot \left(\frac{d_0}{2}\right)^2$ where d_0 is the average initial diameter of the reduced section in mm).

The crosshead movement (in mm) is converted to engineering strain (elongation) by **Equation 3.2** (Bailey *et al.*, 1982):

$$\varepsilon_i (\%) = 100 \cdot \left(\frac{L_i}{L_0} \right) \quad (3.2)$$

where: ε_i is the instantaneous elongation in %, L_i is the instantaneous crosshead movement in mm and L_0 is the initial length of the reduced section in mm.

The calculated stress values are plotted as a function of elongation *i.e.* engineering strain.

3.9.2 Calculation of maximum stress

The maximum stress (S_u), or engineering hot strength, is a significant measurement for continuous casting, enabling prediction and prevention of continuous cast strand deformation, also known as bulging. It is determined as the highest stress value for each hot ductility test. These stress values are plotted as a function of test temperature. The

maximum stress is calculated by dividing the maximum recorded load F (in kN) by the original cross-sectional area A_0 of the reduced section of the specimen (ASTM, 1997b):

$$S_u \text{ (MPa)} = \frac{F}{A_0} \quad (3.3)$$

3.9.3 Calculation of total elongation

The total elongation to fracture (%) is determined at the point where the stress decreases to zero.

3.9.4 Hot ductility measurement

Total reduction of area (R. A.) is a measure of necking strain, and indicates the ability of an alloy to withstand crack propagation (Bailey *et al.*, 1982). It is the most commonly-used measurement to provide quantitative information on the fracture strain (Mintz *et al.*, 1991). Wilcox and Honeycombe (1987) used the total elongation to fracture as a measure of the ductility, and were able to analyze the effect of dynamic recrystallization on hot ductility. Both reduction in area and total elongation to fracture have been included in this work for comparison purposes.

The reduction in area is defined by:

$$R.A. \text{ (\%)} = \frac{A_0 - A_f}{A_0} \cdot 100 \quad (3.4)$$

$$\text{where area } A = \pi \cdot \left(\frac{d}{2}\right)^2 \quad (3.5)$$

A_0 is the initial cross-sectional area of tensile specimen gauge length, A_f is the final reduced cross-sectional area after testing, A is the area, and d is the diameter of the reduced section. The final area is determined by fitting the broken ends of the specimen together and measuring the minimum diameter at the region of fracture.

Due to anisotropy, the circular cross sections often do not remain circular during straining in tension, but can be elliptical. Thus, the area may be calculated by:

$$A = \pi \cdot \left(\frac{d_1 \cdot d_2}{4} \right) \quad (3.6)$$

where d_1 and d_2 are the major and minor diameters respectively.

3.10 METALLOGRAPHY

3.10.1 Specimen preparation

The broken tensile specimens were cut at the fillet and grip intersection on a Discotom[®] cutting machine. The specimens were then mounted, with the longitudinal section from the cut surface to the fracture surface visible for microscopic examination. A carbon-based, thermosetting mounting powder, Konductomet[®], was used as the mounting medium in preference to Perspex[®], as it is harder and provides a flatter reflective surface, improving the focus of the optical microscope. Konductomet[®] is also conductive, and is thus preferred for use in scanning electron microscopy.

The specimens were ground down by ~2 mm to expose the central axis of the specimen, then polished on a Struers RotoPol-25[®] automated polishing machine, ground on 400 and 1200 grit SiC, followed by 9 μm and 3 μm diamond paste and a final polish on 0.2μm alumina paste.

3.10.2 Optical microscopy

A few polished specimens were viewed under the Nikon[®] optical microscope, to examine the internal structure of the specimen and the profile of the fracture surface. Particular attention was paid to non-metallic inclusions (*e.g.* MnS stringers), rows of small particles, and the progression of internal cracking.

As no chemical analysis of inclusions and precipitates is possible on the optical microscope, the decision was made to continue further examination of the mounted specimens on the scanning electron microscope.

3.11 SCANNING ELECTRON MICROSCOPY: JEOL[®] SEM

The mounted and polished specimens were prepared for scanning electron microscopy. The specimen was placed in a specimen holder. Small drops of graphite powder, which had been wet with alcohol, were used to improve the conductivity by bridging the steel specimen to the rim of the holder.

The graphite appeared to contaminate a number of EDS (*Energy Dispersive Spectroscopy*) analyses by showing the presence of carbon.

The SEM was operated at 15 kV in electron backscatter mode to examine the internal structure of the longitudinally-sectioned specimens. EDS analysis was performed on small voids to identify the composition of precipitates. As most of the precipitates were small ($< 2 \mu\text{m}$), the EDS analyses included the surrounding matrix, hence Fe was found in the majority of analyses.

3.12 SCANNING ELECTRON MICROSCOPY: FEI NOVA[®] NANOSEM

Hot tensile test samples from the silicon-killed boron steels were mounted vertically to examine the fracture surfaces by SEM. The type of failure *i.e.* intergranular, transgranular or mixed mode and the size and position of the precipitates were determined. The compositions of the precipitates were determined by EDS.

3.13 TRANSMISSION ELECTRON MICROSCOPY

TEM was performed on the Philips CM20 at IMMRI, University of Pretoria. This part of the investigation focussed on the boron Al-killed and Si-killed steels. Some thin, ion-milled samples were made to look for the presence of FeS and MnS precipitates. Thereafter, extraction replicas were produced to examine the morphology and composition of precipitates by X-ray mapping.

3.14 TEMPERATURE CALCULATIONS: TRANSFORMATION AND PRECIPITATION

The isothermal, equilibrium austenite-to-ferrite transformation start temperatures (Ae_3) and Ae_1 (end of austenite-to-ferrite transformation) were calculated from the three equations in **Table 2.3** in a Microsoft Excel[®] spreadsheet.

The Thermo-Calc[™] modelling package with the FEDAT database for steels was also used to obtain Ae_3 and Ae_1 temperatures for the specific steel compositions used in this work (Cornish, 1999).

Equilibrium dissolution temperatures of relevant precipitates (AlN, BN, Nb(C,N) and MnS) in austenite were calculated in a Microsoft Excel[®] spreadsheet from the solubility equations in **Table 2.2**.

Thermo-Calc[™] modelling was used with the general purpose SSOL2 database to obtain equilibrium dissolution temperatures for various Nb(C,N) precipitates in the niobium microalloyed steels (Cornish, 1999). The Thermo-Calc[™] database, FEDAT (the only steels database available in 2001), does not include AlN and BN solubility data.

The Thermo-Calc[™] modelling was repeated in 2005 – 2006, using the new steel-specific TCFe3 database, which includes AlN and BN solubility data. This work was expanded to show the MnS equilibrium dissolution and solidification temperatures for all the steels.

Also, the updated general materials SSOL4 database was used to determine solubility of various species of Nb(C,N) precipitates.

3.15 ANALYSIS OF INDUSTRIAL BILLET CASTING DATA

Continuous casting data of high sulphur, boron-containing steels from 697 billet casts, showing the number of billets cast, passed and scrapped, were analyzed to determine if there were any distinct trends. The information included chemical analyses and the scrap incidence per cast due to transverse cracking. Regression analysis was performed on the data to ascertain whether any significant trends and dependencies could be seen.

3.16 DATABASE GENERATION

A hot ductility database was developed by the author to enable easy access and comparison of data from literature. This database currently includes data of 340 hot ductility curves sourced from published data in 43 literature references, as well as results from work done by the author and former colleagues at Iscor Ltd. (now Arcelor Mittal) and IMMRI (Industrial Metals and Minerals Research Institute) at the University of Pretoria, and can easily be updated with new information.

Chapter 4: Discussion Overview

4.1 OVERVIEW OF CHAPTER 4

The following chapters 4-8 discuss the results and implication for each steel type (low carbon, niobium, Al-killed boron and Si-killed boron) separately. However, the common element linking the steels is the hot ductility test. The failure mode and the minimum percentage reduction in area required to prevent hot cracking during continuous casting are discussed below. In this chapter, it has been shown that a certain minimum ductility value, usually determined from reduction in area curves, is necessary to minimise or avoid transverse cracking during straightening in continuous casting. In this work, it was found that intergranular cracking was only eliminated at R. A. values approaching 50%.

The relevance and limitations of the laboratory-scale hot ductility test in assessing the likelihood of cracking is discussed. The main areas that are not simulated in the tensile test, *i.e.* oscillation marks, austenite grain size and morphology, and total strain, are discussed.

The hot ductility curve was analysed with specific reference to the low ductility trough, low temperature, high ductility (LT-HD) and the high temperature, high ductility regions (HT-HD). The importance of the minimum R. A. value, the Ae_3 and Ar_3 temperatures, the formation of deformation induced ferrite and the occurrence of dynamic recrystallisation are also discussed.

4.2 DEPENDENCE OF DUCTILITY ON FAILURE MODE

During the microstructural examination by optical microscopy of the tested tensile specimens, it was noted that the ductility (% reduction in area) is closely related to the type of failure. Transgranular ductile failure was found in the specimens with high reduction in area (% *R.A.*) values and intergranular ductile fracture was found in the specimens with low *R.A.* values. A mixture of both transgranular and intergranular failure modes was found in specimens with intermediate *R.A.* values. Many of the specimens with intermediate *R.A.* values showed some internal intergranular cracking, while the fracture surfaces had a ductile, transgranular appearance. These specimens were defined as having “mixed mode” failure.

It is commonly stated in literature that a minimum reduction in area value, typically 40% or 60%, is required to prevent cracking during continuous casting of steel. This is a useful criterion in determining crack susceptibility. Suzuki *et al.* (1988) claimed that there is a critical reduction in area (*R.A._{crit.}*) of 60% above which cracking seldom occurs. However, the means by which this critical ductility is determined is usually empirical, and thus relies on the specific steel and plant conditions.

Nagasaki *et al.* (1999) agreed with the critical reduction in area value of 60% in an investigation of a low carbon steel (0.05% C, 0.26% Mn). They defined the *R.A._{crit.}* as the distinguishing point between transgranular ductile failure (all fracture surfaces are transgranular or not intergranular) and intergranular ductile failure. Below 60%, some intergranular fracture surfaces were observed and below 40% all the fracture surfaces were intergranular.

Mintz (1996) stated that a value of 60% is too conservative and 40% is a more realistic value for *R.A._{crit.}*, especially for low carbon steels, which are not prone to transverse cracking. However, he explained that the actual value would be very dependent on the tensile testing conditions used (in his work the specimen was heated to 1330 °C, cooled at 1.0 °C.s⁻¹, held for 5 minutes before testing, and strained at a strain rate of 3 x 10⁻³ s⁻¹).

Figure 4.1 shows the reduction of area as a function of testing temperature for 86 specimens examined by optical or scanning electron microscopy in this work. The failure modes: transgranular ductile, intergranular ductile and “mixed mode” are indicated on the graph. The graph shows that intergranular failure occurred at $R.A$ values below 50%, “mixed mode” failure between 47–69% and transgranular failure occurred above 57%.

The conservative critical reduction in area used to distinguish transgranular ductile from intergranular failure, as proposed by Nagasaki, would be ~65-68 % $R.A$ and the more lenient $R.A_{crit}$, as used by Mintz, would be ~50% for specimens examined in this work. For the purposes of this work, the 50% criterion was used.

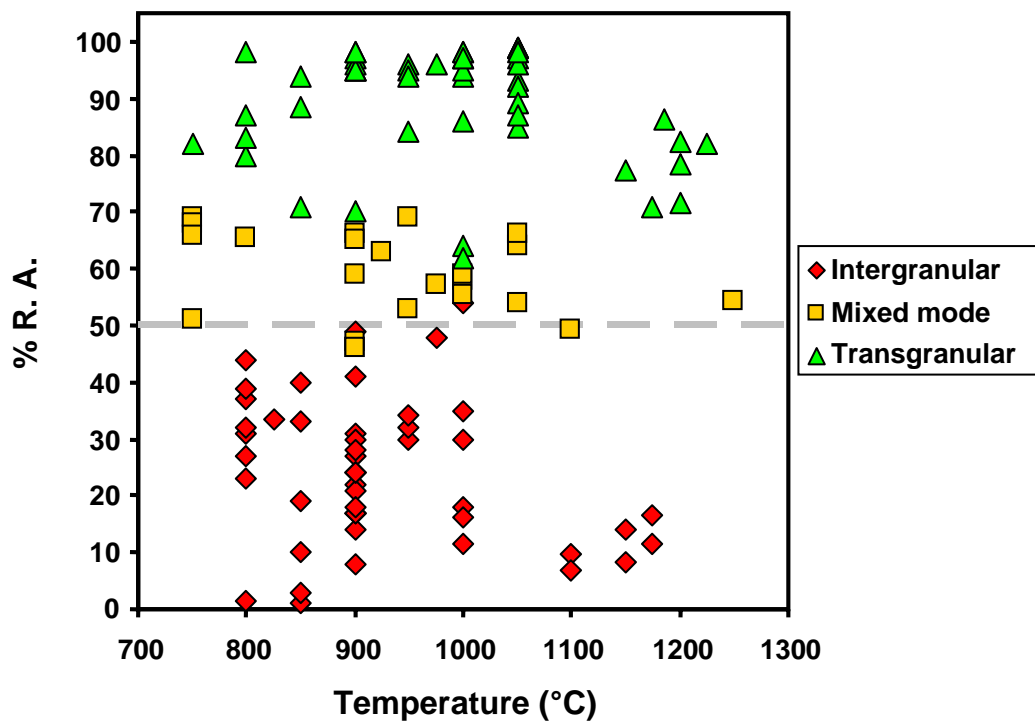


Figure 4.1: Dependence of reduction in area on failure mode in this work.

4.3 RELEVANCE OF THE HOT DUCTILITY TEST IN ASSESSING SUSCEPTIBILITY TO TRANSVERSE CRACKING

4.3.1 Background

The hot tensile test was initially used to study hot ductility, hot shortness and burning in hot working operations in the early 1960s (Lankford, 1972). The first comprehensive group of studies to evaluate the susceptibility of continuously cast steels to transverse surface cracking was conducted by Professor Childs and his graduate students in the late 1960s (referred to in Lankford, 1972). Resistance heated specimens were pulled to failure at high temperatures after *in situ* melting in a Gleeble® thermomechanical machine.

The hot tensile test has been used in many studies relating to crack susceptibility during continuous casting, either with heating directly to the test temperature, reheating to a solution treatment temperature before cooling to the test temperature, or with *in situ* melting before cooling to the test temperature, as discussed in **Sections 2.7.5 to 2.7.8**.

4.3.2 Limitations of the hot tensile testing technique in assessing the problem of transverse cracking

The continuous casting process starts with molten steel, which begins to solidify against a water-cooled copper mould, and is moved vertically down by oscillations of the mould. The strand is then cooled by water sprays between guiding rolls. This induces thermal cycles and thermal stresses on the strand surface. In microalloyed steels such as Nb-containing grades, thermal cycling can have a major influence on the precipitation behaviour of niobium carbonitrides (El-Wazri *et al.*, 1998a).

Owing to the direction of solidification and the strand thickness, there are often large dendrites that develop from the surface towards the solidification front as it progresses towards the centre of the strand. Segregation occurs between the dendrites and interdendritic liquid, often resulting in severe segregation of elements such as S, P, Sn to the interdendritic regions. The steel chemistry and thermal history determine whether the

resulting grain structure is coarse or fine, columnar or equiaxed; whether the oscillation marks are shallow or deep; and whether there is a chill zone between the surface and the columnar zone.

The major limitations of the hot tensile test in simulating the behaviour of the strand surface during continuous casting are:

- Oscillation marks
- Austenite grain size and morphology
- Total strain

Oscillation marks

Takeuchi and Brimacombe (1997) compared the subsurface structure between the top and bottom of oscillation marks. They found that a larger dendrite arm spacing and coarser secondary solidification structure at the bottom of the oscillation marks is linked to a coarse austenitic structure and thus a coarse ferrite-pearlite structure. This is important because transverse cracks are more likely to propagate from the bottom of the oscillation marks. Large regions of positive segregation are often found adjacent to deep oscillation marks, which may promote transverse cracking (Takeuchi and Brimacombe, 1997). The non-uniform structure is related to variations in surface cooling in the mould, as the gap between mould wall and steel surface is not uniform. The heat extraction from the base of the oscillation marks is lower than from the slab surface in contact with the mould wall. The shape of oscillation marks is composition dependent, with peritectic steels having deep, curved oscillation marks, whereas those on high carbon steels are relatively flat and shallow. Tsai *et al.* (2005) found that slab corner cracks initiated from oscillation marks on the broad face in Nb-microalloyed peritectic steels.

Surface strand effects, such as the rough surface with oscillation marks and related segregation effects, cannot be directly simulated in the hot tensile test. Revaux *et al.* (1994; 1996) melted and solidified notched tensile specimens in a purpose-built tensile testing setup with induction heating to simulate oscillation marks with coarse columnar grains perpendicular to the tensile direction. However, in most hot ductility tests, this process is not used, mainly due to the form of heating and difficulty of the tests.

In this work, the typical overall composition of this subsurface region is taken into account by using material sampled from just below the surface of the as-cast strand for the hot ductility specimens. Sampling was also done perpendicular to the casting direction and hence, to the tensile strain direction during straightening. This means that the tensile test is done across the width of the as-cast elongated columnar grains, hence sampling the particular steel chemistry of this region.

Austenite grain size and morphology

The cast strand structure, particularly the grain morphology, is very difficult to simulate in the typical hot tensile test. Whereas low and high carbon steel slabs have small equiaxed surface grains, peritectic steel grades have uneven grain sizes at the surface and columnar subsurface grains due to the mechanism of solidification (Maehara *et al.* 1990). Low carbon steels show primary delta ferrite solidification and high carbon steels show primary austenite solidification. However, in peritectic steels the primary delta ferrite to austenite transformation occurs around the solidification temperature. Peritectic steels show a high tendency for shrinkage, deep oscillation marks and coarse columnar austenite grains at the strand surface due to this solidification behaviour (Mazumdar and Ray, 2001). Cracks can propagate along the coarse austenite grain boundaries (~1 mm diameter) where a soft ferrite film has formed (Tsai *et al.* 2005). In contrast, laboratory hot ductility testing, whether by reheating or by *in situ* melting, generally produces an equiaxed, not columnar, grain morphology. The only exception is when directional solidification is used to promote elongated austenite grains perpendicular to the tensile direction.

Hot ductility is inversely proportional to grain size (Maehara *et al.* 1985). In the hot ductility test, it is recommended that a coarse austenite grain size (~200 μm) be promoted to more closely approximate the size of continuously cast grains. In coarse grained steels, deformation induced ferrite forms as thin films on the austenite grain boundaries, whereas in fine grained steels (grain size ~25 μm) the deformation is more homogeneous, so that the ferrite formation is not so localised (Lewis *et al.*, 1998). The direction of sampling from the as-cast slab is also important. Mintz *et al.* (2000) tested austenitic stainless steel having a coarse columnar structure. They observed that the lowest ductility was obtained for the samples taken parallel to the casting direction *i.e.* the direction containing the

highest density of grain boundaries. As this is also the direction of tensile strain during straightening, it would be more useful to machine the laboratory samples in this direction.

Total strain

Lankford (1972) observed that the strain at straightening was about 1.2% for a bloom casting facility. In the current study, the straightening strains for the different casting operations were found to be approximately 0.7% (Billet casting 1), 0.8% (Thin slab casting), 1.2% (Billet casting 2) and 1.4% (Thick slab casting), as shown in **Table 3.1**. In the hot tensile tests, the specimens are pulled to failure, thus the ductility measurements in this work are based on total strains of ~2-95 % at low strain rates, which are more than one magnitude larger than the straightening strains. Thus the mechanisms occurring during the hot ductility test are not necessarily coincident with those occurring during straightening. This has implications for the formation of deformation induced ferrite and for the occurrence of dynamic recrystallisation, as discussed below.

4.3.3 Analysis of the hot ductility curve

In the temperature region tested in this work, 750 to 1200 °C, there is a low ductility trough with regions of high ductility on either side, as shown in **Figure 4.2**.

Low ductility trough (LD trough)

The low ductility trough (LD trough) is mostly associated with ductile intergranular fracture that occurs due to the formation of PFZs or thin films of deformation induced ferrite (DIF) at austenite grain boundaries, or to grain boundary sliding in single phase austenite (Suzuki *et al.* 1982), as detailed in **Section 2.5.1**. The reduction of area is similar for these mechanisms of intergranular failure, so a discontinuity is seldom seen near the A_{e3} temperature (Mintz *et al.*, 1991). Failure by any of these mechanisms is enhanced by the presence of precipitates, such as MnS, at the grain boundaries (Mintz and Yue, 1993a). These mechanisms, although intergranular, are associated with ductile failure, and can occur during strand straightening.

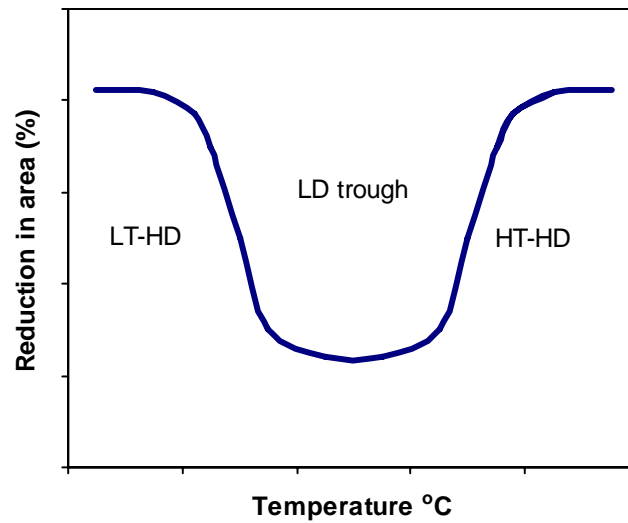


Figure 4.2: Schematic diagram showing the ductility trough (LD trough) flanked by a low temperature high ductility region (LT-HD) and a high temperature high ductility region (HT-HD).

Mintz *et al.* (1991) determined an empirical relationship for the minimum R.A. *i.e.* trough depth, in high Mn (1-1.4% Mn) steels with $S > 0.005\%$:

$$R.A._{\min.} (\%) = 700 d^{-0.5} (1 - 4.3 s^{-0.5}) + 20 (\log \dot{\epsilon} + 2.5) \quad (4.1)$$

where d is the austenite grain size in μm , s is the sum of the interparticle spacing and particle diameter in nm, and $\dot{\epsilon}$ is the strain rate in s^{-1} . The equation appears to apply to both transformation-induced and precipitation-related intergranular failure. This type of relationship is very important for predicting the likelihood of transverse cracking in straightening, as the variables that cause intergranular fracture in the tensile test are the same ones responsible for transverse cracking during straightening.

Low temperature, high ductility region (LT-HD)

In low carbon steels, the ductility recovery in the LT-HD region is characterised by formation of a large amount of ferrite – up to 40-50% (Cowley *et al.* 1998; Mintz *et al.* 1991), either prior to the actual tensile strain being applied (Mintz and Yue, 1993a) or as DIF during straining. This distributes the strain more homogeneously within the grain, thus there is no strain concentration at the grain boundary region. It is not clear, however, whether the low strains associated with continuous casting would be sufficient to form

40% deformation induced ferrite (DIF) during straightening. Mintz (1996) showed that it would be necessary to straighten at ~ 30 °C below the undeformed A_{r3} (transformation temperature on cooling) to ensure that the required large volume of ferrite is formed before straightening. In his latest paper, Mintz (2008) states that narrow trough behaviour, *i.e.* where ductility recovers just below the A_{e3} but above the A_{r3} temperature, is unlikely to occur in commercial casting, as the strain is too low.

High temperature, high ductility region (HT-HD)

The HT-HD region occurs due to one of the following mechanisms:

- Reduced precipitation in the matrix and on grain boundaries, which lowers the formation of PFZs at the higher testing temperatures (Mintz *et al.*, 1991).
- Dynamic recrystallisation of the austenite (Mintz and Yue, 1993a).
- Grain boundary migration, which isolates cracks initiated at grain boundaries (Mintz *et al.*, 1991). Dynamic recrystallisation can provide a high driving force for grain boundary migration.
- Low flow stresses as a result of dynamic recovery, which reduces stress concentration at crack nucleation sites (Mintz *et al.*, 1991).
- The absence of thin ferrite films on austenite grain boundaries at temperatures just above the A_{e3} (Mintz *et al.* 1995).

As-cast grain sizes at straightening are mostly in the range 500 μm to 1 mm. This, together with the fact that the typical strains experienced in straightening operations are small, *i.e.* usually less than 2%, means that only dynamic recovery occurs at and not dynamic recrystallisation (Mintz and Yue, 1993a). However, during tensile testing the strains are much larger and dynamic recrystallisation readily occurs. If dynamic recrystallisation does occur, the ductility increases substantially, but in the absence of dynamic recrystallisation at high temperatures, the reduction in area values remain constant; *i.e.* the ductility does not recover (Mintz *et al.*, 1991). **Figure 4.3** illustrates the difference in reduction of area for carbon and niobium steels with and without dynamic recrystallisation at the high temperature end of the ductility trough (Cowley *et al.*, 1998).

By metallographic examination, Cowley *et al.* (1998) found that the temperatures for the onset of dynamic recrystallisation in C-Mn-Al and C-Mn-Al-Nb steels were ~ 0 -50 °C lower than those determined by analysing the load-elongation curve.

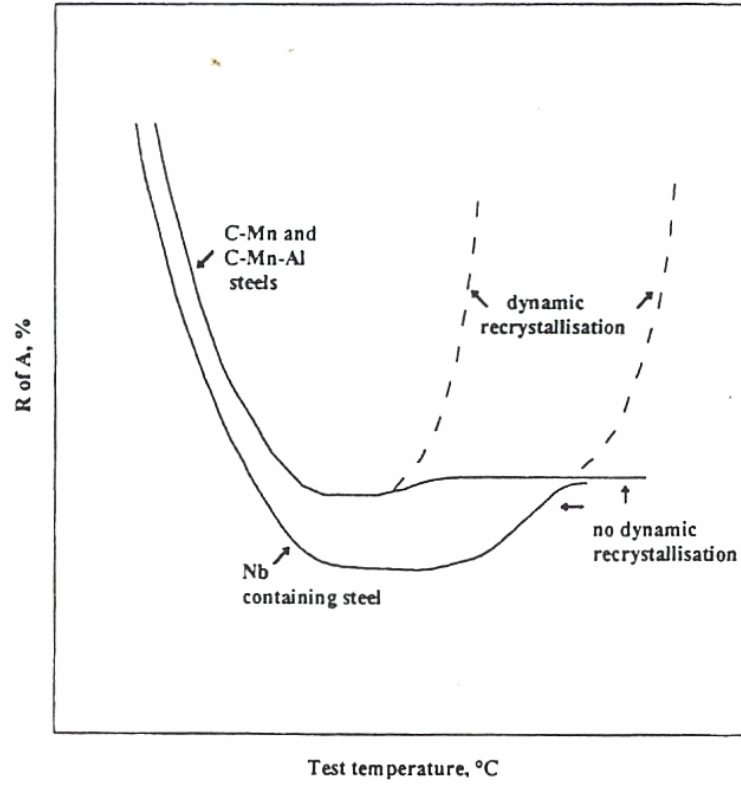


Figure 4.3: Schematic diagram showing the effect of dynamic recrystallisation on reduction of area for carbon and niobium steels (Cowley *et al.*, 1998).

The onset of dynamic recrystallisation occurs when the applied strain at a specific temperature is sufficiently high (Mintz *et al.*, 1998). The strain to the peak stress ε_p is defined as:

$$\varepsilon_p = A D_0^{0.5} Z^{0.15} \quad (4.2)$$

where: A is a constant, D_0 is the austenite grain diameter in μm , and Z is the Zener Holloman parameter in s^{-1} :

$$Z = \dot{\varepsilon} \exp\left(\frac{Q}{RT}\right) \quad (4.3)$$

where $\dot{\varepsilon}$ is the strain rate in s^{-1} , Q is the activation energy in kJ mol^{-1} , R is the universal gas constant and T is the temperature in K. For plain carbon, Al-killed steels, Mintz *et al.* (1998) used values of $A = 6.3 \times 10^{-4}$ (for grain sizes $>200 \mu\text{m}$) and $Q = 290 \text{ kJ mol}^{-1}$. The critical strain for dynamic recrystallisation ε_c is less than ε_p , e.g. $\varepsilon_c = 0.83\varepsilon_p$ or $0.8\varepsilon_p$ (Stumpf *et al.*, 2006) but Mintz *et al.* (1998) suggest using ε_p rather than ε_c , as the dynamic recrystallisation needs to be advanced enough to prevent coalescence of cracks.

Based on the discussion above, the crack susceptibility of the strand surface during continuous casting in this high temperature (HT-HD) region cannot be directly inferred from the total reduction in area value at and above the dynamic recrystallisation temperature (Mintz *et al.*, 1991).

4.4 SUMMARY – USING THE HOT DUCTILITY CURVE TO IMPROVE THE INDUSTRIAL CONTINUOUS CASTING OPERATION

In this chapter, it has been shown that a certain minimum ductility value, usually determined from reduction in area curves, is necessary to minimise or avoid transverse cracking during straightening in continuous casting. In this work, it was found that intergranular cracking was only eliminated at R. A. values approaching 50%.

The relevance of the laboratory-scale hot ductility test in assessing the likelihood of cracking was discussed. The main areas that are not simulated in the tensile test *viz.* oscillation marks, austenite grain size and morphology (especially in peritectic steels), and the total strain, were reviewed.

The hot ductility curve was analysed with specific reference to the low ductility trough, low temperature, high ductility and the high temperature, high ductility regions. The importance of the minimum R. A. value, the Ae_3 and Ar_3 temperatures, the formation of deformation induced ferrite and the occurrence of dynamic recrystallisation were stressed.

Although the hot tensile test has many obvious deviations from the industrial operation, it has been found to be an extremely useful tool to industry in suggesting changes to the temperature at the straightener and changes to the composition of particular steels. The results and discussion in the following chapters should be seen in the light of these limitations.

Chapter 5: Low Carbon Steels

Hot tensile behaviour in the low carbon steels: results, discussion and application

5.1 OVERVIEW OF CHAPTER 5

The low carbon steels with carbon contents ranging from 0.10 to 0.16% C were sampled from thick slab. All five steels contain aluminium, three have high silicon contents, and two have high copper contents (one also with high nickel). The five steels were reheated to 1300 °C, cooled to testing temperatures in the range 750 – 1100 °C at rates of 0.3, 1.2 and 3.0 °Cs⁻¹ and pulled to failure at strain rates of 10⁻⁴ or 10⁻³ s⁻¹.

Increasing the strain rate from 10⁻⁴ to 10⁻³ s⁻¹ improved the hot ductility. Calcium-treatment was shown to be very important in minimising CuS and FeS formation, both which are detrimental to hot ductility. The importance of good steelmaking practice to minimise inclusions remaining in the cast steel was highlighted. It was also shown that a Ni:Cu ratio of ~ 1:1 is needed for acceptable hot ductility in high copper steels.

5.2 TRANSFORMATION IN THE LOW CARBON STEELS

The chemical composition of the low carbon steels is given in **Table 5.1**. It should be noted that steels *LC-3*, *LC-4* and *LC-5* have high levels of Si and steels *LC-4* and *LC-5* have high levels of Cu. Steel *LC-5* is rephosphorised and also has high Ni and Cr contents.

The transformation temperatures from the two equations listed in **Table 2.3**: *GAS* (Deo *et al.*, 1995) and Andrews (1965) and from Thermo-Calc™ ^{iii, iv} are listed in **Table 5.2**. The equilibrium phase transformations as a function of temperature, modelled using the Thermo-Calc™ TCFE3 database, are shown in **Figure 5.5**, **Figure 5.6** and **Figure 5.7**.

Table 5.1: Chemical composition of low carbon steels (in mass %).

Steel	C	Mn	P	S	Si	Al	N	Ni	Cu	Cr	Mo
LC-1	0.10	0.43	0.012	0.006	0.04	0.042	0.0085	0.03	0.02	0.02	-
LC-2	0.12	0.65	0.010	0.009	0.01	0.045	0.0062	0.02	0.01	0.03	0.01
LC-3	0.14	1.10	0.010	0.007	0.25	0.021	0.0038	0.02	0.02	0.02	-
LC-4	0.16	0.72	0.010	0.011	0.18	0.021	0.0091	0.09	0.27	0.02	0.02
LC-5	0.12	0.32	0.100	0.012	0.53	0.028	0.0060	0.26	0.34	0.55	0.02

Table 5.2: Calculated transformation temperatures (in °C) for low carbon steel compositions in this work.

Steel	<i>Ae</i> ₃ (start of ferrite formation)				<i>Ae</i> ₁ (start of austenite formation)		
	<i>GAS</i> ⁱ	<i>And</i> ⁱⁱ	T-C SSOL2 ⁱⁱⁱ	T-C TCFe3 ^{iv}	<i>And</i> ⁱⁱ	T-C SSOL2 ⁱⁱⁱ	T-C TCFe3 ^{iv}
LC-1	855	866	857	862	714	701	714
LC-2	843	852	841	847	708	705	707
LC-3	839	847	846	834	706	681	695
LC-4	830	840	836	837	711	682	700
LC-5	855	934	837	912	753	719	728

ⁱ Genetic Adaptive Search (GAS) equation.

ⁱⁱ *Andrews* formula.

ⁱⁱⁱ Modelled using Thermo-Calc database SSOL2 (1999).

^{iv} Modelled using Thermo-Calc database TCFE3 (2006) – this work.

5.2.1 Ae_3 temperatures

A comparison of the calculated *GAS*, modelled TCFe3 and SSOL2 Ae_3 temperatures with the calculated Andrews Ae_3 temperature is shown in **Figure 5.1**. For the five low carbon steels *LC-1* to *LC-5*, the Ae_3 temperatures were predicted to be in the following ranges:

- *GAS*: 830 – 855 °C
- Andrews: 840 – 934 °C
- Thermo-Calc™ (SSOL2): 830 – 871 °C
- Thermo-Calc™ (TCFe3): 834 – 912 °C

The decrease in Ae_3 from *LC-1* to *LC-2* is due to the increases in the carbon and manganese and decrease in silicon contents. The decrease from *LC-2* to *LC-3* is again due to the increases in the carbon and manganese contents, but in spite of the increase in silicon content.

The *GAS* Ae_3 for *LC-4* is even lower than for *LC-3* because of the ten-fold increase in the amount of copper, the decrease in silicon, and the increase in carbon content.

The *GAS*, SSOL2, TCFe3 and Andrews Ae_3 temperatures vary by less than 12 °C for steels *LC-1* to *LC-4*, but by up to 100 °C for *LC-5*, as *GAS* and SSOL2 predictions do not depend on %P. The higher *GAS* Ae_3 temperature for *LC-5* is due to the high silicon, low

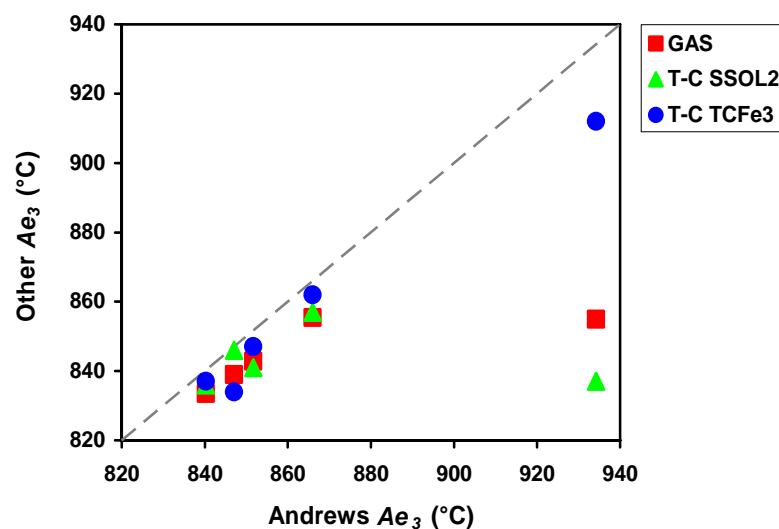


Figure 5.1: Comparison of the calculated *GAS*, modelled TCFe3 and SSOL2 Ae_3 temperatures with the calculated *Andrews* Ae_3 temperature.

carbon and low manganese content and in spite of the increase in nickel, copper and chromium contents. The Ae_3 temperature predicted from the Andrews formula is 79 °C higher than the GAS prediction. This is due to the large dependence of the Andrews Ae_3 formula on phosphorus ($700 * \%P$), which results in a 63 °C increase for an increase of 0.09% P. The TCFE3 Ae_3 is also very sensitive to %P and is high for LC-5 (912 °C).

5.2.2 Ae_1 temperatures

The Ae_1 temperatures for the five low carbon steels LC-1 to LC-5 were predicted to be in the following ranges:

- Andrews: 706 – 753 °C
- Thermo-Calc™ (SSOL2): 681 – 719 °C
- Thermo-Calc™ (TCFe3): 695 – 728 °C

The SSOL2 Ae_1 temperatures are the lowest, and the TCFE3 and Andrews (1965) temperatures vary by less than 25 °C (**Figure 5.2**).

The Andrews Ae_1 temperatures depend on Mn and Ni (which lower the temperature), and more strongly on Si and Cr (which increase the temperature). This explains the higher Ae_1 temperature of LC-5, which has very high Si and Cr contents.

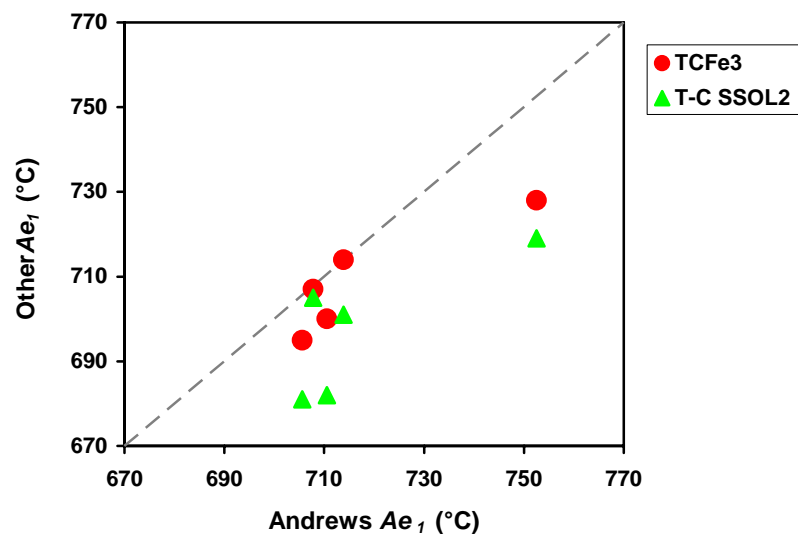


Figure 5.2: Comparison of the modelled TCFE3 and SSOL2 Ae_1 temperatures with the calculated Andrews Ae_1 temperature.

5.3 PRECIPITATE DISSOLUTION IN THE LOW CARBON STEELS

For low solute contents, as in low carbon steels, the total mass concentrations of the dissolved elements, in equilibrium with the precipitated phase, can be used to represent the solubility product discussed in **Section 2.6**.

AlN and MnS precipitates can occur in steels *LC-1* to *LC-5*, together with more complex precipitates, such as oxides and oxysulphides, for which the dissolution temperatures have not been discussed in this work.

An exception to the more commonly used equilibrium solubility is the critical Mn:S ratio calculation (De Toledo, 1993) from **Section 2.5**. The results for the actual Mn:S / critical Mn:S ratio are shown in **Table 5.3**.

Table 5.4 lists the equilibrium dissolution temperatures (T_{diss}) of AlN and MnS precipitates in austenite calculated by the solubility equations in **Table 2.2** for all the low carbon steels. No AlN dissolution temperatures were obtained from the initial Thermo-CalcTM modelling (Cornish, 1999), as the FEDAT and SSOL2 databases do not include aluminium nitride. Subsequent modelling by the author in 2006 on the new TCFE3 database (which includes Al and N) did produce AlN dissolution temperatures. **Figure 5.5**, **Figure 5.6** and **Figure 5.7** show the equilibrium precipitation and transformation as a function of temperature, modelled using the Thermo-CalcTM TCFE3 database.

The T_{diss} is taken to be the highest achievable precipitation temperature for a specific composition. In reality, however, conditions do not approach equilibrium, and the precipitation would occur at significantly lower temperatures, if at all, under cooling conditions.

Table 5.3: Critical and actual Mn:S ratios for all of the steels.

Steel	(Mn:S) _c Critical ^v	(Mn:S) _a Actual	(Mn:S) _a / (Mn:S) _c	Actual > Critical? ^v
LC-1	78	72	0.92	N
LC-2	56	72	1.28	Y
LC-3	69	157	2.28	Y
LC-4	48	65	1.36	Y
LC-5	45	27	0.59	N

Table 5.4: Solubility of precipitates in austenite in the low carbon steels – calculated equilibrium precipitate dissolution temperatures.

Steel	Turkdogan ^{vi}	T-C TCFe3 ^{vii}	Turkdogan ^{vi}	T-C TCFe3 ^{vii}
	AlN	AlN	MnS	MnS
LC-1	1239	1161	1362	1354
LC-2	1204	1141	1474	1442
LC-3	1047	1057	1516	1467
LC-4	1153	1121	1520	1459
LC-5	1136	1127	1415	1405

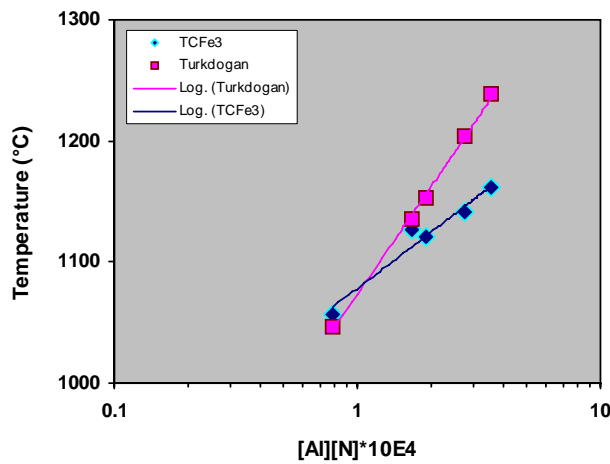


Figure 5.3: Logarithmic dependence of the AlN dissolution temperature on [Al][N] for the low carbon steels (Thermo-CalcTM TCFE3 and Turkdogan equation).

^v Mn/S (actual) > Mn/S (critical) for good hot ductility (De Toledo, 1993).

^{vi} Turkdogan (1987).

^{vii} Modelled using Thermo-CalcTM database TCFE3 (2006) – this work.

The predicted AlN dissolution temperature range is: 1047 °C (*LC-3*) to 1239 °C (*LC-1*) calculated by the Turkdogan equation and 1057 °C (*LC-3*) to 1161 °C (*LC-1*) modelled using the TCFE3 Thermo-Calc™ database (**Figure 5.3**). All the AlN temperatures are lower than the solution treatment temperature (1300 °C), hence all AlN precipitates in the steel before the test would be dissolved, and all Al and N are thus available to potentially form AlN on straining during the tensile test.

All the MnS dissolution temperatures in the low carbon steels were found to be above the solution treatment temperature of 1300 °C. The predicted MnS dissolution temperature range is 1362 °C (*LC-1*) to 1520 °C (*LC-4*) calculated by the Turkdogan (1987) equation and 1354 °C (*LC-1*) to 1467 °C (*LC-3*) modelled using the TCFE3 Thermo-Calc™ database (**Figure 5.4**).

In steel *LC-1*, the possible volume fraction of MnS precipitation should be low due to the low manganese content (0.43% Mn).

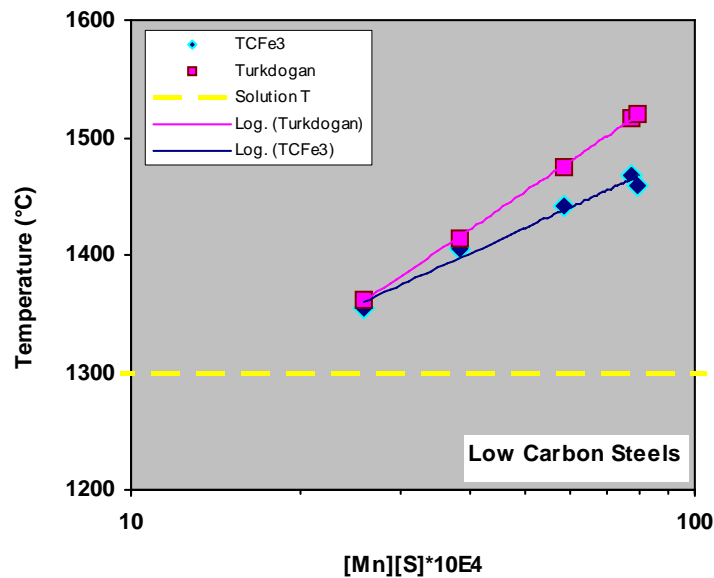
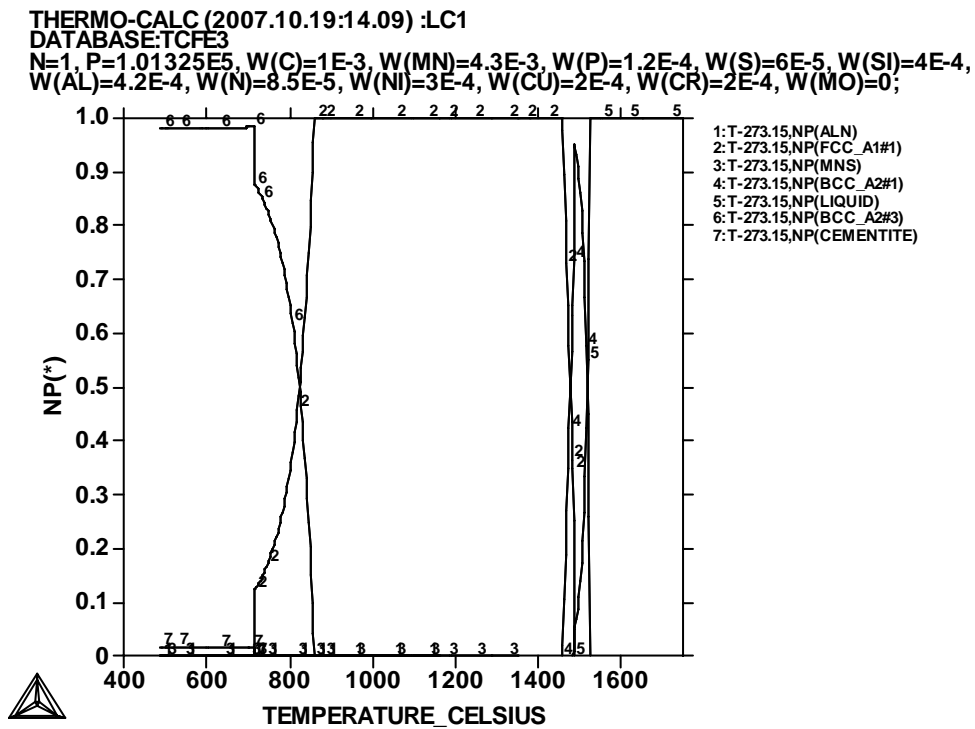
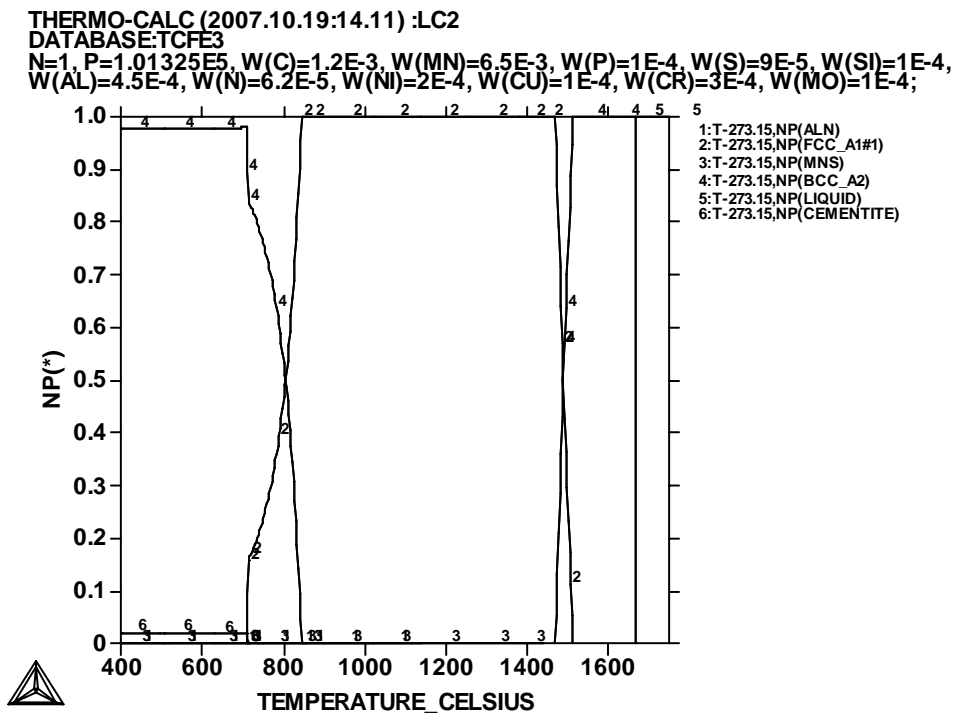


Figure 5.4: Logarithmic dependence of the MnS dissolution temperature on $[Mn][S]$ for the low carbon steels modelled using Thermo-Calc™ and calculated using the Turkdogan (1987) equation.



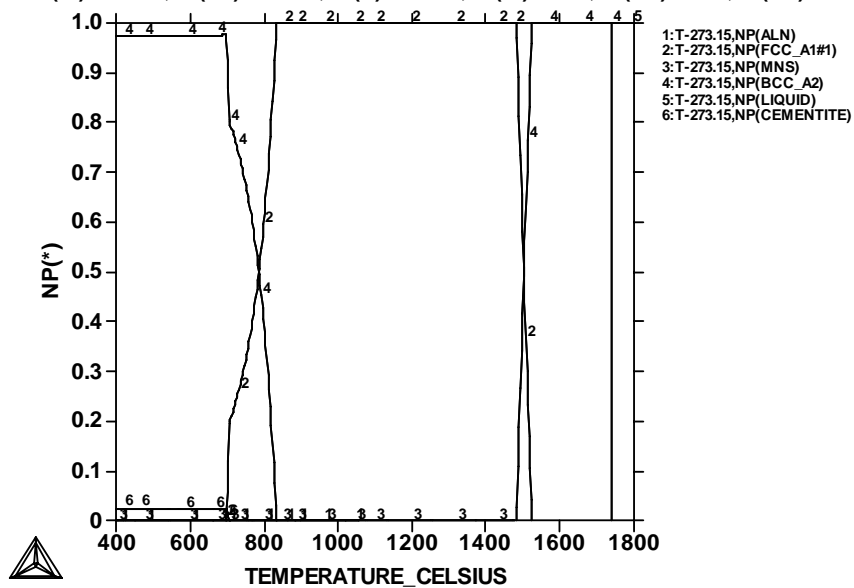
a)



b)

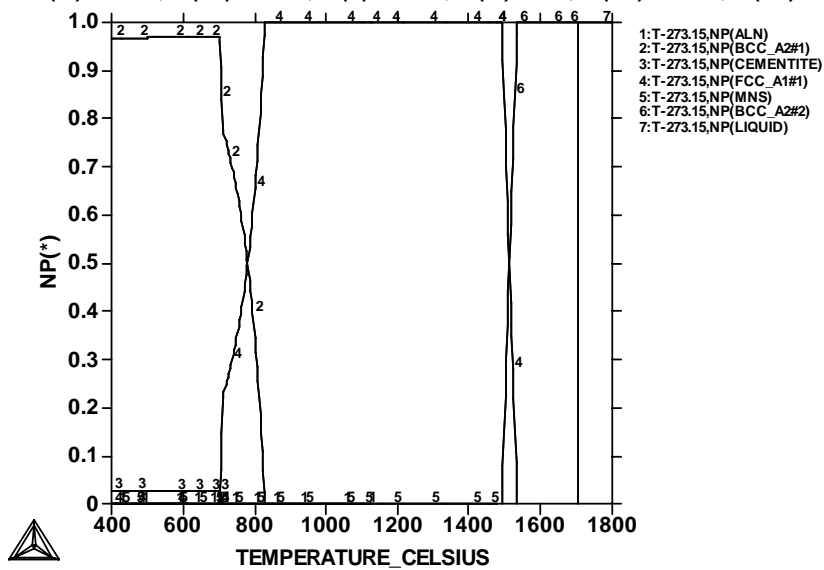
Figure 5.5: Thermo-Calc™ graphs modelled using database TCFe3, showing the equilibrium phases for low carbon steels a) LC-1 and b) LC-2.

THERMO-CALC (2007.10.20:17.31) :LC3
 DATABASE:TCFe3
 N=1, P=1.01325E5, W(C)=1.4E-3, W(MN)=1.1E-2, W(P)=1E-4, W(S)=7E-5,
 W(SI)=2.5E-3, W(AL)=2.1E-4, W(N)=3.8E-5, W(NI)=2E-4, W(CU)=2E-4, W(CR)=2E-4, W(MO)=0;



a)

THERMO-CALC (2007.10.20:17.35) :LC4
 DATABASE:TCFe3
 N=1, P=1.01325E5, W(C)=1.6E-3, W(MN)=7.3E-3, W(P)=1E-4, W(S)=1.1E-4,
 W(SI)=1.8E-3, W(AL)=2.1E-4, W(N)=9.1E-5, W(NI)=9E-4, W(CU)=2.7E-3, W(CR)=2E-4, W(MO)=2E-4;



b)

Figure 5.6: Thermo-Calc™ graphs modelled using database TCFe3, showing the equilibrium phases for low carbon steels a) LC-3 and b) LC-4.

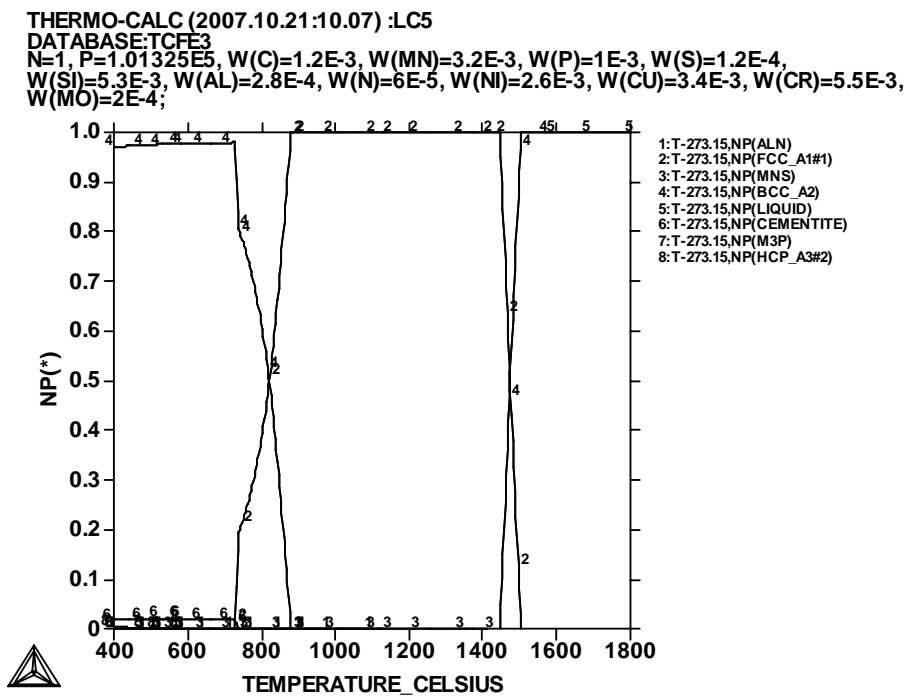


Figure 5.7: Thermo-Calc™ graph modelled using database TCFE3, showing the equilibrium phases for low carbon steel LC-5.

5.4 LOW CARBON STEEL LC-1

5.4.1 Introduction

Figure 5.8 (schedules G, C, H, D and F) shows the engineering stress – elongation curves for steel LC-1. The occurrence of dynamic recrystallisation can be detected on the stress – elongation curves by either an abrupt decrease or oscillations of the flow stress (Abushosha *et al.*, 1991). The onset of dynamic recrystallisation is indicated by arrows on the graphs and the temperatures are listed in Table 5.5.

The maximum strength for all the testing schedules is shown as a function of testing temperature in Figure 5.9.

The percentage reduction in area (% *R. A.*) is shown as a function of testing temperature in **Figure 5.10**. The percentage total elongation is shown as a function of testing temperature in **Figure 5.11**. The modelled Thermo-CalcTM TCF_{e3} A_{e3} transformation temperature of 862°C from **Table 5.2** is indicated on the graphs.

Scanning electron microscopy (SEM) micrographs of the internal precipitates, microvoid coalescence and microcracks are shown in **Figure 5.12** to **Figure 5.14**.

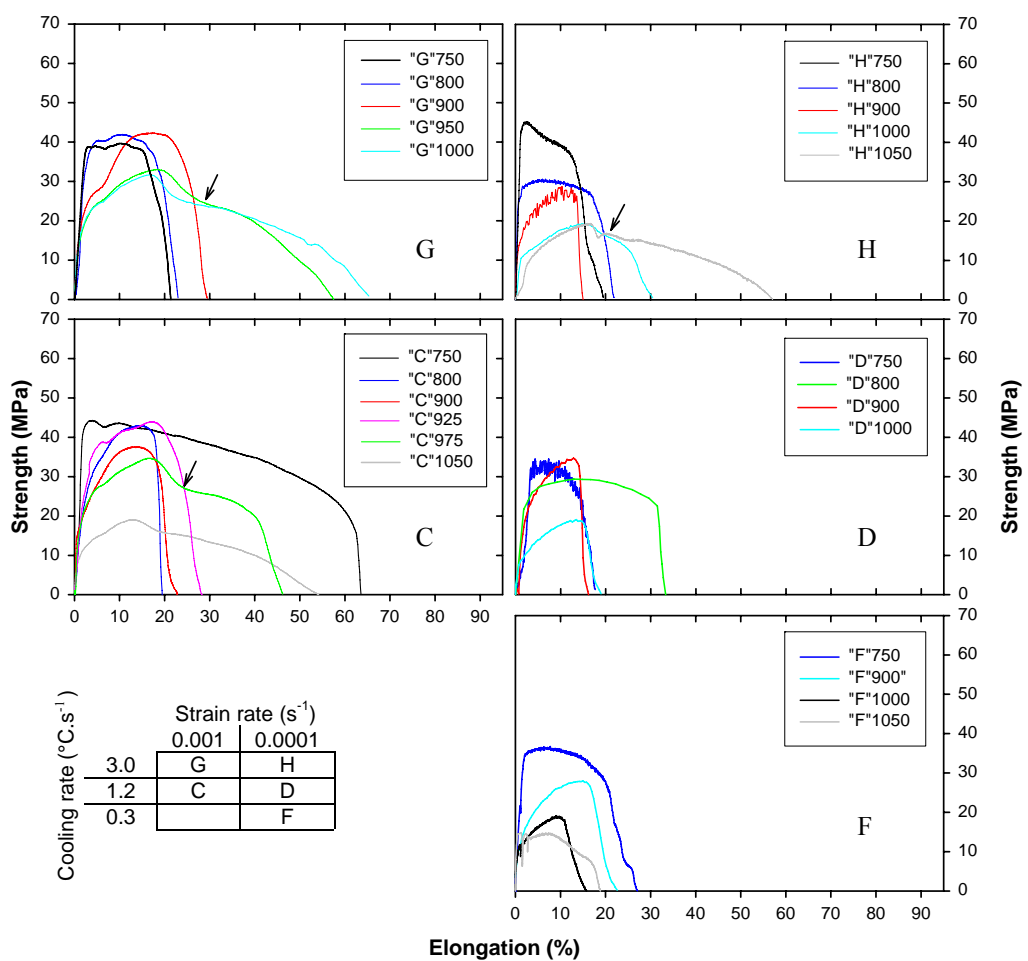


Figure 5.8: Engineering stress as a function of elongation for steel *LC-1*. The key to the testing schedules is also shown. The arrows indicate the onset of dynamic recrystallisation.

5.4.2 Maximum strength

Figure 5.8 shows the differences in the strength – elongation graphs due to the different testing schedules. As can be seen, no dynamic recrystallisation was evident in the tested temperature ranges in schedules D and F.

Figure 5.9 shows a general trend of increasing maximum strength (S_u) with decreasing temperature between 750 – 1050 °C for all testing schedules. The curves fitted 3rd or 4th order polynomial equations ($r^2 = 0.99$) and showed a plateau or slight decrease with decrease in temperature from 900 °C to 750 °C. This temperature oscillation occurred around the Ae_3 temperature of 862 °C.

From 800 – 1000 °C the higher strain rate showed higher S_u values than the lower strain rate and at 750 and 1050 °C there was little difference between S_u values. There was little influence of cooling rate on maximum strength at both strain rates.

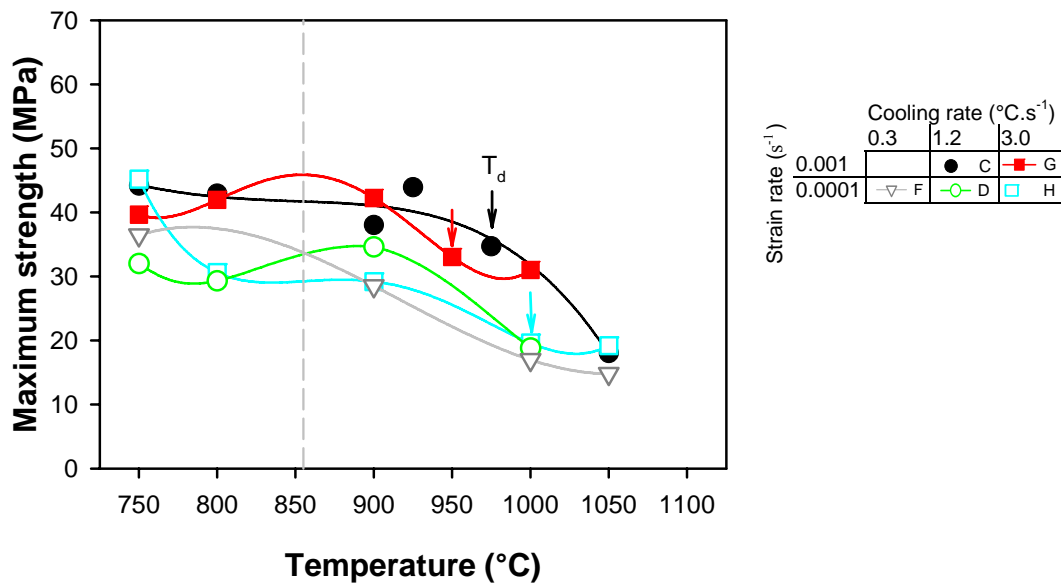


Figure 5.9: Maximum strength for steel LC-1 as a function of testing temperature, strain rate and cooling rate.

5.4.3 Reduction in area

At high strain rate of 10^{-3} s^{-1} : the low and high temperature ductility recovery (taken as 50% R. A.) was moved to lower temperatures by about 50 °C with an increase in cooling rate from 1.2 to 3.0 °C.s⁻¹ as shown in **Figure 5.10**. At 750°C, schedule G (3.0 °C.s⁻¹) showed a lower ductility value than at 800 °C. This either indicates a very wide ductility trough or problems with the initial specimen conditions *e.g.* very large inclusions or an existing crack.

At low strain rate of 10^{-4} s^{-1} : the high temperature ductility recovery (50% R. A.) was shifted to lower temperatures by at least 50 °C with an increase in cooling rate from 0.3 – 3.0 °C.s⁻¹. Considerably wide troughs were found at the low strain rate with low cooling rates (0.3 and 1.2 °C.s⁻¹), where ductility recovery occurred at temperatures above 1050 °C.

A decrease in strain rate decreased the minimum reduction in area (R. A.) value and widened the temperature range of the ductility trough.

The onset of dynamic recrystallisation (T_d) occurred at R. A. values greater than 50% as ductility recovered on the high temperature side of the trough.

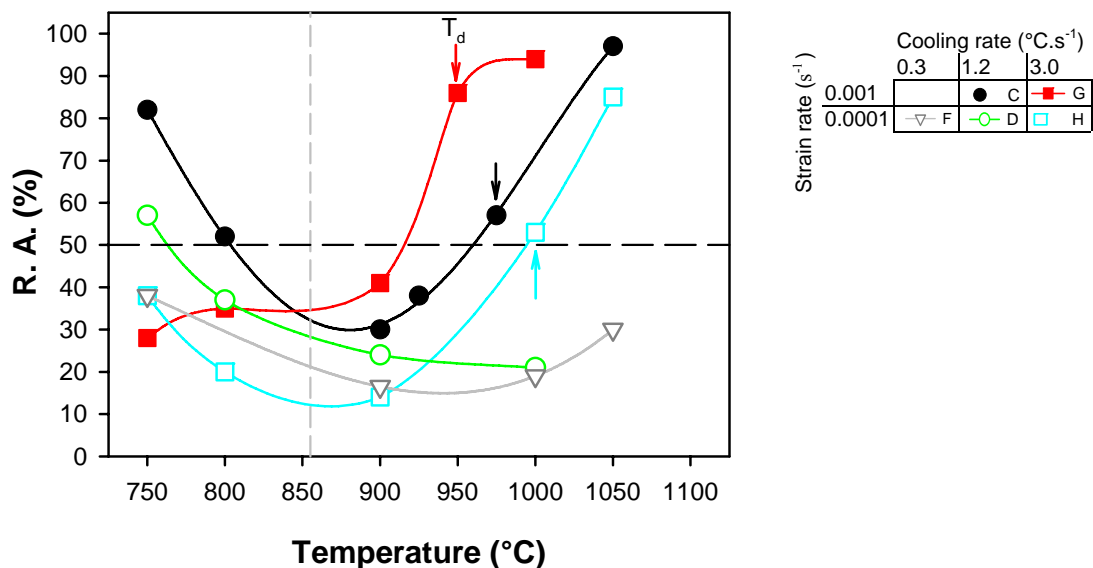


Figure 5.10: Reduction in area for steel LC-1 as a function of testing temperature, strain rate and cooling rate.

5.4.4 Total elongation

Figure 5.11 shows that the total elongation curves follow similar trends to the reduction in area.

At high strain rate of $10^{-3} s^{-1}$: an increase in cooling rate shifted the high temperature elongation recovery to lower temperatures by approximately 50 °C.

At low strain rate ($10^{-4} s^{-1}$): cooling rate appears to have had little influence on the total elongation between 750 – 900 °C. However, an increase in cooling rate from 0.3 to 3.0 °C.s⁻¹ increased the total elongation between 1000 and 1050 °C.

Decreasing the strain rate decreased the elongation at most temperatures, except at 800 °C, where the values were similar. The onset of dynamic recrystallisation (T_d) coincided with elongation recovery at high temperatures.

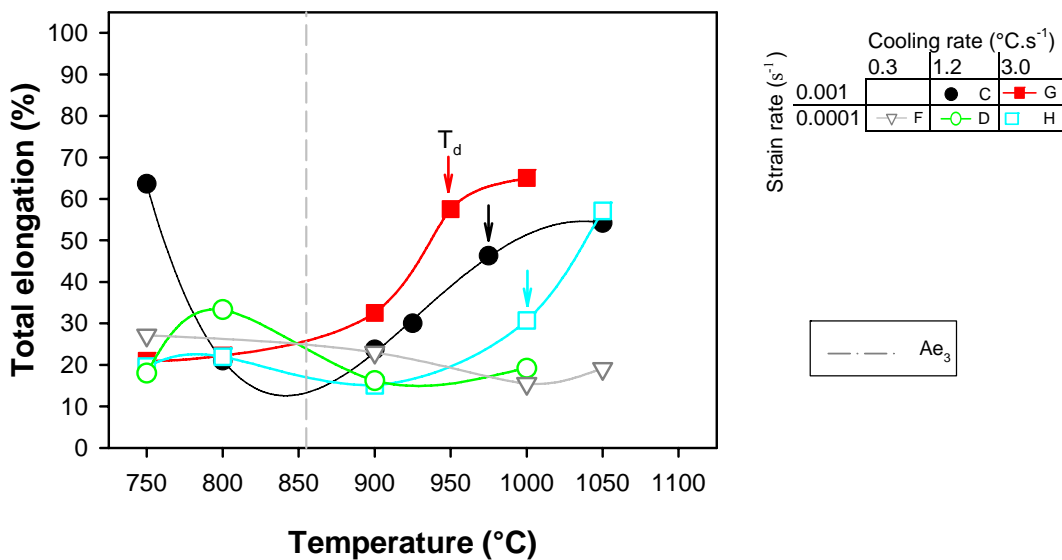


Figure 5.11: Elongation for steel LC-1 as a function of testing temperature, strain rate and cooling rate.

5.4.5 Scanning electron microscopy

High strain rate (10^{-3} s^{-1}):

- $1.2 \text{ }^\circ\text{C}\cdot\text{s}^{-1}$: low ductility at $900 \text{ }^\circ\text{C}$ (**Figure 5.12 a**) was characterized by many small voids in straight lines interconnected by microcracks on or near the prior austenite grain boundaries. EDS analysis of the voids revealed precipitates containing Fe-Mn-Al-O-S. At a higher temperature of $975 \text{ }^\circ\text{C}$ (**Figure 5.12 b**), there were fewer visible precipitates, with less interconnection and cracking than at $900 \text{ }^\circ\text{C}$. No EDS analysis in microvoids was possible, as the precipitates were too small.
- $3.0 \text{ }^\circ\text{C}\cdot\text{s}^{-1}$: in the low ductility sample tested at $900 \text{ }^\circ\text{C}$ (**Figure 5.13 a**) in a few areas one line or two parallel lines of precipitates near prior austenite grain boundaries were seen. There was substantial interconnection of microvoids and cracking. Some precipitates were analyzed as FeS and others contained Al-O. At $1000 \text{ }^\circ\text{C}$ (**Figure 5.13 b**), good ductility was characterised by a limited amount of microvoid coalescence, with no cracking along prior austenite grain boundaries. No precipitate analysis was obtained in the microvoids, as the precipitates were too small.

Low strain rate (10^{-4} s^{-1}):

- For all three cooling rates, cracks caused by microvoid coalescence along prior austenite grain boundaries were observed at a temperature of $900 \text{ }^\circ\text{C}$ (**Figure 5.14 a, d and e**).
- The following precipitates were analyzed:
 - $0.3 \text{ }^\circ\text{C}\cdot\text{s}^{-1}$: FeS and MnS (**Figure 5.14 b**)
 - $1.2 \text{ }^\circ\text{C}\cdot\text{s}^{-1}$: Fe-Al-S-O (**Figure 5.14 c**), MnS (**Figure 5.14 d**) and Fe-S-O
 - $3.0 \text{ }^\circ\text{C}\cdot\text{s}^{-1}$: Fe-Mn-O and Fe-Al-O (**Figure 5.14 e**)
- At a testing temperature of $800 \text{ }^\circ\text{C}$ and cooling rate of $1.2 \text{ }^\circ\text{C}\cdot\text{s}^{-1}$ (**Figure 5.14 c**), an internal crack was seen with a parallel row of microvoids containing precipitates such as Fe-Al-S-O.

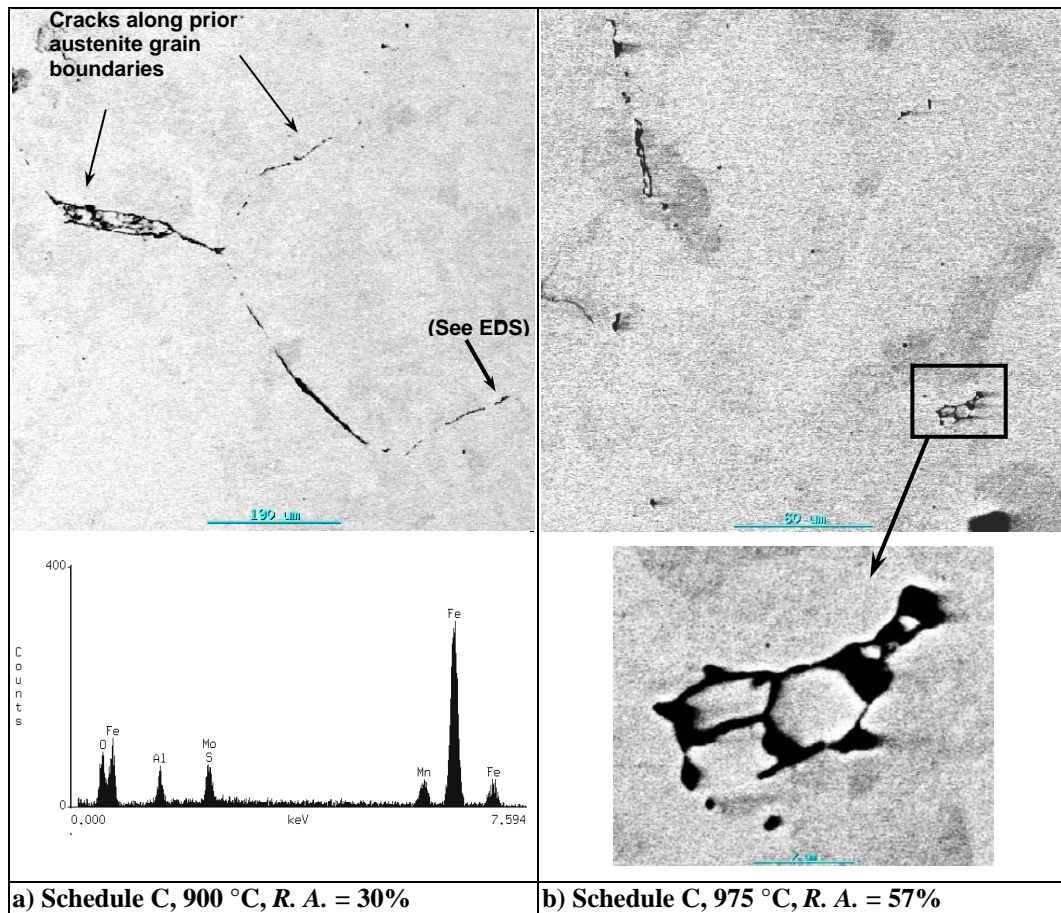


Figure 5.12: SEM backscatter images of steel *LC-1* tested under schedule C conditions, showing microvoid coalescence between precipitates.

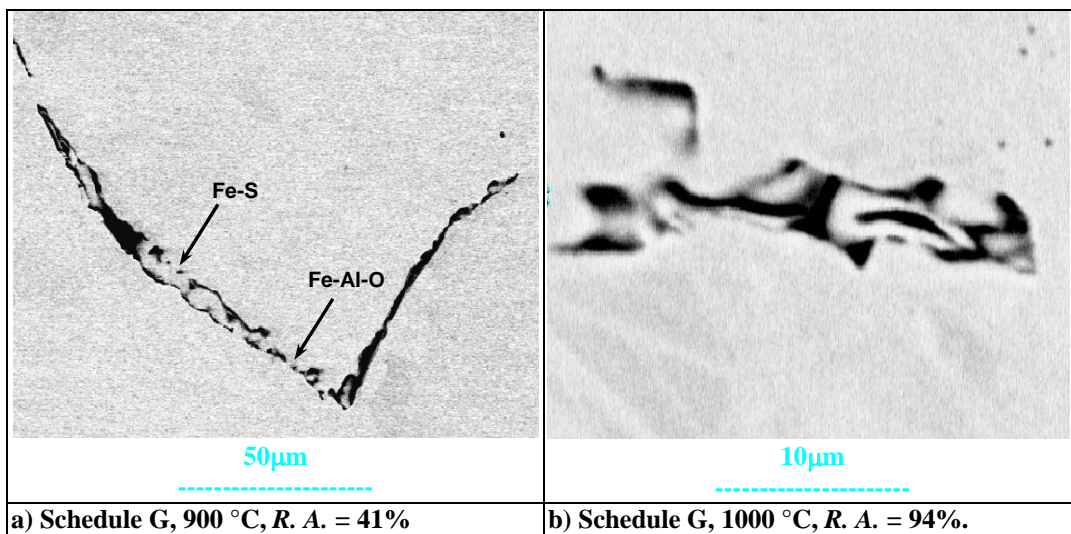


Figure 5.13: SEM backscatter images of steel *LC-1* tested under schedule G conditions, showing cracks along prior austenite grain boundaries formed by microvoid coalescence.

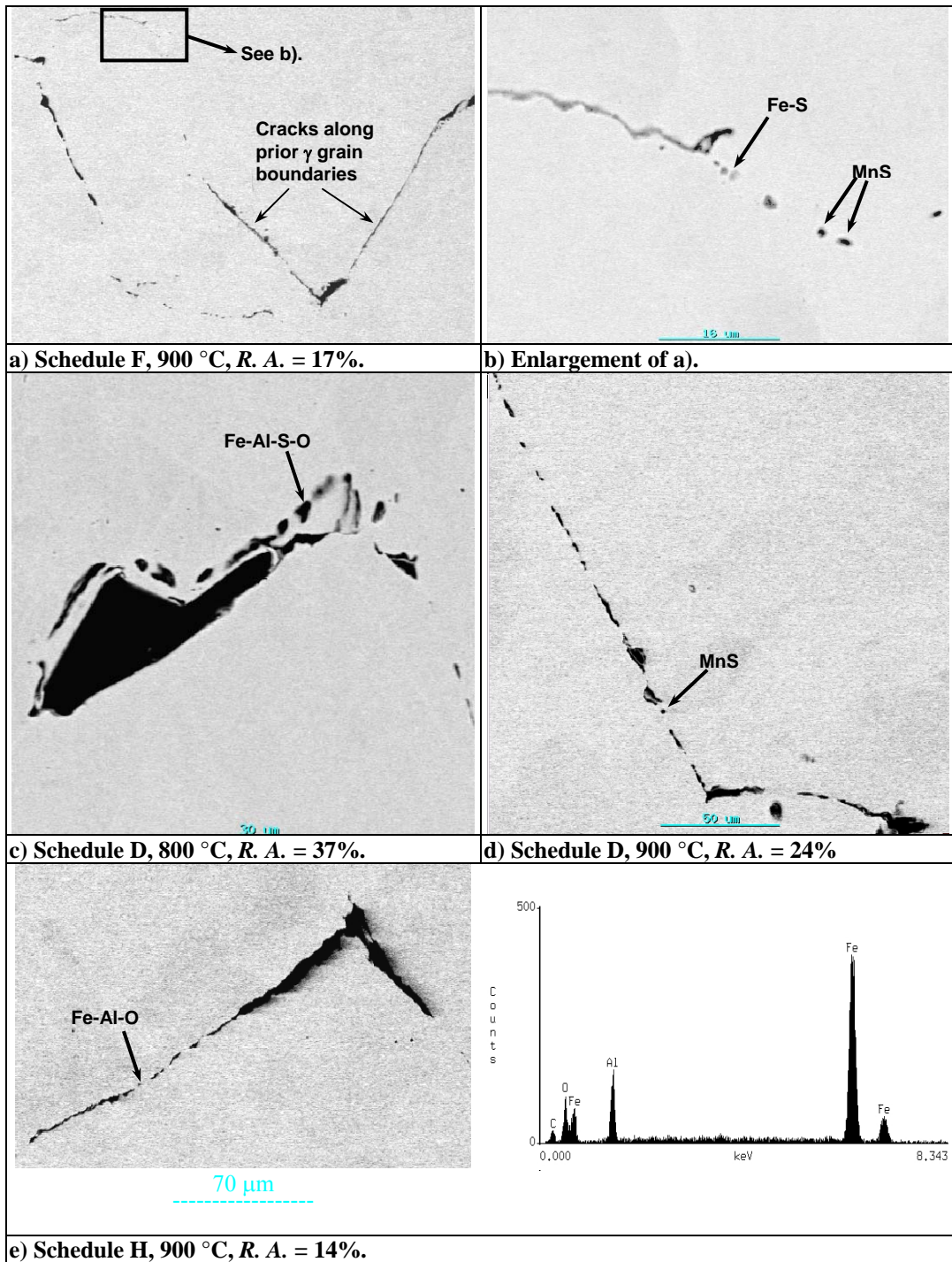


Figure 5.14: SEM backscatter images of steel *LC-1* tested under schedule F, D and H conditions, showing precipitates and cracks along prior austenite grain boundaries.

5.5 LOW CARBON STEEL LC-2

5.5.1 Introduction

The results for LC-2 are shown in **Figure 5.15** to **Figure 5.22** and **Table 5.5**. The Ae_3 transformation temperature of 847°C from **Table 5.2**, modelled using the Thermo-CalcTM TCFE3 database, is indicated on the graphs.

The results obtained at a testing temperature of 900 °C under schedule F conditions were excluded, as a leak into the chamber caused heavy oxidation of the specimen. This caused unusually low ductility results. The schedule G test at 1000 °C was also not valid due to thermocouple problems early in the test. The total elongation result was not obtained for the schedule H test at 1000 °C, as the thermocouple contact was lost near the end of the test. Problems with the infrared furnace prevented repeat testing.

5.5.2 Maximum strength

The stress – elongation results are shown in **Figure 5.15** and the maximum strength – temperature results in **Figure 5.16**. The onset of dynamic recrystallisation is indicated by arrows on the graphs and the temperatures are listed in **Table 5.5**. The occurrence of dynamic recrystallisation can be detected on the stress – elongation curves by either an abrupt decrease or oscillations of the flow stress (Abushosha *et al.*, 1991).

With decreasing temperature there is a trend of an initial increase in maximum strength (S_u) from 1000 to 850 °C, then a decrease or plateau from 850 to 800 °C, followed by an increase from 800 to 750 °C (3rd order polynomial behaviour).

Decreasing the strain rate decreased the amplitude of the S_u oscillation. Cooling rate does not appear to have had any significant effect on the maximum strength.

As temperature decreased, the drop in S_u occurred near the Ae_3 temperature (847 °C). With further decrease in temperature, S_u began to increase below 800 °C. This was more evident at the higher strain rate.

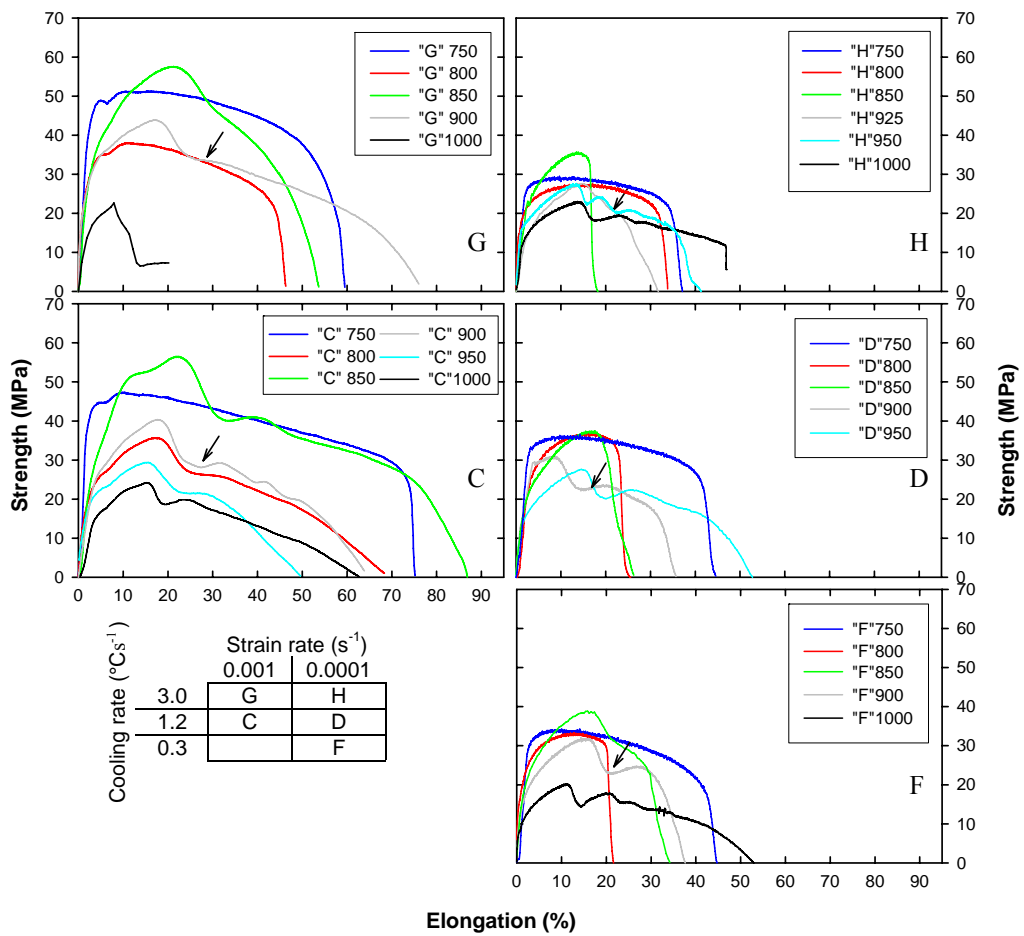


Figure 5.15: Engineering stress as a function of elongation for steel LC-2. The key to the testing schedules is shown above. The onset of dynamic recrystallisation is indicated by arrows on the graphs.

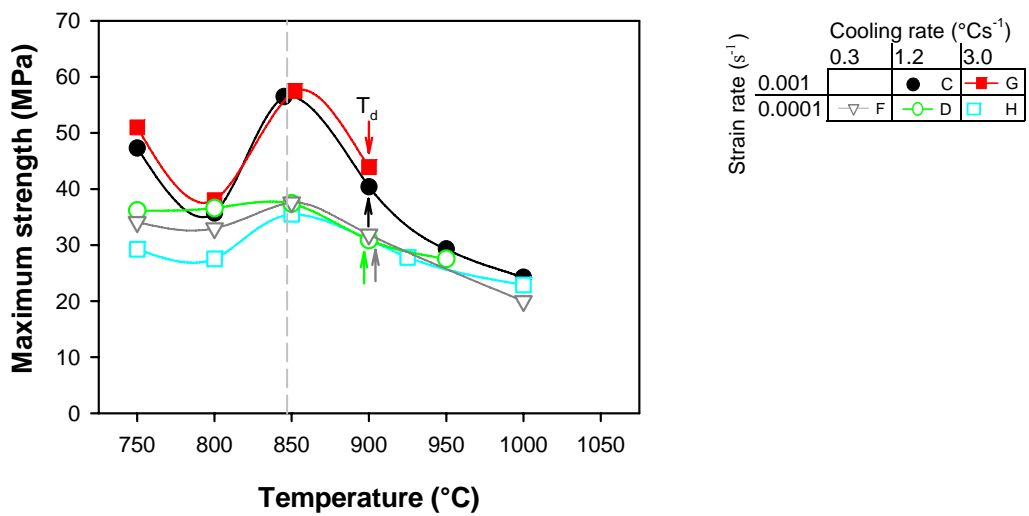


Figure 5.16: Maximum strength for steel LC-2 as a function of testing temperature, strain rate and cooling rate.

5.5.3 Reduction in area

At a strain rate of 10^{-3} s^{-1} : **Figure 5.17** shows that the high temperature ductility recovery was moved to higher temperatures by 30 - 40 °C with an increase in cooling rate from 1.2 to 3.0 °C.s⁻¹. At a cooling rate of 1.2 °C.s⁻¹, the high temperature ductility drop occurred near the Ae_3 temperature. The R. A. minima occurred at ~800 °C.

At a strain rate of 10^{-4} s^{-1} , the R. A. minima were at ~850 °C (1.2 and 3.0 °C.s⁻¹) and the ductility improved below the Ae_3 temperature and for a slow cooling rate (0.3 °C.s⁻¹) the minimum occurred at 800 °C. An increase in cooling rate from 0.3 to 3.0 °C.s⁻¹ deepened the ductility trough by approximately 20%.

A decrease in strain rate moved the high temperature recovery of the ductility trough to higher temperatures by 70 - 80 °C and decreased the minimum reduction in area (% R. A.) values by approximately 20 %.

The onset of dynamic recrystallisation (T_d) occurred at R. A. values higher than 50%, as ductility recovered on the high temperature side of the trough.

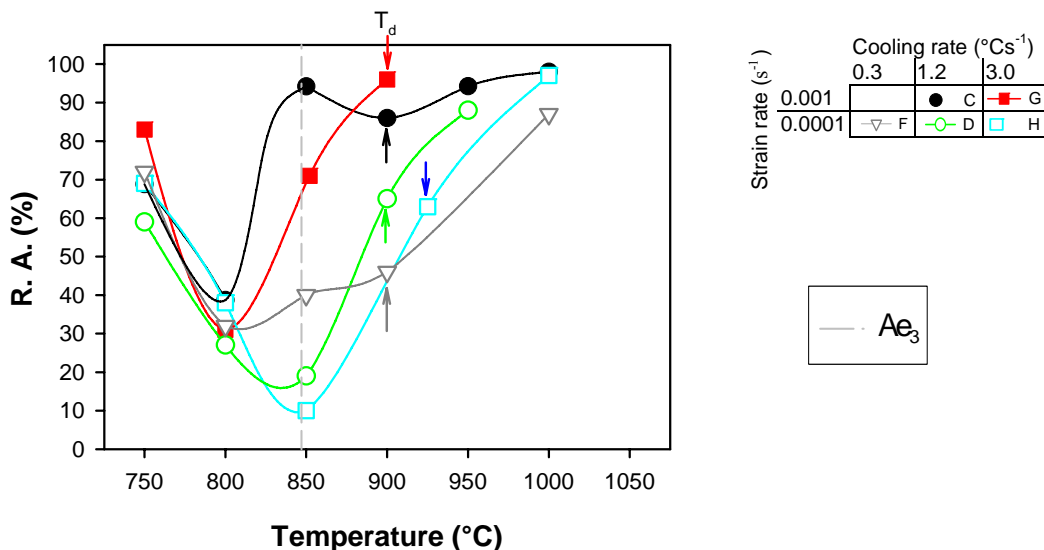


Figure 5.17: Reduction in area for steel LC-2 as a function of testing temperature, strain rate and cooling rate.

5.5.4 Total elongation

The total elongation followed similar trends to the reduction in area as shown in **Figure 5.18**. Decreasing the strain rate decreased the elongation values substantially at temperatures from 750 to 900 °C.

At high strain rate ($10^{-3} s^{-1}$) and $1.2 °C.s^{-1}$ two elongation troughs were noted: from 750 to 850 °C (i) and from 850 to above 1000 °C (ii). Increasing the cooling rate from $1.2 - 3.0 °C.s^{-1}$ (C to G) shifted the high temperature recovery of the first elongation trough (i) to higher temperatures by approximately 50 °C. It is not possible to determine the effect of cooling rate on the second elongation trough, as testing was not performed above 900 °C for schedule G.

At low strain rate ($10^{-4} s^{-1}$): increasing the cooling rate from $0.3 - 3.0 °C.s^{-1}$ (D to H) appears to have moved the elongation trough to higher temperatures by $\sim 30 °C$ between 850 and 925 °C. However, at 1000 °C the elongation values were similar at cooling rates of 0.3 and $3.0 °C.s^{-1}$.

The onset of dynamic recrystallisation (T_d) occurred where elongation was recovering at high temperatures.

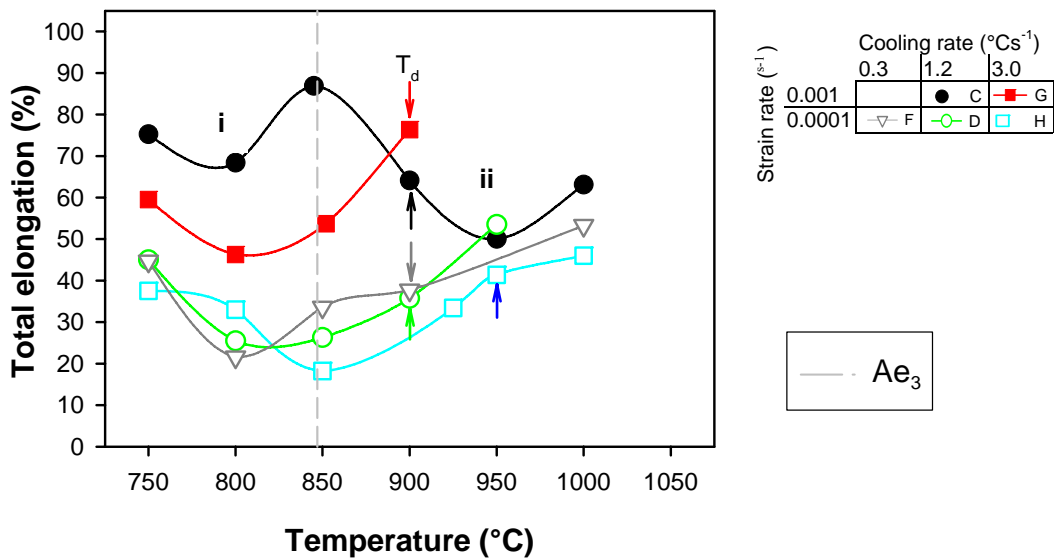


Figure 5.18: Elongation for steel LC-2 as a function of testing temperature, strain rate and cooling rate.

5.5.5 Scanning electron microscopy

High strain rate ($10^{-3} s^{-1}$):

- $1.2 \text{ } ^\circ\text{C}\cdot\text{s}^{-1}$: the internal microstructure of the low ductility sample tested at $800 \text{ } ^\circ\text{C}$ (**Figure 5.19 a and b**) contained lines of precipitates along the prior austenite grain boundaries. Microvoid coalescence and extensive cracking was seen between the MnS precipitates.
- $3.0 \text{ } ^\circ\text{C}\cdot\text{s}^{-1}$: **Figure 5.20 a** shows that at a testing temperature of $800 \text{ } ^\circ\text{C}$, many small precipitates were found along internal crack networks *e.g.* Al-Mn-Fe-S-O and MnS. At $850 \text{ } ^\circ\text{C}$, only a small amount of network cracking was observed (**Figure 5.20 b**) and there was much less internal cracking than at $800 \text{ } ^\circ\text{C}$. A complex precipitate containing Fe-Mn-Ca-Si-O-S was analyzed. The C peak on the EDS analysis is thought to be from the graphite used to enhance the sample conductivity.

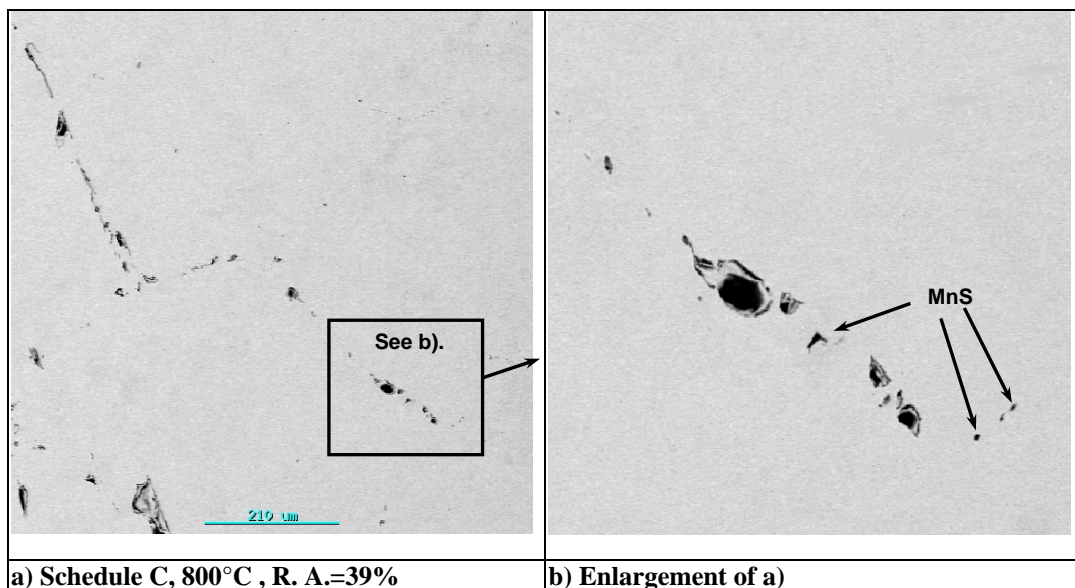


Figure 5.19: SEM backscatter images of steel LC-2 showing precipitation and void formation along austenite grain boundaries ($1.2 \text{ } ^\circ\text{C}\cdot\text{s}^{-1}$, $10^{-3} s^{-1}$).

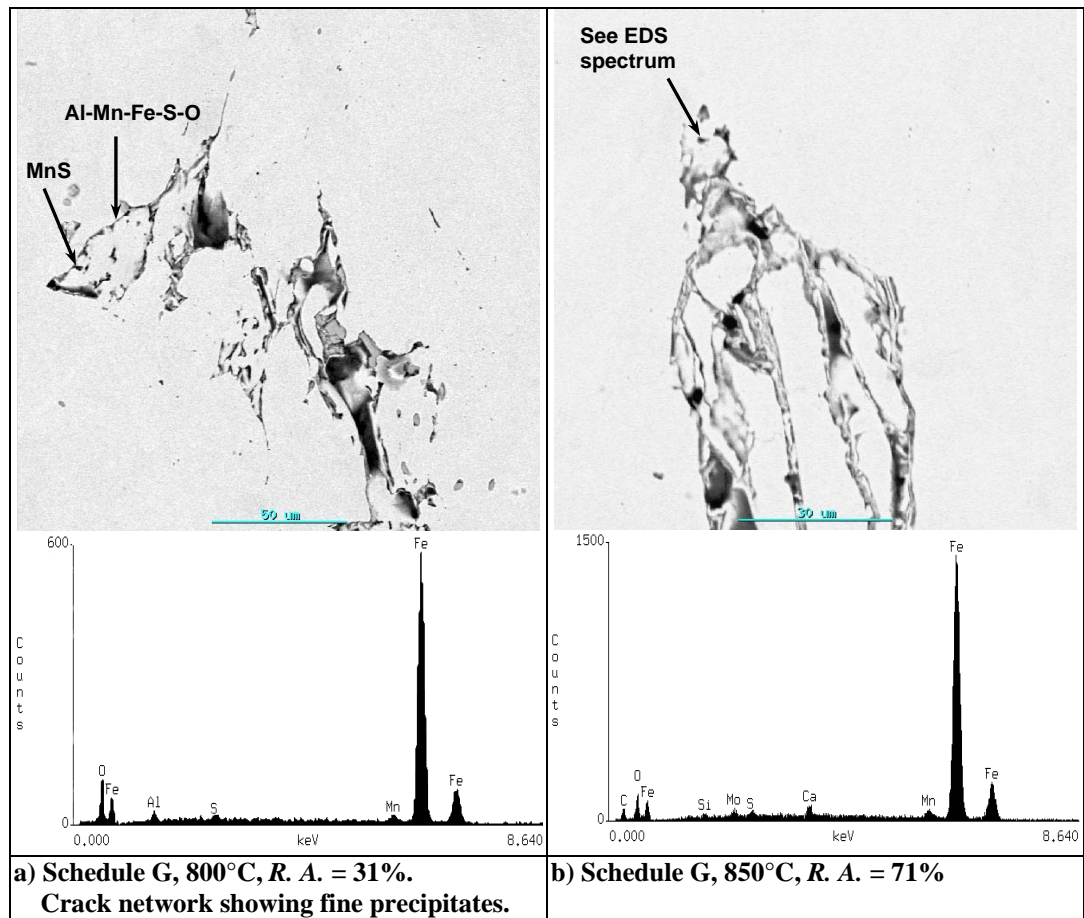


Figure 5.20: SEM backscatter images of steel *LC-2* tested under Schedule G conditions: (10^{-3} s^{-1} , $3.0 \text{ }^\circ\text{C}\cdot\text{s}^{-1}$), showing a) many precipitates and extensive cracking and b) less cracking.

Low strain rate (10^{-4} s^{-1}):

- *Low cooling rate* ($0.3 \text{ }^\circ\text{C}\cdot\text{s}^{-1}$): A few Al-Fe-Mn-O precipitates as well as many 1-2 μm diameter MnS precipitates were observed in the sample tested at 800 $^\circ\text{C}$ (**Figure 5.21 a**). In the sample tested at 850 $^\circ\text{C}$ (**Figure 5.21 b**), many small microvoids were seen, but with only moderate interconnection and internal cracking. Precipitates such as Fe-Mn-Ca-O-S and Fe-Ca-Al-O-S were observed.
- *Medium cooling rate* ($1.2 \text{ }^\circ\text{C}\cdot\text{s}^{-1}$): In the specimen tested at 800 $^\circ\text{C}$ (**Figure 5.21 c**), large spherical MnS precipitates with diameters 1 - 5 μm were seen in rows which were associated with internal cracking. **Figure 5.21 d** shows many small MnS and Mn-Fe-O precipitates along microcracks along prior austenite grain boundaries in the specimen tested at 850 $^\circ\text{C}$.

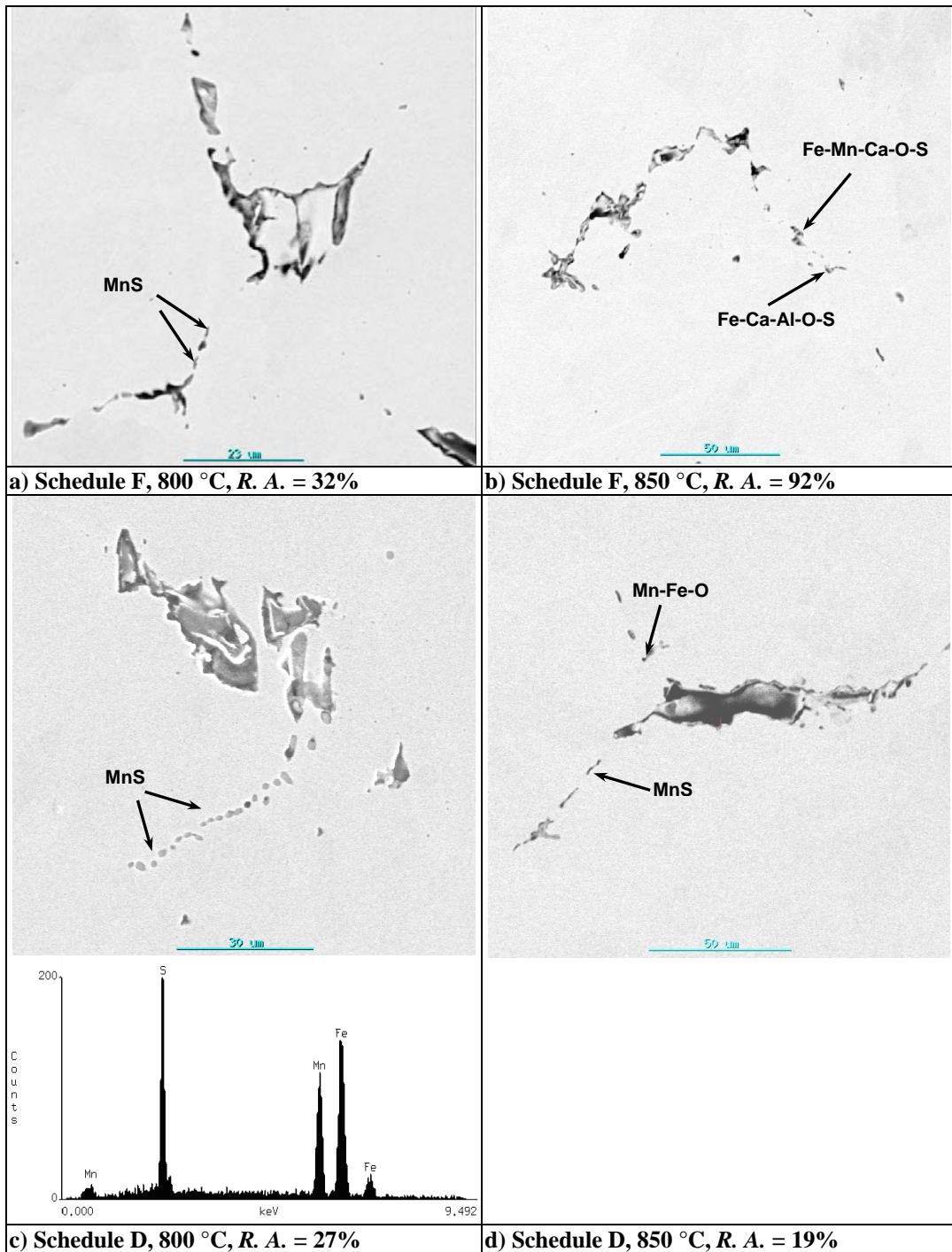


Figure 5.21: SEM backscatter images of steel *LC-2* tested under Schedule F and D conditions: $10^{-4} \text{ s}^{-1} + 0.3$ and 1.2 C.s^{-1} respectively, showing cracking and many precipitates.

- *High cooling rate* ($3.0\text{ }^{\circ}\text{C}\cdot\text{s}^{-1}$): in the specimen tested at $850\text{ }^{\circ}\text{C}$ (**Figure 5.22 a and b**) many MnS precipitates were analyzed in the microvoids which were substantially interconnected by cracks. **Figure 5.22 a** shows outlines of the prior austenite grains, which were measured to be $120 - 200\mu\text{m}$ in diameter.

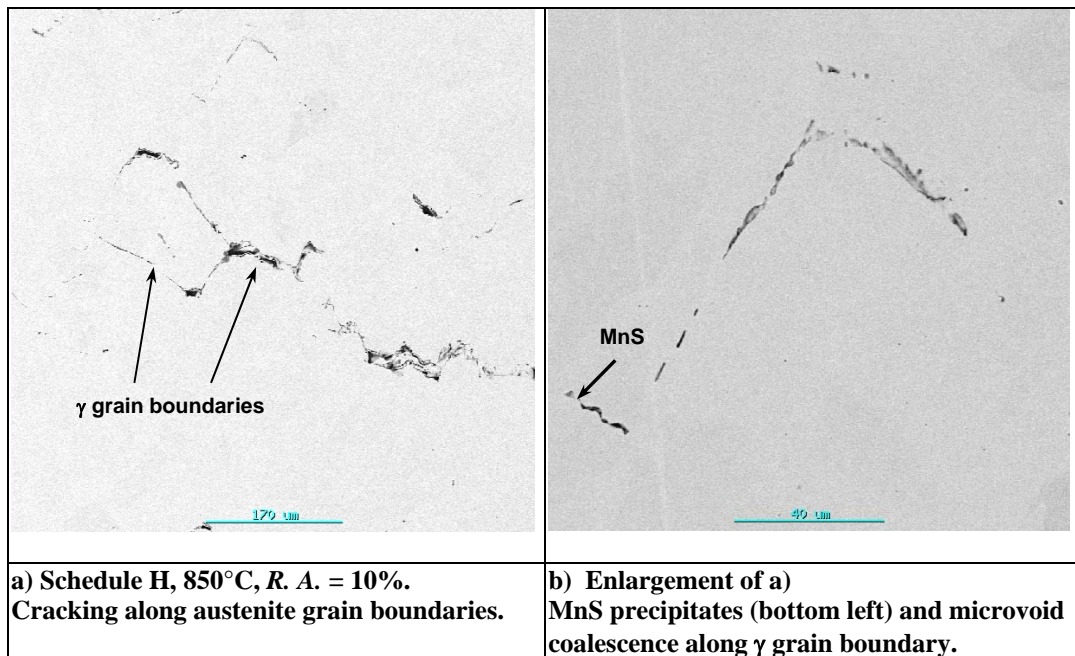


Figure 5.22: SEM backscatter images of steel LC-2 tested under Schedule H conditions: (10^{-4} s^{-1} , $3.0\text{ }^{\circ}\text{C}\cdot\text{s}^{-1}$).

5.6 LOW CARBON STEEL LC-3

5.6.1 Introduction

The results for steel LC-3 are shown in **Figure 5.23** to **Figure 5.27**. The modelled Thermo-Calc™ TCFE3 Ae_3 transformation temperature (834°C) from **Table 5.2** is shown on the graphs.

5.6.2 Maximum strength

Figure 5.23 shows the comparison in engineering stress as a function of elongation for the two testing schedules, C and H. It was not possible to measure the total elongation and reduction in area on the specimen “H”1050, as thermocouple contact was broken before the end of the test. However, the maximum strength value is a valid result. The dynamic recrystallisation occurred at 950 °C (schedule C) and 1000 °C (schedule H).

Figure 5.24 shows increasing maximum strength (S_u) with decreasing temperature from 1050 to 750°C for both testing schedules. The maximum strength increased more sharply from 800 – 750 °C for schedule C than for schedule H. A plateau or slight drop was seen at temperatures just below the Ae_3 . Dynamic recrystallisation occurred at 950 °C (Schedule C) and 1000 °C (Schedule H).

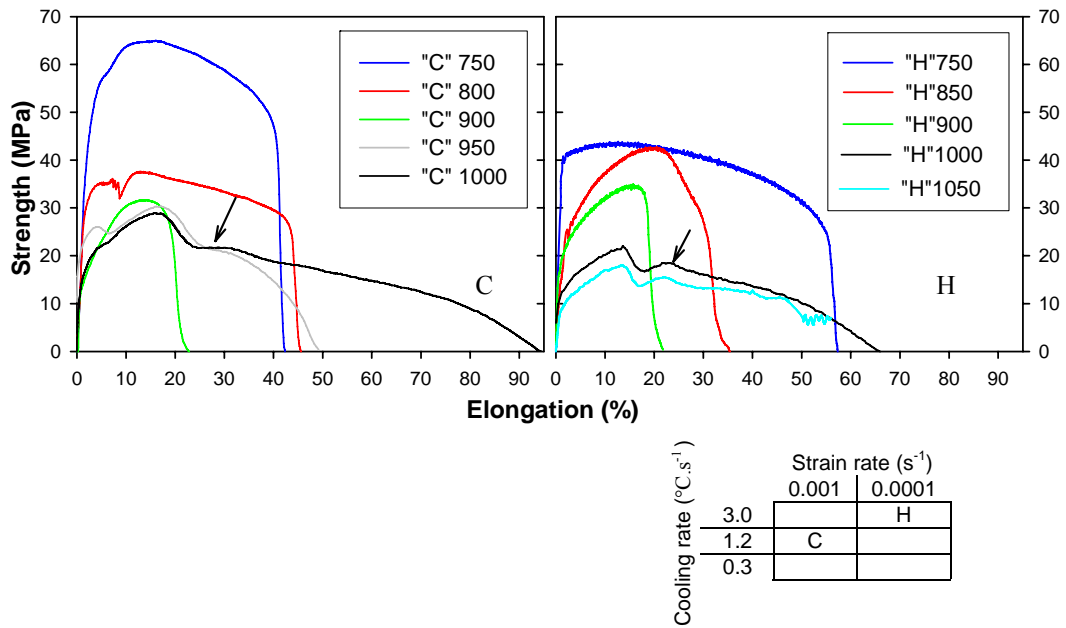


Figure 5.23: Engineering stress as a function of elongation for steel LC-3. The key to the testing schedules is also shown.

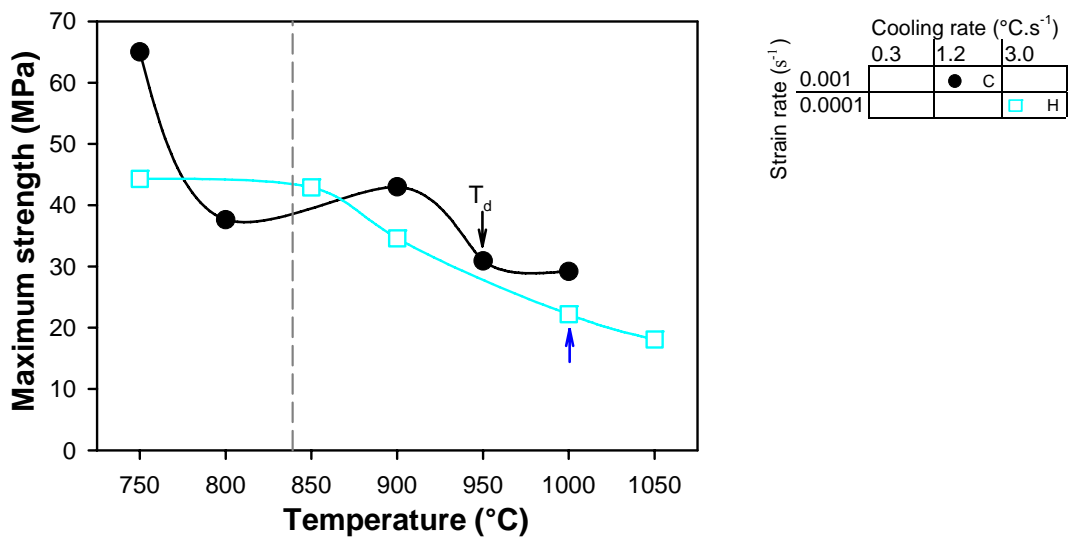


Figure 5.24: Maximum strength for steel LC-3 as a function of testing temperature, strain rate and cooling rate.

5.6.3 Reduction in area

There was a decrease in the minimum reduction in area (*R. A.*) of approximately 20% from schedule C to H *i.e.* deepening of the ductility trough. There appears to be little change in trough width between the two curves *i.e.* where the *R. A.* is below 50%, as shown in **Figure 5.25**.

Ductility recovery (50% *R. A.*) occurred at ~750 °C for both schedules C and H on the low temperature side of the ductility trough. On the high temperature side of the ductility trough, 50% *R. A.* was found to be at ~950 °C. The Ae_3 temperature is close to the minimum ductility values.

The onset of dynamic recrystallisation (T_d) occurred at high *R. A.*: 60% at 950 °C for schedule C and >90% at 1000 °C for schedule H.

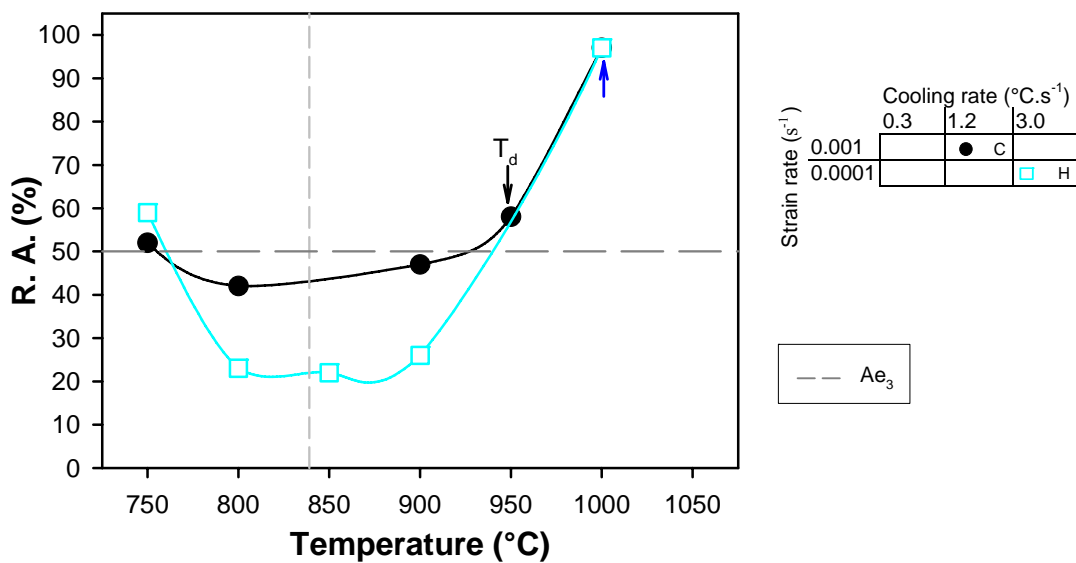


Figure 5.25: Reduction in area for steel LC-3 as a function of testing temperature, strain rate and cooling rate.

5.6.4 Total elongation

The total elongation curves (**Figure 5.0**) showed similar behaviour to the reduction in area: schedule C shows a very shallow elongation trough, whereas schedule H shows a deeper trough than that of schedule C (but narrower than the *R. A.* trough). It also appears that the schedule H elongation minimum was shifted slightly to higher temperatures.

The A_{e3} temperature was found to be $\sim 70^\circ\text{C}$ below the minimum elongation. The onset of dynamic recrystallisation (T_d) occurred where elongation recovered at high temperatures: $\sim 48\%$ for schedule C (950°C) and $\sim 65\%$ for schedule H (1000°C).

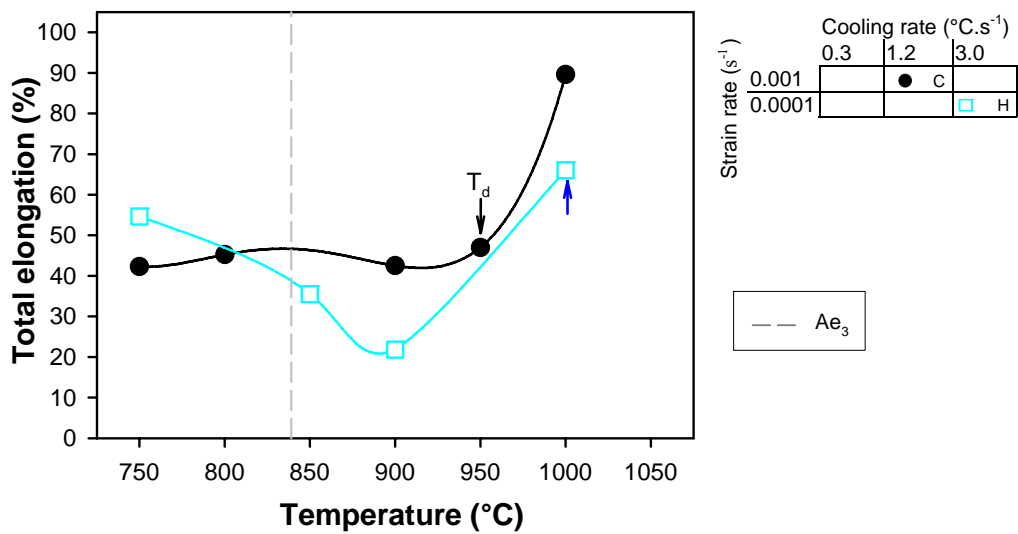


Figure 5.26: Elongation for steel *LC-3* as a function of testing temperature, strain rate and cooling rate.

5.6.5 Scanning electron microscopy

At a high strain rate (10^{-3} s^{-1}), cooling rate of $1.2 \text{ }^\circ\text{C}\cdot\text{s}^{-1}$ and testing temperature of $900 \text{ }^\circ\text{C}$ some interconnection of microvoids was found with precipitates containing Fe-Mn-Si-O, MnS and Mn-Si-S (**Figure 5.27 a**). No substantial internal cracking was observed.

At a low strain rate (10^{-3} s^{-1}), cooling rate of $3.0 \text{ }^\circ\text{C}\cdot\text{s}^{-1}$ and testing temperature of $900 \text{ }^\circ\text{C}$ (**Figure 5.27 b**), many large, complex precipitates were analyzed: Ca-Mn-Al-O, Mn-O and Al_2O_3 . At $1000 \text{ }^\circ\text{C}$ (not shown), Al-Mg-O particles were found –inclusions from the steelmaking process. Many cracks were seen linking the inclusions and precipitates.

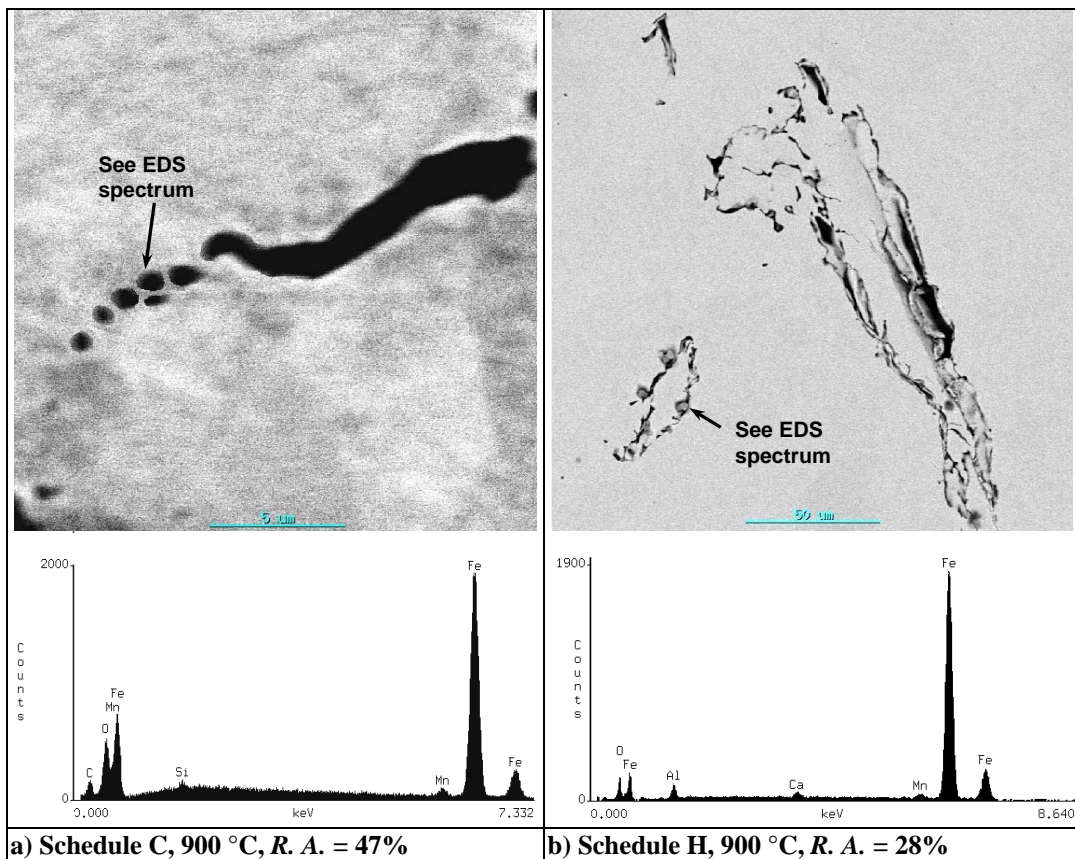


Figure 5.27: SEM backscatter images of Steel LC-3 tested under Schedule C and H conditions: (10^{-3} s^{-1} , $1.2 \text{ }^\circ\text{C}\cdot\text{s}^{-1}$ and 10^{-4} s^{-1} , $3.0 \text{ }^\circ\text{C}\cdot\text{s}^{-1}$ respectively). Dark lines show cracking between precipitates.

5.7 LOW CARBON STEELS *LC-4* AND *LC-5*

The results for steels *LC-4* and *LC-5* are shown in **Figure 5.28** to **Figure 5.33**. The A_{e_3} transformation temperatures of 837 °C and 912 °C respectively from **Table 5.2** modelled using Thermo-Calc™ TCFE3 are indicated on the graphs.

5.7.1 Maximum strength

Figure 5.28 a and **b** shows the tensile behaviour for steels *LC-4* and *LC-5* (both schedule C: 10^{-3}s^{-1} , $1.2\text{ °C}\cdot\text{s}^{-1}$). Dynamic recrystallisation occurred at 900 °C for steel *LC-4* and at 850 °C for steel *LC-5*.

Figure 5.29 shows 3rd order polynomial behaviour for *LC-5* between 750 and 900 °C. With decrease in temperature, the S_u oscillation coincided with the A_{e_3} temperature (855 °C).

LC-4 had a similar maximum strength (S_u) value to *LC-5* at 800 °C and a slightly lower value at 900 °C.

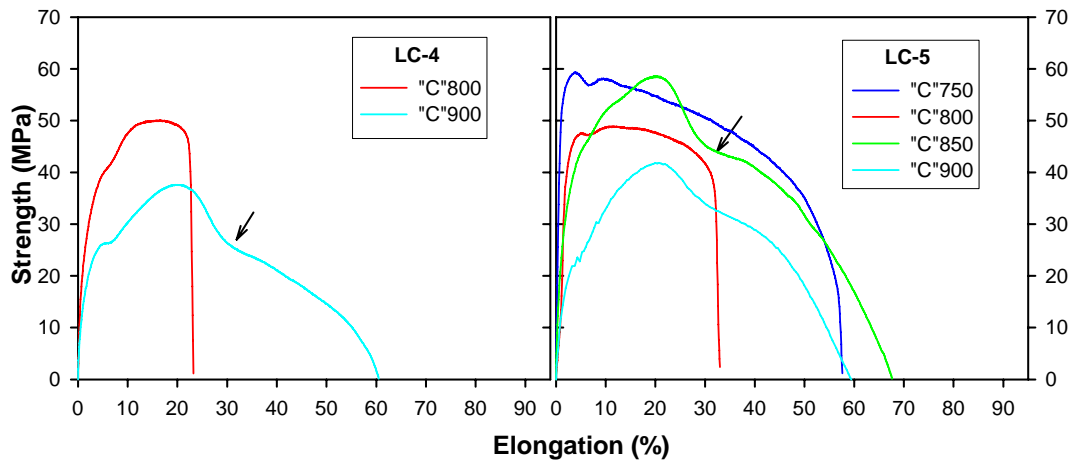


Figure 5.28: Engineering stress as a function of total elongation for steels *LC-4* and *LC-5*. All tests were done according to schedule C conditions ($1.2\text{ }^{\circ}\text{C}\cdot\text{s}^{-1}$, 10^{-4} s^{-1}). Arrows indicate the onset of dynamic recrystallisation.

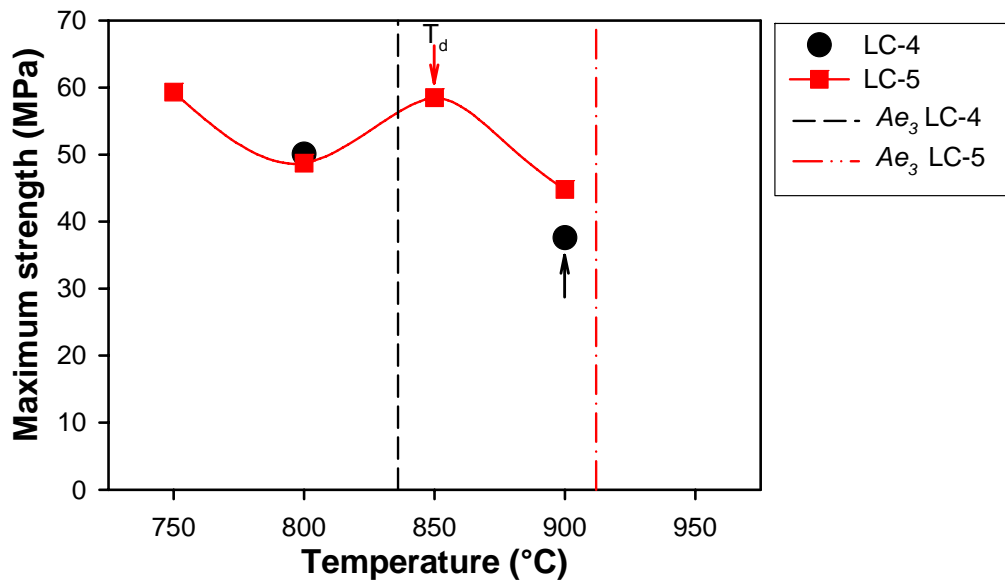


Figure 5.29: Maximum strength for steels *LC-4* and *LC-5* as a function of testing temperature.

5.7.2 Reduction in area

The reduction in area results are shown in **Figure 5.30**. Assuming the trends from the limited results are accurate, a narrow ductility trough of $\sim 100^\circ\text{C}$ was found for *LC-5*, with full ductility recovery at 750°C on the low side and 850°C on the high temperature side of the trough. The 50% *R. A.* values occurred at approximately 780°C and 815°C . The minimum reduction in area of 44% was found at 800°C .

The high temperature ductility recovery of *LC-4* occurred at a higher temperature than for *LC-5*. *LC-4* showed lower ductility than *LC-5* at 800°C (23 % compared with 44 %) and at 900°C (58 % compared with 98 %). The 50% *R. A.* value for *LC-5* is expected to be between $\sim 875\text{-}890^\circ\text{C}$. For both steels, ductility recovery coincided with dynamic recrystallisation.

The A_{e3} temperature for *LC-4* lies below 50% *R. A.*, whereas for *LC-5* it lies well above the onset of the ductility trough.

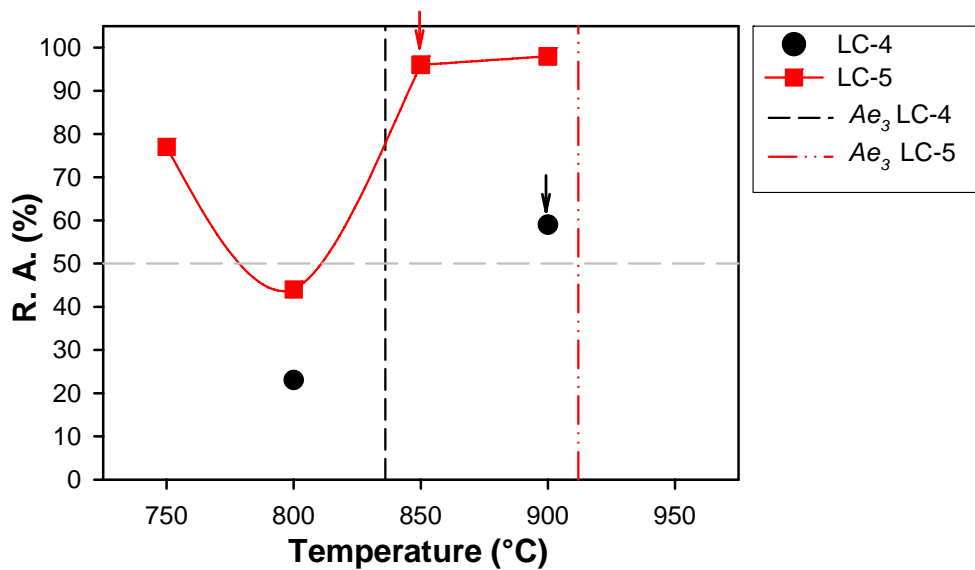


Figure 5.30: Reduction in area for steels *LC-4* and *LC-5* as a function of testing temperature.

5.7.3 Total elongation

The total elongation trough followed similar trends to the reduction in area (**Figure 5.31**). Assuming the accuracy of the data, the elongation trough for *LC-5* extended from 750 - 850 °C. The lowest elongation value occurred at 800 °C (33%). The high temperature elongation decrease occurred near the Ae_3 temperature.

The total elongation of *LC-4* was found to be about 10% lower than for *LC-5* at 800 °C and at 900 °C the elongation values were approximately equal.

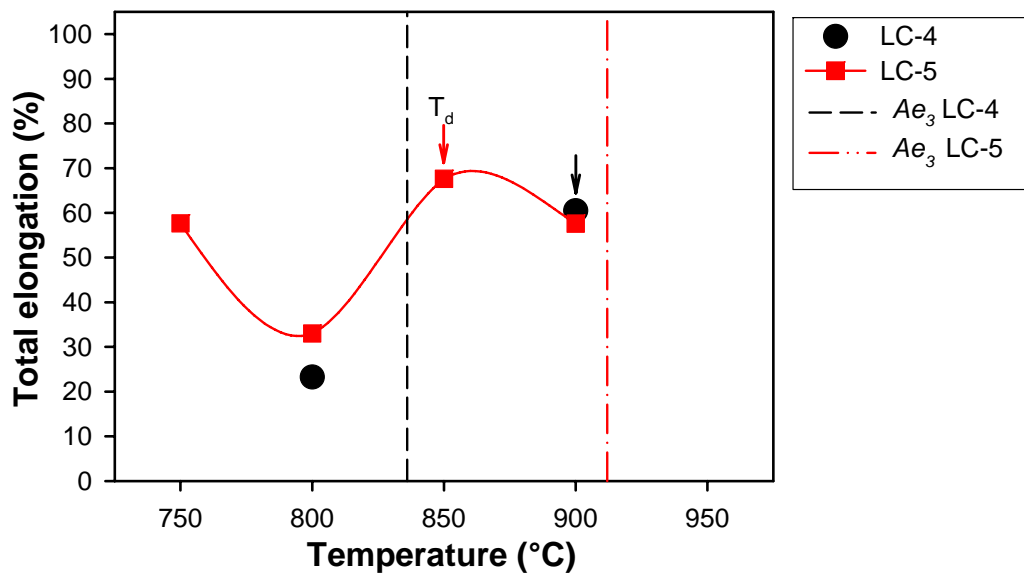


Figure 5.31: Elongation for steels *LC-4* and *LC-5* as a function of testing temperature.

5.7.4 Scanning electron microscopy

Steel *LC-4*:

At a testing temperature of 800 °C, the microstructure contained many small voids in rows on, or parallel to, cracks along prior austenite grain boundaries. **Figure 5.32 a** shows microvoid coalescence and a few discrete voids containing precipitates such as MnS, Fe-Al-Mn-O and Fe-Mn-Si-O-S.

The specimen tested at 900 °C showed fewer precipitates and less microvoid coalescence than at 800 °C. A few large MnS with diameters of 1-3 μm were identified near internal cracks (see **Figure 5.32 b**).

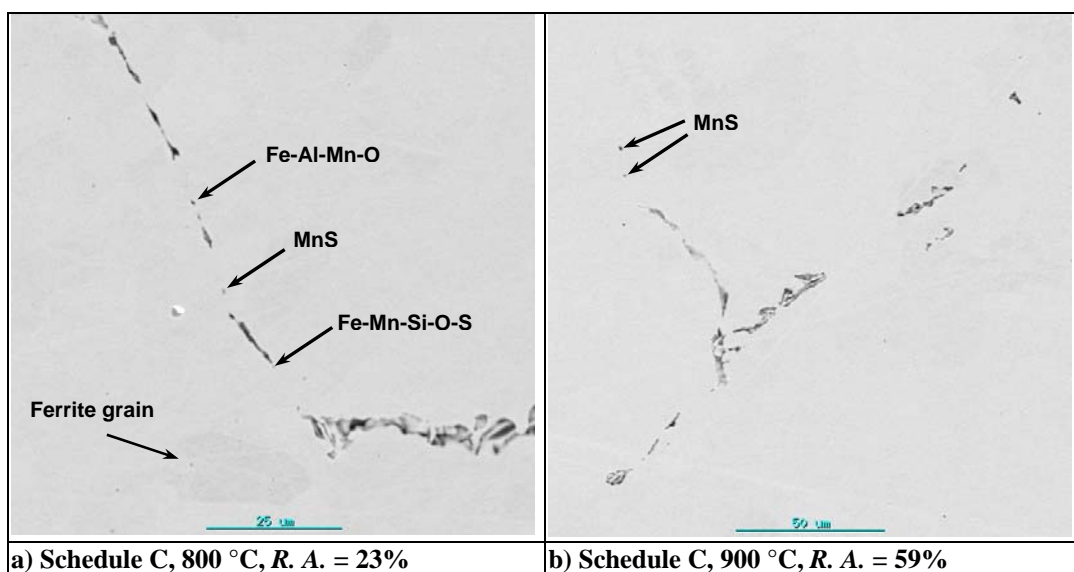


Figure 5.32: SEM backscatter images of steel *LC-4* tested under Schedule C conditions: (10^{-3} s^{-1} , 1.2 °C.s^{-1}), showing microvoid coalescence along prior austenite grain boundaries.

Steel *LC-5*:

In the specimen tested at 800 °C, small MnS and complex precipitates such as Mn-Ca-Si-S and Fe-Al-Si-Ca-Cr-Mn-S-O (**Figure 5.33**) were identified. There was less microvoid coalescence and fewer small precipitates than in the *LC-4* specimen tested at 800 °C. The precipitate analysed below is smaller than 3 µm, so the EDS analysis will include pick up from the matrix. However, for all the analyses performed, the matrix showed very low levels of Mn, Cr, Ca, S and Si.

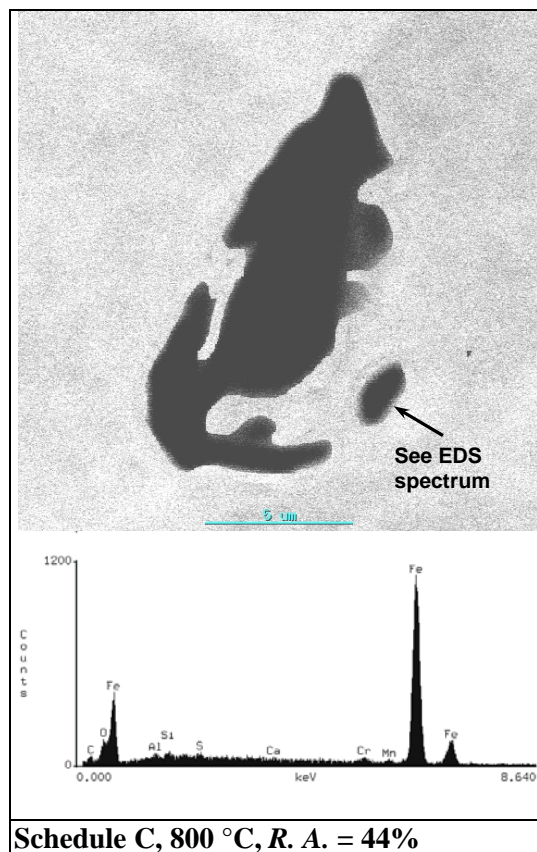


Figure 5.33: SEM backscatter image of steel *LC-5* tested under Schedule C conditions: (10^{-3} s^{-1} , 1.2 °C.s^{-1}), showing precipitate-containing voids.

5.8 SUMMARY OF HOT DUCTILITY RESULTS FOR THE LOW CARBON STEELS

The hot ductility results are summarised in **Table 5.5**, listing the 50% *R. A.* low- and high- temperature ductility recovery temperatures (Low T = 50% low temperature ductility recovery, high T = 50% high temperature ductility recovery), the minimum ductility temperature (and associated % *R. A.*) and the onset temperature of dynamic recrystallisation, T_d (and associated % *R. A.*). The results are ordered according to the steel, strain rates, cooling rates and testing schedule (C, D, F, G and H).

Table 5.5: Summary of the hot ductility results for the low carbon steels.

Steel	Cooling Rate (°Cs ⁻¹)	Strain rate (s ⁻¹)							
		10 ⁻³				10 ⁻⁴			
		Low T (°C)	Min. <i>R.A.</i>	High T (°C)	T _d °C (%)	Low T (°C)	Min. <i>R.A.</i>	High T (°C)	T _d °C (%)
LC-1	0.3					F ~730	900 (18)	>1050	>1050 (>32)
	1.2	C 800	875 (33)	960	975 (57)	D 760	≥1000 (≤25)	>1000	>1000 (>21)
	3.0	G <750	800 (35)	925	950 (86)	H ~730	875 (12)	990	1000 (53)
LC-2	0.3					F 770	800 (32)	900	1000 (87)
	1.2	C 775	800 (40)	815	850 (96)	D 760	840 (17)	880	900 (65)
	3.0	G 775	800 (32)	830	900 (96)	H 790	850 (10)	915	925 (63)
LC-3	1.2	C 750	800 (42)	930	950 (60)				
	3.0					H 770	850 (22)	940	1000 (99)
LC-4	1.2	C <800	≤800 (≤25)	~875	900 (59)				
LC-5	1.2	C 780	800 (45)	815	850 (96)				

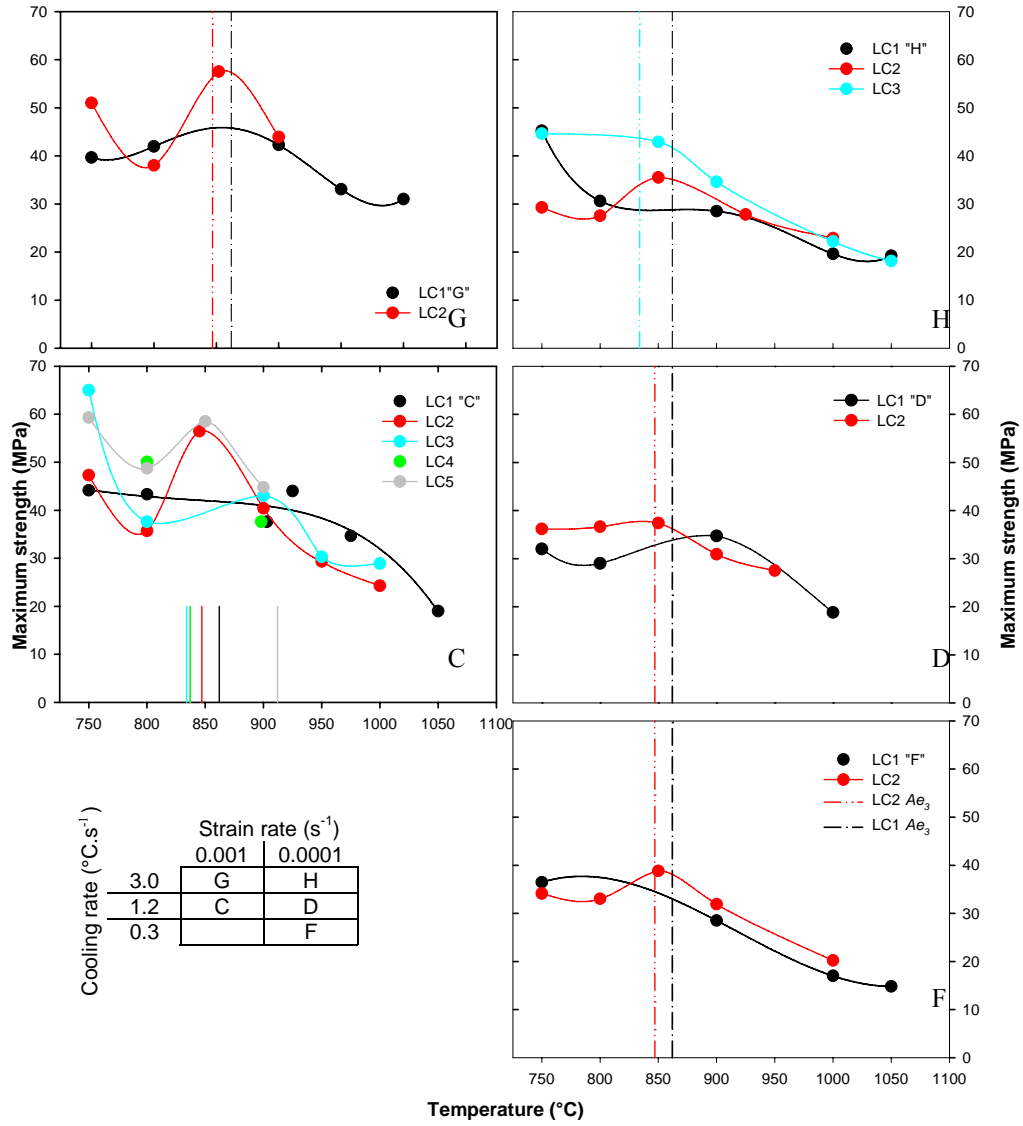


Figure 5.34: Variation in maximum stress between the low carbon steels LC-1 to LC-5, as a function of strain rate cooling rate and testing temperature.

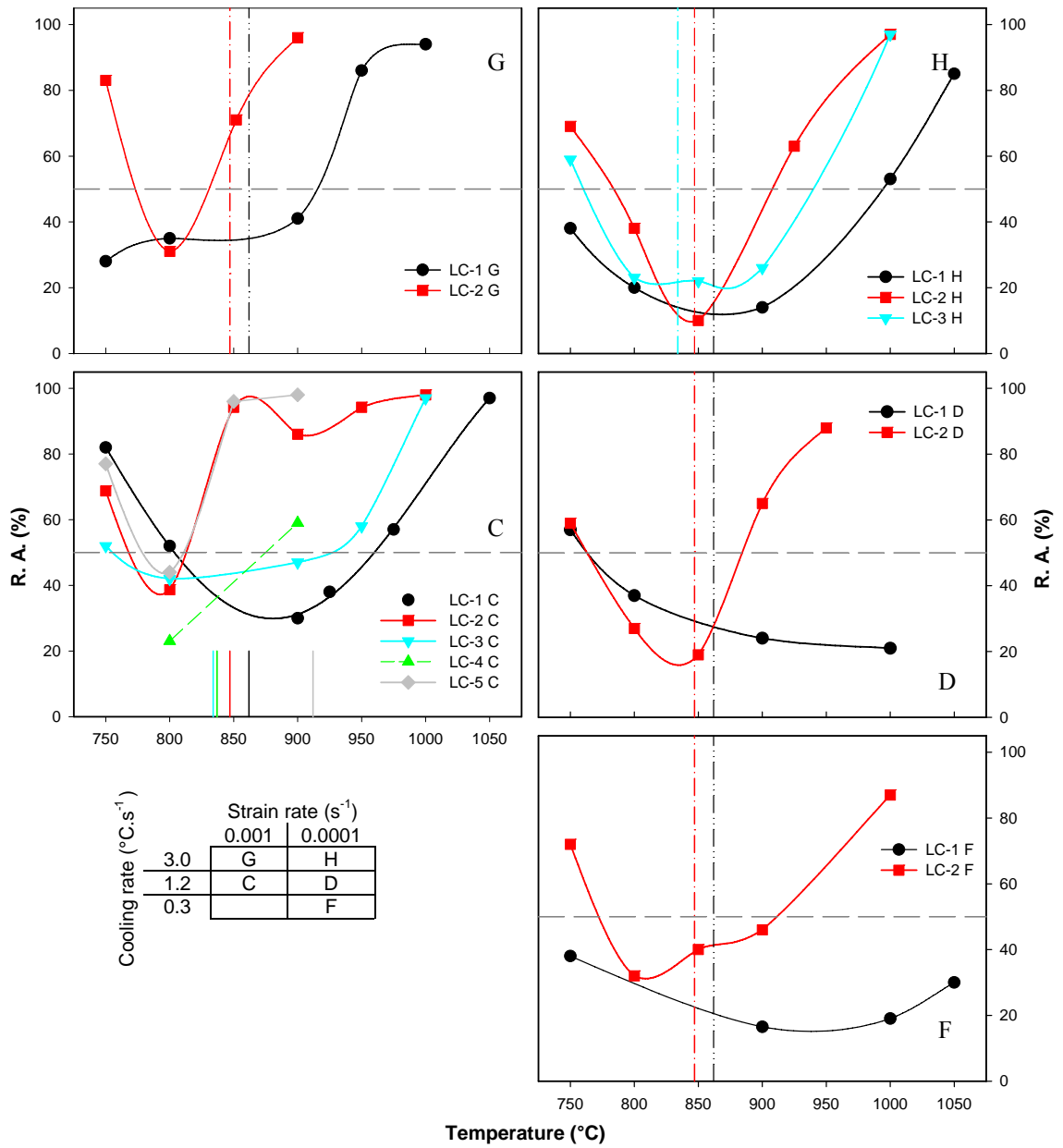


Figure 5.35: Reduction in area for low carbon steels *LC-1* to *LC-5*, as a function of strain rate, cooling rate and temperature.

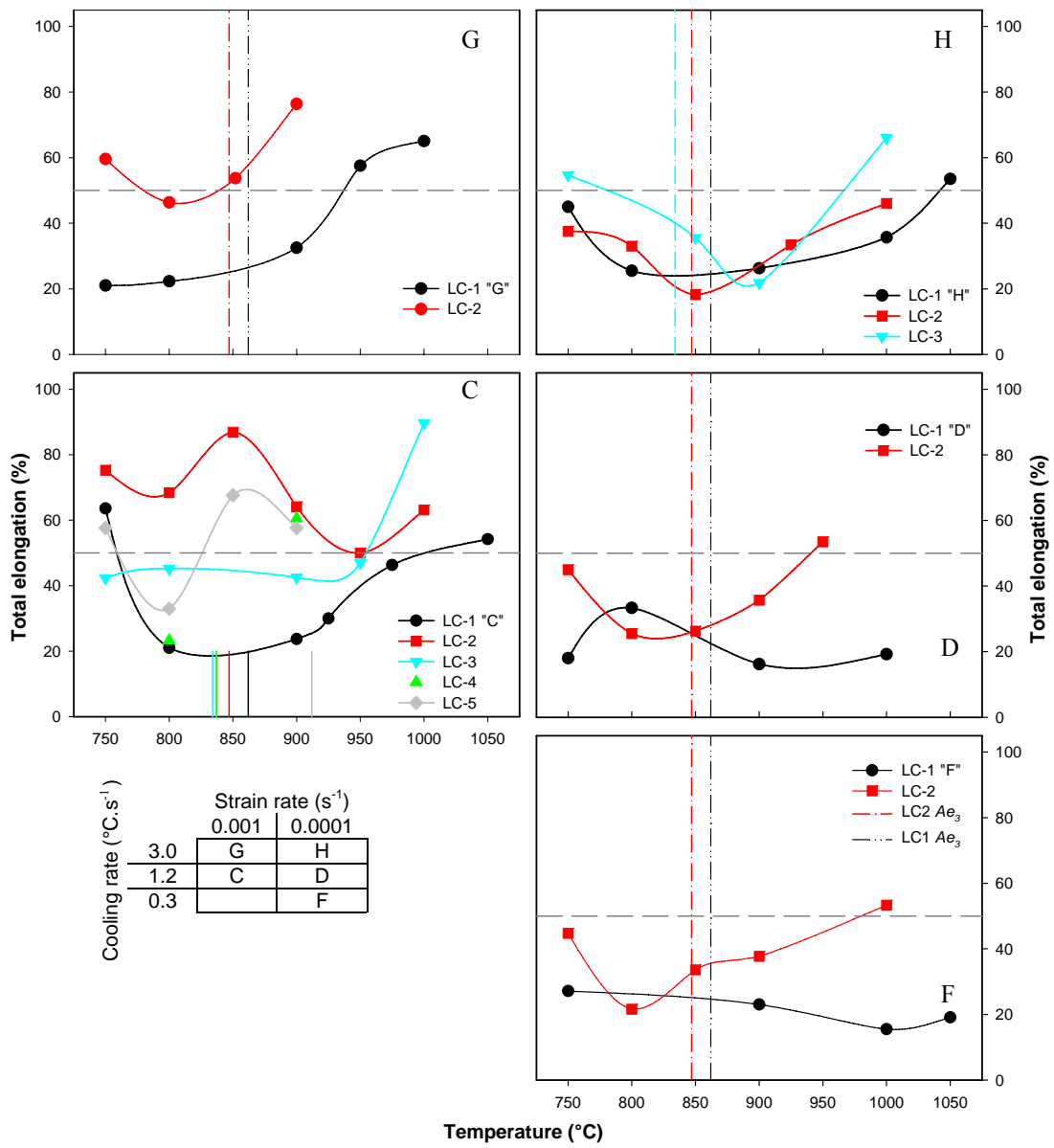


Figure 5.36: Total elongation for low carbon steels *LC-1* to *LC-5*, as a function of strain rate, cooling rate and temperature.

5.9 EFFECT OF STRAIN RATE ON HOT TENSILE BEHAVIOUR IN LOW CARBON STEELS *LC-1* AND *LC-2*

5.9.1 Maximum strength

Decreasing the strain rate from 10^{-3} to 10^{-4} s^{-1} had the following overall effects on the maximum strength, as seen in **Figure 5.34**:

- The maximum strength decreased in the temperature range 750 - 950 °C. At 1000 °C and 1050 °C there was less effect.
- The magnitude of the strength oscillation was decreased in *LC-2*. It is difficult to determine the effect in steel *LC-1*, as testing was not done at 850 °C.
- There was no significant effect on the temperature at which the strength decreased – this remained near the Ae_3 temperature.

These results are in agreement with literature (Mintz *et al.*, 1994). Decreasing the strain rate allows a longer time for grain boundary sliding as well as for the austenite and ferrite to recover and remain soft during deformation, both which decrease the maximum strength.

5.9.2 Hot ductility

Decreasing the strain rate from 10^{-3} to 10^{-4} s^{-1} had the following effects on the hot ductility (reduction in area and total elongation), as seen in **Figure 5.35** and **Figure 5.36**:

- In *LC-1* and *LC-2*, the ductility recovery and minimum *R. A.* were moved to higher temperatures. In *LC-2*, the increase was ~50 °C, causing the minimum *R. A.* to occur near the Ae_3 at low strain rate.
- The minimum reduction in area was decreased in both *LC-1* and *LC-2*, and the minimum elongation was substantially decreased in *LC-2*.
- **Figure 5.37** and **Figure 5.38** clearly show that decreasing the strain rate from 10^{-3} to 10^{-4} s^{-1} is detrimental to the hot ductility in steels *LC-1* and *LC-2*.

A decrease in strain rate causes a drop in ductility as a result of: enhanced grain boundary sliding in the austenite temperature region (Abushosha, 1998), more time for strain-induced precipitation and more time for formation and diffusion-controlled growth of voids around precipitates at grain boundaries (Mintz *et al.*, 1991). One or more of these mechanisms explain the poor high temperature ductility behaviour of *LC-1* and of *LC-2* at low strain rate. This will be clarified further in later sections.

At the high strain rate, the ductility drop below the Ae_3 in steel *LC-2* is explained by the following: ferrite takes a longer time to recover than austenite; so the strain concentrates in the α ferrite films, leading to fracture along the prior austenite grain boundaries (Mintz, 1994).

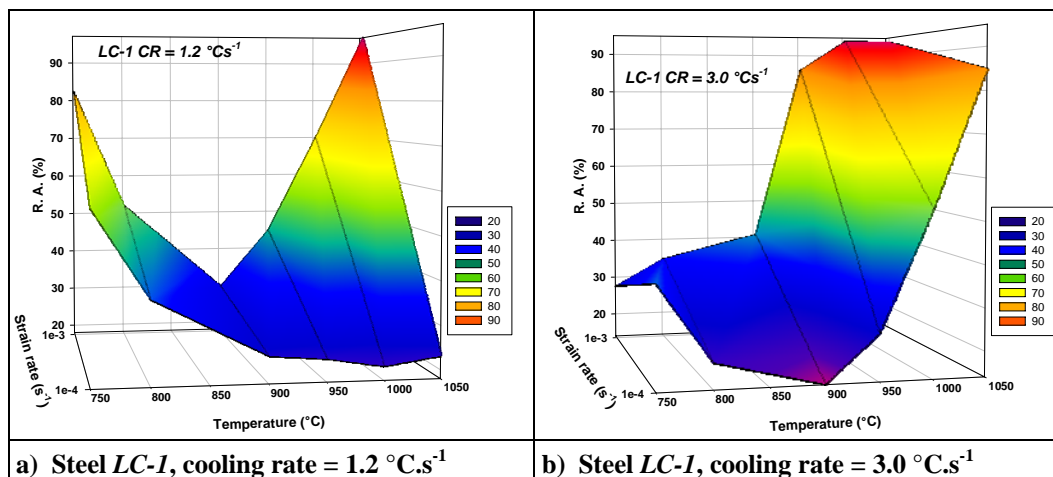


Figure 5.37: The effect of strain rate ($10^{-4} - 10^{-3}\text{ s}^{-1}$) on hot ductility of steel *LC-1*.

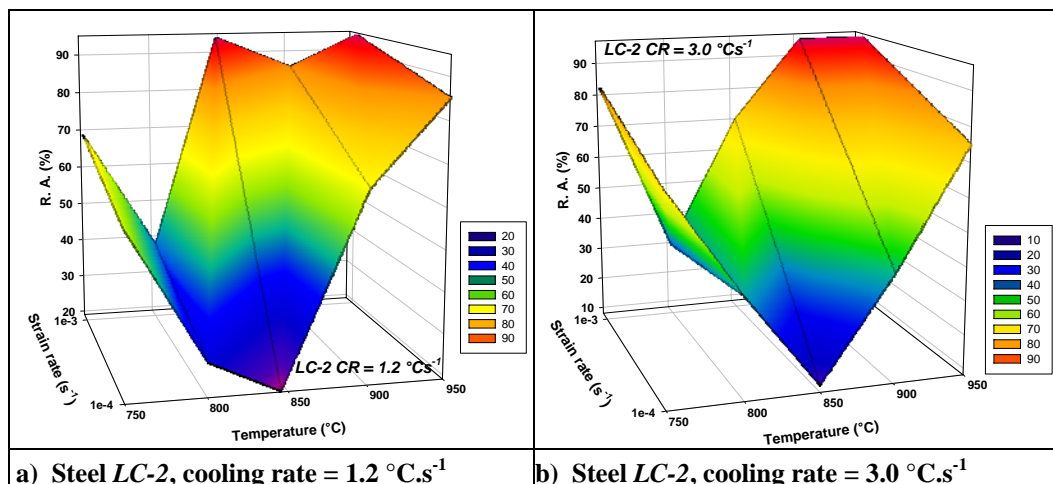


Figure 5.38: The effect of strain rate ($10^{-4} - 10^{-3}\text{ s}^{-1}$) on hot ductility of steel *LC-2*.

5.10 EFFECT OF COOLING RATE ON HOT TENSILE BEHAVIOUR IN LOW CARBON STEELS *LC-1* AND *LC-2*

5.10.1 Maximum strength

Decreasing the cooling rate from $3.0 - 1.2 \text{ }^\circ\text{C}\cdot\text{s}^{-1}$ (strain rate: 10^{-3} s^{-1}), showed no significant difference in maximum strength in both steels *LC-1* and *LC-2*, as seen in **Figure 5.34**.

It is difficult to determine the influence of decreased cooling rate from $3.0 - 0.3 \text{ }^\circ\text{C}\cdot\text{s}^{-1}$ at the low strain rate of 10^{-4} s^{-1} on both steels *LC-1* and *LC-2*, as there appear to be contradictory effects *i.e.* more than one mechanism operating.

5.10.2 Hot ductility

Figure 5.35, **Figure 5.39** and **Figure 5.40** show that decreasing the cooling rate from $3.0 - 1.2 \text{ }^\circ\text{C}\cdot\text{s}^{-1}$ at the high strain rate, and further to $0.3 \text{ }^\circ\text{C}\cdot\text{s}^{-1}$ at the low strain rate was detrimental to the hot ductility for *LC-1*, extending the high temperature ductility recovery to even higher temperatures. Kobayashi (1991) proposed that a decrease in cooling rate increases the amount of sulphur able to segregate to grain boundaries, which has a detrimental effect on hot ductility. This mechanism is substantiated by the increase in FeS(O) and MnS precipitates observed with decrease in cooling rate in steel *LC-1*. The FeS phase can be liquid to temperatures as low as $900 \text{ }^\circ\text{C}$.

However, *LC-2* responded differently, decreasing the cooling rate from $3.0 - 0.3 \text{ }^\circ\text{C}\cdot\text{s}^{-1}$ improved the ductility by moving the high temperature ductility recovery to slightly lower temperatures.

Abushosha *et al.* (1998) found that a decrease in cooling rate resulted in:

- Coarser MnS precipitate distribution in the ferrite surrounding the austenite grains, which decreased the ease of microvoid coalescence. Steel *LC-2* showed this behaviour at the low strain rate, with a substantial increase in MnS diameter from less than $1\mu\text{m}$ at $3.0\text{ }^\circ\text{C}\cdot\text{s}^{-1}$ to $1\text{-}5\text{ }\mu\text{m}$ at $1.2\text{ }^\circ\text{C}\cdot\text{s}^{-1}$ and $0.3\text{ }^\circ\text{C}\cdot\text{s}^{-1}$.
- Wider ferrite films, which decreased the strain concentration, both favoured transgranular failure and improved hot ductility. This is believed to be the mechanism at the high strain rate for *LC-2*, as the high temperature ductility drop occurs below the Ae_3 temperature.

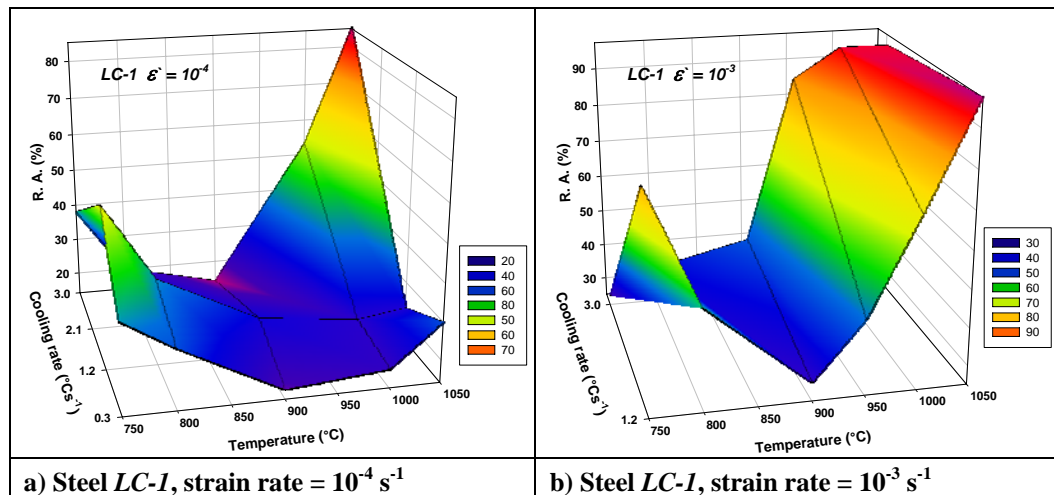


Figure 5.39: The effect of cooling rate on hot ductility of steel *LC-1*.

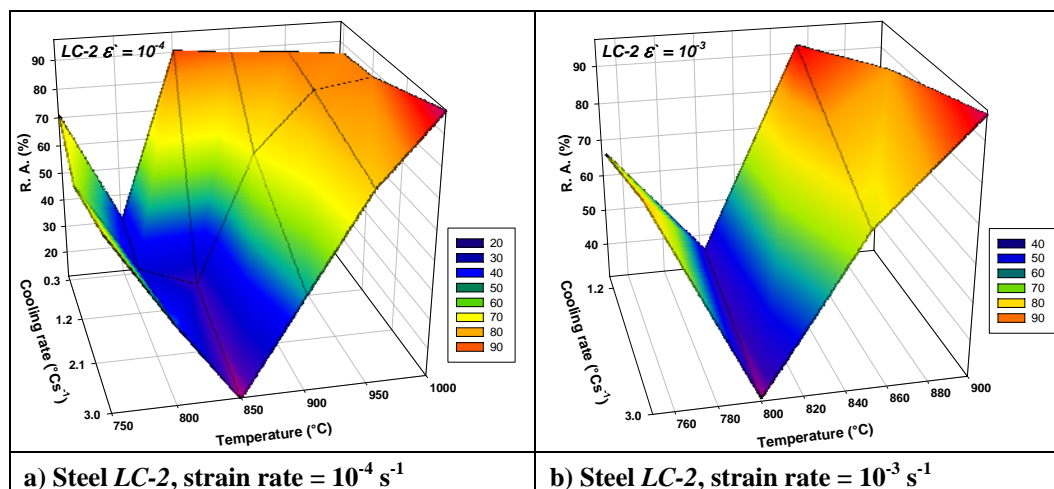


Figure 5.40: The effect of cooling rate on hot ductility of steel *LC-2*.

5.11 PRECIPITATION IN THE LOW CARBON STEELS

The species of precipitates found in the five low carbon steels are discussed below and are summarised in **Table 5.6**.

LC-1:

EDS analysis revealed that Mn was found in very few precipitates in *LC-1*, and the majority of the precipitates contained Fe in combination with S, or S and O. It is well-documented that a low Mn:S ratio, as defined by the calculation in **Section 2.5**, is very detrimental to hot ductility. This is primarily due to the tendency to form fine FeS precipitates, rather than the coarser MnS, near austenite grain boundaries, hence increasing the ease of microvoid coalescence (De Toledo, 1993; Turkdogan, 1987; Lankford, 1972 and Weinberg, 1979). The absence of calcium indicates that the steel has not been calcium-modified, hence the sulphur has not been removed from solution as CaS.

LC-2:

Many MnS and complex precipitates containing Mn and Fe in combination with Al and Ca were found. The Mn:S ratio is the same as that of *LC-1*, but is higher than the critical Mn:S ratio, as defined in **Section 2.5**. This can be seen by the presence of Mn in all analysed precipitates and the absence of FeS, therefore reducing the likelihood of cracking.

LC-3:

Steel *LC-3* contains many complex precipitates with Si and Ca. *LC-3* also has a very high Mn:S ratio, which can be seen by the presence of Mn in most analysed precipitates. There are many inclusions from steelmaking in this steel, as oxides and oxysulphides containing Al, Mg and Si.

LC-4:

Most analysed precipitates were found to be MnS or contained Mn and Fe, with Si and Al, in the form of oxides, sulphides and oxysulphides.

LC-5:

Most precipitates were found to contain Mn, or Mn and Fe in combination with Ca, Si and Cr. Despite the lower than critical Mn:S ratio, the hot ductility of LC-5 is superior to that of steels LC-1, LC-3 and LC-4, and similar to LC-2.

Table 5.6: Summary of the precipitation elements and species found in the low carbon steels.

Steel	Testing conditions	Ductility recovery below Ae_3 ?	Mn:S ratio	Calcium modified?	Precipitate species/ Elements
LC-1	All	No	Low	No	Fe(Mn)S, (Fe,Al)OS, MnS, Al ₂ O ₃ , MnO
LC-2	C,G,F,D	Yes	High	Yes	MnS, Mn(FeCaSiMoAl)OS, MnFeO, CaS(SiMnAlOFe)
	H	No	High	Yes	MnS
LC-3	C, H	No	High	Yes	CaMnAlO, MnSiO, MnS, FeMnSi(SO), MnO, AlMgO, Al ₂ O ₃
LC-4	C	No	High	No	MnAlO, MnS, FeMnSiOS
LC-5	C	Yes	Low	Yes	FeMn(CrCaSi)AlOS, MnCaSi(O)S

5.12 EFFECT OF COMPOSITION ON HOT TENSILE BEHAVIOUR IN THE LOW CARBON STEELS

5.12.1 Maximum strength

It is difficult to determine the effect of composition variation between the low carbon steels on maximum strength from **Figure 5.34**. However, the behaviour of all five low carbon steels is consistent with literature (Marique and Messien, 1990): an oscillation, with a peak, or plateau in the S_u near 850 °C, which is associated with austenite to ferrite transformation at, or just below, the Ae_3 temperature. As the testing temperature decreases in the austenite region, the S_u increases almost linearly. The work hardening of γ is highest at a temperature just prior to transformation, which increases the maximum strength. Austenite begins to transform to ferrite as thin films on the grain boundaries. As the thin α film begins to form with decreasing temperature, the S_u drops substantially. This is as a result of the softer nature of α than γ , as recovery occurs more easily in α at the same temperature (Suzuki *et al.*, 1984). As the temperature drops further below the Ae_3 , the ferrite begins to work harden (less energy available for recovery) and the S_u increases.

5.12.2 Hot ductility

All five steels were tested according to schedule C (10^{-3} s^{-1} and $1.2 \text{ }^\circ\text{C}\cdot\text{s}^{-1}$), *LC-3* was additionally tested according to schedule H (10^{-4} s^{-1} and $3.0 \text{ }^\circ\text{C}\cdot\text{s}^{-1}$) and *LC-1* and *LC-2* were tested under all five schedules. From these results in **Figure 5.35** and **Figure 5.36**, it can be seen that:

- *LC-2* and *LC-5* showed similar hot ductility behaviour: the reduction in area drop occurred just below the Ae_3 temperatures. This means that the failure mode is governed by the formation of a thin ferrite film as discussed in **Section 2.5.1**.
- *LC-4*, *LC-3* and *LC-1* showed increasing ductility recovery temperatures, which occurred above the Ae_3 temperatures for these three steels. Consequently, it can be

stated that the failure mode was governed by the formation of PFZs or by grain boundary sliding, with or without precipitation, as discussed in **Section 2.5.1**.

- *LC-3* showed similar, marginally improved hot ductility behaviour to *LC-1*.
- *LC-2* displayed markedly superior hot ductility to *LC-1* for all tested conditions, with the difference in high temperature ductility recovery (50% *R. A.*) ranging from 40 °C to in excess of 200 °C.

5.13 MECHANISMS OF HOT TENSILE BEHAVIOUR IN THE LOW CARBON STEELS

5.13.1 Zone II embrittlement: High temperature ductility drop above A_{e3} temperature

Zone II embrittlement (see **Section 2.5.1**) occurs in the stable γ region, where cracking occurs along γ grain boundaries due to microvoid coalescence of intergranular precipitates such as sulphides, oxides and oxysulphides (Suzuki *et al.*, 1982), or by grain boundary sliding which is enhanced by particles at the grain boundaries (Mintz *et al.*, 1991).

In steel *LC-1*, under all testing schedules, failure occurred due to intergranular cracking, where the austenite grain boundaries were weakened by copious precipitation of fine (Fe, Mn) oxysulphides and sulphides. The steel is not calcium-modified and the Mn:S ratio is low - both factors that contributed to the enhanced iron sulphide precipitation. A lower manganese content decreases the MnS precipitation temperature (1354 °C for *LC-1*, **Table 5.4**) where the mobility of Mn is lower, thus hindering MnS precipitation. Lankford (1972) stated that this could then lead to liquid drops of FeS forming in planar arrays at austenite grain boundaries; creating paths for easy crack propagation, as the *hcp* FeS precipitates are not coherent with the FCC matrix. Voids then nucleate around the FeS by decohesion from the matrix. In addition, the presence of oxygen promotes the

formation of liquid oxysulphides, such as Mn(O)S, which have a solidus temperature below 1150 °C.

In steel *LC-2*, which was calcium-modified, low ductility above Ae_3 was only seen at low strain rate with fast cooling rates. This is due to grain boundary sliding, usually associated with conditions of creep at low strain rates $< 10^{-4} \text{ s}^{-1}$, which is enhanced by microvoid coalescence between MnS precipitates.

Steel *LC-3* showed poor ductility above Ae_3 , in spite of the presence of Ca, high Si and the high Mn:S ratio, which are usually factors that promote good ductility. However, the presence of copious MnS precipitates and complex oxides and oxysulphides containing Mn, Al, Si and Mg indicates a high inclusion level from a poorly controlled casting process, which had a negative impact on ductility. Crowther and Mintz (1986) found that steels with high manganese levels (~1.4% Mn) always have wide ductility troughs.

Steel *LC-4* has a high Mn:S ratio and contains Si, which is beneficial to ductility. However, this steel was not calcium treated and the precipitates are thus oxides, sulphides and oxysulphides without Ca, but containing Mn, Al, Fe and Si which together with the detrimental presence of 0.27% Cu (melting point of pure Cu = 1080 °C), explains the inferior ductility to that of steel *LC-5*, which also contains copper, but is calcium-treated and contains nickel.

Although steel *LC-5* has a low Mn:S ratio, it is calcium-modified and contains large complex oxides, sulphides and oxysulphides (containing Fe, Mn, Cr, Ca, Si Al) that are incapable of affecting the hot ductility. Mintz (1999) stated that it is necessary to maintain a Ni:Cu ratio of 1.5-2.0 for Ni to increase the solubility of copper in austenite to prevent hot shortness. But Fisher (1969) found that a lower Ni:Cu ratio of 1 can promote oxidation of copper, thus removing it from solution and making it ineffective to influence hot ductility.

5.13.2 Zone III embrittlement: High temperature ductility drop below Ae_3 temperature

Zone III embrittlement occurs in the low temperature γ region (see **Section 2.5.1**), including the $\gamma \rightarrow \alpha$ phase transformation (Cardoso *et al.*, 1989). This only occurred at and below the Ae_3 temperature in steels *LC-2* (high strain rate) and *LC-5* (high strain rate and $1.2 \text{ }^\circ\text{C}\cdot\text{s}^{-1}$). Thin ferrite films can be deformation-induced along γ grain boundaries at temperatures below the Ae_3 and above the Ar_3 (undeformed transformation start temperature after cooling at a constant cooling rate). Preferential strain concentration occurs in the softer ferrite, and decohesion by ductile voiding at precipitates in the ferrite film then proceeds (Mintz *et al.*, 1991). The thickness of the thin α films remains quite constant below the Ae_3 until the Ar_3 is reached. Then the ferrite rapidly thickens and hot ductility recovers, as discussed below in **Section 5.13.3**.

5.13.3 Low temperature ductility recovery below Zone III

In low carbon steels, the Zone III ductility trough extends from the Ae_3 to just below the Ar_3 temperature (Mintz *et al.*, 1993b). In the five tested low carbon steels, the ductility recovery started between 750 and 800 $^\circ\text{C}$. This agrees with literature (Mintz, 1996), where ductility is shown to recover fully $\sim 20 - 30 \text{ }^\circ\text{C}$ below the undeformed Ar_3 (in plain C steels: $\sim 745 \text{ }^\circ\text{C}$ for 0.10% C and $\sim 710 \text{ }^\circ\text{C}$ for 0.16% C). The ductility recovers when $\sim 50\%$ ferrite is present in the sample before deformation (Mintz *et al.*, 1991).

5.14 APPLICATION AND RELEVANCE TO INDUSTRY

All five low carbon steels were tested under conditions simulating thin slab casting with medium secondary cooling (schedule C). *LC-3* was also tested under conditions simulating billet casting with hard cooling (schedule H). *LC-1* and *LC-2* were additionally tested under thin slab [hard cooling], billet [hard] and thick slab [medium and soft] casting conditions. Using the results in this work, the following straightening temperature conditions can be applied for minimal crack susceptibility when considering these steels for use in continuous casting operations, as shown in **Table 5.7**.

Table 5.7: Application of the hot ductility results to casting parameters.

Steel	Testing conditions	Casting type	Secondary cooling rate ($^{\circ}\text{C}\cdot\text{s}^{-1}$) [Cooling pattern]	Straightening temperature ranges ($^{\circ}\text{C}$)
<i>LC-1</i>	C	Thin slab	1.2 [medium]	< 800 or >975
	G	Thin slab	3.0 [hard]	>925
	H	Billet	3.0 [hard]	>950
	D	Thick slab	1.2 [medium]	≤ 750 or $\gg 1100$
	F	Thick slab	0.3 [soft]	Not suitable
<i>LC-2</i>	C	Thin slab	1.2 [medium]	< 775 or >825
	G	Thin slab	3.0 [hard]	< 775 or >825
	H	Billet	3.0 [hard]	< 775 or >925
	D	Thick slab	1.2 [medium]	< 750 or >875
	F	Thick slab	0.3 [soft]	< 775 or >925
<i>LC-3</i>	C	Thin slab	1.2 [medium]	< 750 or >925
	H	Billet	3.0 [hard]	< 750 or >950
<i>LC-4</i>	C	Thin slab	1.2 [medium]	>900
<i>LC-5</i>	C	Thin slab	1.2 [medium]	< 775 or >825

Based on this work, the following compositional limits are recommended to minimise crack susceptibility in low carbon steels:

- Calcium-treatment is required to remove fine sulphide and oxysulphide precipitates such as (Mn,Fe)S and CuS that are detrimental to hot ductility.
- Maintaining the nitrogen below 0.0070% N to reduce strain ageing in downstream processes.
- Maintaining the sulphur below 0.010% S.
- Maintaining a Mn:S ratio of ≥ 30 . As the sulphur control on the steels studied in this work is quite good ($\leq 0.012\%$ S), the Mn content would need to be increased.
- Minimising entrapment of inclusions, *e.g.* silicates, alumina, magnesia, by exercising tighter control over the steelmaking and casting processes.
- Adding nickel to copper-bearing steels in the ratio Ni:Cu ≥ 1.5 to retain Cu in austenite solid solution.

To ensure that the strand temperature does not approach any low ductility region during the straightening process, the minimum recommended straightening temperatures listed in **Table 5.7** should be used for the steel compositions in this work. The maximum straightening temperatures should be limited to ~ 1200 °C, as hot ductility can begin to drop to below 50% *R. A.* at higher temperatures.

It is also important to cast steels in the peritectic composition range with care, especially 0.10-0.17% C with high manganese ($>1.0\%$ Mn), due to the tendency to form coarse columnar austenite grains which are detrimental to hot ductility.

Chapter 6: Niobium Steels

Hot tensile behaviour in the niobium microalloyed steels: results, discussion and application

6.1 OVERVIEW OF CHAPTER 6

The niobium steels were sampled from thick slab. The five steels were reheated to 1300 °C, cooled to testing temperatures between 750 – 1100°C at a rate of 1.2 °Cs⁻¹ and pulled to failure at a strain rate of 10⁻³ s⁻¹. Steel *Nb-5* was cooled at rates of 0.3, 1.2 and 3.0 °Cs⁻¹ and pulled to failure at strain rates of 10⁻⁴ and 10⁻³ s⁻¹.

All five niobium steels showed poor ductility above the A_{e3} temperature *i.e.* in the single phase austenite region, indicating that precipitation of fine Nb(C,N) was the cause of the poor ductility. In addition, the steel that was not calcium-modified showed the poorest ductility.

In steel *Nb-5*, the hot ductility was improved by decreasing the cooling rate and also by increasing the strain rate. Slow thin slab and thick slab casting conditions provided the best hot ductility results for this niobium steel.

6.2 CALCULATED TRANSFORMATION TEMPERATURES IN THE NIOBIUM STEELS

The chemical composition of the niobium steels is given in **Table 6.1**. It should be noted that steel *Nb-4* has a low C content; steel *Nb-4* has a low Si content whereas that of *Nb-5* is high; *Nb-3* has a high N content and *Nb-5* has a high Mn content.

Table 6.1: Chemical composition of niobium microalloyed steels (in mass %).

Steel	C	Mn	P	S	Si	Al	N	Nb	Ni	Cu	Cr	Mo
Nb-1	0.04	0.34	0.009	0.001	0.12	0.047	0.0067	0.018	0.02	0.01	0.02	-
Nb-2	0.07	0.54	0.008	0.003	0.15	0.032	0.0070	0.020	0.02	0.02	0.01	-
Nb-3	0.07	0.87	0.005	0.006	0.19	0.042	0.0106	0.027	0.02	0.01	0.02	-
Nb-4	0.12	0.83	0.007	0.014	0.03	0.045	0.0071	0.028	0.02	0.02	0.02	-
Nb-5	0.16	1.48	0.007	0.008	0.34	0.036	0.0093	0.030	0.01	-	0.02	0.04

The Ae_3 and Ae_1 transformation temperatures from the two equations: GAS^i and $Andrews^{ii}$ (**Table 2.3**) and from Thermo-CalcTM are listed in **Table 6.2**. As the Ae_1 temperatures are at least 200 °C lower than the testing temperatures, they have no influence on this work and are merely noted for interest.

Table 6.2: Calculated Ae_3 and Ae_1 transformation temperatures (in °C) for niobium microalloyed steels in this work.

Steel	Ae_3 (start of ferrite formation).				Ae_1 (start of austenite formation)		
	GAS^i	And^{ii}	T-C SSOL2 ⁱⁱⁱ	T-C TCFe3 ^{iv}	And^{ii}	T-C SSOL2 ⁱⁱⁱ	T-C TCFe3 ^{iv}
Nb-1	884	893	894	893	720	709	718
Nb-2	869	878	872	873	716	700	711
Nb-3	863	870	859	862	709	689	700
Nb-4	840	845	841	842	704	692	702
Nb-5	830	838	821	821	700	685	685

ⁱ Genetic Adaptive Search (GAS) equation. (Deo *et al.*, 1995).

ⁱⁱ Andrews formula (1965).

ⁱⁱⁱ Modelled using Thermo-CalcTM database SSOL2 (Cornish, 1999).

^{iv} Modelled using Thermo-CalcTM database TCFe3 (2006) – this work.

The niobium steels showed a large decrease in predicted Ae_3 temperatures of up to 70 °C from *Nb-1* through to *Nb-5*, due to the increase in carbon and substantial increase in manganese content, and in spite of the variation in silicon.

The calculated and modelled Ae_3 temperatures are very similar, as shown in **Figure 6.1**, and range from:

- GAS: 830 – 884 °C
- Andrews: 838 – 893 °C
- Thermo-Calc™ (SSOL2): 821 – 894 °C
- Thermo-Calc™ (TCFe3): 821 – 893 °C

The *GAS* and Thermo-Calc™ Ae_3 values vary by 1 – 10 °C, whereas the Andrews Ae_3 values are 5 – 9 °C higher than the *GAS* values and range from 1°C lower to 17 °C higher than the Thermo-Calc™ values.

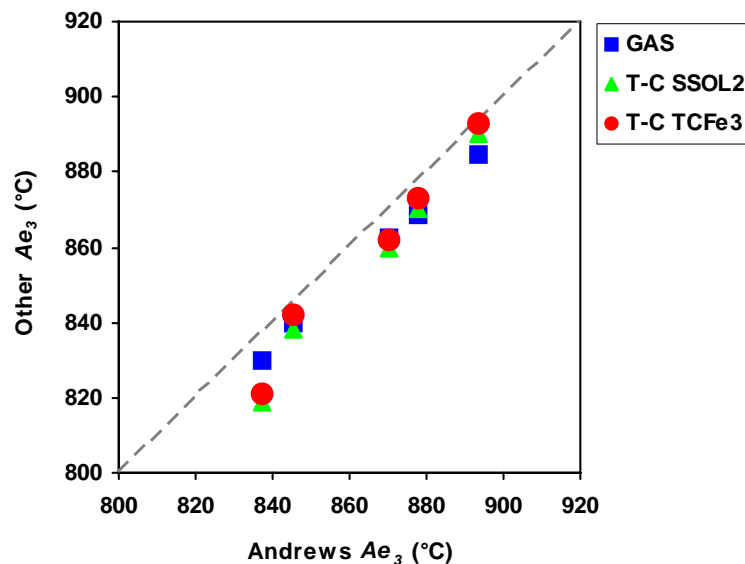


Figure 6.1: Comparison of the calculated *GAS*, modelled TCFE3 and SSOL2 Ae_3 temperatures with the calculated Andrews Ae_3 temperature for the niobium steels.

6.3 CALCULATED PRECIPITATE DISSOLUTION IN THE NIOBIUM STEELS

For low solute contents, as in these low alloy niobium steels, the total mass concentrations of the dissolved elements are assumed to be in equilibrium with the precipitated phase, and can thus be used to represent the solubility product discussed in Section 2.5.

An exception to the more commonly-used equilibrium solubility is the critical Mn:S ratio calculation from Table 2.2 (de Toledo *et al.*, 1993). The results for the actual Mn:S / critical Mn/S ratio are shown in Table 6.3. Table 6.4 lists the equilibrium dissolution temperatures (T_{diss}) of the following precipitates in austenite: AlN, Nb(C,N) and MnS, calculated by the solubility equations in Table 2.2. Table 6.5 lists the various Nb(C,N), AlN and MnS precipitates predicted by Thermo-Calc™.

Table 6.3: Critical (Mn:S)_c and actual (Mn:S)_a ratios for all of the steels calculated using the De Toledo (1993) criterion.

Steel	(Mn:S) _c	(Mn:S) _a	(Mn:S) _a / (Mn:S) _c	Actual > Critical? ^v
Nb-1	323	340	1.05	Y
Nb-2	135	180	1.33	Y
Nb-3	78	145	1.86	Y
Nb-4	40	59	1.49	Y
Nb-5	62	185	2.98	Y

Table 6.4: Solubility of precipitates in austenite in the niobium steels – calculated equilibrium precipitate dissolution temperatures (°C).

Steel	Turkdogan (1987)					Stuart (1981)				
	AlN	MnS	NbC _{.7} N _{.2}	NbC _{.87}	NbN	NbC _{.83} N _{.14}	NbC _{.24} N _{.65}	NbC _{.87}	NbN	NbC
Nb-1	1221	1137	1025	943	1044	1005	1098	849	992	958
Nb-2	1174	1304	1066	1000	1055	1048	1120	896	1004	1019
Nb-3	1272	1458	1098	1031	1111	1076	1168	921	1067	1048
Nb-4	1223	1582	1128	1086	1082	1112	1159	967	1034	1109
Nb-5	1228	1585	1157	1124	1109	1142	1187	997	1065	1150

^v Mn/S (actual) > Mn/S (critical) for good hot ductility (de Toledo *et al.*, 1993).

Table 6.5: Solubility of precipitates in austenite in the niobium steels – Thermo-Calc™ modelled equilibrium precipitate dissolution temperatures (°C).

Steel	SSOL2 ^{vi}		SSOL2 ^{vii}		SSOL4 ^{vii}	TCFe3 ^{vii}	TCFe3 ^{vii}	TCFe3 ^{vii}
	NbC _{.4} N _{.6}	1050	NbC _{.4} N _{.6}	1056	NbC _{.7} N _{.3}	NbC	AlN	MnS
Nb-1	NbC _{.4} N _{.6}	1050	NbC _{.4} N _{.6}	1056	1033	976	1148	1171
Nb-2	NbC _{.55} N _{.45}	1076	NbC _{.55} N _{.45}	1085	1100	1027	1124	1308
Nb-3	NbC _{.45} N _{.55}	1118	NbC _{.45} N _{.55}	1127	1136	1055	1177	1430
Nb-4	NbC _{.7} N _{.3}	1137	NbC _{.7} N _{.3}	1134	1151	1097	1150	1471
Nb-5	NbC _{.7} N _{.3}	1171	NbC _{.7} N _{.3}	1169	1186	1136	1165	1461

The AlN dissolution temperatures ranged from 1174 – 1272 °C calculated using the Turkdogan equation (Turkdogan, 1987) and from 1124 – 1177 °C modelled using the TCFe3 database in Thermo-Calc™. This is shown in **Figure 6.2**, where the dependence of the AlN dissolution temperature on K_{AlN} ($\log [Al][N]$) is plotted. The TCFe3 temperatures are 50 - 100 °C lower than the Turkdogan temperatures.

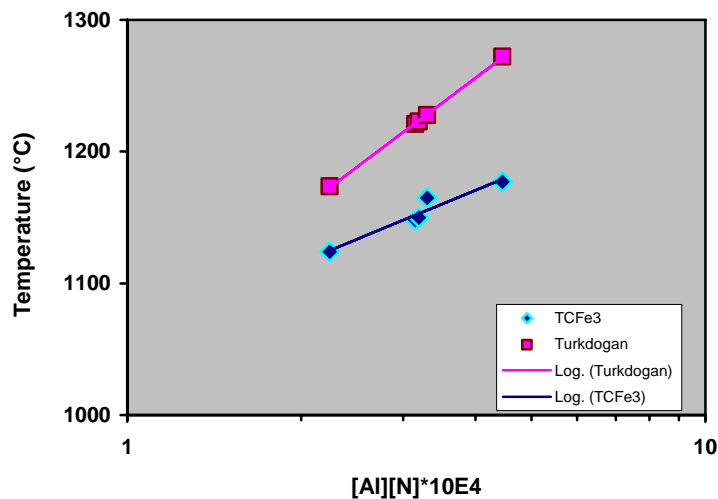


Figure 6.2: Logarithmic dependence of the AlN dissolution temperature on [Al][N] for the niobium steels modelled using Thermo-Calc™ and calculated using the Turkdogan (1987) equation.

^{vi} Modelled using Thermo-Calc database SSOL2 (Cornish, 1999).

^{vii} Modelled using Thermo-Calc databases SSOL2, SSOL4 and TCFe3 (2006) – this work.

The MnS dissolution temperatures in the niobium steels range from 1137 – 1585 °C (Turkdogan equation, 1987) and from 1171 – 1471 °C (Thermo-Calc™ TCFE3) and the dependence on K_{MnS} i.e. $\log [Mn][S]$ is shown in **Figure 6.3**.

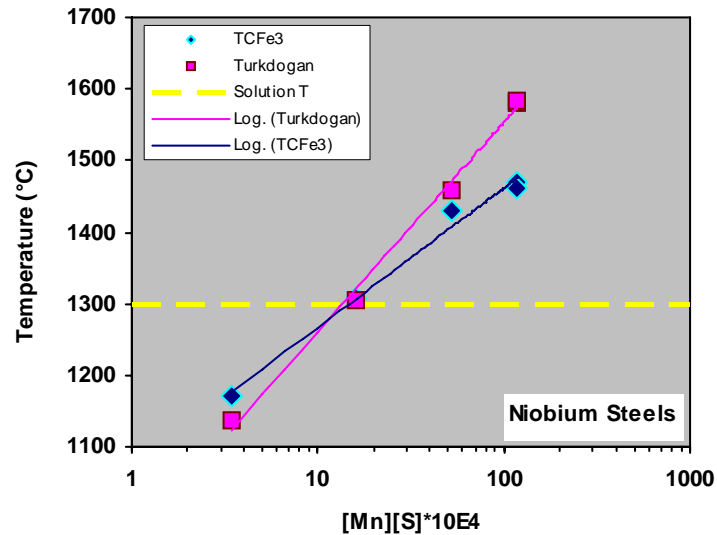


Figure 6.3: Logarithmic dependence of the MnS dissolution temperature on $[Mn][S]$ for the niobium steels using Thermo-Calc™ modelling and the Turkdogan equation (1987).

The equilibrium dissolution temperatures calculated using equations of Turkdogan (1987) resulted in higher $NbC_{0.87}$ temperatures by ~ 60 °C, as well as higher NbN temperatures by approximately 50 °C than by using the equation of Stuart (1981). This is probably due to differences in steel compositions and testing conditions from the data sets used by each author.

Using Thermo-Calc™ (SSOL2, SSOL4 and TCFE3) produced different precipitate species to the other authors. However, the temperatures are in the same region, such as 1134 °C (SSOL2 - $NbC_{0.7}N_{0.3}$) in steel Nb-4, 1151 °C (SSOL4- $NbC_{0.7}N_{0.3}$), compared with 1128 °C ($NbC_{0.7}N_{0.2}$), and 1169 °C (SSOL2 - $NbC_{0.7}N_{0.3}$) in steel Nb-5, 1186 °C (SSOL4- $NbC_{0.7}N_{0.3}$), compared with 1157 °C ($NbC_{0.7}N_{0.2}$) calculated by the Turkdogan (1987) equation. These differences are illustrated in **Figure 6.4**, which shows the

logarithmic dependence of the various Nb(C,N) precipitate dissolution temperatures on $K_{Nb(C,N)}$ i.e. $\log [Nb][C]_x[N]_y$.

The wide range of Nb(C,N) precipitates for which dissolution temperatures have been determined in literature, show that there are many combinations of the elements Nb, C and N, depending on the steel composition, initial state of the microstructure and the specific testing conditions applied to the steel.

Figure 6.5, Figure 6.6 and Figure 6.7 show the Thermo-Calc™ equilibrium phase graphs modelled using database TCFE3 for the niobium steels Nb-1 to Nb-5.

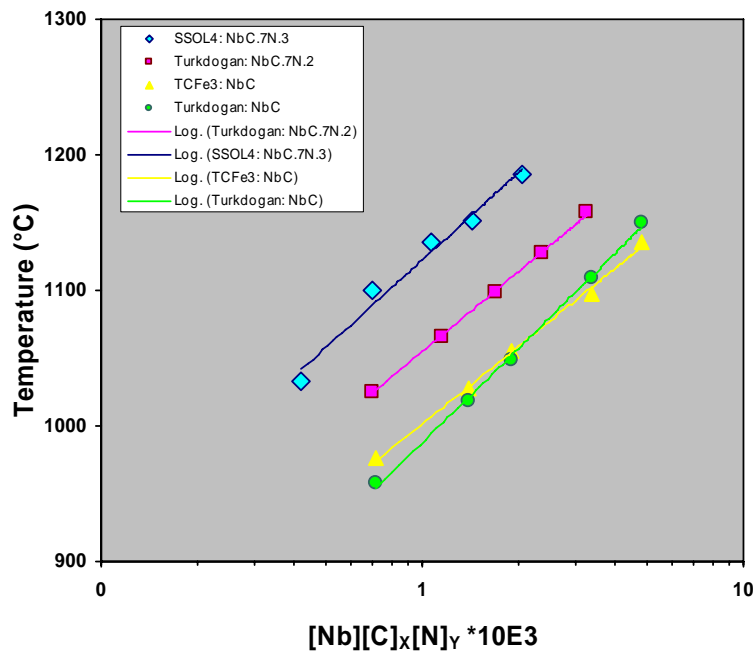


Figure 6.4: Logarithmic dependence of the various Nb(C,N) precipitate dissolution temperatures on $[Nb][C]_x[N]_y$ for the niobium steels, using Thermo-Calc™ TCFE3 and SSOL4, and the Turkdogan equation(1987).

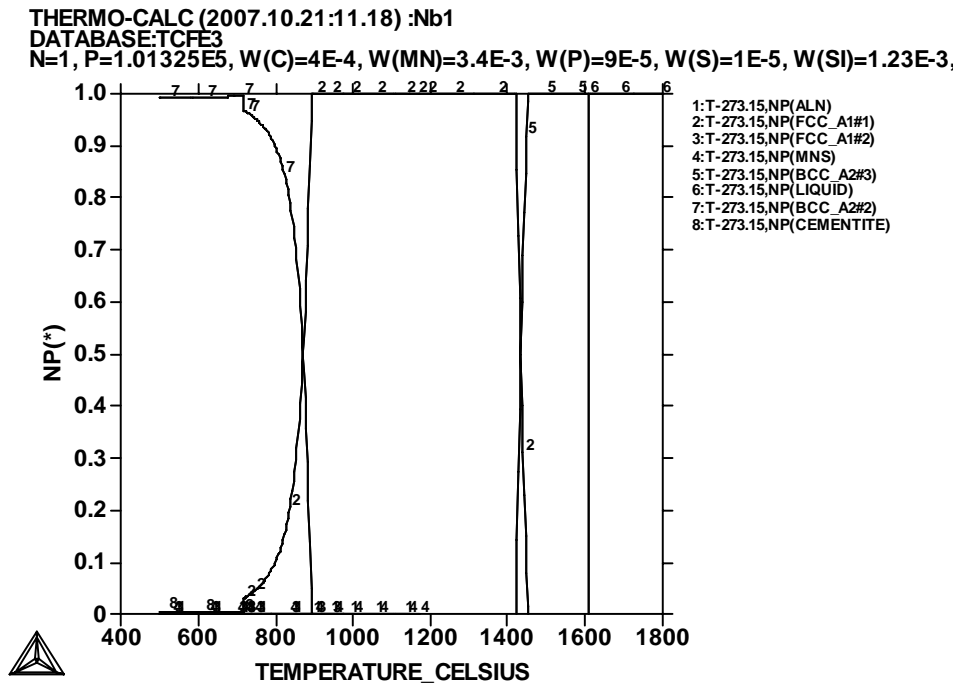
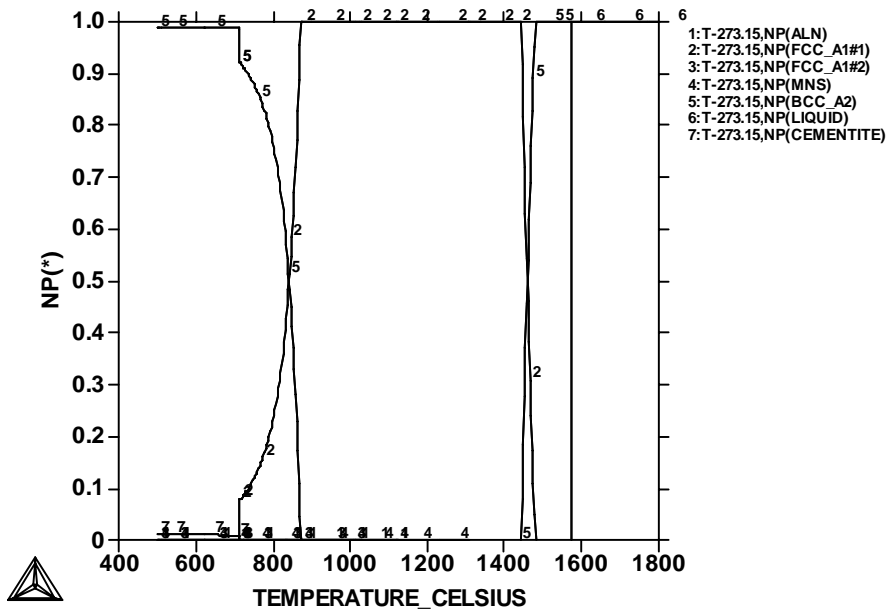


Figure 6.5: Thermo-Calc graph modelled using database TCFe3, showing the equilibrium phases for niobium steel *Nb-1*.

THERMO-CALC (2007.10.21:11.22) :Nb2

DATABASE:TCFE3

N=1, P=1.01325E5, W(C)=7E-4, W(MN)=5.4E-3, W(P)=8E-5, W(S)=3E-5, W(SI)=1.5E-3,
W(AL)=3.2E-4, W(N)=7E-5, W(NB)=2E-4, W(NI)=2E-4, W(CU)=2E-4, W(CR)=1E-4;

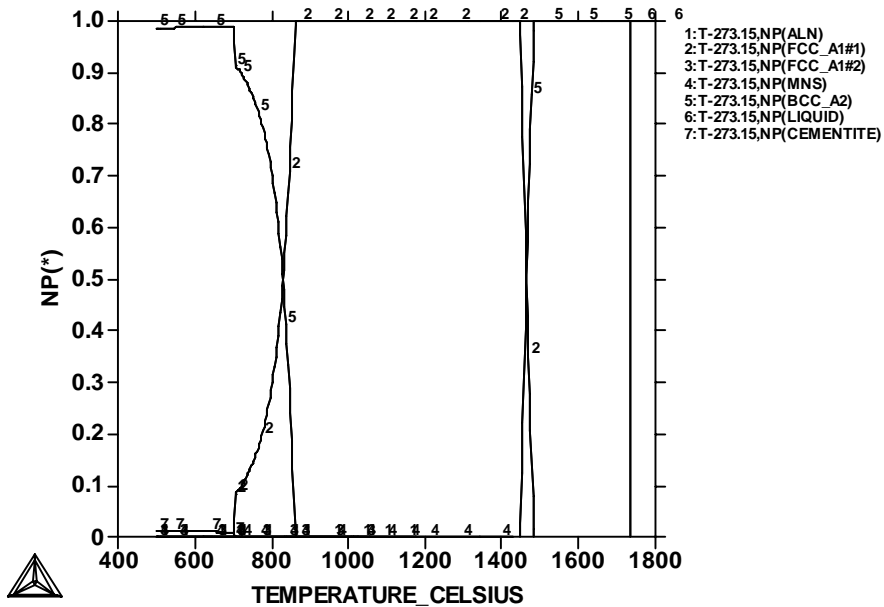


a)

THERMO-CALC (2007.10.21:11.31) :Nb3

DATABASE:TCFE3

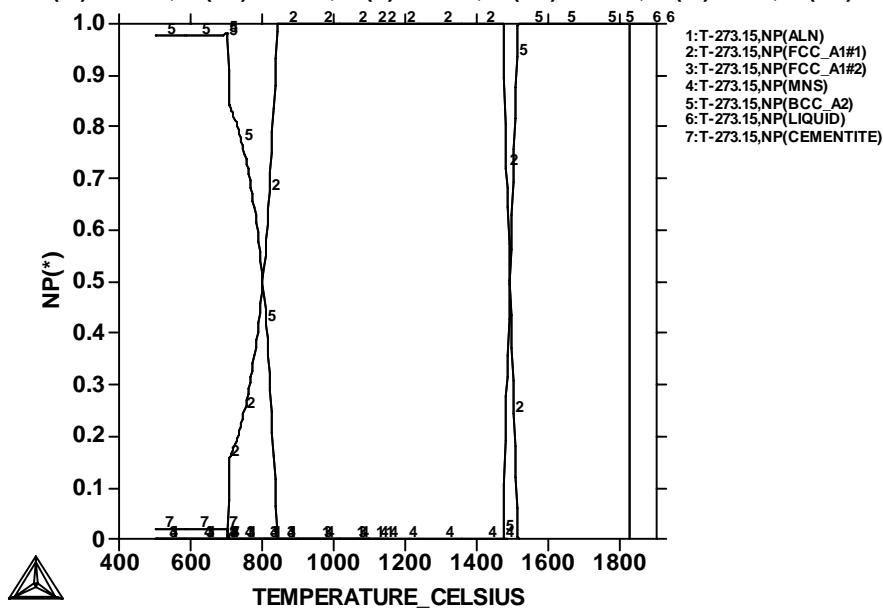
N=1, P=1.01325E5, W(C)=7E-4, W(MN)=8.7E-3, W(P)=5E-5, W(S)=6E-5, W(SI)=1.9E-3,
W(AL)=4.2E-4, W(N)=1.06E-4, W(NB)=2.7E-4, W(NI)=2E-4, W(CU)=1E-4, W(CR)=2E-4;



b)

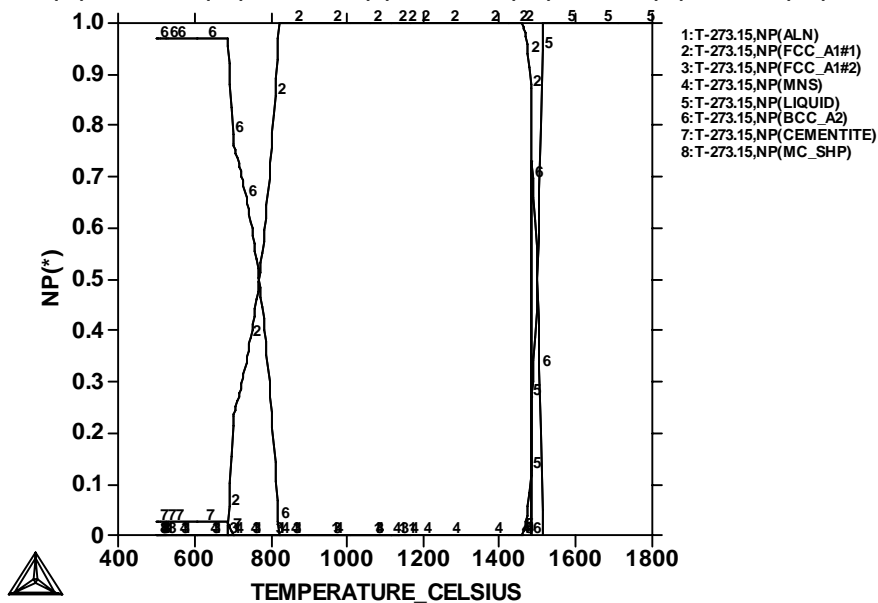
Figure 6.6: Thermo-Calc™ graphs modelled using database TCFE3, showing the equilibrium phases for niobium steels a) Nb-2 and b) Nb-3.

THERMO-CALC (2007.10.21:11.37) :Nb4
 DATABASE:TCFe3
 N=1, P=1.01325E5, W(C)=1.2E-3, W(MN)=8.3E-3, W(P)=7E-5, W(S)=1.4E-4,
 W(Si)=3.2E-4, W(AL)=4.5E-4, W(N)=7.1E-5, W(NB)=2.8E-4, W(NI)=2E-4, W(CU)=2E-4, W(CR)=2E-4;



a)

THERMO-CALC (2007.10.21:11.46) :Nb5
 DATABASE:TCFe3
 N=1, P=1.01325E5, W(C)=1.6E-3, W(MN)=1.48E-2, W(P)=7E-5, W(S)=8E-5,
 W(Si)=3.4E-3, W(AL)=3.6E-4, W(N)=9.3E-5, W(NB)=3E-4, W(NI)=1E-4, W(CR)=2E-4, W(MO)=4E-4;



b)

Figure 6.7: Thermo-Calc™ graphs modelled using database TCFe3, showing the equilibrium phases for niobium steels a) Nb-4 and b) Nb-5.

6.4 NIOBIUM STEEL *Nb-1*

Nb-1 was tested according to schedules A, B and C, as defined in **Table 3.4**. The Thermo-CalcTM TCFE3 modelled Ae_3 transformation temperature (893 °C) from **Table 6.2** is shown on the graphs.

Only 12 machined tensile specimens of steel *Nb-1* were available for testing due to lack of material. One hot ductility test had to be interrupted and cancelled due to problems with thermocouple contact. Thus, there were only two specimens with which to test under Schedule C conditions, which makes interpretation of the results difficult.

6.4.1 Maximum strength

The onset of dynamic recrystallization is shown by means of an arrow on the graph **Figure 6.0 b** at 1000 °C and the temperature is listed in **Table 6.6**.

Figure 6.0 shows a gradual increase in maximum strength with decrease in testing temperature from 1000 to 900 °C for schedules A, B and C. From 900 – 800 °C, the S_u tapers off (schedules A and B). Below 800 °C, there is a large increase in maximum strength (schedule A). This coincides with the progression of the austenite to ferrite transformation down to the Ae_1 temperature (Thermo-CalcTM TCFE3: 718 °C) and limited recovery of the ferrite, leading to work hardening and the subsequent large increase in strength.

The strength values were very similar for schedules A (1 minute solution treatment at 1300 °C, continuous cooling to test temperature) and B (1 minute solution treatment at 1300 °C, thermal oscillation, then continuous cooling to test temperature). The strength values for schedule C (5 minutes solution treatment at 1300 °C, continuous cooling to test temperature) were 5 – 10 MPa lower than for schedules A and B.

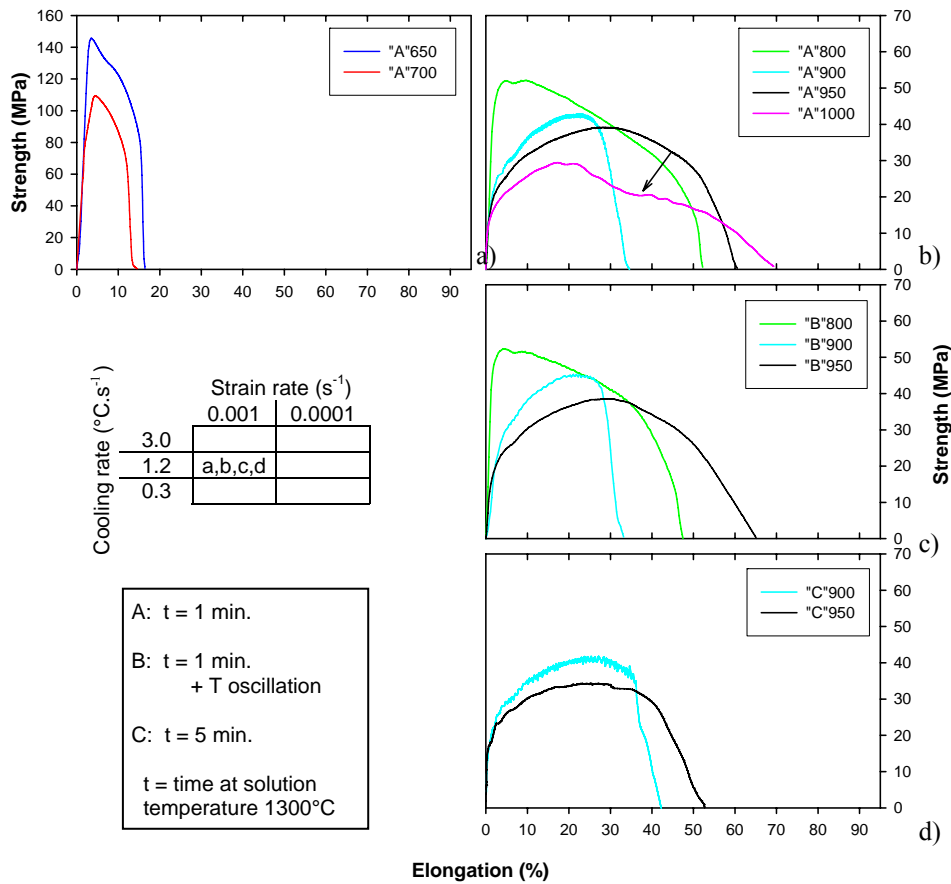


Figure 6.8: Engineering stress as a function of elongation for steel Nb-1. The arrow in b) indicates the onset of dynamic recrystallisation. The key to the testing schedules A, B and C is also shown.

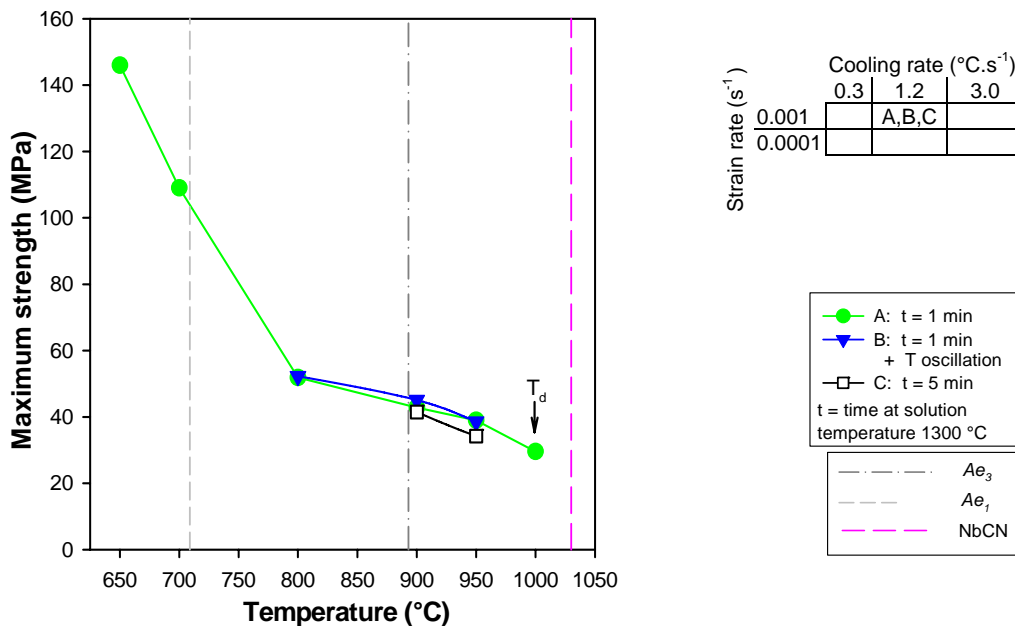


Figure 6.9: Maximum strength for steel Nb-1 as a function of testing temperature, solution treatment time and cooling pattern.

6.4.2 Reduction in area

The reduction in area values for schedules A and B were similar between 800 and 950 °C, as shown in **Figure 6.10**. The ductility of schedule A decreased from 96% (1000 °C) to 84% (950 °C), to a minimum of 32% at 900 °C, followed by an increase to 80% (800 °C). Below 800 °C, the reduction in area dropped to 48% at 700 °C, just below the Ae_1 temperature (718 °C), followed by an increase to 54% at 650 °C. The ductility of schedule B decreased from 96% at 950 °C, to a minimum of 28% at 900 °C, followed by an increase to 84% at 800 °C. The ductility of schedule C showed an increase from 49% at 900 °C to 69% at 950 °C.

The 50% low temperature ductility recovery occurred at 860 °C (schedule A) and 850 °C (B). The 50% high temperature ductility recovery occurred at ~930 °C for schedules A and B and 900 °C for schedule C. Dynamic recrystallisation is only seen at 1000 °C in schedule C.

The Ae_3 (893 °C) occurred at low ductility, at the minimum R. A. values for schedules A and B. Below the Ae_3 , the formation and growth of ferrite grains removes the stress concentration from the austenite grain boundary regions, resulting in a recovery in the reduction of area, and hence, the hot ductility. With temperature drop to below the Ae_1 , the recovery of ferrite is reduced, causing stress concentration, and a resulting drop in the reduction of area.

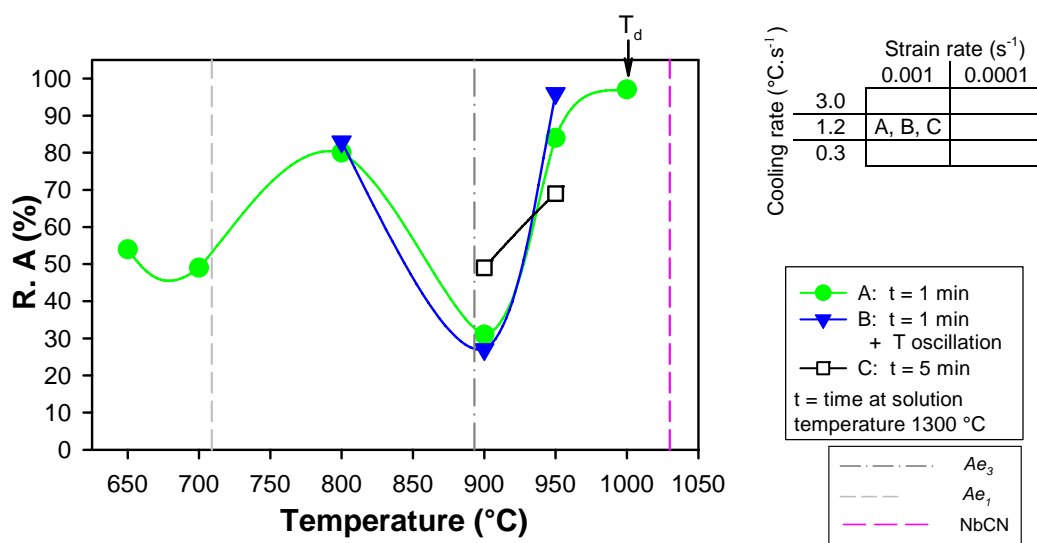


Figure 6.10: Reduction in area for steel Nb-1 as a function of testing temperature, strain rate and cooling rate.

6.4.3 Total elongation

The total elongation graph in **Figure 6.11** shows similar behaviour to the reduction in area graph for all three schedules A, B and C. The total elongation of schedules A and B decreased from ~50% (800 °C) to a minimum of ~35% (900 °C), then increased to ~60% (950 °C). With further increase in testing temperature to 1000 °C, the total elongation for Schedule A increased to ~70%. The total elongation values for Schedule C increased from ~45% (900 °C) to ~55% (950 °C).

The Ae_3 was found to be near the minimum elongation for schedules A and B between 800 and 900 °C. Below the Ae_3 , the formation and growth of ferrite grains removes the stress concentration from the austenite grain boundary regions, resulting in a recovery in the total elongation.

For schedule A there was a substantial decrease in elongation from 800 °C to 700 °C, with some recovery with further decrease in temperature to 650 °C *i.e.* below the Ae_1 temperature.

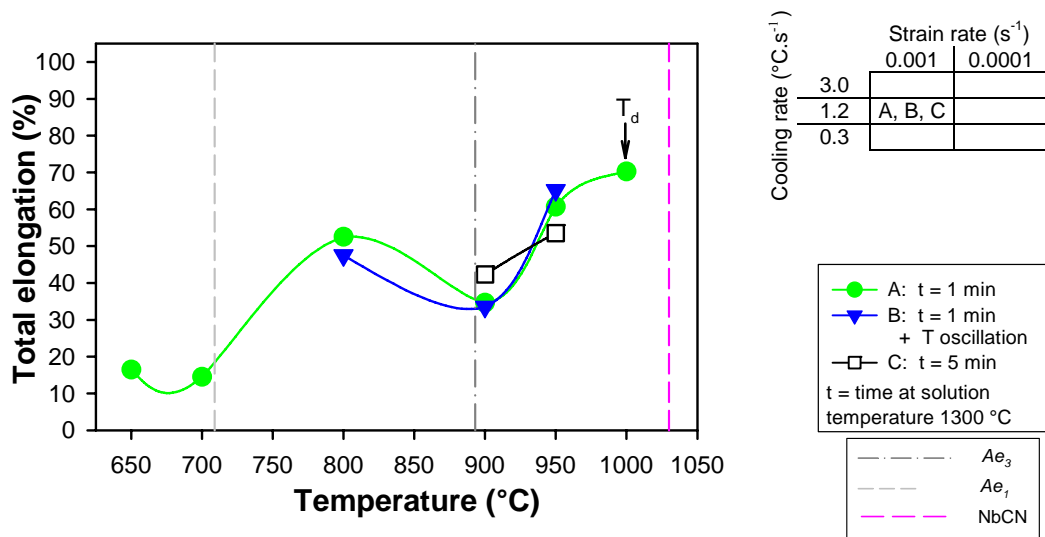


Figure 6.11: Elongation for steel *Nb-1* as a function of testing temperature, strain rate and cooling rate.

6.4.4 Scanning electron microscopy

- *Schedule A (1 minute solution treatment at 1300 °C):*

At 900 °C (**Figure 6.12 a**), fine precipitation was observed in either one row or two parallel rows in between cracks. The precipitate-containing microvoids were joined by coalescence. Typical precipitate analyses indicated Al-Si-O and Fe-Ca-Al-O-C-Nb precipitates, where C and Nb indicate the presence of Nb as Nb(C,N). As these particles are very small, there is pickup from the matrix in the analyses.

At 950 °C (**Figure 6.12 b**), many small precipitates, analyzed as Fe-Mn-Si-Al-O, were seen in the matrix. Little internal cracking was observed.

- *Schedule B (1 minute at 1300 °C, followed by temperature oscillation):*

At 900 °C, rows of precipitate-containing microvoids were found at the tips of internal cracks (**Figure 6.12 c**). Precipitates were analyzed as Al-Mg-O (inclusions from the steelmaking process), Fe-O-S and Fe-Mn-O-S.

- *Schedule C (5 minutes solution treatment at 1300 °C):*

Typical precipitates contained SiO and Fe(Mn)SO. **Figure 6.12 d** (900 °C) shows a row of microvoids joined by coalescence. An adjacent precipitate was analyzed as containing Fe-Mn-S-C-N, which could indicate the presence of Nb as a carbonitride-forming element as Nb(C,N).

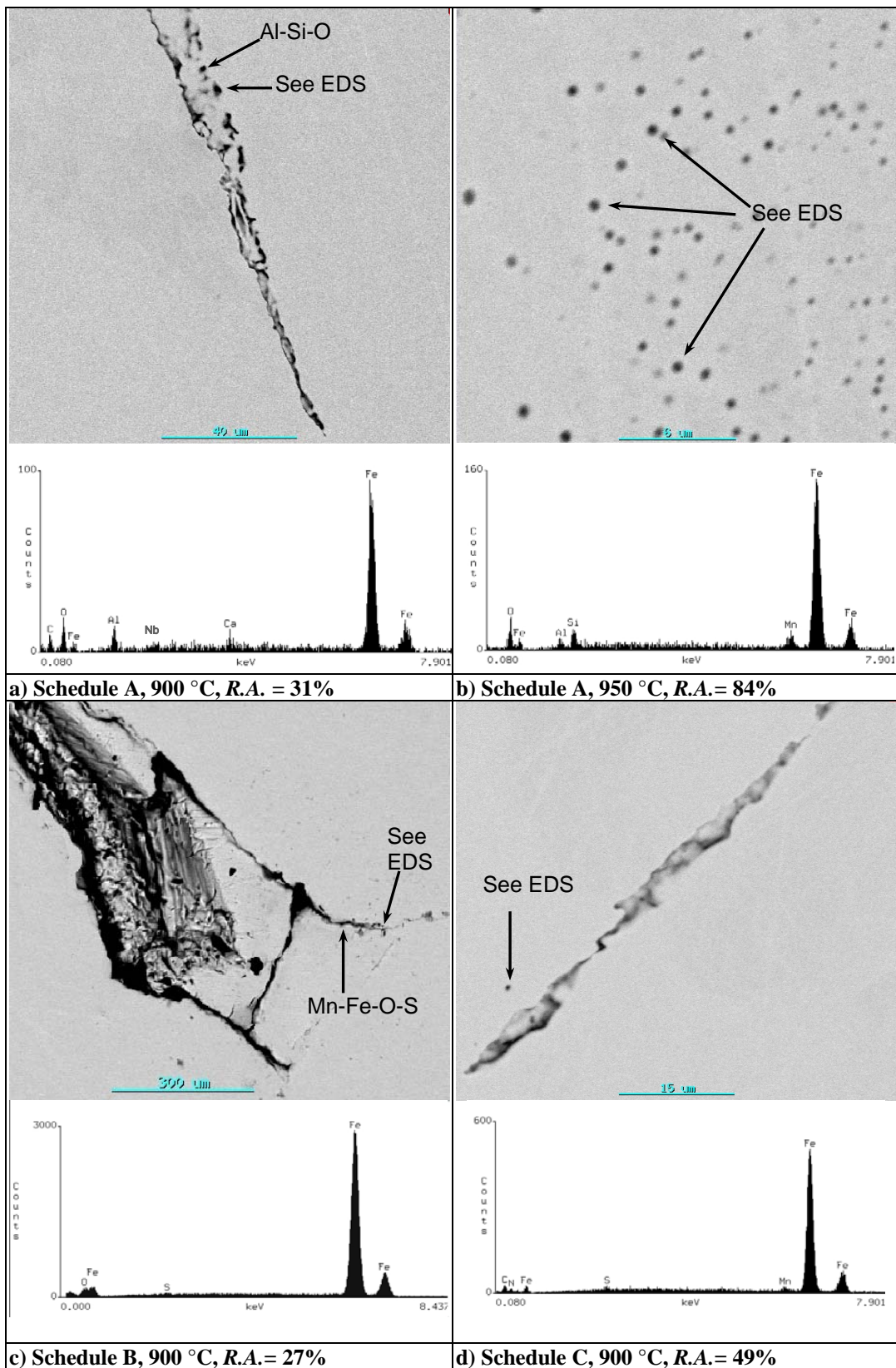


Figure 6.12: SEM backscatter images of steel *Nb-1* tested under schedule A, B and C conditions (cooling rate = $1.2\text{ }^{\circ}\text{C}\cdot\text{s}^{-1}$, strain rate = 10^{-3} s^{-1}), showing discrete precipitates without any cracking (b), microvoid coalescence (a and d) and extensive cracking (c).

6.5 NIOBIUM STEELS *Nb-2*, *Nb-3* and *Nb-4*

All three niobium steels *Nb-1*, *Nb-2* and *Nb-3* were tested under schedule C conditions only, due to the limited amount of steel available for testing. The TCF_{e3} modelled transformation temperatures for *Nb-2* and *Nb-4* from **Table 6.2** are shown on the graphs.

6.5.1 Maximum strength

The engineering stress – elongation graphs are shown in **Figure 6.13** and the maximum strength as a function of temperature is shown in **Figure 6.14**.

Nb-2: The maximum strength result obtained at 900 °C was found to be incorrect, as the temperature fluctuated from 890–970 °C during the test, due to poor thermocouple contact. Thus, the maximum strength decreased slightly with increase in temperature from 950 – 975 °C and then decreased sharply with further increase to 1000 °C.

Nb-3: At 1000 °C, the maximum strength value (34 MPa) was higher than that of *Nb-2* or *Nb-4*.

Nb-4: The maximum strength increased with increase in temperature from 900 – 950 °C, decreased slightly from 950 to 975 °C and then decreased sharply with further increase in temperature to 1000 °C. The maximum strength values for *Nb-4* were approximately 3 MPa higher than for *Nb-2*, except at 900 °C, where the difference was ~11 MPa.

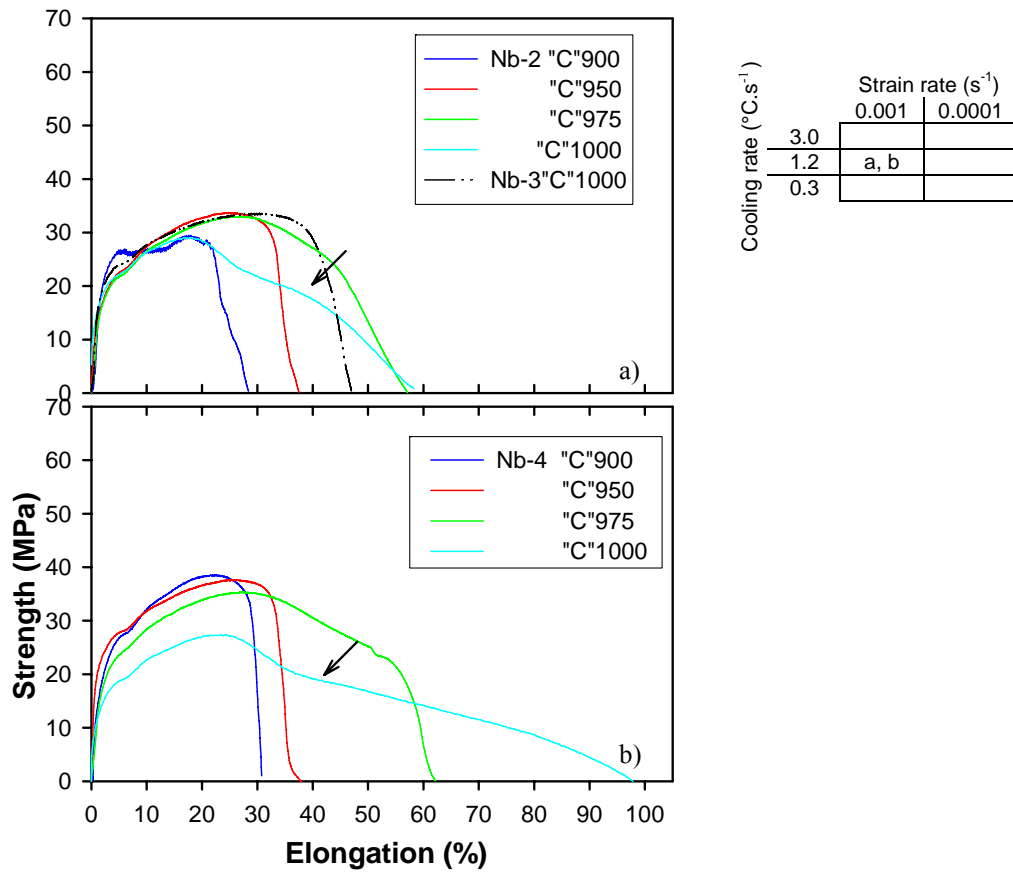


Figure 6.13 Engineering stress as a function of elongation for steels *Nb-2*, *Nb-3* and *Nb-4*. The key to the testing schedules is shown above. Arrows indicate the onset of dynamic recrystallisation

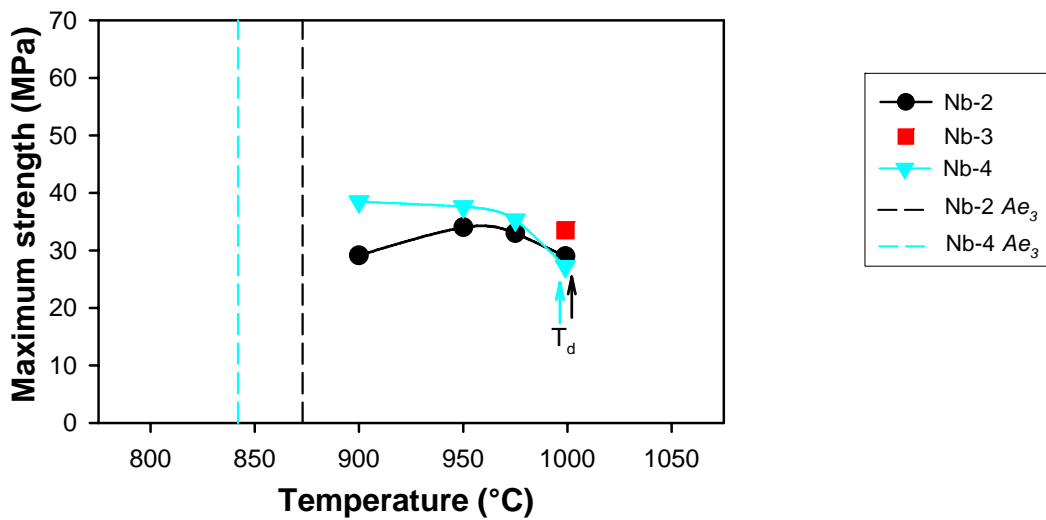


Figure 6.14: Maximum strength for steels *Nb-2*, *Nb-3* and *Nb-4* as a function of testing temperature. All tests were conducted according to Schedule C conditions (10^{-3} s^{-1} , $1.2 \text{ }^\circ\text{C.s}^{-1}$).

6.5.2 Reduction in area

Nb-2: **Figure 6.15** shows that the % *R. A.* increased slightly from 23% at 900 °C, to 30% at 950 °C, then to 96% at 975 °C and 97% at 1000 °C.

Nb-3: At 1000°C the *R. A.* was 64%, which is more than 30% lower than that of *Nb-2* and *Nb-4*.

Nb-4: At 900 °C (26%) and 950 °C (32%) the *R. A.* values were very similar to those of *Nb-2*. However, at 975 °C the *R. A.* only increased to 48% (*Nb-2*: 96%), with a further increase in ductility to 97% at a testing temperature of 1000 °C.

These results show that the ductility recovery at the high temperature side of the ductility trough occurred in these three steels in order of low to high temperature:

Nb-2 → *Nb-4* → *Nb-3*

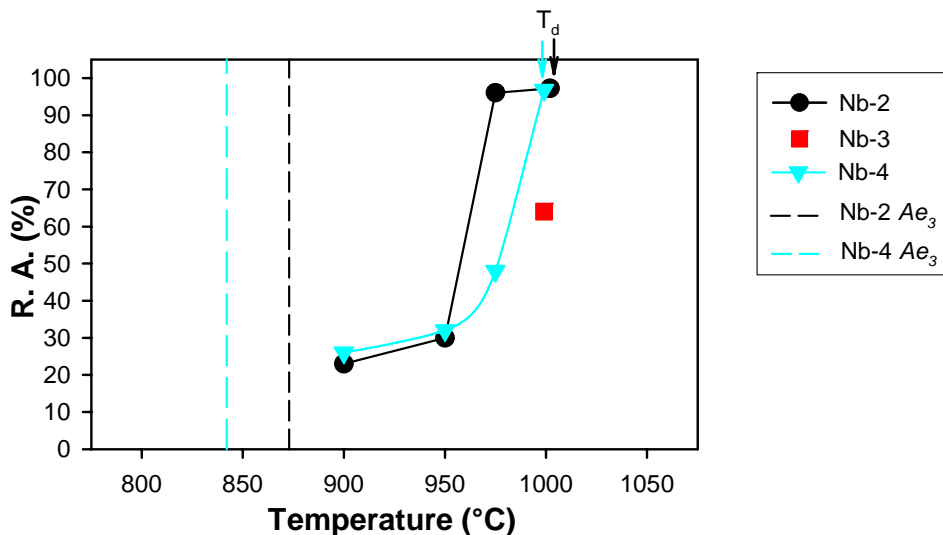


Figure 6.15: Reduction in area for steels *Nb-2*, *Nb-3* and *Nb-4* as a function of testing temperature. All tests were conducted according to Schedule C conditions (10^{-3} s^{-1} , $1.2 \text{ }^\circ\text{C}\cdot\text{s}^{-1}$).

6.5.3 Total elongation

Nb-2: The total elongation increased slightly from ~32% (900 °C) to ~38% (950 °C), then to ~60% (975 °C) as shown in **Figure 6.16**. There was a slight increase in elongation of ~ 3% from 975 to 1000 °C.

Nb-3: At 1000 °C, the total elongation was ~45%, which is much lower than the values for *Nb-2* and *Nb-4*.

Nb-4: The elongation followed the same trend as the reduction in area. The values were the same as for *Nb-2* at 900 and 950 °C, ~2% lower at 975 °C and increased to ~98% at 1000 °C.

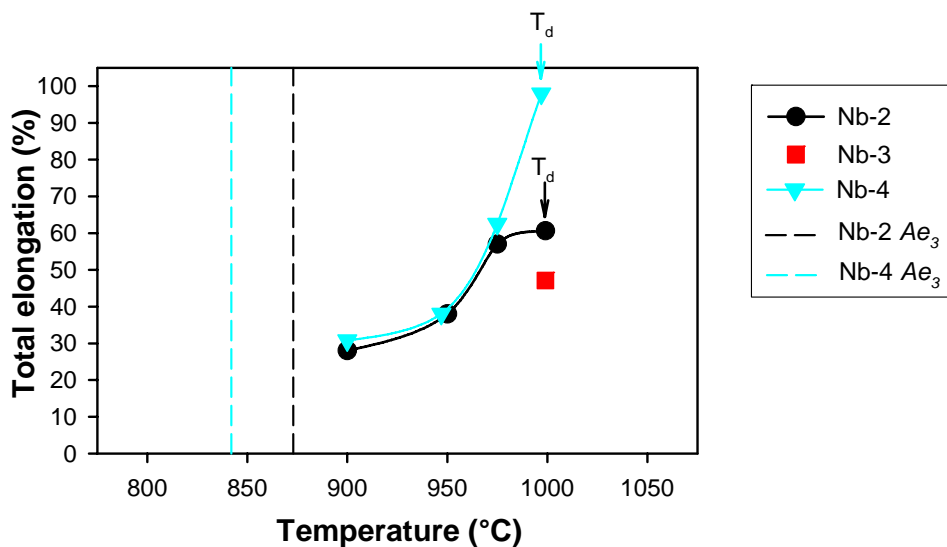


Figure 6.16: Elongation for steels *Nb-2*, *Nb-3* and *Nb-4* as a function of testing temperature. All tests were conducted according to Schedule C conditions (10^{-3} s^{-1} , $1.2 \text{ }^\circ\text{C}\cdot\text{s}^{-1}$).

6.5.4 Scanning electron microscopy

Nb-2: At 900 °C (**Figure 6.17 a**), microvoids joined by internal cracks were seen with precipitates such as Fe-Mn-S.

At 950 °C (**Figure 6.17 b**), a few networks of precipitates joined by microvoid coalescence were observed. The precipitates were mostly too fine to be analyzed accurately, but one precipitate was identified as MnS.

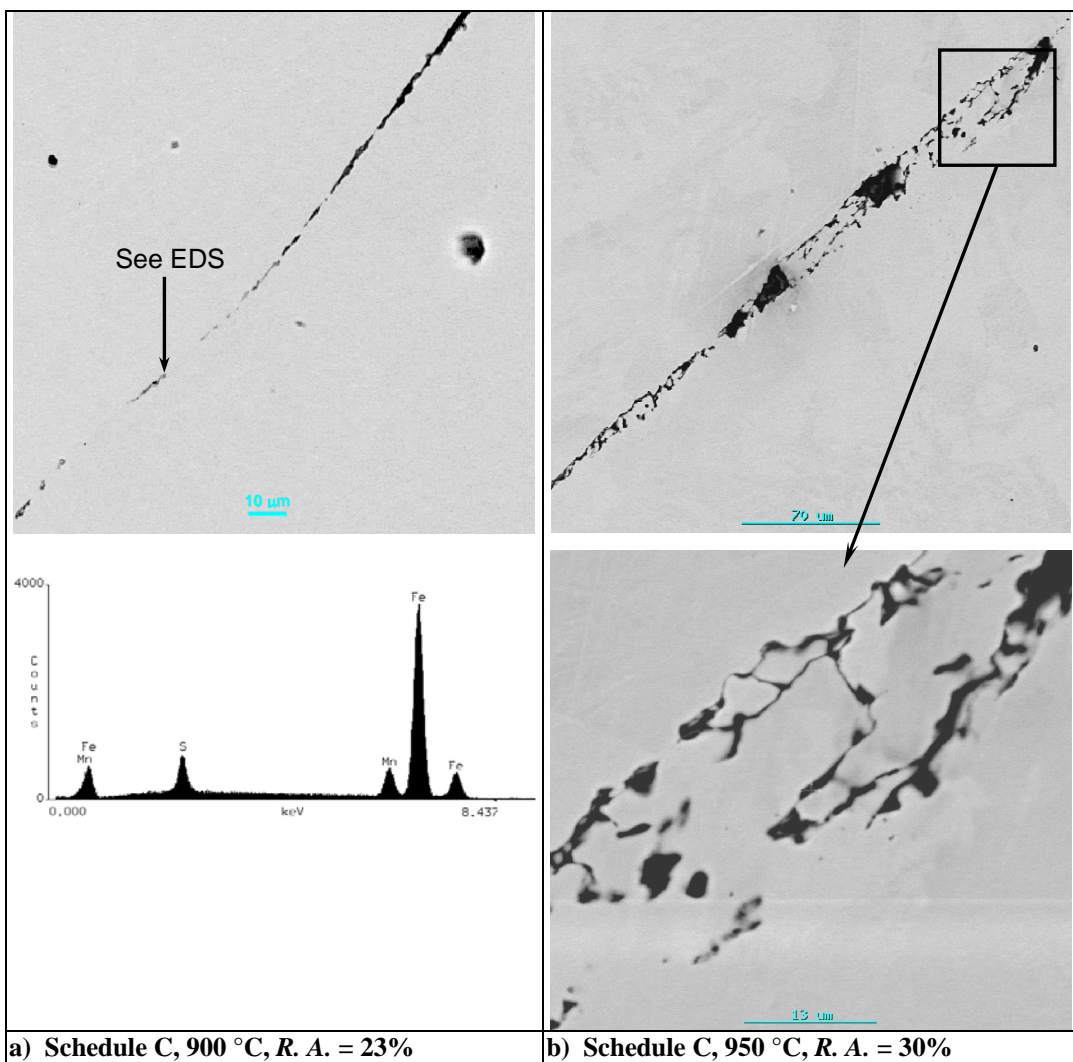


Figure 6.17: SEM backscatter images of steel *Nb-2* tested under schedule C conditions ($1.2\text{ }^{\circ}\text{C}\cdot\text{s}^{-1}$, 10^{-3} s^{-1}), showing microvoid coalescence with single line cracking (a) and network cracking (b).

Nb-3: **Figure 6.18 a** (at 1000 °C), shows a few microvoids connected by short cracks along prior austenite grain boundaries. No extensive cracking was observed. One precipitate was analyzed as Fe-Mn-S-Al-O-Cl-Nb-C, indicating the presence of NbC. The chlorine is thought to be tap water contamination in the void from the polishing process.

Nb-4: At 950 °C (**Figure 6.18 b**), two parallel lines of microvoids can be seen, extending along a prior austenite grain boundary. The distance between the two lines of precipitates is ~5 - 20 μm. Two precipitates were analyzed as Al-O, presumed to be Al₂O₃ inclusions from the deoxidation process during steelmaking.

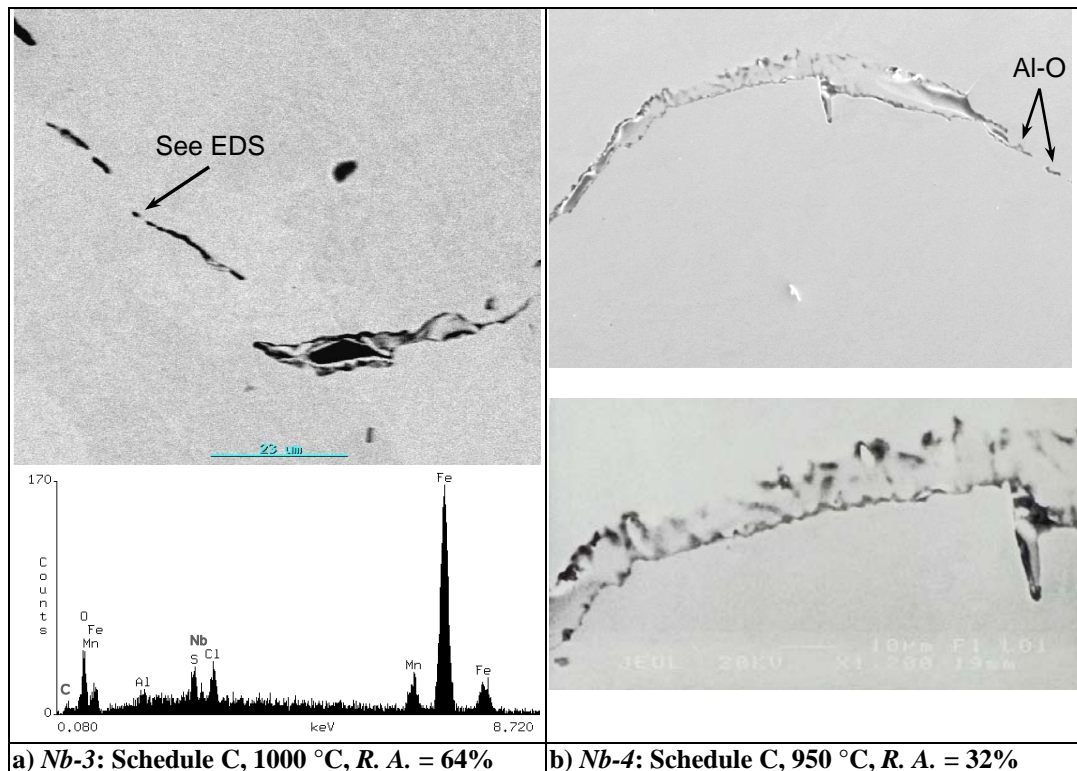


Figure 6.18: SEM backscatter images of steels *Nb-3* and *Nb-4* tested under schedule C conditions ($1.2\text{ }^{\circ}\text{C}\cdot\text{s}^{-1}$, 10^{-3} s^{-1}).

6.6 NIOBIUM STEEL *Nb-5*

The strength and total elongation results for the tests performed at 850 °C under schedule G conditions ($3.0\text{ }^{\circ}\text{C}\cdot\text{s}^{-1}$, 10^{-3} s^{-1}), and at 950 °C under schedule C conditions ($1.2\text{ }^{\circ}\text{C}\cdot\text{s}^{-1}$, 10^{-3} s^{-1}), were measured manually on the data acquisition unit printed graph, as the ASCII files saved on the computer were corrupt. These results were calculated by using measured and ASCII results obtained at 900 °C (schedule G) and 900 °C (schedule C) respectively as benchmarking values. The elongation for the test performed at 1050 °C under schedule D conditions ($1.2\text{ }^{\circ}\text{C}\cdot\text{s}^{-1}$, 10^{-4} s^{-1}) was measured directly from the broken tensile specimen, as the thermocouple-specimen contact was broken before the end of the test. The result was then calculated by using measured and ASCII results obtained at 1000 °C as a benchmarking value. The modelled TCF_{e3} transformation temperature of 821 °C from **Table 6.2** is shown on the graphs.

6.6.1 Maximum strength

Figure 6.19 shows the strength–elongation curves. The arrows show the onset of dynamic recrystallisation. Tests “H”1000 and “F”1000 show small oscillations in the curves as a result of minor fluctuations in temperature during the test caused by thermocouple control problems.

The maximum strength decreased with increase in testing temperature from 71 MPa at 800 °C for schedule H and from 77 MPa at 850 °C for schedule G. This trend was also seen in schedule C, D and F tests from 900 °C to 1050 °C, shown in **Figure 6.20**. Testing at the high strain rate (10^{-3} s^{-1}) resulted in higher maximum strength values than at the low strain rate (10^{-4} s^{-1}). The highest relative maximum strength values were found for schedule G ($3.0\text{ }^{\circ}\text{C}\cdot\text{s}^{-1}$, 10^{-3} s^{-1}) and the lowest maximum strengths were recorded for schedule H ($3.0\text{ }^{\circ}\text{C}\cdot\text{s}^{-1}$, 10^{-4} s^{-1}).

The effect of cooling rate is not clear: for a high strain rate the maximum strength was increased by an increase in the cooling rate from $1.2 - 3.0\text{ }^{\circ}\text{C}\cdot\text{s}^{-1}$, whereas for a low strain rate the maximum strength increased with a change in cooling rate from $3.0 \rightarrow 0.3 \rightarrow 1.2\text{ }^{\circ}\text{C}\cdot\text{s}^{-1}$. However, as these results were based on single tests for each condition, it is evident that even small differences in the maximum strength values may change the perceived effect of cooling rate on the maximum strength.

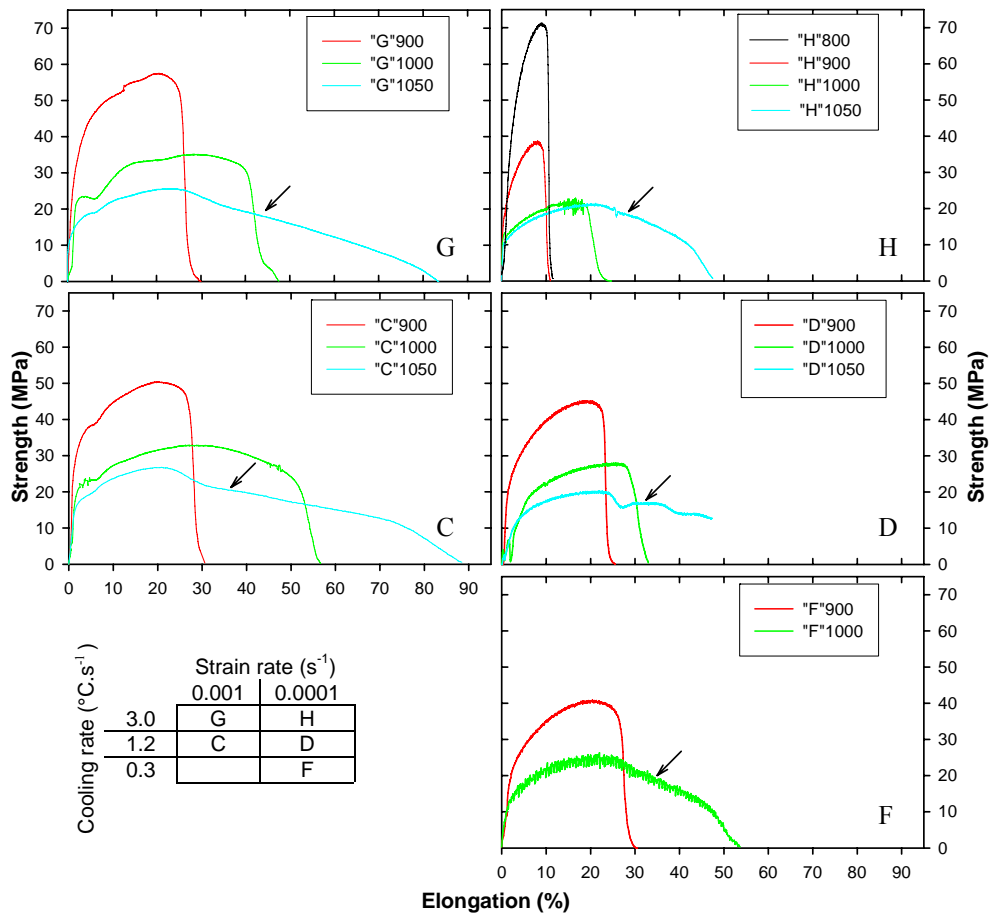


Figure 6.19: Engineering stress as a function of elongation for steel *Nb-5*. The key to the testing schedules is shown above. Arrows indicate the onset of dynamic recrystallisation

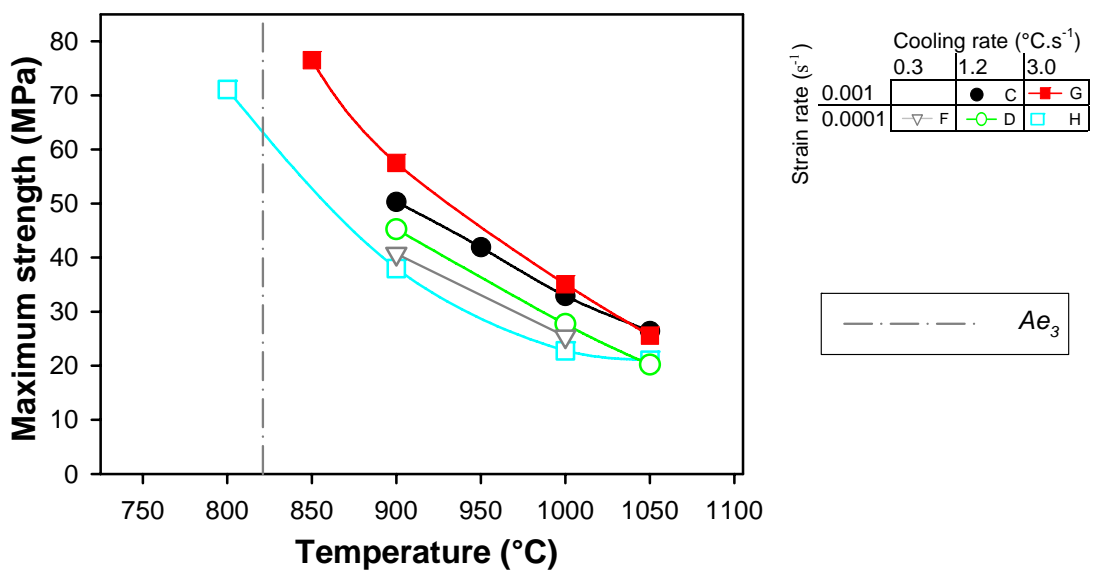


Figure 6.20: Maximum strength for steel *Nb-5* as a function of testing temperature, strain rate and cooling rate.

6.6.2 Reduction in area

The reduction in area curves (**Figure 6.21**) showed similar behaviour for all testing conditions: low ductility at 800 °C, increasing gradually up to 1000°C and a sharper increase in ductility from 1000 – 1050 °C. At 1000 °C, the only ductility above 50% R. A. occurred at conditions of low cooling rate and low strain rate ($0.3\text{ }^{\circ}\text{C}\cdot\text{s}^{-1}$, 10^{-4} s^{-1}) and the lowest R. A. of 16% occurred at high cooling rate and low strain rate ($3.0\text{ }^{\circ}\text{C}\cdot\text{s}^{-1}$, 10^{-4} s^{-1}). At 1050 °C, the ductility recovered to higher than 90% for all testing conditions except schedule H ($3.0\text{ }^{\circ}\text{C}\cdot\text{s}^{-1}$, 10^{-4} s^{-1}), which had a R. A. of 65%.

For both strain rates, an increase in cooling rate increased the 50% ductility recovery temperature.

At cooling rates of 1.2 and $3.0\text{ }^{\circ}\text{C}\cdot\text{s}^{-1}$, a decrease in strain rate increased the 50% ductility recovery temperature and decreased the minimum R. A. values (at $\sim 900\text{ }^{\circ}\text{C}$) by 5 – 10% respectively.

The 50% ductility recovery on the low temperature side of the ductility trough occurred below the tested range *i.e.* below $850\text{ }^{\circ}\text{C}$ (below $800\text{ }^{\circ}\text{C}$ for schedule H).

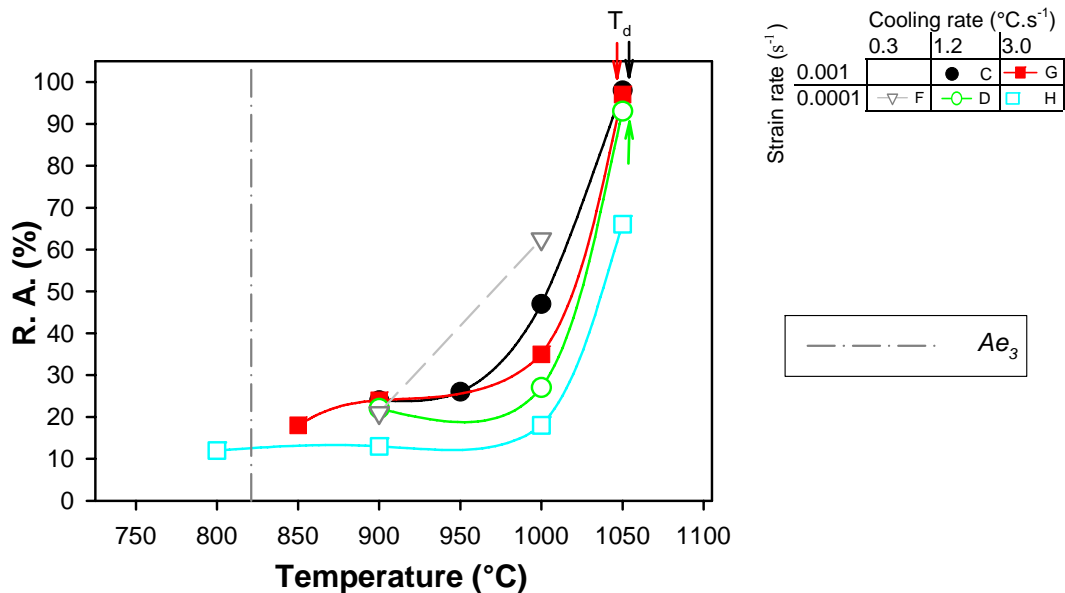


Figure 6.21: Reduction in area for steel Nb-5 as a function of testing temperature, strain rate and cooling rate.

6.6.3 Total elongation

The total elongation followed similar behaviour to the reduction in area (**Figure 6.22**). In the tested range, the total elongation increased with increase in testing temperature from 900 °C (850 °C for schedule G) to 1050 °C.

Both a decrease in strain rate and an increase in cooling rate shifted the elongation recovery to higher temperatures and decreased the elongation values at 900 °C. The highest elongation values at each testing temperature were reported for high strain rate (and 1.2 °C.s⁻¹ conditions at 1000 and 1050 °C) and the lowest elongation values were found under low strain rate and high cooling rate conditions (schedule H: 3.0 °C.s⁻¹, 10⁻⁴ s⁻¹).

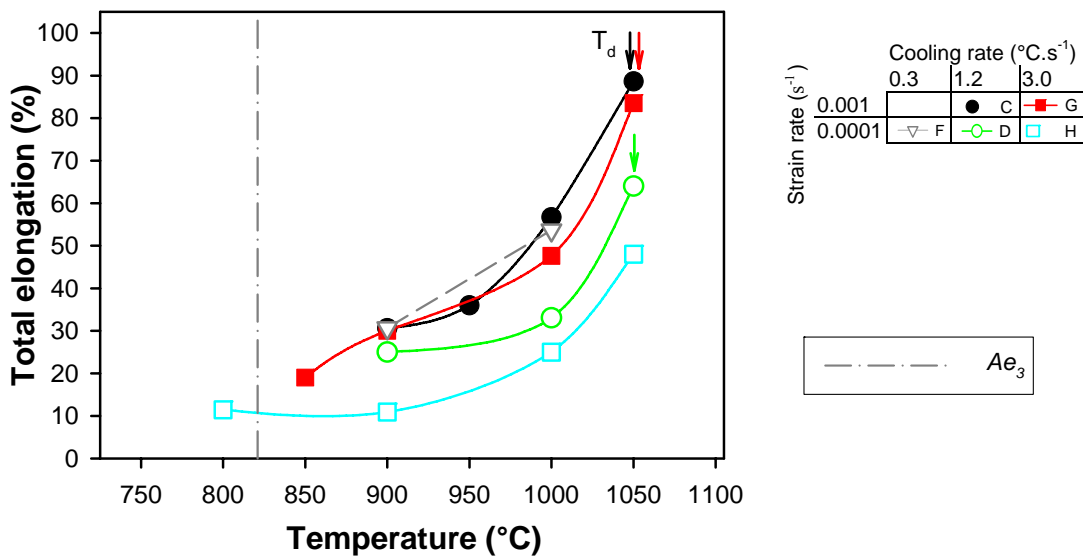


Figure 6.22: Elongation for steel *Nb-5* as a function of testing temperature, strain rate and cooling rate.

6.6.4 Scanning electron microscopy

In all *Nb-5* specimens, Nb(C,N) eutectic structures ranging in size from 10 - 250 μm in size were observed in several places in the matrix, mostly not associated with internal cracking (**Figure 6.23 a** and **c**). Although this is not thought to be directly related to fine precipitation or internal cracking, it is noted that voids and a large crack were found near one such eutectic structure (**Figure 6.23 c**). This eutectic structure and the associated porosity would be associated with the last fraction of solidification and is dependent on the complexity of the solidification process.

At high strain rate (10^{-3} s^{-1}):

Cooling rate 1.2 °C.s⁻¹: At 900 °C (**Figure 6.23 a**), MnS-containing microvoids extensively interconnected by cracks were observed.

Cooling rate 3.0 °C.s⁻¹: At 1000 °C (**Figure 6.23 b**), the microstructure was characterized by intergranular cracking of microvoids. Precipitates were analyzed as MnS, Mn-Al-O and Mn-Si-O.

At low strain rate (10^{-4} s^{-1}):

Cooling rate 0.3 °C.s⁻¹: At 900 °C, **Figure 6.24 a** shows wedge cracking, which is indicative of grain boundary sliding. **Figure 6.24 b** shows parallel cracks along a prior austenite grain boundary, caused by microvoid coalescence and indicating a softer precipitate free zone (PFZ). The analysis of Mn-Fe-Si-O-Nb-C indicates the presence of NbC.

At 1000 °C (**Figure 6.24 c**), complex coarse precipitates such as MnFe(AlSi)ONbC were analyzed, with little interconnection of microvoids.

Cooling rate 1.2 °C.s⁻¹: At 900 °C (**Figure 6.23 c**), extensive cracking between microvoids on prior austenite grain boundaries was observed, containing precipitates such as Al-Mn-S-O.

Cooling rate 3.0 °C.s⁻¹: At 1000 °C (**Figure 6.23 d**), low ductility was characterized by cracking between microvoids. Precipitates were analyzed as Mn-O, MnS and Al-Mn-Fe-S-O.

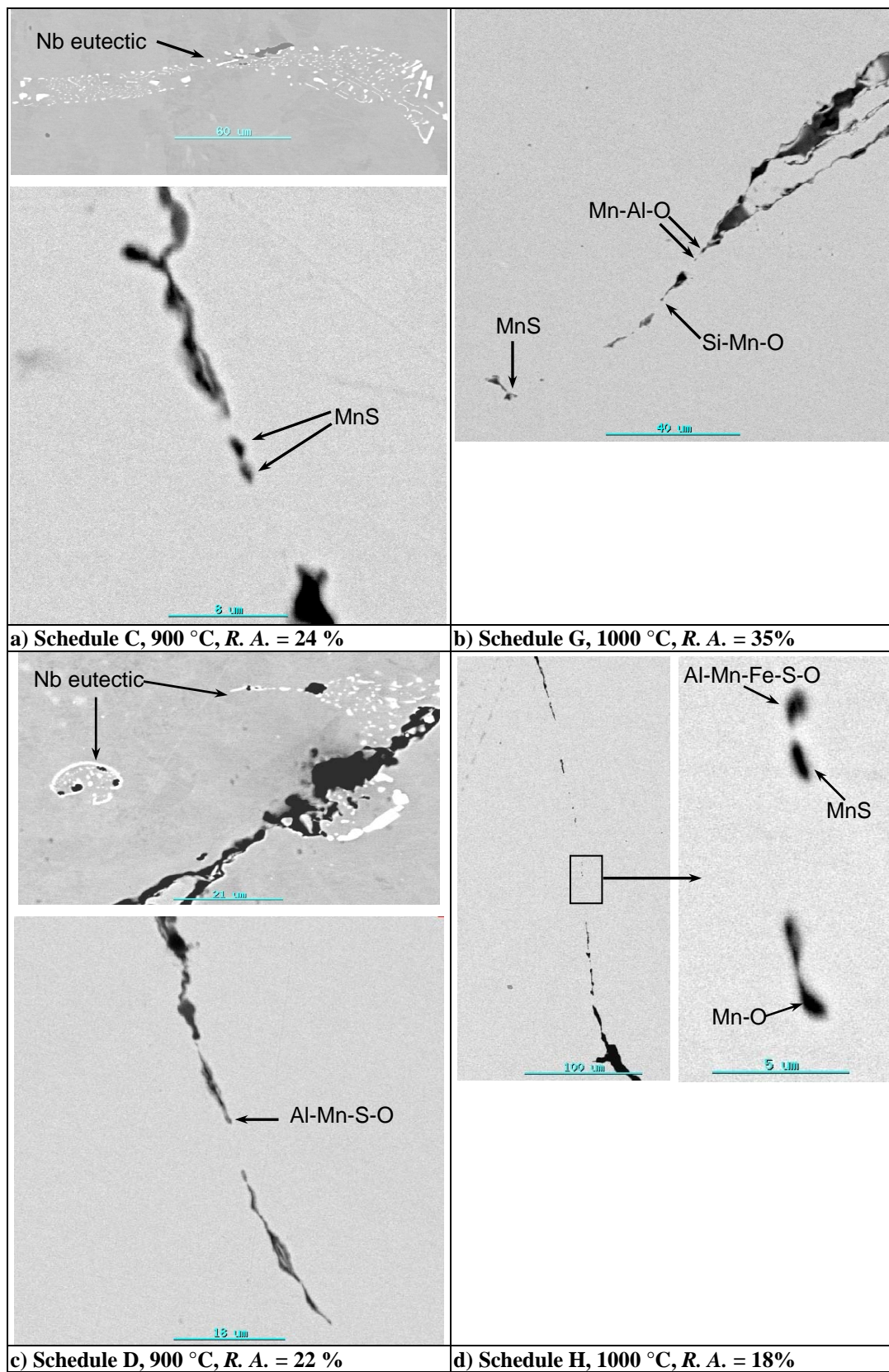


Figure 6.23: SEM backscatter images of steel Nb-5 tested under schedule C, G, D and H conditions, showing precipitates, microvoid coalescence, Nb(C,N) eutectic phase and extensive cracking.

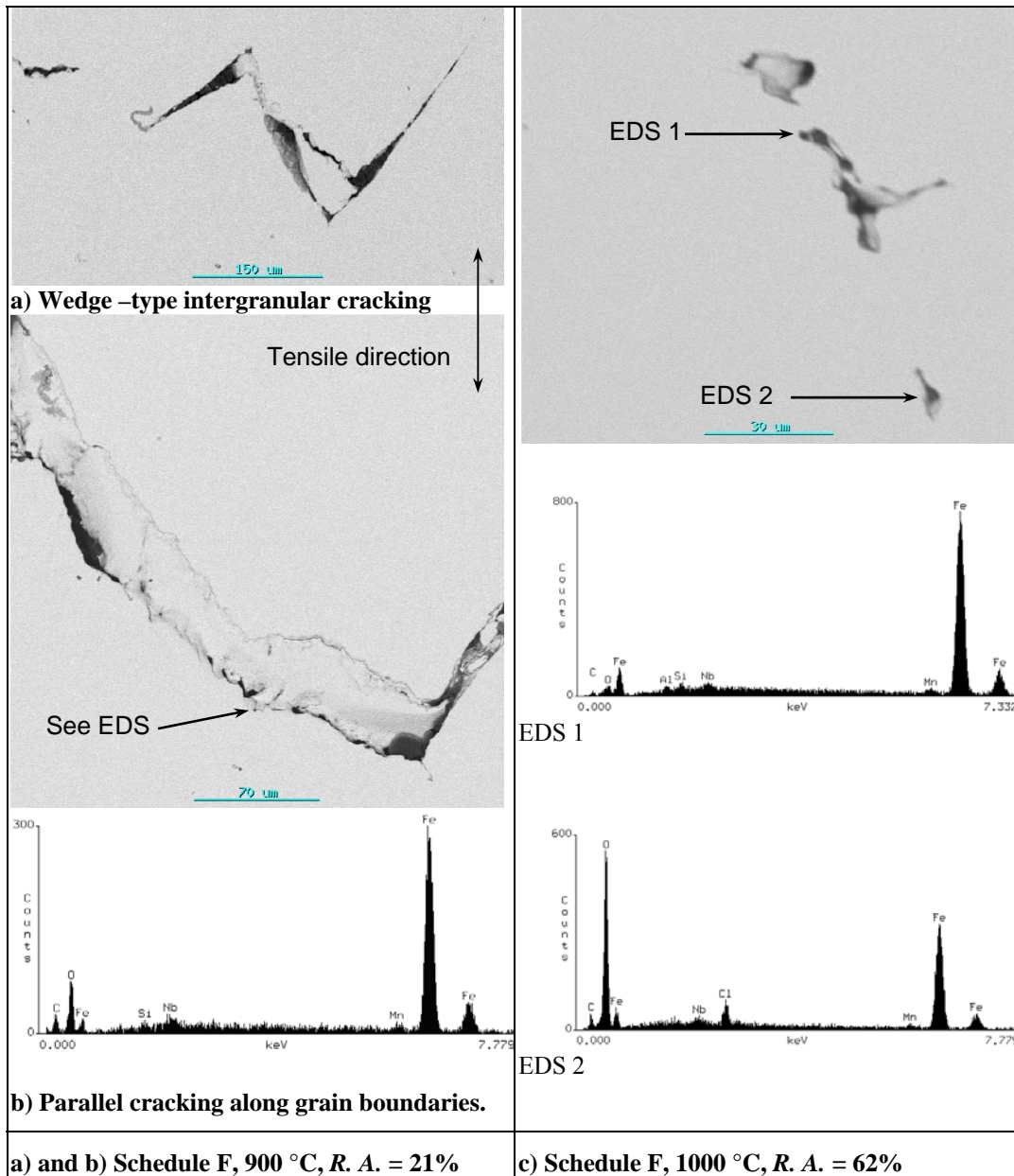


Figure 6.24: SEM backscatter images of steel Nb-5 tested under schedule F conditions, showing three types of intergranular cracking: a) wedge cracking b) parallel cracking along prior austenite grain boundaries and c) limited microvoid coalescence.

6.7 SUMMARY OF HOT DUCTILITY RESULTS FOR THE NIOBIUM STEELS

The hot ductility results are summarised in **Table 6.6** and **Table 6.7**, listing 50% low- and high- temperature ductility recovery temperatures (Low T and high T respectively), the minimum ductility temperature (Min. *R. A.*) and the onset temperature of dynamic recrystallization, T_d (both with associated % *R. A.*). The results are ordered according to the steel, strain rates, cooling rates and Schedule (A, B, C, D, F, G and H).

Steel *Nb-1* was tested under schedule A, B and C conditions to assess the influence of solution treatment time and thermal oscillation. Steels *Nb-2*, *Nb-3* and *Nb-4* were tested under schedule C conditions only, since there were few specimens available for testing. Thus, the influence of strain rate and cooling rate on hot tensile behaviour could only be evaluated in steel *Nb-5*, which was tested under all five schedules C, D, F, G, and H.

Table 6.6: Summary of the hot ductility results for niobium steel *Nb-1*. (Strain rate = 10^{-3} s^{-1} , cooling rate = $1.2 \text{ }^\circ\text{C}\cdot\text{s}^{-1}$).

Steel		Low T ($^\circ\text{C}$)	Min. $^\circ\text{C}$ (<i>R.A.</i> %)	High T ($^\circ\text{C}$)	T_d $^\circ\text{C}$ (%)
Nb-1	A	860	900 (32)	930	1000 (97)
	B	850	900 (28)	930	>950 (>96)
	C			900	>950 (>69)

Table 6.7: Summary of the hot ductility results for niobium steels *Nb-2* to *Nb-5*.

Steel	Cooling Rate (°Cs ⁻¹)	Strain rate (s ⁻¹)					
		10 ⁻³			10 ⁻⁴		
			High T (°C)	T _d °C (%)		High T (°C)	T _d °C (%)
Nb-2	1.2	C	960	1000 (97)			
Nb-3	1.2	C	985	>1000 (>64)			
Nb-4	1.2	C	975	1000 (97)			
Nb-5	3.0	G	1020	1050 (97)	H	1040	>1050 >(66)
	1.2	C	1005	1050 (98)	D	1025	1050 (93)
	0.3				F	950	>1000 >(62)

6.8 EFFECT OF SOLUTION TREATMENT TIME ON HOT TENSILE BEHAVIOUR IN NIOBIUM STEEL *Nb-1*

Increasing the solution treatment time at 1300 °C from 1 to 5 minutes (schedules A and C respectively), while maintaining constant cooling rate and strain rate conditions (1.2 °C.s⁻¹ and 10⁻³ s⁻¹) had the following effects, as shown in **Section 6.4**:

- A slight decrease in maximum strength at 900 °C (which is thought to be insignificant – within 2% experimental error) and at 950 °C.
- An increase in the reduction in area at 900 °C, which could indicate a lower temperature than 900 °C for the minimum of the ductility trough, or an increased minimum reduction in area value.
- The reduction in area value at 950 °C was decreased, which indicates that the ductility trough extends to higher temperatures with an increase in solution

treatment time from 1-5 minutes. Similarly, the elongation value was higher at 900 °C and lower at 950 °C. These results are expected, as an increase in austenite grain size occurs with increase in the reheat time (Yue *et al.*, 1995), leading to an increased number of precipitates per unit area of grain boundary, which has a detrimental effect on hot ductility (Fu *et al.*, 1988).

6.9 EFFECT OF THERMAL OSCILLATION ON HOT TENSILE BEHAVIOUR IN NIOBIUM STEEL *Nb-1*

The change in cooling pattern from a constant 1.2 °C.s⁻¹ (Schedule A) to a series of temperature oscillations (1300-1000-1200 °C: schedule B, as defined in **Table 3.4**) had negligible effects on the maximum strength, reduction in area and total elongation in steel *Nb-1* in the region 800 – 950 °C, as shown in **Section 6.4**.

These results seem to be in conflict with Mintz *et al.* (1987), who showed that oscillated cooling with amplitudes is detrimental to hot ductility in a Nb steel (0.12% C, 1.44% Mn, 0.29%Si, 0.015% Al, 0.035% Nb and 0.010% N). They found that increasing the oscillation amplitude increased the width and depth of the hot ductility trough. However, the negligible effects of temperature oscillation seen in this investigation are due to:

- Temperature oscillations used in this work are at higher temperatures than those used by Mintz (1987).
- Temperatures during oscillated cooling only dropped below the final testing temperature at 1050 °C (Cardoso and Yue, 1989).
- The temperature did not fall below the $\gamma \rightarrow \alpha$ transformation temperature during cooling. Temperature oscillations into the ferrite phase promote fine AlN precipitation, which is detrimental to hot ductility (El-Wazri, 1998b).

6.10 EFFECT OF STRAIN RATE ON HOT TENSILE BEHAVIOUR IN NIOBIUM STEEL *Nb-5*

Decreasing the strain rate from 10^{-3} to 10^{-4} s^{-1} had the following effects, as discussed in **Section 6.4**, which were more pronounced at a high cooling rate of 3.0 $^{\circ}C.s^{-1}$:

- The magnitude of the maximum strength decreased, as there is more time for grain boundary sliding and for the austenite to recover (Mintz and Jonas, 1994).
- The minimum ductility (reduction in area and total elongation) decreased and the high temperature ductility and elongation recovery temperatures moved to higher temperatures. Enhanced Nb(C,N) precipitation (Mintz *et al.*, 1991), increase in grain boundary sliding and increased formation and growth of voids (Mintz *et al.*, 1990) are the possible causes of the decreased ductility with decrease in strain rate (**Section 2.4.2**).

6.11 EFFECT OF COOLING RATE ON HOT TENSILE BEHAVIOUR IN NIOBIUM STEEL *Nb-5*

Decreasing the cooling rate from $3.0 - 1.2$ $^{\circ}C.s^{-1}$ at a high strain rate and from $3.0 - 0.3$ $^{\circ}C.s^{-1}$ at a low strain rate showed the following effects:

- There were contradictory effects on the maximum strength from $900 - 1000^{\circ}C$. At high strain rate, there was a slight decrease in maximum strength. At low strain rate, a slight decrease in the maximum strength value was observed with decrease in cooling rate from $1.2 - 0.3$ $^{\circ}C.s^{-1}$, and an increase occurred with decrease in cooling rate from $3.0 - 1.2$ $^{\circ}C.s^{-1}$.
- At a high strain rate, there was little effect on the reduction in area, as only a 10% increase at 1000 $^{\circ}C$ was observed. However, at a low strain rate, the increase in reduction in area was more pronounced ($18 \rightarrow 27 \rightarrow 63\%$).
- The elongation was increased at all temperatures and for both strain rates.

The improvement in hot ductility with decrease in cooling rate has been found to be as a result of favoured static precipitation (Abushosha *et al.*, 1998b). This removes Nb, N and C from solution before the finer Nb(C,N) can form dynamically on dislocations during straining (Mintz *et al.*, 1991). Static precipitation favours the formation of coarser Nb-C type precipitates (Maehara *et al.*, 1987), whereas fine Nb(C,N) or NbN usually form during straining. This was confirmed in Nb-5 by the presence of coarse precipitates containing Nb and C, but no N. At the high cooling rate of $3.0\text{ }^{\circ}\text{C}\cdot\text{s}^{-1}$, no coarse Nb-containing precipitates were observed; hence, Nb is probably present as precipitates too fine to be analyzed on the SEM.

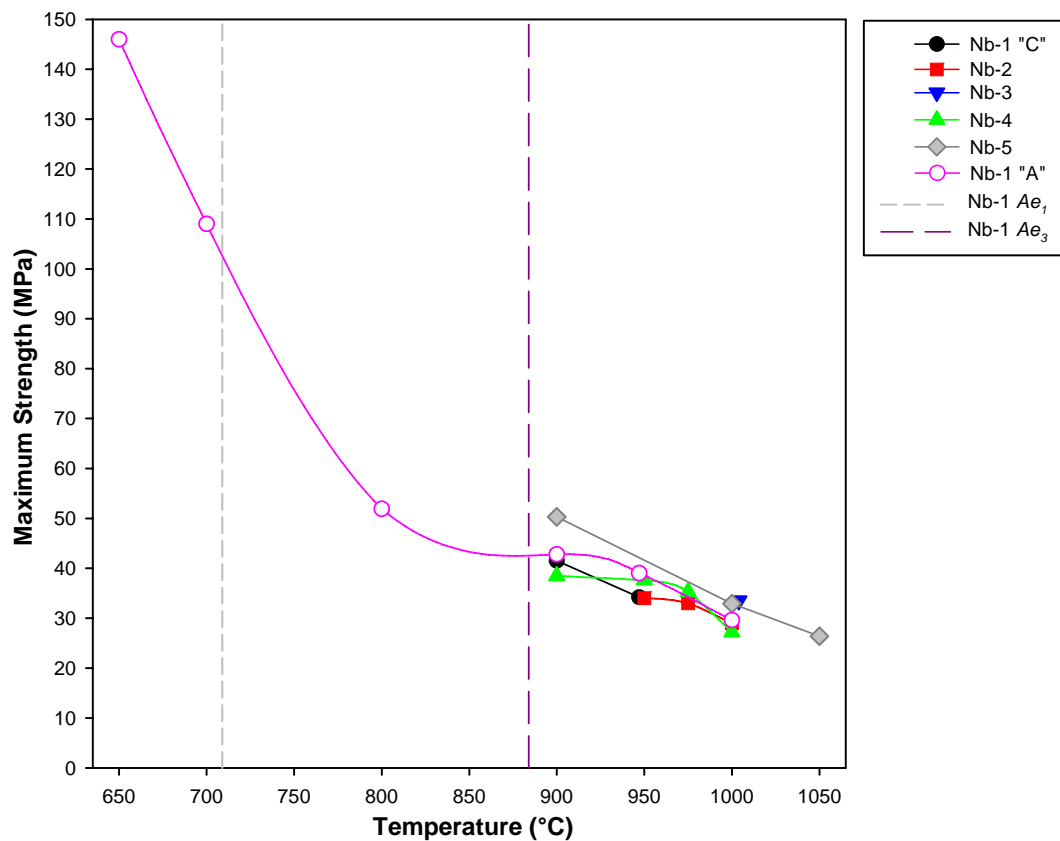
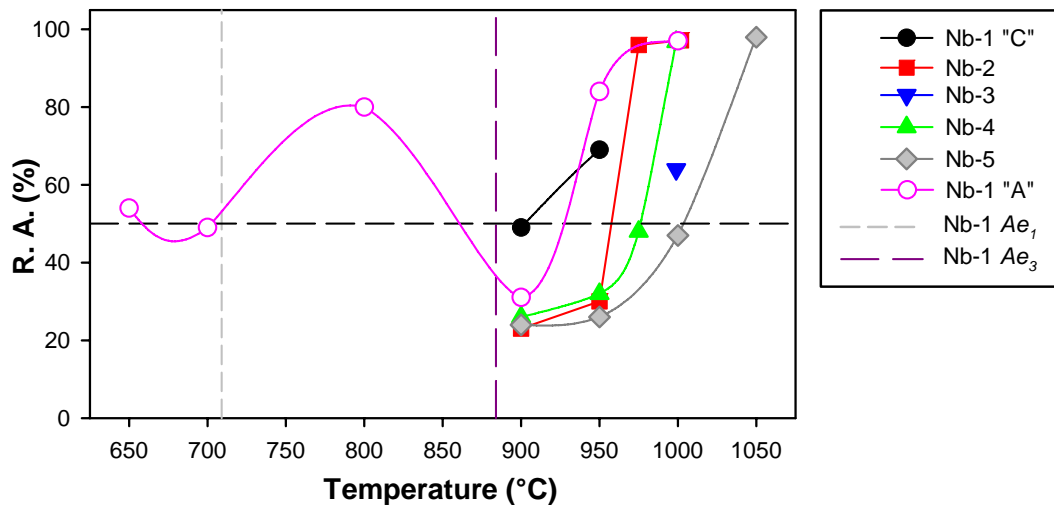
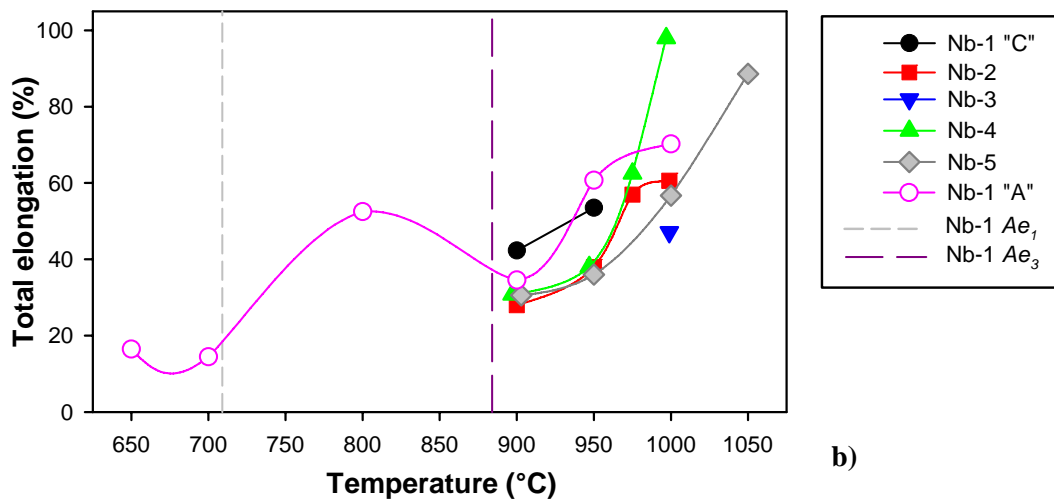


Figure 6.25: Effect of composition on maximum strength in niobium steels Nb-1 to Nb-5. The Ae_3 and Ae_1 temperatures for Nb-1 are shown.



a)



b)

Figure 6.26: Effect of composition on: a) Reduction in area and b) Total elongation in niobium steels *Nb-1* to *Nb-5*. The Ae_3 and Ae_1 temperatures for Nb-1 are shown on the graphs.

6.12 PRECIPITATION IN THE NIOBIUM STEELS

The species of precipitates found in the five niobium steels are discussed below.

Nb-1:

A variety of precipitates ranging from 0.5 – 5 μm diameter were found at cracks along prior austenite grain boundaries: MnS and Fe-S-O (+ Mn), and a various combinations of Al oxide as Al-Ca-O (or oxy-sulphides) and Al-Si-O (+Fe or Mn).

Nb-2:

Small MnS (+Fe), Al-oxide and Ca-oxide precipitates were identified. The alumina and Ca-O precipitates are inclusions remaining from the steelmaking process. Microvoids linked by crack networks were seen, but no precipitate analysis was achieved, as the precipitates were too small.

Nb-3:

This steel contained Ca-oxide (an indication of calcium-modification), Al-O (alumina from steelmaking), Fe-Mn-O and Fe-Mn-Al-S-O precipitates.

Nb-4:

Al oxide, Ca oxide and MnS precipitates were analyzed. Microvoids linked by crack networks were seen along prior austenite grain boundaries, but no precipitate analysis was achieved, due to the small precipitate sizes.

Nb-5:

This is the only niobium steel that had no Ca-containing precipitates, as this steel was not calcium-modified. All identified precipitates contained Mn, such as MnS and Mn-O (with combinations of Al, Si and S). At low strain rate and low cooling rate, larger Nb-containing precipitates were found, such as Mn-Fe-Nb-O-C. In all *Nb-5* specimens, large Nb(C,N) eutectic structures were observed in several places. This indicates an eutectic phase transformation during solidification of the slab from which the tensile samples were machined. Large eutectic Nb(C,N) precipitates form in steels with $>0.07\%$ C (Park *et al.*, 2000). Niobium partitions to the interdendritic liquid phase during solidification. The amount of eutectic increases with increasing Nb in the steel, but also with increasing carbon or slower cooling. Eutectics effectively remove Nb from solution and thus prevent Nb from being able to participate in precipitation strengthening of the matrix.

Table 6.8: Summary of the precipitate species found in the niobium steels (Note: All Nb steels have high temperature ductility recovery above Ae_3 , and have high Mn:S ratios).

Steel	Testing conditions	Calcium-modified?	Precipitate species
Nb-1	A, B, C	Yes	FeAlOCaNbC, MnSNbCN, MnSiAlFeO, AlMgO, Fe(Mn)SO, SiO, AlMgCaSO
Nb-2	C	Yes	MnS, MgO, CaO, Al ₂ O ₃
Nb-3	C	Yes	MnSAlFeONbC, MnS, MgS, CaO, Al ₂ O ₃ , MnSMgAlFeO
Nb-4	C	Yes	MnS, CaO, Al ₂ O ₃ ,
Nb-5	C, G, H, D, F	No	MnS(FeAlSi)ONbC, MnO, Mn(Fe)S, MnFeAlNbN, MnFeONbC Nb(C,N) eutectic

6.13 EFFECT OF COMPOSITION ON HOT TENSILE BEHAVIOUR IN THE NIOBIUM STEELS

The five niobium steels are arranged in order of increasing carbon, manganese and niobium contents from *Nb-1* to *Nb-5*, as shown in **Table 6.1**.

6.13.1 Maximum strength

From **Figure 6.25**, it can be seen that the maximum strength values were similar for steels *Nb-1*, *Nb-2* and *Nb-4* between 900 – 1000 °C. The highest S_u values at each testing temperature are shown for steel *Nb-5* (steel *Nb-3* at 1000 °C). Testing was performed near the calculated Ae_3 temperature only for steel *Nb-1* (only under schedule A conditions, as shown in **Figure 6.0**), which showed a slight levelling off in maximum strength around the Ae_3 (900 - 800 °C), followed by a sharp increase in maximum strength with further temperature decrease to 650 °C.

6.13.2 Reduction in area

Figure 6.26 a shows that from 900 – 950 °C, *Nb-1* exhibited the highest ductility, and *Nb-2*, *Nb-4* and *Nb-5* showed no marked differences in ductility. The ductility trough begins well above the calculated Ae_3 temperatures for all five niobium steels. The 50% high temperature ductility recovery temperatures increased in the order: *Nb-1*, *Nb-2*, *Nb-4*, *Nb-3* to *Nb-5*. At 1000 °C, *Nb-2* and *Nb-4* had reached maximum ductility (> 90% R.A.), *Nb-3* showed ~60% ductility and the reduction in area of *Nb-5* was less than 50% R. A.

The low temperature ductility recovery was only established for *Nb-1* in this work (schedule A -**Figure 6.10**), occurring between 900 – 800 °C which is consistent with literature. Typical low temperature recovery in Nb steels has been found to occur in the temperature range 750 – 850 °C *i.e.* between the Ae_3 and Ae_1 temperatures (Yue *et al.*, 1995). Below the Ae_1 temperature, the ductility dropped to ~50%.

C content

In C-Mn-Nb-Al steels with $\leq 0.03\%$ Nb, carbon has little influence on the position of the hot ductility trough, except at $\leq 0.05\%$ C, when both the width and depth of the trough are reduced *i.e.* an improvement in ductility (Mintz *et al.*, 1989b). For a steel with 0.03% Nb and $\geq 0.05\%$ C, there is little further increase in the volume fraction precipitated, and the hot ductility will be insensitive to carbon level. This explains the improved hot ductility of *Nb-1* when compared to the other Nb steels.

N content

The amount of Nb carbonitride precipitated at a given temperature depends on the amount of N, but to a lesser extent than C (Mintz *et al.*, 1989b). Thus, it is feasible that the high nitrogen contents of *Nb-3* (0.0106% N) and *Nb-5* (0.0093% N) could have contributed to the higher ductility recovery temperatures in these two steels, by increasing the amount of precipitated Nb(C,N).

Ca additions

Nb-5 shows the worst high temperature ductility recovery and is the only Nb steel not treated with calcium-additions, thus there are no large Ca-containing precipitates.

Ductility loss resulting from precipitation of carbides or nitrides can be reduced significantly by a decrease in soluble sulphur content (Maehara *et al.*, 1990). From the trends shown in the current investigation, it is clear that this effect is achieved by calcium addition, which effectively removes sulphur from solution by binding free S in CaS particles (Mintz *et al.*, 1989a).

6.13.3 Total elongation

The lowest elongation recovery temperature was shown by *Nb-1*, then by *Nb-2* and *Nb-4*, followed by *Nb-5* and *Nb-3* (as shown by **Figure 6.26 b**). Between 900 and 950 °C, *Nb-1* exhibited the highest elongation value by ~10%, while steels *Nb-2*, *Nb-4* and *Nb-5* showed similar elongation values. At 1000 °C, the steels showed increasing elongation in the order: *Nb-3*, *Nb-5*, *Nb-2*, to *Nb-4*. Elongation recovery occurred above calculated Ae_3 temperatures for the niobium steels in this work.

6.14 MECHANISMS OF HOT TENSILE BEHAVIOUR IN THE NIOBIUM STEELS

All five niobium steels showed poor ductility well above the Ae_3 temperature, indicating that austenite to ferrite transformation was not responsible for the high temperature ductility drop in these steels. In austenite, grain boundary precipitation can occur during deformation in solution-treated Nb steels. This is frequently accompanied by the formation of precipitate free zones (PFZs) around the grain boundaries. These PFZs are weak, as there is negligible precipitation strengthening effect in this region from fine Nb(C,N) compared to the rest of the matrix. Strain thus concentrates in the PFZ regions. Microvoid coalescence occurs along the grain boundary precipitates such as oxides, sulphides and oxy-sulphides (Maehara *et al.*, 1990), as seen in the niobium steels investigated in this work.

The presence of precipitates such as oxides and sulphides and the absence of Nb(C,N) precipitates in most of the analyses done on the SEM indicates that Nb(C,N) precipitation is too fine to be detected by EDS, which is confirmed by literature (Mintz *et al.*, 1991;

Mintz, 1999). In Nb-microalloyed steels that have been solution treated before cooling to the test temperature, very fine Nb(C,N) precipitates form during deformation in austenite. Grain boundary precipitation occurs, with PFZs of ~500 nm on either side of the grain boundary (Mintz *et al.* 1986). This type of precipitation is occurs with grain boundary sliding and the associated wedge-type cracking seen in some of the low ductility samples in this work.

6.15 APPLICATION AND RELEVANCE TO INDUSTRY

All five niobium steels were tested under conditions simulating thin slab casting with a medium secondary cooling pattern (schedule C). *Nb-5* was additionally tested under thin slab [hard cooling], billet [hard cooling] and thick slab [medium and soft cooling] casting conditions. Using the results in this work, the following straightening temperature conditions can be applied for minimal crack susceptibility when considering these steels for use in continuous casting operations, as shown in **Table 6.9**.

Table 6.9: Application of the hot ductility results to casting parameters.

Steel	Testing conditions	Casting type	Secondary cooling rate ($^{\circ}\text{C}\cdot\text{s}^{-1}$) [Cooling pattern]	Straightening temperature minimum ($^{\circ}\text{C}$)
Nb-1	A, B, C	Thin slab	1.2 [medium]	>900
Nb-2	C	Thin slab	1.2 [medium]	>970
Nb-3	C	Thin slab	1.2 [medium]	>1000
Nb-4	C	Thin slab	1.2 [medium]	>975
Nb-5	C	Thin slab	1.2 [medium]	>1000
	G	Thin slab	3.0 [hard]	>1025
	H	Billet	3.0 [hard]	>1050
	D	Thick slab	1.2 [medium]	>1025
	F	Thick slab	0.3 [soft]	>1000

Based on this work, the following compositional limits are recommended to minimise crack susceptibility in the niobium steels:

- Calcium-treatment is required to remove fine sulphide and oxysulphide precipitates such as (Mn,Fe)SO and CuS that are detrimental to hot ductility.
- Avoiding the peritectic composition range, especially 0.10 - 0.17% C with high manganese (>1.0% Mn).
- Maintaining the nitrogen below 0.0070% N.
- Maintaining the sulphur below 0.010% S.

To ensure that the strand temperature does not approach any low ductility region during the straightening process, the minimum recommended straightening temperatures listed in **Table 6.9** should be used for the steel compositions in this work. The maximum straightening temperatures should be limited to ~1100 °C, as hot ductility can begin to drop to below 50% *R. A.* at higher temperatures.

Chapter 7: Al-killed Boron Steels

Hot tensile behaviour in the aluminium-killed boron microalloyed steels: results, discussion and application

7.1 OVERVIEW OF CHAPTER 7

The Al-killed boron steels were sampled from thick slab. The three steels were reheated to 1300 °C, cooled to testing temperatures between 750 – 1100 °C at rates of 0.3, 1.2 and 3.0 °C.s⁻¹ and pulled to failure at strain rates of 10⁻⁴ or 10⁻³ s⁻¹.

The B:N ratio had the overriding influence on hot ductility and hence on cracking. The steels showed improved hot ductility with increasing B:N ratio from 0.19 to 0.75. Only the steel with a near stoichiometric B:N ratio of 0.75 exhibited no hot ductility trough. Additionally, low Mn:S ratios in all three steels led to formation of (Cu,Mn,Fe)S precipitates, which are detrimental to ductility.

At cooling rates of 0.3 and 1.2 °C.s⁻¹, generally associated with thick slab, bloom and slow thin slab casting, a B:N ratio of ≥0.47 was sufficient to avoid a ductility trough altogether. However, at a high cooling rate of 3.0 °C.s⁻¹, typically experienced in fast thin slab and billet casting, a B:N ratio of 0.75 would be required to provide good hot ductility.

7.2 TRANSFORMATION IN THE AL-KILLED BORON STEELS

The chemical composition of the Al-killed boron steels is given in **Table 7.1**. The main compositional differences in these three steels are the lower aluminium and higher nitrogen contents in *B-1* and the increasing B contents (and B:N ratio) from *B-1* to *B-3*.

Table 7.1: Chemical composition of Al-killed boron microalloyed steels (in mass %).

Grade	C	Mn	P	S	Si	Al	N	B	B:N
B-1	0.036	0.30	0.008	0.016	0.02	0.036	0.0054	0.0010	0.19
B-2	0.026	0.31	0.009	0.005	0.02	0.055	0.0047	0.0022	0.47
B-3	0.033	0.25	0.009	0.015	0.01	0.055	0.0044	0.0033	0.75

The transformation temperatures from the two equations: *GAS* and *Andrews* (**Table 2.3**) and from Thermo-Calc™ (T-C) are listed in **Table 7.2**. The range of Ae_3 temperatures in the Al-killed boron steels *B-1* to *B-3* was found to be small as the steel compositions are similar except for the Al-killed boron contents. However, the small increase in Ae_3 temperatures from *B-1* to *B-3* to *B-2* is due to the decrease in carbon content.

The lowest and highest predicted Ae_3 temperatures from all calculated and modelled predictions are 882 °C and 895 °C respectively, as shown by the temperature ranges:

- *GAS*^{*i*}: 882 – 886 °C
- *Andrews*^{*ii*}: 888 – 893 °C
- *SSOL2*^{*iii*}: 884 – 893 °C
- *TCFe3*^{*iv*}: 888 – 895 °C

Table 7.2: Calculated and modelled transformation temperatures (in °C) for the Al-killed boron steels.

Steel	Ae_3 (start of ferrite formation).				Ae_1 (start of austenite formation)		
	<i>GAS</i> ^{<i>i</i>}	<i>And</i> ^{<i>ii</i>}	T-C <i>SSOL2</i> ^{<i>iii</i>}	T-C <i>TCFe3</i> ^{<i>iv</i>}	<i>And</i> ^{<i>ii</i>}	T-C <i>SSOL2</i> ^{<i>iii</i>}	T-C <i>TCFe3</i> ^{<i>iv</i>}
B-1	882	888	884	888	717	708	718
B-2	886	893	893	895	717	707	718
B-3	884	891	889	895	718	710	721

i Genetic Adaptive Search (GAS) equation (Deo et al, 1995).

ii *Andrews* formula (1965).

iii Modelled using Thermo-Calc database *SSOL2* (Cornish, 1999).

iv Modelled using Thermo-Calc database *TCFe3* (2006) – this work.

The A_{e1} temperatures from the Andrews equation and the TCFE3 database are very similar with a difference from *B-1* to *B-3* of 4 °C.

7.3 PRECIPITATE DISSOLUTION IN THE AL-KILLED BORON STEELS

For low solute contents as in low alloy steels, the total mass concentrations of the dissolved elements in equilibrium with the precipitated phase, can be used to represent the solubility product discussed in **Section 2.5**. The T_{diss} is taken to be the highest achievable precipitation temperature for a specific composition. In reality, conditions do not approach equilibrium, and the precipitation would occur at significantly lower temperatures, if at all, under cooling conditions.

The results for the De Toledo (1993) hot cracking criterion (actual Mn:S / critical Mn:S ratio) are shown in **Table 7.3**. None of the Al-killed boron steels have an actual Mn:S ratio higher than the critical Mn:S ratio, and thus could be susceptible to hot cracking.

No AlN or BN dissolution temperatures could be obtained from the Thermo-Calc™ databases FEDAT and SSOL2, as aluminium and boron nitride are not included in these databases. Later modelling using the SSOL4 and TCFE3 databases produced dissolution temperatures for AlN and BN in these steels.

The equilibrium dissolution temperatures of the following precipitates in austenite: AlN, MnS and BN calculated by the solubility equations in **Table 2.2** are listed in **Table 7.4**. The equilibrium dissolution temperatures of Fe₂B, BN, AlN and MnS modelled using Thermo-Calc™ are listed in **Table 7.5**.

The AlN temperatures modelled using TCFE3 are lower than the calculated temperatures using the Turkdogan (1987) equation (**Figure 7.1**). The very low TCFE3 AlN dissolution temperature for steel *B-3* is due to the larger amount of N tied up by B as BN which precipitates at a higher temperature than AlN, leaving less N for AlN precipitation. All predicted AlN temperatures are lower than the 1300 °C solution temperature used in the hot ductility tests.

The predicted MnS dissolution temperatures for *B-1* and *B-3* are 100 °C higher than the 1300 °C solution treatment temperature, whereas for *B-2* it is 1299 °C, as shown in **Figure 7.2**. The MnS dissolution temperatures modelled using Thermo-Calc™ and calculated using the Turkdogan (1987) equation are similar, having slightly different slopes as a function of the [Mn][S] content.

Equations published by Turkdogan (1987) and Fountain (1962) showed considerable agreement, and provided BN temperatures 60 – 170 °C higher than those given by Maitrepierre (1979). This, again, is probably due to differences in steel compositions and testing conditions in the experimental work of these authors. For ease of reference, only the predicted temperatures given by Fountain (1962) are shown in the following experimental results sections.

The BN equilibrium dissolution temperatures modelled using Thermo-Calc™ database SSOL4 are ~160 °C higher, and using TCFE3 are ~200 °C higher, than the temperatures given by Fountain (1962) as shown in **Figure 7.3**.

The equilibrium phases for the three Al-killed boron steels modelled using the Thermo-Calc™ TCFE3 database are shown in **Figure 7.4** and **Figure 7.5**.

Table 7.3: Critical (Mn:S)_c and actual (Mn:S)_a ratios for the Al-killed boron steels.

Steel	(Mn:S) _c	(Mn:S) _a	(Mn:S) _a / (Mn:S) _c	Actual > Critical?
B-1	36	19	0.52	N
B-2	90	62	0.69	N
B-3	38	17	0.44	N

Table 7.4: Solubility of precipitates in austenite in the Al-killed boron steels – calculated equilibrium precipitate dissolution temperatures.

Steel	Calculated equilibrium dissolution temperatures (°C)				
	Turkdogan (1987)		Maitrepierre (1979)	Fountain (1962)	
	AlN	MnS	BN	BN	BN
B-1	1155	1446	1057	952	1070
B-2	1193	1299	1093	1019	1105
B-3	1184	1411	1113	1057	1124

Table 7.5: Solubility of precipitates in austenite in the Al-killed boron steels – Thermo-Calc™ modelled equilibrium precipitate dissolution temperatures (°C).

Thermo-Calc™ database: equilibrium dissolution temperatures (°C)					
	SSOL2 ^v	SSOL4 ^{vi}	TCFe3 ^{vi}	TCFe3 ^{vi}	TCFe3 ^{vi}
Steel	Fe ₂ B	BN	BN	AlN	MnS
B-1	~900	1232	1257	1088	1415
B-2	~950	1272	1336	1065	1302
B-3	998	1294	1316	910	1393

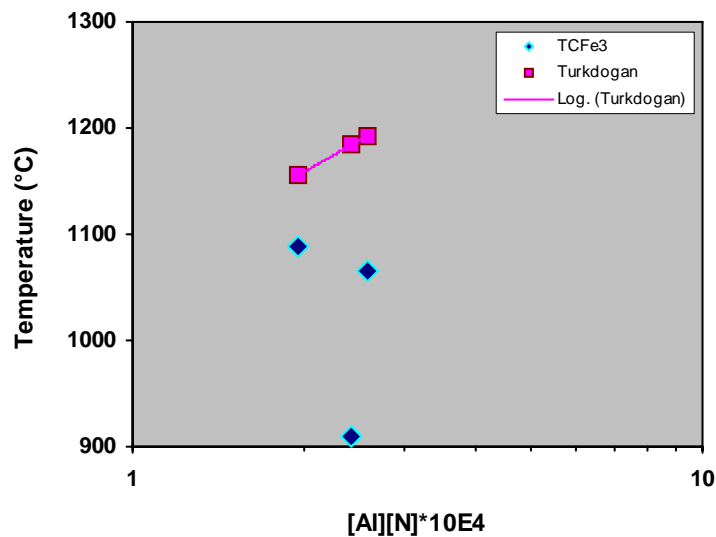


Figure 7.1: Dependence of the AlN dissolution temperature on [Al][N] for the boron steels modelled using Thermo-Calc™ and calculated using the Turkdogan (1987) equation.

^v Modelled using Thermo-Calc™ database SSOL2 (Cornish, 1999).

^{vi} Modelled using Thermo-Calc™ databases SSOL4 and TCFe3 (2006) – this work.

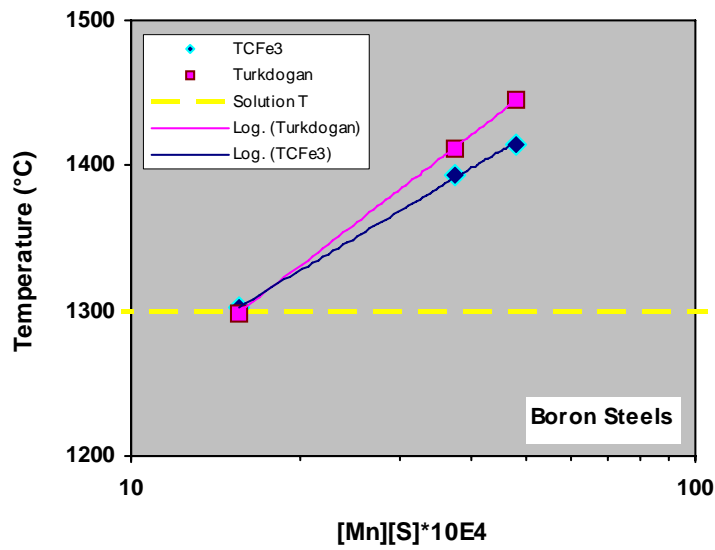


Figure 7.2: Logarithmic dependence of the MnS dissolution temperature on $[Mn][S]$ for the boron steels modelled using Thermo-Calc™ and calculated using the Turkdogan (1987) equation.

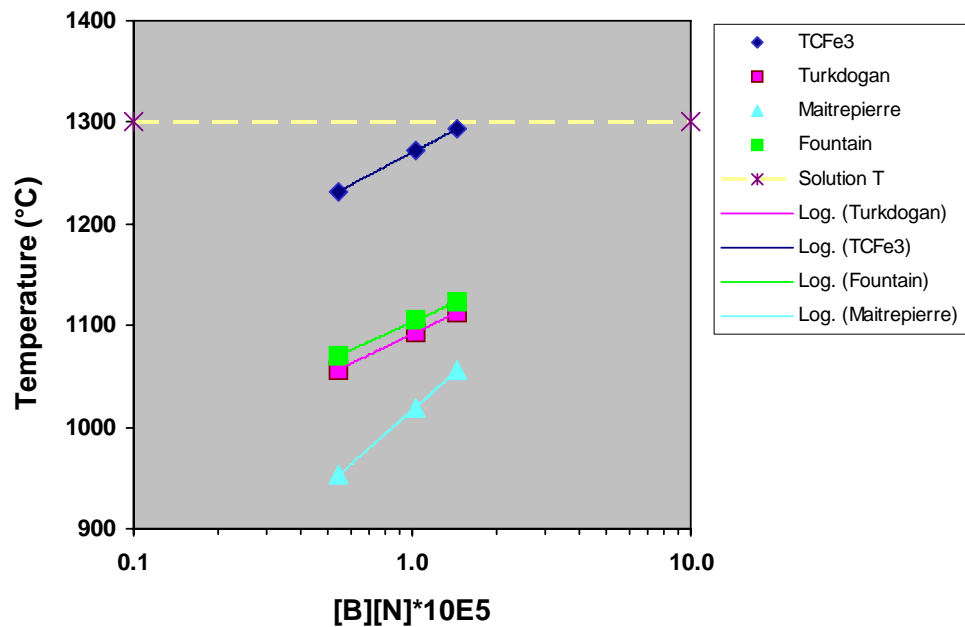
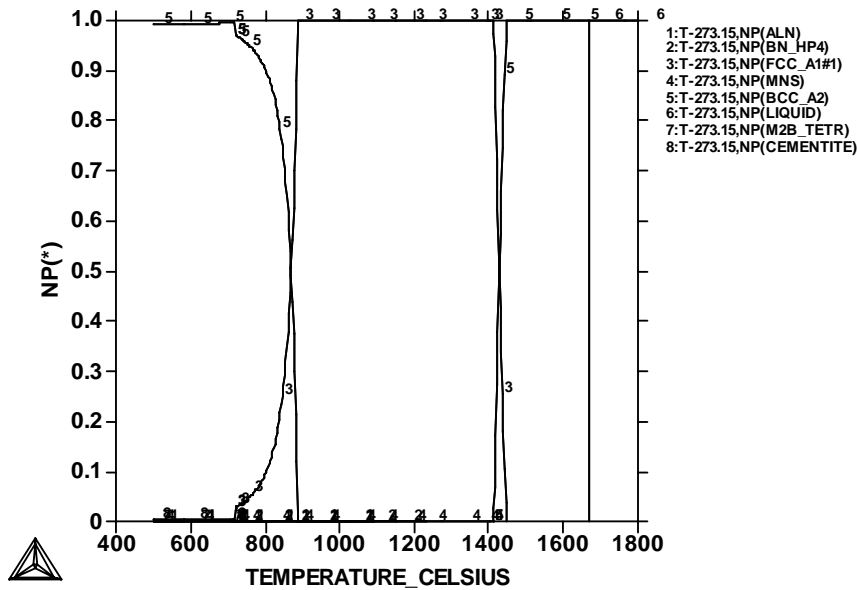


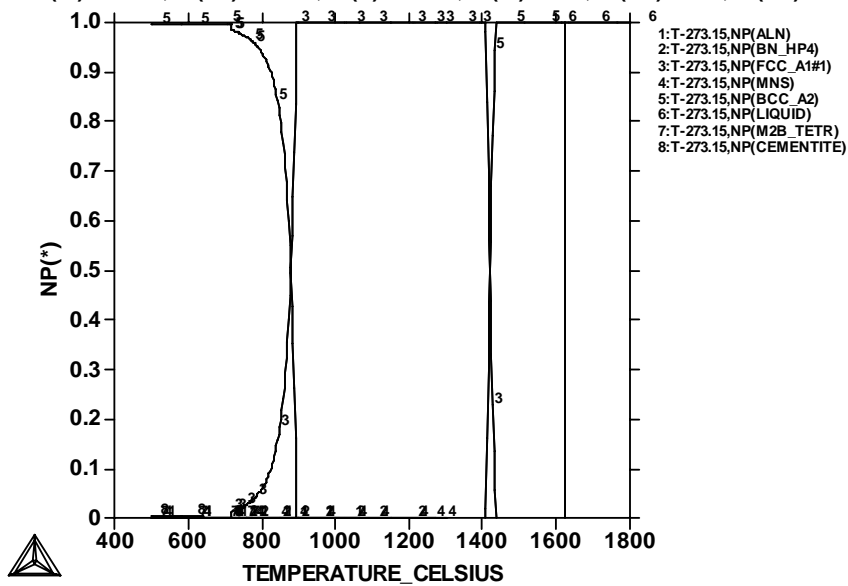
Figure 7.3: Logarithmic dependence of the BN dissolution temperature on $[B][N]$ for the boron steels, calculated using equations published by Turkdogan (1987), Fountain (1962) and Maitrepierre (1979).

THERMO-CALC (2007.10.21:11.07) :B1
 DATABASE:TCFe3
 N=1, P=1.01325E5, W(C)=3.6E-4, W(MN)=3E-3, W(P)=8E-5, W(S)=1.6E-4,
 W(SI)=2.1E-4, W(AL)=3.6E-4, W(N)=5.4E-5, W(NI)=3E-4, W(CU)=1E-4, W(CR)=3E-4, W(B)=1E-5;



a)

THERMO-CALC (2007.10.21:11.10) :B2
 DATABASE:TCFe3
 N=1, P=1.01325E5, W(C)=2.6E-4, W(MN)=3.1E-3, W(P)=9E-5, W(S)=5E-5,
 W(SI)=2.2E-4, W(AL)=5.5E-4, W(N)=4.7E-5, W(NI)=1E-4, W(CU)=1E-4, W(CR)=3E-4, W(B)=2.2E-5;



b)

Figure 7.4: Thermo-Calc™ graphs modelled using database TCFe3, showing the equilibrium phases for boron steels a) B-1 and b) B-2.

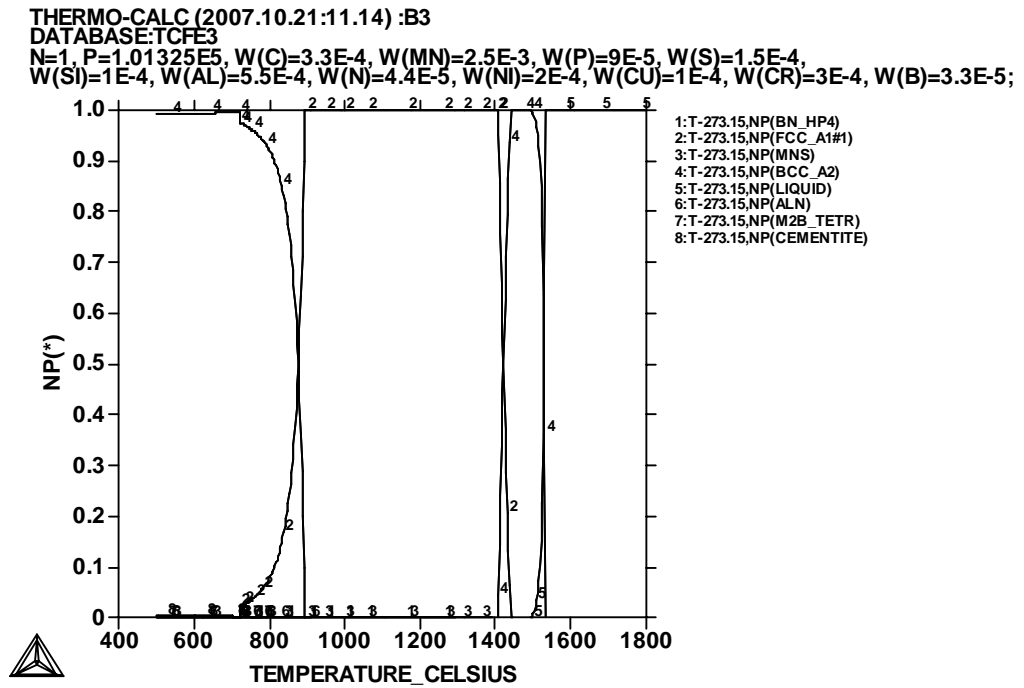


Figure 7.5: Thermo-Calc™ graphs modelled using database TCFE3, showing the equilibrium phases for boron steel B-3.

7.4 AL-KILLED BORON STEEL B-1

7.4.1 Introduction

Figure 7.6 shows the engineering stress – elongation curves for steel *B-1*. The occurrence of dynamic recrystallisation can be detected on the stress – elongation curves by either an abrupt decrease or oscillations of the flow stress. The onset of dynamic recrystallisation is indicated by arrows on the graphs and the temperatures are listed in **Table 7.6**. The maximum strength values are shown as a function of testing temperature in **Figure 7.7**.

The percentage reduction in area (% *R. A.*) is shown as a function of testing temperature in **Figure 7.8** and the percentage total elongation is shown as a function of testing temperature in **Figure 7.9**.

Scanning electron microscopy (SEM) micrographs are shown in **Figure 7.10** to **Figure 7.14** and transmission electron microscopy (TEM) images with X-ray maps are shown in **Figure 7.15** and **Figure 7.16**.

The ASCII data for the test performed at 1050 °C (schedule G) was not retrieved due to diskette problems. However, the maximum strength and elongation were determined by manually measuring the graph on the data acquisition unit printout, and by using another force-elongation curve as a reference (*B-2, G 1000 °C*).

The modelled Thermo-CalcTM TCFE3 calculated Ae_3 temperature (888 °C shown in **Table 7.2**) and the BN temperature (Fountain, 1962) from **Table 7.4** are shown on the graphs.

7.4.2 Maximum strength

All the engineering stress vs. elongation and maximum strength vs. testing temperature curves (**Figure 7.6** and **Figure 7.7**) showed similar behaviour: increasing from 1050 °C to a maximum at ~900 °C and decreasing with further decrease in temperature to 800 °C. The austenite work hardens, increasing the tensile strength, until softer ferrite starts to form just below the Ae_3 temperature (888 °C) and the maximum strength drops. The arrows in **Figure 7.6** show the onset of dynamic recrystallisation.

At high strain rate (10^{-3} s^{-1}), an increase in cooling rate from 1.2 to 3.0 °C.s⁻¹ increased the S_u at 800 °C by approximately 7 MPa, whereas there was no significant effect between 900 – 1000 °C.

At low strain rate (10^{-4} s^{-1}), there was no effect on S_u with increase in cooling rate from 1.2 to 3.0 °C.s⁻¹, but an increase from 0.3 to 1.2 °C.s⁻¹ appeared to have a more significant effect in decreasing the S_u at 900 °C.

An increase in strain rate (10^{-4} to 10^{-3} s^{-1}) showed higher maximum strength by approximately 8 MPa.

The austenite work hardens, increasing the tensile strength, until a drop in the maximum strength occurs near the Ae_3 temperature (888 °C).

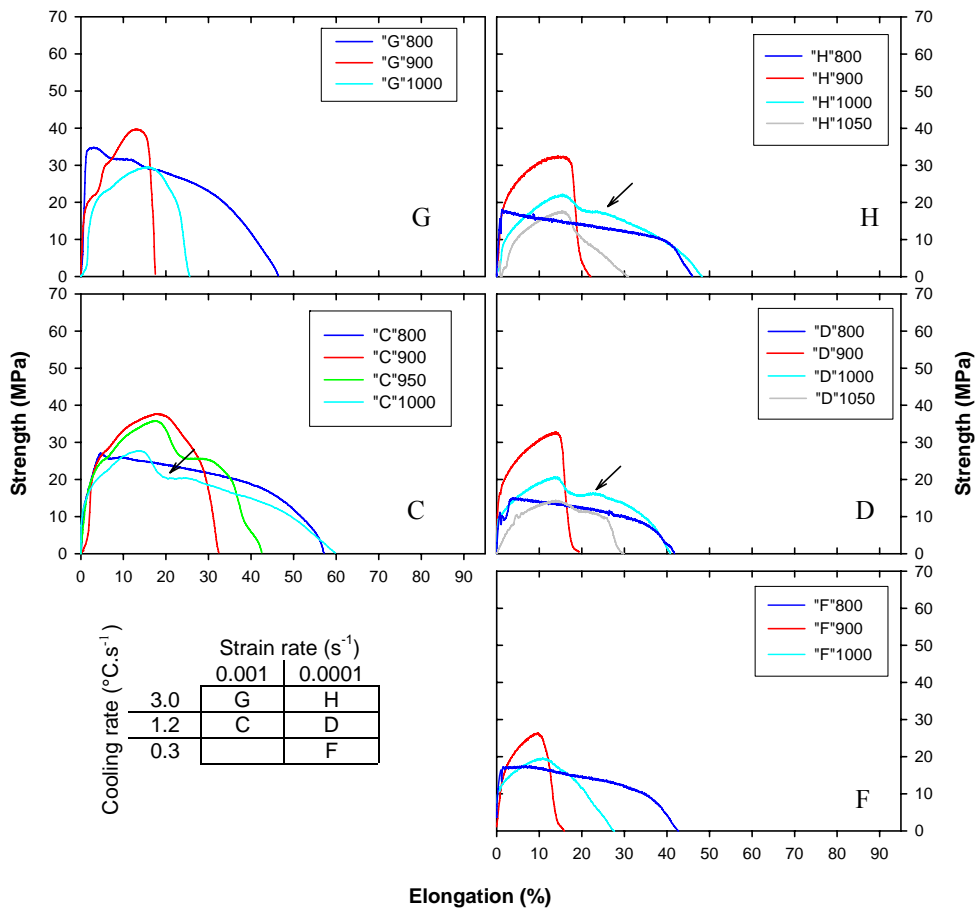


Figure 7.6: Engineering stress as a function of elongation for steel *B-I*. The key to the testing schedules is shown. The onset of dynamic recrystallisation is indicated by arrows on the graphs.

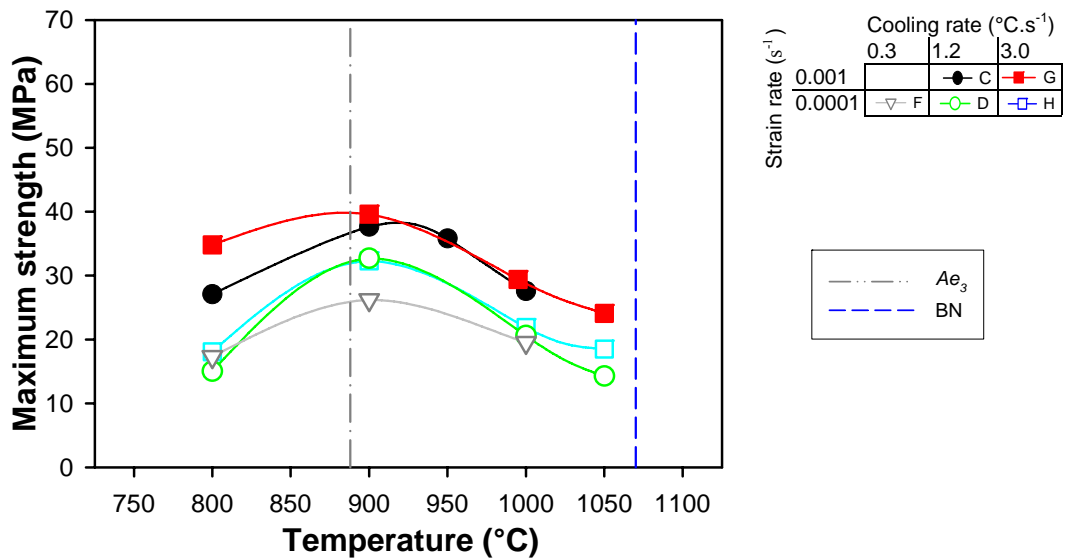


Figure 7.7: Maximum strength for steel *B-I* as a function of testing temperature, strain rate and cooling rate.

7.4.3 Reduction in area

At high strain rate (10^{-3} s^{-1}):

The highest minimum value and narrowest *R. A.* trough occurred at a cooling rate of $1.2 \text{ }^\circ\text{C}\cdot\text{s}^{-1}$ (**Figure 7.8**). An increase in cooling rate from $1.2 - 3.0 \text{ }^\circ\text{C}\cdot\text{s}^{-1}$ deepened the ductility trough by $\sim 20\%$ and widened the trough at 50% *R. A.* by $\sim 40 \text{ }^\circ\text{C}$ on the low temperature side and by $\sim 50 \text{ }^\circ\text{C}$ on the high temperature side. The ductility minima both occurred at $\sim 950 \text{ }^\circ\text{C}$.

At low strain rate (10^{-4} s^{-1}):

The *R. A.* curves showed similar decreases in ductility from $800 - 900 \text{ }^\circ\text{C}$, with minima of $\sim 20\%$ at $\sim 900 \text{ }^\circ\text{C}$. For schedule F (cooling rate = $0.3 \text{ }^\circ\text{C}\cdot\text{s}^{-1}$) the *R. A.* increased to $\sim 97\%$ at $1000 \text{ }^\circ\text{C}$, while for D ($1.2 \text{ }^\circ\text{C}\cdot\text{s}^{-1}$) and H ($3.0 \text{ }^\circ\text{C}\cdot\text{s}^{-1}$) the *R. A.* only increased to $\sim 80\%$. With further increase in temperature to $1050 \text{ }^\circ\text{C}$, the *R. A.* values of schedule D remained at $\sim 85\%$, whereas for schedule H the *R. A.* decreased to $\sim 55\%$. The 50% ductility recovery occurred at temperatures of $\sim 810 \text{ }^\circ\text{C}$ and $\sim 960 \text{ }^\circ\text{C}$.

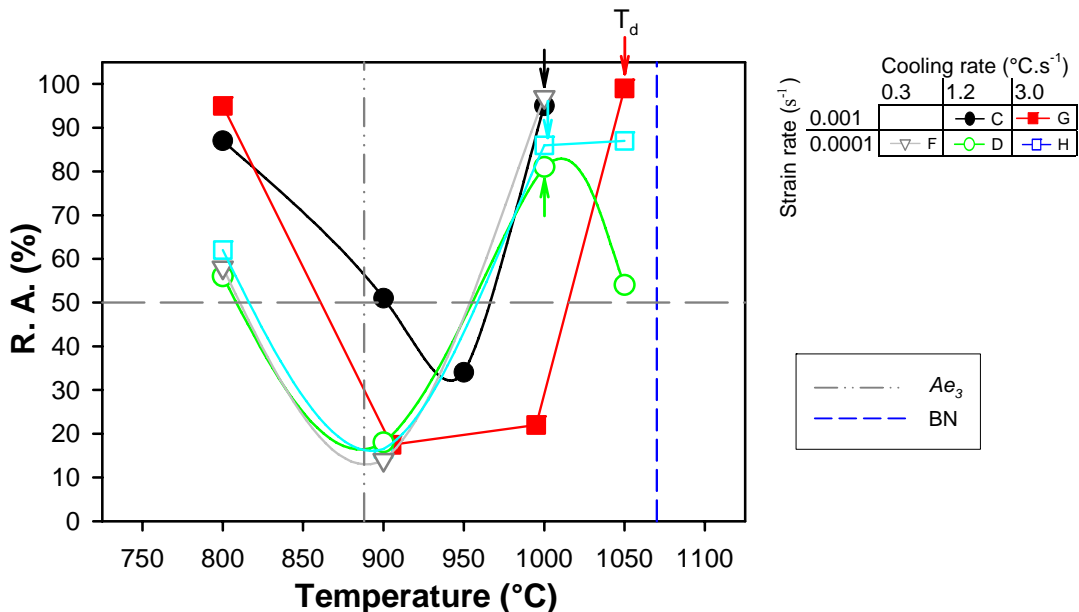


Figure 7.8: Reduction in area for steel B-1 as a function of testing temperature, strain rate and cooling rate.

A decrease in strain rate had little effect on the minimum *R. A.* value for a high cooling rate ($3.0\text{ }^{\circ}\text{C}\cdot\text{s}^{-1}$), but decreased the minimum *R. A.* value by $\sim 15\%$ at a cooling rate of $1.2\text{ }^{\circ}\text{C}\cdot\text{s}^{-1}$. At both cooling rates, the strain rate decrease also lowered the temperature of the minima by $\sim 50\text{ }^{\circ}\text{C}$.

The 50% ductility recovery temperatures were also decreased by a decrease in strain rate:

- By $\sim 90\text{ }^{\circ}\text{C}$ (low temperature) and $\sim 10\text{ }^{\circ}\text{C}$ (high temperature) at $1.2\text{ }^{\circ}\text{C}\cdot\text{s}^{-1}$.
- By $\sim 40\text{ }^{\circ}\text{C}$ (low temperature) and $\sim 75\text{ }^{\circ}\text{C}$ (high temperature) at $3.0\text{ }^{\circ}\text{C}\cdot\text{s}^{-1}$.

At the low temperature end of the trough, the Ae_3 temperature occurred near the *R. A.* minima obtained under low strain rate conditions. Ductility recovery occurred below the Ae_3 temperature.

Ductility recovery at the high temperature end of the trough coincided with the onset of dynamic recrystallisation.

7.4.4 Total elongation

The total elongation curves (**Figure 7.9**) followed similar trends to the reduction in area curves. The minima occurred at temperatures of ~ 900 °C with the possible exception of schedule G, which could occur between 900 and 950 °C.

At a strain rate of 10^{-3} s^{-1} :

The highest minimum elongation and narrowest elongation trough occurred at a high strain rate and intermediate cooling rate ($1.2 \text{ }^\circ\text{C}\cdot\text{s}^{-1}$). Increasing the cooling rate decreased the minimum elongation by ~ 20 % and widened the elongation recovery by ~ 50 °C on both the low and high temperature sides of the trough.

At a strain rate of 10^{-4} s^{-1} :

Increasing the cooling rate from $0.3 - 3.0 \text{ }^\circ\text{C}\cdot\text{s}^{-1}$ had little effect on the elongation from $800 - 900$ °C and increased the elongation between $900 - 1000$ °C. From $1000 - 1050$ °C, the elongation decreased by approximately 10 % for cooling rates of 1.2 and $3.0 \text{ }^\circ\text{C}\cdot\text{s}^{-1}$.

The elongation curves with the lowest minima occurred under the following conditions: low strain rate and low cooling rate (schedule F: 10^{-4} s^{-1} , $0.3 \text{ }^\circ\text{C}\cdot\text{s}^{-1}$) and high strain rate and high cooling rate (schedule G: 10^{-3} s^{-1} , $3.0 \text{ }^\circ\text{C}\cdot\text{s}^{-1}$).

High temperature elongation recovery coincided with the dynamic recrystallisation temperature. Low temperature elongation recovery occurred below the Ae_3 temperature for all tested conditions.

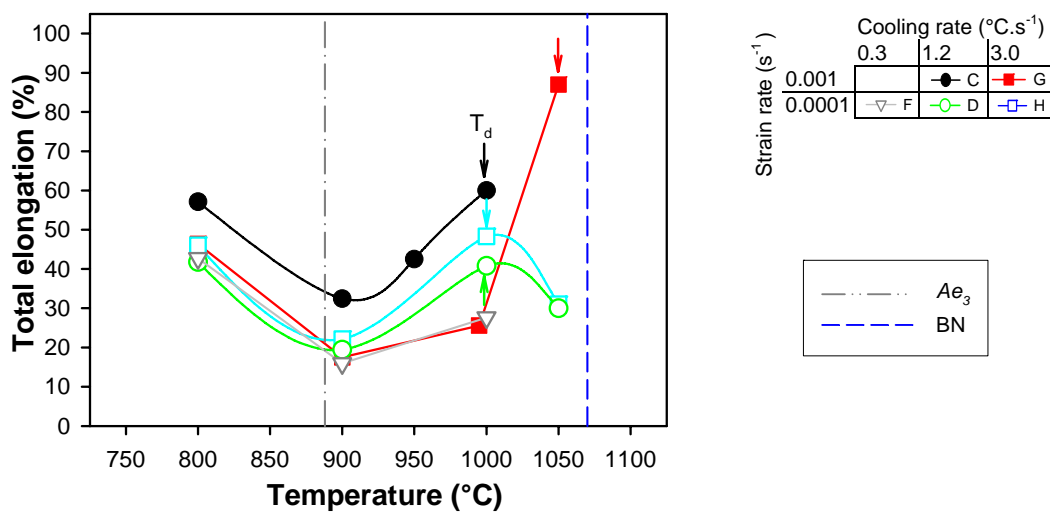


Figure 7.9: Elongation for steel B-1 as a function of testing temperature, strain rate and cooling rate.

7.4.5 Scanning electron microscopy

At high strain rate (10^{-3} s^{-1}):

- *Cooling rate $1.2 \text{ }^\circ\text{C}\cdot\text{s}^{-1}$* : At a testing temperature of $800 \text{ }^\circ\text{C}$ (**Figure 7.10 a and b**), the sample did not show much internal damage as a result of cracking (interconnection of microvoids), but rather as a result of ductile tearing, seen in **Figure 7.10 b**. A few Fe-S-O precipitates were identified around cracks.

At $950 \text{ }^\circ\text{C}$ (**Figure 7.10 c**), many cracks were seen, caused by interconnection of voids containing precipitates such as MnS, Fe-Al-O and Fe-Mn-Al-S-O.

- *Cooling rate $3.0 \text{ }^\circ\text{C}\cdot\text{s}^{-1}$* : At $1000 \text{ }^\circ\text{C}$ (**Figure 7.11 a**) the matrix contained many MnS precipitates. Other precipitates containing Fe-Mn-S-N were identified, which indicate co-precipitation of MnS and BN. Boron is not easily analyzed on the scanning electron microscope, as it is detected at very low energy (0.185 keV), which is near the detection limit.

Figure 7.11 b shows many spherical and a few elongated MnS precipitates in the matrix. Very little internal cracking between microvoids was observed.

At low strain rate (10^{-4} s^{-1}):

- *Cooling rate $0.3 \text{ }^\circ\text{C}\cdot\text{s}^{-1}$* : (**Figure 7.12 a**): At $900 \text{ }^\circ\text{C}$, many precipitates containing MnS, Fe-Al-S-O and Fe-Mn-Al-O were seen in straight lines, connected by internal cracks.

At a testing temperature of $1000 \text{ }^\circ\text{C}$ (**Figure 7.12 b**), many spherical Fe-Mn-Al-Si-O precipitates were observed, with limited interconnection of microcracks.

- *Cooling rate $1.2 \text{ }^\circ\text{C}\cdot\text{s}^{-1}$* : (**Figure 7.13 a**) Many precipitates such as MnS and Fe-Al-Mn-S-O, as well as Fe-Mn-S-N, Fe-N and Fe-Mn-N, all of which are assumed to contain B as the nitride-forming element, were observed at a testing temperature of $900 \text{ }^\circ\text{C}$. There was extensive internal damage caused by cracking between microvoids, which appear to be along prior austenite grain boundaries. The austenite grains are estimated to have an average diameter of $500\text{-}700 \text{ }\mu\text{m}$.

At $1000 \text{ }^\circ\text{C}$ (**Figure 7.13 b**), a few small Fe-O and many Fe-Al-Si-Cr-Mn-O (some with S or P) precipitates were identified. There was limited interconnection of voids, with only a few cracks of $10\text{-}30 \text{ }\mu\text{m}$ observed in the sample.

- *Cooling rate 3.0 °C.s⁻¹*: At 900 °C (**Figure 7.14 a**), many precipitates connected by cracks were seen, such as Fe-Mn-S-O-B-N, Mn-S-B-N and Mn-Ca-Fe-O-C, where the C is thought to be from graphite contamination.

At 1050 °C (**Figure 7.14 b**), many complex precipitates were analyzed, such as: Fe-Mn-S-O, Fe-Mn-Cr-Al-Si-S-O (some containing P) and Fe-B-N-O. Only two long internal cracks (>30 μm) were observed in this specimen.

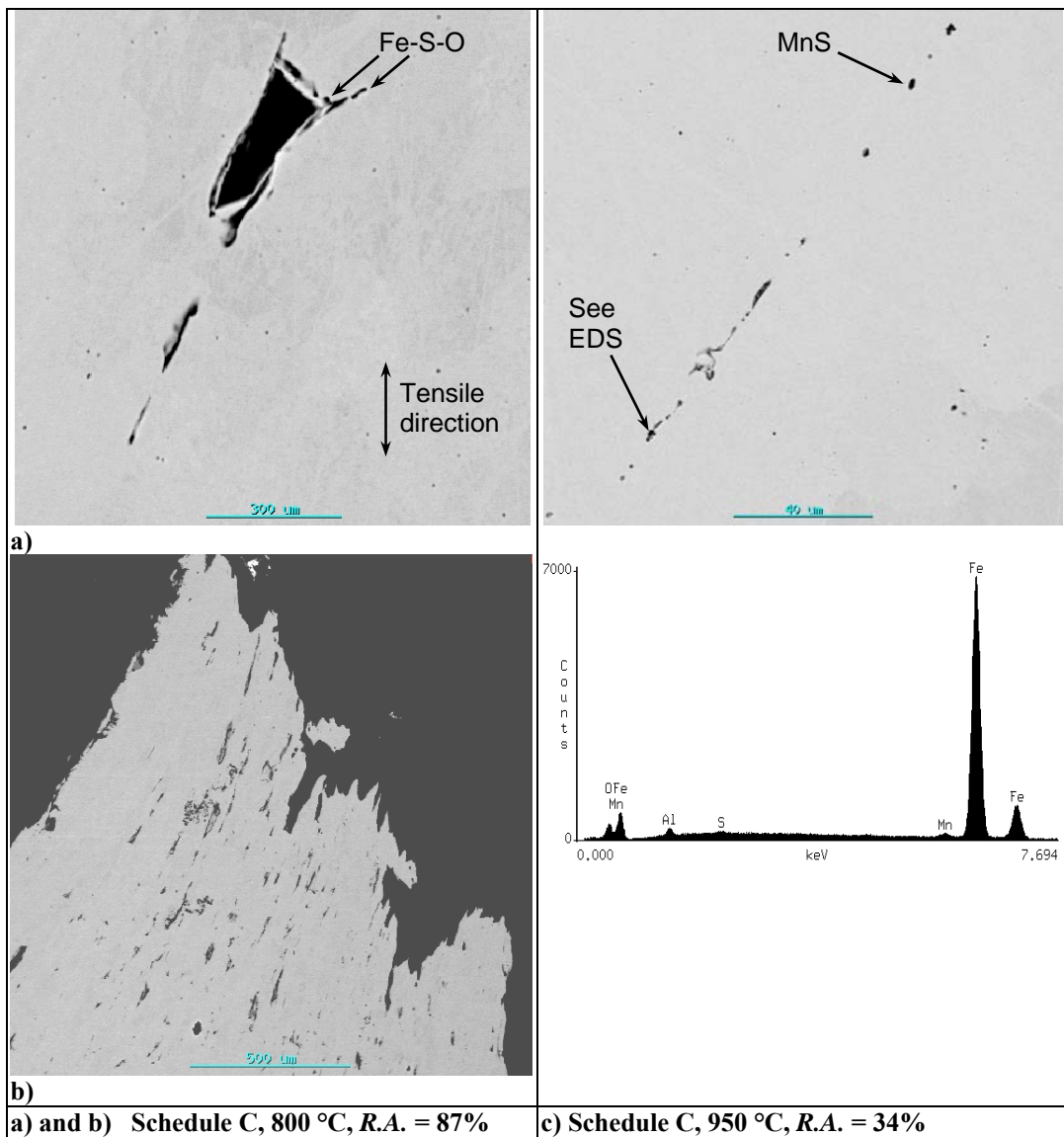


Figure 7.10: SEM backscatter images of Steel *B-1* tested under Schedule C conditions: (10^{-3} s^{-1} , 1.2 °C.s^{-1}).

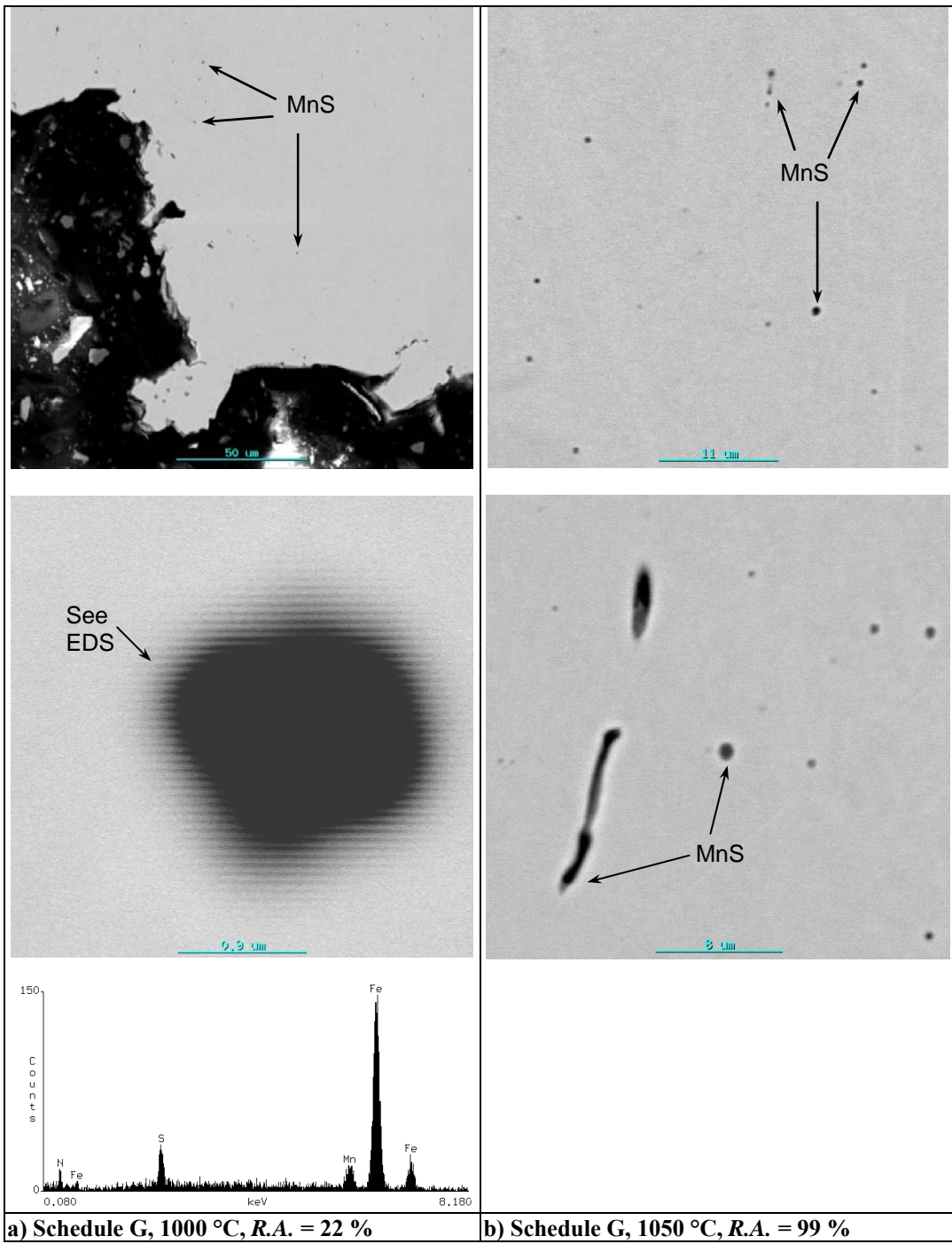


Figure 7.11: SEM backscatter images of Steel *B-1* tested under Schedule G conditions: (10^{-3} s^{-1} , $3.0 \text{ }^\circ\text{C}\cdot\text{s}^{-1}$).

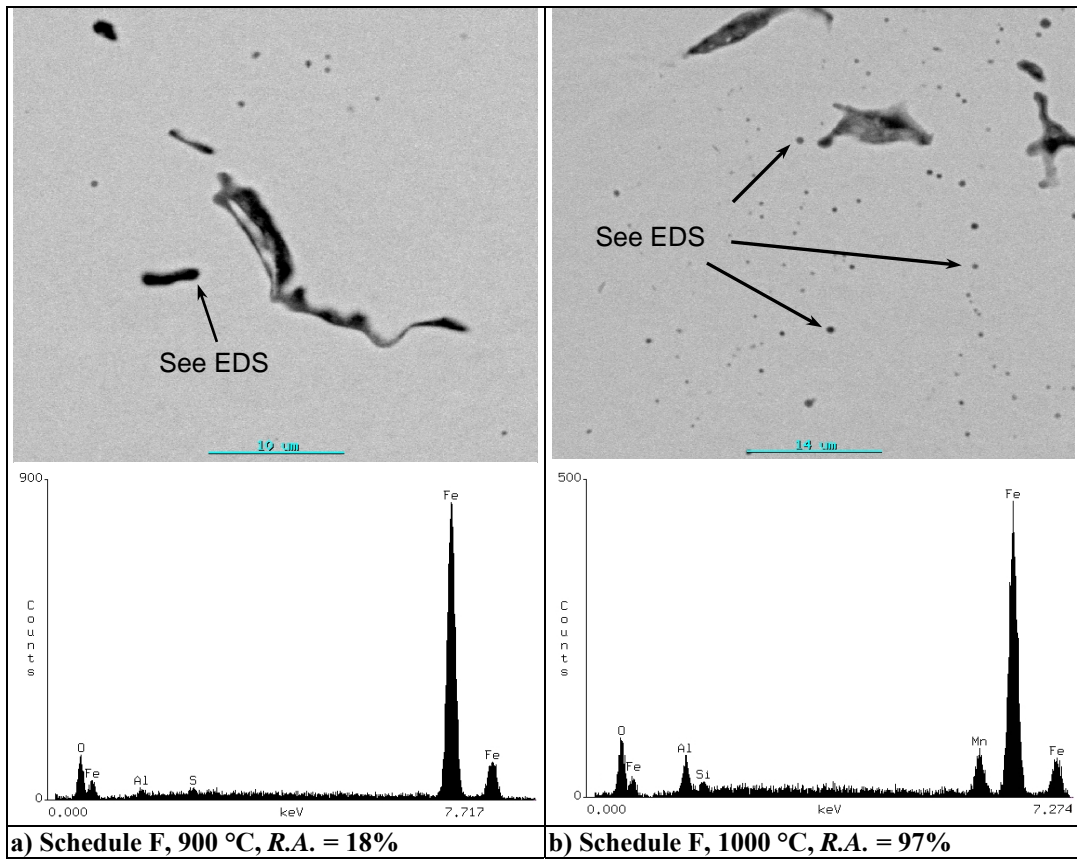


Figure 7.12: SEM backscatter images of Steel *B-1* tested under Schedule F conditions: (10^{-4} s^{-1} , $0.3 \text{ °C}\cdot\text{s}^{-1}$).

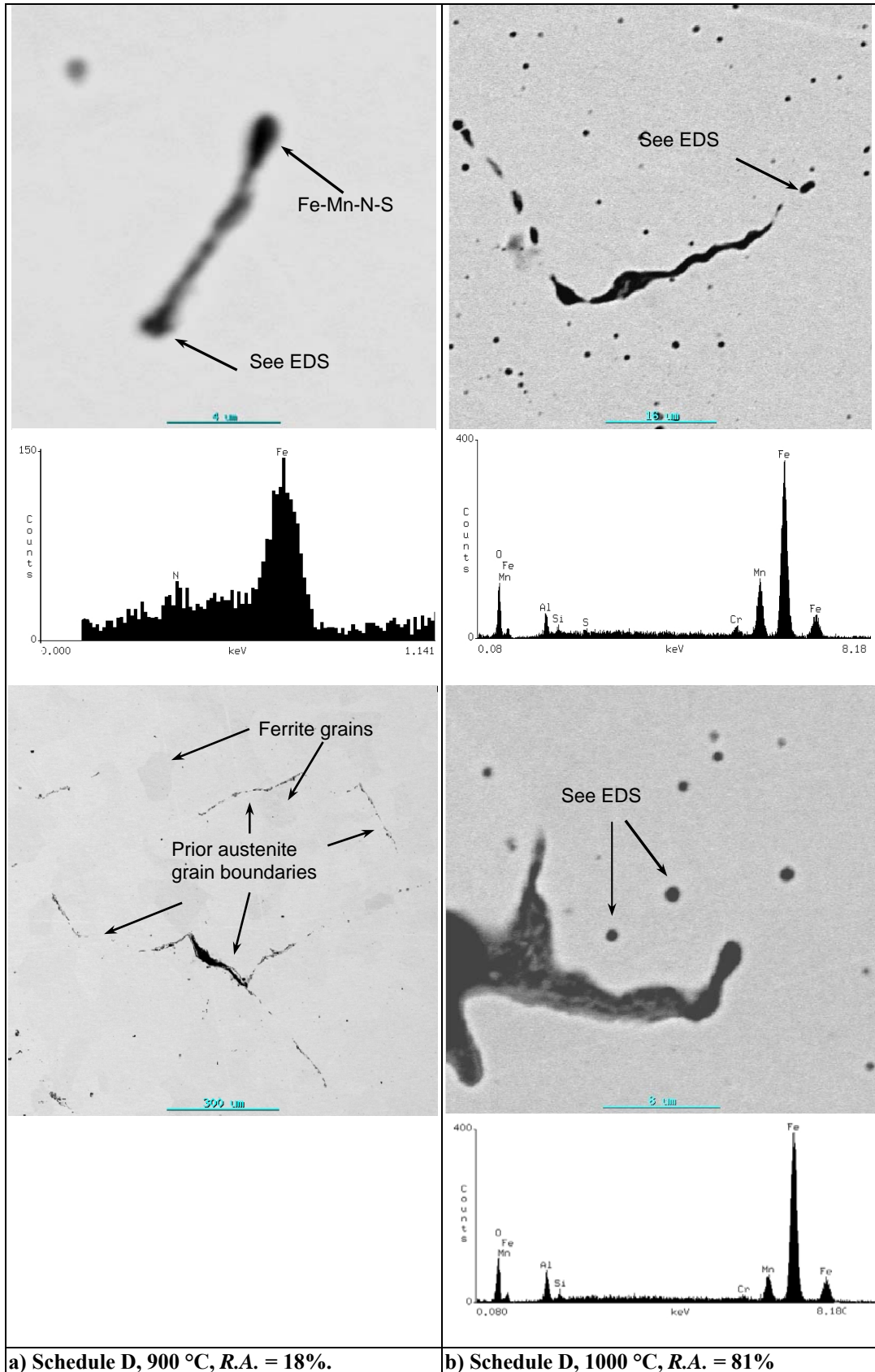


Figure 7.13: SEM backscatter images of Steel B-1 tested under Schedule D conditions: (10^{-4} s^{-1} , 1.2 °C.s^{-1}), showing precipitate-containing microvoids and cracking along prior austenite grain boundaries.

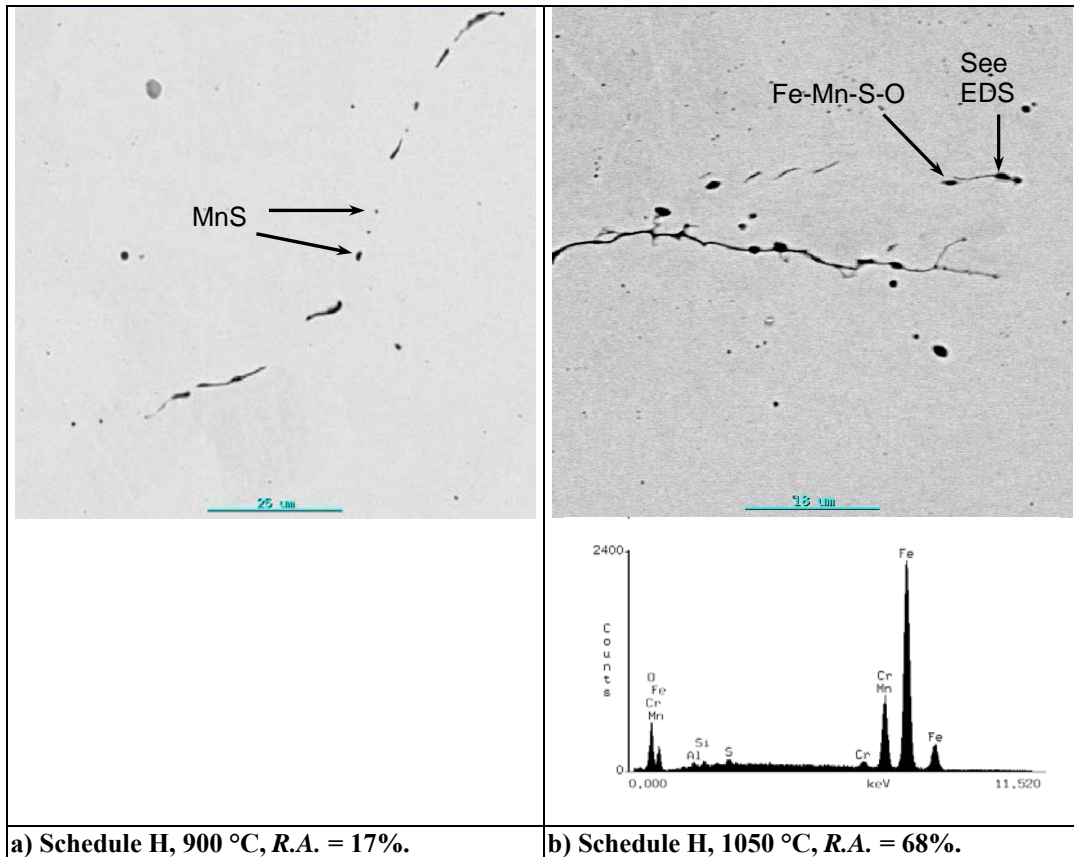
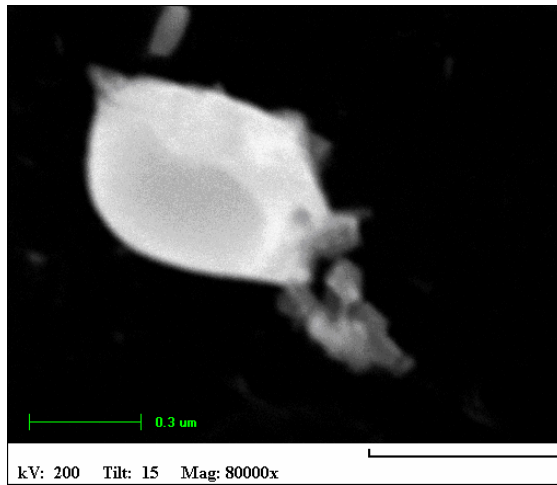


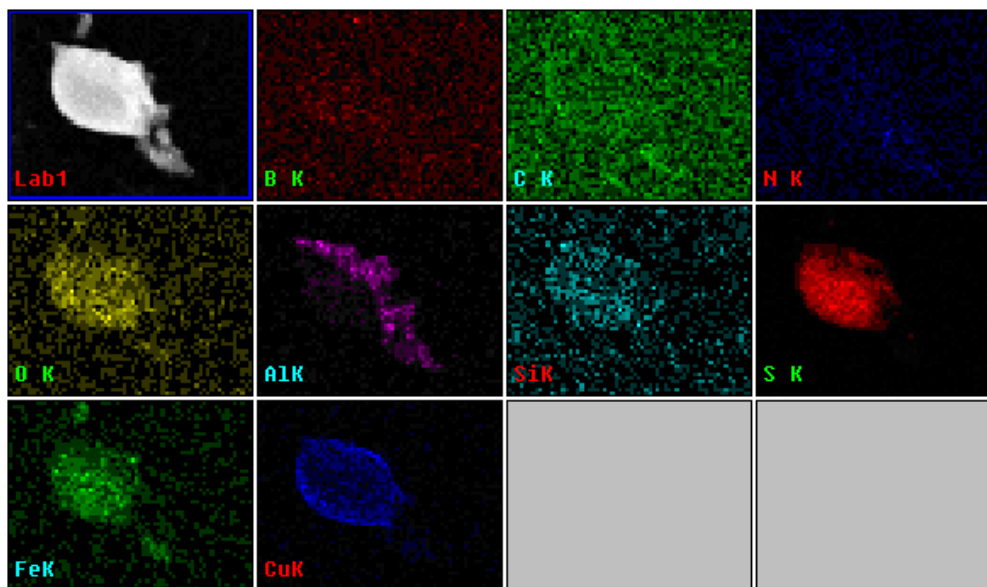
Figure 7.14: SEM backscatter images of Steel *B-1* tested under Schedule H conditions: (10^{-4} s^{-1} , $3.0 \text{ }^\circ\text{C}\cdot\text{s}^{-1}$), showing cracking between microvoids.

7.4.6 Transmission electron microscopy

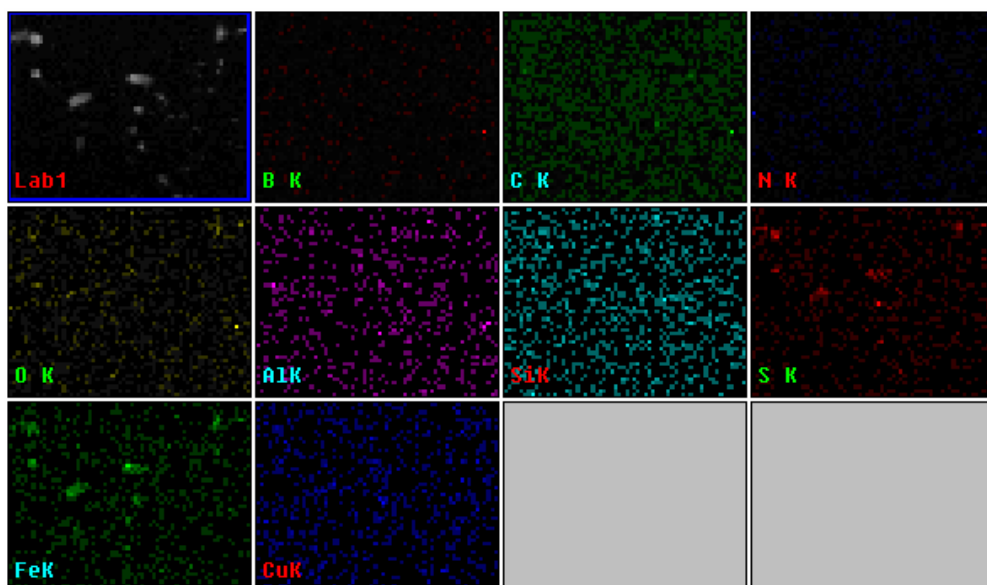
Figure 7.15 and **Figure 7.16** show X-ray maps of Steel *B-1* tested under Schedule F conditions (10^{-4} s^{-1} , $0.3 \text{ }^\circ\text{C}\cdot\text{s}^{-1}$). **Figure 7.15 a** shows a TEM dark field image of a precipitate on an extraction replica. **Figure 7.15 b** shows the X-ray maps, identifying the precipitate as an Fe-S-O-Si particle (originating in steelmaking) with CuS- and AlN-enriched edges. **Figure 7.15 c** shows fine FeS and CuS precipitates. **Figure 7.16 a** shows a dark field image of a 65 nm wide grain boundary filament containing CuS with BN and oxygen (**Figure 7.16 b and c**).



a) TEM dark field image of precipitate on extraction replica.

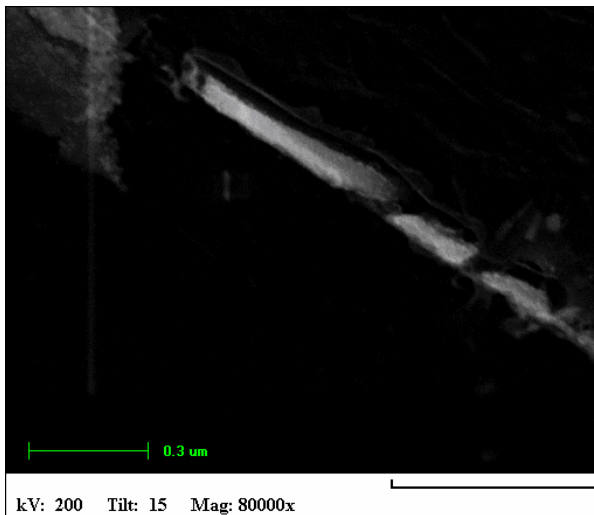


b) Fe-S-O-Si particle with CuS enriched edges.

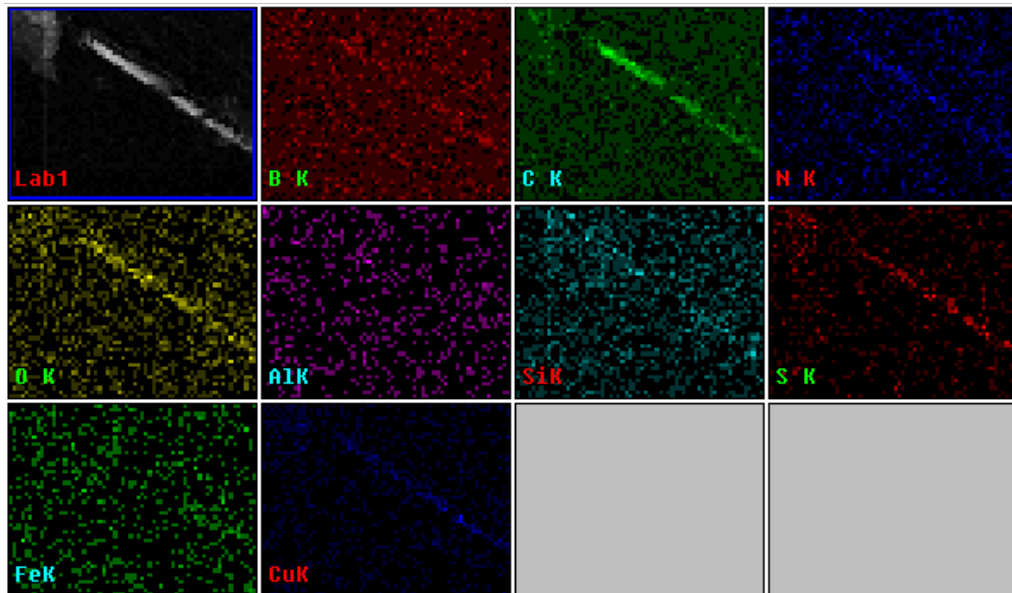


c) Fine FeS and CuS precipitates.

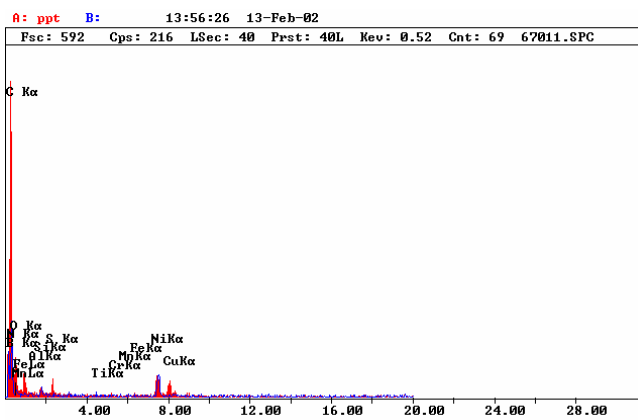
Figure 7.15: X-ray maps of Steel *B-1* tested under Schedule F conditions ($R. A. = 20\%$, $10^{-4} s^{-1}$, $0.3 ^\circ C.s^{-1}$).



a) TEM dark field image of precipitate on extraction replica.



b) X-ray maps showing the presence of CuS, BN and O.



c) EDS spectrum of the filament.

Figure 7.16: X-ray maps of a grain boundary filament in Steel *B-1* tested under Schedule F conditions ($R. A. = 20\%$, $10^{-4} s^{-1}$, $0.3 ^\circ C.s^{-1}$).

7.5 AL-KILLED BORON STEEL *B-2*

7.5.1 Introduction

Figure 7.17 shows the engineering stress – elongation curves for steel *B-1*. The occurrence of dynamic recrystallisation can be detected on the stress – elongation curves by either an abrupt decrease or oscillations of the flow stress (Mintz and Mohamed, 1989; Mintz *et al.*, 1993 and Abushosha *et al.*, 1991). The onset of dynamic recrystallisation is indicated by arrows on the graphs and the temperatures are listed in **Table 7.6**. The maximum strength values are shown as a function of testing temperature in **Figure 7.18**.

The percentage reduction in area (% *R. A.*) is shown as a function of testing temperature in **Figure 7.19** and the percentage total elongation is shown as a function of testing temperature in **Figure 7.20**.

Scanning electron microscopy (SEM) micrographs are shown in **Figure 7.21** to **Figure 7.25** and transmission electron microscopy (TEM) images with X-ray maps are shown in **Figure 7.26** to **Figure 7.26**.

The modelled Thermo-CalcTM TCFE3 calculated A_{e_3} temperature (895 °C, **Table 7.2**) and the BN temperature (Fountain, 1962) from **Table 7.4** are shown on the graphs.

7.5.2 Maximum strength

All the engineering stress *vs.* elongation and maximum strength *vs.* testing temperature curves (**Figure 7.17** and **Figure 7.18**) showed similar behaviour with decrease in temperature: gradual increase in S_u from 1050°C to a maximum value at 900°C (950°C for schedule H and 950 – 1000 °C for schedule D), followed by a decrease with further decrease in temperature to 800°C.

The stress oscillations in the “D”1050 tensile test are due to thermocouple contact problems, which caused small temperature, and hence, small stress fluctuations in the

results. The thermocouple contact was broken during the “D”1000 test, but the maximum strength value is still a valid result.

Increasing the strain rate resulted in higher S_u values and a larger variation in strength, while cooling rate seemed to have little influence on the magnitude of the maximum strength. For schedules C, G and F, the drop in maximum strength occurred below the Ae_3 temperature. As the calculated Ae_3 temperature (895 °C) is very close to the programmed testing temperature 900 °C, the lower S_u values found for schedules D and H could be due to ferrite formation.

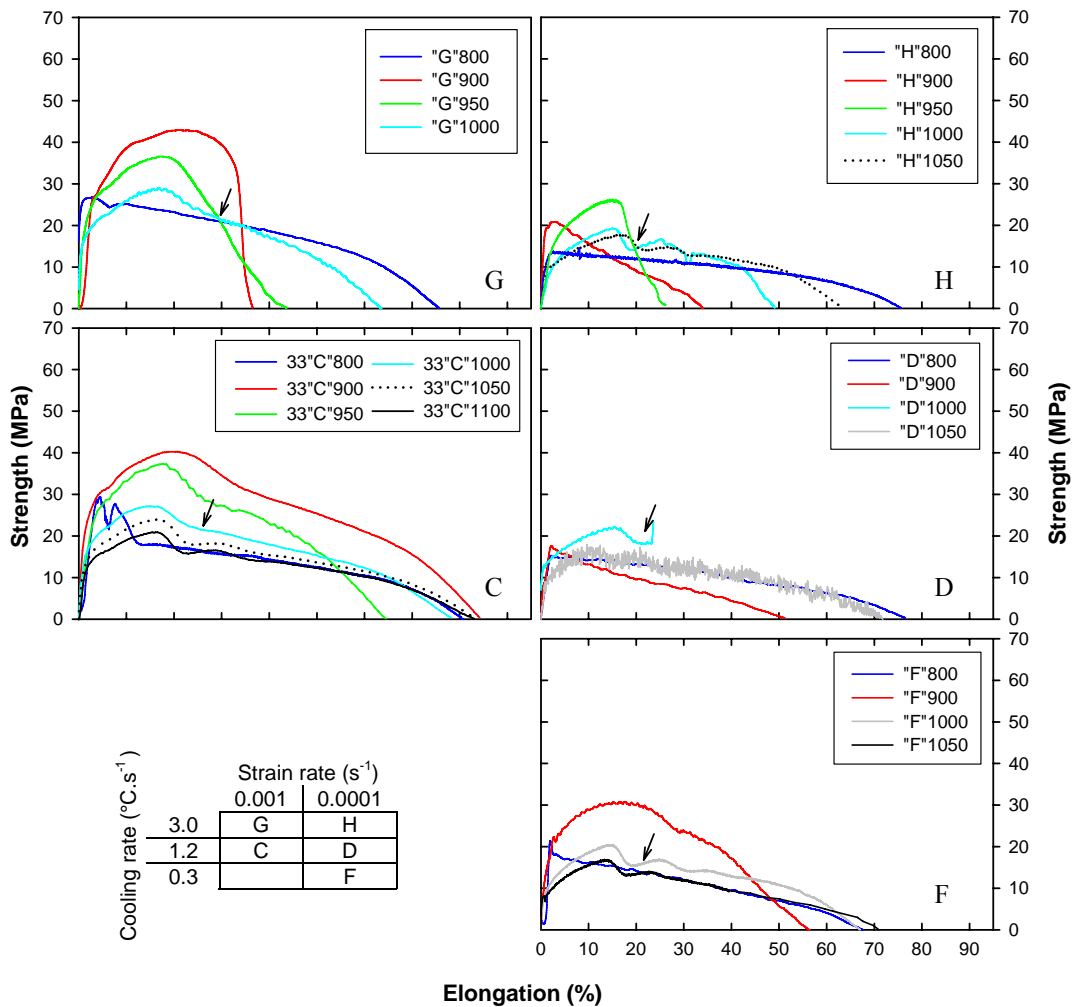


Figure 7.17: Engineering stress as a function of elongation for steel B-2. Arrows indicate the onset of dynamic recrystallisation. The key to the testing schedules is also shown.

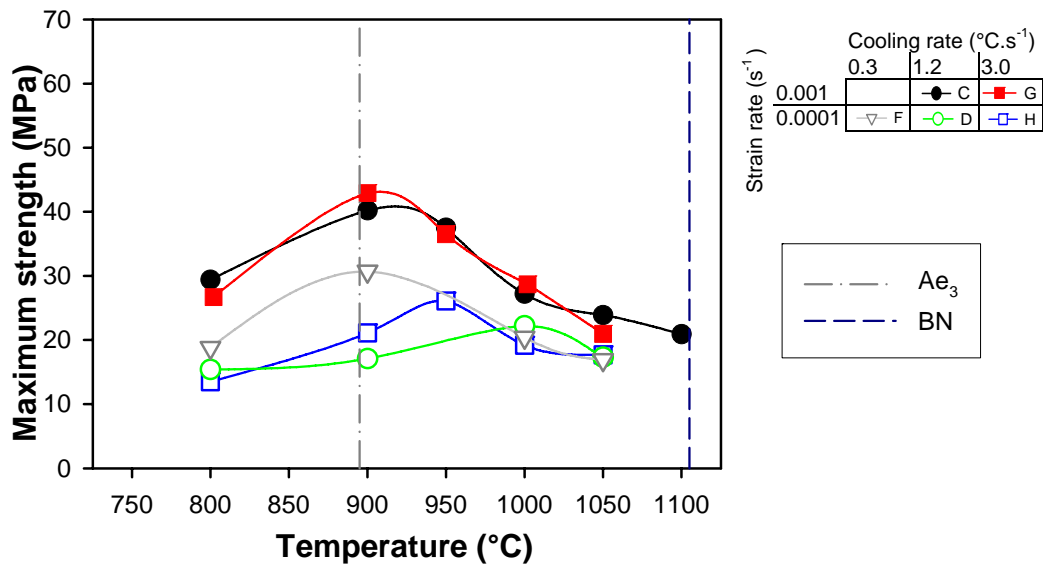


Figure 7.18: Maximum strength for steel B-2 as a function of testing temperature, strain rate and cooling rate.

7.5.3 Reduction in area

Figure 7.19 shows that cooling rate had a significant effect on the reduction in area curves. For both strain rates, the high cooling rate (3.0 °C.s⁻¹) produced deep ductility troughs, approximately 200 °C wide, with minima at ~20-25% R. A. (schedules G and H), while the intermediate cooling rate (1.2 °C.s⁻¹) showed no discernable ductility troughs in the temperature range 800 – 1000 °C.

Increasing the strain rate shifted the ductility minimum from 900 – 950 °C for a cooling rate of 3.0 °C.s⁻¹. The low strain rate and low cooling rate conditions resulted in a shallow ductility trough, 200 °C wide, with a minimum of ~80% at 900 °C (schedule F). The error bars denote the difficulty in measuring the final area on the tensile specimens (800 and 900 °C), as these fracture surfaces occurred by ductile tearing and did not produce smooth ellipsoid areas. The curve was plotted through the mean R. A. value (based on

five measurements taken per specimen) at each testing temperature. The error bars were computed by the SigmaPlot® package as the standard deviation.^{vii}

The Ae_3 temperature occurred near the $R. A.$ minimum obtained under schedule G conditions and approximately 75 °C below the $R. A.$ minimum for Schedule H, implying that the formation of ferrite improves the ductility. For both schedules G and H, high temperature ductility recovery coincided with dynamic recrystallisation.

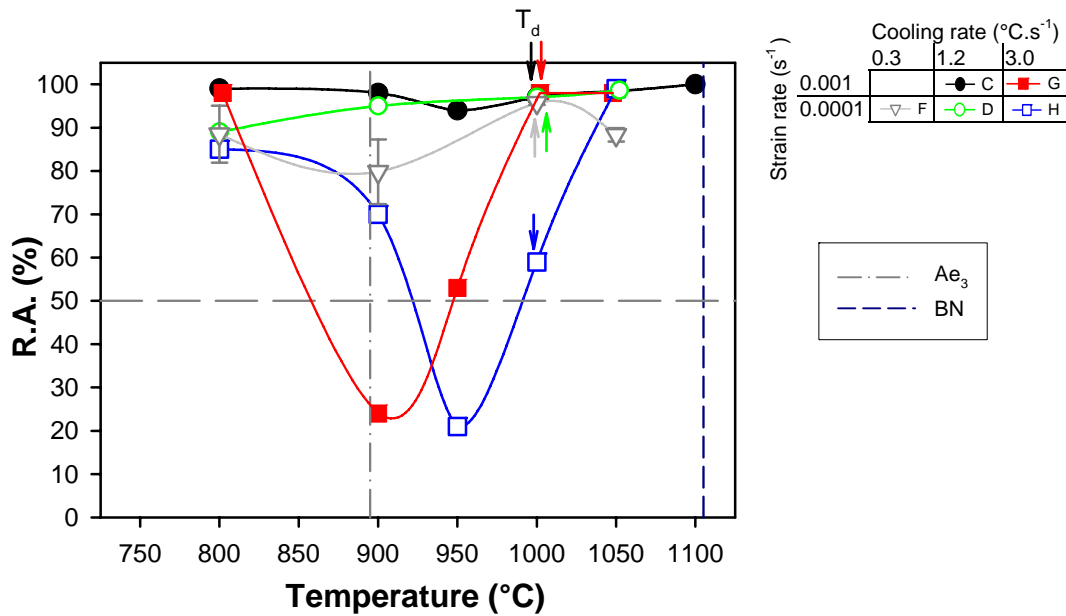


Figure 7.19: Reduction in area for steel B-2 as a function of testing temperature, strain rate and cooling rate.

vii The standard deviation is defined as:
$$S = \left[\frac{1}{n-1} \sum_{i=1}^n (x_i - \bar{x})^2 \right]^{\frac{1}{2}}$$
 x_i is the data sample, \bar{x} is the mean of the data samples and n is the number of samples.

7.5.4 Total elongation

Figure 7.20 shows that the highest elongation values resulted from an intermediate cooling rate ($1.2\text{ }^{\circ}\text{C}\cdot\text{s}^{-1}$) and a high strain rate (10^{-3} s^{-1}).

With increase in cooling rate from $1.2 - 3.0\text{ }^{\circ}\text{C}\cdot\text{s}^{-1}$, the minimum elongation values decreased by $\sim 30\%$ and the width of the elongation trough increased by $\sim 100\text{ }^{\circ}\text{C}$ for both strain rates.

An increase in strain rate moves the elongation recovery to higher temperatures by $\sim 50\text{ }^{\circ}\text{C}$ for the intermediate and fast strain rates.

Under low cooling rate and low strain rate conditions (F), the elongation curve was $\sim 10\%$ below that of the intermediate cooling rate (D) at $800\text{ }^{\circ}\text{C}$.

For each test, the elongation recovery occurred either at or below the Ae_3 temperature, implying that the formation of ferrite improves the elongation.

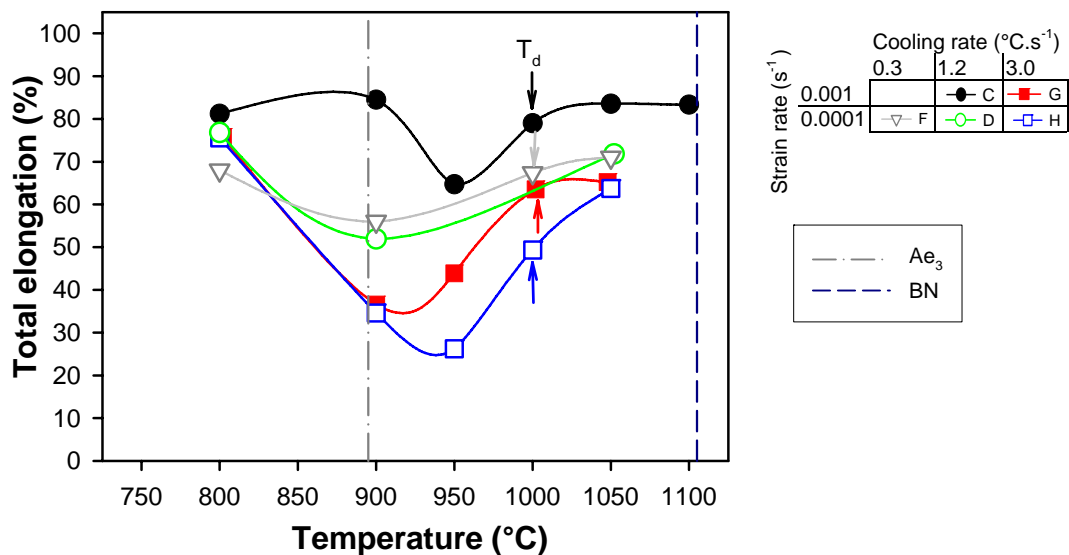


Figure 7.20: Elongation for steel B-2 as a function of testing temperature, strain rate and cooling rate.

7.5.5 Scanning electron microscopy

At high strain rate (10^{-3} s^{-1}):

- *Cooling rate $1.2 \text{ }^\circ\text{C}\cdot\text{s}^{-1}$* : At both $950 \text{ }^\circ\text{C}$ and $1050 \text{ }^\circ\text{C}$ (**Figure 7.21 a** and **b** respectively), voids of $1 - 4 \text{ }\mu\text{m}$ diameter were shown to contain precipitates which were analyzed as Fe-O-B-N and Fe-O-N (with B assumed to be the nitride-forming element). Although these precipitates are small and thus EDS analyses included some of the matrix area, it is still clear that the precipitates are BN-rich, with co-precipitation species such as FeO+BN. No interconnection of voids or internal cracking was seen in these high ductility samples.
- *Cooling rate $3.0 \text{ }^\circ\text{C}\cdot\text{s}^{-1}$* : At a testing temperature of $900 \text{ }^\circ\text{C}$ (**Figure 7.22 a**) many microvoids, containing precipitates such as Fe-O-B-N (with possible C contamination from graphite) and Fe-Mn-S-N *i.e.* FeO+BN and MnS+BN, were seen along prior austenite grain boundaries. These voids were extensively interconnected by cracks, explaining the poor ductility of this sample.

At $1000 \text{ }^\circ\text{C}$ (**Figure 7.22 b**), however, no internal cracking was observed. This is despite the presence of many voids of $1 - 5 \text{ }\mu\text{m}$ diameter, which were shown to contain large B-Fe-N precipitates (diameters $>1 \text{ }\mu\text{m}$), where the Fe is assumed to result from inclusion of the matrix in the EDS analysis.

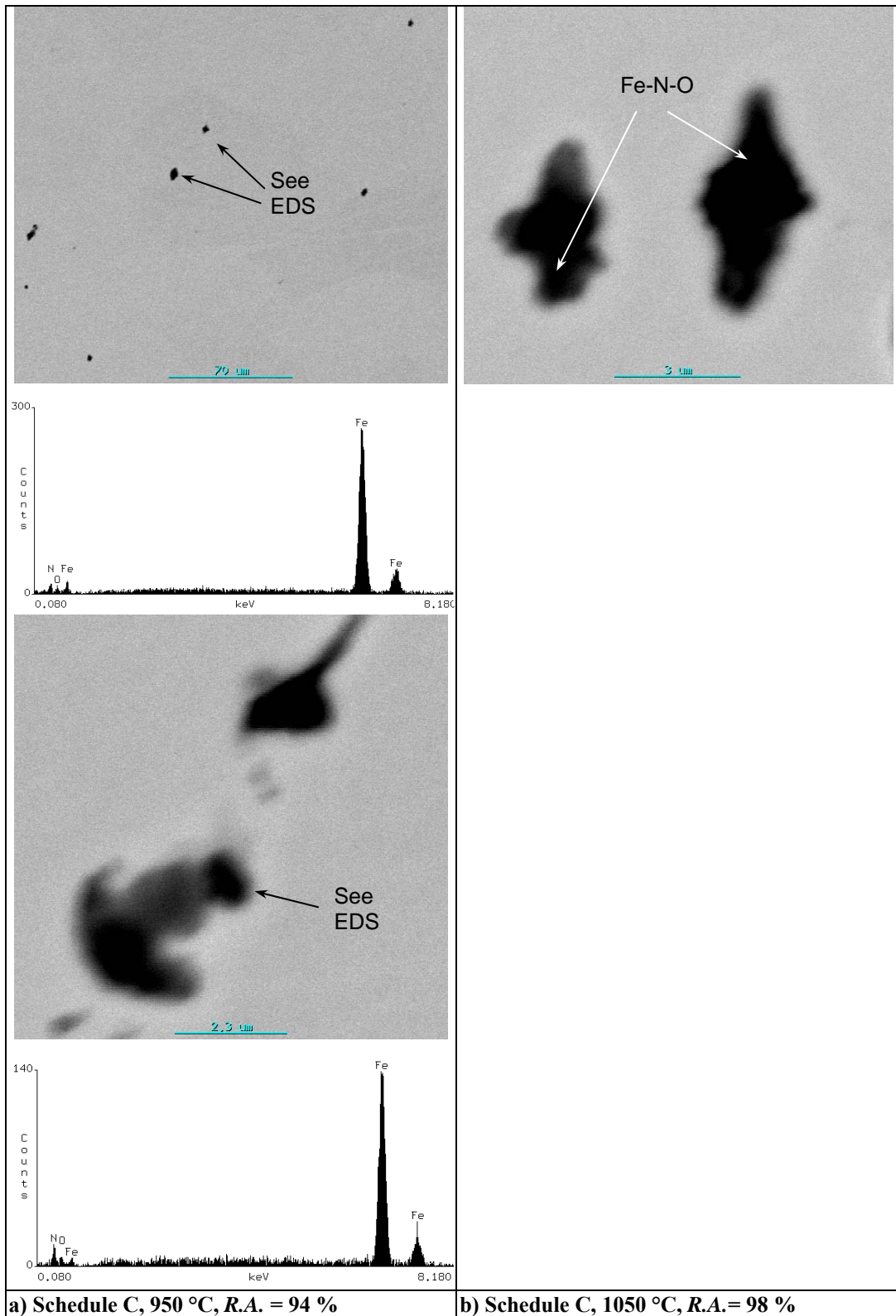


Figure 7.21: SEM backscatter images of Steel B-2 tested under Schedule C conditions: (10^{-3} s^{-1} , $1.2 \text{ }^\circ\text{C}\cdot\text{s}^{-1}$), showing large Fe-O-B-N precipitates.

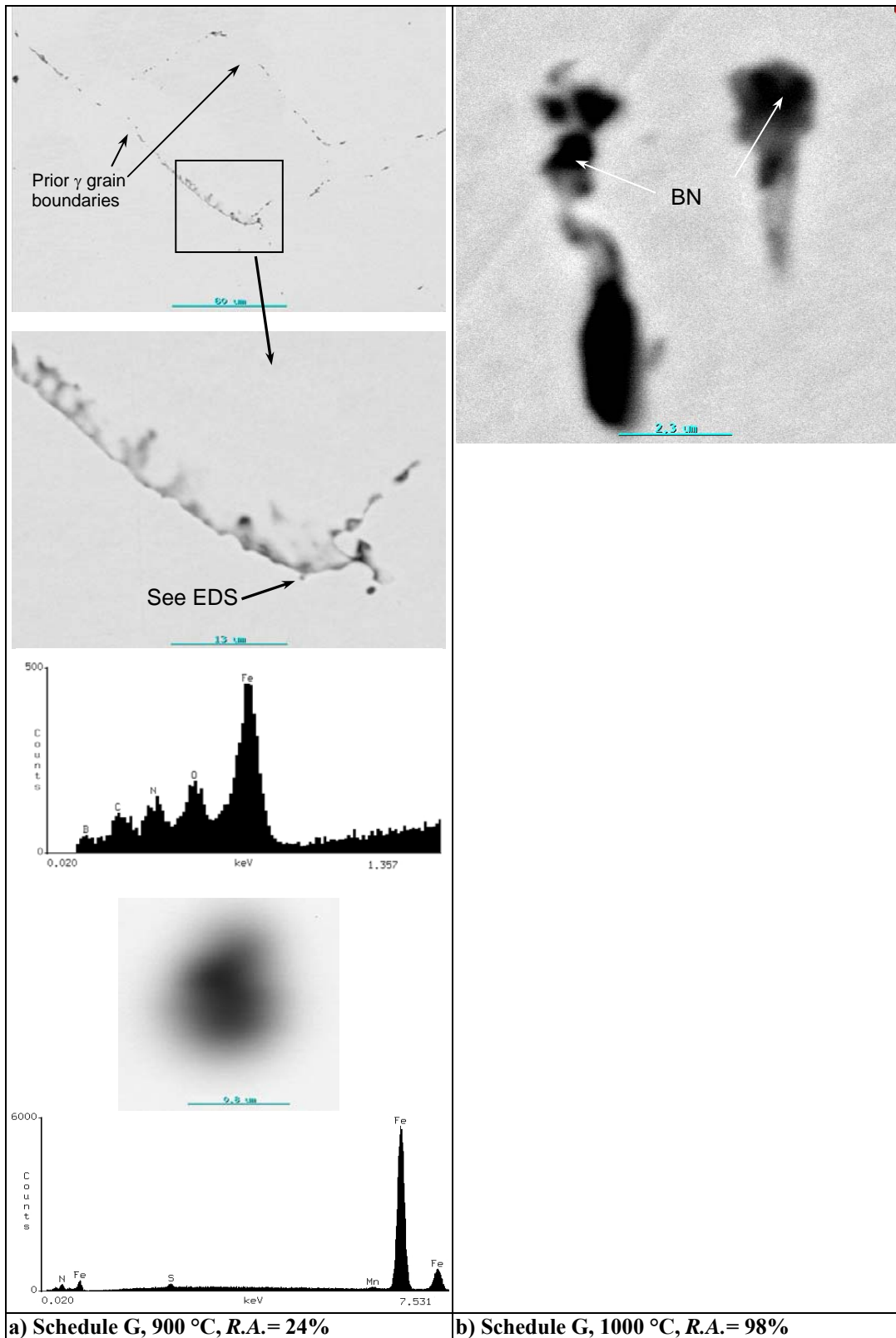


Figure 7.22: SEM backscatter images of Steel B-2 tested under Schedule G conditions: (10^{-3} s^{-1} , $3.0 \text{ }^\circ\text{C}\cdot\text{s}^{-1}$), showing various precipitates and microvoid coalescence.

At low strain rate (10^{-4} s^{-1}):

- *Cooling rate $0.3 \text{ } ^\circ\text{C}\cdot\text{s}^{-1}$* : (**Figure 7.23 a**) shows an EDS analysis of a precipitate containing Fe-Al-B-S-O-N (possibly as $\text{Al}_2\text{O}_3+\text{FeS}+\text{BN}$) in the sample tested at $900 \text{ } ^\circ\text{C}$.

At $1050 \text{ } ^\circ\text{C}$ (**Figure 7.23 b**), many small precipitates such as Fe-Mn-Al-Si-Cr-S-O were seen. The high Fe peak seen in the EDS analysis is due to the matrix interaction volume, as the precipitate is very small. The specimen showed very little internal cracking, and the precipitates were randomly positioned in the matrix.

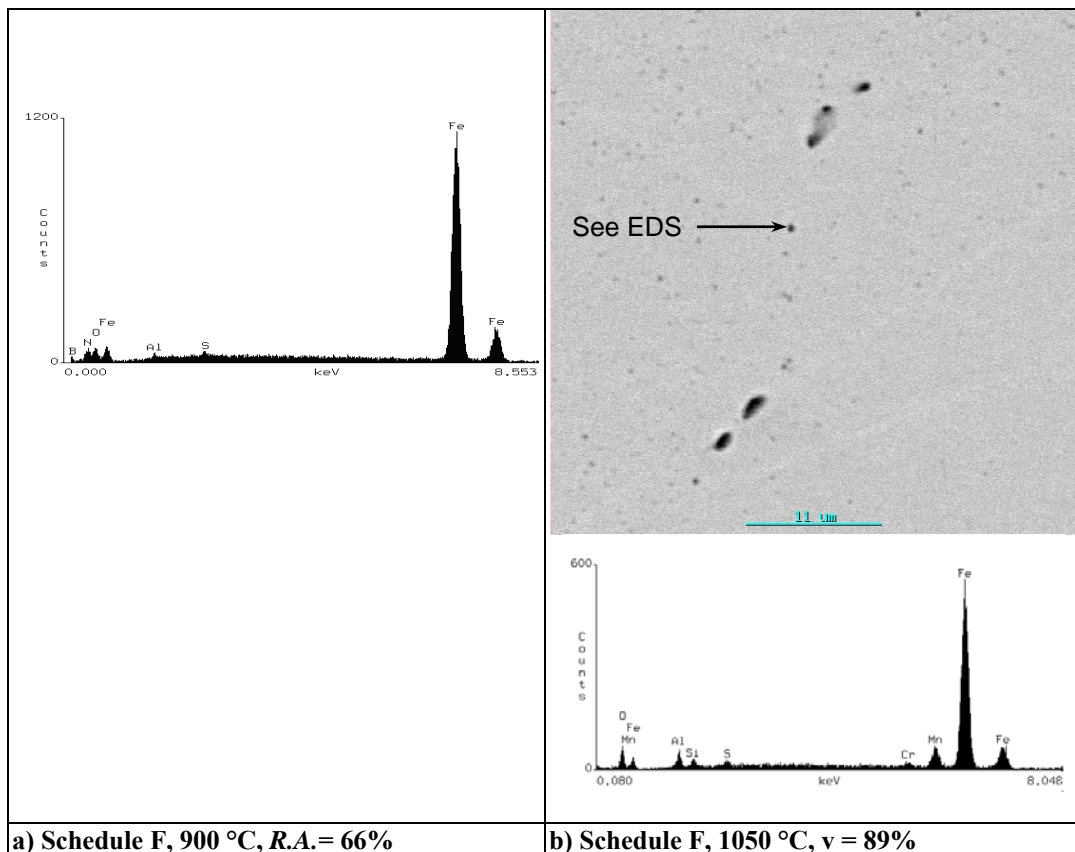


Figure 7.23: SEM backscatter images of Steel B-2 tested under Schedule F conditions: (10^{-4} s^{-1} , $0.3 \text{ } ^\circ\text{C}\cdot\text{s}^{-1}$), showing EDS analyses of various precipitates.

- *Cooling rate 1.2 °C.s⁻¹*: **Figure 7.24 a** (900 °C) shows large Fe-O-N precipitates (assumed to contain B as FeO+BN) in voids of 0.5 - 4 μm diameter. No inter-connection of voids was observed and the precipitates were randomly positioned in the matrix.

At 1050 °C (**Figure 7.24 b**), precipitates containing Al-O (as alumina Al₂O₃) and Fe-Mn-S-N-O (assumed to contain B as FeO+MnS+BN) were analyzed. This specimen also showed no internal damage by microvoid coalescence and the precipitates were randomly positioned in the matrix.

- *Cooling rate 3.0 °C.s⁻¹*: At 900 °C (**Figure 7.25 a**) many precipitates in voids of 1 – 2 μm diameter containing BN and BN+MnS were seen randomly positioned in the matrix.

At 950 °C (**Figure 7.25 b**), wedge-type intergranular cracking was clearly seen. Small precipitates containing MnS together with B, C, Fe and N were analyzed in the microvoids along these cracks (**Figure 7.25 c**).

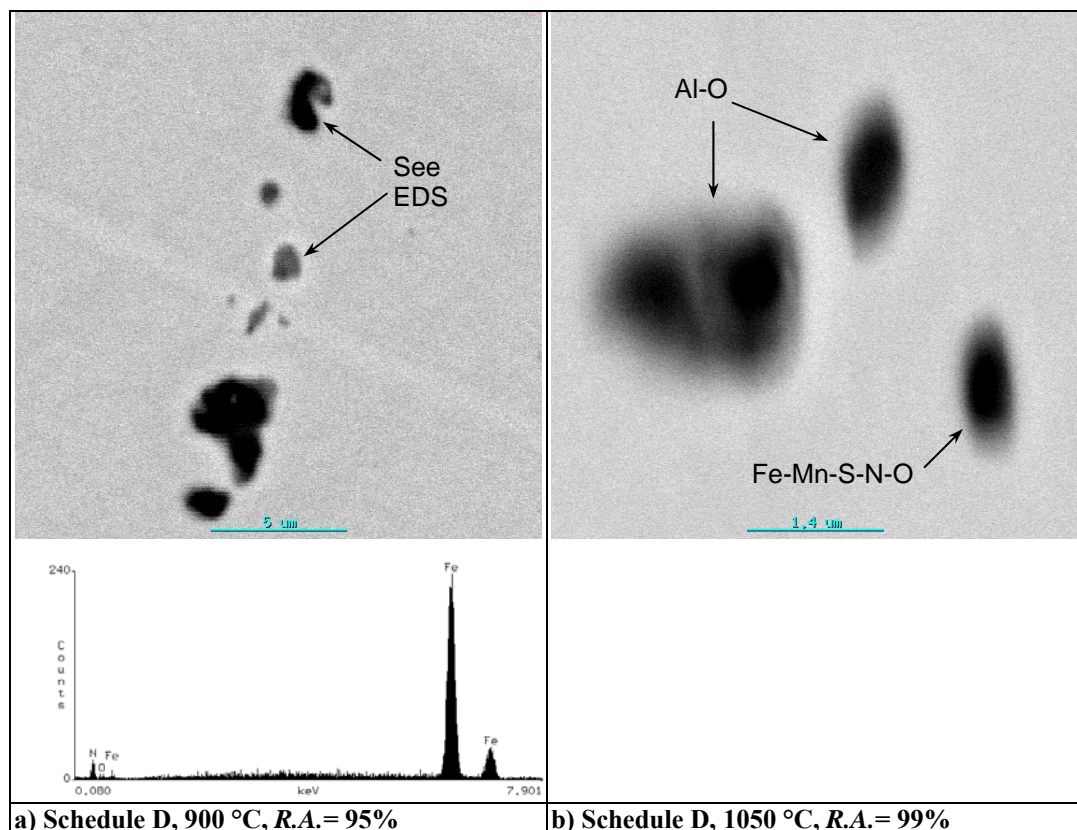


Figure 7.24: SEM backscatter images of Steel B-2 tested under Schedule D conditions (10^{-4} s^{-1} , 1.2 °C.s^{-1}).

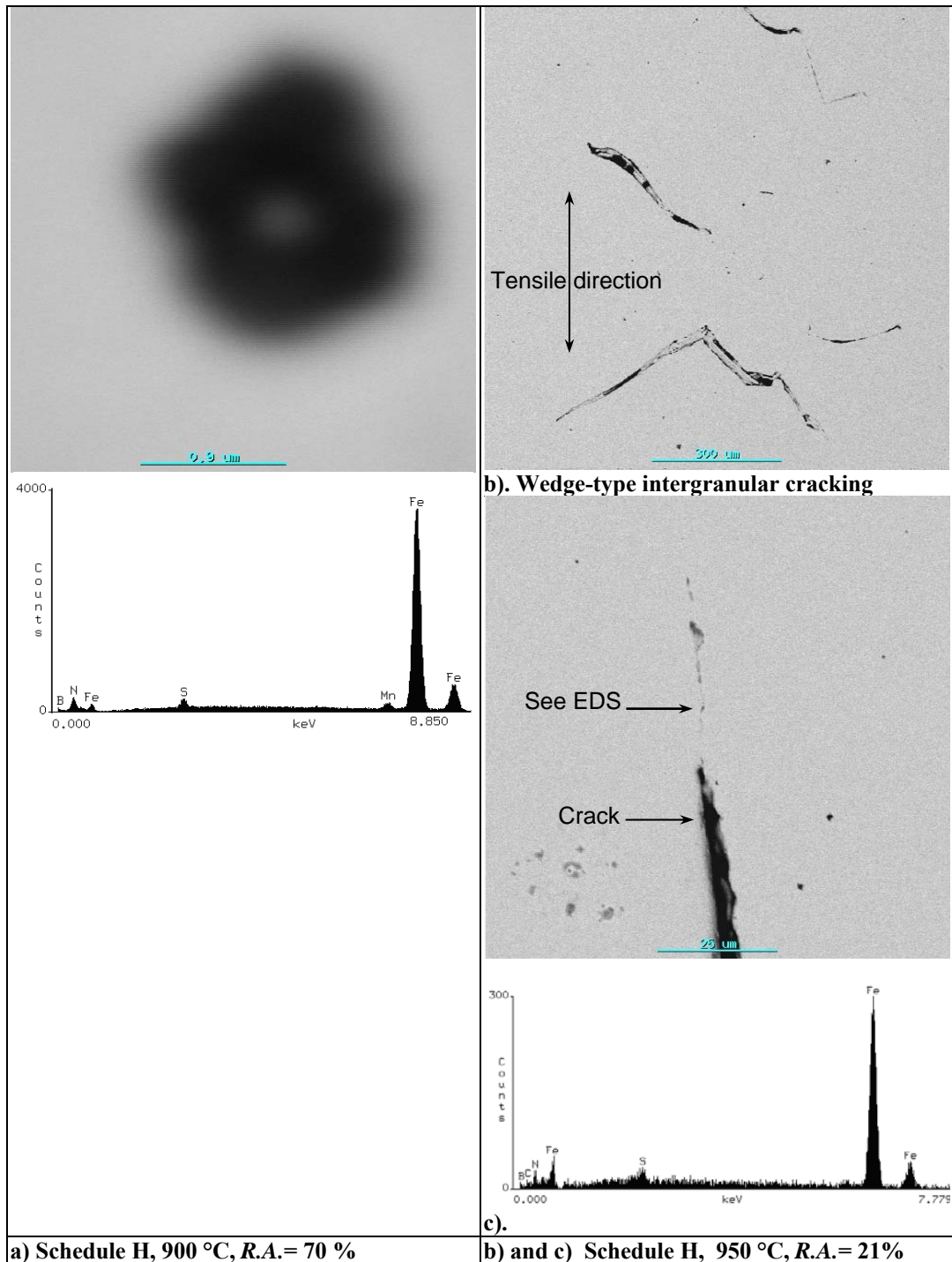


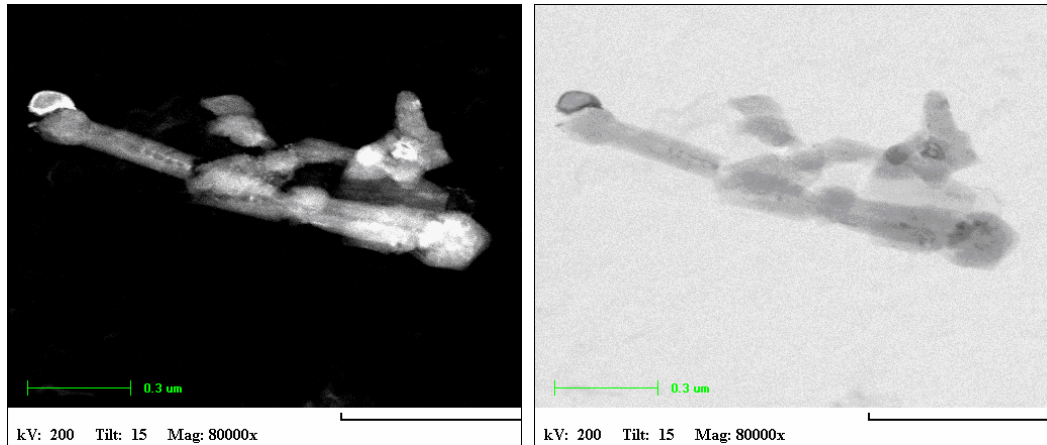
Figure 7.25: SEM backscatter images of Steel B-2 tested under Schedule H conditions (10^{-4} s^{-1} , $3.0 \text{ }^\circ\text{C}\cdot\text{s}^{-1}$), showing various precipitates and intergranular cracking.

7.5.6 Transmission electron microscopy

Figure 7.26 a and b show dark field and bright field images of a complex precipitate on a carbon extraction replica from a low ductility *B-2* sample ($R. A. = 24\%$) tested under Schedule G conditions (10^{-3} s^{-1} , $3.0^\circ\text{C}\cdot\text{s}^{-1}$). The X-ray maps and EDS spectrum (**Figure 7.26 c and d**) show that the filamentous precipitate consists mainly of BN with CuS caps on the ends. The carbon is assumed to come from the extraction replica. The CuS caps are white in the dark field image and dark grey in the bright field image (**Figure 7.26 a and b**).

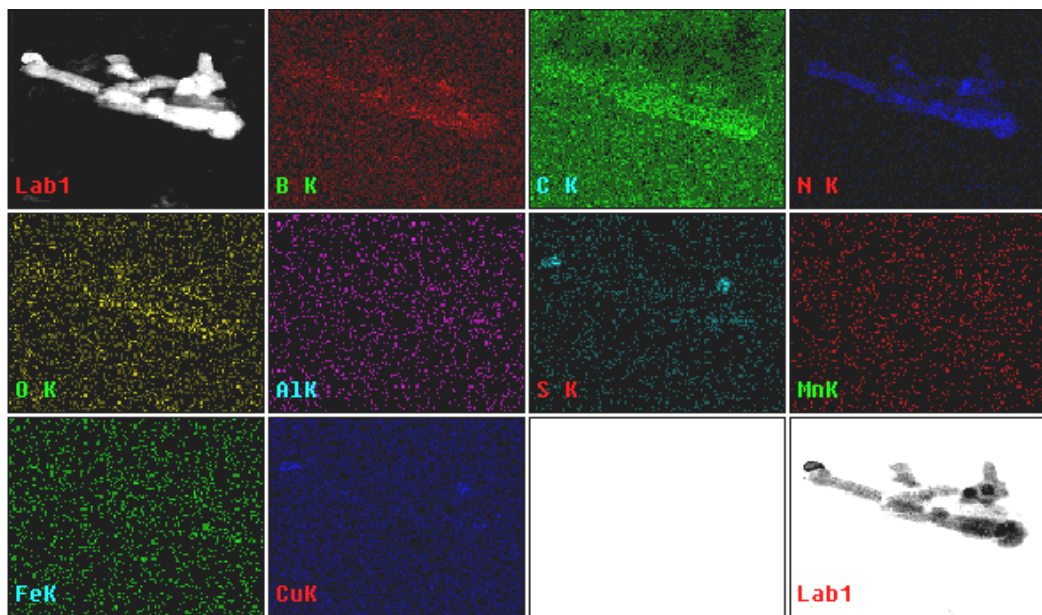
The images in **Figure 7.27** are from the same sample as in **Figure 7.26**. The bright field, dark field and X-ray maps show that the precipitates are shaped as long filaments and small spheres, and are pure Cu-S. The filaments are very fine, at ~ 20 nm wide and are up to $1 \mu\text{m}$ long. The spherical Cu-S precipitates have diameters of ~ 20 nm.

Figure 7.28 shows a dark field image and X-ray maps of a 300 nm diameter alumina inclusion from the steelmaking process covered by BN in steel *B-2* ($R. A. = 66\%$) tested under Schedule F conditions (10^{-4} s^{-1} , $0.3 \text{ }^\circ\text{C}\cdot\text{s}^{-1}$).

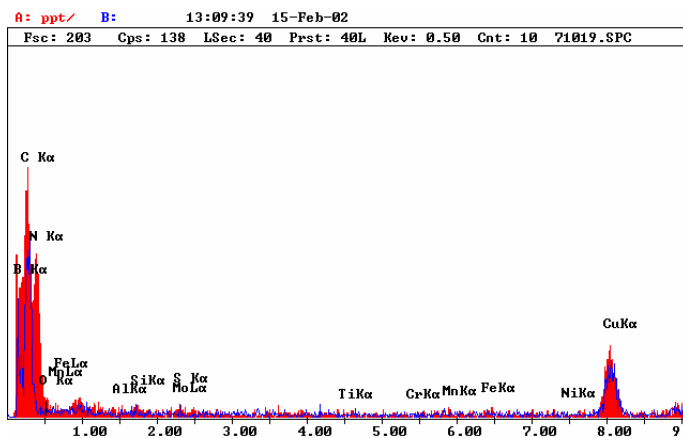


a) Dark field TEM image.

b) Bright field TEM image.

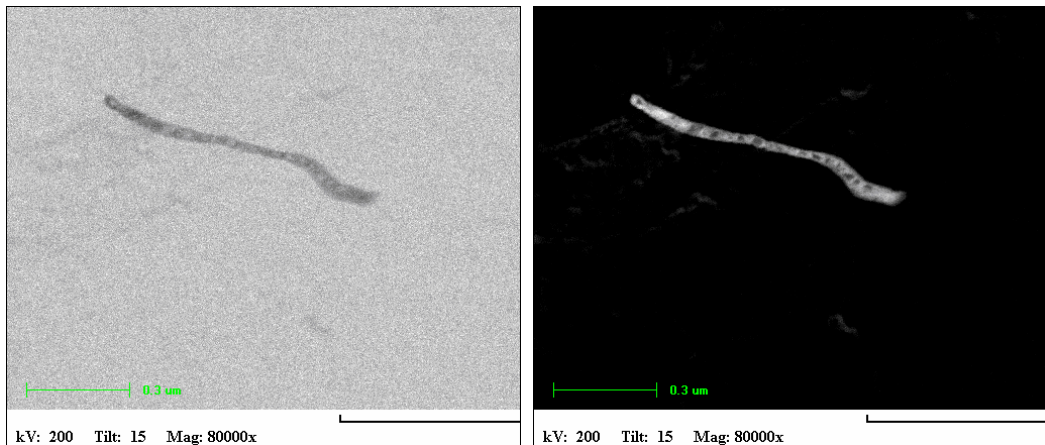


c) X-ray map of precipitate, showing BN core and CuS caps on the ends.



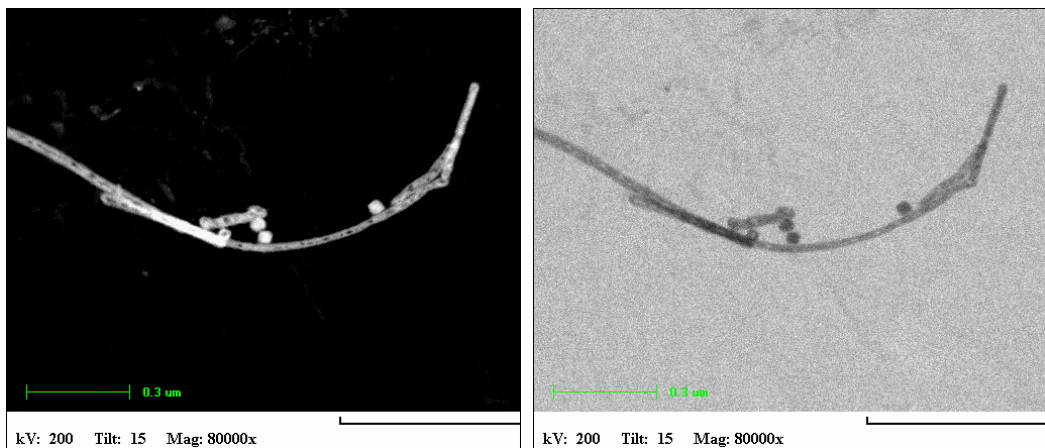
d) EDS spectrum of the precipitate.

Figure 7.26: Dark field image, bright field image, X-ray maps and EDS spectrum of a precipitate in Steel B-2 tested under Schedule G conditions (10^{-3} s^{-1} , $3.0^\circ\text{C}.\text{s}^{-1}$).



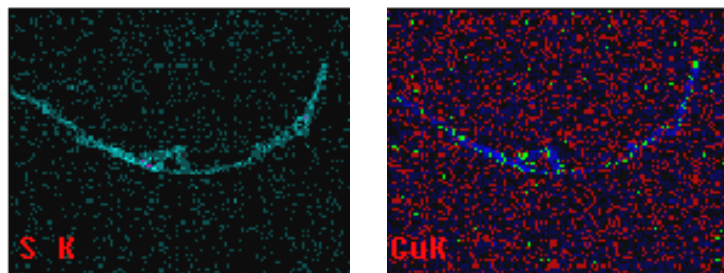
a) Bright field image.

b) Dark field image.



c) Dark field image.

d) Bright field image.



e) X-ray map of CuS filaments and spherical precipitates.

Figure 7.27: Bright field, dark field images and X-ray map of CuS filaments and small spherical CuS precipitates in steel *B-2* tested under Schedule G conditions (10^{-3} s^{-1} , $3.0^\circ\text{C}\cdot\text{s}^{-1}$).

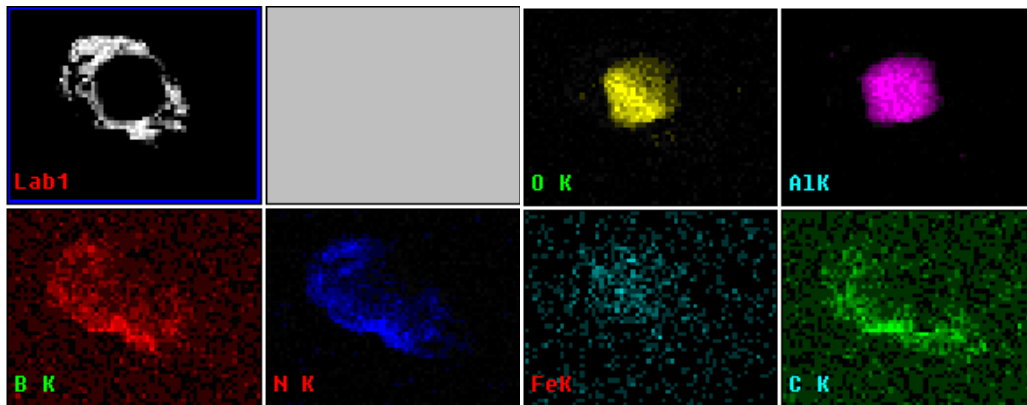
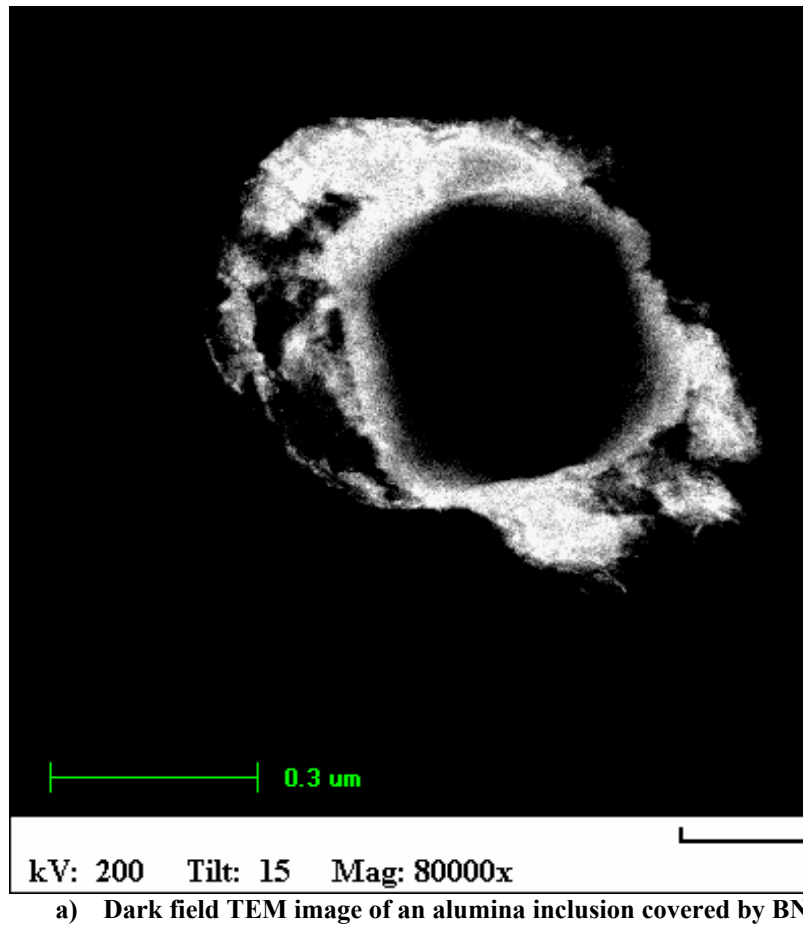


Figure 7.28: Dark field image and X-ray maps of an alumina inclusion covered by BN in steel *B-2* tested under Schedule F conditions (10^{-4} s^{-1} , $0.3 \text{ }^\circ\text{C}\cdot\text{s}^{-1}$).

7.6 AL-KILLED BORON STEEL *B-3*

7.6.1 Introduction

Figure 7.29 shows the engineering stress – elongation curves for steel *B-1*. The occurrence of dynamic recrystallisation can be detected on the stress – elongation curves by either an abrupt decrease or oscillations of the flow stress. The onset of dynamic recrystallisation is indicated by arrows on the graphs and the temperatures are listed in **Table 7.6**. The maximum strength values are shown as a function of testing temperature in **Figure 7.30**.

The percentage reduction in area (% *R. A.*) is shown as a function of testing temperature in **Figure 7.31** and the percentage total elongation is shown as a function of testing temperature in **Figure 7.32**.

Scanning electron microscopy (SEM) micrographs are shown in **Figure 7.33** to **Figure 7.35** and transmission electron microscopy (TEM) images with X-ray maps are shown in **Figure 7.36** and **Figure 7.37**.

The modelled Thermo-Calc™ TCF₃ calculated A_{e_3} temperature (895 °C - **Table 7.2**) and the BN temperature (Fountain, 1962) from **Table 7.4** are shown on the graphs.

Only 10 machined tensile specimens of steel *B-3* were available for testing due to lack of material. Two hot ductility tests had to be interrupted and cancelled due to problems with thermocouple contact. The total elongation results for the test performed at 950 °C under schedule C conditions (1.2 °C.s⁻¹, 10⁻³ s⁻¹), was measured directly from the broken tensile specimen, as the ASCII file saved on the data acquisition unit was corrupt.

Thus, there are only eight sets of data, which makes interpretation of the results difficult. However, the results can still be compared to the other Al-killed boron microalloyed steels.

7.6.2 Maximum strength

The highest S_u (Figure 7.29 and Figure 7.30) was achieved at 900 °C for testing conditions of intermediate cooling rate and high strain rate (schedule C). The lowest S_u values were found from 900 – 1050 °C for low strain rate and high cooling rate conditions (schedule H). The test “H”900 shows small oscillations in the strength-elongation curve in Figure 7.29, which was due to minor fluctuations in the testing temperature caused by over-control of temperature in the tensile test.

The Ae_3 temperature occurred slightly below the maximum S_u found under conditions of low strain rate and low cooling rate (schedule F).

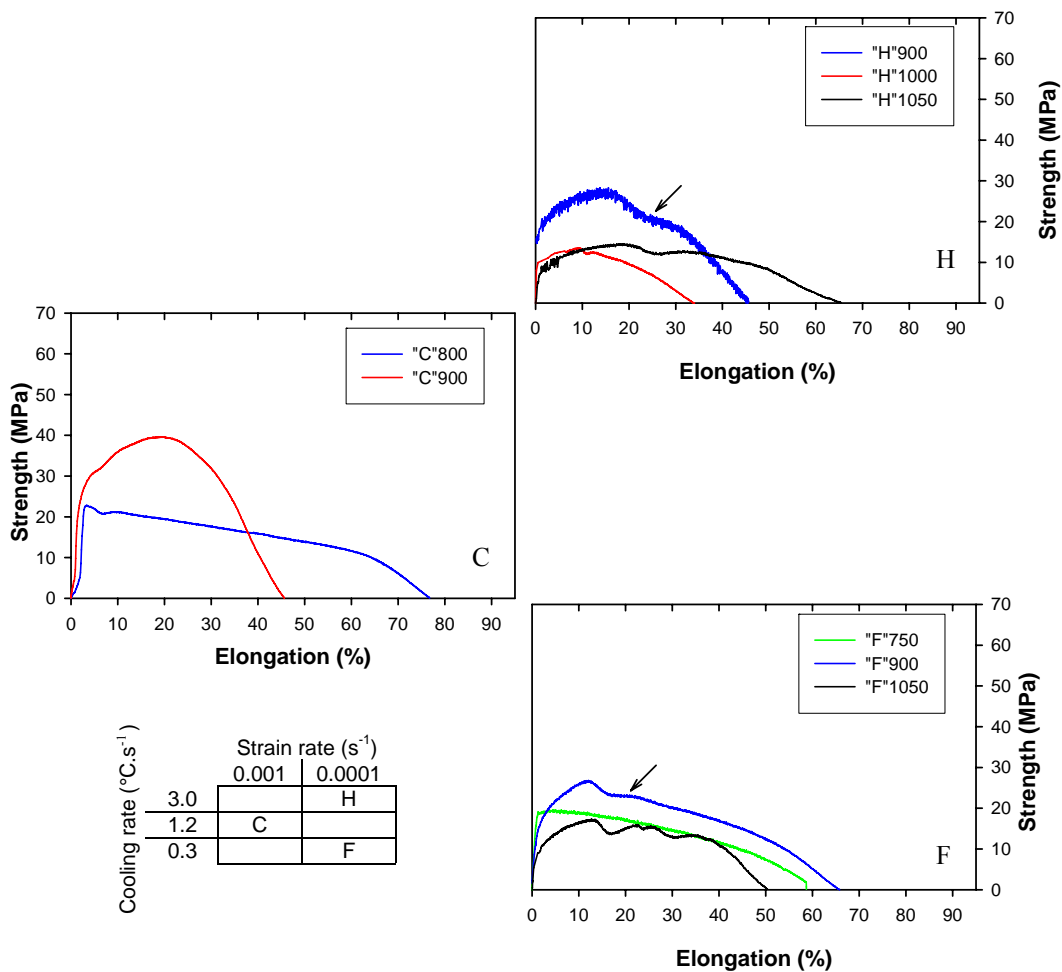


Figure 7.29: Engineering stress as a function of elongation for steel B-3. The key to the testing schedules is also shown. Arrows indicate the onset of dynamic recrystallisation.

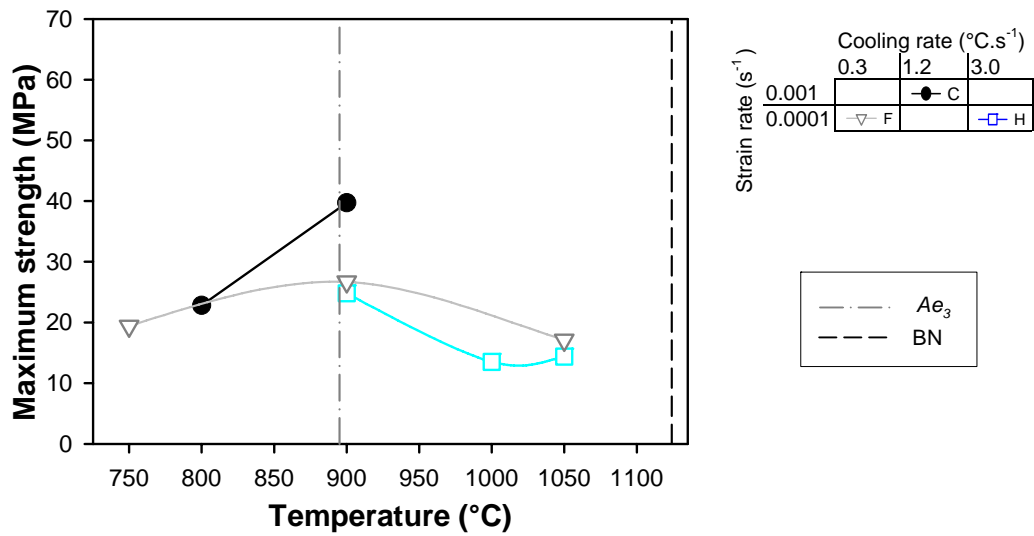


Figure 7.30: Maximum strength for steel B-3 as a function of testing temperature, strain rate and cooling rate.

7.6.3 Reduction in area

For all applied testing conditions, there was no significant change in % R.A. across the entire tested range from 750 – 1050 °C for steel B-3, as shown in Figure 7.31. No hot ductility trough was observed, and the reduction in area remained excellent at 91 – 98%.

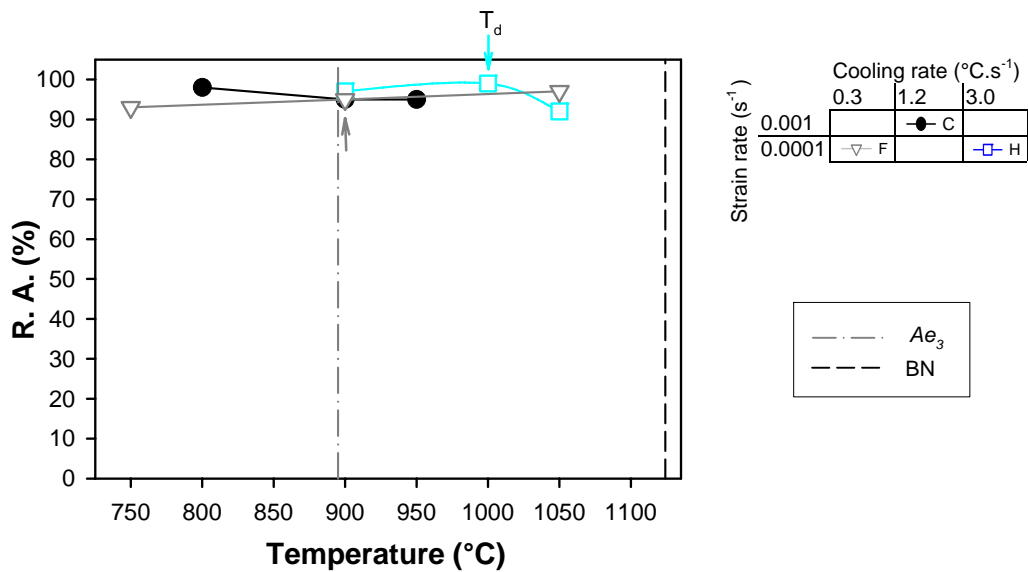


Figure 7.31: Reduction in area for steel B-3 as a function of testing temperature, strain rate and cooling rate.

7.6.4 Total elongation

For testing conditions C and H, elongation troughs were seen (Figure 7.32), with minima at 900 °C (schedule C) and between 900 – 1000°C (schedule H). Conversely, schedule F (low strain rate and low cooling rate) showed a slight maximum at 900 °C, which may be within error limits.

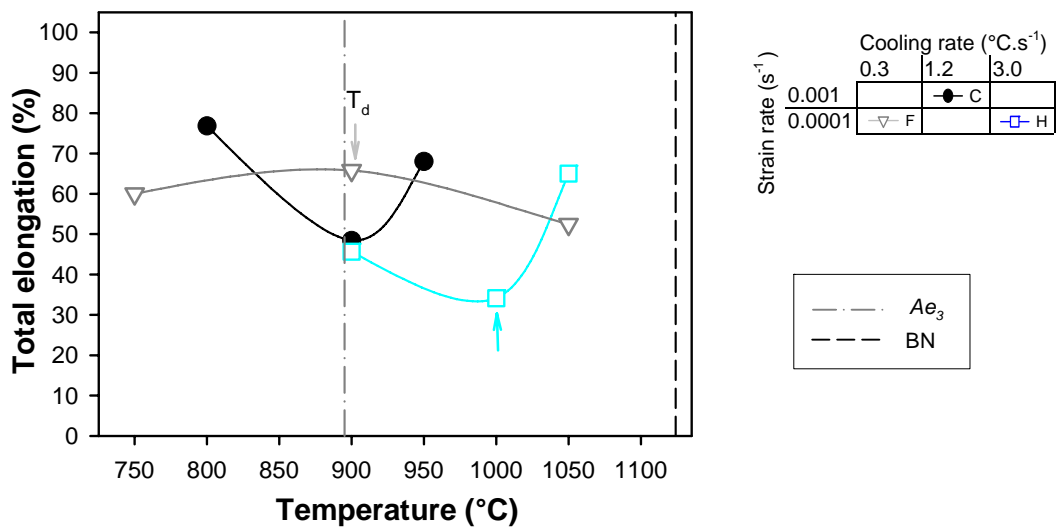


Figure 7.32: Elongation for steel B-3 as a function of testing temperature, strain rate and cooling rate.

7.6.5 Scanning electron microscopy

At high strain rate (10^{-3} s^{-1}):

- *Cooling rate $1.2 \text{ } ^\circ\text{C}\cdot\text{s}^{-1}$* : At $800 \text{ } ^\circ\text{C}$ (**Figure 7.33 a**), many large spherical precipitates containing Fe-Al-Mn-S-O (some also containing Si) were observed in voids with diameters of $0.5 - 2 \text{ } \mu\text{m}$. These voids were well-distributed in the matrix. A few small Fe-N and Fe-Mn-S-N (both assumed to contain B as BN and BN+MnS) precipitates were analyzed in voids of $\sim 0.7 \text{ } \mu\text{m}$ diameter. Limited cracking was seen between voids.

Precipitates containing FeO+MnS+BN were analyzed in the specimens tested at $900 \text{ } ^\circ\text{C}$ (**Figure 7.33 b**), and at $950 \text{ } ^\circ\text{C}$ (**Figure 7.33 c**) and Fe-O-N (FeO+BN) was also seen at $950 \text{ } ^\circ\text{C}$. These are all assumed to contain B, as previously discussed. No internal cracking between voids was seen in these two specimens.

At low strain rate (10^{-4} s^{-1}):

- *Cooling rate $0.3 \text{ } ^\circ\text{C}\cdot\text{s}^{-1}$* : **Figure 7.34 a** ($900 \text{ } ^\circ\text{C}$) shows many $2 - 4 \text{ } \mu\text{m}$ diameter voids containing complex precipitates such as FeO+MnS+BN and FeO+BN. No internal cracking was observed between precipitates.

At $1050 \text{ } ^\circ\text{C}$, (**Figure 7.34 b**), complex precipitates containing pure MnS with FeO+MnS+BN (with C in some areas) were analyzed in voids. No internal cracking was observed between the precipitates.

- *Cooling rate $3.0 \text{ } ^\circ\text{C}\cdot\text{s}^{-1}$* : At $900 \text{ } ^\circ\text{C}$ (**Figure 7.35 a**) large complex precipitates ($>1 \text{ } \mu\text{m}$) containing MnS+BN precipitates and Fe-N-B (BN) were observed, and at $1050 \text{ } ^\circ\text{C}$ (**Figure 7.35 b**), FeO+MnS+BN precipitates were analyzed. No internal cracking was observed in these two specimens.

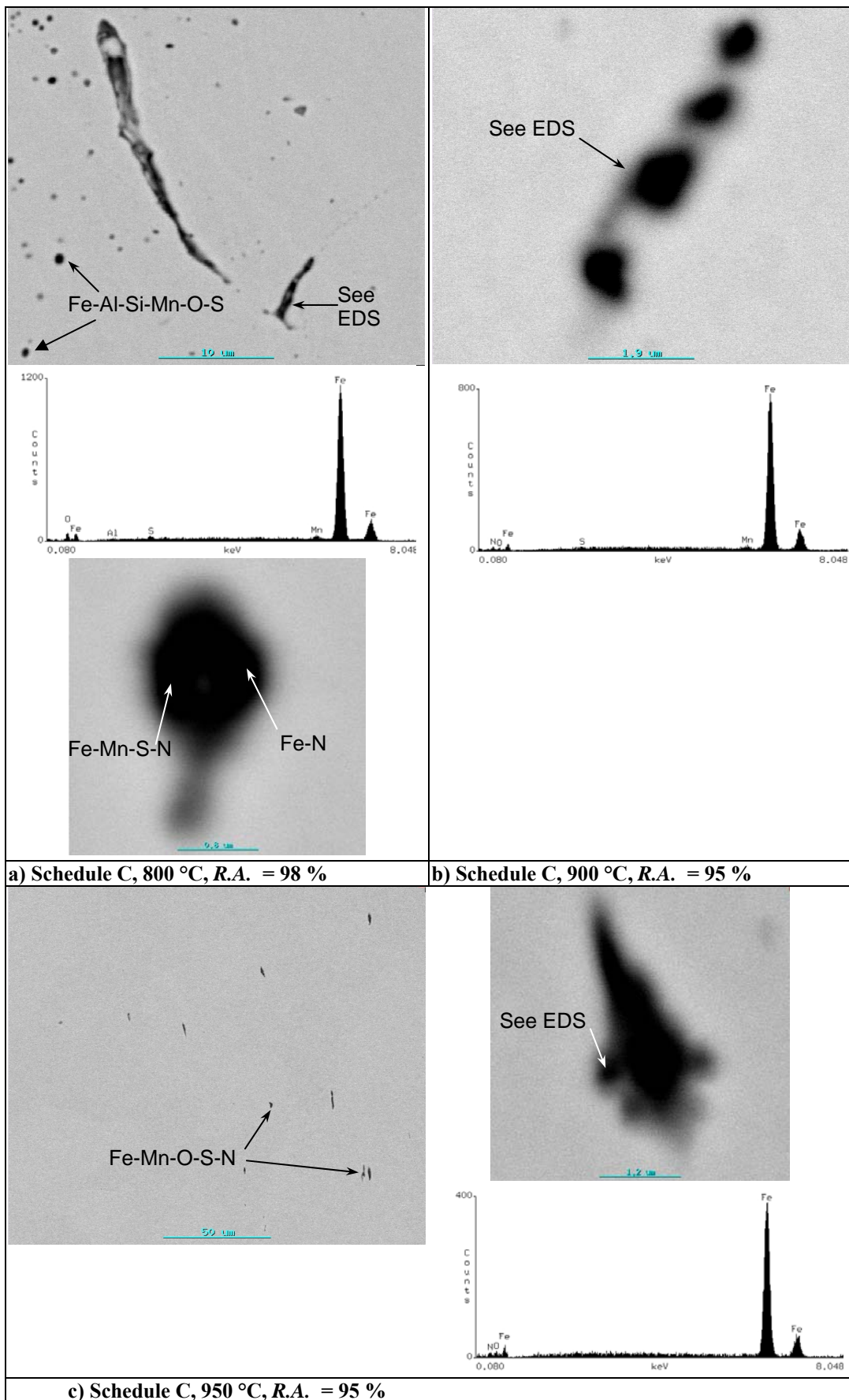


Figure 7.33: SEM backscatter images of Steel B-3 tested under Schedule C conditions: (10^{-3} s^{-1} , $1.2 \text{ }^\circ\text{C}\cdot\text{s}^{-1}$), showing various precipitates.

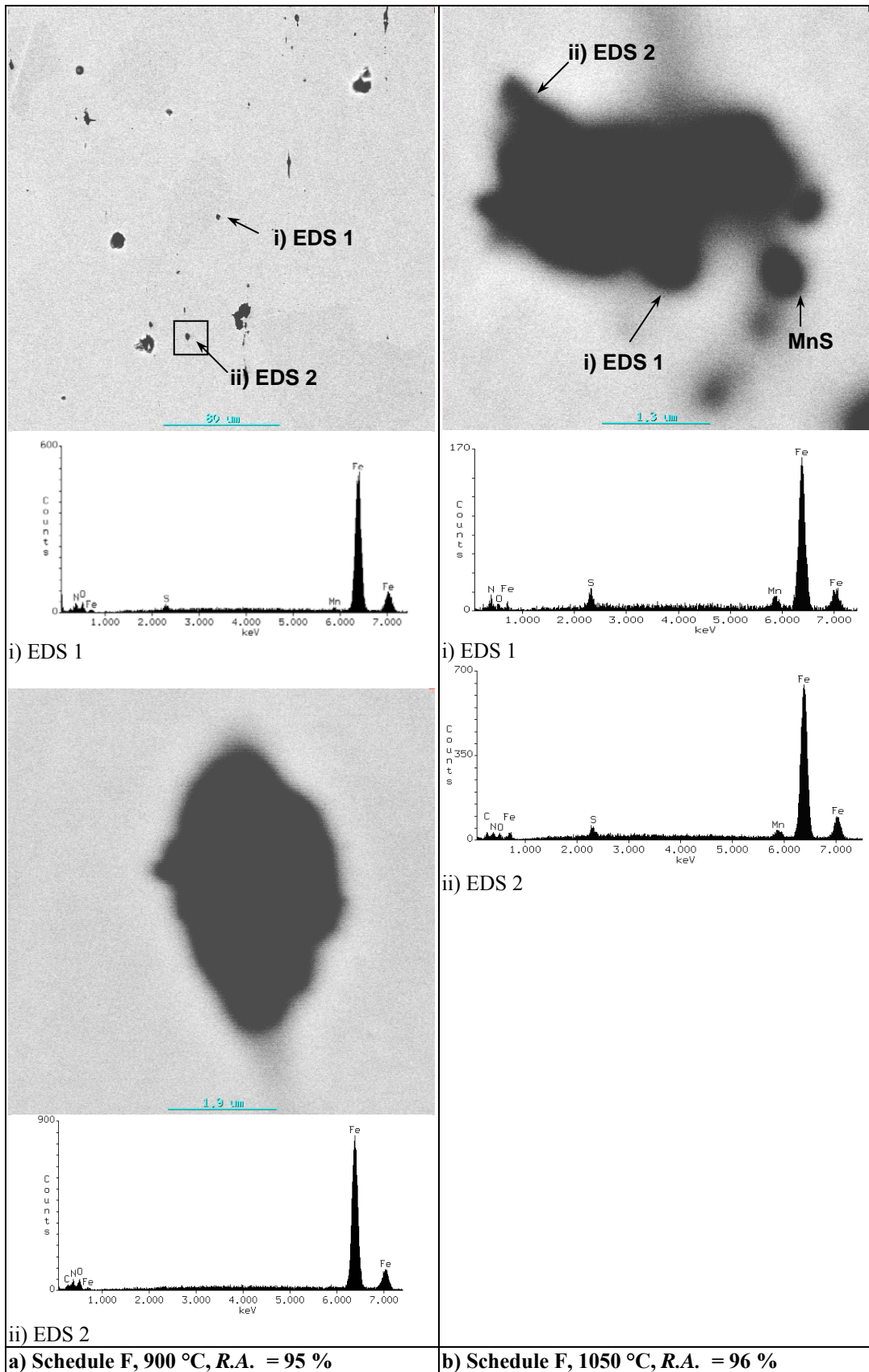


Figure 7.34: SEM backscatter images of Steel B-3 tested under Schedule F conditions: (10^{-4} s^{-1} , $0.3 \text{ }^\circ\text{C}\cdot\text{s}^{-1}$), showing large precipitates with varying compositions.

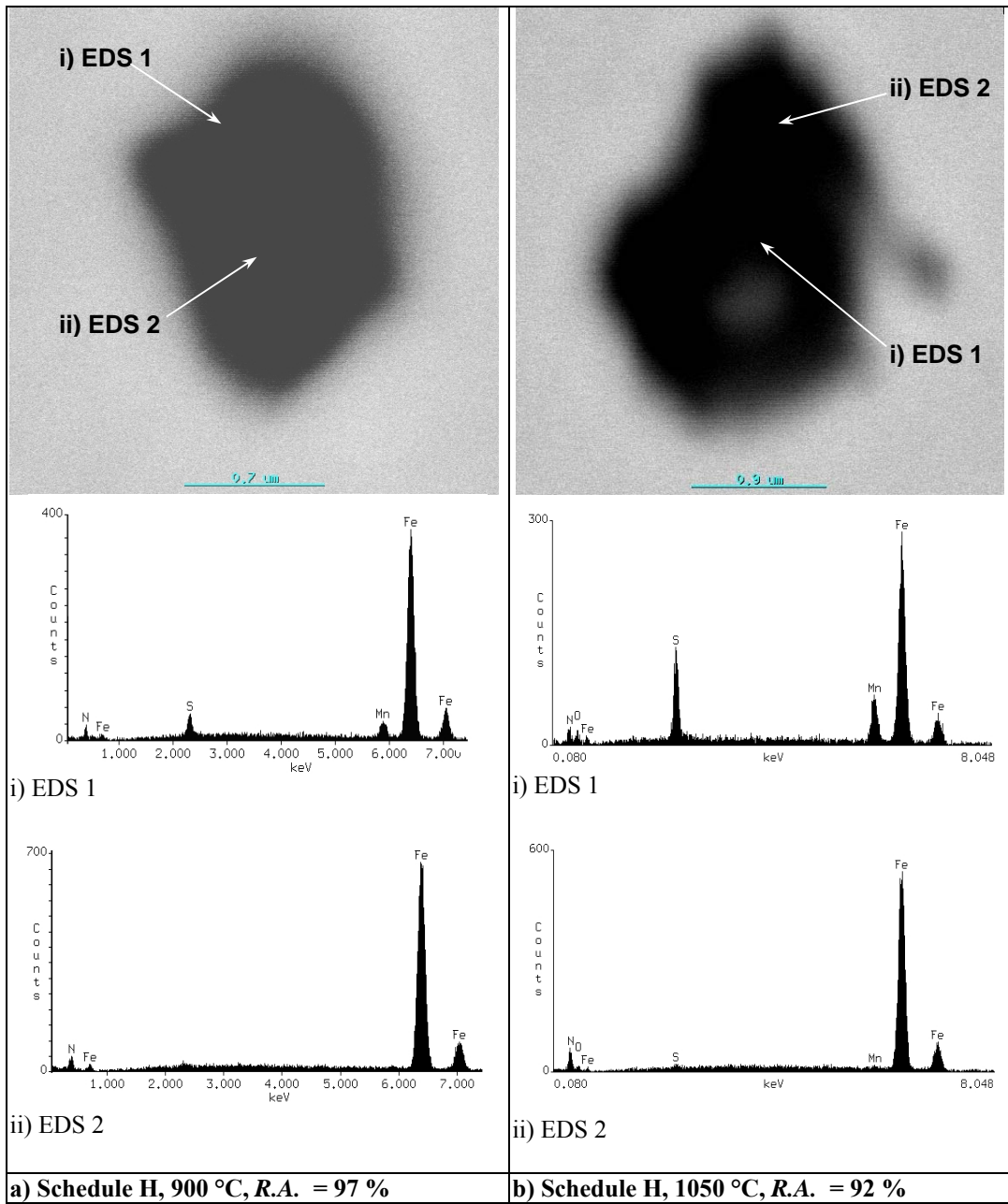
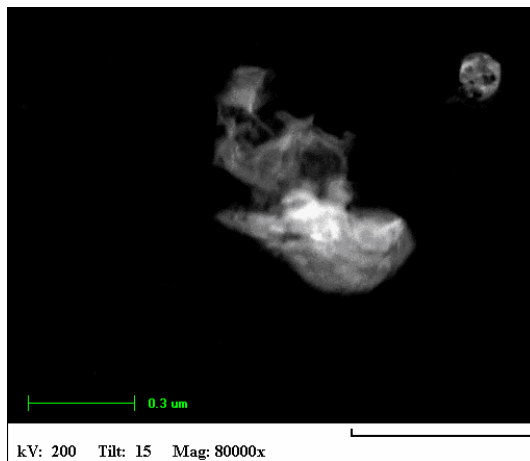


Figure 7.35: SEM backscatter images of Steel B-3 tested under Schedule H conditions: (10^{-4} s^{-1} , $3.0 \text{ }^\circ\text{C}\cdot\text{s}^{-1}$), showing complex precipitates.

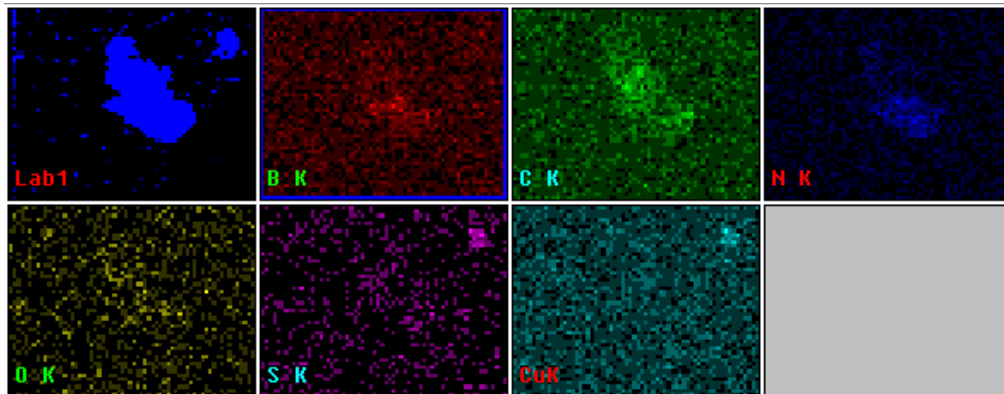
7.6.6 Transmission electron microscopy

Figure 7.36 shows a dark field image and X-ray maps of a ductile sample of Steel *B-3* ($R. A. = 96\%$) tested at $900\text{ }^{\circ}\text{C}$ under Schedule F conditions (10^{-4} s^{-1} , $0.3\text{ }^{\circ}\text{C}\cdot\text{s}^{-1}$). The images show a complex precipitate $\sim 500\text{nm}$ long (oxide with BN and C) and a smaller spherical CuS precipitate of $\sim 80\text{nm}$ diameter in the top right-hand corner.

Figure 7.37 a shows a dark field image another particle in the same *B-3* steel sample as above. **Figure 7.37 b** shows an EDS line scan across the precipitate that indicates a CuS precipitate, with surface areas covered by BN which show up as white on the dark field image (see peak at Point 6). In **Figure 7.37 c**, the X-ray maps also indicate a complex precipitate with a CuS core covered by BN.

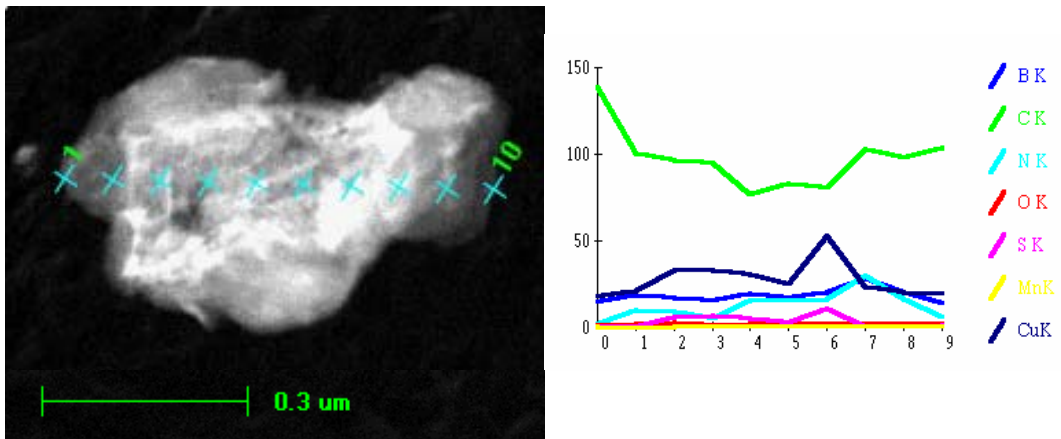


a) Dark field TEM image.



b) X-ray maps of the precipitates, showing BN in the larger precipitate and CuS in the smaller precipitate.

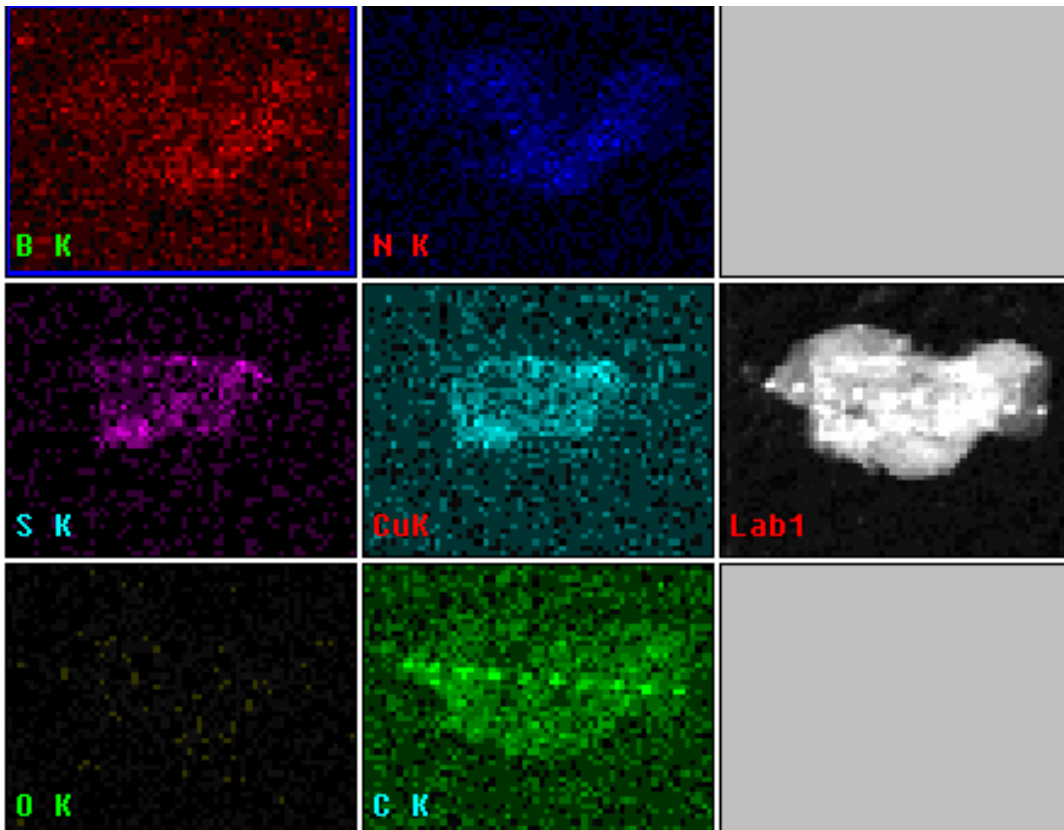
Figure 7.36: a) Dark field image b) X-ray maps of Steel *B-3* tested under Schedule F conditions (10^{-4} s^{-1} , $0.3\text{ }^{\circ}\text{C}\cdot\text{s}^{-1}$), showing a large, complex precipitate (oxide with BN and C) and a smaller CuS precipitate in the top right-hand corner.



kV: 200 Tilt: 15 Mag: 80000x

a) Dark field TEM image.

b) Line scan across the precipitate (see x marks).



c) X-ray map of precipitate, showing that the precipitate is mainly CuS covered by BN. The points from the line scan show as bright spots on the carbon X-ray map.

Figure 7.37: a) Dark field image b) Line scan across the precipitate and c) X-ray map of steel B-3 tested under Schedule F conditions (10^{-4} s^{-1} , $0.3 \text{ }^\circ\text{C}\cdot\text{s}^{-1}$), showing a complex precipitate (CuS+BN).

7.7 SUMMARY OF HOT DUCTILITY RESULTS FOR THE AL-KILLED BORON STEELS

The hot ductility results are summarised in **Table 7.6**, listing 50% low temperature ductility recovery (low T) and 50% high temperature ductility recovery (high T), the minimum ductility temperature (and associated % *R. A.*) and the onset temperature of dynamic recrystallisation T_d (and associated % *R. A.*). The results are ordered according to the steel, strain rates, cooling rates and Schedule (C, D, F, G and H). Note that in B-2 the ductility only decreases below 50% at a cooling rate of $3.0\text{ }^\circ\text{C.s}^{-1}$, and in B-3 the lowest ductility is 92%.

Table 7.6: Summary of the hot ductility results for the Al-killed boron steels.

Steel	Cooling Rate ($^\circ\text{C.s}^{-1}$)	Strain rate (s^{-1})							
		10^{-3}				10^{-4}			
		Low T ($^\circ\text{C}$)	Min. <i>R.A.</i>	High T ($^\circ\text{C}$)	T_d $^\circ\text{C}$ (%)	Low T ($^\circ\text{C}$)	Min. <i>R.A.</i>	High T ($^\circ\text{C}$)	T_d $^\circ\text{C}$ (%)
B-1	3.0	G 850	950 (18)	1020	>1000 (>22)	H 825	900 (20)	950	1000 (86)
	1.2	C 880	950 (30)	970	1000 (96)	D 835	900 (18)	950	1000 (60)
	0.3					F 825	900 (15)	950	1000 (97)
B-2	3.0	G 850	900 (25)	950	1000 (98)	H 925	950 (22)	990	1000 (59)
	1.2	C -	950 (95)	-	950 (95)	D -	800 (90)	-	1000 (97)
	0.3					F -	900 (80)	-	1000 (96)
B-3	3.0					H -	900 (96)	-	1000 (93)
	1.2	C -	900 (94)	-	>900 (>95)				
	0.3					F -	750 (92)	-	900 (95)

7.8 EFFECT OF STRAIN RATE ON HOT TENSILE BEHAVIOUR IN THE AL-KILLED BORON STEELS

7.8.1 Maximum strength

Overall, a decrease in strain rate from 10^{-3} to 10^{-4} s⁻¹ had the effect of decreasing the maximum strength (S_u) in steels *B-1* and *B-2*, as seen in **Figure 7.38**. This can be explained by two possible mechanisms, depending on the testing temperature:

- Increased dynamic recovery of austenite at temperatures above 900 °C *i.e.* around the A_{e3} (Michalak, 1991).
- Increased deformation-induced ferrite, as there is more time available for transformation (Mintz and Jonas, 1994). This would explain the lower S_u values for *B-1* and *B-2* with decrease in strain rate at temperatures below 900 °C. The S_u oscillation appears to have moved to higher temperatures in steel *B-2*. Some $\gamma \rightarrow \alpha$ transformation could have occurred at a programmed testing temperature of 900 °C, which is within 1% experimental error of the A_{e3} temperature (895 °C). The actual testing temperature can vary by up to 10 °C *i.e.* 895 - 905 °C. As the work hardening of γ is highest just prior to transformation, the maximum strength increases. When the softer deformation-induced ferrite film begins to form, the S_u drops substantially, which could account for the lower S_u at a programmed testing temperature of 900 °C.

7.8.2 Reduction in area

The overall influence of strain rate on reduction in area is not clear (**Figure 7.39**). In steel *B-1*, decreasing the strain rate appears to cause a narrower ductility trough at 3.0 °C.s⁻¹ (**Figure 7.40 a**), and a wider trough and a lower minimum *R. A.* at 1.2 °C.s⁻¹ (**Figure 7.40 b**). However, in steel *B-2* at 3.0 °C.s⁻¹, the trough was merely shifted to higher temperatures (**Figure 7.40 c**) and at 1.2 °C.s⁻¹, the excellent ductility remained unchanged with change in strain rate (**Figure 7.40 a**).

7.8.3 Total elongation

The detrimental effects of low strain rate on elongation are much clearer than the effects on reduction in area (**Figure 7.42**). By lowering the strain rate from 10^{-3} to 10^{-4} s^{-1} , the elongation troughs for both *B-1* and *B-2* at 1.2 and 3.0 $^{\circ}C.s^{-1}$ were substantially widened and the minimum elongation values were decreased. Thus, it is clear that decreasing the strain rate had a negative effect on total elongation, and hence, on hot ductility in Al-killed boron steels *B-1* and *B-2*.

7.9 EFFECT OF COOLING RATE ON HOT TENSILE BEHAVIOUR IN THE AL-KILLED BORON STEELS

7.9.1 Maximum strength

Steel *B-1* showed slightly lower maximum strength (S_u) with decreasing cooling rate from 3.0 - 1.2 $^{\circ}C.s^{-1}$ (high strain rate) and from 3.0 – 0.3 $^{\circ}C.s^{-1}$ (low strain rate), as seen in **Figure 7.38**.

At high strain rate there was no difference in S_u with cooling rate in steel *B-2*. At low strain rate there was no marked change in S_u with decrease in cooling rate from 3.0 – 1.2 $^{\circ}C.s^{-1}$, whereas there was an increase in S_u at 900 $^{\circ}C$ with decrease in cooling rate from 1.2 – 0.3 $^{\circ}C.s^{-1}$.

Steel *B-3* showed no significant change in S_u with decrease in cooling rate from 3.0 – 0.3 $^{\circ}C.s^{-1}$ at low strain rate.

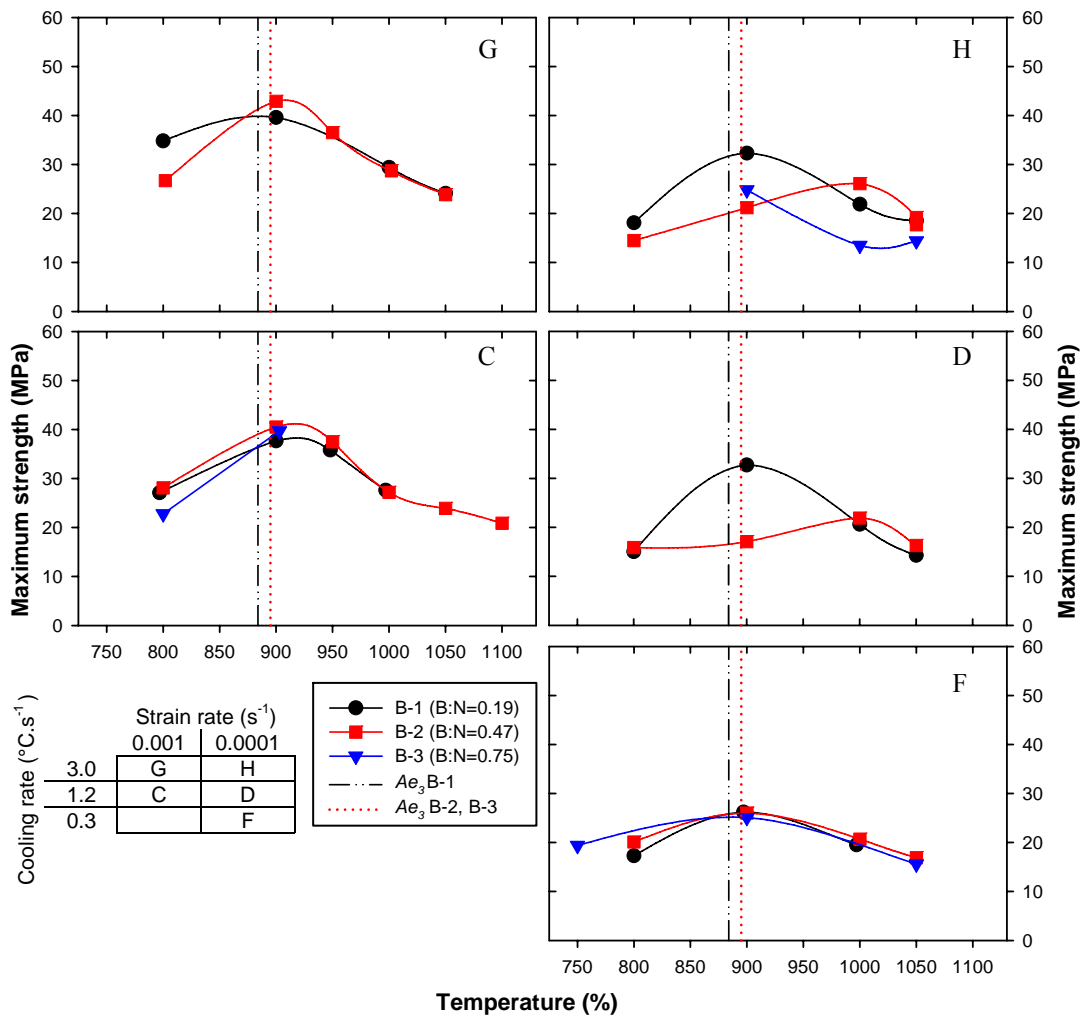


Figure 7.38: The effect of composition (increase in B:N ratio), strain rate and cooling rate on maximum strength in Al-killed boron steels *B-1*, *B-2* and *B-3*. The A_{e3} temperatures of *B-1* (888 °C) *B-2* and *B-3* (both 895 °C) are shown.

7.9.2 Reduction in area

As shown in **Figure 7.39**, decreasing the cooling rate from $3.0 - 1.2 \text{ } ^\circ\text{C}\cdot\text{s}^{-1}$ significantly improved the hot ductility in *B-2* at both strain rates (**Figure 7.41 c and d**), and slightly improved the ductility for *B-1* at 10^{-3} s^{-1} (**Figure 7.41 a and b**). This is also confirmed in the contour plots in **Figure 7.43**, comparing **a**) to **b**) and **c**) to **d**). A possible mechanism is reported by Yamamoto *et al.* (1987), who found marked ductility improvement with decrease in cooling rate from $20 - 0.1 \text{ } ^\circ\text{C}\cdot\text{s}^{-1}$, which promoted matrix precipitation of coarse BN and reduced grain boundary precipitation of BN and $\text{Fe}_{23}(\text{C},\text{B})_6$ (see **Section 2.5.6**). In the tested range, *B-3* was insensitive to both cooling rate and strain rate, as the ductility remained excellent in the temperature range $900 - 1000 \text{ } ^\circ\text{C}$.

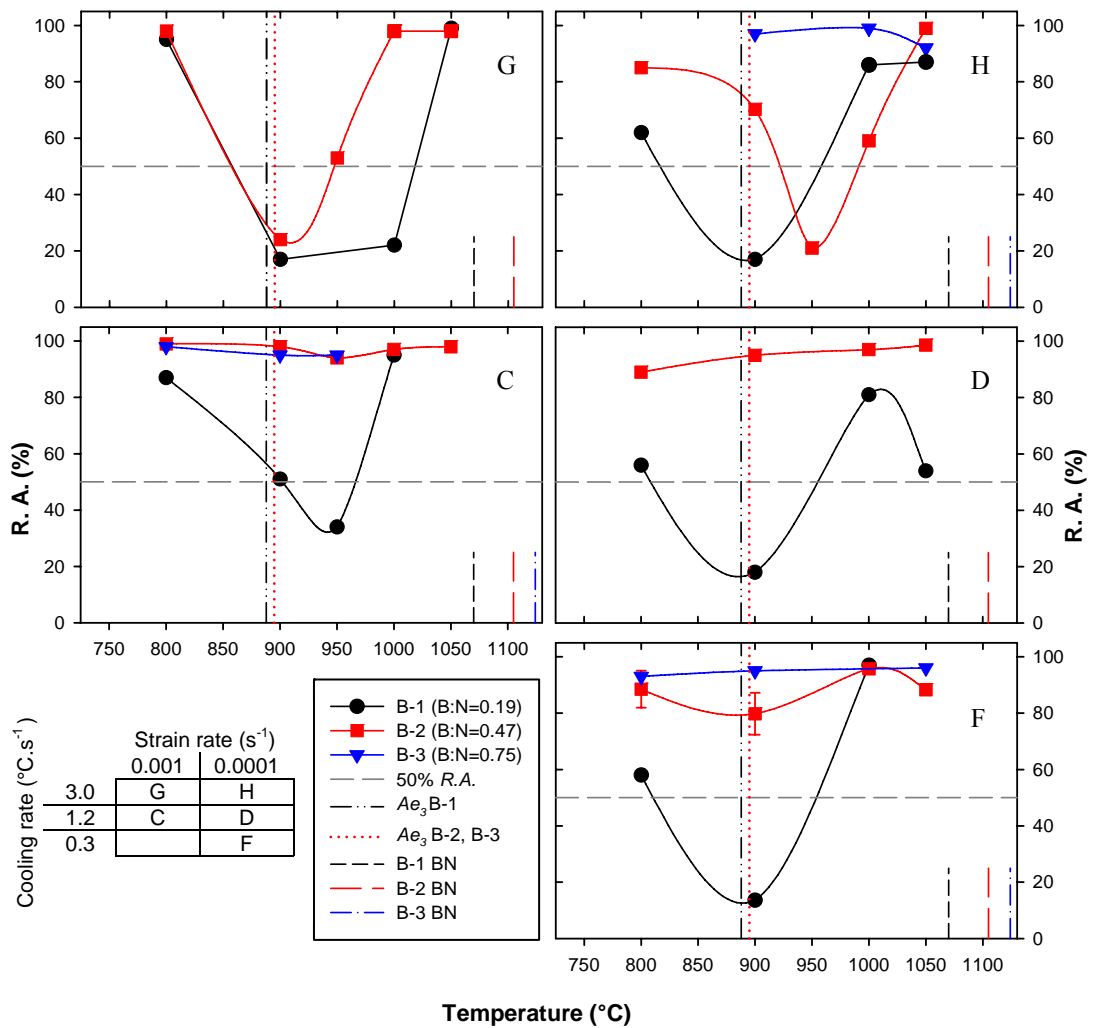
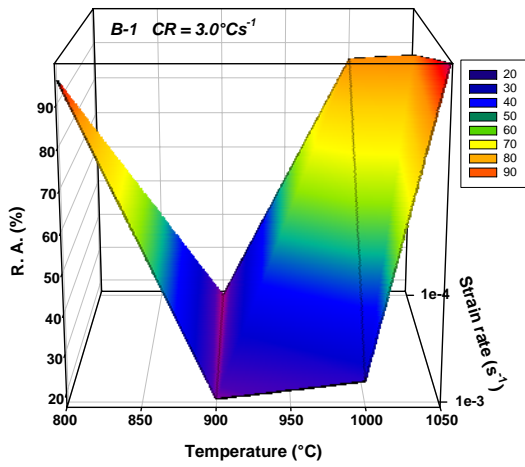
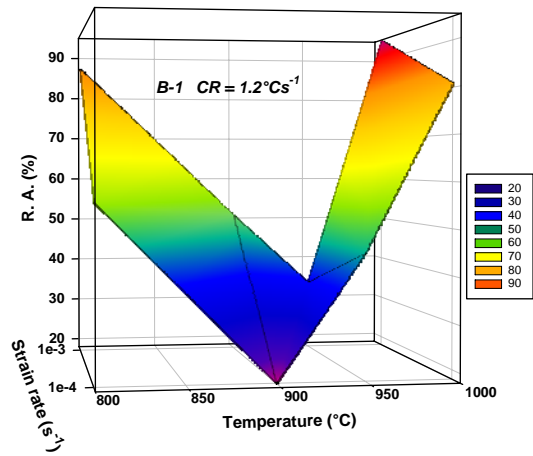


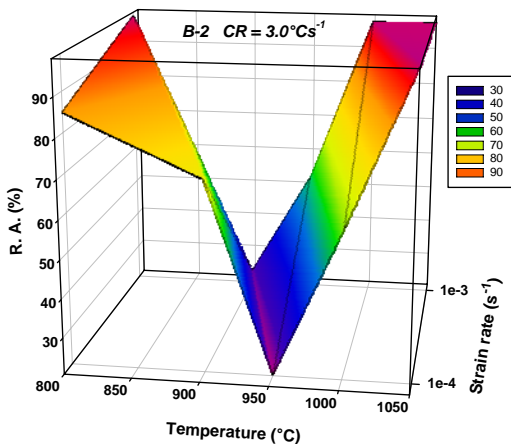
Figure 7.39: The effect of composition (increase in B:N ratio), strain rate and cooling rate on reduction in area in Al-killed boron steels *B-1*, *B-2* and *B-3*. The A_{e_3} and BN dissolution temperatures for the three steels are shown.



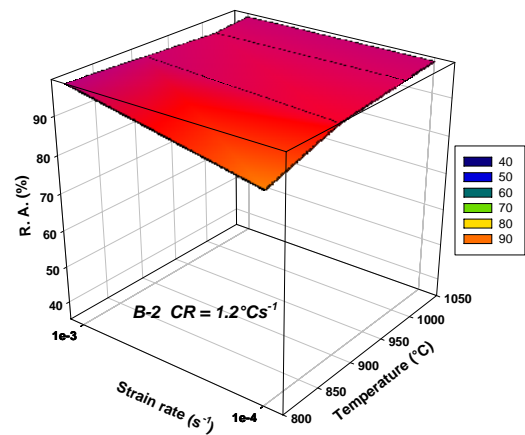
a) Steel *B-1*, cooling rate = $3.0\text{ }^{\circ}\text{C}\cdot\text{s}^{-1}$



b) Steel *B-1*, cooling rate = $1.2\text{ }^{\circ}\text{C}\cdot\text{s}^{-1}$

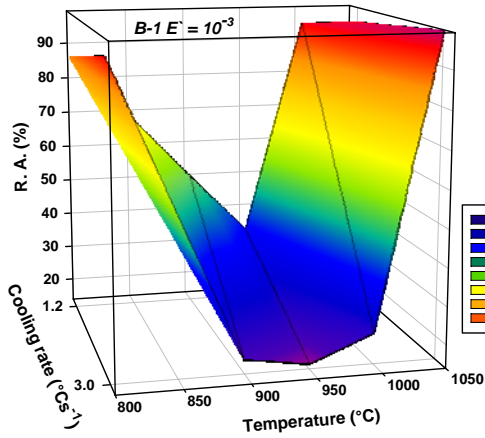


c) Steel *B-2*, cooling rate = $3.0\text{ }^{\circ}\text{C}\cdot\text{s}^{-1}$

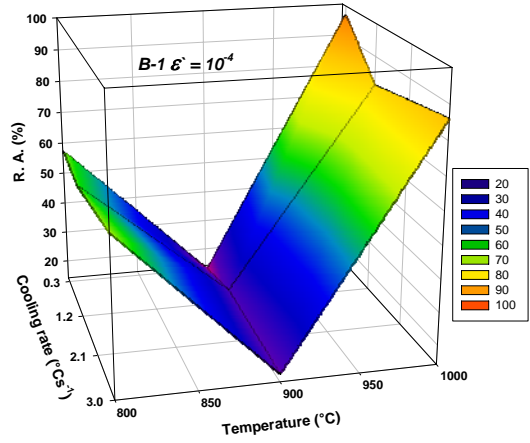


d) Steel *B-2*, cooling rate = $1.2\text{ }^{\circ}\text{C}\cdot\text{s}^{-1}$

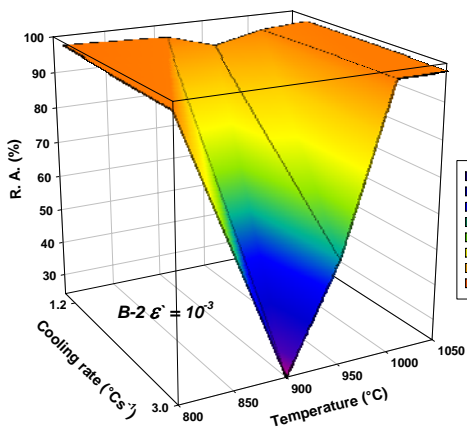
Figure 7.40: Graphs showing the improvement of hot ductility by increasing strain rate from 10^{-4} to 10^{-3} s^{-1} at fast and intermediate cooling rates for steel *B-1* (a and b). There is very little effect of strain rate for steel *B-2* (c and d).



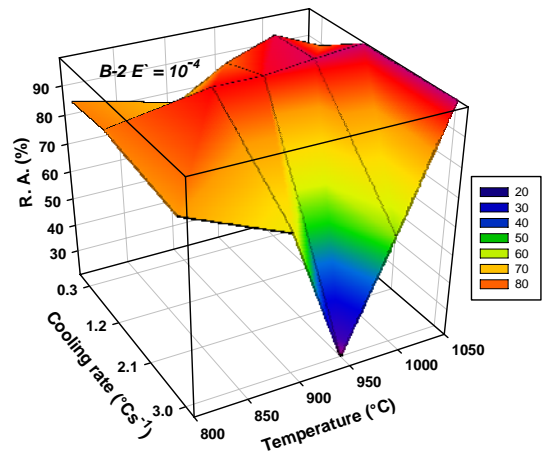
a) Steel *B-1*, strain rate = 10^{-3} s^{-1}



b) Steel *B-1*, strain rate = 10^{-4} s^{-1}



c) Steel *B-2*, strain rate = 10^{-3} s^{-1}



d) Steel *B-2*, strain rate = 10^{-4} s^{-1}

Figure 7.41: Graphs showing the improvement of hot ductility by decreasing cooling rate at high strain rate for steel *B-1* (no change at low strain rate) and at both high and low strain rates for steel *B-2*.

7.9.3 Total elongation

- In steel *B-1*, elongation was significantly improved by decreasing the cooling rate from 3.0 - 1.2 °C.s⁻¹ at high strain rate (**Figure 7.42**). At low strain rate, there was no marked difference in elongation with decrease in cooling rate.
- Steel *B-2* shows a similar trend to *B-1*, as elongation was markedly improved by decreasing the cooling rate from 3.0 - 1.2 °C.s⁻¹ at high strain rate. At low strain rate, there was no clear trend as testing was only done at 950 °C for schedule H.
- In steel *B-3*, the effect of cooling rate on elongation is not clear at low strain rate due to the limited data, although it would appear that slower cooling is beneficial.

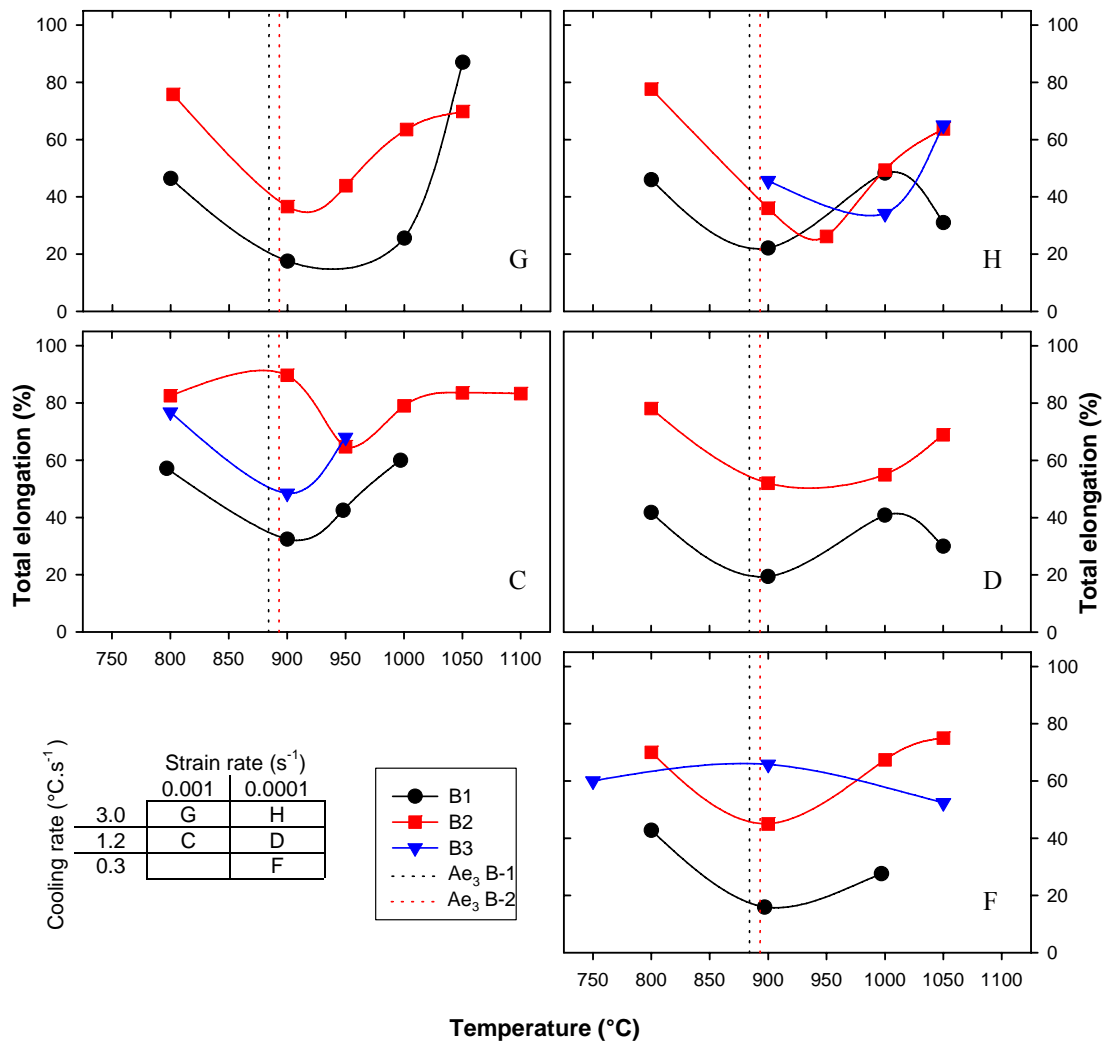


Figure 7.42: The effect of composition (increase in B/N ratio), strain rate and cooling rate on total elongation in Al-killed boron steels *B-1*, *B-2* and *B-3*. The Ae_3 temperatures of *B-1* (888 °C), *B-2* and *B-3* (both 895 °C) are shown.

7.10 PRECIPITATION IN THE AL-KILLED BORON STEELS

The species of precipitates and modes of cracking found in the three Al-killed boron steels are discussed in this section. Scanning electron microscopy of the internal microstructures revealed that all the low ductility specimens (< 40% *R. A.*) had failed by extensive cracking. This intergranular cracking along prior austenite grain boundaries was formed by interconnection of precipitate-containing voids. Precipitates in these voids were analyzed as mostly oxides, sulphides and oxysulphides, containing Fe, Mn, Al and Si, as well as many fine AlN. In only a few specimens, precipitates along intergranular cracks were found to contain BN. CuS and BN filaments up to 500 nm long and ~50 nm wide were seen in steels *B-1* and *B-2*.

The high ductility specimens showed limited or no cracking between precipitate-containing microvoids, and failure was attributed to ductile shear. Many voids with diameters of 1 – 5 μm , which were evenly distributed in the matrix, were shown to contain precipitates such as: MnS+BN, MnS+BN+FeO and BN+FeO. Complex precipitates such as Fe-Mn-Al-Si-Cr-O (some with S) were also well distributed in the matrix. Few voids were seen in lines along prior austenite grain boundaries.

A list of the precipitate species found in all the Al-killed boron steel samples is given in **Table 7.7**. A summary of the relevant precipitates that can have a bearing on hot ductility behaviour in these three Al-killed boron steels is then given in **Table 7.8**.

Table 7.7: List of precipitate species found in the Al-killed boron steels.

Steel	Testing conditions	Mn:S ratio	Precipitate species				
			Small: TEM (≤ 100 nm)	Filaments: TEM (width <50 nm)	Medium: TEM (100 -750 nm)	Large: TEM (>1 μ m)	Large: SEM (≥ 0.75 μ m)
B-1	All	Low	CuFeS AlN AlN-CuS BN Al(Cr)CuOS CuS-Al ₂ O ₃ BN-(Mn,Cu)S	AlO-FeS CuS BN-CuS (along grain boundary)	AlN-Cu(Mn)S (Al)OFeS BN CuS-BN	BN CuS-BN-FeO	MnS, FeO MnS-BN Al ₂ O ₃ , CaO AlMnO FeAlOS FeAlO(CaK) MnCrAlSiO FeMg(Mn,Ca)BCO
B-2	All	Low	(Fe,Mn,Cu)S FeO-CuS BN-CuS AlN (few)	BN BN-CuS CuS	BN Fe(Mn)S Cu(Fe)S CuMnS	BN BN+Al ₂ O ₃	BN AlOMnS(Mg) Fe(MgMn)O FeAl(Mn,Cr,Si)BCO FeOBN Al ₂ O ₃ FeMnS(B,O)
B-3	C, H, F	Low	FeO BN CuS+BN CuS (few)	-	BN, MnS BN on CuS many Cu(MnFe)S CuS on FeO	BNFeS(+Al)	MnS+BN FeO+BN FeOAlMnS(+Cr,Si)

Table 7.8: Summary of the precipitate species relevant to the Al-killed boron steels.

	<i>B-1</i>	<i>B-2</i>	<i>B-3</i>
Small: (≤ 100 nm)	Some AlN, CuSO Many Cu(Fe,Mn)S	Few AlN Many (Cu,Fe,Mn)S	FeO Few Cu(Fe,Mn)S
Medium: (100-750nm)	CuS+BN filaments and complex ppts AlN+(CuMn)S	CuS+BN filaments	Many Cu(Fe,Mn)S
Large: (≥ 750 nm)	Many complex oxides, MnS Few BN (+MnS)	Some complex oxides Some BN (+MnS or +FeO)	Many BN (+FeO or MnS)

The important points to note are:

- Steel *B-1* contains many small and medium sized AlN precipitates, known to be detrimental to hot ductility. Only a few small AlN precipitates were observed in *B-2* and none were seen in *B-3*.
- Steels *B-1* and *B-2* contain many small CuS, CuFeS and CuMnS precipitates. Only a few small CuS were observed in *B-3*.
- Fine filaments of CuS and FeS with widths less than 50 nm were seen in steel *B-1*. In steel *B-2*, BN filaments, some with caps of CuS were observed. No filaments were seen in steel *B-3*.

7.11 EFFECT OF COMPOSITION IN AL-KILLED BORON STEELS

7.11.1 Maximum strength

The behaviour of S_u with temperature in **Figure 7.38** is similar to results found by Marique and Messien (1990) for extra-low carbon steels with and without boron additions (<0.05% C, <0.35% Mn, <0.0060% N) tested at $3 \times 10^{-3} \text{ s}^{-1}$. In all cases, a peak in the S_u was noted between 900-950°C, which was associated with austenite to ferrite

transformation. This implies that the S_u peaks in this work are due to transformation, and not BN precipitation.

B-2 has the highest Thermo-CalcTM Ae_3 temperature (893 °C), followed by *B-3* (889 °C) and then *B-1* (884 °C). The substantially lower S_u of *B-2* compared to *B-1* at 900 °C could be explained by transformation of $\gamma \rightarrow \alpha$ at the Ae_3 temperature as thin films on the austenite grain boundaries. The work hardening of γ is highest just prior to transformation, which increases the maximum strength. As the thin α film begins to form with decrease in temperature, the S_u drops substantially (Suzuki *et al.*, 1984). This is as a result of the softer nature of α than γ , where recovery occurs more easily in α at the same temperature (Mintz *et al.*, 1993b). At the lower testing temperature (800 °C), *B-1* has also transformed to α and has a similar S_u to *B-2*.

7.11.2 Hot ductility

The influence of chemical composition on hot ductility (reduction in area in **Figure 7.39** and total elongation in **Figure 7.42**) in the Al-killed boron steels is detailed below.

Mn:S ratio

In all three steels *B-1*, *B-2* and *B-3*, the actual Mn:S ratio was well below the $Mn:S_{(critical)}$ suggested for good hot ductility by De Toledo *et al.* (1993). If only the calculated $Mn:S_{(actual)}/Mn:S_{(critical)}$ values from **Table 7.3** are considered to have an influence on hot ductility, the steels should have showed ductility improvement in the order: *B-3* to *B-1* to *B-2*, which is clearly not the case. Thus, there must be other factors that exert stronger influences on the ductility behaviour in these three steels.

However, there was copious precipitation of CuS, FeS, CuFeS, CuMnS and MnFeS in steel *B-1*, which are all low melting point phases (as low as 900 °C) and are thus potentially detrimental to the hot ductility. In particular, fine filaments along austenite grain boundaries would provide zones of weakness where intergranular cracks could easily initiate or propagate.

B and N contents

The following observations were made concerning the effect of an increase in B:N ratio (from steel *B-1* to *B-2* to *B-3*) on reduction in area as shown in the contour plots in **Figure 7.43**:

- Under all tested conditions, steel *B-1* (B:N = 0.19) showed a ductility trough.
- Ductility improved with increase in B:N from 0.19 to 0.47 (*B-1* to *B-2*). This improvement was slight at a cooling rate of $3.0\text{ }^{\circ}\text{C}\cdot\text{s}^{-1}$, and substantial at cooling rates of $1.2\text{ }^{\circ}\text{C}\cdot\text{s}^{-1}$ and at $0.3\text{ }^{\circ}\text{C}\cdot\text{s}^{-1}$ (10^{-4} s^{-1}).
- With further increase in B:N to 0.75 (*B-3*), the ductility improved at $3.0\text{ }^{\circ}\text{C}\cdot\text{s}^{-1}$ (10^{-4} s^{-1}) and remained excellent at $1.2\text{ }^{\circ}\text{C}\cdot\text{s}^{-1}$ (10^{-3} s^{-1}) and $0.3\text{ }^{\circ}\text{C}\cdot\text{s}^{-1}$ (10^{-4} s^{-1}).

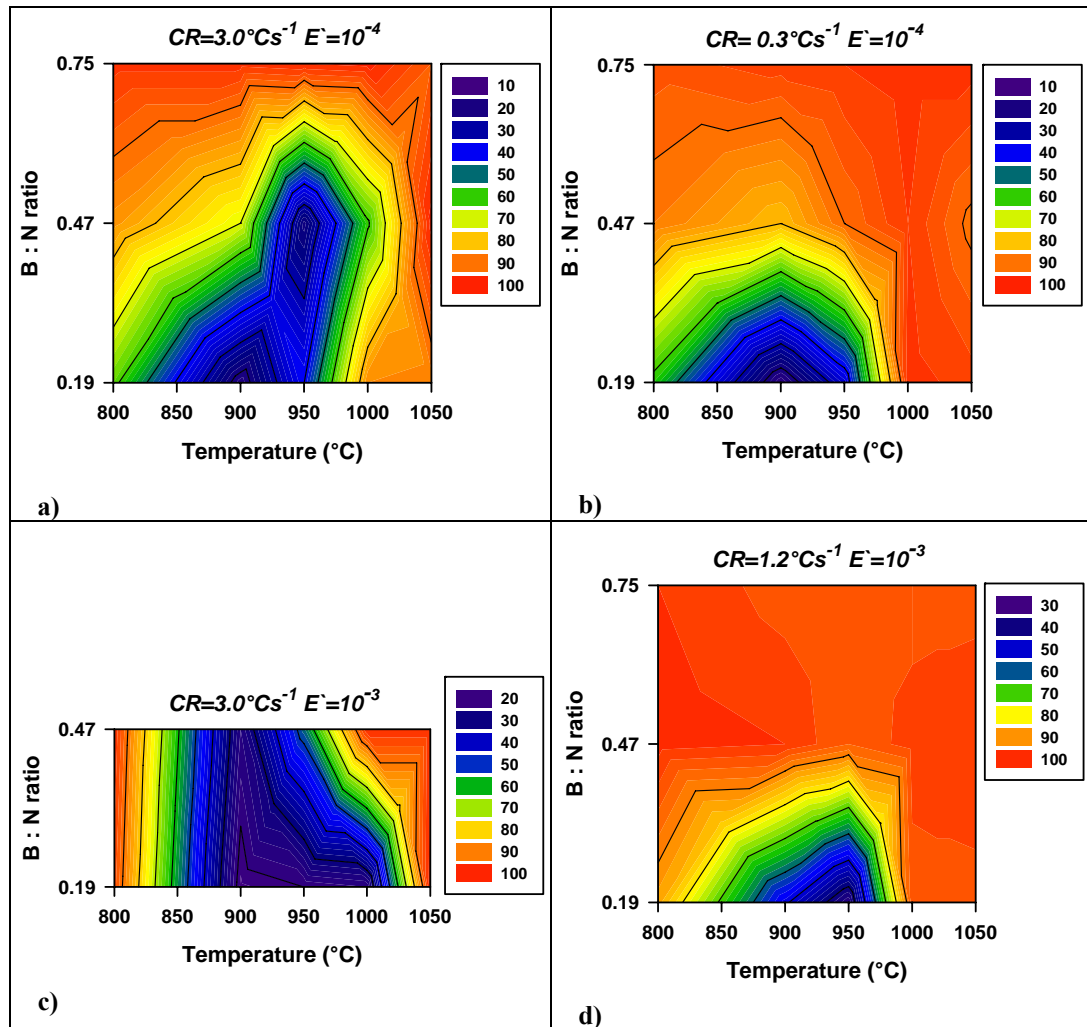


Figure 7.43: Contour plots showing the effects of temperature, cooling rate, strain rate and B:N ratio on reduction in area, and hence on hot ductility, in the Al-killed boron steels.

These results are supported by work done on the same three boron steels by Banks and Verdoorn (1996) under different testing conditions (1250°C reheat temperature; 2 minute soak; 0.4 °C.s⁻¹ cooling rate; 10⁻³ s⁻¹ strain rate), as shown in **Figure 7.44**. They found that only steel *B-1* showed a ductility trough under the specified testing conditions.

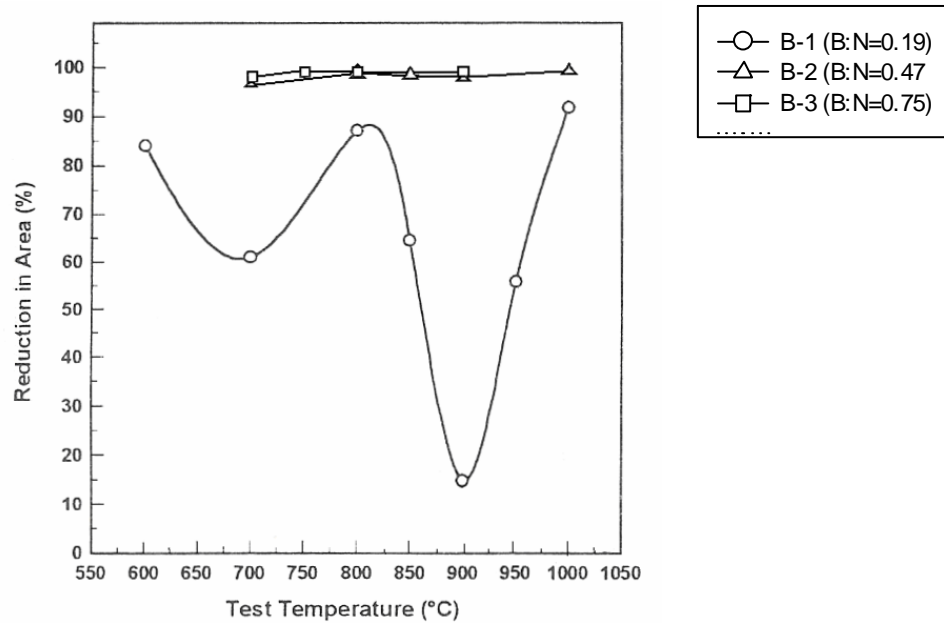


Figure 7.44: Hot ductility in the Al-killed boron steels *B-1*, *B-2* and *B-3* tested by Banks and Verdoorn (1996).

Al and N contents

It is widely accepted that AlN does not precipitate readily in austenite on cooling at the typical cooling rates experienced in slab continuous casting (Wilson and Gladman, 1998). AlN precipitation on cooling is thus even more unlikely under the higher cooling rates experienced in billet and thin slab casting. AlN also precipitates much more readily in ferrite than in austenite. This means that, although the Turkdogan (1987) AlN equilibrium temperatures calculated for these steels are 60-80 °C higher than the calculated BN temperatures, the AlN would only form by strain-induced precipitation during the tensile test (and possibly during strand straightening in continuous casting).

BN forms readily in austenite at temperatures approaching the equilibrium dissolution temperatures. Thus BN would precipitate on cooling before the tensile strain is applied, removing some nitrogen from solution. This would reduce the amount of N available to precipitate as AlN during straining or during transformation of austenite to ferrite. If the B:N ratio is high enough, *i.e.* above stoichiometry, there would be no nitrogen available for AlN formation at temperatures below the BN precipitation temperature.

Table 7.9 shows that after N has been removed from solution to form BN by using the stoichiometric relationship $[N] = 1.30*[B]$ in BN:

- There is an excess of 0.0041% N in steel *B-1*, which has the worst ductility.
- There is also an excess of 0.0018% N after BN formation in steel *B-2* available to form AlN on straining or cooling to the ferrite region.
- In steel *B-3* which has the best ductility, there is only an excess of 0.0001% N, which would have negligible influence on the hot ductility.

This mechanism is supported by the presence of many fine AlN precipitates found in steel *B-1*, fewer AlN found in steel *B-2* and no AlN found in steel *B-3*.

Table 7.9: Chemical composition of the Al-killed boron steels (in mass %), showing the B:N ratio, %N tied up in BN formation, excess %N available for AlN formation and the hot ductility ranking (1: best, 3: worst).

Grade	B	N	B:N	N in BN *	Excess %N**	Ductility ranking
B-1	0.0010	0.0054	0.19	0.0013	0.0041	3
B-2	0.0022	0.0047	0.47	0.0029	0.0018	2
B-3	0.0033	0.0044	0.75	0.0043	0.0001***	1

* % N required in BN for stoichiometric ratio $N = 1.30*B$.

** Excess N remaining after BN formation.

*** No excess N available.

7.12 MECHANISMS OF HOT TENSILE BEHAVIOUR IN THE AL-KILLED BORON STEELS

It is evident that the overall hot ductility of the Al-killed boron steels improved in the order of low to high B:N ratio, $0.19 \rightarrow 0.47 \rightarrow 0.75$ *i.e.* steel *B-1* \rightarrow *B-2* \rightarrow *B-3*. Under all tested conditions, a B:N ratio of 0.19 was not sufficient to ensure adequate hot ductility ($\geq 50\%$ R.A.). At cooling rates of 0.3 and $1.2\text{ }^{\circ}\text{C}\cdot\text{s}^{-1}$, generally associated with thick slab, bloom and slow thin slab casting, a B:N ratio of ≥ 0.47 was sufficient to avoid a ductility trough altogether. However, at a high cooling rate of $3.0\text{ }^{\circ}\text{C}\cdot\text{s}^{-1}$, typically experienced in thin slab and billet casting, a B:N ratio of 0.75 would be required to provide good hot ductility. This is shown in **Figure 7.45**.

BN precipitates readily on cooling in austenite, thus removing some nitrogen from solution. This reduces the amount of N available to precipitate as AlN during straining or during transformation of austenite to ferrite. Boron tends to segregate to high angle grain boundaries, thus sufficient boron on the grain boundaries prevents formation of AlN on intergranular surfaces. If the B:N ratio is high enough, *i.e.* above stoichiometry, there is no nitrogen available for AlN formation at temperatures below the BN precipitation temperature. A lower than stoichiometric B:N ratio only removes some of the nitrogen. This mechanism is supported by the presence of many fine AlN precipitates found in steel *B-1* (B:N=0.19), fewer AlN found in steel *B-2* (B:N=0.47) and no AlN found in steel *B-3* (B:N=0.75).

In addition, the number of fine Cu(Fe,Mn)S precipitates (<100 nm diameter) and CuS filaments (<50 nm width) decreased, and the number of coarse BN precipitates increased, with increase in B:N ratio. The increase in the number of BN precipitates facilitated co-precipitation of CuS with coarse BN. This rendered the CuS ineffective to influence the hot ductility.

It is also clear that transformation was beneficial to hot ductility in these steels, as the low temperature ductility recovery occurred between the Ae_3 and Ae_1 temperatures. This can be ascribed to rapid formation of α at the γ grain boundaries (Mintz *et al.*, 1991), which removes strain concentration from the immediate intergranular area and distributes the strain over a larger area.

7.13 APPLICATION AND RELEVANCE TO INDUSTRY

The Al-killed boron steels *B-1* and *B-2* were tested under conditions simulating thin slab casting with medium and hard secondary cooling, billet [hard] and thick slab [medium and soft cooling]. *B-3* was tested under billet casting with hard cooling (schedule H), thin slab [medium], and thick slab [soft] conditions. Using the results in this work, the following straightening temperature conditions can be applied for minimal crack susceptibility when considering these steels for use in continuous casting operations, as shown in **Table 7.10**.

Table 7.10: Application of the hot ductility results to casting parameters.

Steel	Testing conditions	Casting type	Secondary cooling rate (°C.s ⁻¹) [Cooling pattern]	Straightening temperature ranges (°C)
<i>B-1</i>	C	Thin slab	1.2 [medium]	< 800 or > 975
	G	Thin slab	3.0 [hard]	> 925
	H	Billet	3.0 [hard]	> 950
	D	Thick slab	1.2 [medium]	≤ 750 or >> 1100
	F	Thick slab	0.3 [soft]	Not suitable
<i>B-2</i>	C	Thin slab	1.2 [medium]	< 775 or > 825
	G	Thin slab	3.0 [hard]	< 775 or > 825
	H	Billet	3.0 [hard]	< 775 or > 925
	D	Thick slab	1.2 [medium]	< 750 or > 875
	F	Thick slab	0.3 [soft]	< 775 or > 925
<i>B-3</i>	C	Thin slab	1.2 [medium]	< 750 or > 925
	H	Billet	3.0 [hard]	< 750 or > 950
	F	Thick slab	0.3 [soft]	

Based on this work, the following compositional limits are recommended to minimise crack susceptibility in Al-killed boron steels:

- **B:N ratio 0.78 – 1.0:** The effect of B:N ratio on hot ductility in these boron steels is illustrated in **Figure 7.45**. As the nitrogen control seems to be good *i.e.* <0.0055% N, the B:N ratio should be adjusted by increasing the boron to >0.0035% B.
- **Mn:S ratio >20** (and preferably >30), by increasing manganese to >0.30% Mn and limiting sulphur to <0.015% S, even down to <0.010% S.

To ensure that the strand temperature does not approach any low ductility region during the straightening process, the minimum recommended straightening temperatures listed in **Table 7.10** should be used for the steel compositions in this work. The maximum straightening temperatures should be limited to ~1100 °C, as it has been shown that the hot ductility in these steels begins to drop to below 50% *R. A.* at higher temperatures.

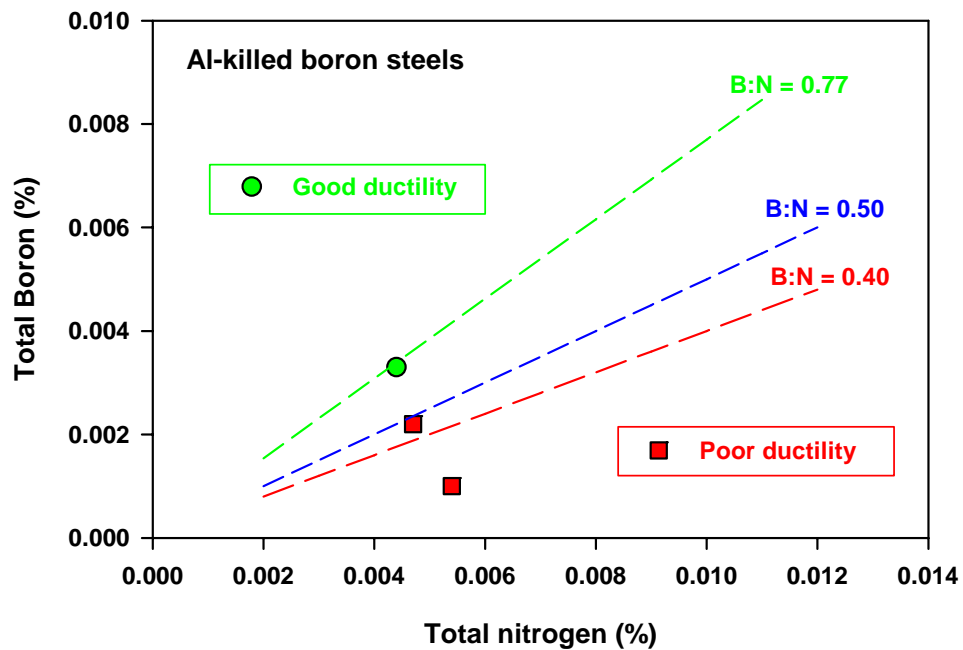


Figure 7.45: The influence of B:N ratio on hot ductility in Al-killed boron steels.

Chapter 8: Silicon-killed Boron Steels

Hot tensile behaviour in the silicon-killed boron microalloyed steels: results, discussion and application

8.1 OVERVIEW OF CHAPTER 8

The silicon-killed boron steels were sampled from square billet. The billet casting plant had been experiencing problems with severe cracking on some billets, but the solution was not obvious. Hot ductility testing was performed using only the calculated parameters that would closely simulate the capabilities of this particular billet caster. This range of steels was subjected to *in situ* melting before cooling to the test temperature.

It was found that the B:N ratio had the overriding influence on hot ductility and hence on cracking, but the Mn:S ratio was also found to play a role.

8.2 TRANSFORMATION IN THE SI-KILLED BORON STEELS

The chemical compositions of the Si-killed boron steels *SiB-1* to *SiB-4* are shown in **Table 8.1**. The Mn:S and B:N ratios are also shown.

Table 8.1: Chemical composition of the Si-killed boron steels (in mass %).

Grade	C	Mn	P	S	Si	N	Ni	Cu	Cr	B	Mn:S	B:N
SiB-1	0.056	0.36	0.025	0.035	0.11	0.0090	0.09	0.15	0.08	0.0040	10.29	0.44
SiB-2	0.048	0.30	0.004	0.025	0.11	0.0100	0.09	0.18	0.07	0.0040	12.00	0.40
SiB-3	0.059	0.44	0.008	0.018	0.15	0.0059	0.07	0.20	0.06	0.0070	24.56	1.19
SiB-4	0.039	0.41	0.014	0.034	0.14	0.0080	0.09	0.15	0.03	0.0080	12.09	1.00

The Si-killed boron steels showed a relatively small variation in predicted Ae_3 temperatures of 9 - 17 °C, as shown in **Table 8.2**. The predicted Ae_3 temperatures ranged from:

- GASⁱ: 870 – 879 °C
- Andrewsⁱⁱ: 879 – 891 °C
- Thermo-Calc^{TM iii}: 872 – 885 °C

Table 8.2: Calculated transformation temperatures (°C) for the Si-killed steels in this work.

Steel	Ae_3 (start of ferrite formation).			Ae_1 (start of austenite formation)	
	GAS ⁱ	And ⁱⁱ	Thermo-Calc TCF _{Fe3} ⁱⁱⁱ	And ⁱⁱ	Thermo-Calc TCF _{Fe3} ⁱⁱⁱ
SiB-1	872	891	879	719	712
SiB-2	876	882	877	720	711
SiB-3	870	879	872	719	711
SiB-4	879	891	885	717	713

The Andrews Ae_3 equation is very sensitive to phosphorous content (+700*X_p), hence an increase in phosphorus from 0.004% P (SiB-2) to 0.025% P (SiB-1) has the effect of

ⁱ Genetic Adaptive Search (GAS) equation (Deo *et al.*, 1995).

ⁱⁱ Andrews formula (1965).

ⁱⁱⁱ Modelled using Thermo-Calc database TCF_{Fe3} (2006) – this work.

increasing the Ae_3 by 14.5 °C. This is only countered slightly by the increase in carbon content. The *GAS* equation does not consider, and is thus not sensitive to, any changes in phosphorus content.

The *GAS* and Thermo-Calc™ Ae_3 values vary by 1-7 °C, whereas the Andrews Ae_3 values are 4-19 °C higher than the *GAS* values and 5-12 °C higher than the Thermo-Calc™ values.

8.3 PRECIPITATE DISSOLUTION IN THE SILICON-KILLED BORON STEELS

For low solute contents, as in low alloy steels, the total mass concentrations of the dissolved elements, in equilibrium with the precipitated phase, can be used to represent the solubility product discussed in **Section 2.5**.

Modelling in 2006 on the new Thermo-Calc™ TCFE3 and SSOL4 databases (which include B and N), did produce BN dissolution temperatures for these steels.

The Mn:S ratios for steels *SiB-1* to *SiB-4* are shown in **Table 8.3**. According to the De Toledo hot cracking criterion (De Toledo *et al.*, 1995), all four steels have lower than critical Mn:S ratios.

Table 8.3: De Toledo (1995) hot cracking criterion, showing critical (Mn:S)_c and actual (Mn:S)_a ratios for the Si-killed boron steels.

Steel	(Mn:S) _c	(Mn:S) _a	(Mn:S) _a / (Mn:S) _c	Actual > Critical?
SiB-1	19	10	0.54	N
SiB-2	25	12	0.48	N
SiB-3	33	25	0.75	N
SiB-4	20	12	0.61	N

The T_{diss} is taken to be the highest achievable precipitation temperature for a specific composition. In reality, conditions do not approach equilibrium, and the precipitation would occur at significantly lower temperatures, if at all, under cooling conditions.

The MnS equilibrium dissolution temperatures calculated using the Turkdogan (1987) equation and modelled using Thermo-Calc™ are shown in Table 8.4. Figure 8.1 shows the logarithmic dependence of the $T_{diss}(MnS)$ on $[Mn][S]$, is the MnS solubility product. The MnS dissolution temperatures from Turkdogan (1987) are much higher than the Thermo-Calc™ temperatures and show a stronger dependence on the solubility product.

Table 8.4: Solubility of precipitates in austenite in the Si-killed boron steels – calculated and Thermo-Calc™ modelled equilibrium precipitate dissolution temperatures (°C).

Steel	Equilibrium dissolution temperatures (°C)				Thermo-Calc™ ^{iv}		
	Turkdogan (1987)		Maitrepierre (1979)	Fountain (1962)	TCFe3	SSOL4	TCFe3
	MnS	BN	BN	BN	BN	BN	MnS
SiB-1	1595	1170	1170	1177	1364	1364	1447
SiB-2	1512	1176	1184	1184	1357	1341	1433
SiB-3	1521	1179	1189	1186	1366	1385	1440
SiB-4	1613	1208	1251	1213	1397	1389	1448

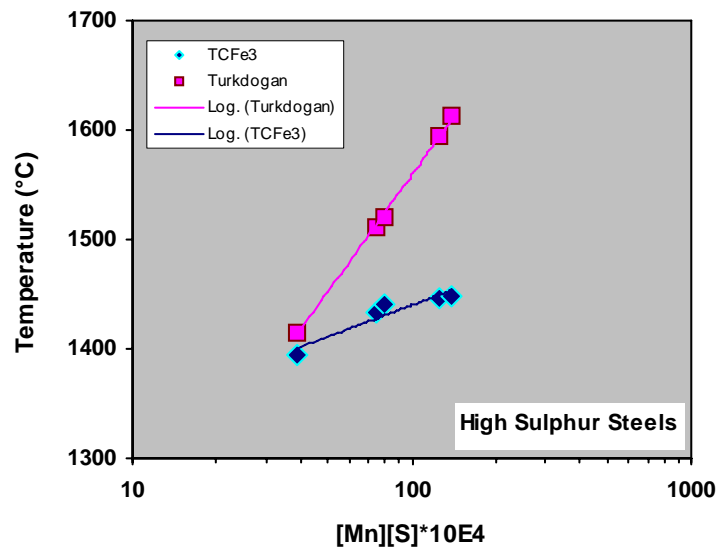


Figure 8.1: Logarithmic dependence of the MnS dissolution temperatures on $[Mn][S]$ for the Si-killed steels using Thermo-Calc™ modelling and calculation using the Turkdogan (1987) equation.

^{iv} Modelled using Thermo-Calc databases SSOL4 and TCFE3 (2006) – this work.

The $T_{diss}(BN)$ temperatures calculated by the Turkdogan (1987), Maitrepierre (1979) and Fountain (1962) equations and modelled using Thermo-CalcTM are also listed in **Table 8.4**. The logarithmic dependence of $T_{diss}(BN)$ on the [B][N] product is shown in **Figure 8.2**. It is clear that the calculated temperatures are quite similar, whereas the Thermo-CalcTM modelled temperatures are significantly higher. This is expected, as Thermo-CalcTM temperatures are derived from tests approaching equilibrium conditions.

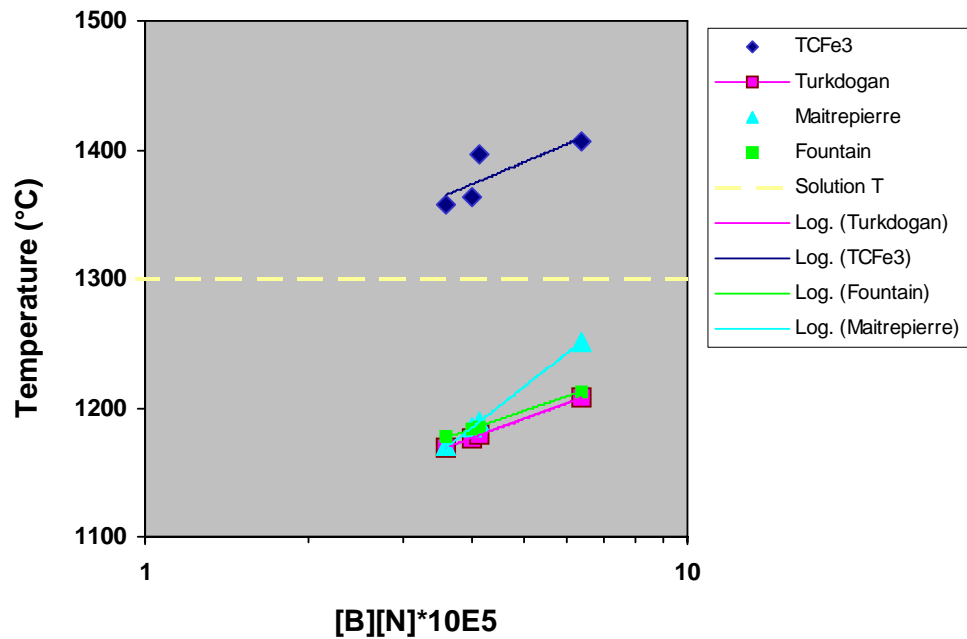


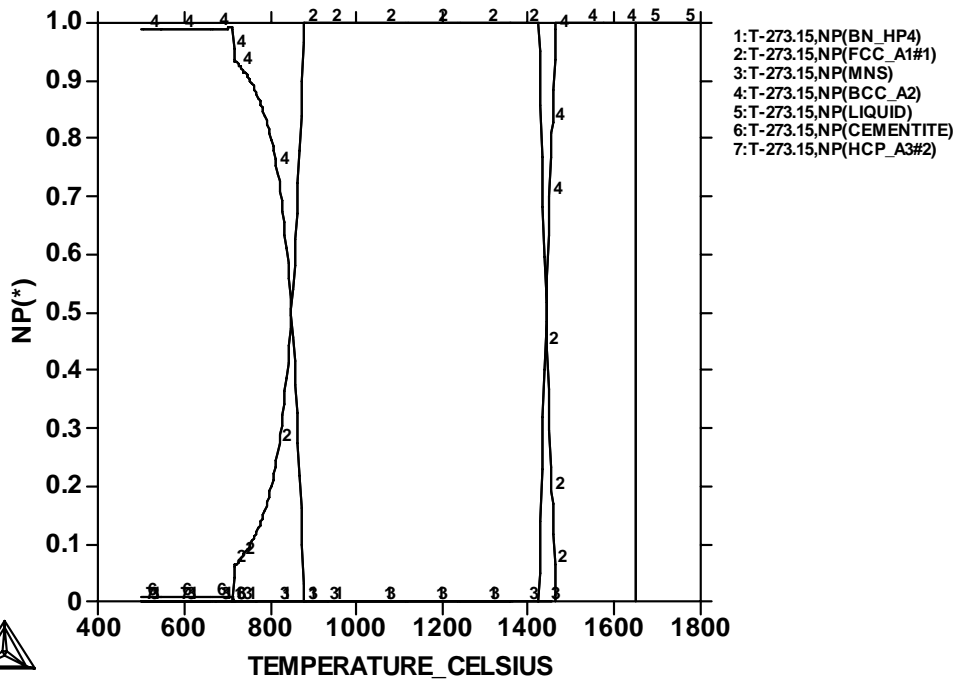
Figure 8.2: Logarithmic dependence of the BN dissolution temperature on [B][N] for the Si-killed boron steels.

Figure 8.3 and **Figure 8.4** show the equilibrium phase transformations for steels *SiB-1* to *SiB-4* respectively, modelled using the Thermo-CalcTM TCFE3 database.

THERMO-CALC (2007.10.21:10.47) :HS1

DATABASE:TCFE3

N=1, P=1.01325E5, W(C)=5.6E-4, W(MN)=3.6E-3, W(P)=2.5E-4, W(S)=3.5E-4,
W(SI)=1.1E-3, W(N)=9E-5, W(NI)=9E-4, W(CU)=1.5E-3, W(CR)=8E-4, W(B)=4E-5;

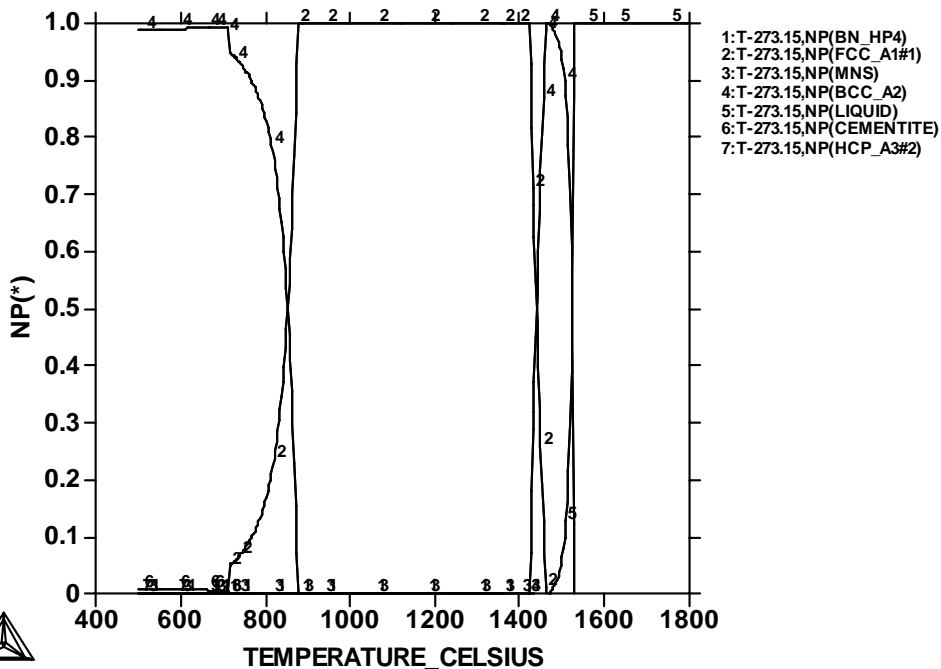


a)

THERMO-CALC (2007.10.21:10.55) :HS2

DATABASE:TCFE3

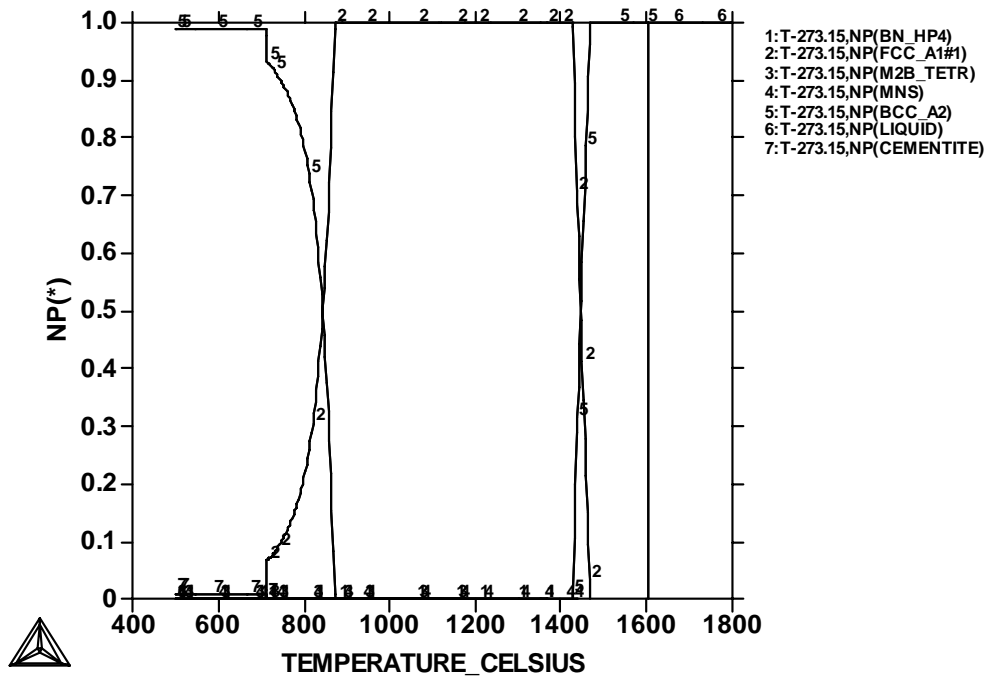
N=1, P=1.01325E5, W(C)=4.8E-4, W(MN)=3E-3, W(P)=4E-5, W(S)=2.5E-4,
W(SI)=1.08E-3, W(N)=1E-4, W(NI)=9E-4, W(CU)=1.8E-3, W(CR)=7E-4, W(B)=4E-5;



b)

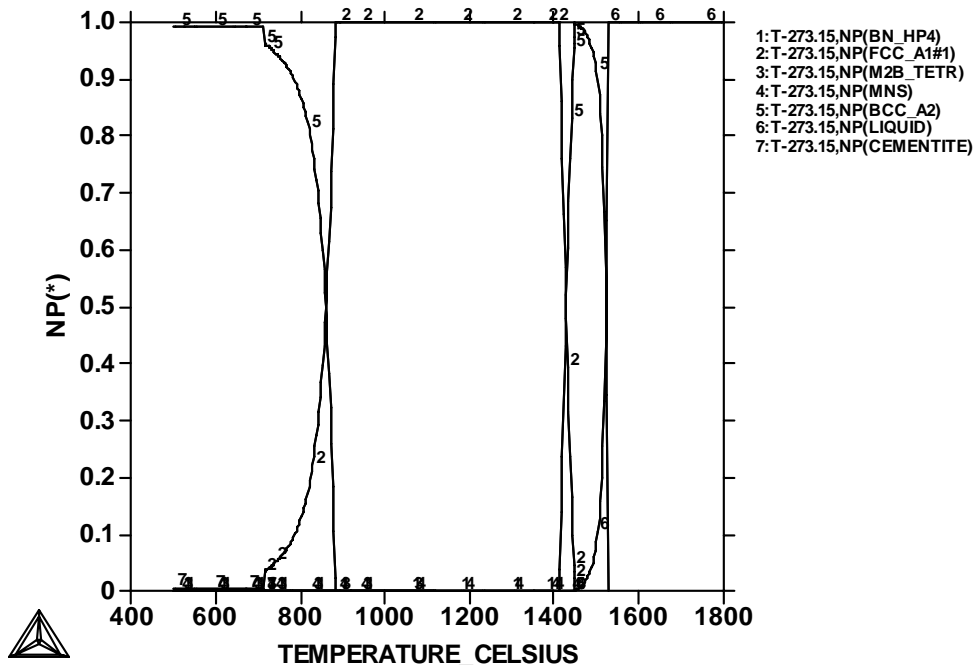
Figure 8.3: Thermo-Calc™ graphs modelled using database TCFE3, showing the equilibrium phase fractions as a function of temperature for steels a) *SiB-1* and b) *SiB-2*.

THERMO-CALC (2007.10.21:10.59) :HS3
 DATABASE:TCFE3
 N=1, P=1.01325E5, W(C)=5.9E-4, W(MN)=4.42E-3, W(P)=8E-5, W(S)=1.8E-4,
 W(SI)=1.5E-3, W(N)=5.9E-5, W(NI)=7E-4, W(CU)=2E-3, W(CR)=6E-4, W(B)=7E-5;



a)

THERMO-CALC (2007.10.21:11.03) :HS4
 DATABASE:TCFE3
 N=1, P=1.01325E5, W(C)=3.9E-4, W(MN)=4.11E-3, W(P)=1.4E-4, W(S)=3.4E-4,
 W(SI)=1.4E-3, W(N)=8E-5, W(NI)=9E-4, W(CU)=1.5E-3, W(CR)=3E-4, W(B)=8E-5;



b)

Figure 8.4: Thermo-Calc™ graphs modelled using database TCFE3, showing the equilibrium phase fractions as a function of temperature for steels a) SiB-3 and b) SiB-4.

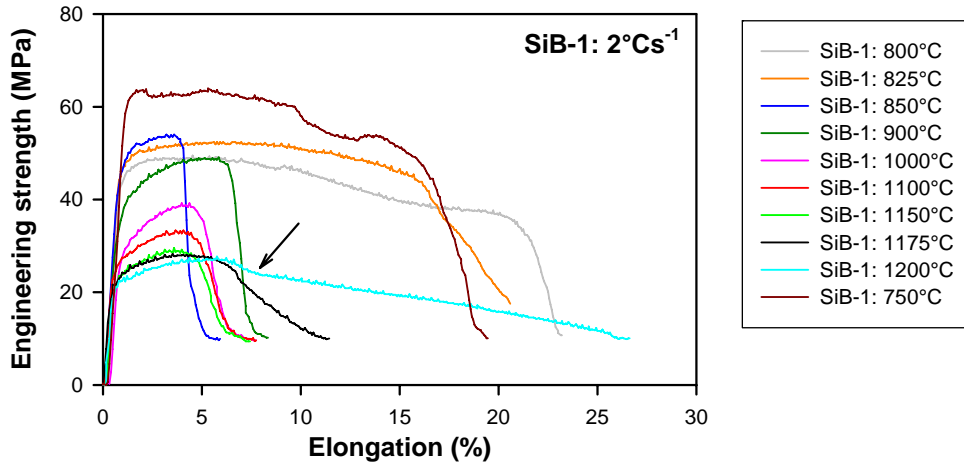
8.4 SI-KILLED BORON STEEL *SiB-1*

8.4.1 Introduction

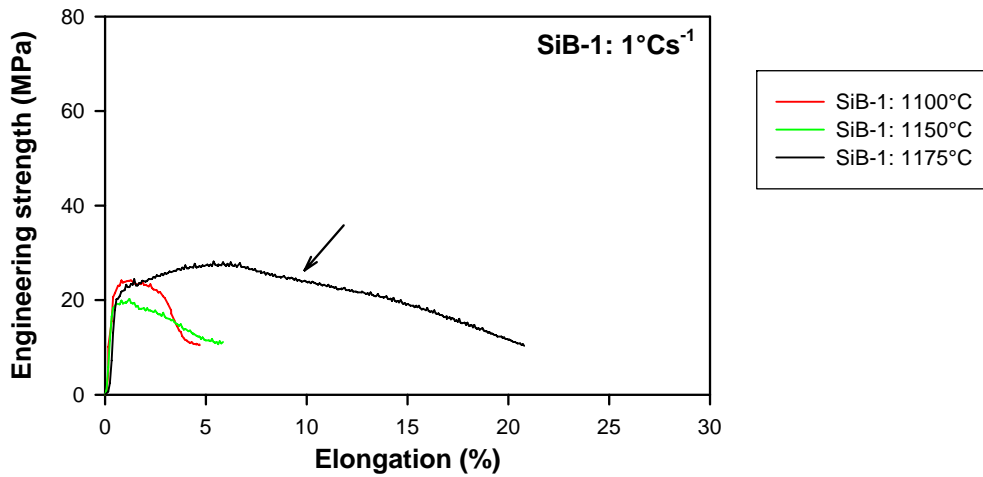
Figure 8.5 a and **b** show the engineering stress – elongation curves for steel *SiB-1* for cooling rates of 1 and 2 °C.s⁻¹ from the melting point. The occurrence of dynamic recrystallisation can be detected on the stress – elongation curves by either an abrupt decrease or oscillations of the flow stress. The onset of dynamic recrystallisation is indicated by arrows on the graphs and the temperatures are listed in **Table 8.5**. The maximum strength values are shown as a function of testing temperature in **Figure 8.6**. The modelled Thermo-CalcTM Ae_3 temperature (879 °C) and Ae_1 temperature (712 °C) from **Table 8.2** are indicated on the graphs.

The percentage reduction in area (% *R. A.*) is shown as a function of testing temperature in **Figure 8.7** and the percentage total elongation is shown as a function of testing temperature in **Figure 8.8**. The modelled Thermo-CalcTM Ae_3 transformation temperature of 879 °C from **Table 8.2** and Ae_1 temperature (712 °C) from **Table 8.2** are indicated on the graphs.

Scanning electron microscopy (SEM) micrographs are shown in **Figure 8.10** to **Figure 8.13**. Transmission electron microscopy (TEM) bright field images are shown in **Figure 8.15**.



a) 2 °C.s⁻¹



b) 1 °C.s⁻¹

Figure 8.5: Engineering stress as a function of elongation for Si-killed steel *SiB-1* after *in situ* melting, followed by cooling to the test temperature at a) 2 °C.s⁻¹ and b) 1 °C.s⁻¹. The key to the tests is shown and the onset of dynamic recrystallisation is indicated by arrows on the graphs.

8.4.2 Maximum strength

Figure 8.5 shows the effect of testing temperature on the strength – elongation curves. The onset of dynamic recrystallisation for Si-killed steel *SiB-1* occurs at $1200\text{ }^{\circ}\text{C}\cdot\text{s}^{-1}$ (cooling rate = $2\text{ }^{\circ}\text{C}\cdot\text{s}^{-1}$) and at $1175\text{ }^{\circ}\text{C}$ (cooling rate = $1\text{ }^{\circ}\text{C}\cdot\text{s}^{-1}$).

Figure 8.6 shows a general trend of near-linear increasing maximum strength (S_u) with decreasing temperature from $1275 - 850\text{ }^{\circ}\text{C}$ for a cooling rate of $2\text{ }^{\circ}\text{C}\cdot\text{s}^{-1}$. With decrease in temperature from $850\text{ }^{\circ}\text{C}$ to $800\text{ }^{\circ}\text{C}$, the maximum strength decreased, then increased with further decrease in temperature below $800\text{ }^{\circ}\text{C}$, *i.e.* between the Ae_3 and Ae_1 temperatures.

At a lower cooling rate of $1\text{ }^{\circ}\text{C}\cdot\text{s}^{-1}$ the S_u values dropped by $\sim 10\text{ MPa}$ from $1175\text{--}1150\text{ }^{\circ}\text{C}$, then increased slightly by $\sim 5\text{ MPa}$ with further decrease in temperature to $1100\text{ }^{\circ}\text{C}$. The absence of a slow increase from the yield strength to the maximum strength in the sample tested at $1150\text{ }^{\circ}\text{C}$ could indicate that this sample had a pre-existing defect, which led to low maximum strength, elongation and reduction in area values. (**Figure 8.5 b** and **Figure 8.6**).

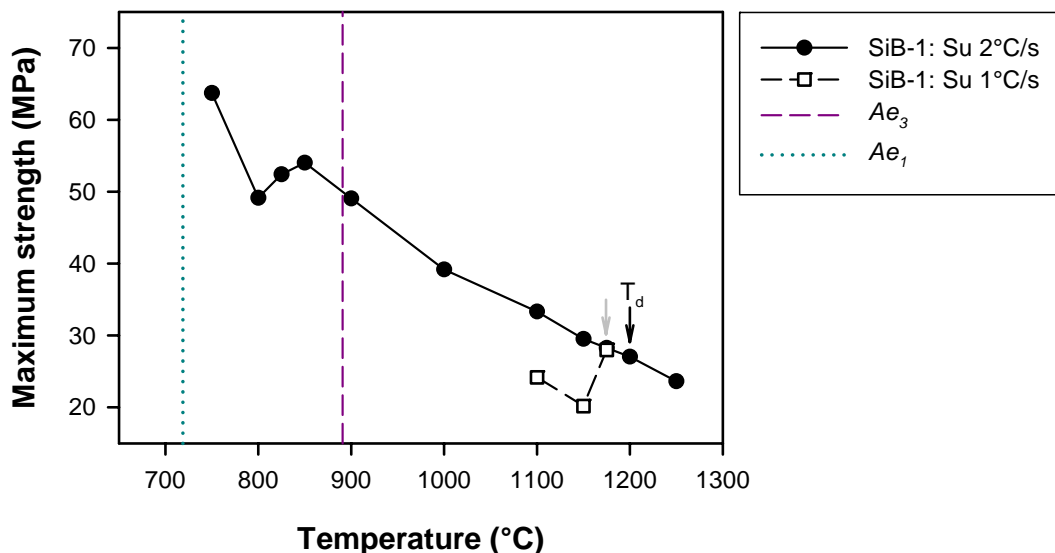


Figure 8.6: Maximum strength for steel *SiB-1* as a function of testing temperature and cooling rate.

8.4.3 Reduction in area

Steel *SiB-1* has a very wide ductility trough that extends from $\sim 1200 - 800$ °C at a cooling rate of 2 °C.s $^{-1}$ (**Figure 8.7**). From 1175 °C down to 850 °C, the ductility is very low (*R. A.* below 20%), with a minimum of 1% *R. A.* at 850 °C. The ductility improvement on the low temperature end coincided with ferrite formation below the A_{e3} temperature.

The onset of dynamic recrystallisation (T_d) occurred at 1200 °C (cooling rate = 2 °C.s $^{-1}$) and at 1175 °C (cooling rate = 1 °C.s $^{-1}$). Here the *R. A.* values are greater than 50% as ductility recovered on the high temperature side of the trough. The reduction in area peaks at 1200 °C, and then drops by $\sim 25\%$ with further temperature increase to 1250 °C.

A lower cooling rate of 1 °C.s $^{-1}$ improved the ductility slightly on the high temperature side of the ductility trough. The drop in *R. A.* occurred 25 °C lower than for a cooling rate of 2 °C.s $^{-1}$.

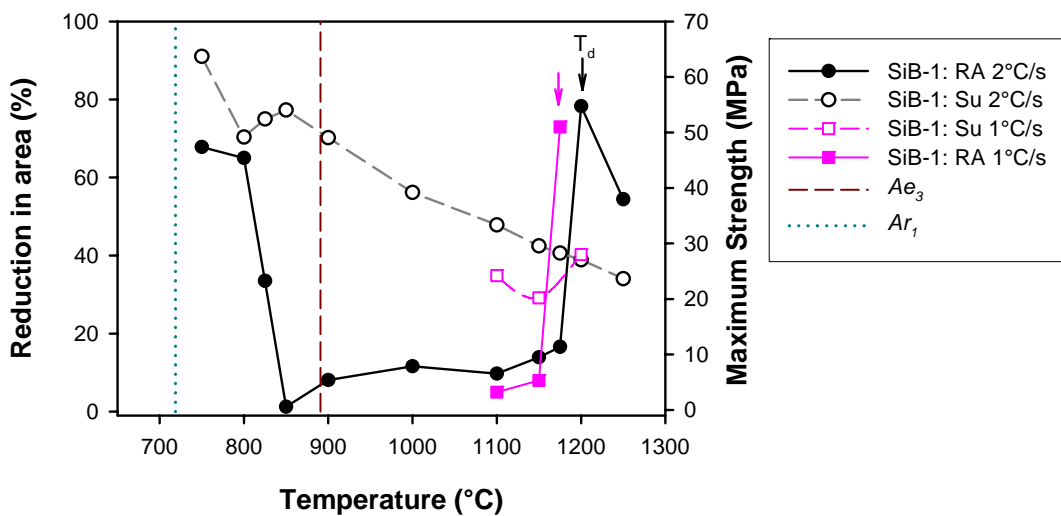


Figure 8.7: Reduction in area for steel *SiB-1* as a function of testing temperature and cooling rate.

8.4.4 Total elongation

Figure 8.8 shows that the total elongation curves follow similar trends to the reduction in area. A wide elongation trough exists from 1175 °C down to 850 °C. Elongation recovery coincides with dynamic recrystallisation on the high temperature end of the trough and with ferrite formation below the Ae_3 on the low temperature end of the trough. Decreasing the cooling rate from 2 - 1 °C.s⁻¹ also improved elongation recovery by ~25 °C on the high temperature side of the trough.

The total elongation peaks at 1200 °C (27%), and then drops by ~10% to 17% with temperature increase to 1250 °C.

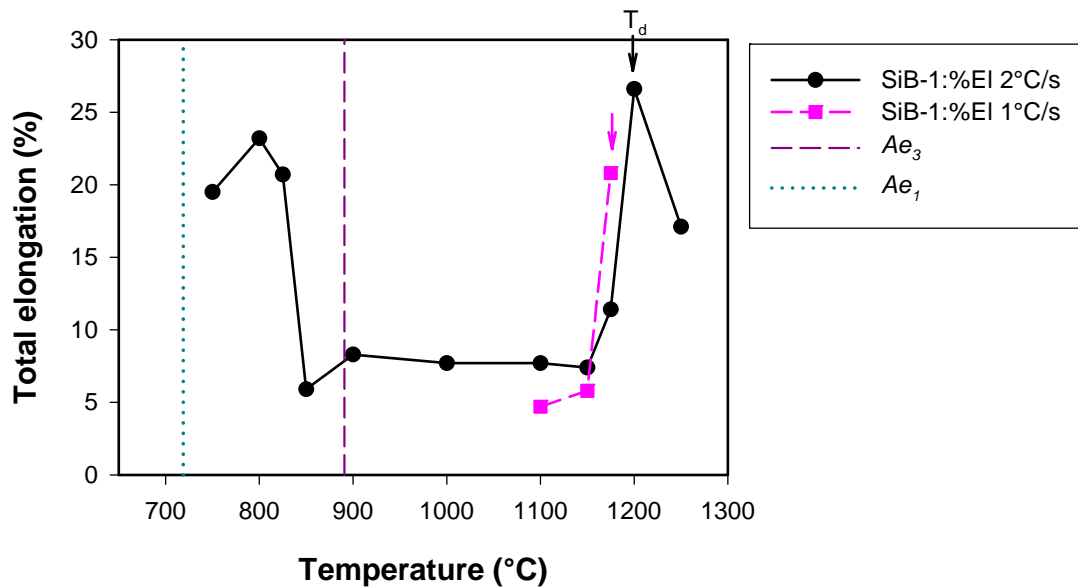


Figure 8.8: Elongation for steel *SiB-1* as a function of testing temperature and cooling rate.

8.4.5 Scanning electron microscopy

Cracked billet - transverse corner crack: **Figure 8.9** shows a photograph highlighting the severity of a transverse corner crack on a section of industrially cast steel *SiB-1* billet. The surface of the crack was heavily oxidised due to atmospheric exposure at high temperatures. However, an unoxidised surface was created by breaking the billet sample open at the crack tip. **Figure 8.10** shows SEM micrographs of this area. Many microvoids were observed, containing mainly MnS precipitates in the 0.5-2 μm size range, but also MnS with B, C, Al, Si and Cu (**Figure 8.10 a and b**). The fracture surface is mostly intergranular along the prior austenite grain boundaries), as shown in **Figure 8.10c and d**.

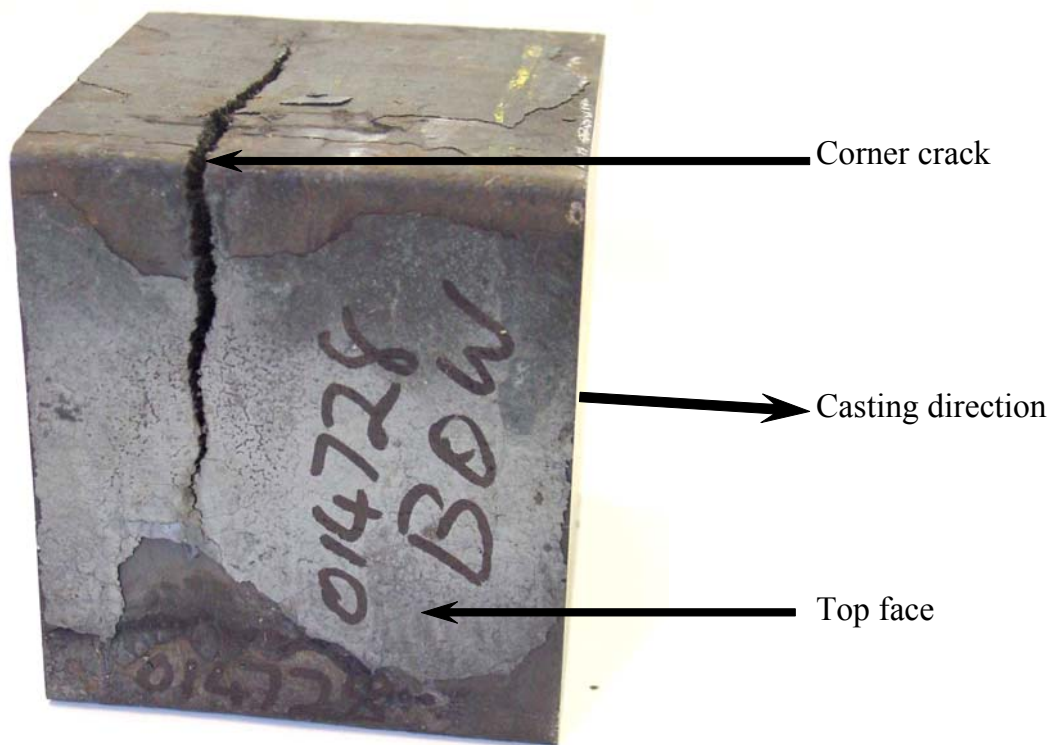


Figure 8.9: Photograph of a section of industrially cast steel *SiB-1* billet, showing a severe transverse corner crack.

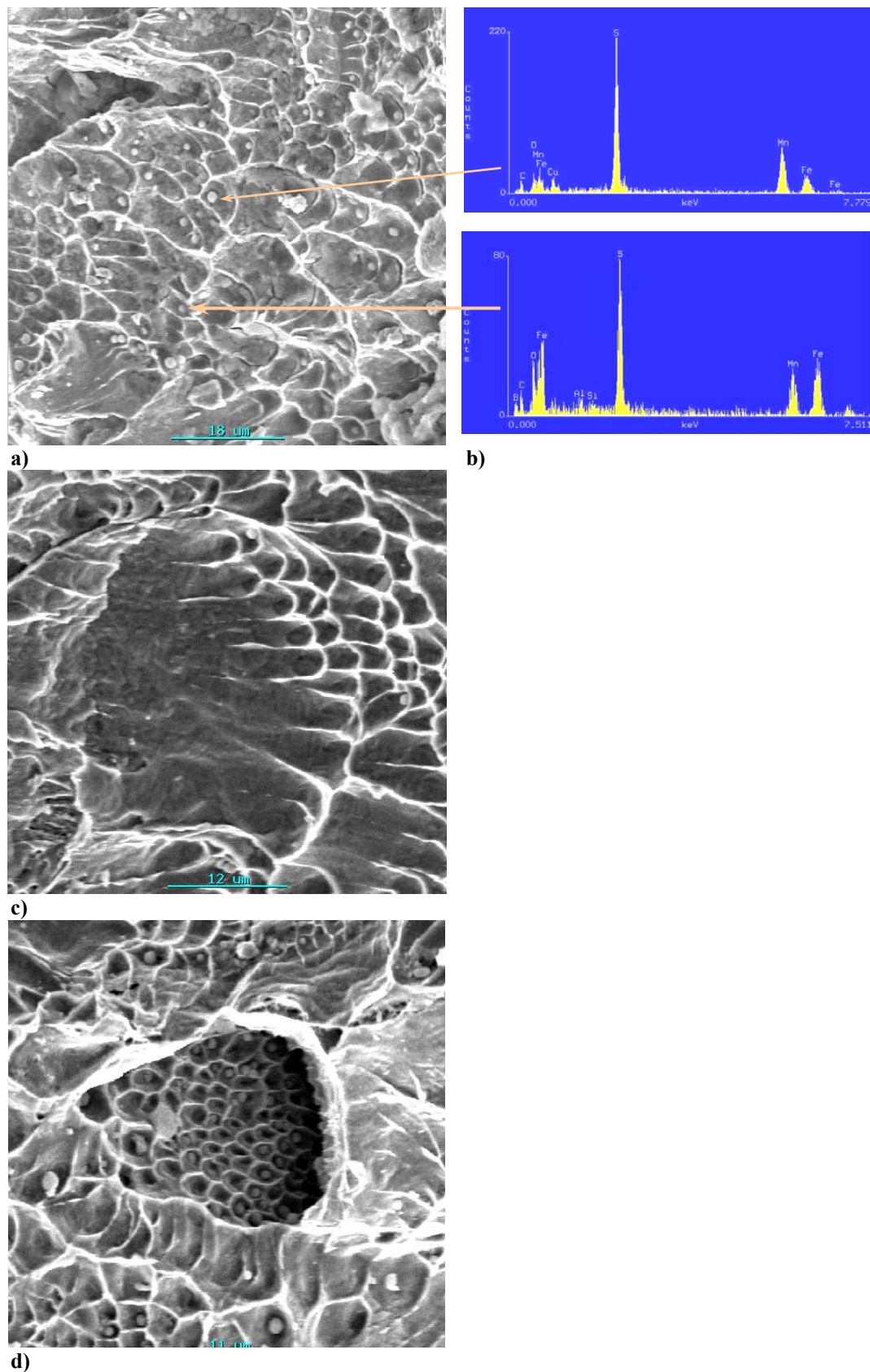


Figure 8.10 : SEM backscatter images of the transverse surface crack in steel *SiB-1*, showing microvoid coalescence, with many large MnS precipitates (1-3 μm) and C, Cu, B, O, Al and Si.

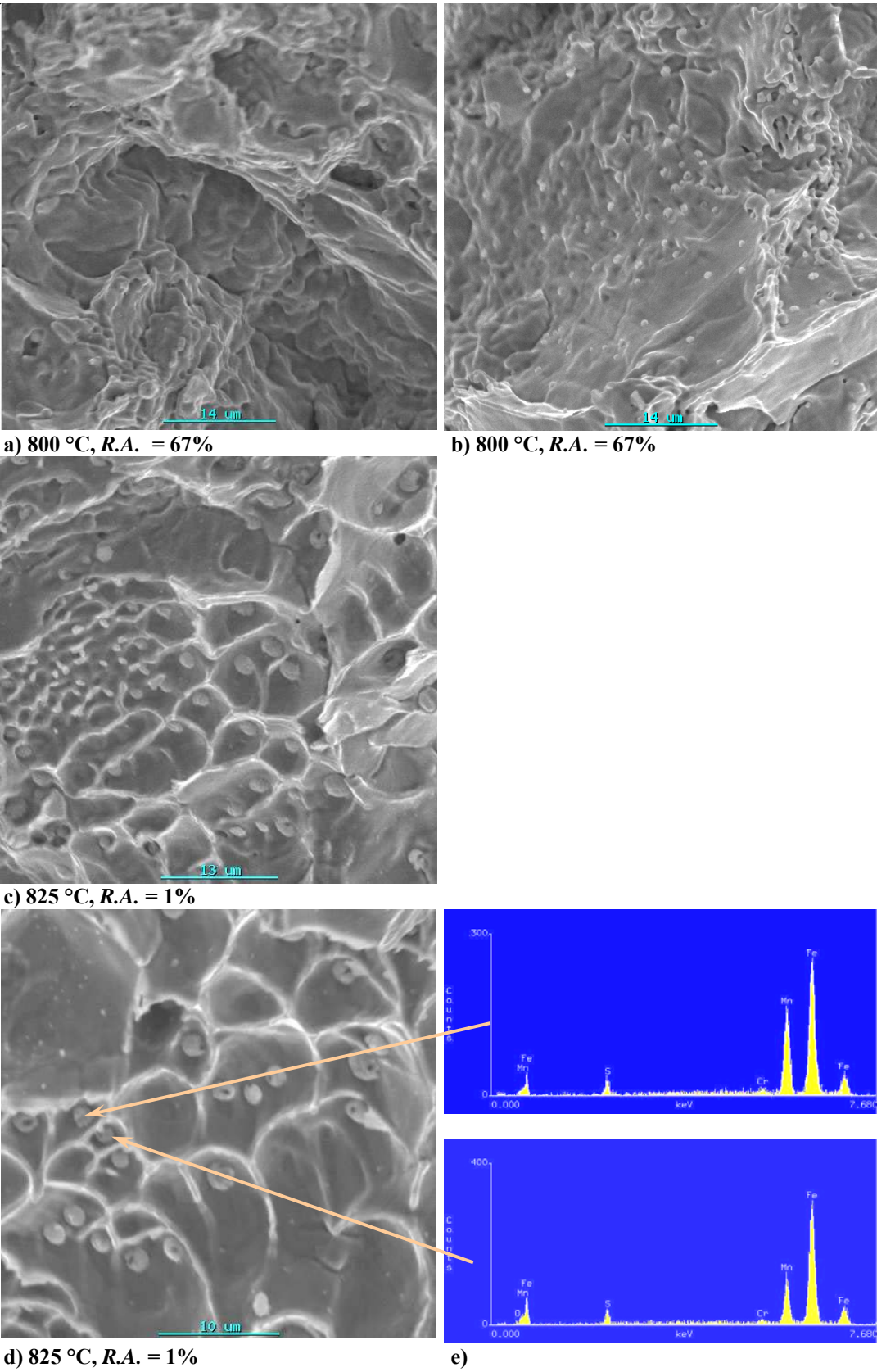
Hot tensile samples: SEM was performed on the fracture surfaces of the hot tensile specimens tested at 800 °C (good ductility: 67%), 825 °C (poor ductility: 1%) and 1175 °C (poor ductility: 17%).

The fracture surface of the ductile specimen tested at 800 °C shows transgranular fracture (**Figure 8.11 a and b**) even though there are many MnS precipitates. In the low ductility sample tested at 825 °C (**c, d and e**), intergranular fracture by microvoid coalescence along prior austenite grain boundaries was evident, with a profusion of microvoids containing MnS(+Cr) precipitates.

Figure 8.12 a–c show SEM backscatter images of the low ductility hot tensile specimen fracture surfaces for testing temperature 825 °C: intergranular fracture and copious precipitation of MnS-rich spherical precipitates. Analyses of MnS particles that range in size from 0.5-3.5 µm. with a darker centre in the low ductility sample tested at 825 °C, show that the centre of these precipitates is almost exclusively MnS, whereas the outer regions contain some B, C and Cr. Pure MnS precipitates first and acts as a nucleus for subsequent precipitation of a combination of MnS with B, C and Cr.

Figure 8.13 shows SEM images of the low ductility hot tensile specimen tested at 1175 °C. The intergranular fracture surfaces are covered with large MnS precipitates and show fine dimpling.

Figure 8.14 shows SEM backscatter electron images of the hot tensile specimen fracture surface (testing temperature 1175 °C) where incipient melting has occurred, indicated by the smooth grain surfaces. The arrows point to grain boundary precipitation, precipitate free zone (PFZ) and matrix precipitation.



a) 800 °C, R.A. = 67%

b) 800 °C, R.A. = 67%

c) 825 °C, R.A. = 1%

d) 825 °C, R.A. = 1%

e)

Figure 8.11: SEM backscatter images of the hot tensile specimen fracture surfaces: a) and b) 800 °C testing temperature (transgranular fracture) and c – e) 825 °C (intergranular fracture).

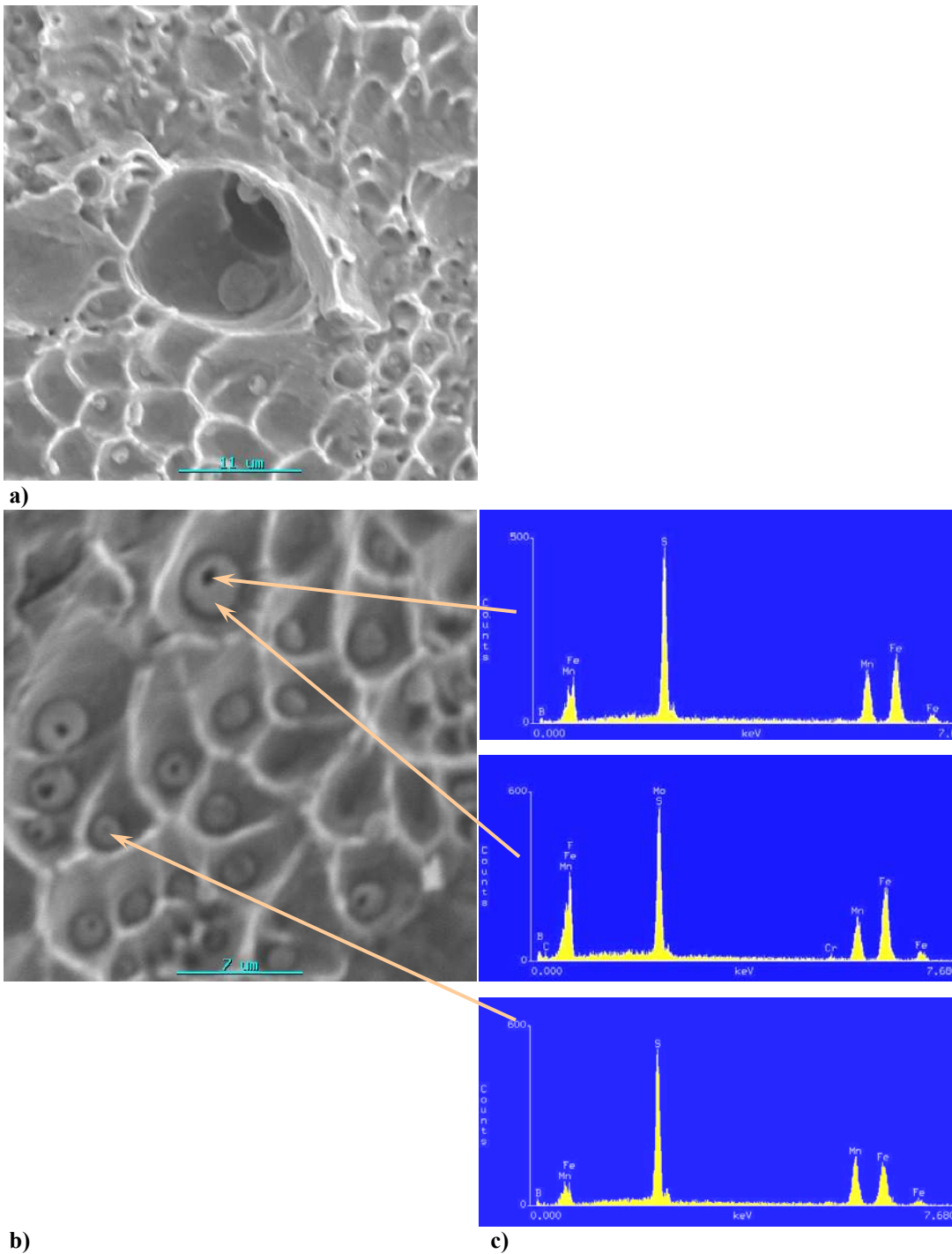
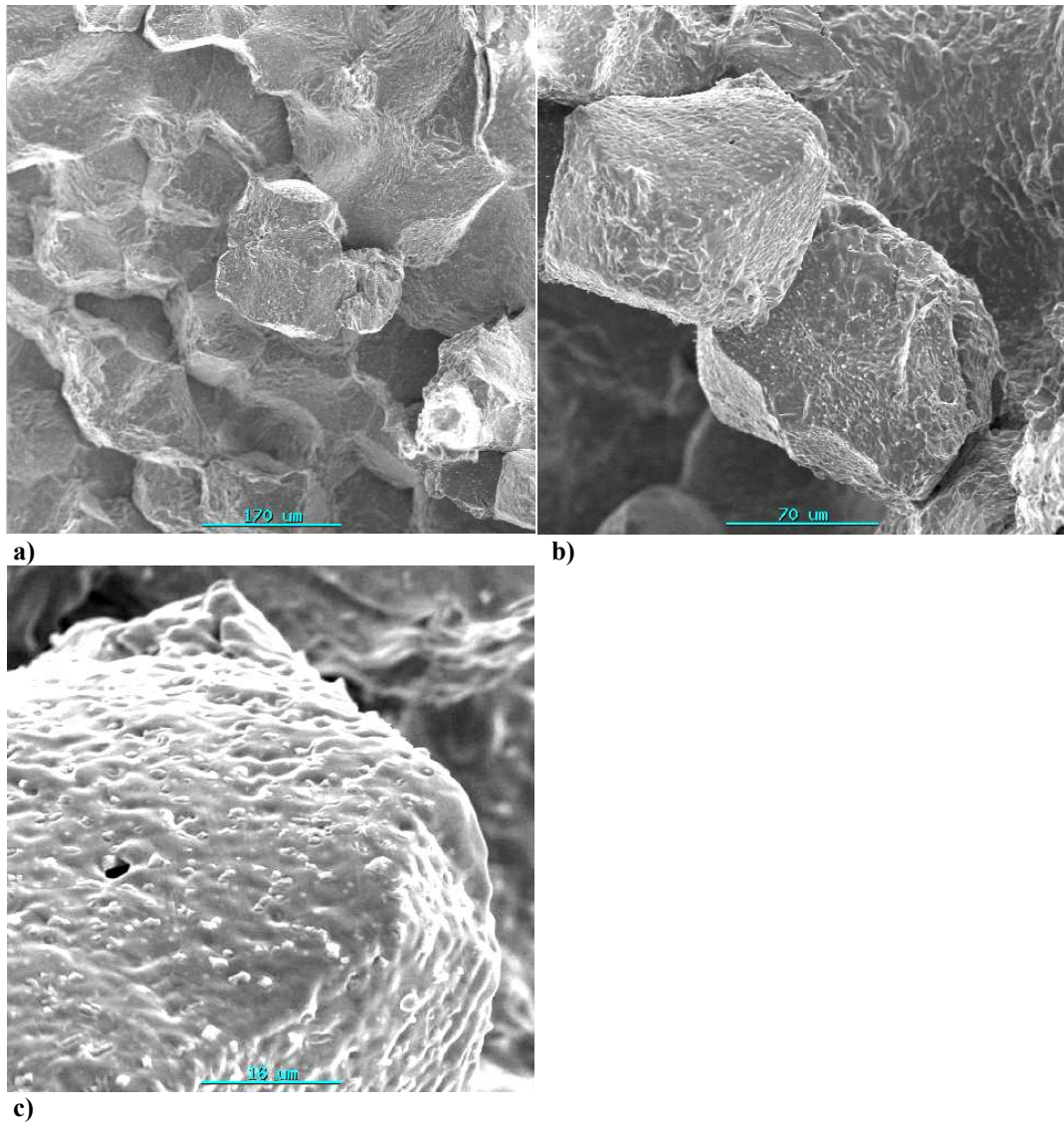


Figure 8.12 a-e: SEM backscatter images of the low ductility hot tensile specimen fracture surfaces for testing temperature 825 °C, showing intergranular fracture and copious precipitation of MnS-rich spherical precipitates.



a)
b)
c)
Figure 8.13 a-c: SEM backscatter electron images of the hot tensile specimen fracture surface (testing temperature 1175 °C) showing intergranular fracture. The fracture surfaces are covered with large MnS precipitates.

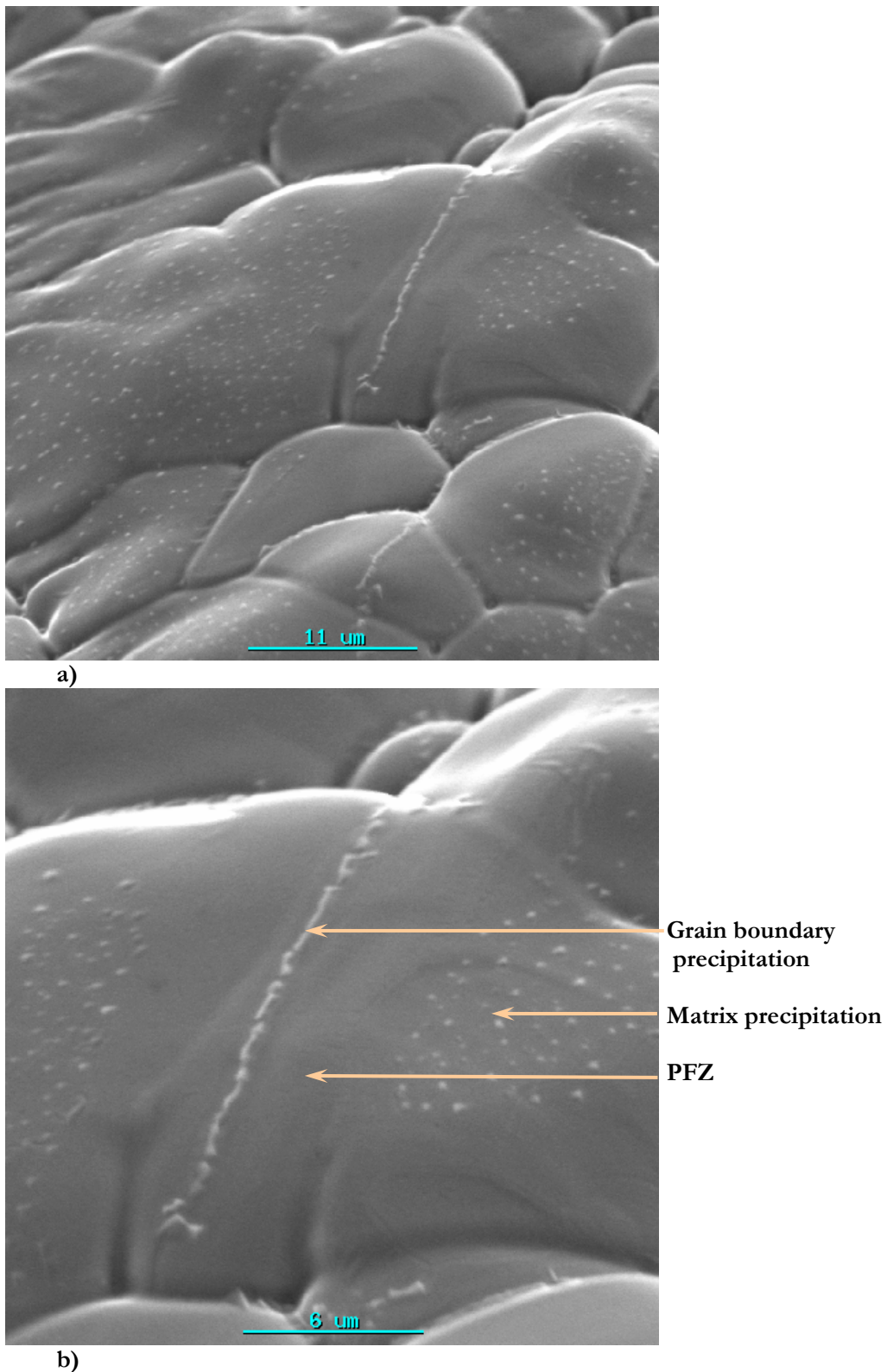


Figure 8.14 : SEM backscatter electron images of the hot tensile specimen fracture surface (testing temperature 1175 °C) showing grain boundary precipitation, precipitate free zone (PFZ) and matrix precipitation.

8.4.6 Transmission electron microscopy

Figure 8.15 shows TEM bright field images of a low ductility hot tensile sample from *SiB-1* cooled at $2\text{ }^{\circ}\text{C}\cdot\text{s}^{-1}$ to a testing temperature of $1175\text{ }^{\circ}\text{C}$. **Figure 8.15 a** and **b** show boron nitride precipitates that had nucleated on iron sulphide precipitates (FeS core $\sim 30\text{-}50\text{ nm}$, BN $\sim 200\text{-}300\text{ nm}$). **Figure 8.15 c** shows a typical BN precipitate with a mean diameter of $\sim 250\text{ nm}$. Fine iron sulphide precipitates with diameters of $\sim 50\text{-}80\text{ nm}$, found only in the low ductility sample and not in the two ductile samples, are shown in **Figure 8.15 d and e**. The small features in these two micrographs may be precipitates, but were not identified.

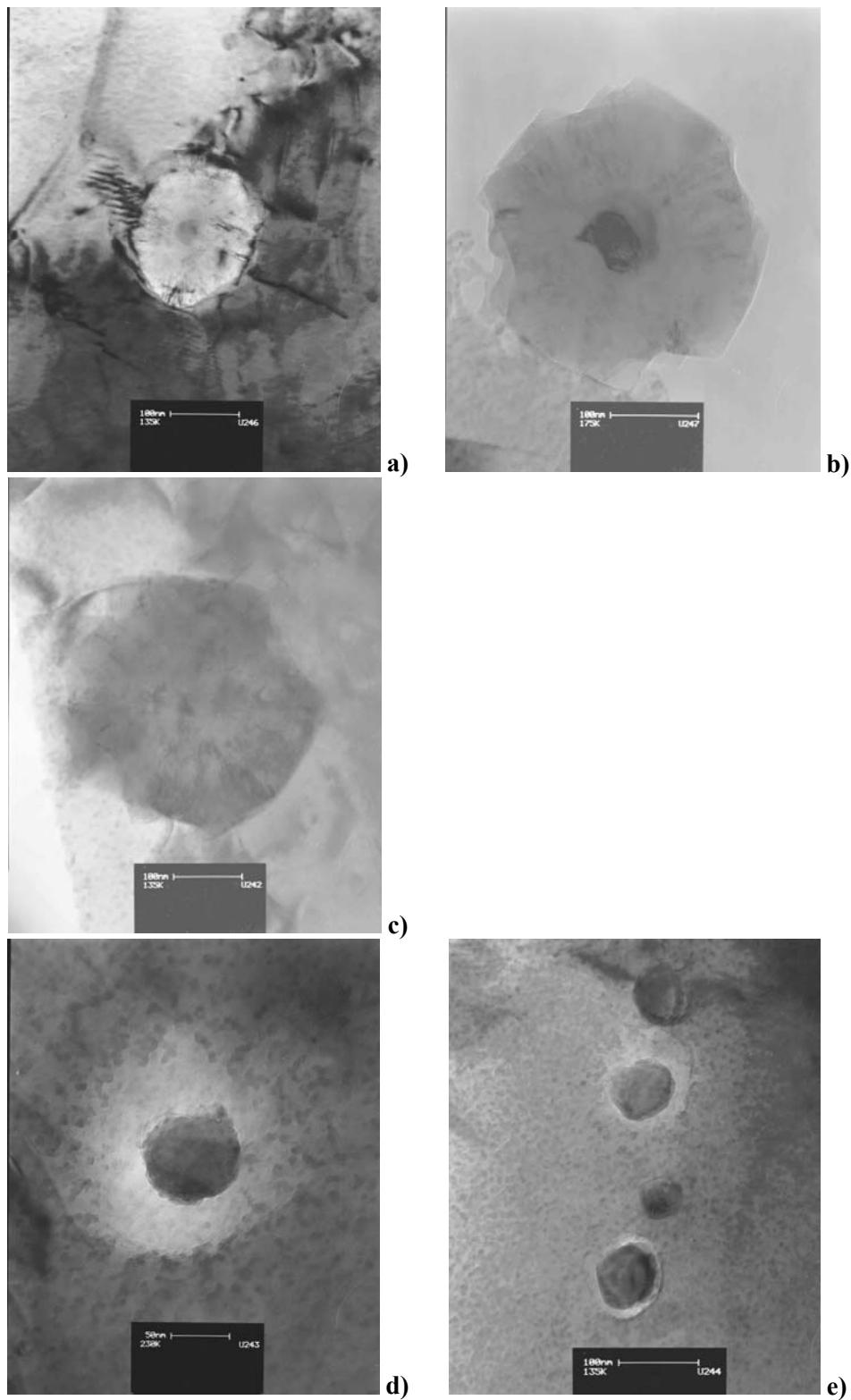


Figure 8.15: TEM bright field images of a low ductility hot tensile sample from *SiB-1* cooled at $2^{\circ}\text{C}\cdot\text{s}^{-1}$ to a testing temperature of 1175°C .
 a) and b) Boron nitride surrounding iron sulphide precipitate (FeS core $\sim 30\text{-}50$ nm, BN $\sim 200\text{-}300$ nm).
 c) Boron nitride (~ 250 nm).
 d) and e) Iron sulphide precipitates ($\sim 50\text{-}80$ nm).

8.5 SI-KILLED BORON STEEL *SiB-2*

8.5.1 Introduction

Figure 8.16 shows the engineering stress – elongation curves for steel *SiB-2*, which was only tested at a cooling rate of $2^{\circ}\text{C}\cdot\text{s}^{-1}$ after *in situ* melting. The onset of dynamic recrystallisation is indicated by an arrow on the graph and the temperature is listed in **Table 8.5**. The maximum strength values are shown as a function of testing temperature in **Figure 8.17**. The modelled Thermo-CalcTM Ae_3 temperature (877°C) and Ae_1 temperature (711°C) from **Table 8.2** are indicated on the graphs.

The percentage reduction in area (% *R. A.*) is shown as a function of testing temperature in **Figure 8.18** and the percentage total elongation is shown as a function of testing temperature in **Figure 8.19**. The modelled Thermo-CalcTM Ae_3 ferrite start transformation temperature of 877°C from **Table 8.2** is indicated on the graphs. Scanning electron microscopy images are shown in **Figure 8.20** to **Figure 8.22**.

8.5.2 Maximum Strength

The engineering stress vs. elongation (**Figure 8.16**) and the maximum strength vs. temperature graphs (**Figure 8.17**) show a similar trend to *SiB-1*: increasing maximum strength (S_u) with decrease in temperature from 1100°C to 850°C , then a sudden decrease in S_u just below the Ae_3 (877°C) followed by an increase as testing temperature drops further. The S_u remains relatively steady from $1100 - 1225^{\circ}\text{C}$ ($\sim 23\text{-}27$ MPa), despite the dynamic recrystallisation at 1200 and 1225°C .

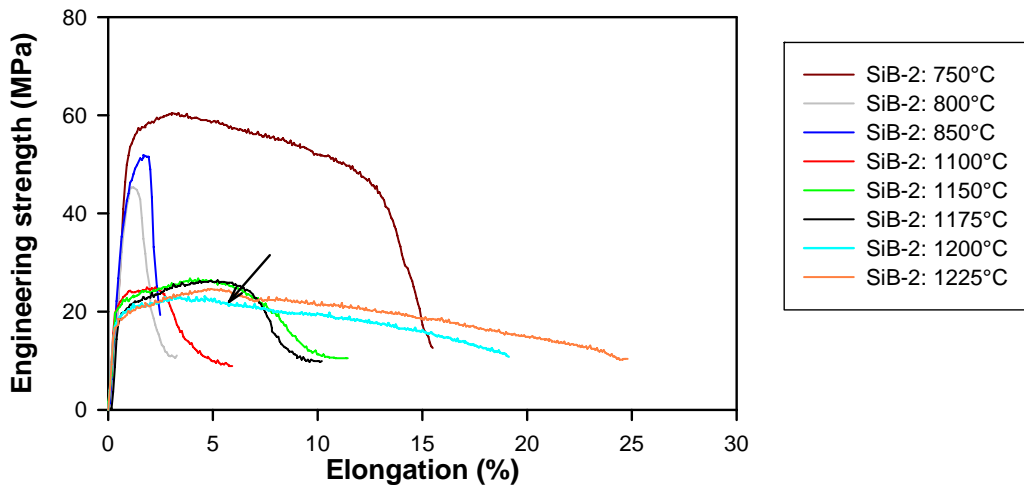


Figure 8.16: Engineering stress as a function of elongation for S-killed steel *SiB-2* after *in situ* melting, followed by cooling to the test temperature at $2^{\circ}\text{C}\cdot\text{s}^{-1}$. The arrow shows the onset of dynamic recrystallisation.

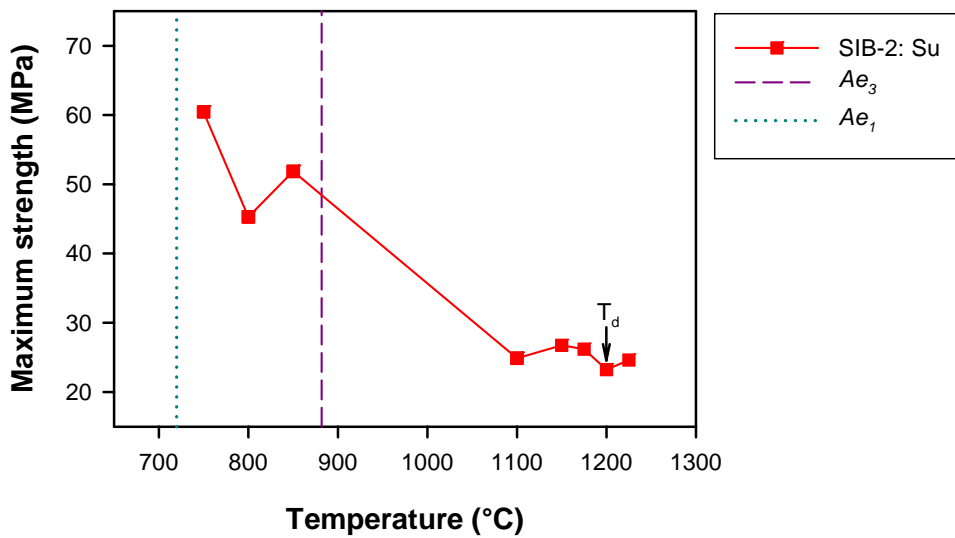


Figure 8.17: Maximum strength for steel *SiB-2* as a function of testing temperature. The arrow shows the onset of dynamic recrystallisation.

8.5.3 Reduction in area

The ductility trough extends from 1200 – 750 °C, as shown in **Figure 8.18**, with extremely low ductility (< 20% *R. A.*) from 1175 – 800 °C, and a minimum *R. A.* of 1.4% at 800 °C. Ductility recovery on the low temperature side of the trough coincides with the formation of ferrite on the austenite grain boundaries, which occurs at temperatures below the A_{e3} (877 °C). Note that the ductility and maximum strength recover simultaneously below 800 °C.

On the high temperature end of the trough, the recovery in ductility occurs at 1200 °C, which coincides with the onset of dynamic recrystallisation.

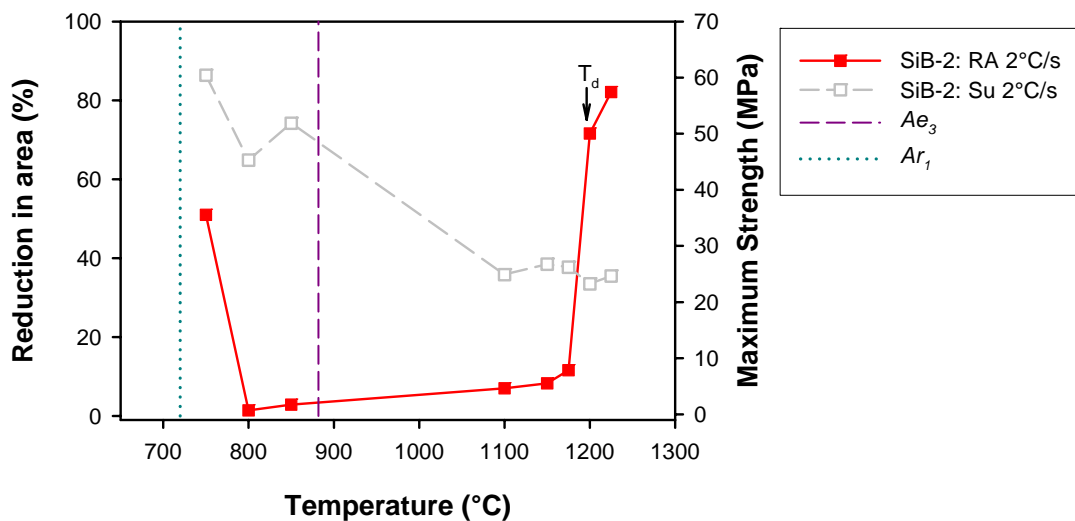


Figure 8.18: Reduction in area for steel *SiB-2* as a function of testing temperature.

8.5.4 Total elongation

The total elongation (**Figure 8.19**) follows a similar trend to the reduction in area. The elongation trough extends from 1200 - 750 °C, with a minimum total elongation of 2.5% at 850 °C. The low temperature recovery in elongation coincides with the formation of ferrite (*i.e.* below the A_{e3} temperature) and the high temperature recovery coincides with the onset of dynamic recrystallisation. The decrease in total elongation from 12-10% between 1150 and 1175 °C is within experimental error and can be ignored.

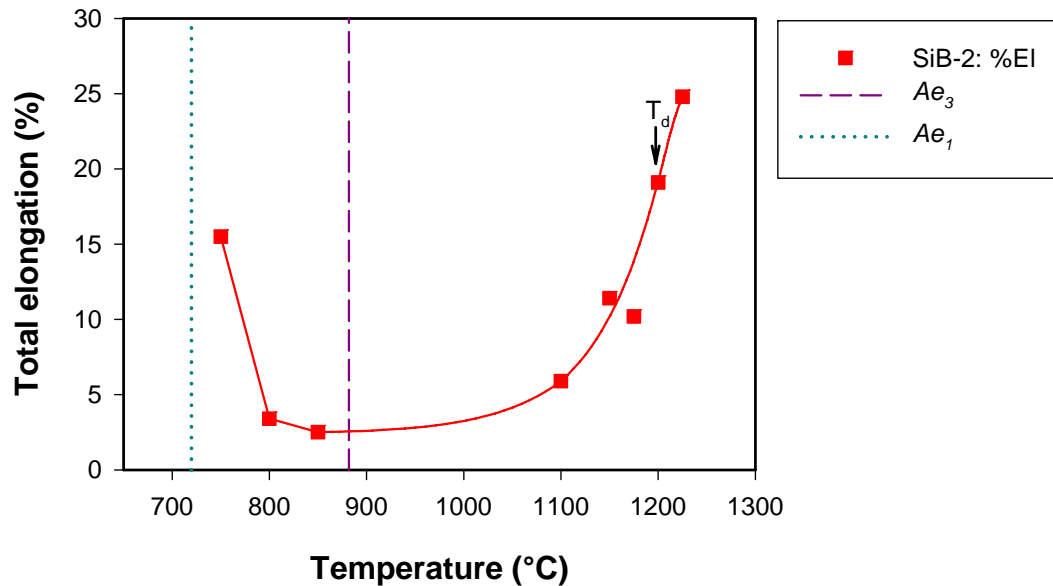


Figure 8.19: Elongation for steel *SiB-2* as a function of testing temperature.

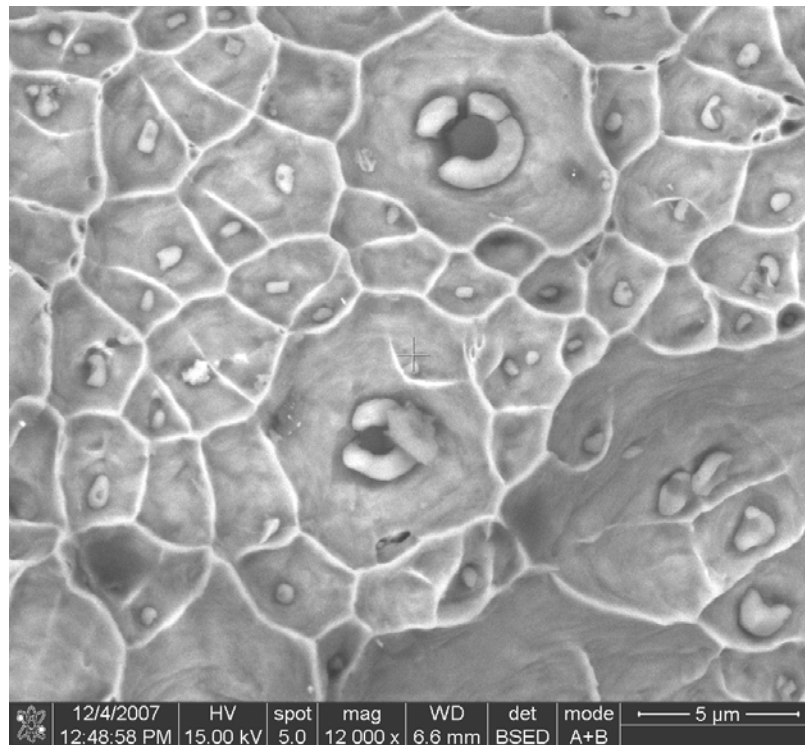
8.5.5 Scanning electron microscopy

SEM backscatter electron images of the fracture surface of a low ductility hot tensile sample from *SiB-2* (tested at 850 °C, *R.A.* = 3%) are shown in **Figure 8.20**, **Figure 8.21** and **Figure 8.22**.

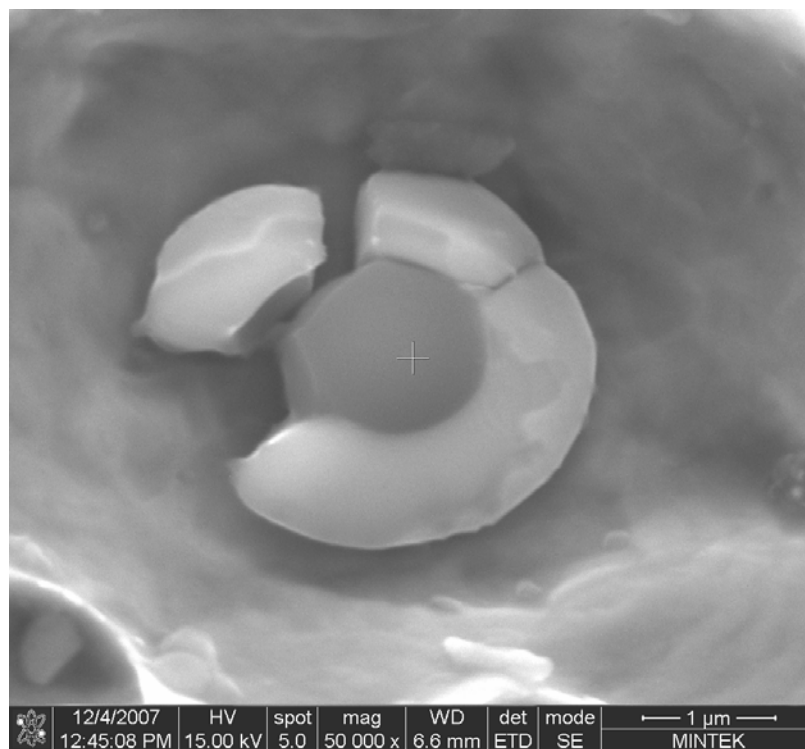
Figure 8.20 a shows voids around complex precipitates. **Figure 8.20 b** shows a fractured complex precipitate (diameter ~3 μm) of MnS around a SiO₂ core (diameter ~1 μm).

Figure 8.21 shows austenite grain boundary triple points with some intergranular cracking (**a**) and microvoid coalescence between MnS precipitates along the austenite grain boundaries with intergranular cracking (**b**).

Figure 8.22 shows matrix and grain boundary precipitation (**a**) and cracking along the austenite grain boundary (**b**).



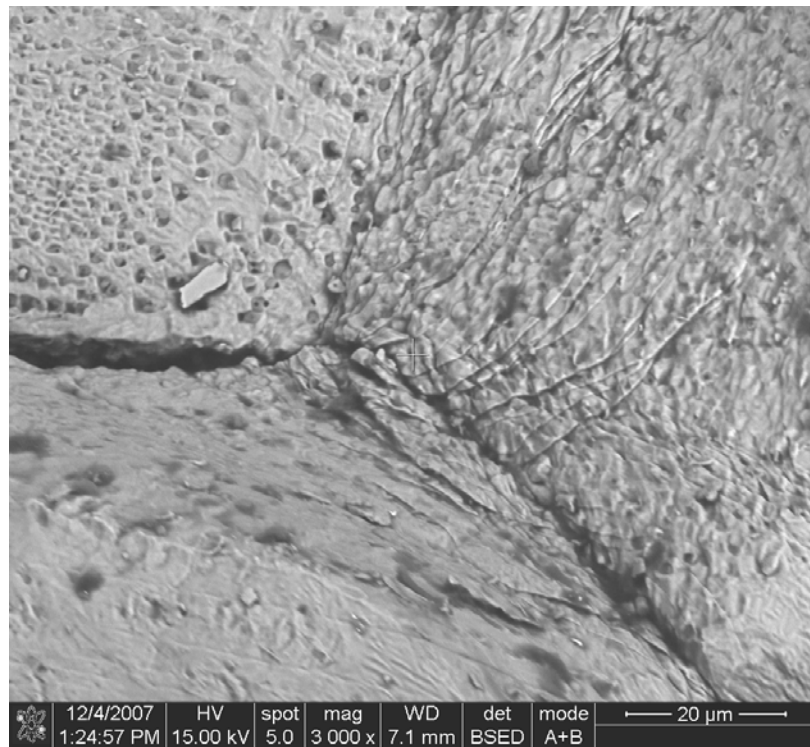
a)



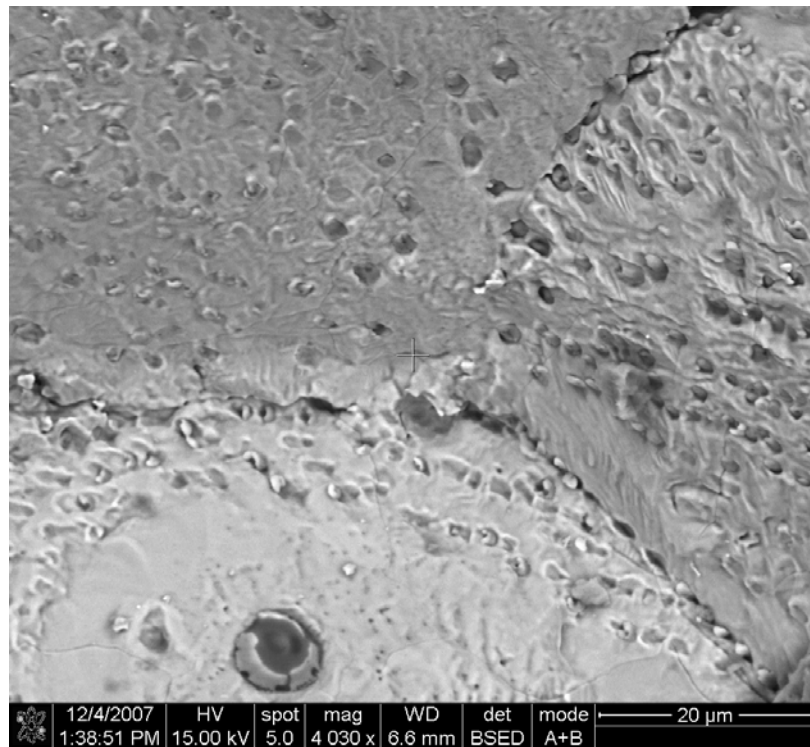
b)

Figure 8.20: SEM backscatter images of the fracture surface of a low ductility hot tensile sample from *SiB-2* (850 °C, *R.A.* = 3%).

- a) **Decohesion around complex precipitates.**
- b) **Fractured complex precipitate showing MnS around a SiO₂ core.**

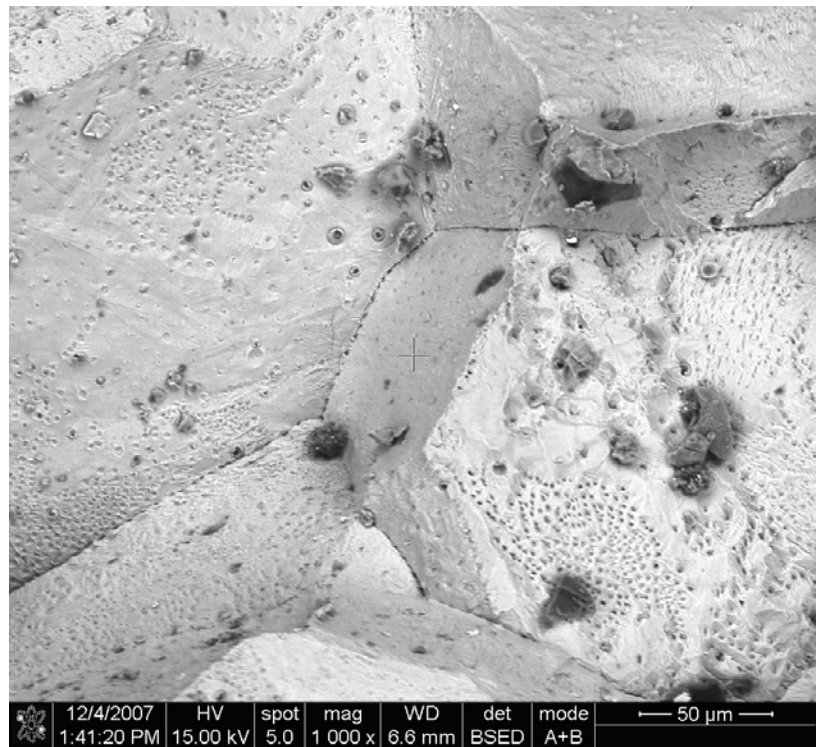


a)

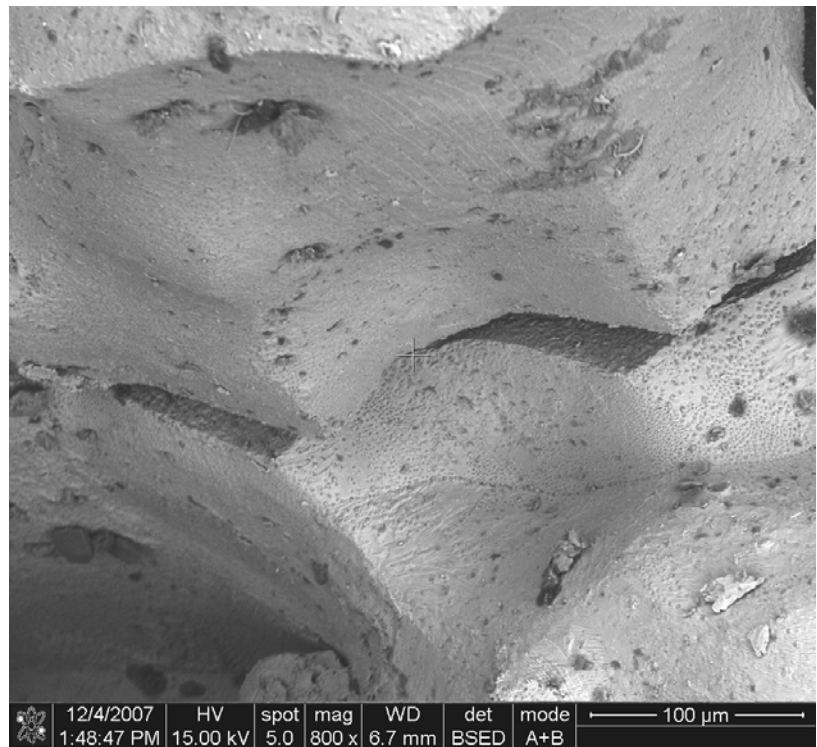


b)

Figure 8.21 a and b: SEM backscatter images of the fracture surface of a low ductility hot tensile sample from *SiB-2* (850 °C, *R.A.* = 3%) showing austenite grain boundary triple points, microvoid coalescence between MnS precipitates and cracking along the austenite grain boundaries.



a)



b)

Figure 8.22: SEM backscatter images of the fracture surface of a low ductility hot tensile sample from *SiB-2* (850 °C, *R.A.* = 3%).

- a) Grain boundary precipitation.
- b) Grain boundary cracking.

8.6 SI-KILLED BORON STEEL *SiB-3*

8.6.1 Introduction

Figure 8.23 shows the engineering stress – elongation curves for steel *SiB-3*. The onset of dynamic recrystallisation is indicated by an arrow on the graph and the temperature is listed in **Table 8.5**. The maximum strength values are shown as a function of testing temperature in **Figure 8.24**. The modelled Thermo-CalcTM Ae_3 temperature (872 °C) and Ae_1 temperature (711 °C) from **Table 8.2** are indicated on the graphs.

The percentage reduction in area (% *R. A.*) is shown as a function of testing temperature in **Figure 8.25** and the percentage total elongation is shown as a function of testing temperature in **Figure 8.26**. The modelled Thermo-Calc Ae_3 transformation temperature of 872 °C and Ae_1 temperature (711 °C) from **Table 8.2** are indicated on the graphs. Scanning electron microscopy images are shown in **Figure 8.27**.

8.6.2 Maximum Strength

Figure 8.23 and **Figure 8.24** show a near-linear trend of increasing maximum strength with decreasing temperature. There is no noticeable drop in S_u between the Ae_3 and Ae_1 , but as there was no test done at 800 °C, this cannot be confirmed. The onset of dynamic recrystallisation occurred at 1150 °C, which is lower than for *SiB-1* and *SiB-2*. The S_u drops to 22.6 MPa at 1200 °C.

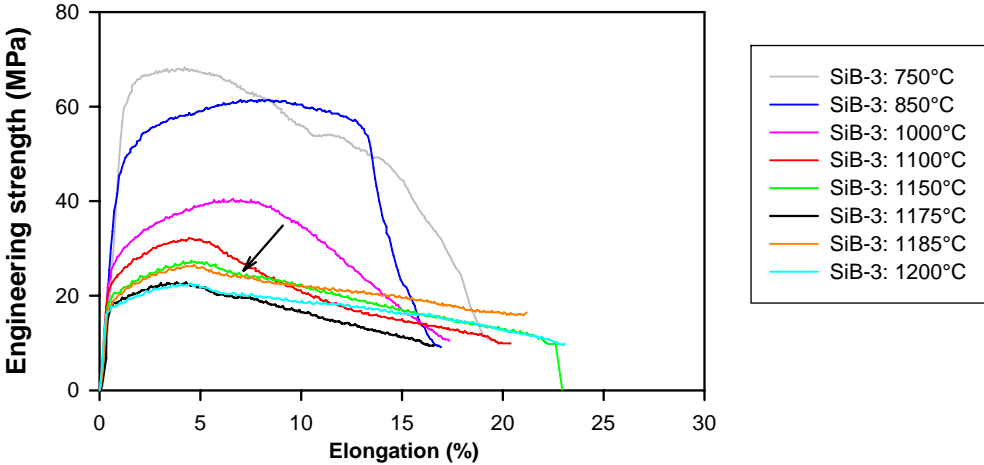


Figure 8.23: Engineering stress as a function of elongation for Si-killed steel *SiB-3* after *in situ* melting, followed by cooling to the test temperature at $2\text{ }^\circ\text{C}\cdot\text{s}^{-1}$. The arrow shows the onset of dynamic recrystallisation.

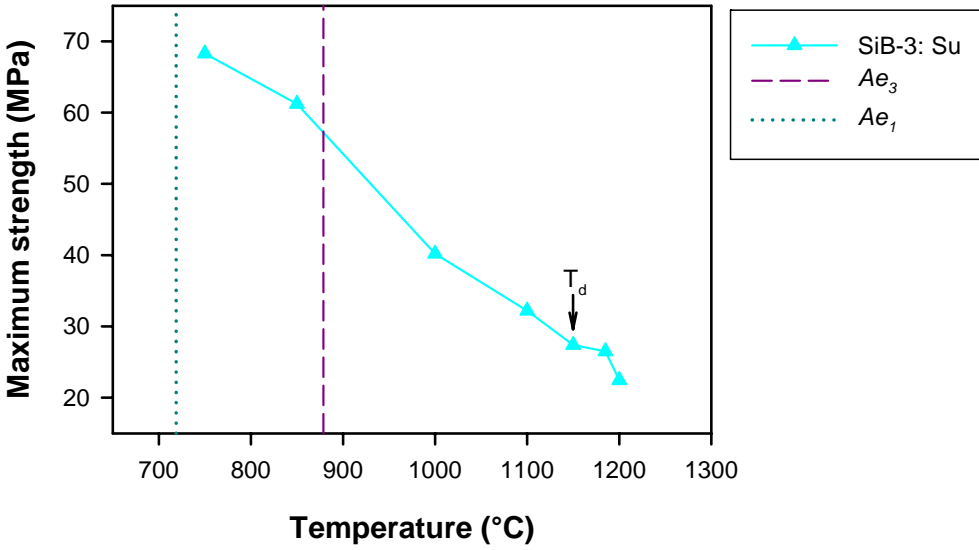


Figure 8.24: Maximum strength for steel *SiB-3* as a function of testing temperature.

8.6.3 Reduction in area

Figure 8.25 shows that Si-killed steel *SiB-3* has two distinct oscillations in the *R. A.* curve. This is in contrast to steels *SiB-1* and *SiB-2*, where single, wide and deep ductility troughs were found.

The shallow high temperature trough extends from 1150 - 1000 °C with a minimum at 1100 °C (49% *R. A.*). The recovery in ductility at 1150 °C coincides with the onset of dynamic recrystallisation. With further increase in temperature, the ductility increases to 86% (1185 °C) and then decreases slightly (1200 °C).

The deeper low temperature trough extends from 1000 - 750 °C, with a minimum at 850 °C (33% *R. A.*). Low-temperature ductility recovery occurs between the Ae_3 and Ae_1 temperatures.

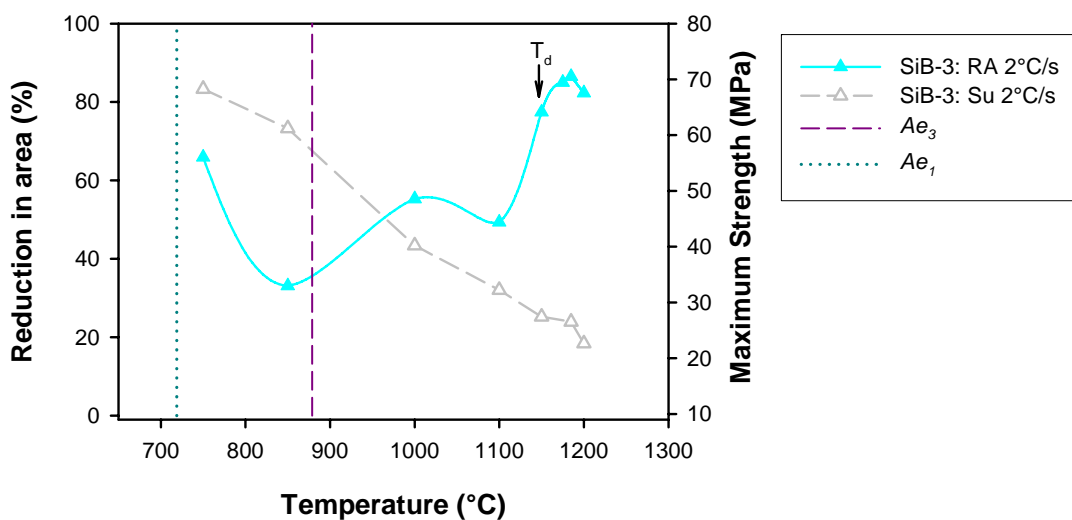


Figure 8.25: Reduction in area for steel *SiB-3* as a function of testing temperature.

8.6.4 Total elongation

Unlike the reduction in area curve, the total elongation curve in **Figure 8.26** has one shallow trough between 1150 - 750 °C, with a minimum of 17% elongation at 850 °C. The maximum elongation value (23 %) is found at 1200 °C. There is a slight variation in the elongation between 1150 and 1200 °C, but this is probably due to experimental error.

Low-temperature elongation recovery occurs between the Ae_3 and Ae_1 temperatures.

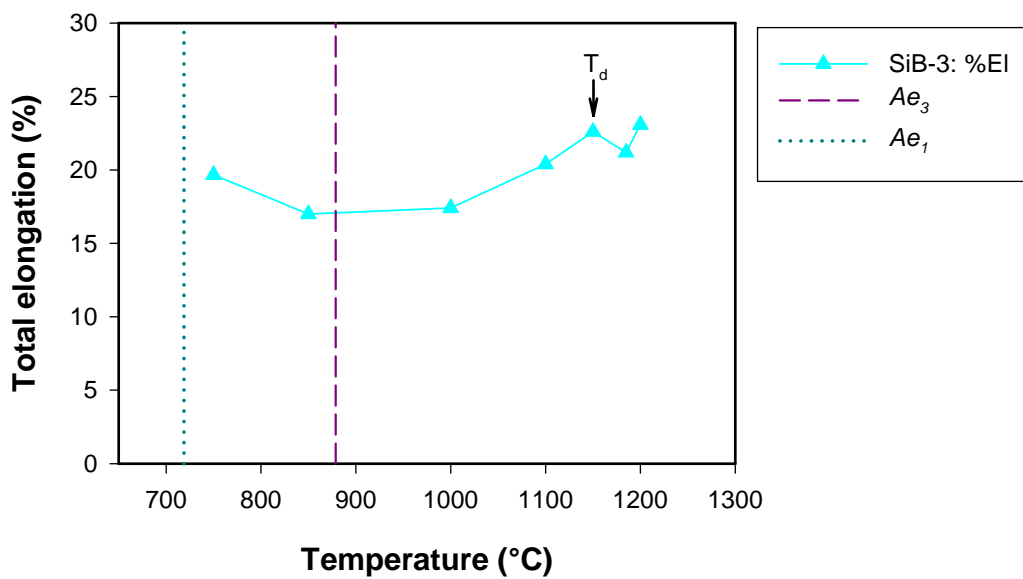
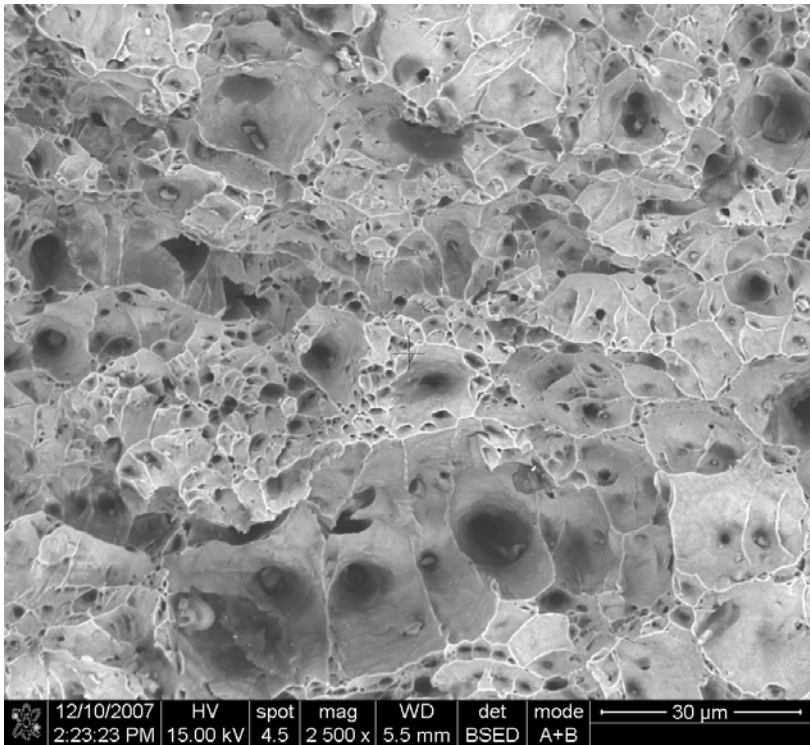


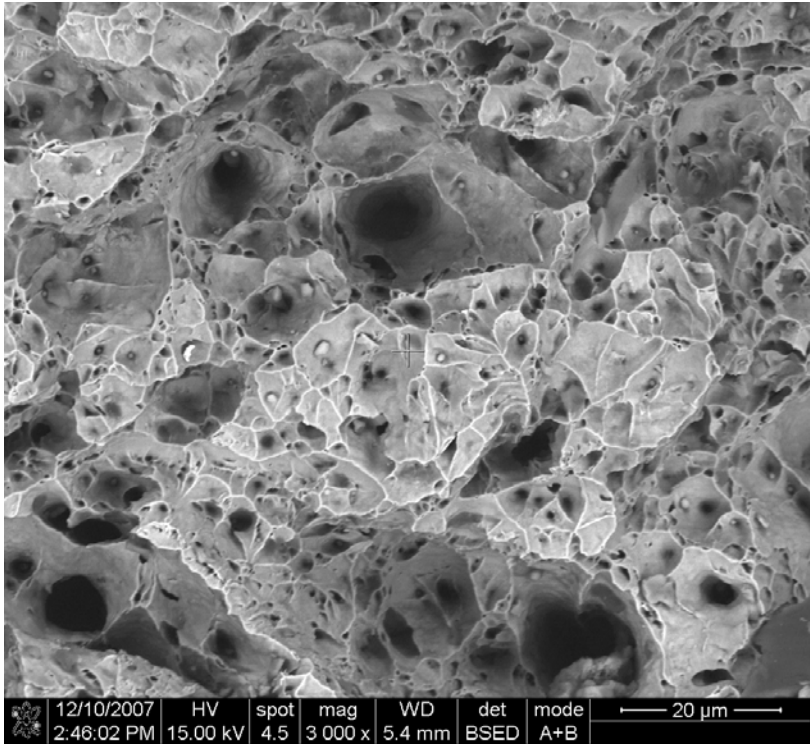
Figure 8.26: Elongation for steel *SiB-3* as a function of testing temperature, strain rate and cooling rate.

8.6.5 Scanning electron microscopy

SEM backscatter electron images of the fracture surface of a ductile hot tensile sample from *SiB-3* (tested at 1185 °C, *R.A.* = 86%) are shown in **Figure 8.27 a** and **b**. The fracture mode is transgranular (no distinct fracture along the austenite grain boundaries) and is covered with voids around precipitates, which are mostly MnS that formed on oxide nuclei such as SiO₂. The voids range in size from less than 1 μm around the small precipitates, to as large as 30 μm around the larger 3-5 μm precipitates.



a)



b)

Figure 8.27 a) and b): SEM backscatter images of the fracture surface of a ductile hot tensile sample from *SiB-3* (1185 °C, *R.A.* = 86%).

8.7 SI-KILLED BORON STEEL *SiB-4*

8.7.1 Introduction

Figure 8.28 shows the engineering stress – elongation curves for steel *SiB-4*. The onset of dynamic recrystallisation is indicated by an arrow on the graph and the temperature is listed in **Table 8.5**. The maximum strength values are shown as a function of testing temperature in **Figure 8.29**.

The percentage reduction in area (% *R. A.*) is shown as a function of testing temperature in **Figure 8.30** and the percentage total elongation is shown as a function of testing temperature in **Figure 8.31**. The modelled Thermo-Calc Ae_3 (885 °C) and Ae_1 (713 °C) transformation temperatures from **Table 8.2** are indicated on the graphs.

8.7.2 Maximum Strength

Figure 8.28 and **Figure 8.29** show a trend of increasing maximum strength with decreasing temperature. As only one test was done below the Ae_3 temperature at 885 °C, the effect of ferrite formation on maximum strength cannot be established. The onset of dynamic recrystallisation occurs at 1175 °C.

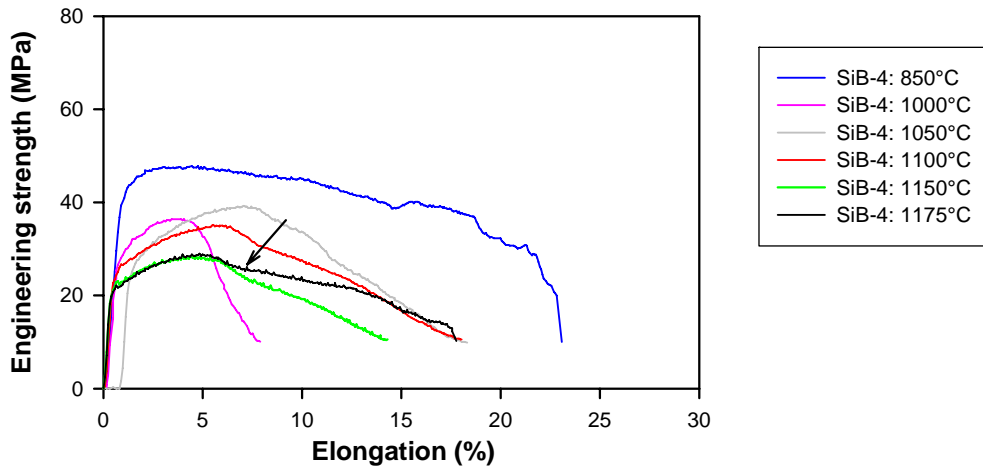


Figure 8.28: Engineering stress as a function of elongation for Si-killed steel *SiB-4* after *in situ* melting, followed by cooling to the test temperature at $2\text{ }^{\circ}\text{C}\cdot\text{s}^{-1}$. Dynamic recrystallisation is shown by an arrow on the graph.

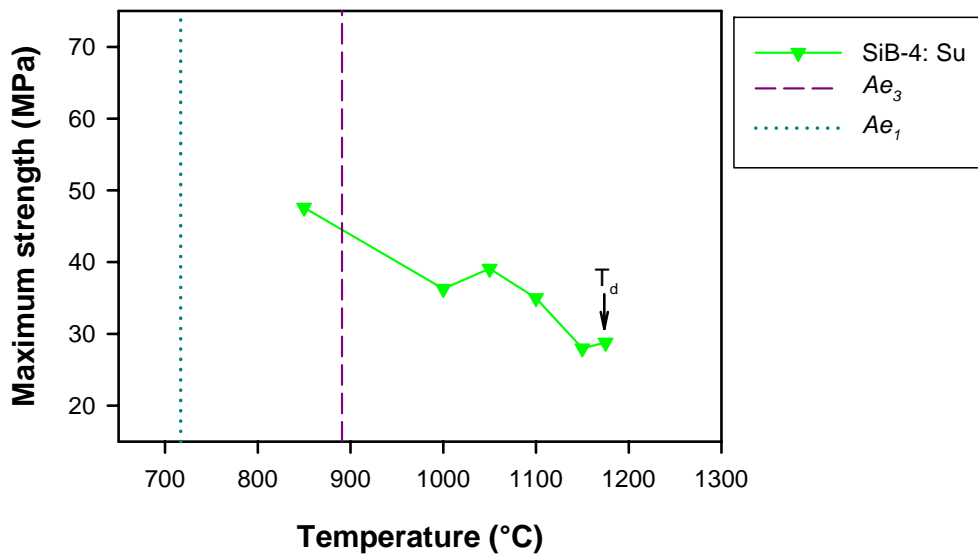


Figure 8.29: Maximum strength for steel *SiB-4* as a function of testing temperature. The arrow shows the onset of dynamic recrystallisation.

8.7.3 Reduction in area

Figure 8.30 shows that, similar to steel *SiB-3*, *SiB-4* has two distinct oscillations in the *R. A.* curve.

The shallow high temperature trough extends from 1175 – 1050 °C, with a minimum between 1100-1150 °C (42% *R. A.*). The recovery in ductility at 1175 °C occurs at the onset of dynamic recrystallisation.

The low temperature trough extends from 1050 - 850 °C, with a minimum at 1000 °C (16% *R. A.*). Low-temperature ductility recovery (88% *R. A.* at 850 °C) occurs between the Ae_3 and Ae_1 temperatures.

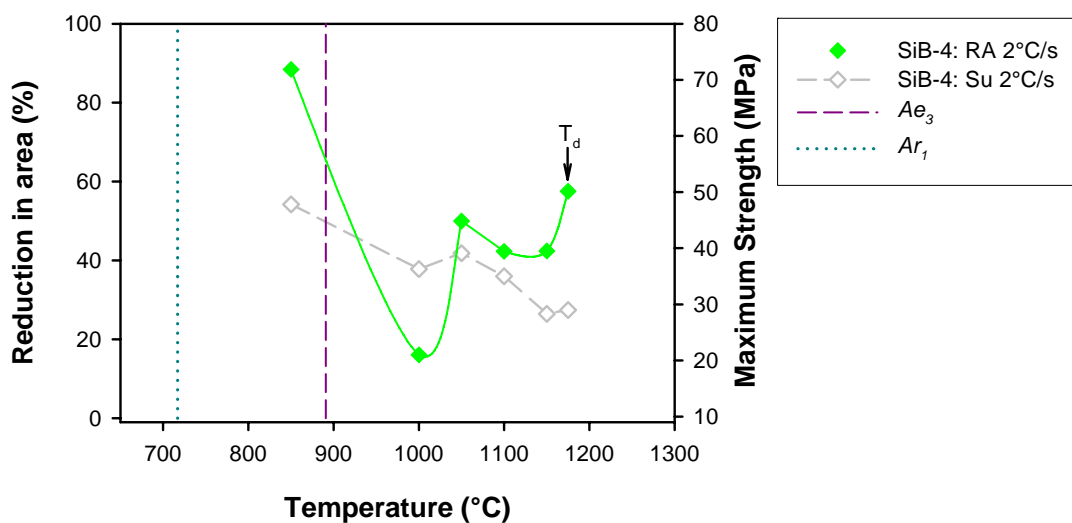


Figure 8.30: Reduction in area for steel *SiB-4* as a function of testing temperature.

8.7.4 Total elongation

Similar to the reduction in area, the total elongation curve in **Figure 8.31** also shows two troughs.

The small high temperature trough extends from 1175 - 1100 °C, with a minimum at 1150 °C. The recovery in total elongation at 1175 °C occurs at the onset of dynamic recrystallisation.

The low temperature trough extends from 1050 - 850 °C, with a minimum at 1000 °C. Low-temperature recovery in total elongation occurs between the Ae_3 and Ae_1 temperatures.

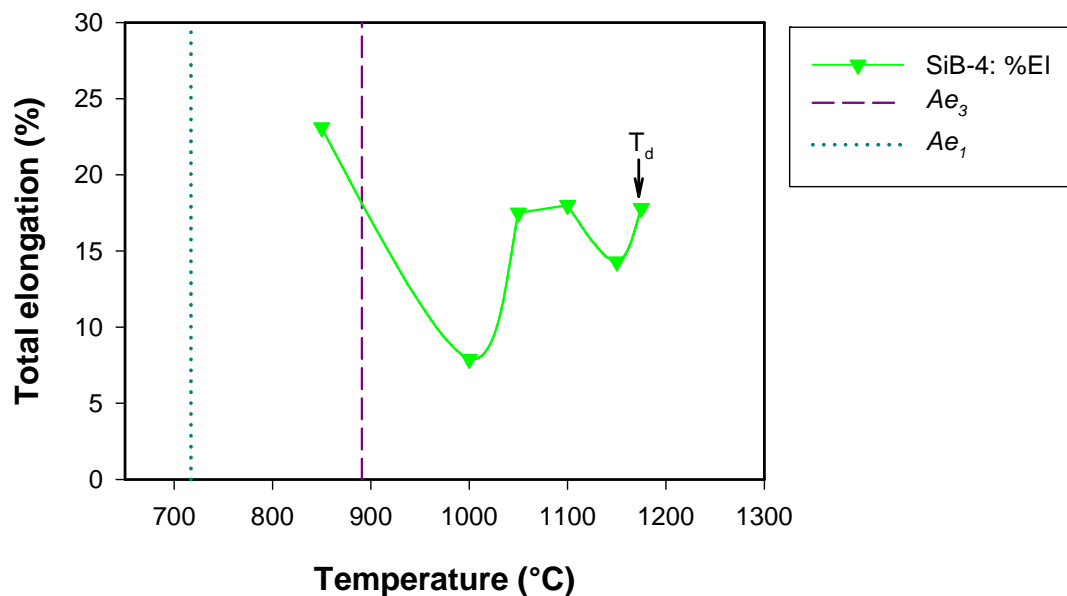


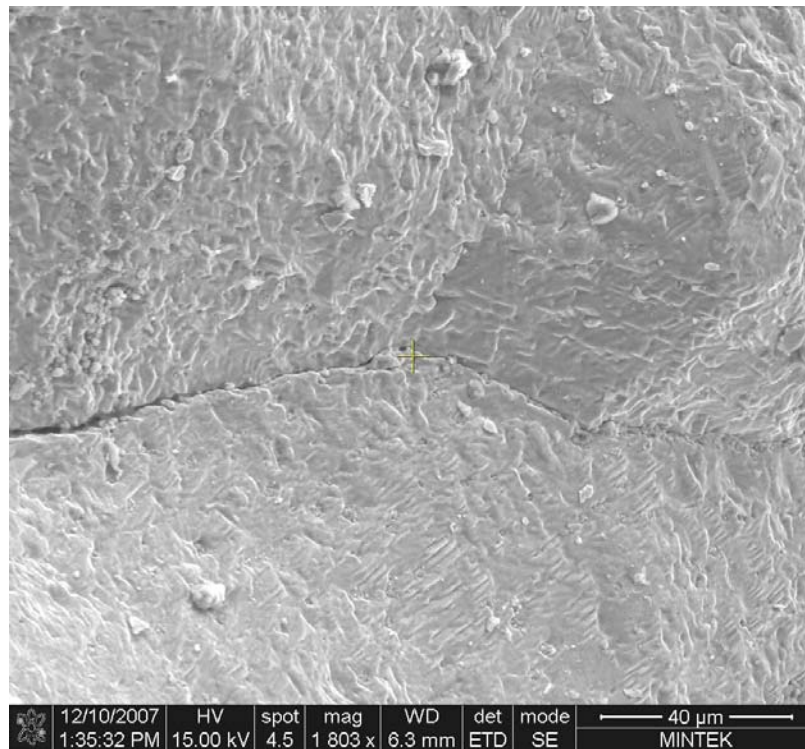
Figure 8.31: Elongation for steel *SiB-4* as a function of testing temperature.

8.7.5 Scanning electron microscopy

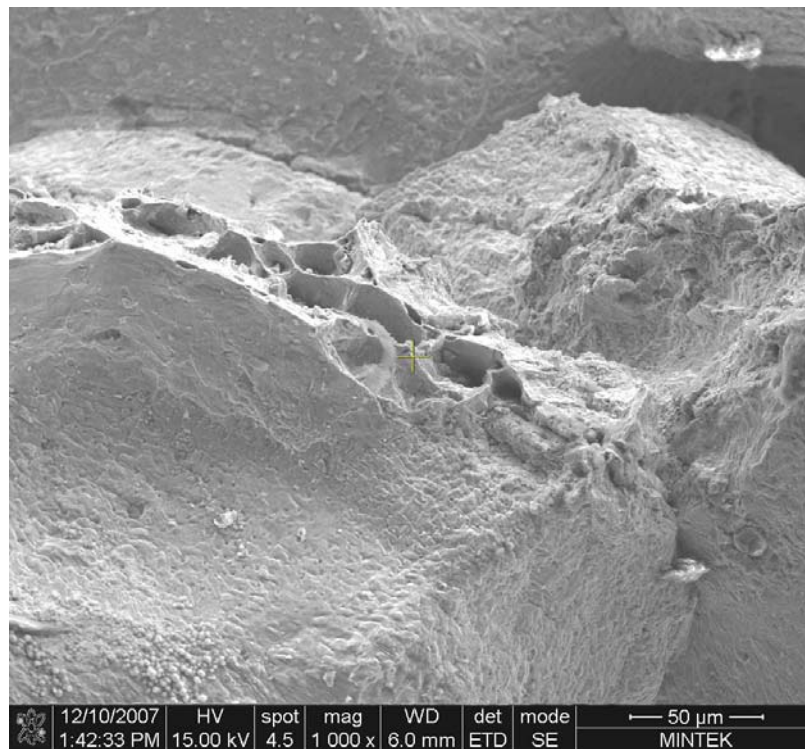
SEM backscatter electron images of the fracture surface of a low ductility hot tensile sample from *SiB-4* (tested at 1000 °C, *R.A.* = 16%) are shown in **Figure 8.32** and **Figure 8.33**.

Figure 8.32 a) shows that some of the fracture surfaces are flat with cracking along austenite grain boundaries. Fine striations were seen on the fracture surface, which are indicative of grain boundary sliding at low strain rates. **Figure 8.32 b)** shows a few precipitate-containing microvoids along grain boundaries.

Figure 8.33 a) and **b)** show that there was very little void formation around the small precipitates (mostly <1µm), which are evenly distributed in the matrix. The fracture surface is relatively smooth. This indicates that grain boundary sliding, and not microvoid coalescence, is the failure mechanism in this sample.

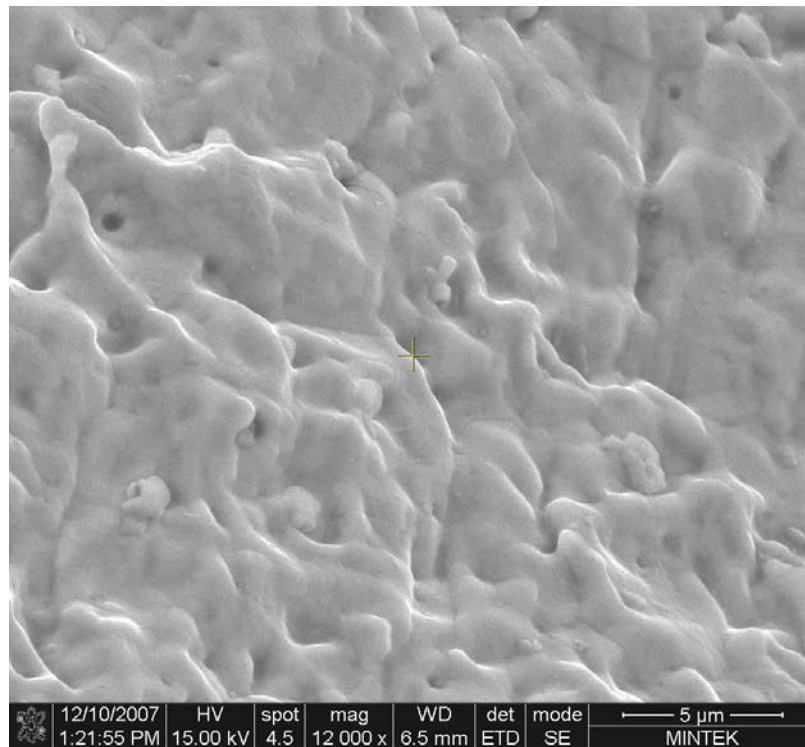


a)

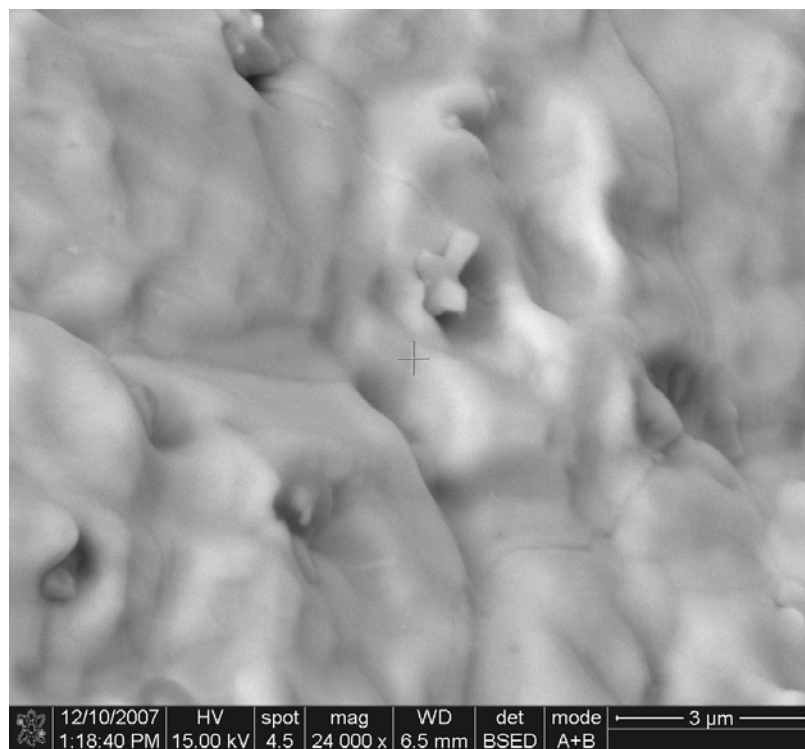


b)

Figure 8.32 a) and b): SEM backscatter images of the fracture surface of a low ductility hot tensile sample from *SiB-4* (1000 °C, *R.A.* = 16%), showing flat fracture surfaces indicative of grain boundary sliding.



a)



b)

Figure 8.33 a) and b) SEM backscatter images of the fracture surface of a low ductility hot tensile sample from *SiB-4* (1000 °C, *R.A.* = 16) showing <1 μm diameter MnS precipitates randomly situated in the austenite matrix.

8.8 SUMMARY OF HOT DUCTILITY RESULTS FOR THE SI-KILLED STEELS

The hot ductility results are summarised in **Table 8.5**, listing low- and high- temperature ductility recovery temperatures (Low T = 50% low temperature ductility recovery, high T = 50% high temperature ductility recovery), the minimum ductility temperature (and associated % *R. A.*) and the onset temperature of dynamic recrystallisation, T_d (and associated % *R. A.*). Note that *SiB-3* and *SiB-4* have two ductility troughs.

Table 8.5: Summary of the hot ductility results for the Si-killed boron steels (low and high temperature recovery, minimum *R.A.* and dynamic recrystallisation temperature).

Steel	Cooling Rate (°C.s ⁻¹)	Low T (°C)	Min. <i>R.A.</i>	High T (°C)	T_d °C (%)
SiB-1	1			1175	1175 (73)
	2	820	850 (1)	1185	1200 (78)
SiB-2	2	750	800 (1)	1180	1200 (72)
SiB-3	2	780	850 (33) and	970	
		1000	1100 (49)	1150	1150 (77)
SiB-4	2	925	1000 (16) and	1050	
		1050	1130 (40)	1180	1175 (60)

8.9 PRECIPITATION IN THE SI-KILLED BORON STEELS

The species of precipitates and modes of cracking found in the four silicon-killed steels are discussed below.

Scanning electron microscopy of the fracture surfaces showed that the low ductility specimens (< 50% *R. A.*) had failed by extensive intergranular cracking. At temperatures low in the austenite region *i.e.* ~875 - 1000 °C, the main mode of failure was microvoid coalescence between precipitate-containing voids on the austenite grain boundaries. At temperatures higher than 1000 °C, grain boundary sliding with no obvious dimpling typical of microvoid coalescence was found to be the main mode of failure.

Many large MnS precipitates ($\geq 3 \mu\text{m}$ diameter), often formed on oxides such as silica, were found in all tested samples of steels *SiB-1*, *SiB-2* and *SiB-3*, while the precipitates in steel *SiB-4* were mostly finer ($\leq 1 \mu\text{m}$ diameter).

TEM was only performed on steel *SiB-1*. BN precipitates were seen in most samples whereas pure FeS precipitates were observed only in low ductility samples. In high ductility samples, BN precipitates nucleated on FeS precipitates, forming complex BN+FeS precipitates.

Table 8.6: List of precipitates found in the Si-killed boron steels.

Steel	Mn:S ratio	Precipitates	
		SEM	TEM
<i>SiB-1</i>	Low	MnS (+B, C, Al, Si, Cu) MnS(+Cr)	Small FeS (30-50nm) BN (+FeS core)
<i>SiB-2</i>	Low	MnS + SiO ₂ core	*
<i>SiB-3</i>	High	MnS + SiO ₂ core	*
<i>SiB-4</i>	Low	Small MnS + SiO ₂ core	*

* TEM not performed on these steels due to lack of TEM equipment availability.

8.10 INTERRUPTED COOLING TESTS

Interrupted cooling tests were performed on samples from steel *SiB-2*. Samples were heated, melted *in situ*, then cooled to either 1220 or 1150 °C, held at that temperature for up to 10 minutes, then tensile tested at 1150 °C, as shown in **Table 8.7** and **Figure 8.34**.

The results of the hot ductility tests at 1150 °C after interrupted cooling are shown in **Figure 8.35** and **Table 8.7**. From these results, it can be seen that holding for 10 minutes at 1150 °C had no effect on the hot ductility (compare I1 and I2). Likewise, increasing holding time at 1220 °C from 5 to 10 minutes had no effect on the hot ductility (compare I3 and I4). However, by increasing the holding temperature from 1150 °C to 1220 °C, the hot ductility improved significantly by ~40% *R. A.*

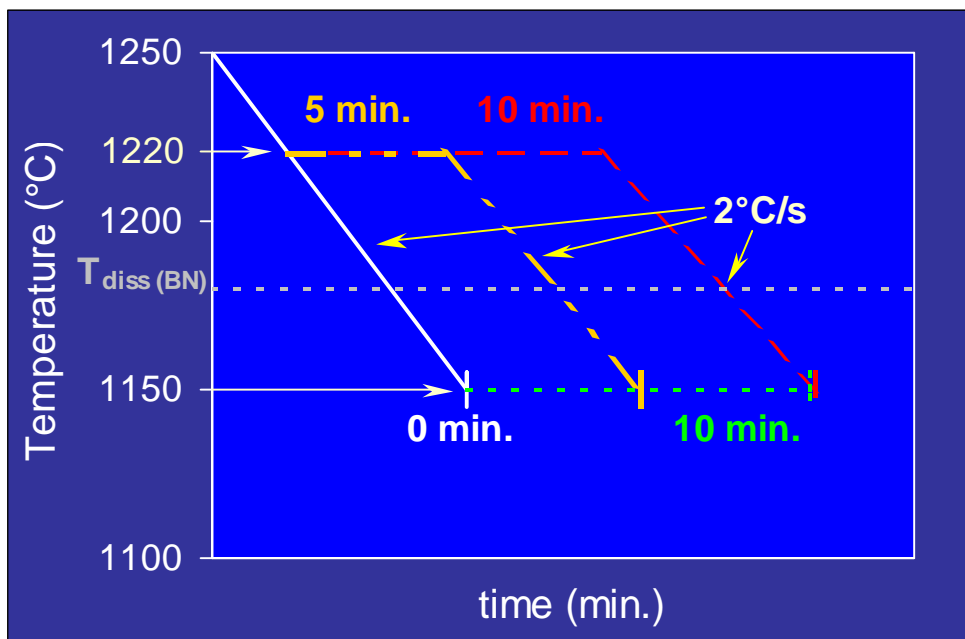


Figure 8.34: Schematic temperature - time diagram showing the hot tensile tests with interrupted cooling.

Table 8.7: Hot ductility (% R.A.) of interrupted cooling tests. All tensile tests were performed at 1150 °C on samples from steel *SiB-2*.

Test no.	Holding temperature (°C)	Holding time (min)	R. A. (%)
I1	1150	0	14
I2	1150	10	11
I3	1220	5	49
I4	1220	10	51

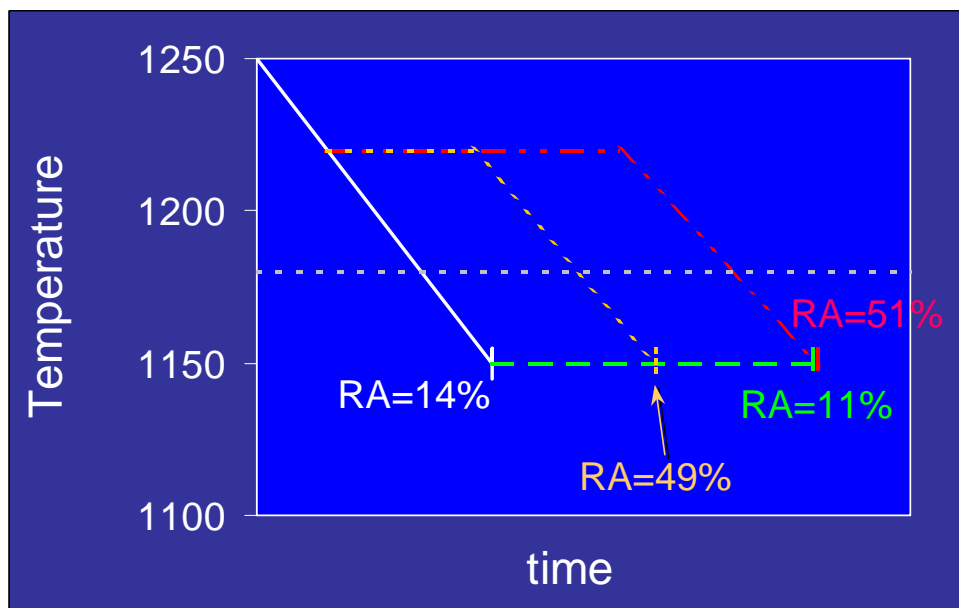


Figure 8.35 Interrupted cooling test results, showing low ductility for samples cooled directly to 1150 °C (no hold: 14%, 10 minutes hold: 11%), and higher ductility for samples cooled first to 1220 °C (5 minutes hold: 49%, 10 minutes hold: 51%).

Based on the results from the interrupted cooling tests, it appears that iron sulphides formed at temperatures below 1220 °C, leading to poor ductility. It is thus postulated that at the holding temperature of 1220 °C, there was sufficient driving force (long time at high temperature) for Mn to migrate to S at the grain boundaries. This would cause preferential formation of MnS, leaving less S available for FeS formation, and thus giving good ductility when tested at 1150 °C. However, with forced cooling directly to 1150 °C, migration of Mn would be inhibited and some MnS precipitation would be suppressed, allowing the formation of FeS. FeS is known to be detrimental to hot ductility, which would explain the poor ductility in those two samples.

In these tests, BN is shown to play no significant role in the hot ductility. The coarse BN precipitates, which are usually beneficial to ductility, would only have precipitated at or below $\sim 1184^\circ\text{C}$ as shown in **Figure 8.35**, so should have resulted in improved ductility at a testing temperature of 1150°C if this was the mechanism, which is clearly not the case.

8.11 EFFECT OF COMPOSITION IN THE SI-KILLED STEELS

8.11.1 Maximum strength

The general trend of maximum strength (S_u) with decreasing temperature is similar for all four Si-killed steels, as shown in **Figure 8.36**: 20-30 MPa at temperatures above 1100°C , increasing with decrease in temperature to $\sim 850^\circ\text{C}$ (just below the Ae_3), then a decrease in S_u down to 800°C , followed by a sharp increase of ~ 15 MPa with further decrease in temperature to 750°C .

It is interesting to note that the small oscillations in maximum strength in the range $1150 - 1200^\circ\text{C}$ are in each case within 25°C of the dynamic recrystallisation temperature. The S_u is decreased by $\sim 3 - 8$ MPa at the T_d .

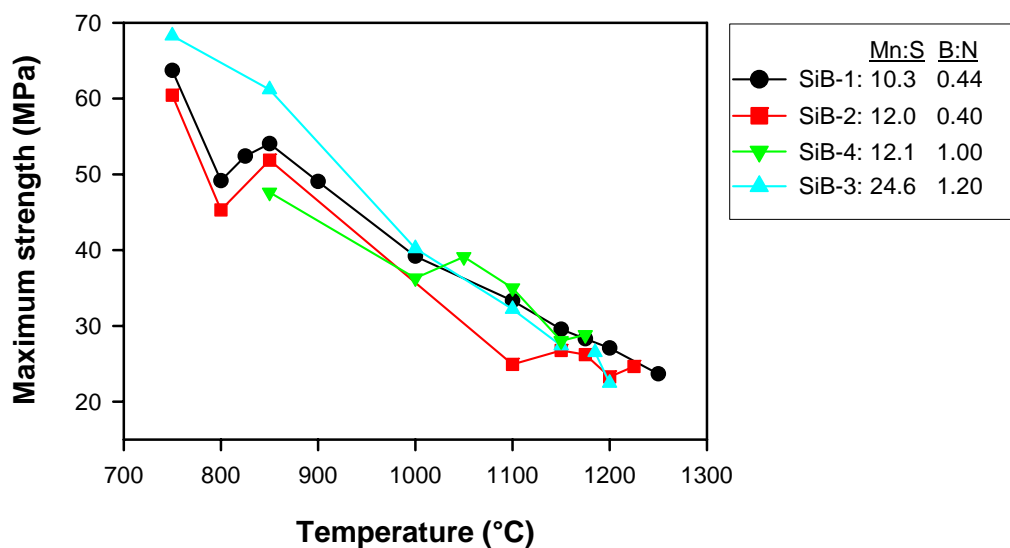


Figure 8.36: Maximum strength results for the Si-killed steels.

8.11.2 Hot ductility

Mn:S ratio

It is clear from the results in this chapter that a Mn:S ratio of 12 can produce either acceptable or poor hot ductility (compare steels *SiB-2* and *SiB-4* in **Figure 8.37** and **Figure 8.38** and see **Table 8.8**). This is shown in **Figure 8.39** where there is a steep increase in *R. A.* from steel *SiB-2* to *SiB-4* at a Mn:S ratio of 12 (the angular shape of the 3-D plot is due to the limited data). The aim for Mn and S levels by the billet casting company is a minimum Mn:S ratio of 14. This is eight times in excess of the stoichiometric ratio needed for Mn and S to combine fully under equilibrium conditions (stoichiometric Mn:S = 1.71).

Ductility improves in the order: $SiB-2 \rightarrow SiB-1 \rightarrow SiB-4 \rightarrow SiB-3$
 (Mn:S = 12.0) \rightarrow (10.3) \rightarrow (12.1) \rightarrow (24.6)

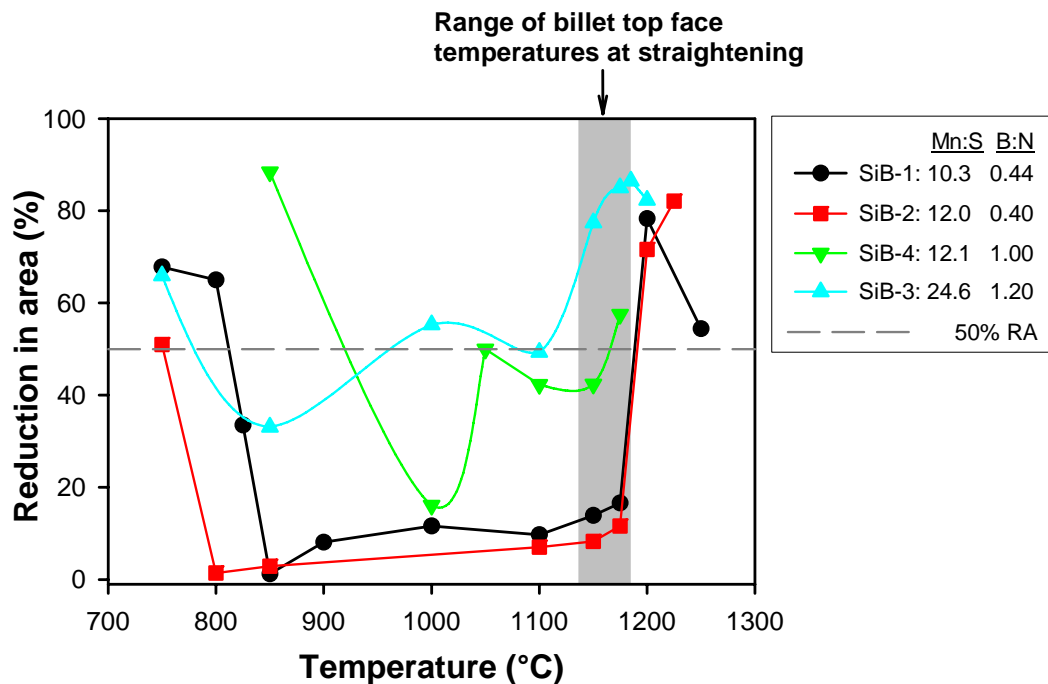


Figure 8.37: Hot ductility results for the Si-killed steels.

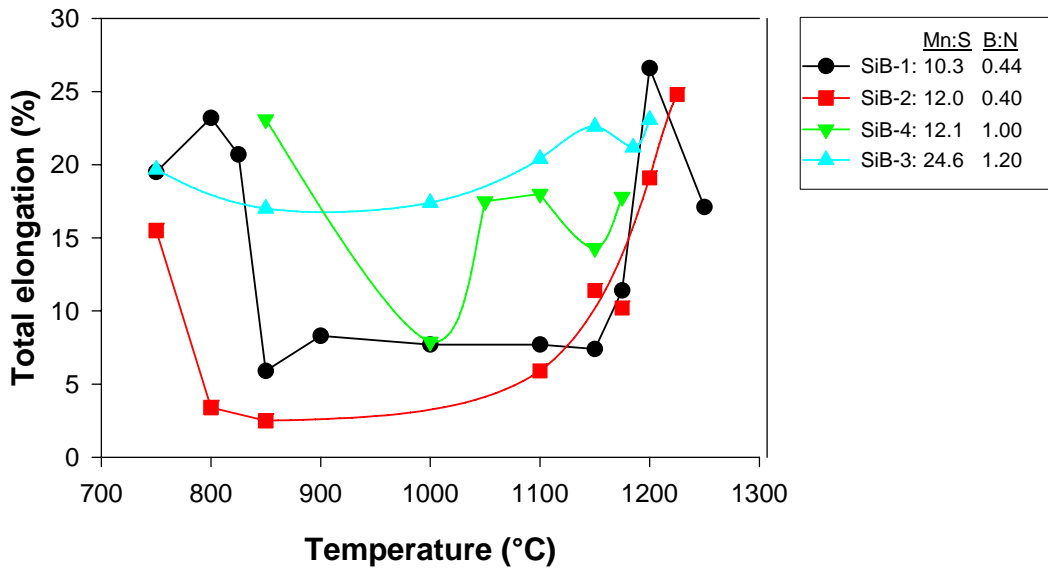


Figure 8.38: Total elongation results for the Si-killed steels.

Table 8.8: Chemical composition of the Si-killed boron steels (in mass %), showing the Mn:S ratio, %S required for MnS formation, excess %S and the hot ductility ranking (1: best, 4: worst).

Grade	Mn	S	Mn:S	S reqd. = Mn/14 *	Excess %S **	Ductility ranking
SiB-1	0.36	0.035	10.29	0.026	0.009	3
SiB-2	0.30	0.025	12.00	0.021	0.004	4
SiB-3	0.44	0.018	24.56	0.032	-0.014 ***	1
SiB-4	0.41	0.034	12.09	0.029	0.005	2

* % S required to meet criterion: Mn = 14*[S].

** Excess S remaining after MnS formation.

*** An excess of 0.19% Mn is indicated by -0.014 %S.

However, the billet casting process is a continuous cooling operation that has a faster cooling rate ($\sim 2.0\text{ }^\circ\text{C}\cdot\text{s}^{-1}$ average cooling rate) than required for equilibrium MnS precipitation. On cooling, the S atoms segregate faster to the grain boundaries than the Mn atoms (up to 1000 times faster at 1090 °C according to Seibel, 1964), which means that there may be many free sulphur atoms at the grain boundaries without Mn.

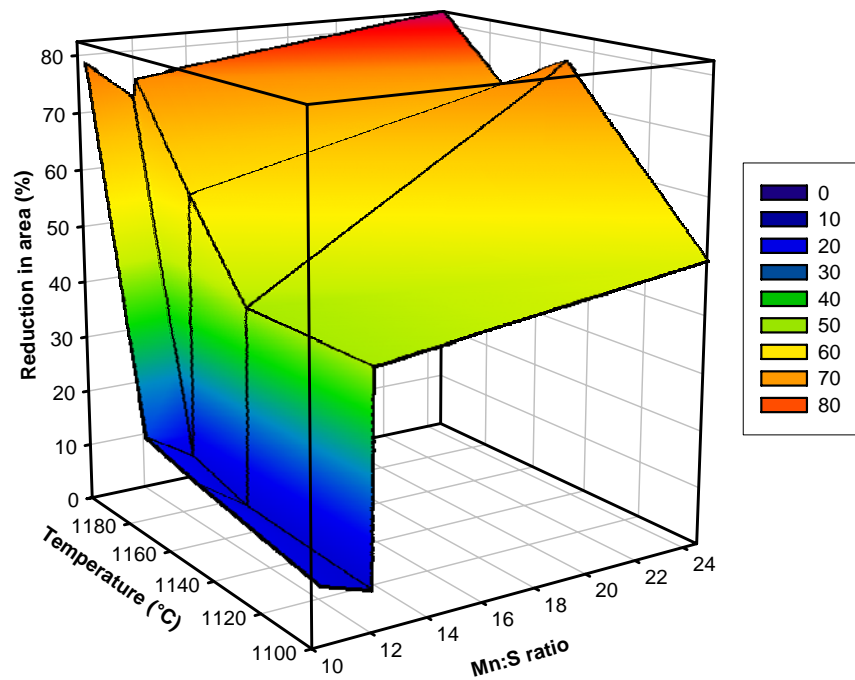


Figure 8.39: Effect of Mn:S ratio on reduction in area in the Si-killed steels (the angular shape of the 3-D plot is due to the limited data).

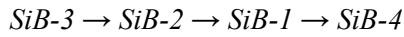
As discussed in **Section 2.5.6**, on rapid cooling from 1400 °C, metastable iron sulphide (FeS) can precipitate at the grain boundaries due to the availability of iron and free sulphur. Iron sulphide is extremely detrimental to hot ductility, as it can form as a liquid on the grain boundary down to temperatures as low as 900 °C, which can lead to extensive intergranular fracture if a tensile stress is applied, such as in billet straightening. The TEM work showed that there were FeS and MnS precipitates in the low ductility sample, but only MnS precipitates in the ductile samples.

Steels *SiB-1*, *SiB-2* and *SiB-4* have Mn:S ratios below 14. This implies that, given an unfavourable combination of casting parameters, cracking can occur due to FeS formation during billet casting, despite the seemingly good hot ductility behaviour of steel *SiB-4*. Using the criterion of $[Mn] = 14*[S]$, **Table 8.8** shows that only steel *SiB-3* contains an excess of Mn which implies that only in steel *SiB-3* will little or no sulphur be available to form FeS, as all sulphur will be tied up as MnS.

Total amount of Mn and S

It is still possible to have poor ductility in a steel that has a sufficiently high Mn:S ratio. Cracking can occur if the total amounts of Mn and S are very high, as the total number or size of manganese sulphides on the grain boundaries can dramatically increase. This is explored in **Table 8.9**, where the stoichiometric volume percent of MnS was calculated.

The potential volume percent MnS that can form in the steels increases in the order:



Many MnS precipitates cause weakening of the grain boundaries, leading to intergranular cracking by microvoid coalescence. Thus, in order to maintain a suitable Mn:S ratio for billet casting *i.e.* >14, it is recommended that the S content should be kept sufficiently low, rather than increasing the Mn content.

Table 8.9: Mn:S ratio, equilibrium volume % MnS of the Si-killed boron steels (composition in mass %) and hot ductility ranking (1: best, 4: worst).

Grade	Mn	S	Mn:S	Vol. % MnS *	Ductility ranking
SiB-1	0.36	0.035	10.29	0.16	3
SiB-2	0.30	0.025	12.00	0.12	4
SiB-3	0.44	0.018	24.56	0.10	1
SiB-4	0.41	0.034	12.09	0.20	2

* Volume % MnS precipitates are calculated from stoichiometry, using %S as the limiting element.

B:N ratio

As discussed in **Chapter 7**, the B:N ratio can play a major role in hot ductility of low carbon steels. It is widely accepted that the aim should be a stoichiometric B:N ratio of 0.77 up to 1.0 in low carbon rod steels, (Marique and Messien, 1990) to bind all N as BN, which minimises strain ageing.

The B:N ratios of the Si-killed boron steels are listed in **Table 8.10** below. Steels *SiB-3* and *SiB-4* have higher than stoichiometric B:N ratios. As can be seen in **Figure 8.37**, these two steels have higher minimum % *R. A.*, have two distinct ductility troughs and high temperature ductility recovery occurs at low temperatures. In contrast, the two low B:N steels (steels *SiB-1* and *SiB-2*) have one large ductility trough with extremely low *R.A.* minima and the high temperature ductility recovery only occurs at ~1200 °C. This is clearly demonstrated in **Figure 8.40**, which shows a direct correlation between good hot ductility and high B:N ratio.

Table 8.10: B:N ratio of the Si-killed boron steels (in mass %) showing the hot ductility ranking (1: best, 4: worst).

Grade	N	B	B:N	Ductility ranking
SiB-1	0.0090	0.0040	0.44	3
SiB-2	0.0100	0.0040	0.40	4
SiB-3	0.0090	0.0070	1.19	1
SiB-4	0.0090	0.0080	1.00	2

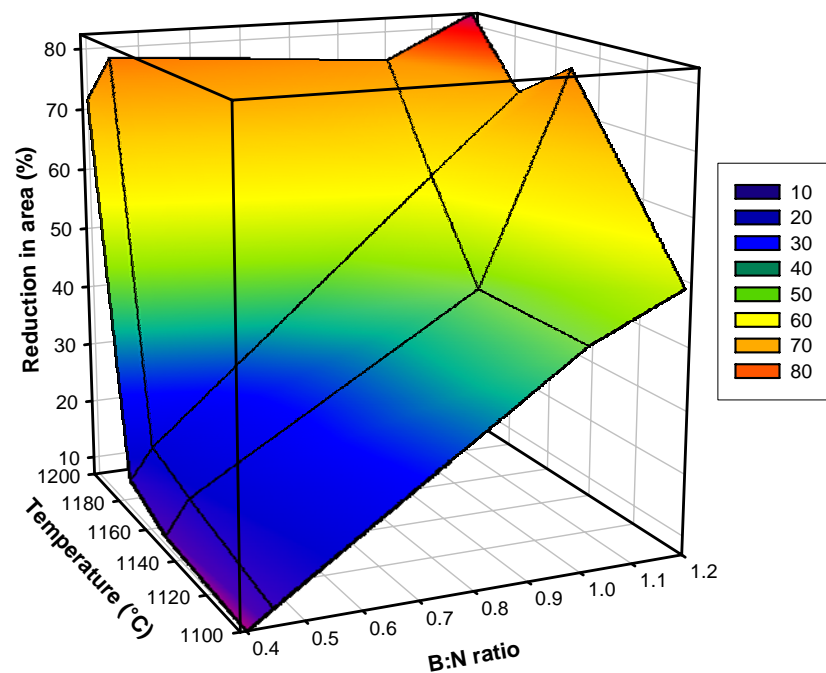


Figure 8.40: Effect of B:N ratio on reduction in area in the Si-killed steels.

Ni:Cu ratio

It is known that 0.3% Ni added to a steel containing 0.3% Cu can suppress surface cracking (Imai, 1997). Mintz *et al.* (2004) showed that in a steel with 0.5% Cu, the addition of 0.3-0.49% Ni (Ni:Cu = 0.6-1.0) prevents precipitation of fine copper sulphides. From **Table 8.11**, it is clear that no clear trend between Ni:Cu and the hot ductility can be seen, as the steel with the best ductility (ductility ranking = 1) has the lowest Ni:Cu ratio.

Table 8.11: Ni:Cu ratio of the Si-killed boron steels (in mass %) showing the hot ductility ranking (1: best, 4: worst).

Grade	Ni	Cu	Ni:Cu	Ductility ranking
SiB-1	0.09	0.15	0.60	3
SiB-2	0.09	0.18	0.50	4
SiB-3	0.07	0.20	0.35	1
SiB-4	0.09	0.15	0.60	2

8.12 ANALYSIS OF PRODUCTION DATA

Production data from 697 industrial billet casts produced from 26 March to 27 May 2001 at the Cape Gate (Pty.) Ltd. billet casting plant, showing the number of billets cast, passed and scrapped, were analysed to determine if there were any distinct trends. It was found that there is a correlation between the actual Mn:S ratio and the percentage billets scrapped due to transverse cracks alone, as shown in **Figure 8.41**.

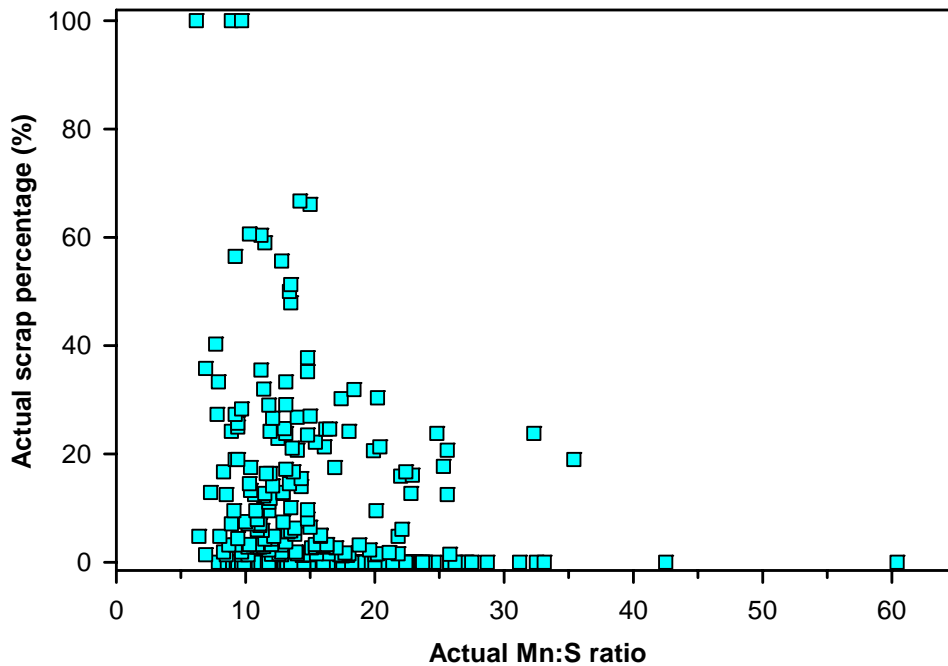


Figure 8.41: Actual scrap percentage as a function of the actual Mn:S ratio.

Figure 8.42 shows the average scrap percentages as a function of average Mn:S ratio. The values were taken as the averages of all data points between Mn:S whole numbers *e.g.* the scrap percentage for all Mn:S values from 12.0 – 12.9 were averaged, and the Mn:S values were also averaged, to give an average Mn:S ratio of 12.5 with an average scrap % of 3.0. The error bars denote the minimum and maximum scrap percentages recorded in that interval. The 5% scrap level, which is the production quality control aim, is indicated. There is a lot of scatter on the graph for average Mn:S values of 25, 26 and 27, where production data from only 5 casts were available, and above an average Mn:S value of 30 there were only one or two casts produced per interval.

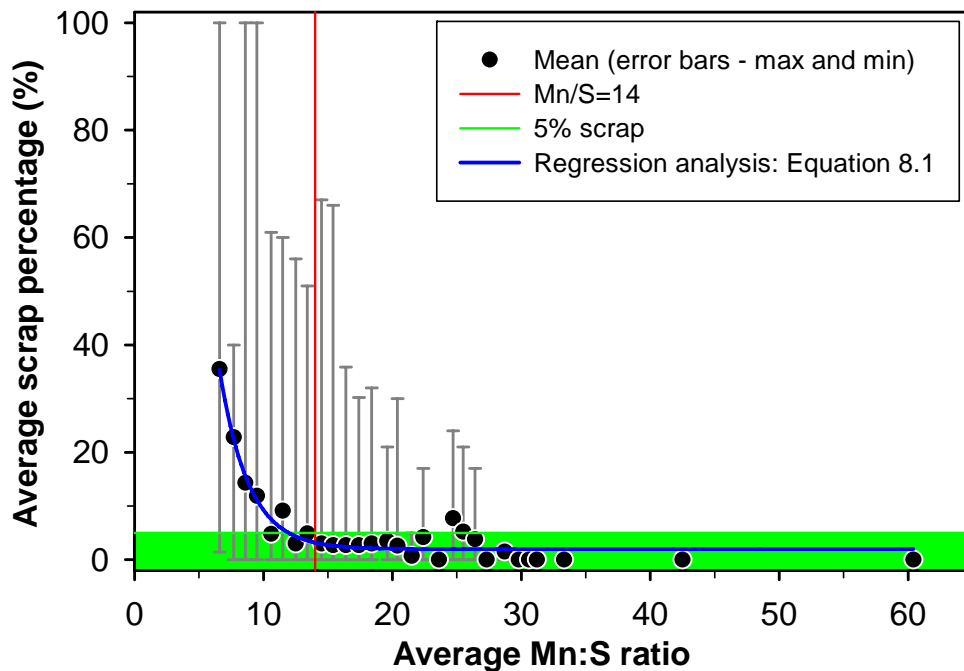


Figure 8.42: Average scrap percentage as a function of the average Mn:S ratio, including the exponential decay equation determined by regression analysis. The 5% scrap level is indicated on the graph.

It is clear that, despite the scatter across the Mn:S range, the average scrap percentages increase rapidly for Mn:S ratios below 14, exceeding 5% scrap for average Mn:S < 14 and exceeding 10% scrap for average Mn:S < 10. Thus it can be seen that the risk of having an exceptionally high % scrap increases exponentially at Mn:S ratios less than 14. The billet casting company's aim Mn:S ratio ≥ 14 is shown on the graph.

An exponential decay equation was determined by regression analysis on this data (this work), and is plotted in **Figure 8.42**:

$$Av. \text{ scrap } \% = 1.963 + 638.2 e^{[-0.447 x]} \quad R^2 = 0.93 \quad (8.1)$$

where x = average Mn:S ratio.

This equation should be used only as an indication of the risk for transverse cracking, as it includes much scatter. The equation can be refined further if more scrap data becomes available from the billet caster.

Using this equation, the predicted scrap percentage of the four Si-killed boron steels used in this work is shown in **Figure 8.43**:

SiB-1 (8.4% predicted scrap), *SiB-2* (5.0%), *SiB-4* (4.9%) and *SiB-3* (2.0%).

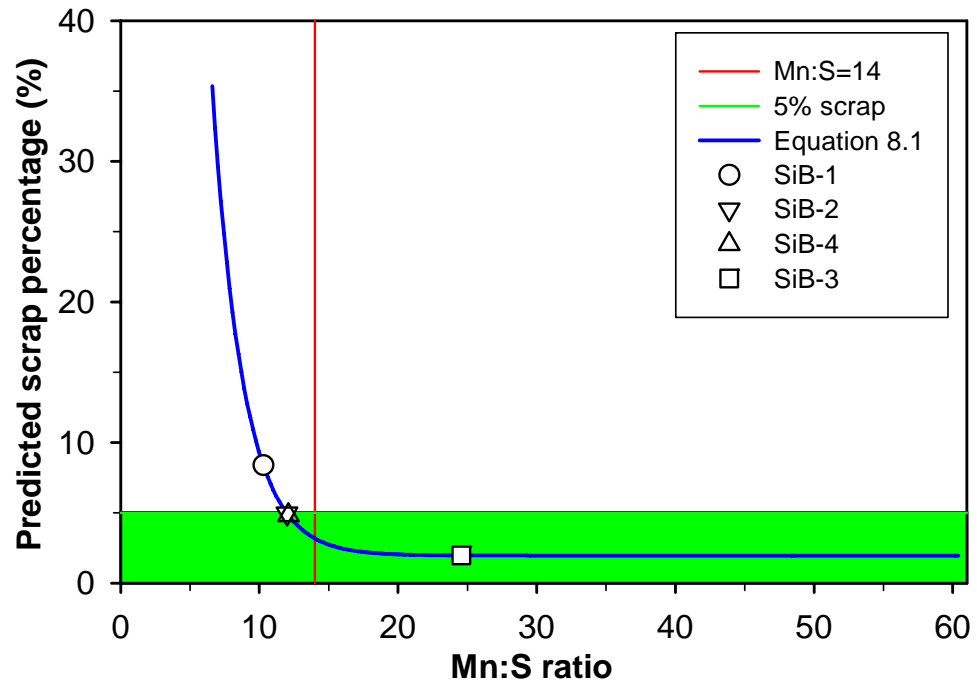


Figure 8.43: Predicted scrap % as a function of Mn:S ratio for the Si-killed boron steels.

The caster had only performed nitrogen analyses on 118 of the 697 casts used in this work for data analysis. Based on the data from these casts, **Figure 8.44** shows that no direct correlation between B:N ratio and the scrap percentage due to transverse cracking was found.

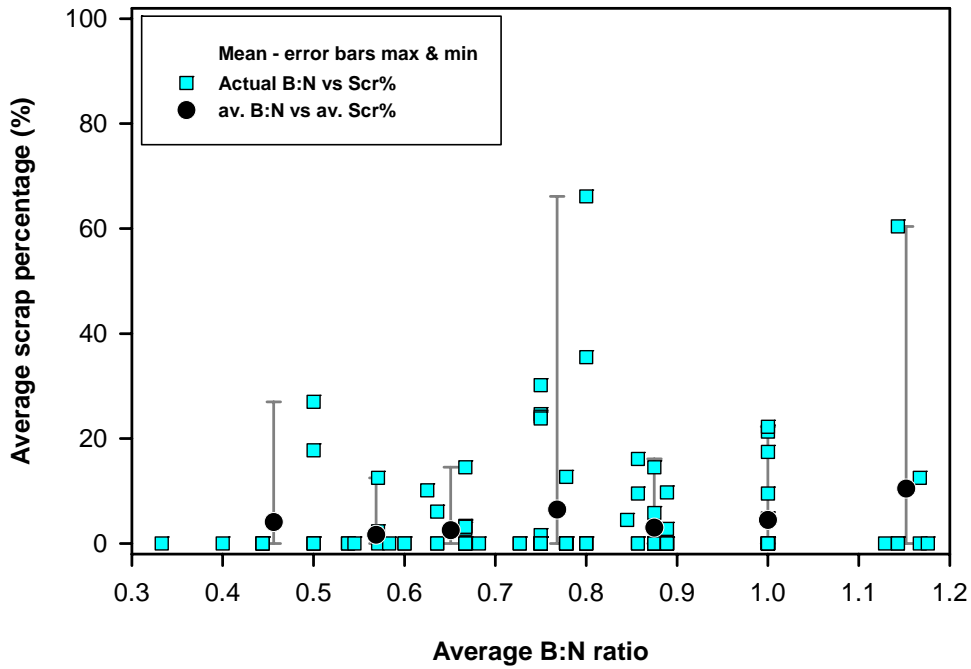


Figure 8.44: Average scrap % as a function of average B:N ratio.

8.13 MECHANISMS OF HOT DUCTILITY FAILURE IN THE SI-KILLED BORON STEELS

The scrap percentage was shown to increase significantly at Mn:S below 14. It was also shown that there was little direct correlation between the industrial scrap percentage due to transverse cracking and the B:N ratio.

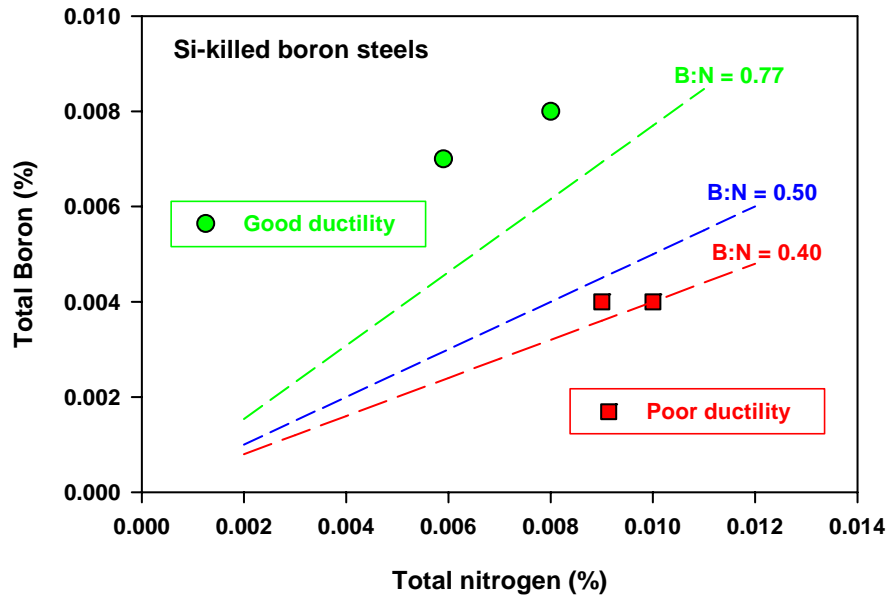
By analysing the industrial casting data, it was shown that an exponential decay relationship exists between the Mn:S ratio (x) and the average scrap percentage due to transverse cracking, *i.e.* due to poor hot ductility, expressed by **Equation 8.1**:

$$\text{Av. scrap \%} = 1.963 + 638.2 e^{-0.447x} \quad R^2 = 0.93$$

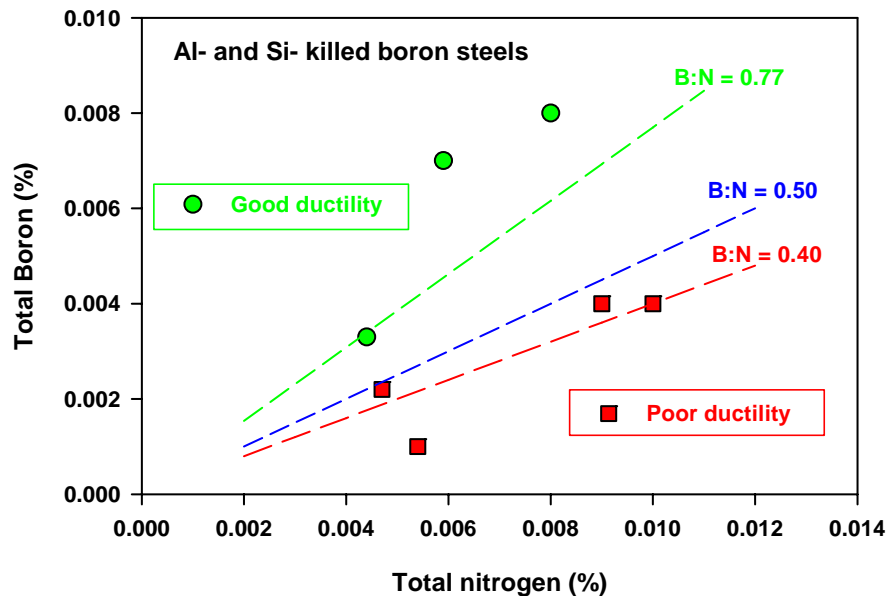
In contrast, hot tensile testing showed an overriding influence of B:N on hot ductility. It was shown that a Mn:S ratio of ~ 12 was on the threshold between poor and good ductility in the Si-killed boron steels. It was at this Mn:S ratio that the overriding influence of the B:N ratio was seen, as the steel (*SiB-4*) with the higher B:N of 1.00 (above stoichiometric) showed superior ductility to the steel (*SiB-2*) with a below-stoichiometric B:N of only 0.40. The hot ductility improved slightly with increase in B:N from 0.40 to 0.44, followed by a marked hot ductility improvement with further increase in B:N from 0.44 to 1.00 and 1.20. **Figure 8.45** shows the B:N effect on ductility for both the Si-killed and the Al-killed steels (from **Chapter 7**).

Boron tends to segregate to interfaces of incoherent particles such as MnS, leading to the formation of complex [MnS+BN] precipitates. In this work, it was also shown that BN formed around 30-50 nm FeS precipitates. The proposed mechanism of ductility improvement in the Si-killed boron steels is that a high B:N ratio forms large complex precipitates with detrimental fine FeMnS precipitates. This rendered them ineffective to influence the hot ductility, especially if the precipitates were on the austenite grain boundaries. With decreasing Mn:S ratios, however, the solidification temperature of the FeMnS precipitates decreases to well below the BN formation temperature. This could lead to localised weakening of the grain boundary.

It is also clear that transformation was beneficial to hot ductility in all four Si-killed boron steels, as the low temperature ductility recovered significantly between the Ae_3 and Ae_1 temperatures. This can be ascribed to rapid formation of α at the γ grain boundaries, which removes strain concentration from the immediate intergranular area and distributes the strain over a larger area.



a)



b)

Figure 8.45: The influence of B:N ratio on hot ductility in a) Si-killed steels and b) Si-killed and Al-killed steels (from Chapter 7).

8.14 APPLICATION AND RECOMMENDATIONS TO INDUSTRY

This work showed the importance of maintaining a high B:N ratio in the Si-killed boron steels and also confirmed that the billet caster aim of Mn:S = 14 was appropriate to minimise transverse cracking. The following is recommended to consistently maintain an acceptable minimum scrap percentage (below 5%):

- B:N higher than 0.78 and preferably not higher than 1.00.
- Chemical analysis of nitrogen to be done on all casts.
- Mn:S higher than 14.
- S level to be kept below 0.025% S
- The exponential decay relationship between the Mn:S ratio (x) and the average scrap percentage due to transverse cracking, *i.e.* due to poor hot ductility, can be used to predict scrap levels in the casting plant:

$$Av. \text{ scrap } \% = 1.963 + 638.2 e^{-0.447x} \quad R^2 = 0.93$$

The billet caster straightening temperature range is ~1138 – 1184 °C. However, even for the Si-killed boron steel with the best ductility, the reduction in area did drop to 60% in this temperature range. In order to ensure that the billet temperature does not approach any low ductility region during straightening, it is recommended that the straightening temperature be kept to a minimum of 1150 °C. **Figure 8.37** shows that ductility may drop slightly at temperatures above 1185 °C, so it is also recommended that a maximum straightening temperature of 1180 °C be specified.

Chapter 9: Hot ductility database

Developing an in-house hot ductility database

9.1 OVERVIEW

In this chapter, a hot ductility database developed by the author is presented. The database was developed so that data from literature could be easily accessed and compared. This database currently includes data of 340 hot ductility curves sourced from published data in 43 literature references (the references relevant to this work are covered in the literature study) as well as work done by the author and colleagues, and is designed to be easily updated with new data. The data are presented in a format where it is easy to select different variables, such as steel type, steel composition, strain rate, cooling rate, reheating temperature and reheating time. The selected data are presented in a spreadsheet table and a graph, which can be exported to the required format.

9.2 HOT DUCTILITY DATABASE PARAMETERS

The database currently groups the steels into the following steel types, with the abbreviations used listed in brackets:

- Ultra-low carbon (ULC): $\leq 0.006\%$ C
- Low carbon (LC): 0.03-0.19% C
- Medium carbon (MC): 0.20-0.49% C
- High carbon (HC): $\geq 0.50\%$ C
- High carbon-boron (HC-B)
- Low carbon-boron (LC-B)
- Boron-titanium (B-Ti)
- Low carbon-chromium (LC-Cr)
- Niobium microalloyed (Nb)
- Niobium-aluminium (Nb-Al)
- Niobium-titanium (Nb-Ti)
- Niobium-vanadium (Nb-V)
- Titanium microalloyed (Ti)
- Vanadium microalloyed (V)
- Vanadium-titanium (V-Ti)
- Chromium-molybdenum-vanadium (Cr-Mo-V)
- Chromium-nickel-aluminium (Cr-Ni-Nb)

To create an automatic display of specific hot ductility data on a graph, the following information can be entered into the “Choose steel type” menu, as shown in **Figure 9.1**:

- Steel type (via a scroll down menu)
- Cooling rate (minimum and maximum)
- Strain rate (minimum and maximum)

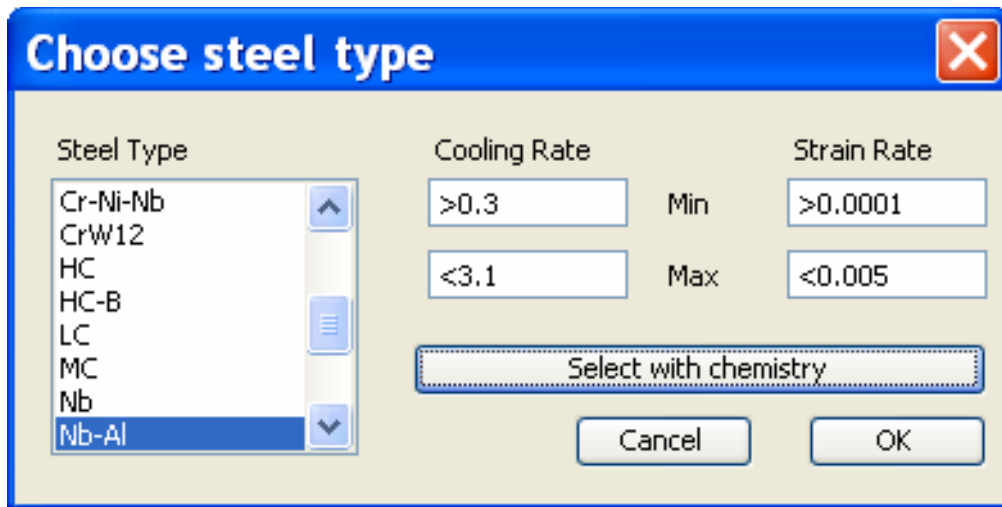


Figure 9.1: “Choose steel type” selection boxes, showing cooling rate and strain rate options.

To select specific chemistry limits within the steel type, the “Select with chemistry” button displays the “Chemical composition” menu shown in **Figure 9.2**. Minimum and/or maximum limits can be set for a wide range of elements to focus in on a narrower group of steel compositions.

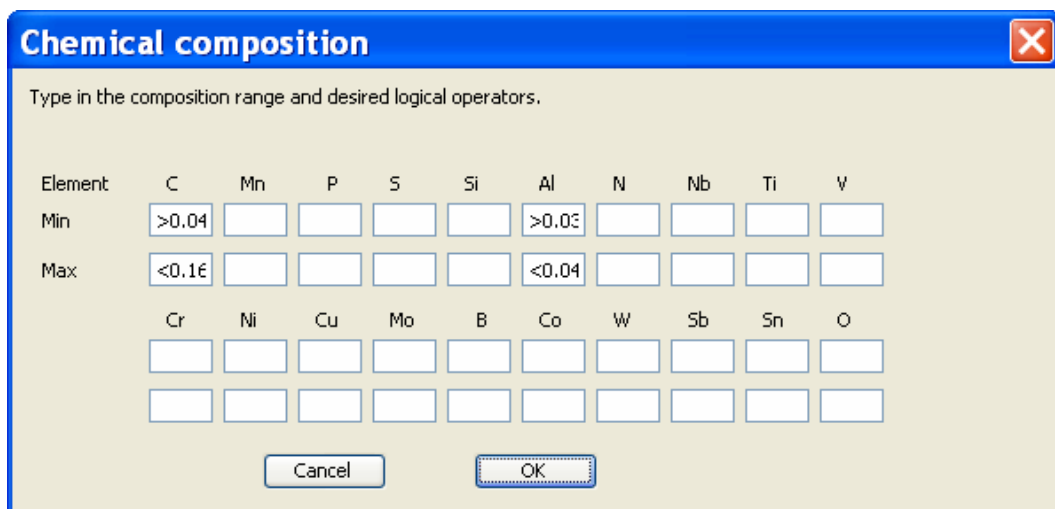


Figure 9.2: “Chemical composition” menu, where minimum or maximum limits can be set for various steel elements.

9.3 HOT DUCTILITY DATABASE EXAMPLE

The results obtained for high carbon steels, with no strain rate, cooling rate or specific element limits selected, is shown in **Table 9.1** and **Figure 9.3**. The Microsoft Excel[®] data and graph can be changed and manipulated to highlight any regions of interest after the graph has been plotted.

Table 9.1: Example of hot ductility database retrieval, showing high carbon steel parameters. Compositions are given in mass %.

#	Ref	Steel	Treheat °C	t rh min	CR °C/s	Str.rate	C	Mn	P	S	Si	Al	N	Cr	Cu
56	46	HC-B	liq + 30	*	10	0.0025	0.83	0.45	0.007	0.008	0.22	*	0.0033	*	*
57	46	HC	liq + 30	*	10	0.0025	0.82	0.52	0.009	0.009	0.21	*	0.0056	*	*
121	59	HC	1330	5	0.4	0.003	0.75	0.91	0.016	0.020	0.22	0.014	0.0060	*	*
199	16	HC	1300	*	100	0.001	1.05	0.50	0.020	0.004	0.20	0.005	0.0037	0.20	0.10
200	16	HC	1300	*	100	0.001	1.05	0.50	0.020	0.004	0.20	0.005	0.0027	0.20	0.10
201	16	HC	1300	*	100	0.001	1.05	0.50	0.020	0.004	0.20	0.005	0.0028	0.20	0.10

- # Steel number in the database
- Ref Literature reference number
- Treheat Reheat temperature in °C (if given). “Liq+30” means liquidus temperature +30 °C.
- t rh Reheat time in minutes (if given)
- CR Cooling rate in °C.s⁻¹ (if given)
- Str.rate Strain rate in s⁻¹ (if given)

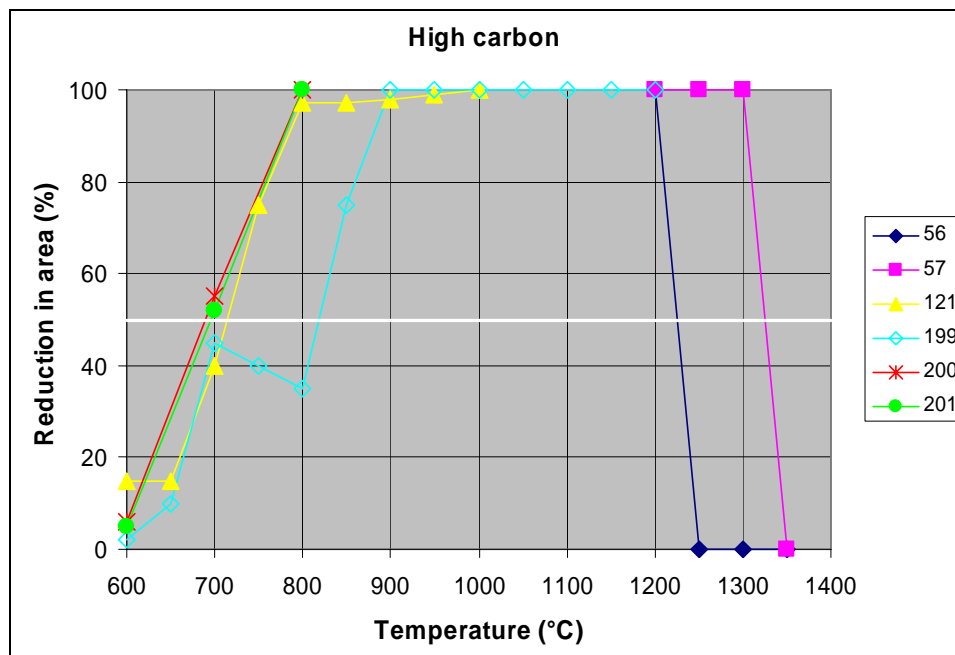


Figure 9.3: Reduction in area (%) results plotted as a function of temperature for the high carbon steel numbers listed in Table 9.1.

9.4 HOT DUCTILITY DATABASE APPLICATION

The ductility results from the steels in this work as well as from unrelated steels tested by the author and former colleagues at Iscor Ltd. have been added to the database. The database has proved to be very useful in comparing and verifying data from this work with information from literature.

This database has also been used in a number of enquiries from Iscor Ltd. (now Arcelor Mittal). In particular, the high carbon steel information was useful to the billet casting plant at the Newcastle Works and the niobium and boron steels information was used by the slab casting plant at the Vanderbijlpark Works.

Chapter 10: Conclusions

10.1 Overview

A study was made to show the effects of composition, strain rate and cooling rate on hot strength, reduction in area and elongation in five low carbon steels, five niobium steels and three aluminium-killed boron steels; and of composition in four silicon-killed boron steels. The techniques used were hot tensile testing by reheating and *in situ* melting, scanning electron microscopy, transmission electron microscopy, Thermo-Calc™ modelling and empirical modelling.

10.2 General Observations

10.2.1 The lenient critical reduction in area ($R.A._{crit}$), as defined by Mintz (1996) was used in determining the minimum reduction in area value required to prevent transverse surface cracking. Failure by intergranular fracture alone occurred at reduction in area values below 50%, ductile + intergranular failure between 47% and 69% and ductile failure above 57%. In this work, the $R.A._{crit}$ was determined to be approximately 50%.

10.2.2 The following general observations showed that the overall hot tensile behaviour of the examined low carbon, niobium, Al-killed boron and Si-killed boron steels were consistent with literature:

- A general increase in maximum hot strength with decrease in testing temperature in the single-phase austenite region.

- Oscillations in the maximum strength caused by a drop in maximum strength (S_u) as dynamic transformation of austenite to ferrite occurred at, or just below, the Ae_3 temperature for the low carbon and boron steels. No S_u oscillation was observed in the niobium steels as the tested temperature range was above most of the calculated Ae_3 temperatures.
 - Hot ductility troughs with low temperature recovery of the reduction in area (50% *R. A.*) occurring below the Ae_3 (~750 – 850 °C) and extending either to near the Ae_3 temperatures, or to much higher temperatures (~1000 °C; 1200 °C for the Si-killed boron steels). Similar behaviour was seen for the total elongation.
- 10.2.3 A decrease in strain rate from 10^{-3} to 10^{-4} s⁻¹ showed the following effect on maximum strength in the low carbon steels *LC-1* and *LC-2*, niobium steel *Nb-5* and Al-killed boron steels *B-1* and *B-2*:
- There was a general trend of decrease in the maximum strength between 750 °C and 950 or 1000 °C.
 - At temperatures above the Ae_3 temperature, this is attributed to increased dynamic recovery of austenite (Mintz and Jonas, 1994) or enhanced grain boundary sliding (Abushosha *et al.* 1998a) with decrease in the strain rate.
 - At temperatures approaching the equilibrium Ae_3 temperature, the lower strength is attributed to deformation-induced transformation of austenite to ferrite (Mintz *et al.* 1991; Marique and Messien, 1990).
 - Below the Ae_3 temperature, there is more time for recovery and softening of ferrite (Mintz and Jonas, 1994).
- 10.2.4 A decrease in strain rate from 10^{-3} to 10^{-4} s⁻¹ caused deterioration in hot ductility (reduction in area and elongation). The high temperature ductility recoveries were moved to higher temperatures and the minimum values were decreased in low carbon steels *LC-1* and *LC-2*, niobium steel *Nb-5* and boron steels *B-1* and *B-2* (elongation only). This can be due to one or more of the following mechanisms: enhanced grain boundary sliding (Mintz and Jonas, 1994), more time for strain-induced precipitation, or more time for formation and growth of voids around precipitates at grain boundaries (Mintz *et al.* 1991).

10.2.5 A decrease in cooling rate from 3.0 to 1.2 °C.s⁻¹ at a strain rate of 10⁻³ s⁻¹ and from 3.0 to 0.3 °C.s⁻¹ at a strain rate of 10⁻⁴ s⁻¹, showed the following effects on ductility:

- In low carbon steel *LC-1*, ductility deteriorated, with the high temperature ductility recovery moved to higher temperatures. This is ascribed to an increase in sulphur segregation to the austenite grain boundaries with decrease in cooling rate (Schmidtman and Merz, 1987), which enhanced precipitation of fine FeS (De Toledo *et al.* 1993).
- In low carbon steel *LC-2*, ductility improved slightly - the high temperature ductility recovery moved to lower temperatures. This is proposed to be due to a decrease in the ease of microvoid coalescence by coarsening of the MnS precipitate distribution along the austenite grain boundaries (Mintz and Jonas, 1994).
- In niobium steel *Nb-5*, ductility improved with a decrease in cooling rate, and a more pronounced effect was observed at low strain rate. This is attributed to favoured static precipitation with a decrease in cooling rate which removes Nb, N and C from solution before dynamic precipitation of fine Nb(C,N), which are detrimental to ductility, can occur (Mintz *et al.* 1991).
- In boron steel *B-1*, a decrease in cooling rate improved the ductility slightly at the higher strain rate. In boron steel *B-2*, a decrease in cooling rate from 3.0 to 1.2 °C.s⁻¹ improved the ductility at both strain rates. This is consistent with literature (Yamamoto *et al.* 1987), as BN precipitation is moved from grain boundaries to the matrix with decreased cooling rate, by coarse precipitation of BN on MnS particles. This is substantiated by the presence of many large BN precipitates.
- However, the cooling rate decrease effected no change in the poor ductility of steel *B-1* or the excellent ductility in steel *B-3* at the lower strain rate.

10.3 Low carbon steels

- 10.3.1 Steel *LC-1* displayed the worst hot ductility of the five low carbon steels. The ductility trough extended to well above the austenite to ferrite transformation temperature (Ae_3), under all tested conditions. In this work, this was found to be due to precipitation of fine iron (oxy) sulphides along austenite grain boundaries. The lack of calcium addition and the low Mn:S ratio are proposed to be the major contributors to the enhanced FeS precipitation.
- 10.3.2 Steel *LC-2* showed low ductility above the Ae_3 temperature only at low strain rate. This is ascribed to either grain boundary sliding (Mintz and Jonas, 1994) or microvoid coalescence between MnS precipitates (Mintz *et al.*, 1991). At high strain rate, this calcium-modified steel, which also had a high Mn:S ratio, showed low ductility only below the Ae_3 temperature. This is ascribed to strain concentration in the thin ferrite films surrounding the austenite grains (Mintz *et al.*, 1991).
- 10.3.3 Steel *LC-3* displayed poor hot ductility, approaching that of *LC-1*, in spite of the presence of calcium, a high silicon content and a very high Mn:S ratio. In this work, the poor hot ductility was found to be due to the poor steelmaking practice, confirmed by the presence of many Al, Mg and Si inclusions as oxides or (oxy) sulphides.
- 10.3.4 The inferior ductility of copper-containing steel *LC-4* compared to *LC-5* is attributed to the absence of beneficial calcium modification in this work. Additionally, the nickel to copper ratio is well below the recommended Ni:Cu ratio of 1:1 for good hot ductility (Fisher, 1969).
- 10.3.5 Steel *LC-5* showed poor hot ductility only below the Ae_3 temperature. The good ductility of this steel is ascribed to calcium modification and the high Ni:Cu ratio in this work.
- 10.3.6 In all five low carbon steels, the low temperature ductility recovery (50% *R. A.*) occurred at or below 750 °C. This is consistent with literature (Mintz, 1996),

which shows that ductility recovers fully between the A_{r3} and A_{e1} temperatures in low carbon steels.

10.4 Niobium steels

- 10.4.1 Increasing the solution treatment time at 1300 °C from 1 to 5 minutes in niobium steel *Nb-1* increased the ductility recovery temperature at the high temperature end. This is consistent with other work (Yue et al. 1995; Fu *et al.* 1998), and is due to coarsening of the austenite grain size, which lowers the grain boundary area per unit volume and increases the precipitate density on the grain boundaries.
- 10.4.2 Changing the cooling pattern from a constant 1.2 °C.s⁻¹ to a series of thermal oscillations in niobium steel *Nb-1* had negligible effects on the hot ductility, which appeared to be contrary to literature (Mintz *et al.*, 1991; Cardoso and Yue, 1989; Mintz *et al.*, 1987). However, this is explained by the smaller oscillation amplitude and that the temperature remained above the tensile testing temperature and the $\gamma \rightarrow \alpha$ transformation temperature in this work.
- 10.4.3 Niobium steel *Nb-1* exhibited improved ductility compared to the four other niobium steels due to the low carbon content (0.04% C), which decreases the volume fraction of detrimental Nb(C,N) precipitation in austenite (Mintz and Mohamed, 1989).
- 10.4.4 It is proposed here that the high nitrogen contents of *Nb-3* and *Nb-5* increased the amount of precipitated Nb(C,N), leading to higher ductility recovery temperatures.
- 10.4.5 In *Nb-5*, it is evident that the poor ductility was exacerbated by the absence of calcium treatment.
- 10.4.6 High temperature ductility recovery occurred well above the calculated A_{e3} temperatures for all five niobium steels, showing the influence of precipitation, and not transformation, on the high temperature ductility drop.

10.5 Aluminium-killed boron steels

10.5.1 The B:N ratio was found to have the overriding influence on hot ductility in the Al-killed boron steels. Overall, the ductility improved in the order of low to high B:N ratio: steel *B-1* (B:N=0.19) → *B-2* (B:N=0.47) → *B-3* (B:N=0.75). This trend was consistent with other published work (Yamamoto *et al.*, 1987).

10.5.2 Low Mn:S ratio in all three Al-killed boron steels led to formation of (Cu,Mn,Fe)S precipitates, which have low melting points and can be detrimental to hot ductility.

10.5.3 The mechanism proposed of ductility loss in the Al-killed boron steels was attributed to a combination of the following:

- A lower than stoichiometric B:N ratio (B:N<0.75) left nitrogen in solution for precipitation of fine AlN on straining or on transformation to ferrite, leading to poor ductility
- A high B:N ratio encouraged the formation of coarse BN which precipitated readily in austenite (often on MnS precipitates) and removed N from solution, hence preventing the formation of AlN
- BN formed large co-precipitates with MnS, CuS or Mn-Fe-O in the matrix, thus rendering these precipitates ineffective to influence hot ductility.

10.6 Silicon-killed boron steels

10.6.1 The Si-killed boron steels were tested by *in situ* melting, then cooling to the test temperature at 2 °C.s⁻¹. The hot ductility troughs of steels *SiB-1* and *SiB-2* were very wide, extending from ~800 °C to ~1150 – 1200 °C. Two slightly shallower ductility troughs were seen in steels *SiB-3* and *SiB-4*.

10.6.2 In steel *SiB-1*, a lower cooling rate of 1 °C.s⁻¹ improved the ductility slightly on the high temperature side of the ductility trough. The drop in %R. A. occurred 25 °C lower than for a cooling rate of 2 °C.s⁻¹.

- 10.6.3 In the Si-killed boron steels, an overriding influence of B:N on hot ductility was found. The hot ductility improved slightly with increase in B:N from 0.40 to 0.44, followed by marked hot ductility improvement with further increase in B:N to 1.00 and 1.20.
- 10.6.4 It was shown in this work that a Mn:S ratio of ~12 was on the threshold between poor and good ductility in the Si-killed boron steels. It was at this Mn:S ratio that the overriding influence of the B:N ratio was seen, as the steel (*SiB-4*) with the higher B:N of 1.00 (above stoichiometric) showed superior ductility to the steel (*SiB-2*) with a below-stoichiometric B:N of only 0.40.
- 10.6.5 In the Si-killed boron steels, the industrial scrap percentage due to transverse cracking was shown in this work to increase significantly at Mn:S below 14 by analysis of scrap data. It was also shown that there was little direct correlation between the industrial scrap percentage and the *B:N* ratio.
- 10.6.6 An exponential decay relationship between the Mn:S ratio (x) and the average scrap percentage due to transverse cracking was found by analysing the industrial casting data:

$$\text{Av. scrap \%} = 1.963 + 638.2 e^{-0.447x} \quad \mathbf{R^2 = 0.93}$$

- 10.6.7 In this work, the mechanism of hot ductility failure in the Si-killed boron steels tested was found to be complex and involves both the B:N ratio and the Mn:S ratio. The mechanism of ductility improvement in the Si-killed boron steels proposed here is that a high B:N ratio formed large complex precipitates of BN+(Fe,Mn)S precipitates. This rendered the (Fe,Mn)S precipitates ineffective to influence the hot ductility. However, with decreasing Mn:S ratios, *i.e.* increasing Fe content in the precipitates, the solidification temperature of the (Fe,Mn)S precipitates decreased to well below the BN formation temperatures. This prevented formation of complex BN+(Fe,Mn)S precipitates, leaving small (Fe,Mn)S precipitates (30-50 nm diameter), or even thin films of molten FeMnS, at the intergranular regions. This then led to localised weakening and decohesion of the grain boundary regions by microvoid coalescence.

10.7 Hot ductility database

A hot ductility database was designed and developed by the author so that data from literature could be easily accessed and compared. This database currently includes data of 340 hot ductility curves sourced from published data in 43 literature references, as well as work done by the author and colleagues, and is designed to be easily updated with new data.

Chapter 11: Recommendations

- 11.1** A number of problems occurred during the reheated (Instron[®]) hot tensile testing that caused oxidation of the specimen and poor thermocouple-specimen contact. Changes to the equipment setup should be made to ensure an adequate protective atmosphere and, thus, a scale-free specimen.
- 11.2** During the *in situ* melting (Gleeble[®]) tests, the control of the molten zone was not ideal, as in some tests, boiling of the molten zone occurred which introduced porosity and in others, the sample failed on cooling to the test temperature due to the natural shrinkage of the steel. To provide a consistent, repeatable test, more work needs to be done to determine the melting/solidification parameters for various steels.
- 11.3** Ideally, there are a few tests that should be repeated, or tests performed midway between tested temperatures, to confirm the hot tensile results. Unfortunately, as mentioned in Chapters 5 to 8, a lack of testing material was the key obstacle in executing further tests.
- 11.4** As the magnification on the SEM is too low to detect fine precipitates, it is recommended that further TEM work should be done, especially on the low carbon, niobium and Si-killed boron steels. This should take the form of thin foil specimens and extraction replicas to look for grain boundary precipitates, matrix precipitates and precipitate free zones. Analysis of the precipitates by EDS or X-ray mapping should also be performed.

- 11.5** To really understand the precipitation behaviour, such as static versus strain-induced precipitation, specimens should be quenched prior to, and after, deformation, and then analyzed on the TEM.

- 11.6** More industrial data (if available) should be added to the Si-killed boron steel database to further refine the relationship between billet composition and crack susceptibility due to transverse cracking.

- 11.7** The Hot Ductility Database should be regularly updated with data from literature to expand the range of steel types and testing conditions.

Chapter 12: References

- Abushosha, R., Ayyad, S. and Mintz, B. (1998a)**, *Mater. Sci. Technol.*, vol. 14, Mar. 1998, pp. 227-235.
- Abushosha, R., Ayyad, S. and Mintz, B. (1998b)**, *Mater. Sci. Technol.*, vol. 14, Apr. 1998, pp. 346-351.
- Abushosha, R., Vipond, R. and Mintz, B. (1991)**, *Mater. Sci. Technol.*, vol. 7, July 1991, pp. 613-621.
- Adams, C.J. (1971)**, *Open Hearth Proc.*, vol. 54, 1971, pp. 290-302. Cited in ref. Brimacombe (1977).
- Andrews, K. W. (1965)**, *J. Iron Steel Inst.*, vol. 203, 1965, pp. 721-727. Cited in ref. Mintz (1991).
- Anelli, E., Mollo, A. and Oulhadj, A. (1993)**, *34th Mech. Work. Steel Process. Conf. Proc.*, ISS-AIME, vol. XXX, 1993, pp. 399-407.
- ASTM (1997a)**, *E8M-97: Standard Test methods for Tension Testing of Metallic Materials [metric]*, *Annual Book of ASTM Standards*, 1997, pp. 77-97.
- ASTM (1997b)**, *E21-92: Standard Practice for Elevated Temperature Tension Tests of Metallic Materials*, *Annual Book of ASTM Standards*, 1997, pp. 129-136.
- ASTM (1997c)**, *E112-96: Standard test method for determining average grain size*. *Annual Book of ASTM Standards*, 1997, pp. 227-249.
- ASTM (1997d)**, *E407-93: Practice for microetching metals and alloys*, *Annual Book of ASTM Standards*, 1997, pp. 439-456.
- Bailey, R. E., Shiring, R.R. and Black, H.L. (1982)**, *Workability testing techniques*, A.S.M., Ed. G.E. Dieter, 1982, pp. 73-94.
- Banks, K.M. and Verdoorn, F.A. (1996)**, *ITEC R&D Internal Report to ISCOR Vanderbijlpark*, Dec. 1996, pp. 1-6.
- Barber, B. and Perkins, A. (1989)**, *Ironmaking Steelmaking*, vol. 16, no. 6, 1989, pp. 406-411.

- Barber, B., Patrick, B., Watson, P. York, R., Kitching, F., Sha, H., Kraushaar, K. and Spitzer, K. H. (1996)**, *Rev. Metall. - CIT*, Nov. 1996, pp. 1403-1412.
- Barber, B. (1997)**, *Steel Times*, April 1997, pp. 154-155.
- Bernhard, C., Reiter, J. and Preßlinger, H. (2007)**, *AISTEch2007Conf. Proc.*, 2007, pp. S1 - S10.
- Blake, N.W. (1987)**, *Report MRL/AMP/87/5*, BHP, Melbourne, July 1987. Cited in ref. Mintz (1991).
- Boratto, F., Weidig, C. Rodrigues, P. and Gnzalez, B.M. (1993)**, *Wire J. Int.*, May 1993, pp. 86-89.
- Brimacombe, J. K. and Sorimachi, K. (1977)**, *Metall. Trans. B*, vol. 8B, no. 3, Sept. 1977, pp. 489-505.
- Brimacombe, J.K. and Samarasekera, I.V. (1997)**, *Iron Steelmaker*, Nov. 1997, pp. 29-39.
- Cardoso, G.I.S.L. and Yue, S. (1989)**, *29th Mech. Work. Steel Process. Conf. Proc.*, vol. XXXI, 1989, pg. 585.
- CBMM website**: <http://www.cbmm.com.br/portug/sources/techlib/report/toosteel/toosteel.htm>, © CBMM, 2007.
- Cepeda, L.E., Rodrigues-Ibabe, J.M., Urcola, J.J. and Fuentes, M. (1989)**, *Mater. Sci. Technol.*, vol. 5, 1989, pg. 1191. Cited in ref. Mintz (1991).
- Chimani, C.M., Resch, H., Mörwald, K. and Kolednik, O. (2005)**, *Ironmaking Steel-making*, vol. 32, no. 1, 2005, pp. 75-79.
- Cho, Y.R. and Kim, S.I. (2004)**, *Iron Steel Technol.*, May 2004, pp. 46-51.
- Christ, B. (1991)**, *Metals Handbook: Tension Testing*, 1991, pg. 31.
- Chung, I-S.; Cho, S-G. (1993)**, *J. Korean Inst. Met. Mater.*, vol. 31, no. 1, Jan. 1993, pp. 64-72
- Cicutti, C., Petroni, J., Di Gresia, G., Dziuba, M. and Lagos, E. (1997)**, *Steelmaking Conf. Proc.*, 1997, pg. 365.
- Comineli, O., Luo, H., Liimatainen, H-M. and Karjalainen, L.P. (2003)**, *IX Congreso de Ciencia y Tecnologia de Materiales, Ref: 204/CTM 2003*, pp. 1-6.
- Cornish, L.A. (1999)**, Report to the CSIR: *Application of Thermo-Calc to deduce phases and precipitation temperatures in continuously cast steels*, University of the Witwatersrand, Johannesburg, South Africa, Oct. 1999, pp. 1-40.
- Cowley, A., Abushosha, R. and Mintz, B. (1998)**, *Mater. Sci. Technol.*, vol. 14, Nov. 1998, pp. 1145-1153.
- Crowther, D.N. and Mintz, B. (1986)**, *Mater. Sci. Technol.*, vol. 2, Nov. 1986, pp.1099-1105.

- Daelen, R. M. (1890)**, Notes on Recent Improvements in German Steel-Works and Rolling Mills, *Trans. AIME*, vol. XIX, 1890, pg.523. Cited in ref. Irving (1993).
- Deisinger, M. and Tacke, K.-H. (1997)**, *Ironmaking Steelmaking*, vol. 24, no. 4, 1997, pp. 321-328.
- Deo, B., Gupta, A., Girish, B.V.S. and Jena, A.K. (1995)**, *37th Mech. Work. Steel Process. Conf. Proc.*, vol. 33, 1995, pp. 565-577.
- Deprez, P., Bricout, J.-P and Oudin, J. (1993)**, *Mater. Sci. Eng.*, vol. A168, 1993, pp. 613-621.
- De Toledo, G.A., Campo, O. and Lainez, E. (1993)**, *Steel Research*, vol. 64, no. 6, 1993, pp. 187-217.
- Diederichs, R. and Bleck, W. (2006a)**, *Steel Res. Int.*, vol. 77, no. 3, 2006, pp. 202-209.
- Diederichs, R. and Bleck, W. (2006b)**, *Steel Res. Int.*, vol. 77, no. 4, 2006, pp. 256-264.
- DSI Gleeble manual (1986)**, *Dynamic Thermal/Mechanical Metallurgy with the Gleeble 1500*, Second Edition, Duffers Scientific Inc. pp. 1-185.
- El-Wazri, A.M., Hassani, F. and Yue, S. (1998a)**, *Iron Steelmaker*, Jan. 1998, pp. 37-41.
- El-Wazri, A.M., Hassani, F., Yue, S., Es-Sadiqi, E., Collins, L.E. and Iqbal, K. (1998b)**, *ISIJ Int.*, vol. 39, no. 3, 1998, pp. 253-262.
- Fisher, G. L. (1969)**, *J. Iron Steel Inst*, vol. 207, no.7, pg. 1010.
- Fountain, R.W. and Chipman, J. (1962)**, *J. Trans. AIME*, 1962, vol. 224, pg. 599.
- Fu, J.Y., Garcia, C.I. and deArdo, A.J. (1988a)**, *8th P.T.D. Conf. Proc.*, 1988, pp. 43-49.
- Fu, J.Y., Garcia, C.I., Pytel, S. and A.J. deArdo (1988b)**, *Processing, microstructure and properties of HSLA steels*, AIME, 1988, pg. 27. Cited in ref. **Mintz (1991)**.
- Fuchs, A. (1975)**, *ESTEL – Berichte aus Forschung und Entwicklung unserer Werke*, no. 3, 1975, pp. 127-135. Cited in ref. Brimacombe (1977).
- Gladman, T. (1997)**, *The physical metallurgy of microalloyed steels*, IOM, 1997, pp.81-135.
- Hannerz, N. E. (1985)**, *Trans. Iron Steel Inst. Jpn.*, vol. 25, 1985, pp. 149-158.
- Harbottle, J. E. and Fisher, S. B. (1982)**, *Nature*, 299, 9 Sept. 1982, pp. 139 – 140.
- Hassani, F. and Yue, S. (1993)**, *34th Mech. Work. Steel Process. Conf. Proc.*, ISS-AIME, vol. XXX, 1993, pp. 409-417.
- Howe, A. A. (1991)**, *Segregation and phase distribution during solidification of carbon, alloy and stainless steel*, *EUR 13303*, ECSC, Luxembourg. Cited in ref. **Pierer, R. and Bernhard, C. (2006)**.

- ISI (1995)**, *Continuous casting of steel 1985 – a second study*, 1985. Cited in ref. Irving (1993), pg. 95.
- Imai, N., Komatsubara, N. and Kunishige, K. (1997)**, *ISIJ Int.*, vol. 37, 1997, pp.224-231.
- Irving, W.R. (1993)**, *Continuous casting of steel*, I. O. M., 1993, pp. 1-120.
- Kiessling, R. and Lange, N. (1966)**, *ISI Publication No. 100*, 1966, pp. 104-114.
- Kobayashi, H. (1991)**, *ISIJ Int.*, vol. 31, no. 3, 1991, pp. 268-277.
- Kobayashi, Y. and Nagai, K. (2005)**, *NIMS NOW Int.*, vol. 3, no. 9, Sept. 2005.
- Kumar, S., Samarasekera, I.V. and Brimacombe, J.K. (1997)**, *Iron Steelmaker*, June 1997, pg. 56.
- Kuo, C.-H., Lu, M.-J. and Chung, Y.-H. (1991)**, *China Steel Technical Report*, no. 5, 1991, pp. 74-83.
- Lankford, W.T. (1972)**, *Metall. Trans.*, vol. 3, 1972, pp. 1331-1353.
- Lee, B.-J., Sundman, B., Kim, S. I. and Chin, K.-G. (2007)**, *ISIJ Int.* vol. 47, 2007, no. 1, pp. 163-171.
- Lewis, J., Jonas, J.J. and Mintz, B. (1998)**, *ISIJ Int.*, vol. 38, no. 3, 1998, pp. 300-309.
- Liu, D., Huo, X., Wang, Y. and Sun, X. (2003)**, *J. Univ. of Sci. and Technol. Beijing*, vol. 10, no. 4, Aug. 2003, pp. 1-6.
- Liu, Z., Kobayashi, Y. and Nagai, K. (2004)**, *ISIJ Int.*, vol. 44, no. 9, 2004, pp. 1560-1567.
- Liu, Z., Kobayashi, Y., Nagai, K., Yang, J. and Kuwabara, M. (2006)**, *ISIJ Int.*, vol. 46, no. 5, 2006, pp. 744-753.
- Luo, H-W.; Zhao, P.; Zhang, Y.; Dang, Z-J. (2001)**, *Mater. Sci. Technol.*, vol. 17, no. 7, July 2001, pp. 843-846
- López-Chipres, E., I. Mejía, C. Maldonado, A. Bedolla-Jacuinde and J.M. Cabrera (2007)**, *Mater. Sci. Eng. A*, vol. 460 - 461, 15 July 2007, pp. 464-470.
- Maehara, Y., Yasumoto, K., Sugitani, Y. and Gunji, K. (1985)**, *Trans. Iron Steel Inst. Jpn.*, vol. 25, 1985, pp. 1045-1052.
- Maehara, Y., Yasumoto, K. and Tomono, H. (1987)**, *Trans. Iron Steel Inst. Jpn.*, vol. 27, 1987, pp. 222-228.
- Maehara, Y., Yasumoto, K., Tomono, H., Nagamichi, T. and Ohmori, Y. (1990)**, *Mater. Sci. Technol.*, vol. 6, Sept. 1990, pp. 793-806.
- Maehara, Y. and Nagamichi, T. (1991)**, *Mater. Sci. Technol.*, vol. 7, Oct. 1991, pp. 915-921.
- Mahapatra, R. B., Brimacombe, J. K. and Samarasekera, I.V. (1991)**, *Metall. Trans. B*, vol. 22B, Dec., 1991, pp. 875-888.

- Maitrepierre, P. (1979)**, *Int. Symposium on boron steels*, AIME, 1979, pp. 421-447. Cited in ref. **Franks, A.J. and Kirkaldy, A. Wire Journal Int.**, May 1998, pg. 102.
- Marique, C. and Messien, P. (1990)**, *Rev. Metall. – CIT*, June 1990, pp. 599-609.
- McLean, D. (1957)**, *Grain boundaries in metals*, Oxford University Press.
Cited in ref. **Lankford (1972)**.
- McPherson, N.A. and McLean, A. (1997)**, *Continuous Casting – ISS Continuous Casting Volume Eight*, Iron and Steel Society/AIME, 410 Commonwealth Drive, Warrendale, PA 15086-7528, USA, 1997, pp.1-46.
- Michalak, J.T. (1991)**, *Metals Handbook: Plastic deformation structures in iron and steel*, ASM, 1991, pp. 218-220.
- Mintz, B. and Arrowsmith, J. M. (1979)**, *Met. Technol.*, vol. 6, 1979, pp. 24-32.
- Mintz, B., Stewart, J.M. and Crowther, D.N. (1987)**, *Trans. Iron Steel Inst. Jpn.*, vol. 27, 1987, pp. 959-964.
- Mintz, B., Mohamed, Z. and Abushosha, R. (1989a)**, *Mater. Sci. Technol.*, vol. 5, no. 7, 1989, pp. 682-688, Cited in ref. De Toledo (1993).
- Mintz, B. and Mohamed, Z. (1989b)**, *Mater. Sci. Technol.*, vol. 5, Dec. 1989, pp. 1212-1219.
- Mintz, B. and Mohamed, Z. (1989)**, *7th Int. Conf. On Fracture Proc.*, vol. 4, 1989, pg. 2545. Cited in ref. **Mintz (1991)**.
- Mintz, B., Yue, S. and Jonas, J.J. (1990)**, *Proc. Int. Conf. Recrystallization in Metallic Materials*, AIME, 1990, pg. 553. Cited in ref. **Mintz (1991)**.
- Mintz, B., Yue, S. and Jonas, J.J. (1991)**, *Int. Mat. Rev.*, vol. 6, no. 5, 1991, pp. 187-217.
- Mintz, B. and Yue, S. (1993a)**, *34th Mech. Work. Steel Process. Conf. Proc.*, vol. XXX, 1993, pp. 391-398.
- Mintz, B., Abushosha, R. and Shaker, M. (1993b)**, *Mater. Sci. Technol.*, vol. 9, Oct. 1993, pp. 907-914.
- Mintz, B., Abushosha, R. (1993c)**, *Ironmaking Steelmaking*, vol. 20, no. 6, 1993, pp. 445-452.
- Mintz, B. and Jonas, J.J. (1994)**, *Mater. Sci. Technol.*, vol. 10, Aug. 1994, pp. 721-727.
- Mintz, B., Crowther, D.N. and Abushosha, R. (1995)**, *Mater. Sci. Technol.*, vol. 11, May 1995, pp. 474-481.
- Mintz, B. (1996)**, *Mater. Sci. Technol.*, vol. 12, Feb. 1996, pp. 132-138.
- Mintz, B., Abushosha, R. and Cowley, A. (1998)**, *Mater. Sci. Technol.*, vol. 14, Mar. 1998, pp. 222-226.

- Mintz, B. (1999), *ISIJ Int.*, vol. 39, no. 9, 1999, pp. 833-855.
- Mintz, B., Comineli, O. and Karjalainen L. P. (2004), *59th Annual Conference of Associação Brasileira de Metalurgia e Materiais - ABM São Paulo – Brazil*, - 22-24 July - REF. 3638 July 2004, São Paulo, pp. 1-7.
- Nachtrab, W.T. and Chou, Y.T. (1986), *Metall. Trans. A*, vol. 17A, Nov, 1986, pg. 1995.
- Nagasaki, C. and Kihara, J. (1999), *ISIJ Int.*, vol. 39, no. 1, 1999, pp. 75-83.
- Nozaki, T., Matsuno, J., Murata, K., Ooi, H. and Kodama, M. (1978), *Trans. Iron Steel Inst. Jpn.*, vol. 18, 1978, pp. 330-338.
- Offerman, C., Däcker, C.Å. and Enström, C. (1997), *Continuous Casting Volume Eight*, 1997, pp. 149-153.
- Ouchi, C. and Matsumoto, K. (1982), *Trans. Iron Steel Inst. Jpn*, vol. 22, 1982, pp. 181-189.
- Ouchi, C., Sampei, T. and Kozasu, I. (1982a), *Trans. Iron Steel Inst. Jpn*, vol. 22, 1982, pg. 214.
- Park, J.S., Ajmal, M. and Priestner, R., (2000), *ISIJ Int.*, vol. 40, no. 4, 2000, pp. 380-385.
- Patrick, B., Barber, B., Scoones, D.J., Heslop, J.L. and Watson, P. (1992), *Metall. Italiana*, vol. 84, no. 9, 1992, pp. 605-611.
- Patrick, B. and Ludlow, V. (1994), *Rev. Metall. - CIT*, July-Aug. 1994, pp. 1081-1089.
- Pierer, R. and Bernhard, C. (2006), *MS&T 06 Conf. Proc., Mater. Sci. Tech.*, Conference and Exhibition, Cincinnati, USA, 15-19 Oct. 2006, pp. 793-803.
- Reiter J., Bernhard C., Preßlinger H. (2006), *MS&T 06 Conf. Proc., Mater. Sci. Tech.*, Conference and Exhibition, Cincinnati, USA, 15-19 Oct. 2006, pp. 805-816.
- Revaux, T., Deprez, P., Bricout, J.-P and Oudin, J. (1994), *ISIJ Int.*, vol. 34, no. 6, 1994, pp. 528-535.
- Salter, W. J. M. (1979), *Institute of Materials: Inclusions*, vol. Monograph, no. 3, 1979, pp. 29-46.
- Schmidtman, E. and Merz, M. (1987), *Steel Research*, vol. 58, no. 4, 1987, pp. 191-196.
- Seibel, G. (1964), *Mem. Sci. Rev. Met.*, vol. 61, 1964, pg. 413.
- Seo, S.J., Asakura, K. and Shibata, K. (1997), *Iron Steelmaker*, Sept. 1997, pp. 51-55.
- Shieldalloy Metallurgical Corporation (2002), <http://www.shieldalloy.com/>, Ferroalloys and Alloying Additives Handbook, original authors: Paul Deeley, Konrad J.A. Kundig, and Howard R. Spindelov, Jr (1981), (<http://www.shieldalloy.com/calciumpage.html>), 2002.

- Shimazu, T., Chikuma, K. Sakai, T and Tanino, M. (1984)**, *Tetsu-to-Hagané*, vol. 70, 1984, pg. S568. Cited in reference Liu (2004).
- Song, S-H., Guo, A-M., Shen, D-D., Yuan, Z-X. Liu, J. and Xu, T-D. (2003)**, *Mater. Sci. Eng.*, vol. A360, 2003, pp. 96-100.
- Sridhar, G., Das, S. K. and Mukhopadhyay, N.K. (1999)**, *Eng. Failure Anal.*, vol. 6, 1999, pp. 155-172.
- Stuart, H. (1981)**, *Editor: Proc. of the Int. Symposium Niobium '81*, Nov. 1981, pg. 710.
- Suzuki, H.G., Nishimura, S. and Yamaguchi, S. (1982)**, *Trans. Iron Steel Inst. Jpn.*, vol. 22, 1982, pp. 48-56.
- Suzuki, H.G., Yamamoto, K., Ohno, Y. and Miyamura, K. (1983)**, *U. S. Patent no: US4379482*, 1983, pp. 1-12.
- Suzuki, H.G., Nishimura, S., Imamura, J. and Nakamura, Y. (1984)**, *Trans. Iron Steel Inst. Jpn.*, vol. 24, 1984, pp. 169-177.
- Suzuki, H.G., Nishimura, S. and Yamaguchi, S. (1988)**, *Physical Simulation of Welding, Hot Forming and Continuous Casting Conf. Proc.- CANMET*, Canada, May 1988, pp. 1-25.
- Suzuki, H.G. (1997)**, *ISIJ Int.*, vol.37, no. 3, 1997, pp. 250-254.
- Takeuchi, E. and Brimacombe, J.K. (1997)**, *Continuous Casting Volume Eight*, vol. 8, 1997, pp. 93-113.
- Tanino, M. (1983)**, *Nippon Steel Tech. Rep.*, vol. 23, 1983, pp. 331-337.
- Turkdogan, E. T. (1987)**, *Steelmaking Conf. Proc.*, I.S.S., vol. 70, 1987, pp. 399-415.
- Turkdogan, E.T. (1996)**, *Fundamentals of Steelmaking*, IOM, 1996, pp. 305-316.
- Vodopivec, F., Torkar, M. and Jakupovic, M. (1987)**, *Mater. Sci. Tech.*, vol. 3, May 1987, pp. 372-377.
- Walmag, G., Schmidt, A. and Marique, C. (2002)**, *4th European Continuous Casting Conf.*, Birmingham, vol. 2, 14-16 Oct. 2002, pp. 840-848.
- WebElements (2007)**, <http://www.webelements.com/webelements/compounds/text/Cu/Cu2S1-22205454.html>, The periodic table on the WWW, © 1993-2007, Mark Winter, The University of Sheffield and WebElements Ltd, UK, 24 July 2007.
- Weinberg, F. (1979a)**, *Metall. Trans. B*, vol. 10B, June 1979, pp. 219-227.
- Weinberg, F. (1979b)**, *Metall. Trans. B*, vol. 10B, Dec. 1979, pp. 513-520.
- Weiss, I. and Jonas, J.J. (1979)**, *Metall. Trans. A*, 10A, 1979, pg. 831. Cited in ref. Abushosha, 1998b.

- Wenying, L., Weiqing, C., Hui, Y. and Yongdong, L. (2006), *Steel Wire Products*, vol. 32, no. 2, 2006, pp.38-41.
- Wilber, G.A. Savage, W.P. and Childs, W.J. (1975), *Metall. Trans. A*, vol. 6A, 1975, pg. 1727. Cited in ref. Nagasaki, 1999.
- Wilcox, J. R. and Honeycombe, R.W.K. (1987), *Mater. Sci. Technol.*, vol. 3, Oct. 1987, pg. 849.
- Wilson, F.G. and Gladman, T. (1998), *Int. Mater. Rev.*, 1988, vol. 33, no. 5, pp. 221–86.
- Wintz, M., Bobadilla, M., Lehmann, J. and Gaye, H. (1995), *ISIJ Int.*, vol. 35, no. 6, 1995, pp. 715-722.
- Wolańska, N. Lis, A.K. and Lis, J. (2007), *J. of Achievements in Mater. and Manuf. Eng.*, vol. 20, issue 1-2, Jan-Feb 2007, pp. 291-294.
- Wolf, M.M. and Kurz, W. (1981), *Metall. Trans. B*, vol. 12B, 1981, pg. 85. Cited in ref. Mintz, 1999.
- Wolf, M.M. (1991), *Proc. 1st European Conf. on Continuous Casting- AIM*, vol. 2, 1991, pp. 2.489-2.499.
- Wolf, M.M. (1997), *Initial solidification and Strand Surface Quality of Peritectic Steels - Continuous Casting Volume Nine*, Iron and Steel Society/AIME, 410 Commonwealth Drive, Warrendale, PA 15086-7528, USA, 1997, pp. 59-65.
- Yamamoto, K., Suzuki, H.G., Ohno, Y. and Noda, N. (1987), *Tetsu-to-Hagané*, vol. 73, no. 1, 1987, pp. 115-122.
- Yoshida, N., Umezawa, O. and Nagai, K. (2003), *ISIJ Int.*, vol. 43, no. 3, 2003, pp. 348-357.
- Yu, H., Kang, Y-L., Zhao, Z. and Sun, H. (2006), *J. Iron Steel Res. Int.*, vol. 13, no. 5, 2006, pp. 30-36.
- Yue, S. and Jonas, J. J. (1990), *Materials Forum.*, vol. 14, 1990, pp. 245-252.
- Yue, S., Jonas, J. J. and Mintz, B. (1995), *13th PTD Conf. Proc.*, 1995, pp. 45-52.
- Zheng, L., Hongtao, Z. and Baorong, W. (1990), *Steel Research*, vol. 61, no. 12, 1990, pg. 620.

Appendix I

Publications, presentations and contributions to literature

This Appendix contains the following publications and presentations on this work:

- A.1 L. H. Chown and L. A. Cornish, Investigation of hot ductility in Al-killed boron steels, *Materials Science and Engineering A*, vol. 494, 2008, pp. 263-275..... A-2
- A.2 L. H. Chown and A. S. Tuling, (2002) The influence of cooling rate on hot ductility in a low carbon boron steel, *15th International Congress on Electron Microscopy (ICEM) Conference Proceedings*, Sep. 2002, vol. 2, pp. 767-768 A-16
- A.3 L. H. Chown, A. P. Bentley and F. A. Verdoorn, (2001) The influence of sulphide precipitation on hot ductility in a boron steel, *40th Microscopy Society of Southern Africa (MSSA) Conference Proceedings*, Dec. 2001, vol. 31, pg. 25. [ANASPEC Award: “The Best Application in Industry” Presentation] A-18
- A.4 L.H. Chown, The effects of boron, cooling rate and strain rate on hot ductility of extra low carbon steel, *SAIMM Colloquium*, Pretoria, 18 July 2000..... A-19
- A.5 L.H. Chown, Continuous casting of steels: prediction and prevention of cracking, *Centre of Excellence in Strong Materials Colloquium*, University of the Witwatersrand, Johannesburg, 20 February 2005..... A-21

APPENDIX I.1

Investigation of hot ductility in Al-killed boron steels

L. H. Chown^{a,b,c*} and L. A. Cornish^{a,c}

^a Department of Chemical and Metallurgical Engineering,
University of the Witwatersrand, Johannesburg, Private Bag 3, WITS, 2050, South Africa

^b Advanced Materials Division, Mintek,
Private Bag X3015, Randburg, South Africa

^c DST/NRF Centre of Excellence in Strong Materials,
University of the Witwatersrand, Johannesburg,
Private Bag 3, WITS, 2050, South Africa

Abstract

The influence of boron to nitrogen ratio, strain rate and cooling rate on hot ductility of aluminium-killed, low carbon, boron microalloyed steel was investigated. Hot tensile testing was performed on steel samples reheated in argon to 1300°C, cooled at rates of 0.3, 1.2 and 3.0°Cs⁻¹ to temperatures in the range 750 to 1050°C; and then strained to failure at initial strain rates of 1x10⁻⁴ or 1x10⁻³ s⁻¹. It was found that the steel with a B:N ratio of 0.19 showed deep hot ductility troughs for all tested conditions; the steel with a B:N ratio of 0.47 showed a deep ductility trough for a high cooling rate of 3.0°Cs⁻¹ and the steel with a near-stoichiometric B:N ratio of 0.75 showed no ductility troughs for the tested conditions. The ductility troughs extended from ~900°C (near the Ae₃ temperature) to ~1000 or 1050°C in the single phase austenite region. The proposed mechanism of hot ductility improvement with increase in B:N ratio in these steels is that the B removes N from solution, thus reducing the strain-induced precipitation of AlN. Additionally, BN co-precipitates with sulphides, preventing precipitation of fine MnS, CuS and FeS, and forming large, complex precipitates that have no effect on hot ductility.

Keywords: Al-killed steel; hot ductility; boron nitride; aluminium nitride; sulphides

* Corresponding author. Tel.: +27 (11) 709 4097 or +27 (11) 849 8244; Fax: +27 (11) 709 4480.
E-mail address: Lesley@mintek.co.za

APPENDIX I.2

15th International Congress on Electron Microscopy (ICEM) Proceedings,
Durban, Sep. 2002, vol. 2, pp. 767-768.

THE INFLUENCE OF COOLING RATE ON HOT DUCTILITY IN A
LOW CARBON BORON STEEL

L. H. Chown and A. S. Tuling

Industrial Metals and Minerals Research Institute, Pretoria, South Africa

In the steel industry, continuous casting processes are characterized by variations in secondary cooling rate and strain rate during unbending. Fine cracks can initiate on the strand surface and form transverse corner or transverse facial cracks that lead to costly surface dressing or scrapping of the affected strand. Low carbon steels with boron additions are prone to this phenomenon during thick slab¹ and billet² casting. It has been reported that a minimum B:N mass ratio of 0.8 should be maintained in billet casting to bind all nitrogen as BN, reducing transverse crack susceptibility.³ However, the crack susceptibility of boron steels during thin slab casting has not been widely reported.

In this work, the relationship between precipitation and hot ductility under thick slab, thin slab and billet casting conditions was investigated in a boron, extra low carbon steel with a B:N mass ratio of 0.47 (0.026% C, 0.31% Mn, 0.005% S, 0.02% Si, 0.055% Al, 0.0047% N, 0.0022% B). Hot tensile tests, where hot ductility is related to reduction in area or % R.A., were performed to determine the crack susceptibility. After holding at 1300 °C for 5 minutes, the specimens were cooled at rates between 0.3 and 3.0 °C.s⁻¹ to testing temperatures ranging from 750 to 1050 °C. The specimens were then pulled at initial strain rates of 1 x 10⁻⁴ or 1 x 10⁻³ s⁻¹. These testing parameters were chosen to approximate the different industrial casting conditions (Table 1).

The fast cooling conditions (3.0 °C.s⁻¹) found in billet and fast cooled thin slab casting showed poor minimum ductility (<30% R.A.), as shown in Figure 1. The intermediate cooling conditions (1.2 °C.s⁻¹), typical of fast cooled thick slab and slow cooled thin slab showed high ductility (95% R.A.) in the temperature range tested. A small drop in ductility to 80% R.A. was seen in the slow cooled thick slab simulation (0.3 °C.s⁻¹).

Scanning electron microscopy revealed that the ductile specimens failed by ductile shear, with limited intergranular cracking. Large, complex precipitates (containing B, N, Mn, Cu, S, Al, O) of 1–5 µm diameter, were well distributed in the matrix. The TEM study confirmed that there were few precipitates along prior austenite boundaries.

Yamamoto *et al.*¹ have shown that hot ductility of B steels improves with decrease in cooling rate from 20 to 0.1 °C.s⁻¹. Additionally, they found that for a steel with B:N ratio as high as 0.47 the ductility should be above 50% R.A., even at a high cooling rate of 20 °C.s⁻¹. However, we have shown (Figure 1) that there is poor hot ductility even at 3.0 °C.s⁻¹, which corresponds to billet casting and thin slab fast cooling conditions. SEM study revealed that the low ductility specimens (<30% R.A.) had failed by extensive intergranular cracking. This cracking along prior austenite grain boundaries was formed by coalescence of precipitate-containing voids containing oxides, sulphides and boron nitrides (Figure 2). Further study using TEM extraction replicas showed BN and Cu-S filaments along the prior austenite grain boundaries (Figure 3).

The slight deterioration in ductility with decrease in cooling rate from 1.2 to 0.3 °C.s⁻¹, as shown in Figure 1, was an unexpected result, as it is generally accepted that a decrease in cooling rate improves hot ductility.¹ This result was shown to be due to fine precipitation of intergranular AlN (< 100 nm diameter).

This study has shown that there is a risk of transverse cracking during billet and thin slab casting with fast cooling. This is attributed to precipitation of BN and Cu-S filaments along prior austenite grain boundaries.

Table 1. Testing parameters as related to industrial continuous casting processes.

Strain Rate (s ⁻¹)	0.001	Thin slab	Thin slab
	0.000	Thick	Billet
		0.3	1.2
		Approx. cooling rate (°C. s ⁻¹)	

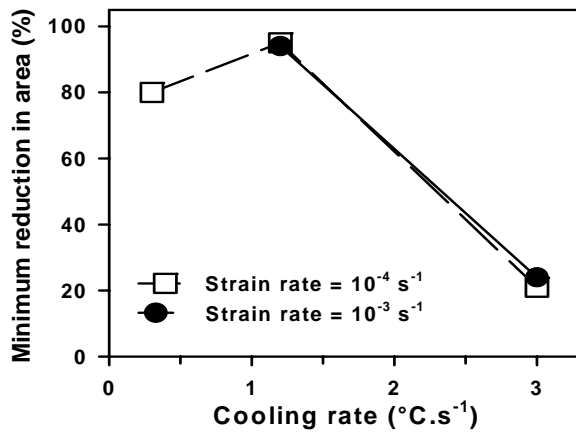


Figure 1. Minimum reduction in area as a function of strain rate and cooling rate.

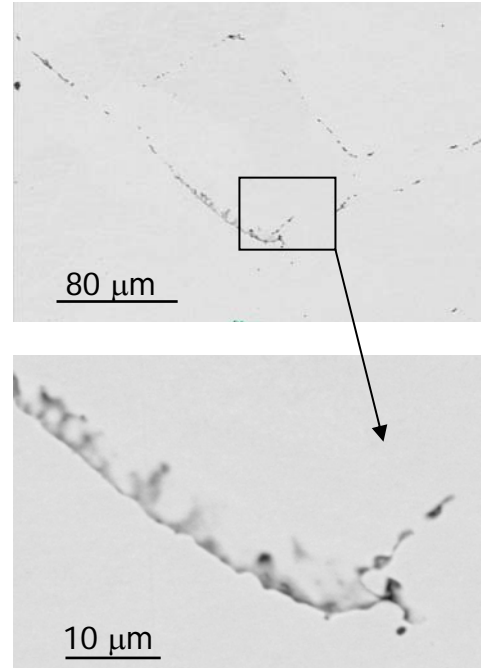


Figure 2. SEM backscatter image of microvoid coalescence along prior austenite grain boundaries.

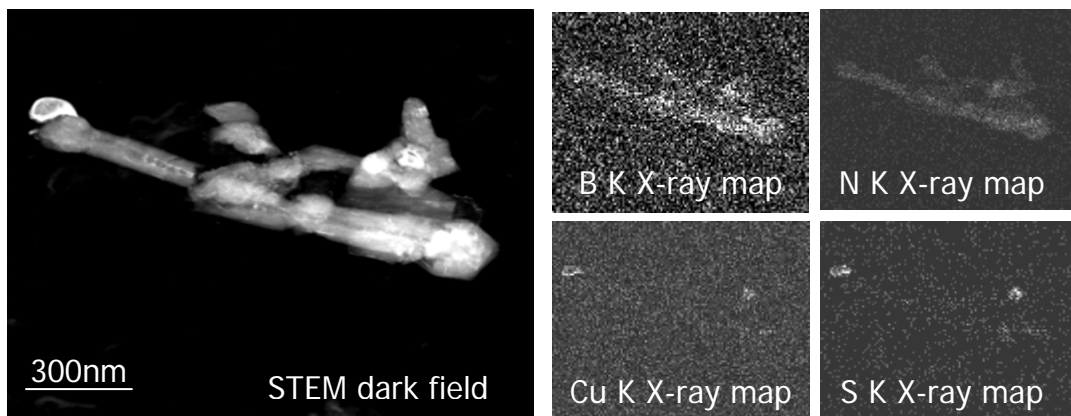


Figure 3. STEM dark field image and X-ray maps of a BN filament capped with Cu-S.

References

1. Yamamoto, K., Suzuki, H.G., Ohno, Y. and Noda, N., (1987), Tetsu-to-Hagané, 73 (1), 115.
2. Chown, L.H., Bentley, A.P. and Verdoorn, F.A., (2001), Proc. Microsc. Soc. of Southern Africa, 31, 25.
3. Marique, C. and Messien, P., (1990), La Revue de Métallurgie –CIT, (6), 599.

APPENDIX I.3

MSSA (Microscopy Society of Southern Africa) 2001 Proceedings, Pretoria, December 2001, vol. 31, pg. 25. [ANASPEC Award: "The Best Application in Industry" Presentation]

THE INFLUENCE OF SULPHIDE PRECIPITATION ON HOT DUCTILITY IN A BORON STEEL

L. H. Chown, A. P. Bentley and F. A. Verdoorn

Industrial Metals and Minerals Research Institute (IMMRI), University of Pretoria, Pretoria.

Boron is added to low carbon wire rod and strip steels for deep drawing applications, to react with free nitrogen, forming boron nitride (BN). The benefits are reduced nitrogen-related strain ageing, improved formability and decreased work hardening.¹ However, it has been found that boron-containing steels are susceptible to transverse surface cracking during straightening in the continuous casting operation.² The ductility trough caused by precipitation of boron-containing compounds along austenite grain boundaries can extend from 600°C to as high as 1050°C.³ Also, in low carbon steels containing sulphur, transverse surface cracking during straightening has been attributed to the sulphur segregation at grain boundaries,⁴ fine MnS precipitation⁵ and fine FeS precipitation⁶ at austenite grain boundaries.

An investigation was undertaken to find the cause of transverse cracking in a boron-containing low carbon billet steel, with composition: 0.056% C, 0.36% Mn, 0.035% S, 0.0090% N and 0.0040% B. Hot ductility testing was done on the Gleeble 1500[®] servo-hydraulic machine, with testing parameters simulating billet casting conditions. Samples were melted *in situ*, cooled to the testing temperature at cooling rates of 1 or 2°C.s⁻¹ and strained to failure at a strain rate of $1 \times 10^{-3} \text{ s}^{-1}$.

The hot ductility (% reduction in area) results are shown as a function of testing temperature in Fig. 1. Suzuki et al.³ found that boron steels containing in excess of 0.0020% B should have low crack susceptibility. Thus, the hot ductility troughs were ~100°C wider than expected, extending from 800 to 1200°C. Decreasing the cooling rate from 2 to 1°Cs⁻¹ slightly improved the ductility at the high temperature end of the trough, so that ductility recovery occurred 25°C lower at 1175°C.

Investigation by SEM and TEM showed copious precipitation of fine and coarse manganese sulphides and only a few coarse boron nitrides. Good ductility (e.g. sample #1 at 1175°C and #3 at 1200°C) was characterized by precipitation of many large and medium sized MnS precipitates. Lines of fine FeS particles were found in low ductility sample #2 tested at 1175°C (Fig. 2), whereas no FeS precipitates were found in the ductile samples.

The mechanism of ductility loss in this steel is proposed to be precipitation at temperatures below 1200°C of fine grain boundary (Fe, Mn)S and FeS, which become regions of stress concentration under tensile load, leading to embrittlement by void coalescence. Under equilibrium conditions, only MnS and no FeS should form, as the Mn/S ratio is six times higher than required by stoichiometry. Thus, the testing conditions used in this work are non-

equilibrium, providing sufficient S in solution below 1200°C for FeS formation. Super-saturated sulphur, and the volume fraction of fine FeS precipitation, increases with decrease in testing temperature at constant cooling rate, and with increase in cooling rate from 1 to 2°C.s⁻¹ at constant testing temperature. Hence, in spite of the excess of Mn, FeS can form in the boron steel under the tested conditions in this work, causing poorer than expected hot ductility. For this steel grade, it has been recommended that a Mn/S ratio in excess of 15 should be maintained to minimize cracking during billet casting.

References

- Faulring, G.M. (1989) Proc. Elec. Furn. Conf., 155.
- Marique, C. (1990) La Rev. Met. CIT 87(6), 599.
- Suzuki, H., Yamamoto, K., Ohno, Y. and Miyamura, K. (1983) U.S. Pat. 4,379,482.
- Kobayashi, H. (1991) ISIJ Int. 31(3), 268.
- Yasumoto, K., Maehara, Y., Ura, S., Ohmori, Y. (1985) Mat. Sci. & Tech. 1(2), 111.
- Nagasaki, C. and Kihara, J. (1999) ISIJ Int. 39(1), 75.

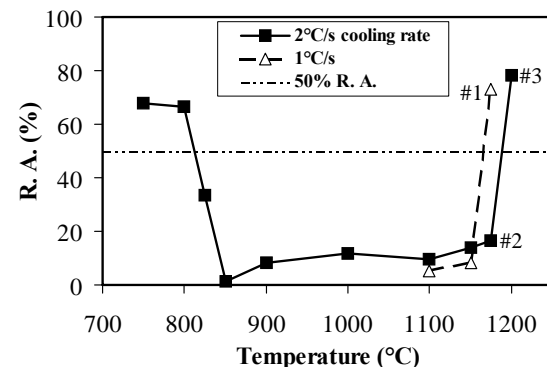


Fig. 1: Hot ductility (% R.A.) vs. testing temperature for a low carbon, boron steel.

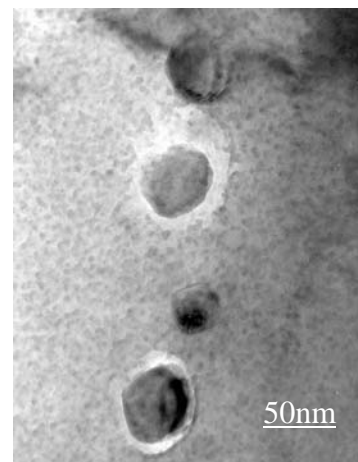


Fig. 2: TEM bright field image showing fine FeS precipitates in low ductility sample #2 tested at 1175°C

APPENDIX I.4

SAIMM Colloquium

University of Pretoria, 18 July 2000

POWERPOINT PRESENTATION SLIDES

The effects of boron, cooling rate and strain rate on hot ductility of extra low carbon steel

Lesley Chown
IMMRI
SAIMM Colloquium
18 July 2000

1

Transformation and precipitate dissolution temperatures

Grade	Ae ₃ (°C)	T _{diss} (°C) [BN]	T _{diss} (°C) [AIN]
B-1	884	1070	1155
B-2	893	1105	1193
B-3	889	1124	1184

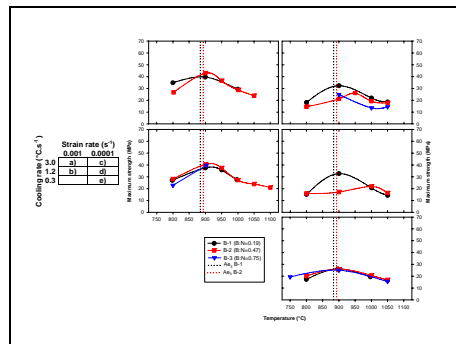
* from Thermo-Calc

4

Background

- Extra low carbon steels with boron → transverse cracking
- Cracks propagate during straightening (Slab cracking project)

2



5

Project Goals

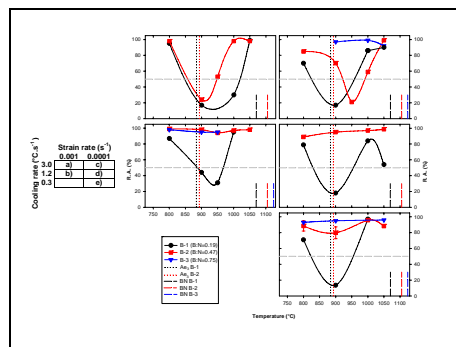
Relationships between:

2° Cooling rate
Strain rate

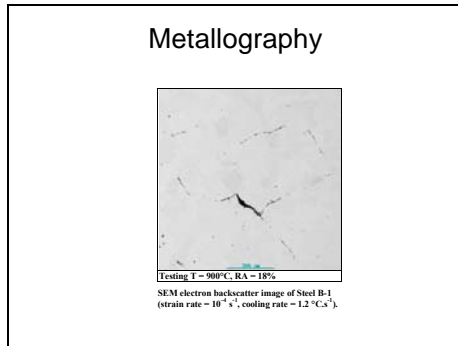
Transformation
Precipitation

Maximum strength
Hot ductility

3



6

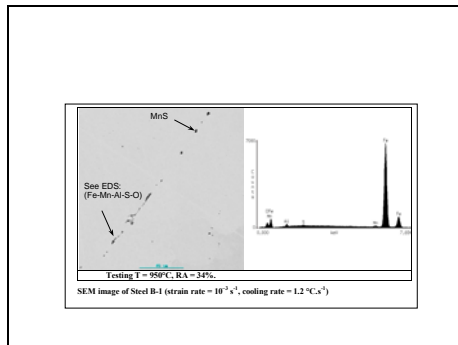


7

Conclusions (cont.)

- Ductility improved by:
 - Transformation from $\gamma \rightarrow \alpha$
 - \uparrow B:N ratio from 0.19 \rightarrow 0.47 \rightarrow 0.75
 - \downarrow cooling rate from 3.0 \rightarrow 1.2 °C.s⁻¹
 - Effect of strain rate not clear

12

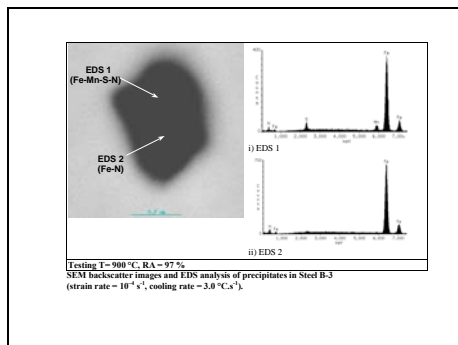


8

Application

- B:N = 0.19: **Not suitable for any CC**
- B:N \geq 0.47: **Thick slab**
- B:N \geq 0.75: **Thick, thin slab and billet**

13



10

Further work

Transmission electron microscopy
Examine precipitation

- type (e.g. BN, AlN)
- distribution

14

Conclusions

- Maximum strength
 - Influenced by transformation
 - \uparrow by \uparrow in strain rate (10^{-4} to 10^{-3} s⁻¹)
 - Effect of cooling rate not clear



11

APPENDIX I.5

DST/NRF Centre of Excellence in Strong Materials

University of the Witwatersrand, Johannesburg, 14 March 2006



POWERPOINT PRESENTATION SLIDES

**DST/NRF CENTRE OF EXCELLENCE
IN STRONG MATERIALS**

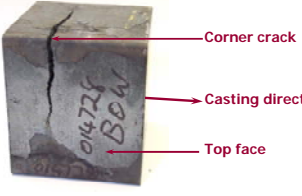


Lesley H. Chown

**Focus Area:
Strong Metallic Alloys**



1

Transverse cracking

5

**Continuous casting of
steels:
Prediction and
prevention of cracking**






2

Steel compositions

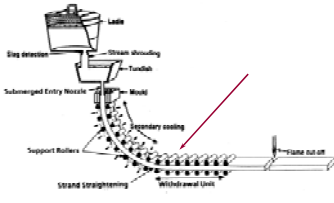


- All low carbon steels:
 - Low S and high S (5 steels)
 - Niobium HSLA (5 steels)
 - Boron + extra-low carbon (3 steels)
 - Boron + high S * (5 steels)

** Successfully implemented in industry (2002)*

6

Problem definition




3

Tensile testing facility (UP)- Instron



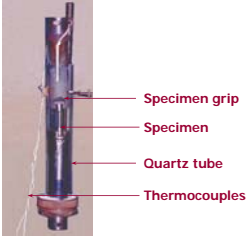




7

4

Hot tensile specimen setup

8

Tensile testing facility- Gleeble

MINTTEK

9

SEM: backscatter images of a brittle sample

Microvoid coalescence

$\dot{\epsilon} = 1 \times 10^{-3} \text{ s}^{-1}$
 $CR = 3.0 \text{ } ^\circ\text{C} \cdot \text{s}^{-1}$
 $T = 900 \text{ } ^\circ\text{C}$
 $R.A = 24\%$

MINTTEK

13

Hot ductility tests

Temperature

Time

melt/1300°C

0.3, 1.2, 3.0°C/s

1175°C

MINTTEK

10

Brittle (intergranular) fracture

MnS

L.H. Chown, A. P. Bentley & F. A. Verdoorn,
 40th MSSA, 2001, vol.31, pg. 25.
 (ANASPEC award-winning presentation).

MINTTEK

14

Hot ductility tests

Strain rate (s^{-1})

Cooling rate ($^\circ\text{C} \cdot \text{s}^{-1}$)

0.0010 TSC TSC
 0.0001 CC CC Billet

0.3 1.2 3.0

MINTTEK

11

X-ray maps of a BN filament capped with Cu-S

300nm

L.H. Chown & A. S. Tuling, ICEN-15, Vol. 2,
 p.p. 767-768, Durban, South Africa. 2002

MINTTEK

15

Hot ductility results

Reduction of Area (%)

Temperature ($^\circ\text{C}$)

Thin slab (fine coating) $CR = 3.0 \text{ } ^\circ\text{C} \cdot \text{s}^{-1}$ $\dot{\epsilon} = 10^{-3} \text{ s}^{-1}$

Thin slab (fine coating) $CR = 1.2 \text{ } ^\circ\text{C} \cdot \text{s}^{-1}$ $\dot{\epsilon} = 10^{-3} \text{ s}^{-1}$

Thin slab (fine coating) $CR = 0.3 \text{ } ^\circ\text{C} \cdot \text{s}^{-1}$ $\dot{\epsilon} = 10^{-3} \text{ s}^{-1}$

Thick slab (fine coating) $CR = 3.0 \text{ } ^\circ\text{C} \cdot \text{s}^{-1}$ $\dot{\epsilon} = 10^{-3} \text{ s}^{-1}$

Thick slab (fine coating) $CR = 1.2 \text{ } ^\circ\text{C} \cdot \text{s}^{-1}$ $\dot{\epsilon} = 10^{-3} \text{ s}^{-1}$

Billet $\dot{\epsilon} = 10^{-3} \text{ s}^{-1}$

Strain rate (s^{-1})

Cooling rate ($^\circ\text{C} \cdot \text{s}^{-1}$)

0.0010 TSC TSC
 0.0001 CC CC Billet

0.3 1.2 3.0

MINTTEK

12

Precipitation: NbC, NbC_{0.87} and NbN

Temperature ($^\circ\text{C}$)

Log[10]C

NbC, NbC_{0.87} and NbN dissolution temperatures

Temperature ($^\circ\text{C}$)

Log[10]C

Legend:
 - NbC (red circles)
 - NbC_{0.87} (black squares)
 - NbN (blue triangles)
 - NbC (red circles)
 - NbC_{0.87} (black squares)
 - NbN (blue triangles)

MINTTEK

16

Progress

- Hot ductility ✓ done
- Continuous casting data ✓ done
- SEM ✓ done
- Hot ductility/precipitation tests ✓ done
- HRSEM/TEM ✓ x some to do
- DTA ✓ done (analysis incomplete)
- Modelling (precipitation/ transformation
 ↑ hot ductility) ✓ x some to do
- Modelling: Thermo-Calc™ ✓ x some to do
- Writing up: ✓ x some to do

MINTTEK

17

Appendix II

Summary of the work done by Lesley Chown and the work done by colleagues and industry

The following summary clarifies the work that was performed by the student, colleagues or industry.

Industrial continuous casting conditions:

Casting conditions, such as casting speed, were obtained by the student from communication with personnel at various slab and billet casting plants. Caster dimensions, such as radius and straightening zone length, were determined by the student from blueprint diagrams of continuous casting machines.

Instron® hot tensile tests:

The student designed the specimen chamber at Iscor R&D in 1995 (shown in Figure 3.6) to minimize oxidation of the hot tensile specimens during testing. The specimen grips were designed by the student and a colleague, Johan van Wyk. The initial reheated tensile tests on the low carbon steels and niobium steels were performed by an operator (Johan van Wyk) at Iscor R&D, but planned and interpreted by the student. As the work was not part of a specific funded project at Iscor after 1997, The student then began doing the tests herself after hours. Most of the boron hot ductility tests were conducted by the student, at Iscor R&D and then later at IMMRI, Pretoria University.

Gleeble® hot tensile tests:

The *in situ* melting tests (boron steels) were performed by the technician in charge of the Gleeble (Francois Verdoorn) at IMMRI, Pretoria University. The tests were planned, programmed into the Gleeble computer, and interpreted by the student.

Thermo-Calc™ modelling:

Initial modelling was done by Prof. L.A. Cornish (supervisor) using Thermo-Calc™ database SSOL2 (Cornish, 1999).

Lesley Chown then modelled the phase transformation and precipitate dissolution temperatures using the updated Thermo-Calc™ database TCFE3 in 2006.

SEM work:

After SEM training by Carel Coetzee, all SEM work related to this thesis was performed by the student herself. Many of the samples were cut, mounted and polished by Thomas Mabena of Iscor Ltd.

TEM work:

TEM work related to this thesis was performed by Alan Bentley and Alison Tuling at IMMRI, Pretoria University.

Interrupted cooling tests (Section 8.10)

These tests were planned by Alan Bentley and performed by Francois Verdoorn. Interpretation of the results was done by Lesley Chown.

Analysis of industrial billet casting data:

This was done by the student after receiving the relevant information (composition, number of cracked billets, etc.) from the specific casting plant.

Database generation:

The database was created entirely by the student. A colleague (Jevon Buirski) created the Visual Basic® macros to enable selection and sorting of the data by various criteria.